24 July 2009 | $10

Science

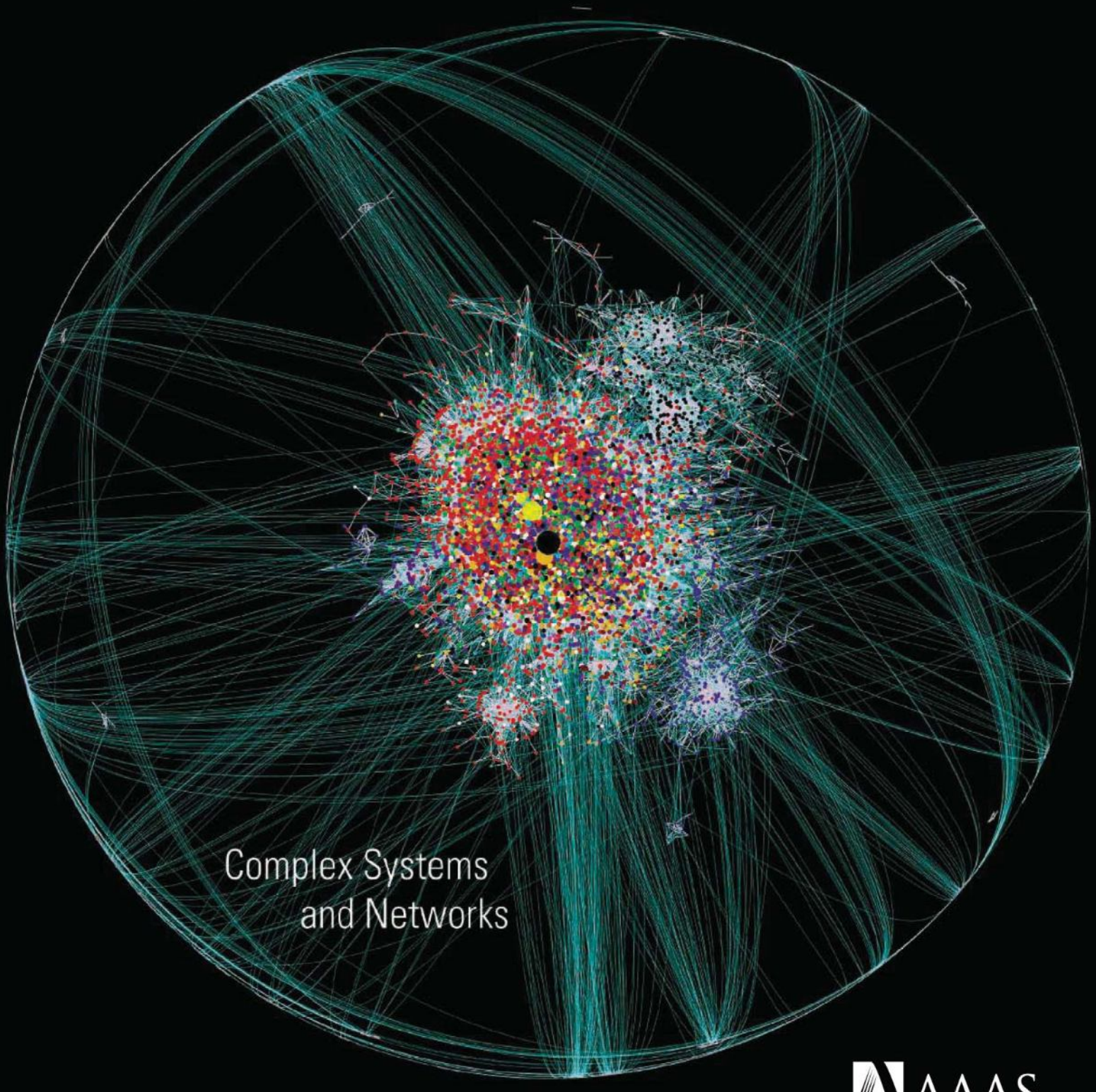

Complex Systems and Networks

AAAS

Gene expression and function analysis sample and assay technologies by QIAGEN

Enjoy first-time success

Rely on QIAGEN's manual and automated workflow solutions for:

- **Sample collection and disruption**
- **RNA stabilization and purification**
- **Real-time PCR and RT-PCR and gene expression assays**
- **RNAi and gene silencing**
- **miRNA purification and assays**
- **Methylation analysis in epigenetics research**
- **Protein sample preparation and assays**

Making improvements in life possible — www.qiagen.com

QIAGEN®

GEPart1030951WW

Sample & Assay Technologies

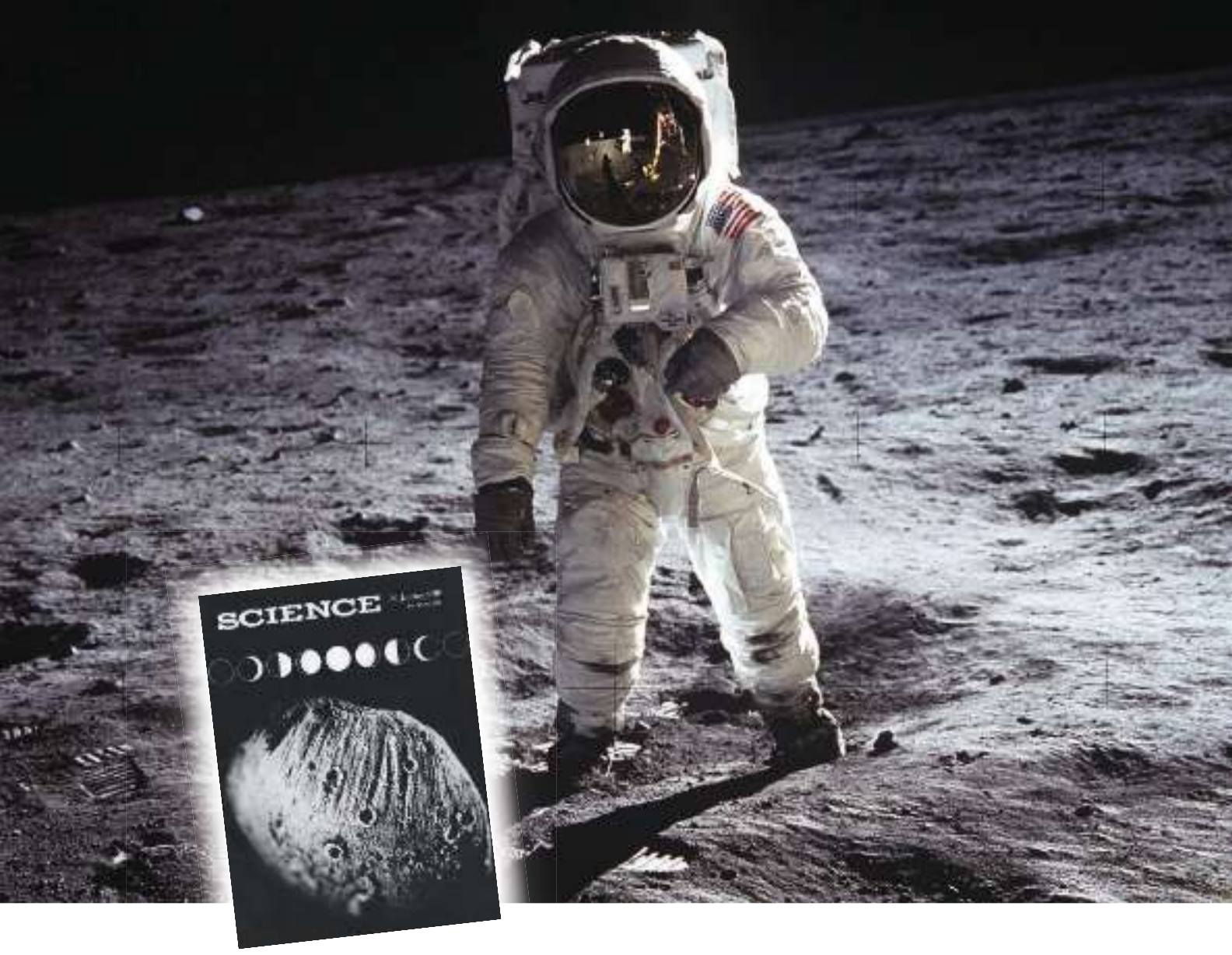

From the *Science* Archives: Apollo 11

On July 20, 1969, Neil Armstrong and Edwin "Buzz" Aldrin achieved one of the most significant scientific breakthroughs of the 20th century by becoming the first men to walk on the moon.

In 1970, *Science* published a special issue devoted to this remarkable achievement, filled with analyses of the lunar samples the astronauts brought home and experiments they conducted on the moon.

In honor of the 40th anniversary of this historic event, *Science* is opening its online archives, *Science* Classic, to make this commemorative issue free with registration.

To get your free access visit *Science* Classic online at:
www.sciencemag.org/apollo11

Science Classic
AAAS

For full access to *Science* Classic, become a AAAS/*Science* member at AAAS.org/join or recommend *Science* Classic to your librarian at http://sciencemag.org/cgi/recommend_subscription

Biacore systems

from inspiration ...to publication

Highest quality, information-rich interaction data from Biacore™ systems deepen your understanding of molecular mechanisms and interaction pathways and enable you to add function to structure.

Select the perfect solution for your application and draw conclusions with confidence – from the company that continues to set the standard for label-free protein interaction analysis.

For further information or register to have one of our scientific experts contact you, please visit **www.gelifesciences.com/biacore-science**

Biacore T100
unmatched performance

Biacore X100
ready to run research system

Biacore Flexchip
array-based comparative profiling

imagination at work

SPECIAL SECTION

Complex Systems and Networks

INTRODUCTION

NEWS

PERSPECTIVES

REVIEW

>> See also related Policy Forum on p. 396, and http://www.sciencemag.org/complexity/ for additional material from Science Signaling *and* Science *Careers*

CELEBRATE THE 40TH ANNIVERSARY OF THE APOLLO 11 MOON LANDING

The scientific results of that mission and samples returned from the Moon, published in our 20 January 1970 issue, are now freely available with registration at www.sciencemag.org/apollo11.

EDITORIAL

NEWS OF THE WEEK

NEWS FOCUS

LETTERS

CONTENTS continued >>

COVER

A computer-generated map showing relationships between Internet blogs (colored spots), where lines represent links between individual blogs. In this map, blogs within the inner core cover technical topics and gadgetry, and blogs in the outer sphere involve nontechnical discussions and link back to the technical ones. See the special section on complex systems and networks beginning on page 405.

Image: Matthew Hurst

DEPARTMENTS

Rats

the Gene Knockout You Always Wanted

ADD. DELETE. SWAP.

EDIT FOR THE BETTER.

The next scientific breakthrough is here, and it's a knockout!

CompoZr™ ZFN technology, a breakthrough that enables simple and efficient genomic editing–exclusively from Sigma Life Science. Zinc Finger Nuclease (ZFN) technology allows easy creation of novel cell lines and model organisms with precise and heritable gene additions, deletions or modifications. With direct embryo injection of ZFNs, embryonic stem cell limitations are no longer a barrier to your knockout animal research. ***Now it's all possible.***

SIGMA® Life Science

The future of genomic research is at your fingertips.
Discover the ZFN technology at ***compozrzfn.com***

BOOKS *ET AL.*

POLICY FORUM

PERSPECTIVES

BREVIA

RESEARCH ARTICLES

REPORTS

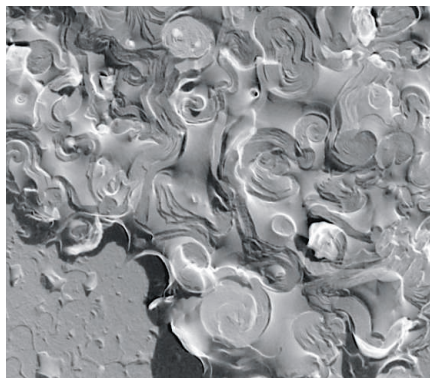

pages 402 & 456

page 464

CONTENTS continued >>

Published by AAAS

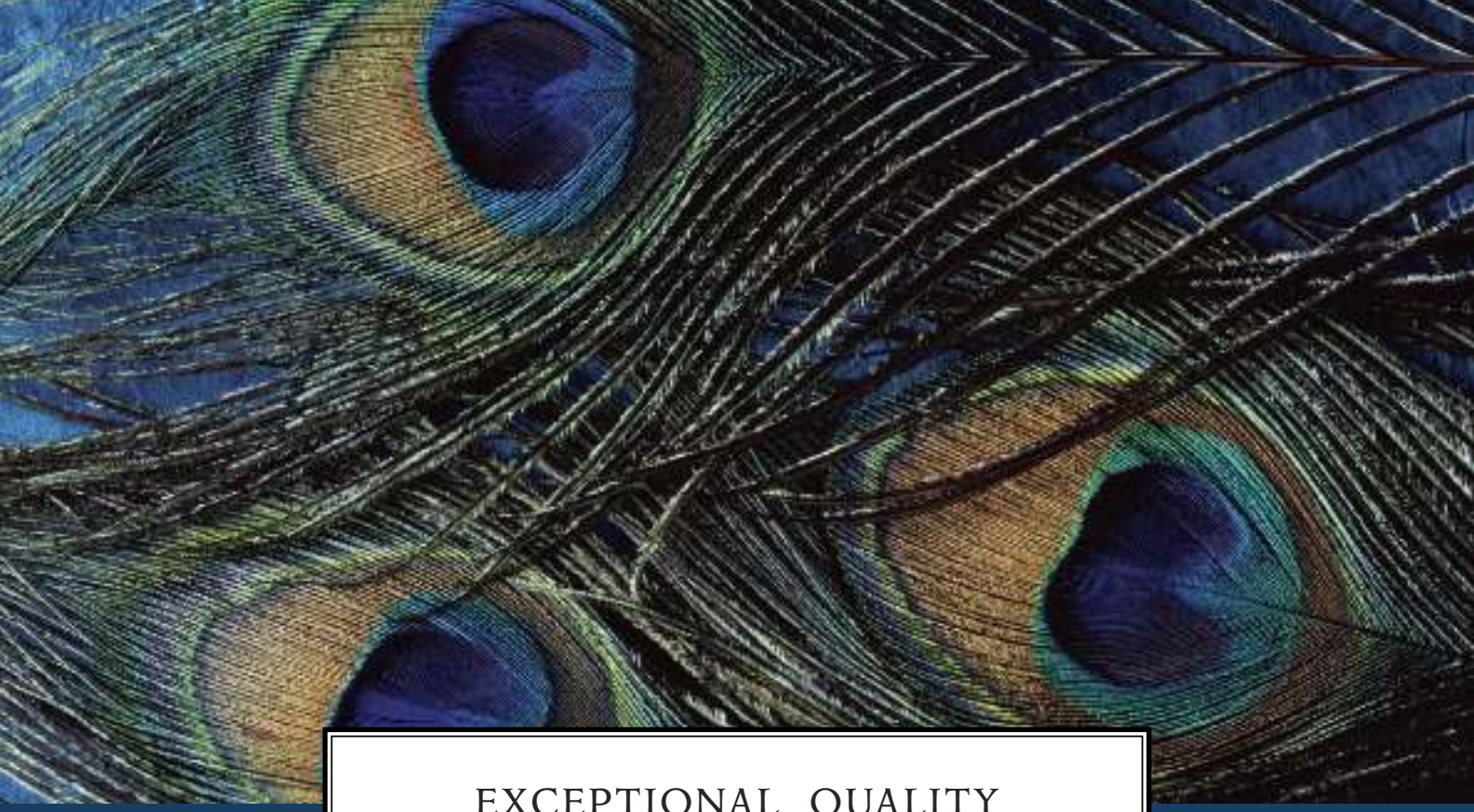

EXCEPTIONAL QUALITY

Restriction Enzymes from New England Biolabs

With 35 years of experience in enzyme technology, New England Biolabs leads the industry in quality, selection and innovation for restriction enzymes. Our expertise in purification coupled with a reliance on recombinant technology results in highly pure enzymes suitable for even the most sensitive applications. Additionally, stringent quality controls ensure that our enzymes deliver optimal performance. For quality you can count on, make NEB restriction enzymes your first choice.

Power and purity of NEB Restriction Enzymes

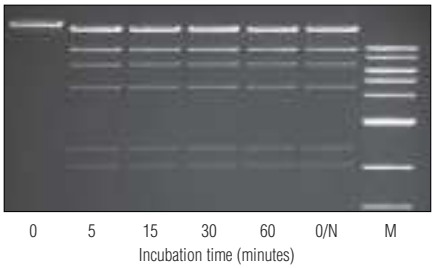

Recombinant HindIII is powerful enough to digest 1 µg of DNA in 5 minutes, but can also be used in overnight digests with no indication of nuclease contamination. Marker (M) is the 1 kb DNA Ladder (NEB #N3232).

RR *Choose recombinant enzymes for a higher quality product with lot-to-lot consistency*

Advantages:

- **Selection** – More specificities than any other supplier
- **Convenience** – Optimal activity for over 160 enzymes in a single buffer NEB 4
- **Quality** – State-of-the-art production and stringent QCs
- **Innovation** – HF enzymes engineered for reduced star activity
- **Performance** – Guaranteed

NEW ENGLAND BioLabs® Inc.
enabling technologies in the life sciences

CLONING & MAPPING	DNA AMPLIFICATION & PCR	RNA ANALYSIS	PROTEIN EXPRESSION & ANALYSIS	GENE EXPRESSION & CELLULAR ANALYSIS

www.neb.com

SCIENCEONLINE

SCIENCEXPRESS
www.sciencexpress.org

Coupling Mechanics to Charge Transport in Carbon Nanotube Mechanical Resonators
B. Lassagne et al.
10.1126/science.1174290

Strong Coupling Between Single-Electron Tunneling and Nanomechanical Motion
G. A. Steele et al.
Individual electrons tunneling onto and out of a carbon nanotube can be used to tune its oscillatory motion.
10.1126/science.1176076

Motile Cilia of Human Airway Epithelia Are Chemosensory
A. S. Shah et al.
Airway epithelia directly sense and respond to noxious substances.
10.1126/science.1173869

SDH5, a Gene Required for Flavination of Succinate Dehydrogenase, Is Mutated in Paraganglioma
H.-X. Hao et al.
Analysis of a yeast mitochondrial protein reveals a human tumor susceptibility gene.
10.1126/science.1175689

Bcl6 Mediates the Development of T Follicular Helper Cells
R. I. Nurieva et al.
A transcription factor controls follicular T helper cell differentiation.
10.1126/science.1176676

SCIENCENOW
www.sciencenow.org
Highlights From Our Daily News Coverage

How a Raindrop Is Like an Exploding Parachute
High-speed videos reveal secret to raindrop size.

No Risk in Disclosing Genetic Risks
Researchers find that patients suffer no adverse mental effects after hearing bad news.

Elephants Don't Always Keep It in the Family
When decimated by humans, elephants turn to friends to beef up their numbers.

SCIENCESIGNALING
www.sciencesignaling.org
The Signal Transduction Knowledge Environment

RESEARCH ARTICLE: SIK1 Couples LKB1 to p53-Dependent Anoikis and Suppresses Metastasis
H. Cheng et al.
Loss of SIK1 suppresses cell death resulting from loss of cell anchorage and promotes metastasis in the absence of primary tumors.

RESEARCH ARTICLE: Intracellular Delivery of a Cell-Penetrating SOCS1 That Targets IFN-γ Signaling
A. DiGiandomenico et al.
The proinflammatory responses of cells to interferon-γ can be suppressed by a cell-penetrating, inhibitory protein.

EDITORIAL GUIDE: Signals to Neurodegeneration
W. Wong
Investigation of signaling pathways that are perturbed in neurodegenerative diseases may improve treatment options.

RESEARCH ARTICLE: Inhibition of mTOR Signaling in Parkinson's Disease Prevents L-DOPA–Induced Dyskinesia
E. Santini et al.

PERSPECTIVE: Thwarting Dyskinesia by Targeting mTORC1
E. Klann
Blocking mTORC1 activity may decrease the unwanted involuntary movements associated with L-DOPA treatment.

PERSPECTIVE: Functional Amyloids Signal Their Arrival
M. P. Badtke et al.
Several peptide and protein hormones are stored in an amyloid configuration in secretory granules.

PODCAST
W. Wong and A. M. VanHook
A small G protein may limit the toxicity of mutant huntingtin to the brain.

SCIENCECAREERS
www.sciencecareers.org/career_magazine
Free Career Resources for Scientists

Math Education Researchers in Demand
C. Wald
In 2007, 40 percent of faculty positions in mathematics education went unfilled.

Tangled Webs: Careers in Network Science
S. Carpenter
The booming science of networks reveals hidden connections in just about everything.
>> Complex Systems and Networks section p. 405

Funding News
GrantsNet Staff
The Funding News, published weekly, provides the latest sources of research and education grants.

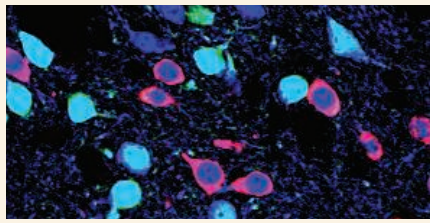

SCIENCESIGNALING
Neurons from Parkinsonian mice.

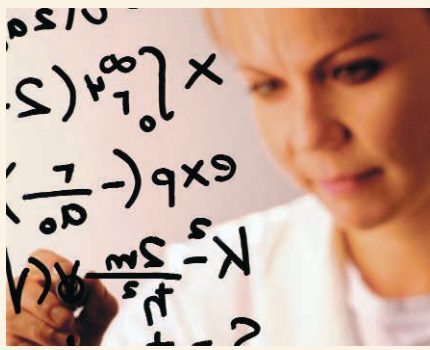

SCIENCECAREERS
Researchers studying math education.

SCIENCEPODCAST
www.sciencemag.org/multimedia/podcast
Free Weekly Show
Download the 24 *Science* Podcast to hear about how clouds impact climate, research on complex socioeconomic systems, policing nuclear testing, and more.

ORIGINSBLOG
blogs.sciencemag.org/origins
A History of Beginnings

SCIENCEINSIDER
blogs.sciencemag.org/scienceinsider
Science Policy News and Analysis

SCIENCE (ISSN 0036-8075) is published weekly on Friday, except the last week in December, by the American Association for the Advancement of Science, 1200 New York Avenue, NW, Washington, DC 20005. Periodicals Mail postage (publication No. 484460) paid at Washington, DC, and additional mailing offices. The title SCIENCE is a registered trademark of the AAAS. Domestic individual membership and subscription (51 issues): $146 ($74 allocated to subscription). Domestic institutional subscription (51 issues): $835; Foreign postage extra: Mexico, Caribbean (surface mail) $55; other countries (air assist delivery) $85. First class, airmail, student, and emeritus rates on request. Canadian rates with GST available upon request, GST #1254 88122. Publications Mail Agreement Number 1069624. **Printed in the U.S.A.**

Change of address: Allow 4 weeks, giving old and new addresses and 8-digit account number. **Postmaster:** Send change of address to AAAS, P.O. Box 96178, Washington, DC 20090–6178. **Single-copy sales:** $10.00 current issue, $15.00 back issue prepaid includes surface postage; bulk rates on request. **Authorization to photocopy** material for internal or personal use under circumstances not falling within the fair use provisions of the Copyright Act is granted by AAAS to libraries and other users registered with the Copyright Clearance Center (CCC) Transactional Reporting Service, provided that $20.00 per article is paid directly to CCC, 222 Rosewood Drive, Danvers, MA 01923. The identification code for *Science* is 0036-8075. *Science* is indexed in the *Reader's Guide to Periodical Literature* and in several specialized indexes.

AAAS
ADVANCING SCIENCE, SERVING SOCIETY

CREDITS: (*SCIENCE SIGNALING*) EMMANUEL VALJENT/KAROLINSKA INSTITUTE; (*SCIENCE CAREERS*) PHOTODISC

EDITED BY STELLA HURTLEY

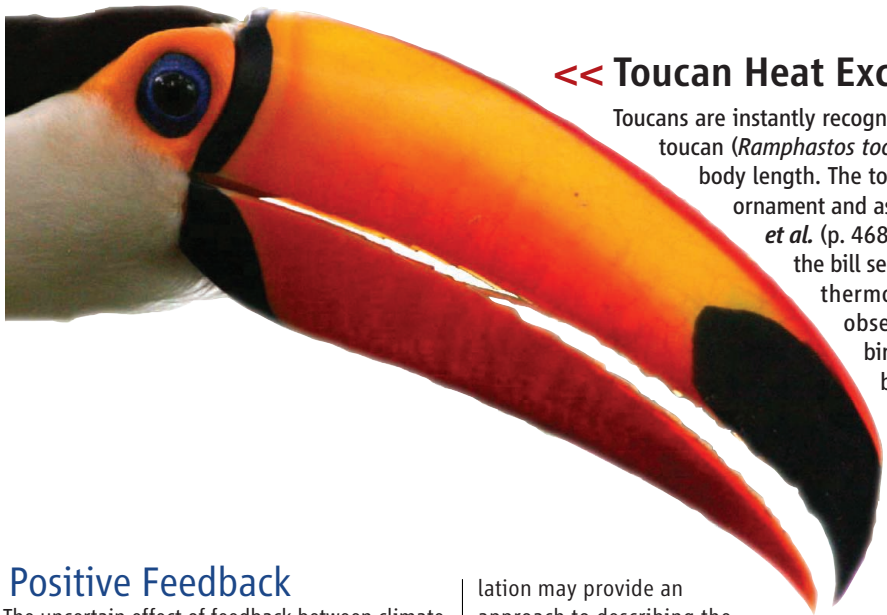

<< Toucan Heat Exchanger

Toucans are instantly recognizable by their large bills, which in the toco toucan (*Ramphastos toco*) accounts for about one-third of the total body length. The toucan's bill has been interpreted as a sexual ornament and as an adaptation for handling fruit. **Tattersall *et al.*** (p. 468) explore an alternative explanation in which the bill serves primarily as a thermoregulator. Infrared thermography techniques, which allow detailed observations with minimal disturbance to the birds, show that the birds alter blood flow to the bill according to ambient conditions, effectively using it as a radiator to "dump heat."

Positive Feedback

The uncertain effect of feedback between climate and clouds is one of the largest obstacles to producing more confident projections of global climate. **Clement *et al.*** (p. 460) examined how clouds, sea surface temperature, and large-scale atmospheric circulation vary in the Northeast Pacific region. Change in cloud coverage was the primary cause of sea surface temperature variations, and clouds provided a positive feedback to temperature variations. Furthermore, regional atmospheric circulation patterns were linked to patterns of cloudiness. One model produced realistic covariability between cloud cover, sea surface temperatures, and atmospheric circulation for the 20th century.

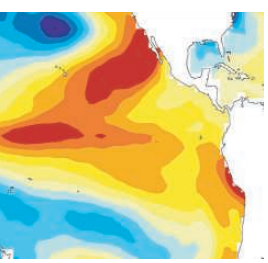

String Theory and Condensed Matter

The complex interactions involving highly correlated electron systems can give rise to "exotic behavior" in electronic systems, such as quantum criticality and superconductivity. The usual theoretical tools, however, are limited when describing these states. String theory is a highly mathematical approach initially developed to describe gravity and high-energy particle physics. Certain aspects of string theory may be relevant to describe condensed matter systems. **Čubrović *et al.*** (p. 439; published online 25 June) take one such approach, and show that the characteristic properties of a Fermi liquid can emerge from string theory. The formulation may provide an approach to describing the exotic states of matter that arise in condensed matter systems.

Threonine Required

Embryonic stem (ES) cells divide rapidly, raising the possibility that they might exist in a metabolic state that facilitates rapid growth. By monitoring the abundance of common metabolites in mouse ES cells, **Wang *et al.*** (p. 435; published online 9 July) found altered levels of metabolites involved in carbon metabolism. Measurement of messenger RNA levels revealed unusually high expression of the gene encoding threonine dehydrogenase. In addition, in growth experiments, mouse ES cells were critically dependent on the amino acid threonine.

Black Hole Energy Boost

More than 20 galaxies are known to emit photons with energies a trillion times higher than those of visible light, but it is not known where this emission originates. These galaxies are part of a class of active galactic nuclei believed to harbor supermassive black holes in their centers from which relativistic plasma jets emerge, reaching out many thousands of light years into the intergalactic medium. **Acciari *et al.*** (p. 444, published online 2 July; see the Perspective by **Begelman**) present simultaneous radio and very-high-energy γ-ray observations of the nearby active galaxy Messier 87, revealing very-high-energy flaring activity accompanied by a radio flare originating from the core of the galaxy. The findings imply that the highest energy emission from active galaxies has its origin in the immediate vicinity of the black hole.

Bright Shiny Beetles

The beautiful iridescent colors found on the wings of butterflies and on the bodies of beetles have attracted the attention of brilliant minds over the past centuries, starting with Newton, who understood that these colors must involve ''thin film structures." In 1911 Michelson described the metallic appearance of these beetles, and in the late 1960s Neville and Caveney discussed the optical properties in the context of cholesteric liquid crystals. **Sharma *et al.*** (p. 449; see the Perspective by **Vukusic**) examined the metallic green beetle *Chrysina gloriosa*, which selectively reflects left circularly polarized light when illuminated with unpolarized light. The underlying cellular structure of the beetle exoskeleton is organized primarily in a hexagonal pattern, with variations in the pentagonal and heptagonal arrangements depending on the local curvature. Thus, the ordering of the cells in concentric, nested arcs is indeed analogous to the ordering of the molecules in a cholesteric (or chiral nematic) liquid crystal.

Packing Bananas and Boomerangs

Assembling achiral molecules typically generates achiral domains. However, odd things can happen when the molecules are banana- or boomerang-shaped—their cores can twist out of plain to form left- or right-handed helices, which can then pack into chiral domains that will polarize light (see the Perspective by **Amabilino**). **Hough *et al.*** (p. 452) show that if you make the situation even more complex by frustrating the packing of adjacent layers, you can create a material that appears to be macroscopically isotropic with only very local positional and

CREDITS (TOP TO BOTTOM): THIAGO FILADELPHO; CLEMENT *ET AL.*

Published by AAAS

orientational ordering of the molecules but still shows an overall chirality. In a second paper, **Hough *et al.*** (p. 456) also show that if you change the chemistry of the molecules to allow for better overall packing, you can create a situation where helical filaments form that also tend to pack in layered structures. However, the frustration between the two types of packing leads to macroscopically chiral and mesoporous structures.

Little Lambs

In changing environments, ecological and evolutionary dynamics are intimately intertwined. However, understanding the dynamics of phenotypic traits under natural conditions is still rudimentary. **Ozgul *et al.*** (p. 464; published online 2 July) dissected the dynamics of a phenotypic trait in the context of the contributing ecological and evolutionary processes. In a wild population of Soay sheep where mean body size has fluctuated substantially over the past 25 years and has, on average, gotten smaller, an ecological response to environmental variation is the major driver of the dynamics; evolutionary change has contributed relatively little: The sheep have become smaller because climate change has modified the way that density-dependence influences lamb growth rates.

"Swine Flu" Pathology

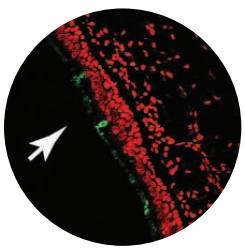

The clinical spectrum of disease caused by the swine-origin 2009 A(H1N1) influenza virus and its transmissibility are not completely understood. **Munster *et al.*** (p. 481; published online 2 July) and **Maines *et al.*** (p. 484; published online 2 July) used ferrets, an established model for human influenza, to evaluate the pathogenesis and transmissibility of a selection of 2009 A(H1N1) virus isolates compared with representative seasonal H1N1 viruses. The results help explain the atypical symptoms seen so far, including the gastrointestinal distress and vomiting observed in many patients. Although results were variable, it seems that the 2009 A(H1N1) virus may be less efficiently transmitted by respiratory droplets in comparison to the highly transmissible seasonal H1N1 virus, suggesting that additional virus adaptation in mammals may be required before we see phenotypes observed in earlier pandemics.

Making Connections

Endoplasmic reticulum (ER)–mitochondria connections have been implicated in many physiological processes, including calcium homeostasis, signaling, membrane biogenesis, and apoptosis. **Kornmann *et al.*** (p. 477, published online 25 June; see the Perspective by **Wiedemann *et al.***) looked for a proteinaceous link between the ER and mitochondria and, using combinations of synthetic biology and classical yeast genetics, found a protein complex that tethers the two organelles. A large-scale genetic interaction map suggests that these ER-mitochondria connections are important for interorganellar phospholipid exchange.

All Together Now (Sometimes)

Motile cilia and flagella protrude from the surface of many eukaryotic cells. Understanding how cilia and flagella operate is important for understanding ciliated cells in metazoans, the ecology and behavior of motile microorganisms, and the mechanisms of molecular motors and signal transduction. Using very-high-speed video microscopy, **Polin *et al.*** (p. 487; see the Perspective by **Stocker and Durham**) discovered that the biflagellated cells of the single-cell alga *Chlamydomonas rheinhartii* switch between synchronous beating, which keeps the cells traveling forward, and asynchronous beating, which allows the organisms to make sharp turns. This random progression occurs in the dark and allows cells to diffuse, and it may underpin directional movement toward light in the same way that the run-and-tumble behavior of prokaryotes allows them to move up chemical gradients.

Keeping Calm

Benzodiazepines are the most prescribed anxiolytics and are used by a broad population. However, benzodiazepines can cause unwanted side effects, including sedation, development of tolerance, and withdrawal symptoms after long-term administration. **Rupprecht *et al.*** (p. 490; published online 18 June) now find that a translocator protein (18-kD) ligand, XBD173, is a fast-acting anxiolytic agent, both in animals and humans, which lacks the unwanted side effects of benzodiazepines and provides a promising target for novel clinically effective anxiolytic drugs.

CREDIT: MAINES *ET AL.*

Published by AAAS

Research Data in the Digital Age

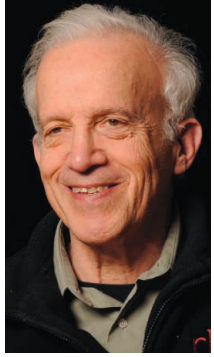

Daniel Kleppner is the Lester Wolfe Professor of Physics, Emeritus, at the Massachusetts Institute of Technology, Cambridge, MA.

Phillip A. Sharp is Institute Professor at the Massachusetts Institute of Technology, Cambridge, MA.

THIS WEEK, THE U.S. NATIONAL ACADEMIES RELEASED AN OVERVIEW REPORT* ON THE CHALLENGES of maintaining the integrity of scientific research data in an age of revolutionary digital technologies. The report, *Ensuring the Integrity, Accessibility, and Stewardship of Research Data in the Digital Age*, provides a framework for dealing with the challenges to the community generated by the onrush of digital technology. As chairs of the report committee, we hope that it moves the research community forward, collectively, to consider the integrity of data in ways that best support the advancement of scientific, engineering, and medical knowledge, as well as the maintenance of public trust.

In 2007, Ralph Cicerone, president of the U.S. National Academy of Sciences, received letters from the editors of several journals† expressing concern about the manipulation of digital images in scientific manuscripts. It soon became apparent that this was but one of many issues related to the treatment of data with the advent of digital technologies. As a result, the National Academies appointed a committee of scientists to examine their impact on acquiring, sharing, and storing data across scientific disciplines.

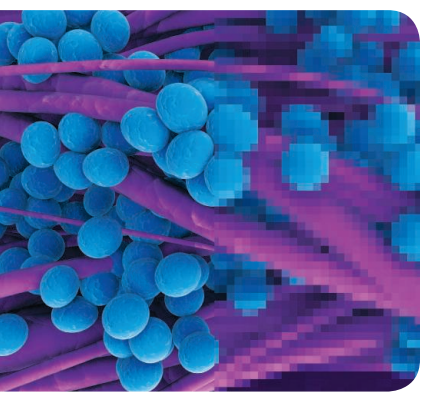

Digital technologies have transformed every facet of research, from the questions asked and the methods used, to the ways in which researchers interact. In the face of this transformation, researchers must take the lead in maintaining the integrity of data that lies at the heart of science. The guiding principle continues to be that researchers are responsible for their findings, and peer review remains the gold standard for evaluating the quality of research.

Digital technologies have raised many concerns about the methods traditionally used to ensure the integrity and utility of data. Because each research field has its own conventions and procedures for acquiring, analyzing, and disseminating data, it is not possible to provide specific recommendations that apply across disciplines. Nevertheless, the committee has identified several broad principles that extend across all fields of research, thus providing a framework for moving forward.

Standards for ensuring the integrity of digital research data must be developed and enforced by researchers, research institutions, funding agencies, professional societies, and journals. The report lays out broad principles for producing such standards, including such issues as the legal requirements for maintaining records, copyright, and ownership. It is also essential that researchers, educators, and students receive appropriate training in the proper management of research data. The report provides guidance for developing such programs. Research data and other information integral to publicly reported results should be publicly accessible. Although legitimate reasons may exist for keeping some data private or delaying their release, the default assumption must be that research data and the information needed to interpret them will be publicly accessible in a timely manner to allow verification of findings and facilitate future discoveries.

The questions of who is responsible for storing research data and who pays for maintaining the archive are urgent. The value of the huge quantities of data generated by digital technologies to contemporary and future research requires not only preserving and sharing the data, but also documenting the instruments and procedures used to generate it. Such tasks are time-consuming and costly, and there is no consensus on how to tackle these issues. However, researchers need to work with their institutions, funding agencies, and professional societies to formulate and implement data management plans. The National Academies' Board on Research Data and Information will address this agenda at an upcoming meeting in September.

Many of the issues raised by the report apply to all efforts to derive new knowledge in science as technologies evolve, and the very process of modifying the practices and daily activities of researchers provides a valuable opportunity to reinforce and extend the traditional openness and collaborative spirit of science.

– Daniel Kleppner and Phillip A. Sharp

10.1126/science.1178927

*www.nap.edu/catalog.php?record_id=12615 †The study was supported in part by the American Association for the Advancement of Science, the publisher of *Science*.

CREDITS: (LEFT) JUPITERIMAGES; (TOP RIGHT) GREG HREN; (BOTTOM RIGHT) PHILLIP SHARP

ATMOSPHERIC SCIENCE

An Eye for Ammonia

Ammonia is a trace gas of considerable importance for atmospheric chemistry, aerosol particle formation, and fertilization of the biosphere. Its global emissions have grown to more than twice their preindustrial values, mainly as a consequence of expanded agriculture and associated use of fertilizers. Yet large uncertainties in emissions budgets, due to the lack of adequate observational data, have hindered a confident assessment of the strengths of ammonia sources geographically. Clarisse *et al.* present infrared spectra obtained by satellite to map global atmospheric ammonia concentrations in 2008. They find that there is good qualitative agreement between these data and modeled values, but that large quantitative discrepancies exist, especially in regions above 30°N latitude. Additionally, they find a number of emission hot spots, all in the Northern Hemisphere, leading them to suggest that Northern Hemispheric ammonia emissions have been underestimated. These data, and this technique, should enhance our broader understanding of the global nitrogen cycle. — HJS

Nat. Geosci. **2**, 479 (2009).

SYSTEMS BIOLOGY

Figuring Out What to Aim At

A pervasive problem in identifying promising drug targets is that it can be difficult to ascertain which component of a complicated signaling network should be perturbed in order to produce the desired alteration of the system readout. Schoeberl *et al.* show the feasibility of a systems-level analysis for this purpose. Cancer is a known consequence of excessive signaling through the ErbB receptor tyrosine kinase family, which includes four related receptors and a dozen or so ligands (such as epidermal growth factor or EGF) that can act in various combinations. Their computational model suggested that binding to the ErbB3 receptor (which itself is mute with respect to kinase activity) with an affinity in the low nanomolar range in addition to disrupting binding by the ligand HRG1-β and signaling in response to the ligand betacellulin would be key. MM-121 is a monoclonal antibody with these in vitro attributes, and it also inhibited tumor xenografts in mice. — LBR

Sci. Signal. **2**, ra31 (2009).

CHEMISTRY

Fate of Fluoropolymers

The synthetic materials we rely on in everyday life are typically required to pass a series of laboratory tests before they can be used in consumer products. Outside the controlled environment of the lab, however, some approved compounds may degrade into potentially harmful byproducts. Washington *et al.* explored the capacity of a fluorotelomer polymer, similar to those commonly used in stain-resistant clothing and firefighting foam, to degrade into potentially toxic perfluorooctanoic acid when added to soil columns. In general, such studies face substantial challenges in unraveling the complex chemical and microbial pathways at play in real soil (often first-generation byproducts must be inferred from observation of their own induced byproducts). Moreover, analysis of this specific type of degradation is hampered by the tendency of the byproduct to cling to the parent polymer and so elude sampling. The authors therefore developed a multistep extraction protocol involving the successive use of several different solvents. Their experiments yielded a degradation half-life on the order of 1000 years, consistent with prior studies; however, modeling of the data suggested great sensitivity of the kinetics to exposed surface area, potentially raising the degradation rate by two orders of magnitude for commercial polymers more finely grained than the authors' test samples. The exact degradation pathway remains unknown but could involve local microorganisms. — NW

Environ. Sci. Technol. **43**, 10.1021/es9002668 (2009).

IMMUNOLOGY

No Accessories Needed

In response to infection, $CD4^+$ T cells differentiate into distinct effector subsets, which include T helper type 1 (T_H1), T_H2, T_H17, and regulatory T cells. How do naïve T cells choose? The cells that present major histocompatibility complex (MHC) class II–bound antigens to T cells also deliver cues in the form of secreted cytokines that initiate lineage-specific differentiation programs. It has long been thought that dendritic cells are the bearers of this information, yet previous studies had found a limited activation of dendritic cells in response to T_H2-inducing antigens and a lack of interleukin-4, which is the cytokine critical for directing T_H2 cell differentiation.

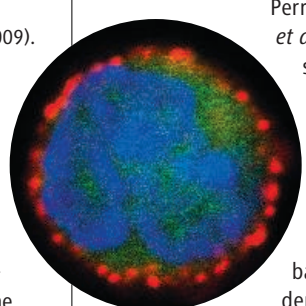

Basophil (blue) expressing interleukin-4 (green) and MHC II (red).

Perrigoue *et al.*, Yoshimoto *et al.*, and Sokol *et al.* show that for T_H2 $CD4^+$ T cells—which mediate responses to parasitic helminths, protease allergens, and allergy-inducing immune complexes—basophils, rather than dendritic cells, are the antigen-presenting cells that initiate T_H2 cell responses in mice. These studies push basophils into the limelight and will potentially lead to further understanding of allergic reactions. — KLM

Nat. Immunol. **10**, 697; 706; 713 (2009).

CREDITS (TOP TO BOTTOM): JUPITERIMAGES; PERRIGOUE AND YOSHIMOTO

WHAT'S Next™

Introducing Stemedia™. Culture Stem Cells

Stemedia™. Rationally Designed. Affordable.

Healthy cell cultures are the bedrock of biological research. And Stemgent knows that the hardest cells to maintain properly are stem cells. Your ability to keep your stem cells healthy, in an efficient and affordable manner, requires media that are consistent, reliable, and completely free of contaminants. That's why we've introduced a new line of Stemedia™: the Stemgent way to culture stem cells.

- ❑ **Designed from the ground up with components chosen for stem cell utility.**
- ❑ **Support long-term culture of stem cells.**
- ❑ **Enhance every step in cell culture.**

MORE www.stemgent.com/ns2

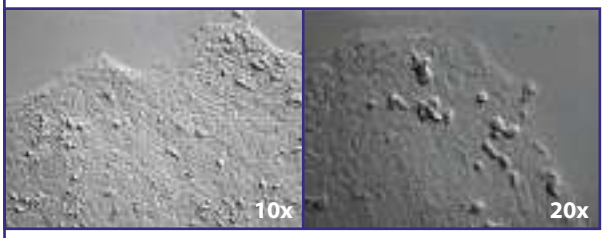

Morphology hESC (H1) morphology at passage 5 in NutriStem™

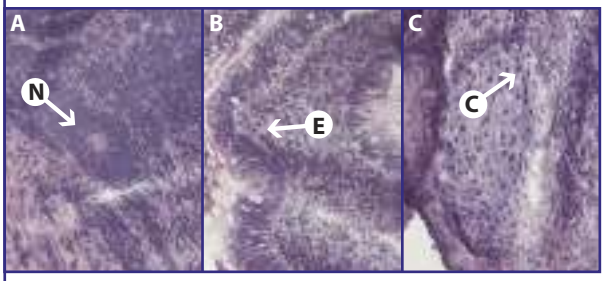

Teratoma Formation hESCs (H1) cultured with NutriStem™ for 14 passages were injected subcutaneously into SCID mice. Teratomas were harvested after 8 weeks and processed for histological analysis. Tissue types from all three germ layers could be identified in the sections (A–C). (A) ectoderm with neural rosette (arrow marked N); (B) endoderm with columnar epithelium (arrow marked E); (C) mesoderm with cartilage (arrow marked C).

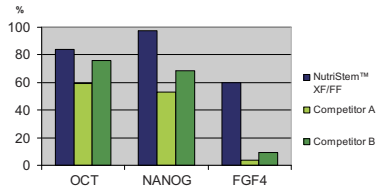

Q-PCR
Q-PCR levels of gene expression %GAPDH Passage 2, Matrigel™

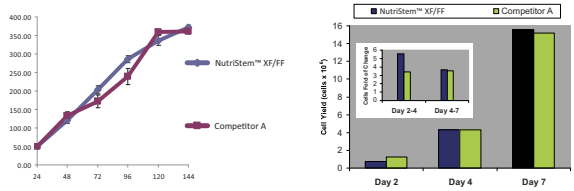

Proliferation I. hESCs (H1, passage 6) were seeded in 96-well plates (Matrigel™ coated) in the different media. Media were changed every 24 hours. The number of cells was determined using CyQuant™ cell proliferation assay kit. II. Evaluation of NutriStem™ hESCs (H9.2) using Matrigel™ as a matrix. Growth promotion for hESCs cultured in NutriStem™ versus competitor A. Cell counts are reported for days 2, 4, and 7.

The First Stemedia Product Available Now: NutriStem™ XF/FF Culture Medium

The first medium in the line, NutriStem™ XF/FF Culture Medium, is the only xeno-free human embryonic stem cell culture medium on the market.

- ❑ **A proprietary, animal component-free, serum-free medium formulation eliminates risk of animal virus contamination.**
- ❑ **Low bFGF-formulation reduces cost and allows you to better control your cell culture system.**
- ❑ **NutriStem™ XF/FF Medium is a complete, ready-to-use formulation (containing Alanyl-glutamine).**
- ❑ **Supports expansion of hES cells in feeder-free culture conditions (on Matrigel™) or on feeder layers (human foreskin fibroblasts, MEFs).**

MORE www.stemgent.com/ns4

MORE www.stemgent.com/xxx

Get to the precise information you need faster. When you see one of these link bars, go to Stemgent.com and add the /xxxx extension. It's a direct link to the info you're looking for.

With New Media From Stemgent.

Stemgent Raises the Bar For Human Embryonic Stem Cell Media.

Stemgent is committed to producing a complete system of cell culture products, including media, substrates, cytokines, and enzymes.
Our scientific advisory board represents a unique association of some of the most accomplished minds in stem cell science. Our work is not only inspired by our board, but everything we produce must maintain their high standards through every step of production, delivery, and support.

- ❑ **All Stemedia are rigorously tested by Stemgent and at board members' labs.**
- ❑ **Batch to batch consistency reduces unnecessary variables in your culture.**
- ❑ **Better performance and lower cost mean a more efficient laboratory for you.**

MORE www.stemgent.com/ns6

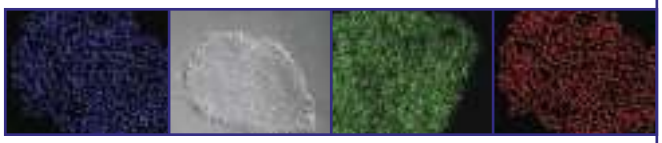

DAPI Phase SSEA4 OCT4

Immunostaining hESCs (H1) show expected morphology and immuno- fluorescence staining of pluripotency markers

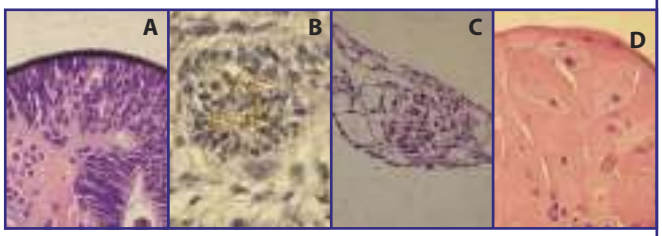

Embryoid Body Formation hESCs (H9.2) were cultured with NutriStem™ using Matrigel™ matrix for 16 passages and tested in vitro for pluripotency by EB formation. After being transferred to suspension culture using serum-supplemented medium, the cells spontaneously formed EBs containing cells representing embryonic germ layers. Histological sections of 14-day old EBs showed the following cell types: (A) neural rosette (ectoderm), (B) neural rosette stained with anti-tubulin, (C) primitive blood vessels (mesoderm) and (D) megakaryocytes (mesoderm). H&E stain.

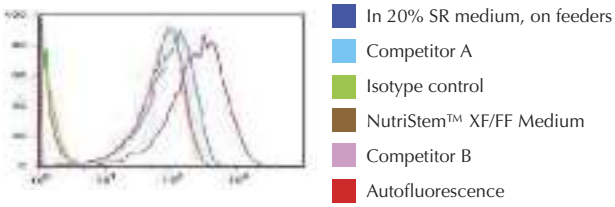

SSEA4 expression: hESCs (H1) were cultured in different media for 6 passages.

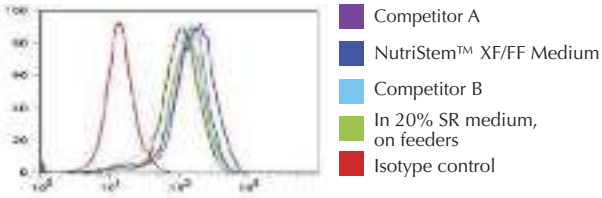

OCT4 expression: hESCs (H1) were cultured in different media for 6 passages.

Gene Expression Analysis by Flow Cytometry

Our Mission.

Our purpose is to move stem cell science forward. To that end, two things are required. First we need to work with the world class scientists responsible for the breakthroughs that make stem cell research possible in the first place. Second, we need to make that science available in a virtually failsafe way, so that your work benefits from their work. That means that our product offerings are proven.They work.They do what we say they will do. After all, we're not doing experiments, you are.

Come to www.stemgent.com/sci13 for more information. Or call 877-228-9783 (toll-free) or +1-617-245-0098 (international).

STEMGENT™

REPROGRAMMING THE REAGENT™

BOSTON | www.stemgent.com/sci13 | SAN DIEGO

Developed and manufactured by Biological Industries

Co-developed in collaboration with the Technion R&D Foundation

www.sciencemag.org

Science

1200 New York Avenue, NW
Washington, DC 20005
Editorial: 202-326-6550, FAX 202-289-7562
News: 202-326-6581, FAX 202-371-9227
Bateman House, 82-88 Hills Road
Cambridge, UK CB2 1LQ
+44 (0) 1223 326500, FAX +44 (0) 1223 326501

Subscription Services For change of address, missing issues, new orders and renewals, and payment questions: 866-434-AAAS (2227) or 202-326-6417, FAX 202-842-1065. Mailing addresses: AAAS, P.O. Box 96178, Washington, DC 20090-6178 or AAAS Member Services, 1200 New York Avenue, NW, Washington, DC 20005

Institutional Site Licenses please call 202-326-6755 for any questions or information

Reprints: Author Inquiries 800-635-7181
Commercial Inquiries 803-359-4578

Permissions 202-326-7074, FAX 202-682-0816

Member Benefits AAAS/Barnes&Noble.com bookstore www.aaas.org/bn; AAAS Online Store www.apisource.com/aaas/ code MKB6; AAAS Travels: Betchart Expeditions 800-252-4910; Apple Store www.wapple/eppstore/aaas; Bank of America MasterCard 1-800-833-6262 priority code FAA3YU; Cold Spring Harbor Laboratory Press Publications www.cshlpress.com/affiliates/aaas.htm; GEICO Auto Insurance www.geico.com/landingpage/go51.htm?logo=17624; Hertz 800-654-2200 CDP#343457; Office Depot https://bsd.officedepot.com/portalLogin.do; Seabury & Smith Life Insurance 800-424-9883; Subaru VIP Program 202-326-6417; VIP Moving Services www.vipmayflower.com/domestic/index.html; Other Benefits: AAAS Member Services 202-326-6417 or www.aaasmember.org.

science_editors@aaas.org	(for general editorial queries)
science_letters@aaas.org	(for queries about letters)
science_reviews@aaas.org	(for returning manuscript reviews)
science_bookrevs@aaas.org	(for book review queries)

Published by the American Association for the Advancement of Science (AAAS), *Science* serves its readers as a forum for the presentation and discussion of important issues related to the advancement of science, including the presentation of minority or conflicting points of view, rather than by publishing only material on which a consensus has been reached. Accordingly, all articles published in *Science*—including editorials, news and comment, and book reviews—are signed and reflect the individual views of the authors and not official points of view adopted by AAAS or the institutions with which the authors are affiliated.

AAAS was founded in 1848 and incorporated in 1874. Its mission is to advance science, engineering, and innovation throughout the world for the benefit of all people. The goals of the association are to: enhance communication among scientists, engineers, and the public; promote and defend the integrity of science and its use; strengthen support for the science and technology enterprise; provide a voice for science on societal issues; promote the responsible use of science in public policy; strengthen and diversify the science and technology workforce; foster education in science and technology for everyone; increase public engagement with science and technology; and advance international cooperation in science.

Information for Authors
See pages 807 and 808 of the 6 February 2009 issue or access www.sciencemag.org/about/authors

EDITOR-IN-CHIEF **Bruce Alberts**
EXECUTIVE EDITOR **Monica M. Bradford**
NEWS EDITOR **Colin Norman**
MANAGING EDITOR, RESEARCH JOURNALS **Katrina L. Kelner**
DEPUTY EDITORS **R. Brooks Hanson, Barbara R. Jasny, Andrew M. Sugden**

Editorial senior editors/commentary Lisa D. Chong, Brad Wible; **senior editors** Gilbert J. Chin, Pamela J. Hines, Paula A. Kiberstis (Boston), Marc S. Lavine (Toronto), Beverly A. Purnell, L. Bryan Ray, Guy Riddihough, H. Jesse Smith, Phillip D. Szuromi (Tennessee), Valda Vinson, Jake S. Yeston; **associate editors** Kristen L. Mueller, Nicholas S. Wigginton, Laura M. Zahn; **online editor** Stewart Wills; **associate online editors** Robert Frederick, Tara S. Marathe; **web content developer** Martyn Green; **book review editor** Sherman J. Suter; **associate letters editor** Jennifer Sills; **editorial manager** Cara Tate; **senior copy editors** Jeffrey E. Cook, Cynthia Howe, Harry Jach, Barbara P. Ordway, Trista Wagoner; **copy editors** Chris Filiatreau, Lauren Kmec; **editorial coordinators** Carolyn Kyle, Beverly Shields; **publications assistants** Ramatoulaye Diop, Carlos L. Durham, Joi S. Granger, Jeffrey Hearn, Lisa Johnson, Scott Miller, Jerry Richardson, Jennifer A. Seibert, Brian White, Anita Wynn; **editorial assistants** Emily Guise, Michael Hicks, Patricia M. Moore; **executive assistant** Sylvia S. Kihara; **administrative support** Maryrose Madrid

News deputy news editors Robert Coontz, Eliot Marshall, Jeffrey Mervis, Leslie Roberts; Contributing Editors Elizabeth Culotta, Polly Shulman; **news writers** Yudhijit Bhattacharjee, Adrian Cho, Jennifer Couzin, David Grimm, Constance Holden, Jocelyn Kaiser, Richard A. Kerr, Eli Kintisch, Andrew Lawler (New England), Greg Miller, Elizabeth Pennisi, Robert F. Service (Pacific NW), Erik Stokstad; **interns** Michael Torrice, Brittany Johnson, Preyanka Makadia; **contributing correspondents** Dan Charles, Jon Cohen (San Diego, CA), Daniel Ferber, Ann Gibbons, Robert Koenig, Mitch Leslie, Charles C. Mann, Virginia Morell, Evelyn Strauss, Gary Taubes; **copy editors** Linda B. Felaco, Melvin Gatling, Melissa Raimondi; **administrative support** Scherraine Mack, Fannie Groom; **bureaus** New England: 207-549-7755; San Diego, CA: 760-942-3252, FAX 760-942-4979; Pacific Northwest: 503-963-1940

Production director James Landry; **senior manager** Wendy K. Shank; **assistant manager** Rebecca Doshi; **senior specialists** Steve Forrester, Chris Redwood; **specialist** Anthony Rosen; **Preflight director** David M. Tompkins; **manager** Marcus Spiegler; **specialist** Jason Hillman

Art director Yael Kats; **associate art director** Laura Creveling; **senior illustrators** Chris Bickel, Katharine Sutliff; **illustrator** Yana Greenman; **senior art associates** Holly Bishop, Preston Huey, Nayomi Kevitiyagala; **art associates** Jessica Newfield, Matthew Twombly; **photo editor** Leslie Blizard

***Science* International**

Europe (science@science-int.co.uk) **editorial: international managing editor** Andrew M. Sugden; **senior editor/commentary** Julia Fahrenkamp-Uppenbrink; **senior editors** Caroline Ash, Stella M. Hurtley, Ian S. Osborne, Peter Stern; **associate editor** Maria Cruz; **locum editor** Helen Pickersgill; **editorial support** Deborah Dennison, Rachel Roberts, Alice Whaley; **administrative support** John Cannell, Janet Clements, Louise Moore; **news: europe news editor** John Travis; **deputy news editor** Daniel Clery; **contributing correspondents** Michael Balter (Paris), John Bohannon (Vienna), Martin Enserink (Amsterdam and Paris), Gretchen Vogel (Berlin); **intern** Claire Thomas

Asia Japan Office: Asca Corporation, Eiko Ishioka, Fusako Tamura, 77 Tenjin-cho, Shinjuku, Tokyo 162-0808, Japan; +81 3 6802 4616, FAX +81 3 6802 4615, inquiry@sciencemag.jp; **asia news editor** Richard Stone (Beijing: rstone@aaas.org); **contributing correspondents** Dennis Normile [Japan: +81 (0) 3 3391 0630, FAX +81 (0) 3 5936 3531; dnormile@gol.com]; Hao Xin [China: +86 (0) 10 6307 4439 or 6307 3676, FAX +86 (0) 10 6307 4358; cindyhao@gmail.com]; Pallava Bagla [South Asia: +91 (0) 11 2271 2896; pbagla@vsnl.com]

EXECUTIVE PUBLISHER **Alan I. Leshner**
PUBLISHER **Beth Rosner**

Fulfillment Systems and Operations (membership@aaas.org); **director** Waylon Butler; **senior systems analyst** Nomuna Nyamaa; **customer service supervisor** Pat Butler; **specialists** Latoya Casteel, LaVonda Crawford, Vicki Linton, April Marshall; **data entry supervisor** Cynthia Johnson; **specialists** Shirlene Hall, Tarrika Hill, William Jones

Business Operations and Administration director Deborah Rivera-Wienhold; **assistant director, business operations** Randy Yi; **manager, business analysis** Michael LoBue; **manager, business operations** Jessica Tierney; **financial analysts** Priti Pamnani, Celeste Troxler; **rights and permissions: administrator** Emilie David; **associate** Elizabeth Sandler; **marketing director** Ian King; **marketing managers** Allison Pritchard, Alison Chandler, Julianne Wielga; **marketing associates** Aimee Aponte, Mary Ellen Crowley, Adrian Parham, Wendy Wise; **marketing executive** Jennifer Reeves; **director, site licensing** Tom Ryan; **director, corporate relations** Eileen Bernadette Moran; **publisher relations, eresources specialist** Kiki Forsythe; **senior publisher relations specialist** Catherine Holland; **publisher relations, east coast** Phillip Smith; **publisher relations, west coast** Philip Tsolakidis; **fulfillment supervisor** Iquo Edim; **fulfillment coordinator** Carrie MacDonald; **marketing associate** Mary Lagnaoui; **electronic media: manager** Lizabeth Harman; **project manager** Trista Snyder; **assistant manager** Lisa Stanford; **senior production specialists** Christopher Coleman, Walter Jones; **production specialists** Nichele Johnston, Kimberly Oster

Advertising director, worldwide ad sales Bill Moran

Product (science_advertising@aaas.org); **midwest/west coast/w. canada** Rick Bongiovanni: 330-405-7080, FAX 330-405-7081; **east coast/e. canada** Laurie Faraday: 508-747-9395, FAX 617-507-8189; **uk/europe/asia** Roger Goncalves: TEL/FAX +41 43 243 1358; **japan** Mashy Yoshikawa: +81 (0) 3 3235 5961, FAX +81 (0) 3 3235 5852; **senior traffic associate** Deiandra Simms

Commercial Editor Sean Sanders: 202-326-6430

Project Director, Outreach Brianna Blaser

Classified (advertise@sciencecareers.org); **u.s.: sales manager** Daryl Anderson: 202-326-6543; **midwest** Tina Burks: 202-326-6577; **east coast** Alexis Fleming: 202-326-6578; **west/south central** Nicholas Hintibidze: 202-326-6533; **sales coordinators** Rohan Edmonson, Shirley Young; **international: sales manager** Tracy Holmes: +44 (0) 1223 326525, FAX +44 (0) 1223 326532; **sales** Susanne Kharraz, Dan Pennington, Alex Palmer; **sales assistant** Lisa Patterson; **japan** Mashy Yoshikawa: +81 (0) 3 3235 5961, FAX +81 (0) 3 3235 5852; **advertising support manager** Karen Foote: 202-326-6740; **advertising production operations manager** Deborah Tompkins; **senior production specialist/graphic designer** Amy Hardcastle; **senior production specialist** Robert Buck; **senior traffic associate** Christine Hall

AAAS Board of Directors retiring president, chair James J. McCarthy; **president** Peter C. Agre; **president-elect** Alice Huang; **treasurer** David E. Shaw; **chief executive officer** Alan I. Leshner; **board** Alice Gast, Linda P. B. Katehi, Nancy Knowlton, Cherry A. Murray, Julia M. Phillips, Thomas D. Pollard, David S. Sabatini, Thomas A. Woolsey

AAAS
ADVANCING SCIENCE, SERVING SOCIETY

EDITED BY CONSTANCE HOLDEN

A Streetcar Named Darwin

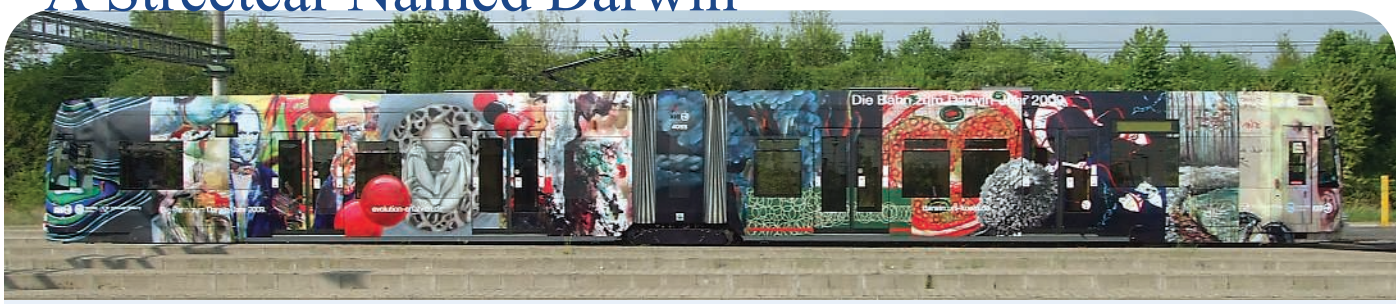

Some streetcar riders in Cologne, Germany, are getting a dose of evolutionary biology during their daily commute. Twenty art students at the University of Cologne, directed by biologist Daniel Dreesmann, artist Volker Saul, and art professor Silke Leverkühne, celebrated the Darwin Year by creating the "Evolution Erfahren" (experience evolution) streetcar, which will run for the rest of the year on the city's regular routes. The car is covered inside and out with artwork exploring Darwin-related themes, including the evolution of birds, evolution and medicine, and "evolution in our backyard"—for example, a recently evolved fish species that lives in the Rhine. "It's not a moving textbook," Dreesmann says. "It's designed to make people curious." For those who can't catch the streetcar in person, the Volkswagen Stiftung, which funded the project, this week published a catalog of the artworks created for the project (www.evolution-erfahren.de).

CREDITS (TOP TO BOTTOM): WWW.EVOLUTION-ERFAHREN.DE; INTERNATIONAL CRANE FOUNDATION; WWW.EP-PRESIDENT.EU; D. HOFFMAN *ET AL.*, *GEOPHYSICAL RESEARCH LETTERS*

Dam Threatens Cranes

Conservationists are blasting plans to dam Poyang Lake, the largest freshwater lake in China and a mecca for migratory birds, including most of the world's Siberian cranes. The lake rises during the summer flood season and drops by as much as 10 meters in winter, offering vast shallows and mudflats where hundreds of thousands of waterfowl feed on fish and dig for tubers. A dam would keep the water level up year-round.

Chen Qixing, an official of Jiang Xi Province, says the project will control water levels so the ecology won't be harmed. But attendees at this month's International Congress for Conservation Biology in Beijing denounced the plan. No other wetland in China offers conditions so favorable to water birds, says James T. Harris, vice president of the International Crane Foundation in Baraboo, Wisconsin. "All the areas where the Siberian crane and other birds feed would be deeply flooded," says Chen Kelin, director of Wetlands International. Food supplies would become unpredictable, he says. Vegetation would shift to the edges of the lake, but this would force birds to move to shore areas where disturbance from human activities would be much greater. Last month, Chen and 15 other scientists sent a letter to Premier Wen Jiabao protesting the plan.

Engineer to Head E.U. Parliament

Jerzy Buzek, former Polish prime minister and a strong supporter of research, has been elected the new president of the European Parliament. Buzek, 69, made headlines last week as the first citizen of a former Eastern Bloc nation to hold the office, one of the three top posts in the European Union (E.U.). A chemical engineer by training, Buzek was active in the Solidarity trade union movement in Poland and was the country's prime minister from 1997 to 2001.

"Jerzy Buzek's election is a blessing" for the future of the European Research Council (ERC), a grantmaking body formed in 2005, says ERC Vice-President Helga Nowotny of the Vienna Science and Technology Fund. Nowotny says Buzek could help ERC gain more financial autonomy from the E.U. It will be "an arduous political process" requiring Parliamentary approval, Nowotny says, so "we must get it done [while] Buzek is in office." That doesn't leave much time. In a political compromise typical of the E.U., Buzek, a member of a center-right party, won by agreeing to serve just 2.5 years of the 5-year term. He is expected to be succeeded by Germany's Martin Schulz, a leader of the Parliament's Social Democrats.

CHINA'S HUMAN VOLCANO

China is apparently trying to catch up with Mount Pinatubo in dirtying the stratosphere, researchers say.

The country's explosive increase in sulfur pollution has penetrated Earth's most remote and seemingly pristine reaches. In an upcoming paper in *Geophysical Research Letters*, atmospheric scientist David Hoffman of the National Oceanic and Atmospheric Administration in Boulder, Colorado, and colleagues finger Chinese coal burning for a steady increase since 2000 of the sulfurous haze 20 to 30 kilometers up. Mount Pinatubo's powerful 1991 eruption boosted stratospheric haze, shading and cooling the globe for a few years while destroying ozone. But 50 million tons or so of global annual sulfur emissions hadn't made a noticeable dent until China's economy took off, increasing its sulfur emissions more than 60% between 2000 and 2005. That accounts for the observed 4% to 7% per year thickening of stratospheric haze, the group reports.

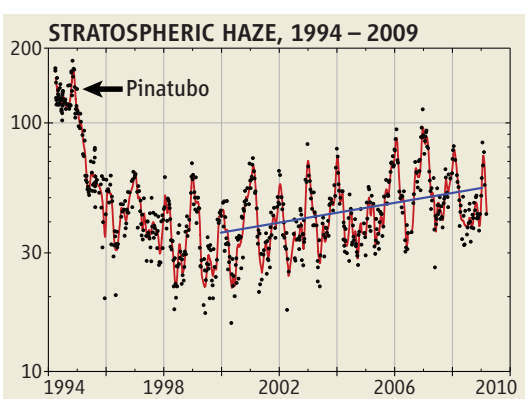

Published by AAAS

Exxon puts big bet on biofuels
379

Test ban monitoring passes a test
382

SOUTH KOREA

Forensic Finds Add Substance to Claims of War Atrocities

HAMPYEONG, KOREA—Early in the Korean War, the South's army was fighting on two fronts: against the North, which had invaded in June 1950, and against homegrown Communist guerillas. In February 1951, the army's 11th Division and police in the divided peninsula's southwest were closing in on guerillas holed up on Bulgap Mountain in Hampyeong County. Operation Full Moon—an assault on Bulgap—was planned for the night of 20 February. But the rebels caught wind of the impending attack and, knowing they'd be routed if they made a stand, slipped the cordon. In the meantime, villagers fleeing advancing troops had sought refuge on Bulgap. When soldiers and police stormed the ridge and found only civilians, survivors claim, they dug a long trench, forced the civilians to kneel inside, and then shot them or thrust sharpened bamboo sticks down their throats. Women and children were among the victims.

That's the story South Korea's Truth and Reconciliation Commission (TRCK) heard when it began to investigate the Bulgap massacre last year. "It was controversial," says sociologist Kim Dong-Choon, a commissioner and director of the Human Rights and Peace Center of Sungkonghoe University in Seoul. Some commissioners, he says, doubted the recollections of elderly survivors who had lived in Hampyeong when the atrocity occurred but had not witnessed it. "A few of my colleagues thought the victims really were guerillas," says Kim.

But the survivors have been vindicated by new forensic finds. Last week, TRCK revealed evidence from an ongoing excavation confirming Bulgap as one of the Korean War's darker chapters. Anthropologist Noh Yong-Seok, who leads TRCK's excavations with help from forensic scientists at Chungbuk National University, says the team has found adult skeletons bent at the knees with finger bones clasped behind their skulls and artifacts that rebel soldiers would have had no use for, such as a woman's hairpin and toys. Investigators here have unearthed bones of several children, the first such verified remains from a Korean War–era massacre site, says Noh.

The Hampyeong dig is one of the more stunning revelations to date from the truth commission, which in the past 3 years has documented mass killings in the war's early years of more than 100,000 South Korean civilians, deemed "traitors," by the country's own military and police. Hundreds of thousands more were slain by indiscriminate aerial bombing and ground fire by U.S. and Korean forces, says Kim. "We know now that the Korean War was like a war with no frontline. Everyone was killing each other, whoever was beside them," says TRCK President Ahn Byung-Ook, a historian at Catholic University of Korea in Seoul.

Digging up the truth. Excavation leader Noh Yong-Seok holds a woman's hairpin, evidence of a civilian massacre.

CREDIT: R. STONE/*SCIENCE*

As TRCK rewrites history books, it is rushing to wind up investigations before its legal mandate expires in April 2010. President Lee Myung-bak's conservative Administration has not hidden its disdain for the truth commission, which was created by the liberal government of his predecessor, Roh Moo-hyun. "We would prefer to lay the past to rest and solve today's problems, like our economic crisis," an Administration official told *Science*.

Commission officials insist it will be impossible to wrap up active investigations by April. That leaves sociologists wondering whether South Koreans—especially those born after the war ended—will ever come to terms with the incidents TRCK is uncovering. "I don't blame younger generations for lack of interest," says Ahn. "But I expect them to learn a more accurate account of history."

Untold stories

It is monsoon season in Korea, and after an early downpour, wispy fog clings to Hampyeong's hills and rice paddies. Paintings of butterflies adorn bus stops and farm outbuildings, and an entire hillside's vegetation is trimmed neatly in the shape of a butterfly. These days, Hampyeong is known for its annual butterfly festival—that and for onions, umpteen numbers of which are stacked in bales along the roads.

After an arduous half-hour slog up a muddy path on Bulgap Mountain, Chang Jae-soo helps two college-age excavators peel back a blue tarp brimming with standing water. The 74-year-old, who lived in a nearby village 6 decades ago, has remarkable stamina—perhaps, he says, because the exhumation has revitalized him. "I feel like I am getting my honor back," he says.

A row of tarps, each about 3 meters wide, extends for 50 meters or so along the ridge. Noh's team has been excavating here for about a month. So far they have unearthed remains of about 100 individuals from the shallow

Published by AAAS

Bats and turbines don't mix
386

Plant bacteria that bring color and disease
388

grave. Noh crouches and reaches behind a skull and picks up a humerus, several centimeters long, that Chungbuk National University scientists estimate belonged to a 12-year-old child. Spent bullet casings lie scattered among the bones, as do some rusted spoons. "Spoons are one possession the villagers surely would have brought with them. They had to eat," says Noh. He lays the bone down gently. Nearby is a tiny pale blue ball—a marble. "This is one of the few toys children back then would have had." They have found bones here of toddlers as young as 3 or 4.

Although some victims here may have been guerillas, forensic evidence of a civilian massacre, Noh says, is now incontrovertible. About a quarter of the dead were women and children. Noh has led TRCK exhumations at 13 sites that so far have yielded remains of about 1700 people; no other site has such young victims. Hampyeong, he says, "is the most tragic one of all."

It's not surprising that villagers would have fled to Bulgap. A month before the Hampyeong incident, troops shot dead Chang's parents, his uncle and aunt, and three younger sisters. Chang, 16 at the time, escaped and later found his way to an elder sister's home across the peninsula. For years after the armistice, Korean society spurned people deemed to be Communist sympathizers—even those like Chang who had nothing to do with the guerillas but were tainted merely by having lost family members in massacres. "People hardly got a chance to get an education or a job," says Chang, who made ends meet as a traveling salesman.

Under the military dictatorships that ruled after the war, Noh explains, "we were taught to not question the government or the army." At one notorious massacre site, Gyeongsan Cobalt Mine, victims were shot and dumped down shafts. Noh's crew there has so far recovered remains of 240 of an estimated 3500 victims. "Many people knew about the cobalt mine, but for 50 years they didn't say anything. It was taboo," says Noh, who grew up in the area. In the 1990s, a rising chorus called for an investigation into alleged crimes against civilians, ranging from when Korea was a colony of Japan before World War II, the Korean War era, and up through democracy movements lasting into the 1980s. Roh bowed to pressure and established the commission in December 2005. Roh, who committed suicide 2 months ago, apologized to victims on behalf of the nation in January 2008. "It was the first time in our history that the government acknowledged the war's civilian victims," says Ahn.

Seeking closure. Seven members of Chang Jae-soo's family were killed.

TRCK's creation opened a floodgate: More than 10,000 petitions have poured in, and several thousand cases are still pending. Investigators have interviewed hundreds of victims and alleged perpetrators; many of the latter have shown little or no remorse. "Offenders justify what they did as inevitable," says Ahn. However, he notes, "our aim is not to put perpetrators on trial. It is to reconstruct the past through the victims' eyes."

Last December, Chang and others formed the Bulgap Mountain–Yongcheon Temple Provincial Union of Bereaved Families of Civilian Victims—one of 100 or so such unions across the country. The union plans to sue the government for compensation once the excavation is finished. But more important than money, Chang insists, is that he and other victims are finally putting the bitter years of postwar discrimination behind them. Using words one would expect from a perpetrator, he says, "We're not seen as sinners anymore."

–RICHARD STONE

CREDIT: R. STONE/*SCIENCE*

CAREER SUPPORT

DOE Puts Up $85 Million for Grants to Young Scientists

The U.S. Department of Energy (DOE) has committed $85 million next year for a new program to help 50 young scientists establish their research careers. It is the latest federal agency to try to lend a hand to this vulnerable population.

The program (www.science.doe.gov/SC-2/early_career.htm) is financed by the $1.6 billion given to DOE's Office of Science earlier this year in the government-wide stimulus package. As such, the money must be spent quickly, with the expectation that it will provide jobs and help pull the nation out of its economic doldrums. DOE officials say the program also responds to the recommendations of several expert panels, including the 2005 National Academies' *Rising Above the Gathering Storm*. Several other agencies already have programs that target this population, including a greatly expanded effort in the past 2 years by the Department of Defense (*Science*, 14 November 2008, p. 1037).

The 5-year awards will be divvied up between tenure-track university scientists and those holding full-time jobs at a DOE national laboratory. Applicants must be within 10 years of having received their Ph.D. Awards for academic scientists can range up to $750,000, whereas lab scientists are eligible for as much as $2.5 million. (DOE will be paying only summer salaries for university researchers, while it foots the entire salary for its lab employees.) The awards "are meant to support proposals from individual PIs [principal investigators], in areas that serve DOE's mission," explains DOE's Linda Blevins, who will manage the program within the Office of Science.

Applicants are asked to submit a letter of intent by 3 August, Blevins says, so that DOE can get an idea of the level of interest and the nature of the proposals to be reviewed. "We really don't know how many applicants we'll get, but it's certainly generated a lot of interest from the community," she adds. Full proposals are due by 1 September, with awards to be announced next spring.

Although the stimulus money will cover only the first round of awards, Blevins says "we anticipate growing the program" in subsequent years if DOE receives adequate funding from Congress.

–JEFFREY MERVIS

Published by AAAS

CLIMATE CHANGE

Clouds Appear to Be Big, Bad Player in Global Warming

Climate researchers have long viewed clouds' reaction to greenhouse warming as the key to understanding the world's climatic fate. As rising carbon dioxide strengthens the greenhouse, will some clouds thicken and spread, shading the planet and tempering the warming? Or will they thin and shrink, letting in more sunshine to amplify the warming? The first reliable analysis of cloud behavior over past decades suggests—but falls short of proving—that clouds are strongly amplifying the warming. If that's true, then almost all climate models have got it wrong.

The new study "confirms with observations that low clouds are critical for the climate system's response," says climate modeler Gerald Meehl of the National Center for Atmospheric Research in Boulder, Colorado. But "it's really a challenge for models" to simulate that response, he adds. If real-world cloud amplification works the way the study indicates, researchers say, global warming could be even worse than the typical model predicts.

Clouds have been a climate conundrum in part because no one has been keeping an eye on them the way the weatherman has been recording temperature for more than a century. On page 460, climate researcher Amy Clement of the University of Miami in Florida and colleagues consider the two best, long-term records of cloud behavior over a rectangle of ocean that nearly spans the subtropics between Hawaii and Mexico. Other researchers had compiled one of the records from eyeball estimates of cloud cover made by mariners who passed through the region from 1952 to 2006. The other record, which runs from 1984 to 2005, came from satellite measurements, which Clement and her colleagues adjusted to account for calibration shifts from one satellite to the next.

Between them, the observations recorded the two major climate shifts that roiled the North Pacific during the periods they covered. In a warming episode that started around 1976, the ship-based data showed that cloud cover—especially low-altitude cloud layers—decreased in the study area as ocean temperatures rose and atmospheric pressure fell. One interpretation, the researchers say, is that the warming ocean was transferring heat to the overlying atmosphere, thinning out the low-lying clouds to let in more sunlight that further warmed the ocean. That's a positive or amplifying feedback. During a cooling event in the late 1990s, both data sets recorded just the opposite changes—exactly what would happen if the same amplifying process were operating in reverse. "All of the elements of a positive feedback are there," Clement says.

Even so, positive low-cloud feedback was only a supposition until the group looked at another sort of satellite measurement of the second natural climate shift. That showed that when decreasing cloud cover let the sun leak through, the additional solar heating was large enough to account for much of the ocean warming. A positive feedback operating in the decades-long climate shifts "is real," Clement concludes. And other studies link cloud changes in the northeastern tropical Pacific to atmospheric changes across the Pacific.

But is such a feedback actually working to amplify global warming? To get some indication, Clement and her colleagues checked the archives of a study in which the international Coupled Model Intercomparison Project compared the results of 18 global climate models run under standardized conditions. Clement and her colleagues tested whether each model was properly simulating each element of the positive cloud feedback they had found in the northeastern Pacific.

When the results were in, only two models showed low clouds producing a positive feedback as observed. One of them stood out from the pack. The HadGEM1 model from the U.K. Met Office's Hadley Center in Exeter produced patterns of warming and circulation changes during greenhouse warming that resembled those of all 18 models averaged together—the best guide available. The group also concluded that HadGEM1's simulation of meteorological processes in the lowermost kilometer or two of the atmosphere—where the key low-lying clouds reside—is particularly realistic.

As it happens, the HadGEM1 model is among the most sensitive of the 18 models to added greenhouse gases. When carbon dioxide is doubled, the model warms the world by 4.4°C; the median of the models for a doubling is 3.1°C. That gap raises a red flag for Clement. "We tend to focus on the middle of the range of model projections and ignore the extremes," she says. "I think it does suggest serious consideration should be given to the upper end of the range."

Climate researchers agree that Clement and her colleagues may be on to something. "There's been a gradual recognition that this rather boring type of [low-level] cloud is important in the climate system," says climate researcher David Randall of Colorado State University, Fort Collins. "They make a good case that in [decadal] variability there is a positive feedback. The leap is that the same feedback would operate in global climate change." The study tends to support an important role for marine low clouds in amplifying global warming, he says, but it doesn't prove it.

One clear contribution of the study, Randall says, is to point the way toward more reliable climate models. The paper "is definitely a reasonable approach to deciding which models to pay the most attention to," he says. In its previous international assessments, Randall notes, the Intergovernmental Panel on Climate Change assumed that all models are created equal. "I think we have to get away from that."

–RICHARD A. KERR

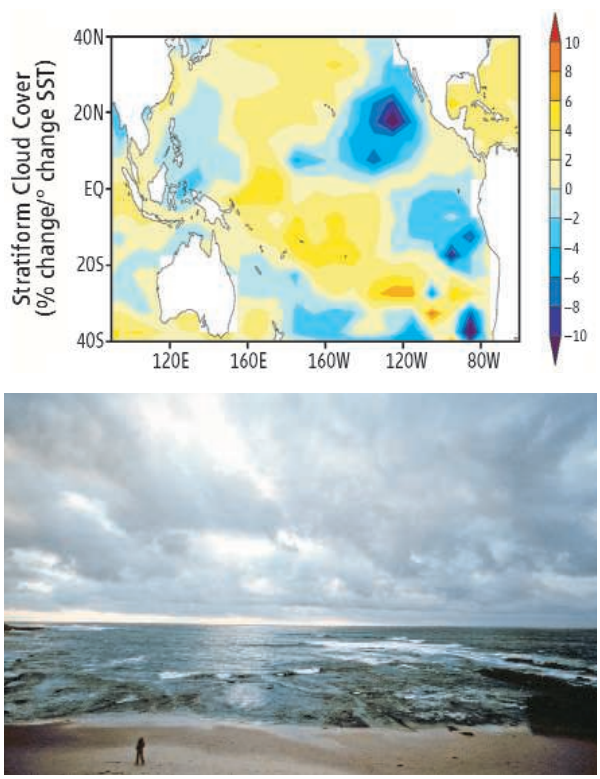

Leaky clouds. Decades-long records show that when sea surface temperature (SST) warms, cloud cover—especially from low clouds (*bottom*)—decreases (blues, *top*), letting in more sunlight.

CREDITS (TOP TO BOTTOM): CLEMENT *ET AL.*, *SCIENCE*; NOAA

Published by AAAS

ENVIRONMENTAL MONITORING

Spy Satellites Give Scientists A Sharper Image of Field Sites

Hajo Eicken has spent the past 10 years monitoring the freezing and melting of sea ice along the 900 kilometers of northern Alaskan coastline. Each winter, the geophysicist at the University of Alaska, Fairbanks, visits a handful of field sites and fills in the gaps with satellite images. But last week, thanks to the U.S. intelligence community, he saw pictures that will allow him to model the breakup at a level of detail he never imagined.

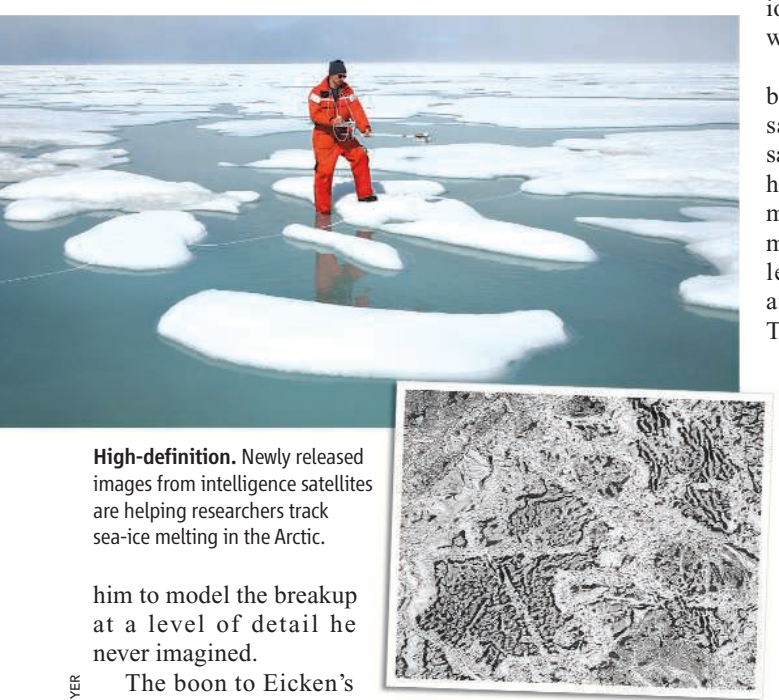

High-definition. Newly released images from intelligence satellites are helping researchers track sea-ice melting in the Arctic.

The boon to Eicken's research—plotting the interplay of ocean currents, tides, and winds—comes courtesy of the National Civil Applications Program at the U.S. Geological Survey (USGS). For the past decade, the program has maintained a library of scientifically useful images taken by intelligence-gathering satellites that have been available only to federal scientists with security clearances. Last week, USGS posted 1199 pictures, taken at 22 environmentally significant sites across the continental United States and six around the North Pole, with a resolution up to 30 times sharper than what Eicken could obtain from commercial satellites (gfl.usgs.gov). The new images will enable researchers to "chart the progression of ice decay in great detail," Eicken says, to the level of "individual melt ponds."

The U.S. government began collecting these images in the late 1990s under a program called Medea. With few exceptions, the images have been available only to federal scientists. Last fall, as part of a planned release, the intelligence agencies asked the U.S. National Academies whether producing unclassified versions of the images—essentially by stripping out information that might telegraph the satellites' technological prowess or jeopardize national security—would be worthwhile to scientists.

The panelists were blown away. "What we saw was unbelievable," says Stephanie Pfirman, head of the environmental sciences department at Barnard College in New York City and chair of the panel. The panel recommended the release of the images. On the eve of the report's publication, the panelists briefed intelligence officials, who promised that the images would be available the very next day. Two hours after the report was released, they were posted. "The response was faster than any of us had expected," says Thorsten Markus, a researcher at NASA's Goddard Space Flight Center in Greenbelt, Maryland, who served on the panel along with Eicken and three other scientists.

"We are thrilled that this imagery is coming out," says Peter Jutro, an Environmental Protection Agency official who sits on the Civil Applications Committee and was a member of the Medea program. James Devine, a senior adviser to the USGS program, says "we are in the process of preparing several hundred more" images, with funding from the intelligence community.

The panel also recommended that the satellites expand their breadth by tracking moving ice as well as fixed sites. "The community is going to want more," says Pfirman. "It would be great to add dynamic image collection."

–YUDHIJIT BHATTACHARJEE

CREDITS (LEFT TO RIGHT): UNIVERSITY OF ALASKA, FAIRBANKS; (INSET) DOI/USGS; GEORGE WITTEMYER

ScienceNOW.org

From *Science*'s Online Daily News Site

Exploding Raindrops
Here's a question for a rainy day: How do clouds create such a wide variety of raindrop sizes? The answer, according to stunning new high-speed movies, is much simpler than physicists thought. Drops don't crash into each other as they fall; rather, they balloon like a parachute, then explode. Watch a movie here: http://bit.ly/qG00c

No Risk in Disclosing Genetic Risks
Sitting in your doctor's office, you get the bad news: Thanks to a faulty gene, you're 15 times more likely than the average person to develop Alzheimer's disease. But despite the diagnosis, you're unlikely to become more anxious or depressed within the next year, according to a new study. http://bit.ly/uZhFj

Ancient Climate-Change Puzzle
Carbon dioxide gets a bad rep for contributing to global warming, and deservedly so. But scientists say they can't entirely blame the greenhouse gas for a curious spike in Earth's temperature 55 million years ago. New research reveals that something else also seems to have warmed the planet during that time, though no one's quite sure what it was. http://bit.ly/zgvmx

Elephants Don't Always Keep It in the Family
In elephant society, nothing is more important than family. From traveling packs of mothers and calves to larger groups that include aunts and cousins, all segments of the creatures' complex social structure are typically composed of relatives. But what happens when these populations are decimated by humans? New research reveals that elephants sometimes bring in nonkin to keep their social groups viable. http://bit.ly/3aSyD1

Read the full postings, comments, and more on **sciencenow.sciencemag.org**.

Published by AAAS

Old and new. This NOAA Cessna will fly around the country toting the gravimeter, an improvement over the traditional method of surveying and siting National Geodetic Survey markers.

GEODESY

NOAA Project to Measure Gravity Aims to Improve Coastal Monitoring

How high is up? The U.S. government has launched a 10-year, $38 million research project to answer that question in hopes of improving its management of coastal regions and reducing the damage from severe storms and rising sea levels.

Calculating the elevation of any point on the globe isn't a simple undertaking. The traditional method relied upon surveyors traipsing around the country, repeatedly lining up a telescope on a tripod with a leveling rod to measure the position difference between two points of reference with respect to sea level. Those efforts have produced the National Spatial Reference System (NSRS), a network of more than 1.5 million survey markers throughout the United States that record latitude, longitude, and elevation above sea level. Federal and local agencies use NSRS to help with construction plans, mapping, floodplain management, tropical storm preparation, and many other endeavors.

Unfortunately, changes in Earth's surface—from earthquakes and other factors—erode the accuracy of those markers over time. The current NSRS contains elevation errors ranging from 40 centimeters to nearly 2 meters, says Juliana Blackwell, director of the National Geodetic Survey (NGS), a branch of the National Oceanic and Atmospheric Administration (NOAA) that operates the reference system. "The accuracies are not what we'd like them to be," Blackwell says.

A newer technology, the Global Positioning System (GPS), also generates elevation data—but of the wrong sort. GPS instruments provide what's known as ellipsoid height, based on a model of Earth as a smooth, flattened sphere. Although that's a good fit for the actual shape of the planet, heights measured from it are not useful for generating a topographic map that will show how water flows, for example.

To do that, you need an accurate depiction of Earth's gravity field, which represents how the pull of gravity varies from place to place because of the planet's irregular surface and makeup. "Water will always follow the gravity field because the gravity field predicts water flow," says NGS's Vicki Childers. "The gravity field helps determine sea level. And sea-level surface is used to base measurements on."

Measuring the gravity field allows scientists to update their model of the geoid—a fictional surface warped so that Earth's gravity is constant everywhere on it. In turn, the geoid provides a basis to measure a point's orthometric height (*orthos* being Greek for straight or correct).

The new project is called Gravity for the Redefinition of the American Vertical Datum (GRAV-D). The key instrument is an airborne gravimeter coupled with GPS. Placed inside NOAA's Cessna Citation II jet, the gravimeters will measure the acceleration of gravity at the same time that GPS instruments aboard NASA's Gravity Recovery and Climate Experiment Satellite measure the plane's vertical acceleration. Thus, equipped researchers can produce large-scale regional land and sea surveys without the inconsistencies of leveling, says Childers, project manager for GRAV-D.

"[GRAV-D] is a logical progression," says Thomas Herring, a geophysicist at the Massachusetts Institute of Technology in Cambridge. He says it makes no sense for NGS to rely on a "labor-intensive technique" like leveling when something better exists. "It's part of transforming from historical methods to much less expensive and more reliable methods with GPS," Herring says.

Under the first phase of GRAV-D, NGS carried out airborne surveys over Puerto Rico in January and conducted test flights last year in Alaska and along the coast of the Gulf of Mexico. NGS didn't receive money last year to ramp up the project. So NOAA tried again this year, including $4 million for GRAV-D in its request for fiscal year 2010, which begins in October. Although the budget process is still under way, last month spending panels in both the House of Representatives and the Senate exceeded NOAA's overall request for research, all but ensuring that the project can proceed.

Each leg of the survey takes about a month, Childers says. The project is expected to take 10 years to complete, beginning with the coastal areas and then extending inland. When it's done, scientists will have a new geoid model from which orthometric heights can be calculated more accurately.

Those heights offer crucial information to public officials responsible for civil infrastructure—roads, buildings, bridges, airports, and other structures along the country's vast coastline and inland floodplains. A recent study NOAA commissioned estimated that the new geoid model will save the country $3.6 billion over 15 years through improved flood control and other steps taken as a result of better knowledge of the height of low-lying areas.

More precise measurements alone would not have saved New Orleans and the Gulf Coast from the ravages of Hurricane Katrina. But NGS scientists say that arming public officials with more accurate height data about the regions they must manage is bound to save lives and money in the long run.

–BRITTANY JOHNSON

CREDITS: NOAA

Published by AAAS

BIOFUELS

ExxonMobil Fuels Venter's Efforts To Run Vehicles on Algae-Based Oil

The floodgates are officially open. After years of skepticism about the promise of biofuels, ExxonMobil has decided to make one of the biggest biofuel bets so far.

Last week, the world's second largest company announced that it will spend up to $600 million over 5 to 6 years to produce biofuels from algae. Half the money will go to Synthetic Genomics Inc. (SGI), a San Diego, California–based start-up run by genomics pioneer J. Craig Venter. Exxon will spend another $300 million on in-house research including attempts to scale up biofuels production from algae and refine the resulting oils into finished fuels. "This is not going to be easy, and there are no guarantees of success," says Emil Jacobs, vice president of research and development for Exxon's research division.

Venter says SGI has already reengineered some strains of algae to secrete hydrocarbons from their cells. That achievement allows them to produce the compounds continuously in bioreactors. That's a big advantage over traditional "farming" methods, in which algae are grown in shallow ponds from which they are harvested and split open for oil that is then refined into fuel. The company plans to build a large facility in San Diego to test thousands of algal species in hopes of finding or reengineering strains to turn out oils at a high rate. Jacobs says Exxon's investment hinges on SGI's meeting a series of research milestones.

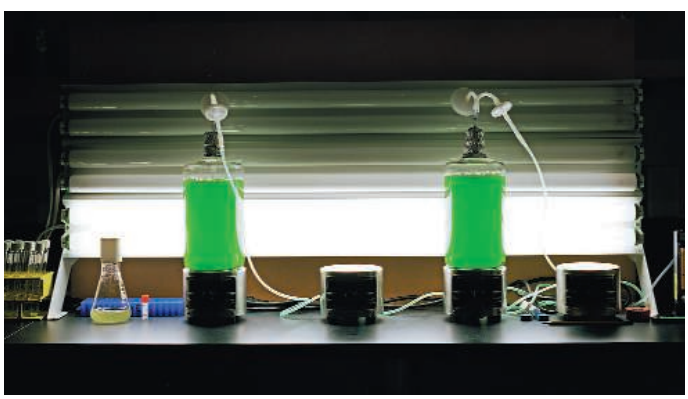

Chemical plant. ExxonMobil will pay SGI to make biofuels from algae.

CREDIT: MARK MAHANEY

"The deal is tremendous for biofuels," says Bill Haywood, CEO of LS9 Inc., a biofuels start-up based in South San Francisco, California. "A move like that tells me they are serious about the future of biofuels." Exxon is the last major oil company to move into biofuels, notes Divya Reddy, an energy and natural resources analyst in Washington, D.C., with the Eurasia Group, an international policy risk assessment firm. The size of its investment "solidifies that trend," she says.

The technology's backers say algae have inherent advantages over other biofuels. They can be grown on nonagricultural land, absorb carbon dioxide, and the oils they produce can be refined into conventional transportation fuels that can be distributed using existing infrastructure. The market has begun to recognize those strengths: In 2006, Algenol Biofuels, a Florida-based company, announced an $850 million project with Mexico's Sonora Fields S.A.P.I. de C.V. to produce ethanol from algae. More recently, two algae fuel makers, Sapphire Energy in San Diego and Solazyme in South San Francisco, have raised $100 million and $76 million, respectively, from venture capitalists.

But although the area is hot, many obstacles remain. Among the biggest are reengineering algae to produce more hydrocarbons and to make molecules that more closely resemble refined gasoline. But Stephen Mayfield, a cell biologist at the Scripps Research Institute in San Diego, California, and a founder of Sapphire Energy, thinks the tallest hurdle is scaling up the process. "That's a key component Exxon will bring to this deal," Mayfield says.

The race to market has already begun. LS9, which uses engineered *Escherichia coli* instead of algae to make fuel, hopes to open a large-scale production facility in Brazil by 2013. Aurora Biofuels in Alameda, California, expects to have a commercial algae biodiesel facility online in 2012, and Algenol plans to begin selling fuel from its facility in Mexico later this year.

Mayfield and others aren't worried about the competition. Given the global $1-trillion-a-year market for energy, Mayfield says the more biofuels players, the better. "We will use every molecule of renewable energy we can get," he says. **–ROBERT F. SERVICE**

ScienceInsider

From the *Science* Policy Blog

India's new environment minister, **Jairam Ramesh**, says **India will not agree to mandatory reductions** in carbon emissions. Ramesh spoke at a news conference with visiting U.S. Secretary of State Hillary Clinton. "We are simply not in a position to take over legally binding emission reduction targets," Ramesh said. Clinton said the United States would not impose targets on India or "do anything that would limit India's economic progress."

The planned restart of the **Large Hadron Collider** will be pushed back from September to at least November because of newly discovered "vacuum leaks" in two sections of the accelerator. CERN disclosed the bad news in the latest issue of its online newsletter.

Thirty-four U.S. Nobel laureates last week called on President Barack Obama to push for **a steady funding mechanism** in upcoming climate legislation **to support clean energy research**. Many billions of dollars are already flowing from stimulus funding, they note in a letter to Obama, but the money will run out in October 2010. The Nobelists want the president to follow through on an earlier pledge to spend **$15 billion a year for 10 years** for research on clean energy.

Norman Augustine, who is chairing a blue-ribbon panel examining alternative futures for the U.S. human space-flight effort, hinted last week that **the panel might shy away from advocating an expensive human mission to the moon, Mars, or an asteroid**. Recommendations to the White House are expected by the end of August.

The **Chinese government has banned** the controversial application of **electroconvulsive therapy** for so-called Internet addiction after a clinic gained notoriety for applying electric shocks to unanesthetized teenagers being treated against their will (*Science*, 26 June, p. 1630).

For other science policy news, go to **blogs.sciencemag.org/scienceinsider.**

Published by AAAS

IMAGING

With 'Phenomics,' Plant Scientists Hope to Shift Breeding Into Overdrive

MELBOURNE, AUSTRALIA—Last May, a scrawny grass, *Brachypodium distachyon*, joined the exclusive club of plants whose genomes have been sequenced. *Brachypodium* may look unassuming, but under the hood it is a geneticist's dream. It has a short life cycle and a small genome with one pair of chromosomes (wheat, for instance, has three pairs) that readily reveals the effects of genetic modification. In short, the temperate grass is a superb model organism for cereals like wheat and rice and for biofuels like switchgrass. But *Brachypodium*'s genome alone cannot revolutionize plant breeding.

Enter plant phenomics. Borrowing imaging techniques from medicine, phenomics offers plant scientists new windows into the inner workings of living plants: infrared cameras to scan temperature profiles, spectroscopes to measure photosynthetic rates, lidar to gauge growth rates, and MRI to reveal root physiology. "Phenomics will give plant scientists the tools to unlock the information coded in genomes," says Mark Tester, director of the Australian Plant Phenomics Facility (APPF), a new $40 million venture with headquarters in Adelaide.

Institutes worldwide are racing to build facilities with instrument arrays that can scan thousands of plants a day in an approach to science akin to high-throughput DNA sequencing. "This will allow plant physiology to 'catch up' with genomics," says Tester. APPF, the first national lab of its kind in the world, consists of two nodes. One is a High Resolution Plant Phenomics Centre (HRPPC) in Canberra, which opened last week. A debut project of the center is an international collaboration to screen *Brachypodium* variants for drought-tolerance and for less lignin in their cell walls. The second node is the Plant Accelerator in Adelaide, a screening facility that Tester will run and aims to get online by December.

"Australia is leading the way," says David Kramer, a spectroscopist at the Institute of Biological Chemistry at Washington State University, Pullman. But other countries are ramping up fast. In Germany, for example, the Institute for Phytosphere Research (IPR) in Jülich in 2007 established the Jülich Phenomics Centre, which carries out a variety of screens and is developing root imaging. And the Leibniz Institute of Plant Genetics and Crop Plant Research in Gatersleben is carrying out high-throughput screening on crops such as barley and wheat using instruments such as infrared cameras to chart transpiration and fluorescent microscopy to assess photosynthesis.

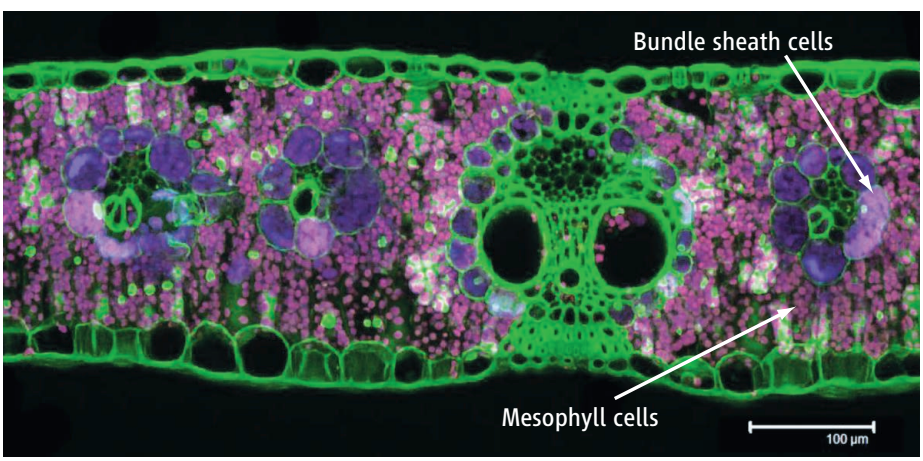

A-maizing transformation. In this maize leaf, laser confocal microscopy reveals a clear distinction between high activity of photosystem II in mesophyll cells (pink fluorescence) and low activity in bundle sheath cells (purple)—a distinction typical of C4 plants. The green fluorescence comes mainly from lignin in cell walls.

CREDIT: R. WHITE AND ROBERT FURBANK/CSIRO AND SUSANNE VON CAEMMERER/ANU

From feel to phenomics

Plant breeders are known for their "feel": the ability to select subtle traits that enhance a plant's performance. They might key in on the way a plant curls its leaves, for example, or a particular shade of green whose significance escapes the uninitiated. Such craftwork delivered enormous agricultural gains through the mid 1990s. But with yields of many crops having hit plateaus, green thumbs are no longer enough. Modern plant breeders need the equivalent of a watchmaker's magnifying glass and tweezers to tinker with complex and intertwined traits. Phenomics, says Uli Schurr, director of IPR, promises to usher in "precision agriculture and predictive breeding."

One trait Australia has in its cross hairs is salt tolerance. High salinity affects one-fifth of the world's irrigated land and two-thirds of Australian cereal crops. But selecting plants for salt tolerance has generally flopped. "We can end up with plants like mangroves that are salt-tolerant but slow growing and not much use," says Tester. He and Rana Munns of CSIRO Plant Industry in Black Mountain, Canberra, recently found that salt tolerance is connected with a plant's ability to resume growth after osmotic shock—the shutdown in cell growth occurring fractions of a second after a plant is exposed to high salt concentrations.

Exploiting that trait, Tester's lab earlier this year used a three-dimensional camera to record minute changes in growth responses after wheat plants transplanted into salty soil went into osmotic shock. After crossing varieties and laboriously screening hundreds of plants, one of Tester's Ph.D. students, Karthika Rajendran, appears to have pinpointed a gene that helps plants resist osmotic shock.

Such mind-numbing screening will be automated and sped up when the Plant Accelerator roars to life. It will have a throughput of 2400 plants a day—10 times the capacity of current labs. Plants will travel by conveyer belt to stations that measure growth rate and color, a sign of tissue health.

Also expected to get a phenomics boost is an effort to replace rice's inefficient C3 photosynthetic pathway with the C4 pathway found in maize and 40 other plant species. For the same input of water and nitrogen, maize produces twice the carbohydrate content of rice. Researchers have tried to assemble the C4 pathway in rice using maize enzymes, but the efforts failed, perhaps because rice's subcellular structure prevented the enzymes from working in synchrony.

Phenomics tools can provide snapshots of cellular structure and diagnose steps along the way toward C4 metabolism in live plants. The International Rice Research Institute (IRRI) in Los Baños, Philippines, is screening rice varieties for those with a cellular architecture best suited to house the C4 enzyme assembly. In C4 plants, mesophyll cells turbocharge photosynthesis by delivering carbon dioxide

at 10 times atmospheric concentration to sugar-producing bundle sheath cells that surround the veins. For this transfer to work, there can be no more than three to four cells between the veins. IRRI's initial screens are for rice varieties with narrower spacing between the veins. Promising varieties will be shipped to HRPPC, which will use fluorescence microscopy and other tools to interrogate the plants. One approach is to look for a fluorescent signature from a complex of light-absorbing molecules called photosystem II: If these molecules' activities are muted in bundle sheath cells, it means the plant is becoming more C4-like.

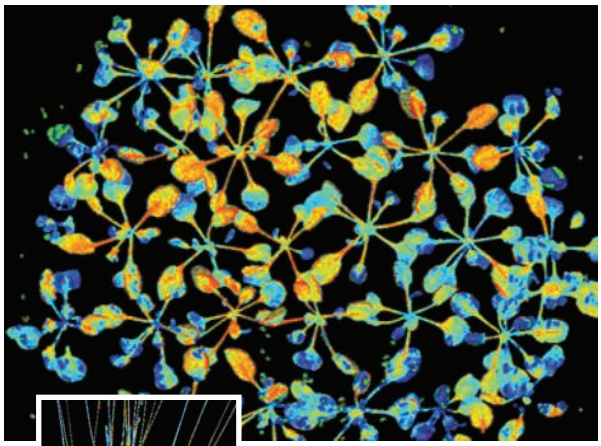

Energy efficient? Chlorophyll fluorescence, a measure of photosynthesis, in *Arabidopsis* seedlings and a wheat ear (*inset*). Blue depicts high photosynthetic rate, red depicts low. Large numbers of plants can be screened for stress response, for example, or for high yield.

Kramer's lab in Pullman, meanwhile, is examining the split-second reactions that capture some energy of impinging sunlight while dissipating more than 80% to prevent damage. "If we could reduce this regulatory loss by 1%, we might double yields," he says.

Plants vary in how much light they dissipate. The photosynthetic rate of giant cane (*Arundo donax*), a potential biofuel source, is many times that of rice. Most crops are less efficient and "far too conservative for biofuels use," Kramer says. "They're playing it too safe."

Breeders have never seriously attempted to rev up the photosynthetic rate, says Kramer. Indeed, some high-yield rice varieties have reduced photosynthetic rates. The problem is that the switches that set the photosynthetic rate are poorly understood. To penetrate this mystery, Kramer plans to use the equivalent of a car engine dynamometer: a spectrometer that gauges the photosynthetic engine. The cogs of the engine—carotenoids, plastocyanins, and cytochrome complexes—emit unique spectral signatures in their excited states.

Kramer hopes to probe the "wear and tear" costs of photosynthesis with an "idea spectrometer," a device his group designed that is inspired by the "tricorder" of *Star Trek* fame. At the moment, the spectrometer, the size of a pint of beer, must be wired to a leaf; the goal is to be able to wave it over a plant like the fictional tricorder. Kramer says he would freely provide the device to colleagues to compile a global database of plant performance. "We can push our crop plants harder," says Kramer. "The question is how far."

Kramer and other adherents think the emerging discipline of phenomics will help foment the next green revolution. We now have the tools "to make quantum leaps in crop breeding," says plant physiologist Robert Furbank, director of HRPPC. "These are the tools we need to feed and fuel the world." **–ELIZABETH FINKEL**

Elizabeth Finkel is a writer in Melbourne, Australia.

CREDITS: ROBERT FURBANK AND SUSANNE VON CAEMMERER

SCIENTIFIC PUBLISHING

Data Integrity Report Sends Journals Back to the Drawing Board

It seemed like a good idea: With digital data routine in nearly every scientific field, and growing concerns about doctored images and demands to share data, why not convene a set of experts to come up with general data-handling guidelines? But a National Academies panel found this task impossible. Instead, its report, released today, offers broad principles for dealing with data but calls on disciplines to work out the details themselves.

One trigger for the study was a particularly egregious case of scientific fraud: the faking of stem cell data by South Korean researcher Woo Suk Hwang, including cut-and-pasted cell images in a 2005 paper in *Science*. Faced with other examples of data manipulation, a group of journal editors asked the academies for advice in 2006. Academies officials added a second controversy they considered related: demands from a global-warming skeptic in Congress for data from the scientists who published the so-called hockey stick paper in 1998 in *Nature* that shows rising global temperatures since 1900. Then the academies convened 17 experts in fields from physics to sociology to look at issues of treating, sharing, and archiving research data.

Their conclusions, described in a report* this week (see Editorial, p. 368), boil down to three "principles" that are as uncontroversial as motherhood and apple pie: Researchers are responsible for ensuring the integrity of their data; data from published papers should be publicly accessible; and data should be properly archived.

The report also offers 11 recommendations urging scientists, institutions, journals, and other players to develop standards and provide proper training. The suggestions include a few new points—for example, data-sharing should include not just the raw data but also the computer programs used to analyze it. But there are no detailed guidelines.

The problem was that every time a panelist made a detailed proposal, another member would say it would not work in their field, says co-chair Phillip Sharp, a molecular biologist at the Massachusetts Institute of Technology (MIT) in Cambridge. So the committee couldn't be too specific, Sharp says. For example, says co-chair and emeritus MIT physicist Daniel Kleppner, astrophysicists don't really have issues with image manipulation because they work with public data sets, and if someone doctors an image, colleagues "can go right back and look" and catch it.

Journal editors seem a bit disappointed. The National Institutes of Health's Kenneth Yamada, an editor of *The Journal of Cell Biology*, which has worked out ways to screen for manipulated images that other journals have followed, calls the report's principles "an excellent foundation on which fields can build." But he suggests a "Phase Two" academies study focusing on digital imaging in biology. Katrina Kelner, managing editor, research journals at *Science*, who calls the report "welcome" and the principles "useful," expects journals themselves may have to work out the specifics. **–JOCELYN KAISER**

*Ensuring the Integrity, Accessibility, and Stewardship of Research Data in the Digital Age, The National Academies Press

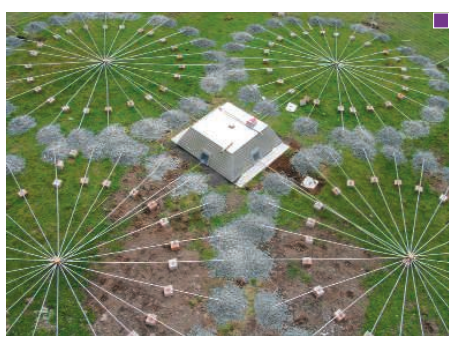

Test Ban Monitoring: No Place to Hide

A nearly complete global network can reliably spot secret nuclear explosions, researchers say. Will holdout nations now ratify the test ban?

VIENNA—On 9 October 2006, the collection of nations known to possess nuclear weapons gained a new member: North Korea. The country had tested a small nuclear device, equivalent to less than 1000 tons, or 1 kiloton (kT), of conventional explosives. It highlighted a vexing question for those trying to curb the spread of nuclear weapons: If the world community outlaws nuclear bomb tests, can it set up an effective system to police that ban?

A network of sensors designed to do exactly this—by detecting nuclear blasts anywhere on Earth—was taking shape when the North Koreans ran their test. It was being built under the auspices of the Comprehensive Nuclear-Test-Ban Treaty (CTBT), an international agreement that grew out of the Cold War and was codified in the 1990s. A decade later, it is still waiting to come fully into force.

CTBT is unique among nuclear treaties in that it includes a worldwide verification system financed by the signatories, an array of 337 sensor stations and laboratories scattered across 89 countries. The stations pick up seismic tremors in the earth, listen for acoustic signals in the air and oceans, and sniff out radionuclides carried on the wind. Although this monitoring network was only 60% complete in 2006, more than 20 of CTBT's seismic stations—one as far away as South America—immediately picked up signals from the North Korean test. In less than 2 hours, it delivered an automatic analysis of the blast's estimated time, location, and magnitude to states that had signed the treaty.

The network performed again in May of this year when North Korea carried out a second test. This time, the bomb was detected by 61 seismic stations, reflecting its larger blast and the network's growth. Within 48 hours, CTBT experts had narrowed down the location of the explosion to an area in North Korea just 10 kilometers across. "There could not be a clearer indicator of the need for these verification tools," say Tibor Tóth, head of the CTBT Organization (CTBTO).

Yet the treaty remains hamstrung: Although 181 nations have signed CTBT and 148 ratified it, the treaty does not ban tests, nor can it use its full arsenal of verification measures until all 44 states with nuclear weapons or reactors have ratified it. Nine have yet to do so, including the United States. In 1999, the U.S. Senate debated and rejected CTBT. Critics argued that the verification system would not be sensitive enough to detect cheating and, with a little ingenuity, a purposeful nation could conceal a test. But during the 2008 presidential election campaign, candidate Barack Obama said he would tackle this issue: "As president, I will reach out to the Senate to secure the ratification of CTBT at the earliest practical date."

Much has changed since the Senate rejected the treaty a decade ago. CTBT's monitoring system, barely begun in 1999, is now nearly 75% complete. And it has been scrutinized over the past year by hundreds of outside researchers. CTBT managers offered them access to data from the network so that they could test its readiness, probe its strengths and weaknesses, and suggest improvements. "This was potentially danger-

Network's four senses. Clockwise from top left: an auxiliary seismic station at Kerman, Iran; laying cable to an offshore hydroacoustic station, Juan Fernández Islands, Chile; radionuclide station, Resolute, northern Canada; infrasound detectors, Tristan da Cunha, southern Atlantic Ocean.

CREDITS: CTBTO

Published by AAAS

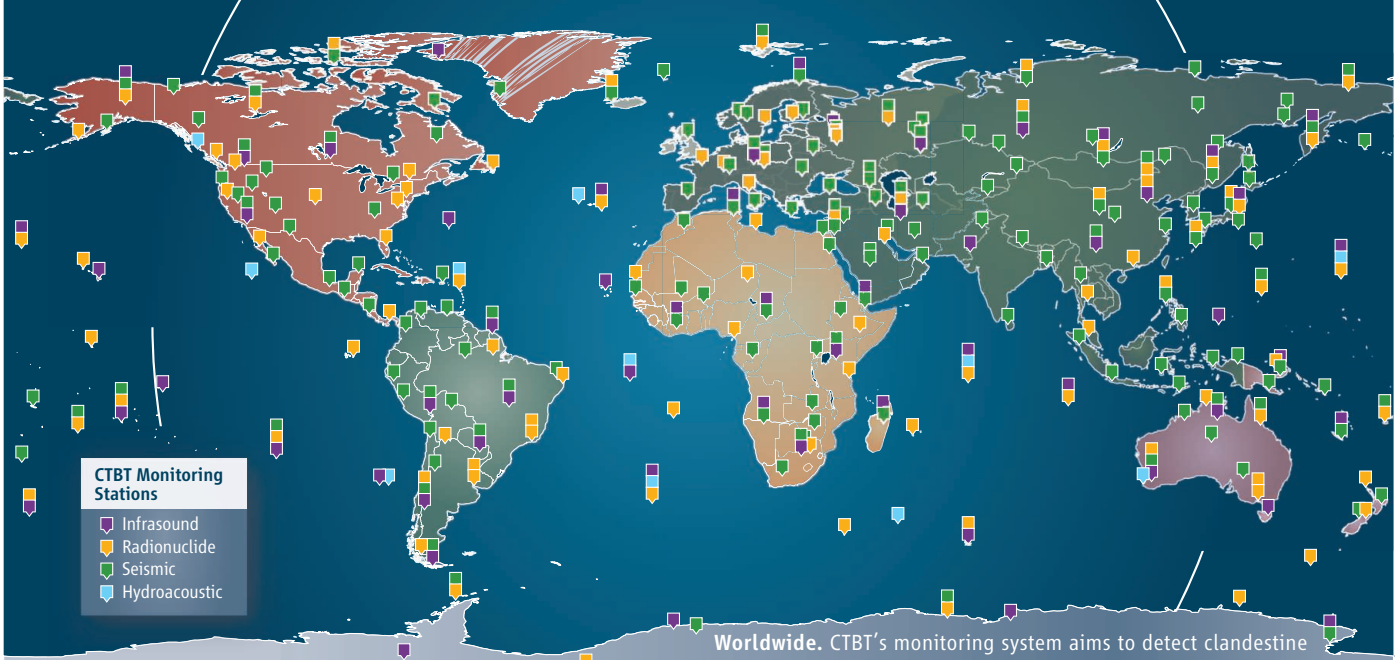

Worldwide. CTBT's monitoring system aims to detect clandestine nuclear explosions anywhere in the world with 337 stations using four different sensing techniques.

ous. They could have spotted flaws," says planetary scientist Raymond Jeanloz of the University of California, Berkeley.

Last month, those researchers were invited to Vienna for the first conference of this International Scientific Studies (ISS) program. The reviews were mostly positive: Many lauded CTBT's International Monitoring System (IMS) for the quality and global coverage of its data, declaring that in many parts of the world the network is more sensitive than the treaty requires. "[The ISS] was an amazingly successful process," Jeanloz says. Now supporters of CTBT are returning to the political challenge, trying to persuade holdout nations to come on board. "If we don't make this step, the whole thing is vulnerable to falling apart," says David Hafemeister of the Center for International Security and Cooperation at Stanford University in Palo Alto, California.

An ear to the ground

Because the best way to hide a nuclear test is to carry it out underground, the backbone of IMS is an array of 170 seismic stations: 50 primary stations that are online around the clock and 120 auxiliary stations that send data on request.

The treaty bans all nuclear explosions, no matter how small, but for practical reasons IMS is designed to detect an explosion equivalent to 1 kT or bigger. This corresponds to a seismic shock of roughly magnitude 3.5. (The bomb that was dropped on Hiroshima was about 15 kT.) This cutoff was chosen in part to reduce noise in the system, because hundreds of earthquakes and mining explosions every day produce shocks below this level. A threshold lower than 1 kT would overwhelm the CTBT's International Data Center (IDC) in Vienna with events requiring analysis for signs of a nuclear test. And weapons experts have said that blasts smaller than 1 kT would not be militarily useful to a fledgling nuclear power.

Seismic events produce a variety of waves that can be picked up by monitoring stations. Body waves, which travel deep through the earth, come in both P-waves, which oscillate in the direction of travel, and S-waves, which vibrate crosswise. Surface waves are slower, but they do the damage following earthquakes. Researchers have learned to identify which direction body waves are coming from, and the differences in arrival times reveal the distance of the source. Surface waves give information on the depth of the event and its magnitude. The tricky part of nuclear weapons verification is distinguishing nuclear tests from the natural and innocent manmade events.

Online
sciencemag.org
Podcast interview with author Daniel Clery.

"Different events produce different wave types in different proportions," says seismologist Paul Richards of the Lamont-Doherty Earth Observatory of Columbia University in Palisades, New York. However, a mine collapse in Germany in 1989 and two others in 1995 in Russia and the United States cast doubt on the precision of seismic fingerprinting because all three looked disturbingly like nuclear tests to seismologists. After much analysis, researchers found an unmistakable difference: The signal from a mine collapse starts with a trough as the ground moves inward, whereas an explosion always starts with a peak.

This knowledge gave seismologists confidence that IMS would be able to spot nuclear explosions. The nascent system was put to the test in August 1997 when stations detected an event of magnitude 3.3 close to Novaya Zemlya, the Soviet Union's old Arctic test site. It seemed as though Russia might be testing the abilities of CTBT. Analysis of the signal soon showed the source to be offshore beneath the Kara Sea, but the surface waves were too weak to be of any use in distinguishing between a blast and a quake. Researchers used a new technique, which looks at "regional" seismic waves that have traveled less than 1000 kilometers through the crust and upper mantle. By comparing the magnitudes of the P-waves and S-waves, they were able to confirm that the event was an earthquake.

Researchers at the ISS meeting pointed out that in certain areas, such as around former nuclear test sites, stations have been sited carefully to ensure that monitoring is more sensitive than required by the treaty. At Novaya Zemlya, a test of 0.1 kT would probably not go undetected. This resolution is something "we dreamed of" 15 years ago, says Yves Caristan, director of the Saclay Institute of Nuclear Studies of France's Atomic Energy Commission. "There has been significant improvement over the past few years, particularly in the use of regional seismic data," says Jay Zucca of the Lawrence Livermore National Laboratory (LLNL) in California.

Some researchers said detection could be improved with more stations around the Southern Ocean and in India and Pakistan. (Neither has signed the treaty.) And some

SOURCE: CTBTO

Published by AAAS

Comprehensive Test Ban: The Long Road

In the early 1950s as the extent of radioactive fallout from atmospheric blasts became widely known, the calls grew louder for a ban on nuclear weapons testing. Steps over the next half-century led to the current effort for a comprehensive ban.

1963 The Partial Test Ban Treaty forbade nuclear tests in the atmosphere, oceans, and space. The treaty did not have its own verification measures but relied on monitoring by signatory states.

1976 An ad hoc Group of Scientific Experts (GSE) began assessing whether it was possible to police a complete testing ban. GSE was made permanent by the United Nations Conference on Disarmament in 1982. Although there was little diplomatic movement during the Cold War years, GSE honed its skills at detecting nuclear explosions.

1991 Countries that had signed the partial test ban agreed to work toward a total ban; formal negotiations began in 1993.

1996 After 3 years of intense bargaining, the Comprehensive Nuclear-Test-Ban Treaty (CTBT) was opened for signature in September at the United Nations headquarters in New York City; it was signed that day by all five nuclear weapon states and 66 others. To date, 181 countries have signed, leaving only 14 outside of it. The treaty also requires ratification, a political process—usually a parliamentary vote—that legally binds the country to abide by CTBT. Some 148 have ratified it so far. But the negotiators set a high bar for the treaty to come into full force: They compiled a list of all countries that in 1996 had either nuclear weapons or reactors for power or research and required that all 44 must ratify. Nine have yet to do so—China, North Korea, Egypt, India, Indonesia, Iran, Israel, Pakistan, and the United States.

1999 The U.S. Senate failed to ratify CTBT by a vote of 51–48 in October.

2008 Candidate Barack Obama said: "As president, I will reach out to the Senate to secure the ratification of the CTBT at the earliest practical date." To be approved, the treaty must be endorsed by two-thirds of the Senate.

–D.C.

called for boosting the network further by using auxiliary stations more regularly and gathering data from the many thousands of civilian seismic stations. Gideon Frank, vice chair of the Israel Atomic Energy Commission, made a pitch for basic research: "Noise is still a problem. We need to develop a much deeper understanding of natural events to improve screening," he says.

Watching the waves

IMS also has a smaller network of sensors to listen for explosions carried out underwater, just above the ocean surface, or below the ocean bottom. Sound travels very efficiently in water: Kiyoshi Suyehiro of the Institute for Research on Earth Evolution in Kanagawa, Japan, says a 20-kilogram test charge of TNT was detected 16,000 kilometers away. As a result, IMS has just 11 hydroacoustic stations positioned around the vast expanses of the Atlantic, Pacific, and Indian Oceans in the Southern Hemisphere. Sound propagates in deep water especially well at a depth of about 1000 meters in what is known as the sound fixing and ranging (SOFAR) channel. Six of the IMS's hydroacoustic stations consist of SOFAR hydrophones in deep water as much as 100 kilometers from the coast of remote islands. Each is a set of three hydrophones anchored to the seabed and connected to shore-based stations by cable.

In addition to hydrophones, IMS has five stations to detect T-phase waves, the third or tertiary waves, after P and S, from a seismic tremor. These seismic stations pick up waves that have traveled into the ocean as hydroacoustic waves and then back into the ground. To get the best results, such stations need to be sited near coasts or on small islands. Researchers here were enthusiastic about the scientific spinoff of the hydroacoustic network because nothing on this scale has been available before. "The data from this network are unprecedented. Many applications … we haven't even touched yet," says Harry Miley of the Pacific Northwest National Laboratory in Richland, Washington.

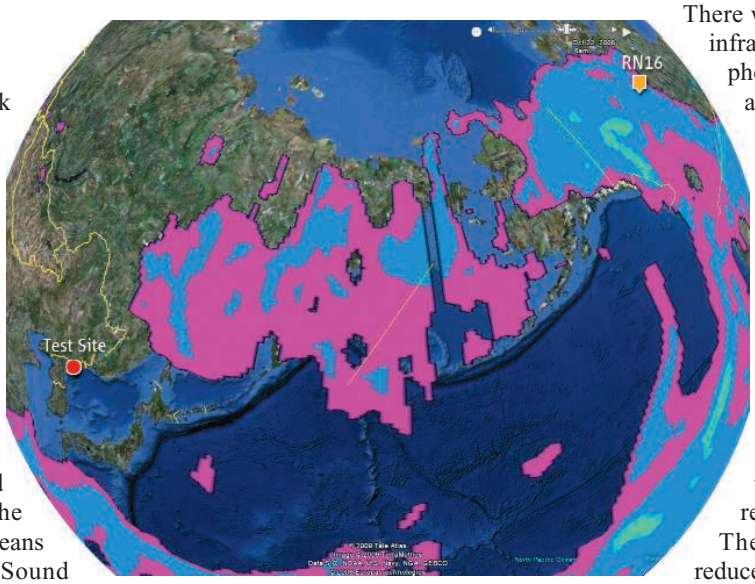

Blowing in the wind. This atmospheric transport model shows how radionuclides spread from North Korea's 2006 nuclear test (*bottom left*) to the RN16 monitoring station in Yellowknife, Canada (*top right*).

To listen for test explosions in the atmosphere, IMS has revived the almost-forgotten science of infrasound. Very low frequency sound, or infrasound, was first detected in 1883 following the eruption of Krakatoa in Indonesia. Infrasound waves shattered windows hundreds of kilometers away and circled the globe seven times, leaving a trace on microbarometers far from the volcano. There was much scientific interest in infrasound during the era of atmospheric testing, but it died away as atmospheric testing was curtailed. CTBT has caused a "renaissance" in infrasound research, says Elisabeth Blanc of France's Atomic Energy Commission.

An infrasound detector consists of two dozen pipes, each about 3 meters long, radiating from a central chamber. Arriving infrasound waves travel down the pipes; the minute changes in pressure they cause in the chamber are registered by a microbarometer. The pipe arrangement serves to reduce noise from wind, and at windy sites a number of detectors are combined to further improve the signal-to-noise ratio. Thirty-nine of a planned 60 infrasound stations are now operating and appear to be working well. The 2004 eruption of Manam in Papua New Guinea was detected by 13 IMS stations, some more than 1000 kilometers away. In 2005, five IMS stations, up to 1500 kilometers distant, picked up the Buncefield oil depot explosion north of London. In 2008, a bolide that exploded over Oregon and the explosion of

CREDIT: ADAPTED FROM CTBTO

an ex-military ammunition depot in Gërdec, Albania, were both detected. "This is far larger and more sensitive than any previous network," says Alexis Le Pichon of France's Atomic Energy Commission. Although challenges remain, he says, including dealing with wind noise and seasonal changes to propagation, "the 1-kT goal [for IMS] is fully achieved."

Irrefutable evidence

No matter how well CTBT seismic and sound networks function, there's no "smoking gun" evidence of the nuclear nature of an explosion unless radionuclides are detected. For that reason, IMS's fourth and final pillar is dedicated to radionuclide monitoring. Although this system can confirm that an explosion was nuclear, it has a disadvantage: It can be days or weeks after an event before any data are recorded. Fifty-six out of a total of 80 radionuclide stations are already operational. All will have particle detectors, essentially air filters that gather specks of dust carried on the wind and which are removed and checked daily in a gamma-ray detector for radioactive isotopes.

Half the stations will also be equipped to detect radioactive noble gases, including xenon. Noble gases do not react with anything and so are more likely to escape through cracks in the rock into the air following an underground test. Some xenon isotopes have half-lives measured in hours or days; detecting them suggests that an event happened recently. "The network can detect tests well below 1 kT anywhere in the world," says Wolfgang Weiss of Germany's Federal Office for Radiation Protection.

To compensate for the time lag between the release of radionuclides from a detonation and their detection, IDC uses sophisticated atmospheric transport models that can reconstruct the likely travel paths particles might have followed. The computers are constantly fed weather information from the World Meteorological Organization (WMO). IDC staff can run these models backward to see where detected radionuclides might have come from and whether this corresponds with a suspected test. "The technology has come a long way in the past 10 years, especially with the use of satellite data," says WMO's Peter Chen.

The radionuclide network worked perfectly following the 2006 North Korean test. Twelve days after the seismic signal was recorded, xenon was detected at a station at Yellowknife in Northern Canada, and transport models showed it could have come from Korea. This success was all the more reason for surprise when, after this year's North Korean test, no radionuclides were detected. "The sensors were working fine," says Anders Ringbom of the Swedish Defence Research Agency. "If there was a prompt release, … we would have seen it."

This unexpected blank has renewed debate about evasion scenarios: methods by which a potential cheat could try to fool IMS into not recognizing a test. Decoupling, for example, is a way of reducing the seismic signal of an underground explosion by carrying it out in the center of a large cavity. This is even more effective if the surrounding rock is soft. The only successful fully decoupled test was carried out by the United States in 1966: a 0.38-kT blast in a 34-meter-wide salt cavity. But such small tests are not militarily useful. Researchers estimate that to fully decouple a 5-kT explosion would require a cavity 85 meters across, almost large enough to accommodate the Statue of Liberty with its pedestal. "It would require an engineering effort akin to building the World Trade Center. … It's possible but not really practical," says Andreas Persbo of the Verification Research, Training and Information Centre in London.

Similarly, it is possible to contain radionuclides by exploding a bomb of the right size in a rock that will melt to form a glassified cage impervious to gases. Such evasion takes skill and considerable experience with nuclear weapons, neither of which experts believe North Korea yet has. Many at the ISS meeting think that on this occasion the North Koreans just got lucky. "Maybe it was well-contained purely by chance. It is clear from the seismology that it was a huge explosion," says Lars Ceranna of Germany's Federal Institute for Geosciences and Natural Resources.

The puzzle created by the North Korean blast this year, CTBT proponents say, highlights the importance of forging ahead and ratifying the treaty. Once it is fully in force, its Executive Council, if faced with a suspected test like the one in May, can call for CTBT's ultimate verification measure: an on-site inspection. Within days of a suspected test, a team of up to 40 people can be on the scene and scouring an area up to 1000 square kilometers using overflights, mobile radionuclide detectors, microseismic arrays to detect aftershocks, gamma-ray detectors, ground-penetrating radar, magnetic and gravitational field mapping, and electrical conductivity measurements. CTBTO held a full-scale dress rehearsal of an on-site inspection last year in Kazakhstan. "Recent events in Korea point up the importance of on-site inspection," says LLNL's Zucca. "There was obviously an explosion; there was no measured xenon. On-site inspection can resolve these questions."

CTBT officials were pleased by the positive report card from the researchers at the ISS meeting. Their approval may even help persuade some of the holdout governments to reconsider their position on the treaty. But in the end, the decision on whether to put the treaty to use will not be a technical one. "How good is good enough?" asks Jenifer Mackby of the Center for Strategic and International Studies in Washington, D.C.: "That's for the politicians to decide."

–DANIEL CLERY

CREDIT: CTBTO

Ground truth. Inspectors collect air samples to test for radioactive argon during a 2008 full-scale field trial of an on-site inspection in Kazakhstan.

Elusive. Migrating bats have proven tough to study.

ECOLOGY

Deadly Flights

Massive wind turbines seem to be killing more and more migratory bats, prompting research into these neglected creatures and efforts to minimize the toll

On a warm, late-April night, Volker Kelm drives his battered station wagon across a bleak expanse of scrubby fields a few kilometers from the German border with Poland. The site is a brown coal strip mine owned by the German energy giant Vattenfall; the only other vehicles on the access roads are massive earthmovers. The Berlin-based environmental consultant parks on a dirt access road and pulls out what looks a bit like an old-fashioned tape recorder but is actually a monitor capable of picking up ultrasonic calls from bats ranging up to 120 kilohertz.

Tuning the detector to the 32-kilohertz range favored by *Nyctalus noctula*, one of Europe's most common bat species, Kelm starts scanning the sky. At 20:59, just as the day's last light dwindles away, the bat detector begins to chirp. Kelm watches as a trio of *Nyctalus* bats—known as the common noctule all across Europe—makes their way across the field in the direction of a long line of blinking red lights on the horizon: dozens of wind energy turbines, a night's flight away.

With 40-meter blades whose tips move at up 360 kilometers per hour, wind turbines are what bring Kelm out tonight to spy on bats. Vattenfall wants to build a new wind farm on a tapped-out part of the mining site, but the turbines have a reputation for killing bats and European regulations compel the company to hire someone to conduct an environmental assessment. At a glance, the mine-scarred ground seems an unlikely home to bats. "For bats, the countryside here is not that interesting," Kelm says. "There are no meadows, no rivers—it's really a desert here."

But scientists have learned that even if there are no bat roosts nearby, wind turbines can pose a threat. Like many birds, some bat species are migratory, moving long distances on a seasonal basis, usually from summer feeding grounds to winter hibernation sites. The common noctule, for example, lives in forests during the warm summer and fall months, but may travel hundreds of kilometers to caves to hibernate. Fortunately for Vattenfall, the three *Nyctalus* bats spotted by Kelm are the only migratory species he will see all night, despite also using night-vision goggles.

Kelm's surveys won't always bring such good news. With wind power booming around the world—in Germany alone, nearly 20,000 wind-energy installations have been built since 1990—researchers are seeing a marked increase in dead bats. The turbines simply rotate their blades too quickly for the winged mammals to avoid. "There's nothing that fast in nature," Kelm says. "They're using sonar to look for butterflies and insects, not windmill blades."

The deaths have led to a flurry of research on migratory bats and their behavior. "The problem with bats and wind energy has pushed a lot of work that wouldn't have occurred otherwise," says Edward Arnett of the Austin, Texas–based nonprofit Bat Conservation International. Indeed, at a January conference in Berlin on migratory bats, wind farms were a dominant theme. Scientists are racing to figure out what brings the bats in contact with wind turbines, and what can be done to save them.

There are no easy answers, in part because little is known about migratory bats. "There are huge questions: 'How big are the populations? Where do they migrate? Are they really being killed by wind farms?' Sometimes it looks like that, but we don't know," says Martin Wikelski, an expert on bat migration at the Max Planck Institute for Ornithology in Radolfzell, Germany. And without concrete data, persuading government regulators and energy companies to relocate proposed wind farms, let alone change the operations of existing turbines or shut them down, is difficult.

Bat signals

The first hints of a problem were reported in Europe almost a decade ago, when ornithologists and environmental consultants looking for evidence of bird collisions at wind-energy sites began noticing dead bats on the ground. The bat fatalities became particularly apparent in Germany, which has the most wind-energy facilities in the world and is a central location in Europe that makes it a crossroads for migratory birds and bats.

Still, getting definitive death counts wasn't easy. Bats are small, light, and hard to spot without experience and training. "They look like little rocks on the ground. They sort of blend in because of their size and color," says Boston University bat biologist Thomas Kunz. By the time the sun comes up on a field full of bat casualties, scavengers such as foxes and coyotes may have made off with many of the carcasses, skewing the true number of bat kills even further.

In the fall of 2003, consultants looking for bird kills at Mountaineer, a wind-energy facility located atop a wooded, West Virginia mountain ridge, found large numbers of eastern red bats and hoary bats dead near the turbine blades. "There were a few hundred bat fatalities, unlike anything in the literature," says Paul Cryan, a U.S. Geological Survey research biologist based in Fort Collins, Colorado. Adjusting for the limitations of ground surveys, researchers estimated that the Mountaineer windmills alone were killing between 1400 and 4000 bats a year (*Science*, 9 April 2004, p. 203). Suddenly, the problem was no longer just a European one.

As dead bats were tallied on both sides of the Atlantic, one thing rapidly became clear: Wind-energy plants aren't equal-opportunity killers. "Migratory bats are the ones that die in wind parks, not the locals," Kelm says. Indeed, in Germany, 90% of bat fatalities at wind farms are from just five species, all migratory. North American researchers found similar patterns.

Unfortunately, migratory bats are notoriously uncooperative research subjects: They're nocturnal, solitary, and too small to be tracked with current GPS or radio transmitter tags, which at a minimum of 16 grams weigh almost as much as the average 20-gram bat. The traditional method to study these bats has

been banding—attaching lightweight metal tags to a bat's forearm—but that relies on someone finding and reporting the tag, either by catching the bat somewhere along its migration route or finding a dead one. Still, thanks to banding programs that date back almost a century, German researchers have a general idea of European bat migration. It tends to be latitudinal, as opposed to the north-south migrations of birds, for example, but the data are frustratingly vague.

U.S. bat scientists have had it even worse. Because of concerns among biologists over disturbing bats during their hibernation period, there has been a moratorium on bat banding in North America for decades. As a result, there's almost no information on where migratory bats in the United States come from. "We don't really know where they are for much of the year," says Cryan. "They're not an easy animal to follow."

With no way to document the migration corridors the animals use, researchers have turned to what biologist Erin Baerwald of the University of Calgary in Canada calls "destructive sampling," examining the corpses of dead bats found below turbines for clues to their diet during migration, brain development, genetics, age, and cause of death. Dissecting these bats has yielded some surprises. A study out last summer showed that many are killed not by collisions with turbine blades, but by barotrauma, fatal bubbles or ruptures in bats' lungs and hearts caused by the low-pressure zones the massive blades create in their wake.

Biologists are also deploying a rapidly advancing array of technological tools to study how bats interact with the blades and towers, some of which now reach as high as 150 meters. Researchers can now install "batcorders" inside turbines that are capable of recording hundreds of hours of bat calls. Other techniques include thermal imaging to watch bat behavior around turbines and night-vision goggles to spot their flight paths.

The data provided by these gadgets are yielding new insights into migratory bat behavior and clues as to how to reduce the impact of wind farms. Christian Voight, a behavioral physiologist at the Leibniz Institute for Zoo and Wildlife Research in Berlin, notes that during their long-distance travels and hunting forays, migratory bats don't stick as close to the ground as locals do, and that may put them on a collision course with the blades of windmills.

There's even a possibility the turbines actively attract bats. Researchers have observed tree bats flocking around tall trees during mating season, perhaps using them as rallying points for mating and roosting. As the most prominent object on the horizon, windmills may look like particularly tall trees to migrating bats crossing unfamiliar landscapes. That has led to concerns that preconstruction surveys like Kelm's are not that useful, because bat activity could increase after a turbine is built.

Lethal blades. Hoary bats (*Lasiurus cinereus*) are among the bats most often found dead (*inset*) near wind turbines in North America.

CREDITS: PAUL CRYAN

Minimizing the danger

Amid all the uncertainties, scientists are gathering potentially useful data. The activity of migratory bats spikes in the late summer and early fall, when the animals have given birth to their young and are actively hunting to store up energy for winter hibernation. "During the fall migratory period, there's twice as many bats and birds out there as in the spring," Kunz says.

And bat recorders placed on and around windmills detect the highest levels of bat calls on warm, dry nights when wind speeds are below 6 meters per second—ideal conditions for insects, and for the bats that feed on them. Drawing on such data, Arnett and bat biologist Oliver Behr of the University of Erlangen-Nürnberg in Germany have set up separate experiments in the United States and Germany to see if feathering windmills—shifting the angle of the blade so that it's parallel to the wind—on nights when bats are most likely to be active reduces bat fatalities. Arnett, for example, worked with Portland, Oregon–based Iberdrola Renewables to randomly feather windmills at a Pennsylvania facility over the course of 3 months last year. The results were encouraging: Daily ground surveys during the study found between 53% and 87% fewer bat fatalities at the inactive windmills.

And because bats tend to be most active on nights with low wind speeds, Arnett says the financial impact of "operational mitigation" would be minimal. "The projected loss to the facility was 0.3% to 1% of annual production," Arnett says. "We think it's worth it to reduce the fatalities." This summer, Arnett is continuing the study and also testing acoustic devices that might drive bats away from windmills by interfering with their sonar abilities, much as marine biologists have similarly warned dolphins away from fishing nets.

For his part, Kelm will be back at the German strip mine every 10 days for the next 5 months, listening for the calls of the common noctule. Ironically, the very wind turbines that threaten these creatures of the night have helped scientists understand them better. "In the last 15 years, people have started really talking about bats, really brought them out of the darkness and into the light, so to speak," Kelm says. "Wind energy provoked research and has provided results."

–ANDREW CURRY

Andrew Curry is a freelance writer based in Berlin.

MICROBIOLOGY

Phytoplasma Research Begins to Bloom

Spread by insects, bacteria called phytoplasmas co-opt plant development, sometimes creating beauty but more often bringing devastation

Tainted beauty. Commercial poinsettias owe their lushness to a bacterial infection.

Ancient Chinese rulers and lovers of Christmas decorations have been unwitting fans of an obscure group of bacteria called phytoplasmas. When these microbes infect peonies, the plants' flowers can emerge not in the typical red or yellow colors, but in a delicate green. This hue was considered so attractive and valuable about 1000 years ago in China that the Song Dynasty's imperial court received a special annual tribute composed of the blossoms. More recently, phytoplasmas have helped brighten winter holidays by transforming otherwise gangly poinsettias, with their eye-catching red leaves, into bushy ornamentals.

But most effects of these microbes on plants are far from pretty. They shrivel grapes in Europe and Australia; stunt corn growth in South America; destroy pears and apples in the United States and Europe; ruin peanuts, sesame, and soybean in Asia; and sicken elms, coconuts, asters, and hydrangeas on multiple continents. Just one 2001 phytoplasma outbreak in apple trees caused a loss of about €25 million in Germany and about €100 million in Italy. Epidemics among coconut palms have destroyed the livelihoods of many people in Africa and the Caribbean who depend on the trees for nourishment, building materials, and income. And as the world warms up, these attacks on food crops, lumber and shade trees, and ornamental flowers will likely grow, in part because the insects that transmit the bacteria are expected to expand their ranges north and south.

For all the destruction that phytoplasmas inflict, one might expect that dozens of agricultural companies and academic labs have generated abundant amounts of information about them. But study of these plant pathogens got off to a slow start. For almost half a century, plant pathologists thought phytoplasmas were viruses. To this day, the inability to grow these bacteria outside plants or insects hinders efforts to get a handle on their biology and genomes. However, the knowledge scientists have managed to glean has nurtured their appreciation for the diverse talents that these bacteria demonstrate.

Indeed, whereas phytoplasmas are more petite and possess smaller genomes than most bacteria, they manage a complex life cycle that involves two distinct environments: the sugar-conducting tissue—or phloem—of plants and various organs of the sap-sucking insects that spread them. It's "pretty amazing" that "they seem to do so well in both situations," says Amy Charkowski, a plant pathologist at the University of Wisconsin, Madison.

In 2004, scientists published the first full phytoplasma genomic sequence and, since then, they've completed three additional ones. For the small band of biologists studying these microbes, sequencing the genomes is "the most exciting thing that's happened in the last decade," says Assunta Bertaccini, a plant pathologist at the University of Bologna in Italy. With that information, researchers have begun to elucidate how phytoplasma proteins manipulate plant physiology and insect behavior, findings that might inspire novel measures to stem the devastating agricultural infections around the world.

Viral blinders

In the 1920s, researchers began to go astray when they tried to pin down the cause of aster yellows, a disease that destroys crops, orchards, and ornamental plants. Scientists established that insects spread this malady, an observation that fostered the notion that it was yet another viral blight transmitted by the creatures. Indeed, some symptoms of the disease, including the yellowing that begat its name, resembled those of known viral infections. For those reasons and more, scientists spent the next 40 years convinced that a virus, or viruses, causes yellows-type diseases and additional insect-transmitted scourges where there was no standard evidence of bacteria or fungi. "The most prominent people knew it was a virus, so we looked for a virus," recalls virologist Karl Maramorosch of Rutgers University in New Brunswick, New Jersey. "But we didn't find it."

Scientists missed clues about the true culprit, says Maramorosch. In 1957, he noticed that insects injected with both the antibiotic tetracycline and material containing the infectious agent did not subsequently give aster yellows to plants. But Maramorosch knew that tetracyclines have no effect on viruses, so he concluded at the time that unusually high temperatures in the greenhouse—rather than the drug—prevented pathogen transmission. "I missed the boat by … years because I didn't repeat that experiment," Maramorosch says.

Finally, in 1967, Yoji Doi and colleagues at the University of Tokyo used electron microscopy to discover structures that resembled bacteria called mycoplasmas in plant tissue afflicted with presumptive viral infections. Like mycoplasmas—which cause respiratory ailments and other diseases in people and animals—the plant microbes were unusually small and lacked rigid cell walls. Additional tests established that the pathogens succumbed to antibiotics.

Doi's findings stimulated a flurry of research that linked these mycoplasma-like organisms to many other "atypical virus" plant diseases. In the 1980s, scientists began isolating pieces of bacterial DNA from afflicted plants. They developed diagnostic techniques and categorized the microbes based on shared sequences and other DNA patterns. The plant bacteria proved to be only distantly related to mycoplasmas and, in 1994, researchers coined the name phytoplasma.

CREDIT: ISTOCK.COM

Unlike most bacteria that sicken plants, phytoplasmas reside within cells rather than in the surrounding space. They duplicate only inside plants or insects, a property that makes them hard to study. The inability to grow pure cultures in laboratory broth renders even some basic experiments impossible. For example, scientists can't purify a suspect phytoplasma and inoculate healthy plants to test whether it causes a given disease. Even sequencing their genomes proved challenging because the bacterial DNA must be separated from that of the plants or insects they infect.

Sowing host changes

Phytoplasmas trigger symptoms that suggest they interfere with normal plant development. The bacteria tend to promote vegetative growth—producing plants with extra leaves, shoots, and branches—and to quash reproductive activities such as flower formation. The microbes also promote dwarfism, turn normally nongreen parts green, elicit general yellowing, and cause "witches' broom," a condition in which branches cluster and grow dense.

With the genomes in hand, researchers have begun to look for proteins that enable phytoplasmas to hijack plant processes. Using computer programs, they have pinned down genes for proteins that the bacteria likely secrete into the cells they infect.

Earlier this year, molecular biologist Saskia Hogenhout of the John Innes Centre in Norwich, U.K., identified such a gene from Aster Yellows-Witches' Broom (AY-WB) phytoplasma. The gene contains a "nuclear localization" sequence, which suggests that the protein it encodes might be able to access the host cell's DNA. This observation intrigued Hogenhout because it raised the possibility that the protein, secreted AY-WB protein 11 (SAP11), alters plant-cell gene activity. The *sap11* gene turns on in AY-WB-infected plants and, as predicted by the presence of the localization sequence, its protein accumulates in plant cell nuclei, Hogenhout's team reported in the January issue of *Molecular Plant-Microbe Interactions*.

Like other phytoplasmas, AY-WB is found only in the phloem, yet the researchers documented SAP11 in other tissues, suggesting that the protein could exert widespread effects on plants. Indeed, Hogenhout says that when her team engineered *Arabidopsis thaliana* to manufacture SAP11 in almost all of its cells, the mustard plant displayed many signs of AY-WB infection, providing additional evidence of the protein's role in disease. SAP11 production or AY-WB infection modifies the activity of plant genes that participate in development, she adds, "so that's satisfying."

Shigetou Namba, a plant pathologist at the University of Tokyo, and colleagues have uncovered a different virulence protein, this one from the OY phytoplasma, which causes a disease called *Tengu-su* (Tengu's nest). Affected plants develop small, short branches that look like the nest of Tengu, a supernatural creature from Japanese folklore.

The Tokyo team began its study by identifying 30 proteins that are likely to be secreted from OY phytoplasma, based on DNA sequences. They next put the gene for each of these proteins into an herb called *Nicotiana benthamiana*, one per plant. Twenty-nine of the plants looked normal, but the 30th developed witches' broom and dwarfism, the researchers reported in the 14 April issue of the *Proceedings of the National Academy of Sciences*. They called that symptom-causing bacterial protein TENGU. Like SAP11, TENGU appears outside the phloem in infected plants. "The molecules can reach farther than the bacterium," says Namba. "These kinds of small proteins might [aid the] survival of microorganisms that are restricted to phloem tissues."

Studies of *A. thaliana* engineered to contain the *tengu* gene revealed that the activity of more than 900 genes changed in response to the protein. Among the many genes whose activity levels dropped, at least a dozen contribute to signaling by the hormone auxin, which normally ensures that plants grow from their upper tips. Suppression of those genes might explain the witches' broom, Namba suggests.

The possibility that SAP11 and TENGU govern plant-gene activity challenges the prevailing idea in the field that phytoplasmas cause symptoms by depleting nutrients or growth regulators, says Nigel Harrison, a plant pathologist at the Fort Lauderdale Research and Education Center of the University of Florida. The new work "implies that phytoplasma parasitism does not just involve eating the sap," he explains. "The bacteria are influencing plant development, maybe to produce more of what they want, by regulating the plant genome."

Who knows what phytoplasmas "want," but the myriad ways they modify plants increase the longevity and breeding success of some insects that the bacteria use for transmission. The mechanism of this phenomenon is currently unknown, but researchers note that the additional vegetative tissues induced by infection expand the territory where insects can feed and lay eggs. Hogenhout's preliminary work with the leafhopper *Macrosteles quadrilineatus* shows that feeding it plants engineered to produce SAP11 increases the insect's reproductive output. "That's really cool because it means that phytoplasma molecules exert control beyond their direct interactions with plants," says Hogenhout. "Phytoplasmas that can generate more insect vectors are more likely to survive and spread."

The bacteria can even broaden an insect's host range, somehow making normally inhospitable plants more welcoming. Decades ago, Maramorosch noticed that aster yellows disease lengthens the normally short survival time of *Dalbulus maidis* on asters.

What's more, phytoplasmas lure to plants the very insects needed to spread the microbes. The phytoplasma *Candidatus* P. mali causes apple proliferation disease, a condition characterized by witches' broom and small, tasteless fruit. The microbe prods apple trees to produce a substance that attracts a sap-sucking insect called *Cacopsylla picta*, chem-

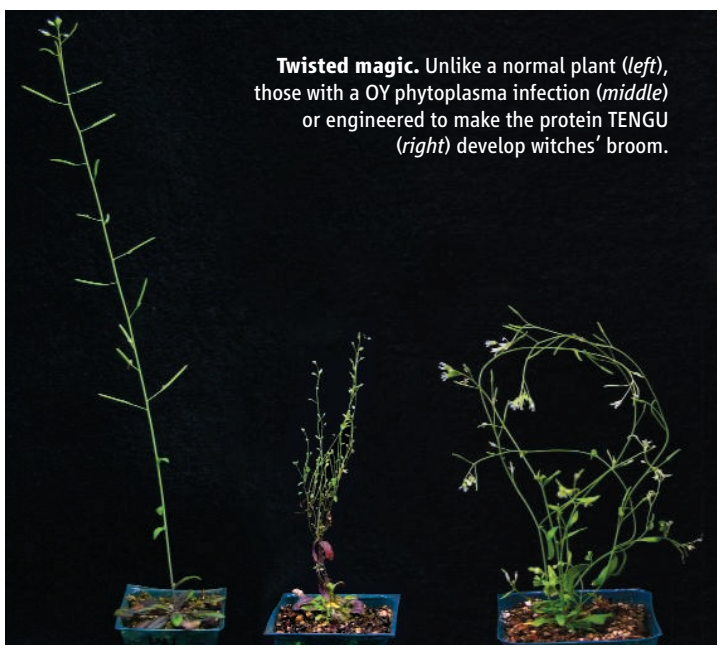

Twisted magic. Unlike a normal plant (*left*), those with a OY phytoplasma infection (*middle*) or engineered to make the protein TENGU (*right*) develop witches' broom.

CREDIT: SHIGETOU NAMBA

ical ecologist Jürgen Gross of the Federal Research Centre for Cultivated Plants in Dossenheim, Germany, and colleagues reported in the August 2008 issue of the *Journal of Chemical Ecology*. The phytoplasma-induced apple-tree compound is a chemical called β-caryophyllene that preferentially attracts *C. picta* over other insects, the researchers subsequently showed. Gross's team has now exploited this preference, creating an insect trap that might help monitor or capture *C. picta* in the field.

Analyses of the phytoplasma genome sequences hint that researchers still have a lot to learn about these formidable microbes. Three of the four genomes contain large amounts of repeated DNA sequence, and even the fourth one carries multiple copies of almost 100 genes, a noteworthy observation, given that phytoplasmas have unusually small genomes, even for bacteria. The repeats might allow phytoplasmas to "try something new" by adapting genes and other DNA to new functions without losing essential capabilities, speculates Robert Davis, a plant pathologist at the Agricultural Research Service at the U.S. Department of Agriculture in Beltsville, Maryland.

The phytoplasmas with sequenced genomes represent only a few twigs on the genus's evolutionary tree—and this collection does not include any from the branch that contains the majority of *Candidatus* phytoplasma species, which cause significant diseases and carry some of the smallest phytoplasma genomes. Screening healthy plants might reveal additional phytoplasmas, including ones that live peacefully within these hosts, say researchers. Harvesting genome sequences from this group of organisms could provide valuable information for understanding symbiosis and fuel ongoing studies of evolution as well as pathogenesis.

Fighting back

Given the damage phytoplasmas wreak, researchers want to develop ways to keep the microbes in check, but they need more basic knowledge to curb transmission, says Phyllis Weintraub, an entomologist at the Agricultural Research Organization of Gilat Research Center in Israel. Most control tactics depend on identifying the insects that carry a given pathogen, so researchers have information about how the vectors reproduce and migrate, how far they can fly, and what else they feed on. However, "there are a great number of [phytoplasma] diseases for which the vector is unknown," Weintraub says.

In addition, the complex ecology of phytoplasmas and their hosts plagues plant pathologists. A given phytoplasma species can infect a few or many kinds of plants and cause a wide range of symptoms. Furthermore, different phytoplasmas can cause nearly identical-looking plant diseases, and a single insect can carry multiple varieties of the microbes.

In some crops, the bacteria are not abundant enough to spot, nor are they uniformly distributed in the phloem. "If you don't detect something, you don't know if you've just sampled the wrong bit of plant, or [sampled] at the wrong time, or if it's really not there," says Matthew Dickinson, a plant pathologist at the University of Nottingham in the United Kingdom.

Even with the right knowledge in hand, horticulturists and others find that traditional control measures—pesticides, culling infected plants, or destroying weeds and other plants that can serve as a reservoir for phytoplasmas—are only moderately effective. All too often, "an insect will get through" and the bacteria will spread, says Dickinson. Injecting tetracycline into trunks can limit infections in trees, but that's a pricey strategy and doesn't always work. Furthermore, using this drug in agriculture worries many human-disease experts because the practice could exacerbate clinical antibiotic resistance.

Some researchers are trying to find or create plants that fend off a phytoplasma attack or remain healthy while carrying the microbes. Dickinson is assessing whether some coconut palms harbor the bacteria without succumbing to disease, for example. "We've got some preliminary evidence" that such resistant trees exist, he says.

Other scientists are considering making plants distasteful to a phytoplasma-ferrying insect by engineering compounds into them that deter feeding. Such a scheme has shown promise in a leafhopper-transmitted disease in rice, Harrison and Weintraub say.

Infecting plants with mild forms of phytoplasmas also holds potential. Evidence suggests that such strains can guard against damage from those that produce more severe symptoms. Alternatively, scientists might employ other kinds of harmless bacteria to compete with phytoplasmas inside the insects, Weintraub says.

Researchers are turning to the newly sequenced phytoplasma genomes—and following up on recent results—to identify additional ways of interfering with crucial interactions between host proteins and phytoplasma virulence molecules. In addition, DNA sequence comparisons among different phytoplasmas could help scientists work out why some of the bacteria benefit insects while others harm them or seem to have no effect. Such findings, in turn, may suggest new control strategies.

After eluding identification for decades, phytoplasmas are finally giving up some of their secrets. Exploiting those revelations to save trees and crops remains a challenge, however. But in a different tack, some scientists are already contemplating whether they can create plants with only the positive attributes of an infection. Perhaps adding a single phytoplasma gene to a plant's DNA could create bushy poinsettias or green peonies that don't carry the pesky pathogens.

–EVELYN STRAUSS

Hassling plants, helping insects. Phytoplasmas trouble grapevines (*top left*), raspberries (*top right*), and coneflowers (*bottom left*) but can boost reproductive prowess of leafhoppers (*bottom right*) that spread the bacteria.

CREDITS: (TOP LEFT, TOP RIGHT, BOTTOM LEFT) BOJAN DUDUK; (BOTTOM RIGHT) ANDY DAVIS, JIC PHOTOGRAPHY

Symbolic art. Tauba Auerbach (*left*) and Byron Cook.

MATHEMATICS

A Good Sign

When existing notation for explaining a complex mathematical problem wasn't enough, Byron Cook teamed up with an artist to design his own

Mathematical signs have the power to squeeze hundreds of pages of work into a few neat lines. But as math gets more complex, the symbols can show their limitations. Byron Cook, a senior researcher at Microsoft's research laboratory in Cambridge, U.K., and a professor of computer science at Queen Mary, University of London, learned this recently while solving a 70-year-old puzzle called the halting problem.

Halting is the reason some computer programs occasionally get stuck in endless loops. It plagues PC users with the hourglass icon that never disappears, and Mac users with the rainbow-colored "spinning wheel of death." Scientists have known for decades that there is no universal solution to the glitch. But in 2008, Cook made a breakthrough that could help to prove whether most real-life computer programs would come to an end or hang forever.

Fellow computer scientists agreed that Cook's approximate solution was important, but the complicated set theory he used wasn't easy to explain. "When I was giving lectures or talking to product developers, I needed to get a lot of information across quickly, and this was getting difficult," says Cook. Things got even tougher when he began to write a book on the subject.

Mathematicians in this kind of pickle often devise shorthand notation to trim down the maze of formulae. "Historically, the abbreviation of complex texts has allowed some problems to be solved that were otherwise intractable," says Patrick Ion, associate editor of *Mathematical Reviews* for the American Mathematical Society. "The introduction many centuries ago of, say, zero, or the equals sign, are thought to be turning points." Roughly 2500 symbols are in use today, most of them variations on earlier symbols or letters of the alphabet.

Cook decided to take a bigger leap. He enlisted the help of a friend, New York City–based artist Tauba Auerbach, a former professional sign writer whose artwork has played with language and technology. For example, her 2005 show "How to Spell the Alphabet" explored the analog and digital ways we express characters, from the optician's eye chart to patterns in binary code. "I often read about math and physics, and they're integral to my art," Auerbach says. "But there was of course a limit to how much of Byron's work I could understand. I brainstormed for days, and my goal was to capture the motion or trajectory of each function—the way the sets of numbers were being grouped or moved in a certain direction."

But when Cook tested the first drafts of the new notation on colleagues, they hated them. Some of the symbols were too ornate to be drawn freehand. One was binned for resembling a swastika; another for being too similar to a Japanese language character.

Through trial and error, Cook and Auerbach learned that new symbols should build on old ones, so they make intuitive sense at first glance. "I knew that Tauba had been successful after I used her final symbols in a lecture and people hardly noticed. Before I knew it, my students were using them, too," says Cook, as he sketches the nine symbols they created onto his whiteboard. The simplest one, representing a mathematical operation that gathers only the right-hand coordinates of a set of pairs of numbers, is a rounded, inverted "L" with an arrow at the end, pointing rightward. In two strokes, it expresses a concept that would otherwise take two lines to explain. Another symbol, which constructs a new numerical relationship for a set of variables using a mapping, is an L-shape with a "greater-than" symbol inside it.

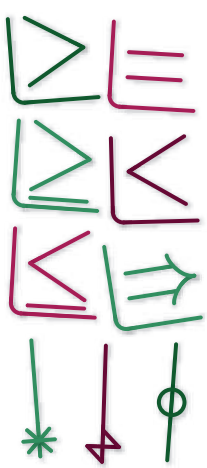

Sensible addition. These new math symbols are designed to be understood intuitively.

"I rather like their notations," says David Bressoud, president of the Mathematical Association of America and a professor of mathematics at Macalester College in St. Paul, Minnesota. "It will be interesting to see if they get picked up beyond the computer science community." That is likely to depend more on the value of Cook's research than on the beauty of the designs, Bressoud adds.

Still, says Ion, "good notation has a tendency to beat out bad notation." Leonhard Euler's decision to use the letter "e" for the base of the natural logarithm around 250 years ago, for example, was so successful that we still use it today. The battle continues, however, between Newton's choice to use a dot over "x" to represent a derivative, and Leibniz's "dx/dt" notation for the same thing.

Although the verdict from his colleagues is still out, Cook says the new notation has made a "dramatic" difference to his own work. He estimates that more than 100 of his students and colleagues already recognize the symbols. Next, he hopes to have them implemented in LaTeX, the typesetting package that mathematicians commonly use to publish their work electronically. After that, Cook says, "our plan is to see what else needs simplification. We might invent some more."

Ion predicts that mathematical symbols are due for a bigger shakeup: "The way we think about notation is evolving. Color may come in, and as technology advances, maybe even animation." **–ANGELA SAINI**

Angela Saini is a freelance writer based in London.

CREDITS (TOP TO BOTTOM): COURTESY OF TAUBA AUERBACH; MICROSOFT RESEARCH; TAUBA AUERBACH

LETTERS

edited by Jennifer Sills

Promoting Engineering

IN HIS EDITORIAL "SCIENCE IN THE WHITE HOUSE" (1 MAY, P. 567), Office of Science and Technology Policy (OSTP) Director John Holdren outlined the role that OSTP plays in the formulation of science and technology policy in President Obama's White House.

America's science, technology, and engineering infrastructure can be used to drive America's economic recovery. Now is the time to add "Engineering" to Dr. Holdren's title and the organization he directs. Engineering is the practical application of science to commerce or industry. The multitude of economic recovery options outlined by the president (for example, a new energy grid, green energy solutions, and efficacious health care) cannot happen without engineering expertise. History shows us an encyclopedia of technological advances that simply would not have occurred without strong engineering expertise. From radar, to nuclear weapons and energy, to space travel, to robotic surgery and engineered tissue implants, the tripartite arrangement of science, technology, and engineering has always been the combination for successful advancement.

Director John P. Holdren. Is it time to add "Engineering" to the Office of Science and Technology Policy?

What better way to raise the stature of engineering than to include it in the title of the individual tasked with advising the president on how to capitalize on America's science, technology, and engineering expertise? This change is fully consistent with President Obama's stated desire that more young people choose engineering as their career.

EUGENE C. ECKSTEIN

Department of Biomedical Engineering, University of Memphis, Memphis, TN 38152, USA. E-mail: eckstein@memphis.edu

Do Not Underestimate Science

IN THE LETTER "THE HARD PROBLEM" (24 April, p. 463), E. J. Neafsey comments on a previous Letter by M. J. Farah and N. Murphy ("Neuroscience and the soul," 27 February, p. 1168), which claimed that neuroscience may eventually be able to explain all aspects of being human. Neafsey asserts that Farah and Murphy's Letter demonstrates "a somewhat naïve and simple faith in scientific progress." He then refers approvingly to the philosopher David Chalmers's characterization of consciousness as the "hard problem" that will forever defy a reductionist, scientific explanation (*1*).

However, philosophers deal in belief systems and personal opinions, not in natural laws and facts. They ask interesting questions and pose challenging dilemmas, but they have an unimpressive historical record of prognostication. August Comte, father of positivism, wrote in 1835 that we shall never know what stars are made of (*2*). A few decades later, the chemical composition of stars was deduced by spectral analysis of their light (*3*).

Francis Crick, a scholar with a far better track record of prediction, stated in an interview in 1996, "It is very rash to say that things are beyond the scope of science" (*4*).

CHRISTOF KOCH

Department of Biology, California Institute of Technology, Pasadena, CA 91125, USA. E-mail: koch@klab.caltech.edu

References

1. D. Chalmers, *J. Consciousness Stud.* **2**, 200 (1995).
2. A. Comte, *Cours de Philosophie Positive* (1830–1842).
3. G. R. Kirchhoff, R. Bunsen, *Ann. Phys.* (1860); pp. 110, 160.
4. Interview "The scientific search for the soul" with Jeffrey Mishlove as part of the *Thinking Allowed* series, NPR (1996).

Immune System: Success Owed to a Virus?

IN HIS NEWS FOCUS STORY "ON THE ORIGIN of the immune system" (1 May, p. 580), J. Travis addresses the mysterious origins of the immune system's ability to create specific antibodies. He first describes how this occurs: *RAG* enzymes mediate a recombination process that results in specific lymphocyte receptors and immunoglobulin. He then explains the prevailing theory about the origins of the process: These *RAG* enzymes were originally transposons. However, no specific transposon with these properties has been identified. In fact, the closest transposon relative to the *RAG1* protein is the so-called transib family of DNA transposons, which do not contain anything resembling a *RAG2* protein (*1*).

I recently proposed an alternative explanation. Numerous other enzymes—including retroviral integrases, RNAse H, the RNA Induced Silencing Complex Argonaute proteins, and possibly other DNA viruses—use a similar magnesium-dependent catalytic site

Letters to the Editor

Letters (~300 words) discuss material published in *Science* in the previous 3 months or issues of general interest. They can be submitted through the Web (www.submit2science.org) or by regular mail (1200 New York Ave., NW, Washington, DC 20005, USA). Letters are not acknowledged upon receipt, nor are authors generally consulted before publication. Whether published in full or in part, letters are subject to editing for clarity and space.

CREDIT: J. SCOTT APPLEWHITE/AP PHOTO

Published by AAAS

Scarab beetle iridescence

398

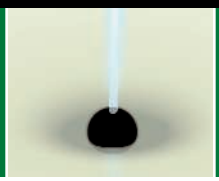

Acceleration from a black hole

399

for nucleic acid cleavage (*2*). More plausible than a "*RAG* transposon" is the insertion of an infectious DNA virus resembling a herpes virus adjacent to the *RAG2* protein in a primordial deuterostome (*3*). DNA viruses such as the herpes viruses encode a recombinase resembling the *RAG1* protein more closely than that of DNA transposon transposases, and they are also part of the regulatory network shared by the *RAG* genes and recombination of the VDJ regions, consistent with the subsequent arms race between herpes viruses and the immune system.

DAVID H. DREYFUS

Department of Pediatrics, Yale School of Medicine, New Haven, CT 06511, USA. E-mail: dhdreyfus@pol.net

References

1. V. V. Kapitonov, J. Jurka, *PLoS Biol*. **3**, e181 (2005).
2. D. H. Dreyfus, *Ann. Allergy Asthma Immunol*. **97**, 567 (2006).
3. D. H. Dreyfus, *PLoS ONE* **4**, e5778 (2009).

Immune System: "Big Bang" in Question

J. TRAVIS'S NEWS FOCUS STORY "ON THE origin of the immune system" (1 May, p. 580) strengthens the idea that there exists a "Big Bang" in the evolution of the immune system, namely the move from innate to adaptive immunity. Yet evidence accumulated during the past 10 years has shown that this idea requires caution, for at least three reasons: (i) Immune memory, supposedly a characteristic of adaptive immunity and therefore of higher vertebrates, does in fact exist in invertebrates (*1*, *2*). (ii) Nonvertebrate immunity no longer appears to be "unspecific"; many forms of immune specificity exist in animals, and even in plants (*3*). (iii) The adaptive immune system never works on its own [a little-known fact first revealed 20 years ago (*4*) but subsequently neglected]. An antigen that is recognized by the adaptive immune system but not by the innate immune system will not, in general, trigger an immune response (*5*).

These studies show that immunity is ubiquitous in nature and that the boundary between adaptive and innate immunity is not as clear cut as has been claimed for decades (*6*). In light of these results, looking for evidence for the immunological "Big Bang" is probably an inadequate strategy for studying the evolution of immunology.

THOMAS PRADEU

Institut d'Histoire et de Philosophie des Sciences et des Techniques, Paris-Sorbonne University, Paris, 75006, France. E-mail: thomas.pradeu@paris-sorbonne.fr

References

1. J. Kurtz, K. Franz, *Nature* **425**, 37 (2003).
2. K. Kurtz, S. A. O. Armitage, *Trends Immunol*. **27**, 493 (2006).
3. B. J. DeYoung, R. W. Innes, *Nat. Immunol*. **7**, 1243 (2006).
4. C. A. Janeway, *Cold Spring Harbor Symp. Quant. Biol.* **54**, 1 (1989).
5. R. M. Steinman, D. Hawiger, M. C. Nussenzweig, *Annu. Rev. Immunol*. **21**, 685 (2003).
6. E. Vivier, B. Malissen, *Nat. Immunol*. **6**, 17 (2005).

Immune System: Promethean Evolution

IN HIS NEWS FOCUS STORY "ON THE ORIGIN of the immune system" (1 May, p. 580), J. Travis overlooked some important components of the Darwinian evolution of the acquired immune response. Travis, quoting molecular biologists, ascribes the "Big Bang" in immunological evolution to the adaptation of *RAG1* and *RAG2* enzymes from transposons (or something similar) to gene-segment splicers. However, it is possible that a mechanism that permitted this splicing function existed previously and that the true "Big Bang" was the development of the multiple V, D, and J regions—those regions that are spliced in order to create specific antibodies.

But even this is not the most interesting aspect of immunological evolution. Many years ago, Susumo Ohno, citing the Greek legend of the Titan brothers—forward-looking Prometheus and backward-looking Epimetheus—speculated that in contrast to almost all other physiological functions, immunology has developed an anticipatory mechanism (*1*, *2*). Most physiological functions are Epimethean: They start with a primitive mechanism and then gradually adapt to meet environmental challenges. Thus, everything in Epimethean evolution depends on the response to past events and challenges.

In contrast, immunology functions as a forward-looking system (*3*). The evolution of the various B cell gene segments, together with the adaptation of mechanisms to join them combinatorially, has enabled the generation of a magnificently large repertoire of specific antibodies. Almost any new pathogenic component will thus be covered, which is important in an environment where pathogens change far faster than the vertebrates can adapt.

Here was the real "Big Bang." But then normal Darwinian (Epimethean) evolution intervened, as might have been expected. It entered the process in many forms. For example, given that the generator of diversity would necessarily produce lymphocytes that are specific to both foreign and self antigens, the latter had to be down regulated by various mechanisms to avoid the development of compromising autoimmunities.

We do not know precisely when the change from Epimethean (reacting) to Promethean (anticipating) took place, and there are no satisfactory intermediate forms ("missing links") to indicate the steps along the way. But absence of proof is not proof of absence. We may with confidence recognize the Promethean "Big Bang" in immunology as one of the high points in the workings of Darwinian evolution.

ARTHUR M. SILVERSTEIN

38 Fells Road, Falmouth, MA 02540, USA. E-mail: arts@jhmi.edu

References and Notes

1. S. Ohno, *Perspect. Biol. Med*. **19**, 527 (1976).
2. S. Ohno *et al.*, *Progr. Immunol*. **4**, 577 (1980).
3. The neural networks of the brain are the only other known system with this capability.

CORRECTIONS AND CLARIFICATIONS

News Focus: "A medical mystery in middle China" by R. Stone (12 June, p. 1378). On page 1380, in the first paragraph, the recommended daily intake of selenium should have been 70 micrograms, not 70 milligrams.

News of the Week: "Report finds no gender bias in faculty hiring, resources," by J. Mervis (5 June, p. 1250). Sally Shaywitz, Yale University professor of pediatrics and co-director of the Center for Dyslexia and Creativity, served as co-chair of the report by the National Research Council, *Gender Differences at Critical Transitions in the Careers of Science, Engineering, and Mathematics Faculty*.

News Focus: "Biologists struggle to solve bat deaths" by R. Zimmerman (29 May, p. 1134). On page 1135, the statement that bats "arouse and triple their body temperature" was incorrect. During an arousal, the body temperature of a bat will increase approximately 10°C to about 24° to 30°C.

Reports: "Human substantia nigra neurons encode unexpected financial rewards" by K. A. Zaghloul *et al.* (13 March, p. 1496). Equation 1 in this paper was incorrect. The correct equation is as follows:

$$E_d[n] = 0.5 + 0.5\sum_{i=1}^{n-1} R_d[n-i]\alpha i^{-\tau}\ n = 2, \ldots, N$$

ANTHROPOLOGY

The Cooking Ape

Andreas Keller

If we believe that the difference between humans and chimpanzees is more remarkable than the difference between leopards and cheetahs or that between nightingales and stonechats, then we need an evolutionary explanation for the rapid changes in our lineage. Explanations of "what makes us human" often focus on a single event or capacity and consider many human-specific behaviors and abilities to be a consequence of it. Among such proposed accelerators of biological and cultural change are opposable thumbs, bipedalism, language, and trade.

Catching Fire
How Cooking Made Us Human
by Richard Wrangham
Basic Books, New York, 2009. 315 pp. $26.95, C$33.95. ISBN 9780465013623.

Fire
The Spark That Ignited Human Evolution
by Frances D. Burton
University of New Mexico Press, Albuquerque, 2009. 245 pp. $34.95. ISBN 9780826346469.

These arguments often include a bridge between culture and biology. Their basic structure involves a cultural accomplishment that can accelerate genetic changes by reshaping the selective forces. The genetic changes improve cognitive abilities. Improved cognitive abilities drive cultural progress, which again alters the selective forces. This positive feedback loop between culture and genes could propel the cognitive abilities and behavior of humans away from those of the chimp. An inherent problem for these types of scenarios is that most major cultural accomplishments happened very recently, whereas biological changes that are the result of positive selection are generally believed to spread rather slowly (*1*).

Two new books by anthropologists Frances Burton and Richard Wrangham, released within weeks of each other, now argue that learning to control fire a few million years ago "made us human" or "ignited human evolution." Each comes in a black dustjacket with the title and author's name written in white and yellow above the picture of a campfire. Each draws on evidence from anthropology, archaeology, and comparative primatology to provide a fascinating account of how fire was first used and controlled. However, the similarities end there.

The reviewer is at the Laboratory of Neurogenetics and Behavior, Rockefeller University, 1230 York Avenue, Box 63, New York, NY 10021, USA. E-mail: kellera@mail.rockefeller.edu

In *Fire: The Spark That Ignited Human Evolution*, Burton (University of Toronto) argues that the light from campfires extended the day for our ancestors and therefore decreased their melatonin levels. She discusses the effects of melatonin on cognitive abilities, reproduction, and other physiological processes, but she does not directly connect the light from a campfire to accelerated genetic changes. At the conclusion of her account, she describes the ultimate effect of light as "accelerating processes of mind, body, disease, and society in the transformation to us."


Fueling bigger brains?

Wrangham (Harvard University) presents evidence that it's the heat and not the light of fire that was important. *Catching Fire: How Cooking Made Us Human* offers a convincing argument that cooking allowed us to do the work of chewing and digesting outside of our bodies. Wrangham presents evidence (sometimes strong and always interesting) that the energy our bodies saved by outsourcing digestion was redirected toward our brains. For example, he discusses the rapid evolution of the beaks in Galapagos finches in response to dietary changes, a self-experiment in which he determines that adding leaves to raw goat meat makes it easier for him to chew, and the food preferences of the gorilla Koko. (She likes her vegetables cooked.)

But is cooked food really energetically superior to raw food? It is intuitive that cooking reduces the time and energy necessary to chew and digest a potato or a steak. The potential advantages of cooking are less obvious, however, for foods such as bananas, eggs, or fish. Cooking also produces hard-to-digest protein compounds and destroys vitamins. When meats are heated, fat melts and drips off, reducing their caloric content.

Nonetheless, Wrangham concludes that cooking increases the amount of energy we can obtain from food. As evidence, he cites the weight loss in humans who shift to a diet consisting of mostly raw foods and the accelerated growth and increased milk production in cows that are fed cooked food. Furthermore, he informs us that all known human societies cook and that there are no reports of lost explorers or adventurers surviving on raw food for more than a few weeks.

If Wrangham's arguments convince you that cooking increases caloric content, then it is easy to see that selection would favor anatomical and physiological adaptations to the new foods we created. Cooking would free more energy for the brain, which could then increase in size and advance culture. And so on through the positive feedback loop.

Along with this main thesis, *Catching Fire* presents other original ideas about the consequences of controlled fire on human evolution. Some of cooking's consequences may be seen in human social relationships. One individual can cook for a group, and Wrangham claims that this led to the establishment of pair bonds between individual men and women in early societies. The importance of cooking in relationships is seen in hunter-gatherer societies in which "when a woman feeds a man, she is immediately recognized as being married to him."

Fire, Wrangham acknowledges, has other uses than cooking. The one that receives the most attention from him is to keep predators away. He suggests that when our ancestors no longer needed to climb trees for protection at night but slept around a campfire, "natural selection rapidly favored the anatomical changes that facilitated long-distance locomotion and led to living completely on the ground."

Because Wrangham does not mention potential effects of the lengthening of the day on human physiology, his and Burton's books complement one another. Both books lead to testable hypotheses. Burton calls the question of whether a campfire produces enough light to affect melatonin levels the "crux" of her book. This suggests an experiment in which melatonin is assayed in subjects in a controlled environment with or without a campfire artificially prolonging the day. Wrangham, surprisingly, could not find a single study that compares human participants on controlled diets of food that is either eaten raw or cooked.

Published by AAAS

Such experiments together with the evidence and the innovative ideas Burton and Wrangham present would help us better understand what made us who we are today.

References

1. G. Cochran, H. Harpending, *The 10,000 Year Explosion: How Civilization Accelerated Human Evolution* (Basic Books, New York, 2009).

10.1126/science.1176069

RESEARCH MISCONDUCT

Neglecting the Crucial "Why?"

Donald Eigler

The "outliers"—the data points that deviate far from the norm—invariably draw our attention. We know from statistical analysis that they should be there, yet we somehow are never fully at ease to accept them as belonging to part of the whole. I suspect this comes from a deeply rooted need to create order in our world through classification schemes that not only allow us to differentiate normal from deviant behavior but also predispose us toward being inclusive of the former and exclusive of the latter. Nowhere is this more true or more deeply rooted in our psyche than in our response to human behavior.

Human behavior at this normal-deviant boundary has been the grist of great literature. Shakespeare was drawn here. Dostoyevsky's masterworks, *Crime and Punishment* and *The Brothers Karamazov*, drew from this font. It was then with high expectations and the hope of some valuable insight into perplexing questions regarding deviant human behavior in the scientific community that I began to read Eugenie Samuel Reich's *Plastic Fantastic*—a book about an outlier.

Reich (a Boston-based science journalist) chronicles the case of scientific fraud committed by Jan Hendrik Schön, the golden boy of Bell Laboratories at the turn of the millennium. I was disappointed to find that her book does little more. I say this because I wanted it to do more. Schön's fraud had dominated the "scandal du jour" entrée of physicists' lunch-time conversation menu for a very long time. Whereas so many of these conversations revolved around questions of what Schön had done, I was always drawn to the more disturbing questions of psychomechanics: how and why had Schön destabilized. What lessons could be learned?

I had high expectations of *Plastic Fantastic* for another reason. Long ago, I had read a transcript of Irving Langmuir's classic 1953 talk "Pathological Science" (*1*), in which Langmuir addressed the topic of how a scientist can be fooled, especially by himself. As the Schön affair unfolded, I repeatedly consulted Langmuir to see if I could extract understanding. I could not. The reason for this, in retrospect, is that Langmuir was addressing the questions of how one gets fooled or how one fools oneself, whereas the questions I harbored about Schön were largely about how and why he came to commit and justify fraud. I was interested in how he went astray. Reich doesn't go after these meaty questions. Instead, her avowed purpose is to examine the widely held belief that science is "self-correcting." She barely does this, and only in the epilogue.

Plastic Fantastic
How the Biggest Fraud in Physics Shook the Scientific World

by Eugenie Samuel Reich

Palgrave Macmillan, London, 2009. 270 pp. $26.95, C$29.95, £15.99. ISBN 9780230224674.

Plastic Fantastic is by and large a history—sometimes anecdotal, sometimes mixed with smatterings of critical examination—of the Schön affair. Unfortunately, it is repetitive and poorly organized, vacillating back and forth in time and topic. The editing, spelling, and grammar are a constant irritation, e.g., "Schon" instead of "Schön," "silicone" instead of "silicon."

At times, the book seems to have been written for the general public. The author makes an admirable attempt to explain everything from transistors to composite fermions to her audience. The unfortunate professional who reads these descriptions should be warned: prepare to cringe. Her explanations are often wrong and sometimes horribly botched. The curious lay reader should be cautioned to seek an understanding elsewhere.

At other times, the book seems targeted at the scientific community. This is no more apparent than in the book's epilogue when Reich at last turns to her raison d'etre, the question of whether science is self-correcting. Her tone here is more of someone wanting to grind an axe (and grind it against scientists) rather than to illuminate or understand.

In all, *Plastic Fantastic* disappointed me. The book is not what I had hoped for, an insightful study of the mechanisms through which a scientist's ethics can be corrupted. Nor does it provide a thoughtful examination of the self-correcting nature of science, what Reich claims her book is all about.

References

1. I. Langmuir, *Phys. Today* **42**, 36 (1989) [transcribed, Ed., R. N. Hall].

10.1126/science.1175487

The reviewer is at the IBM Almaden Research Center, Department K-10/801, 650 Harry Road, San Jose, CA 95120–6099, USA. E-mail: eigler@almaden.ibm.com

SOCIOLOGY

Can We Reinvent the Internet?

To build a better Internet may require us to rewire the social communities that created its code.

Viktor Mayer-Schönberger

Recently, researchers who support "network neutrality" have become worried that the Internet may lose its innovative edge. They are concerned that control could be shifting from the edges of the Internet toward the service providers at the center, which would allow the providers to have "gatekeeper" capacity and would contradict the Internet's "end-to-end" principle (*1*–*3*). This core tenet states that control over information flows should take place, to the extent possible, at the end points of the network (*4*). President Obama supported net neutrality during his campaign (*4*) and in recent statements (*5*), and the European Parliament has added net neutrality to its recent telecom bill (*6*). Taking the end-to-end principle from protocols to users, Jonathan Zittrain has called for maintaining the Internet's "generativity," the ability of users at the network's end points to create, distribute, and run whatever software code they choose (*7*). There are good reasons to preserve network neutrality and generativity, but it is unclear whether these are sufficient to ensure continued innovation. The larger issue is what policies are optimal to foster innovation on the Internet?

Innovation and the Internet

Given that the Internet connects general-purpose processors, most of the innovation happens in software code, which, once released, is rapidly distributed through the network. A new version of Apple's Safari achieved 11 million downloads in 3 days (*8*); many open-source software packages are compiled nightly to be ready for (automated) download the next morning. A combination of global Internet connectivity, automatic software updates, and centralized code management makes this rapid distribution possible. But these updates are mostly minor changes to software already installed on user machines. Although the ability to rapidly react to hacks and bugs by pushing down a software update is no doubt beneficial, it tells us little about the Internet as a system that enables code innovation.

In contrast, new software products or radically new versions of existing software often face a difficult time getting accepted in the marketplace. Perceived costs incurred when switching from one software product to another, e.g., the cost of data conversion and training, make users keep the software they already have installed (*9*). Costs are higher still if a code switch necessitates hardware changes, as well (especially when, owing to its complexity and specialization, the required hardware is expensive). Moreover, positive network effects ensure a pull toward the popular and established, but not necessarily the most innovative, software products. A superior new software product may attract relatively few users for a prolonged period of time, before finally, rapidly taking off (*10*). Conservative user choice, in turn, influences product development, pushing most vendors to alter their software titles only incrementally to avoid the risk of losing their user base. Microsoft's woes in converting users from Windows XP to Windows Vista offers a powerful case in point, so does the painfully slow switch from the network protocol IPv4 to IPv6 (*11*). This tilts development of new code toward incremental innovation.

The Social Network of Users and Coders

Peer production of software (facilitated by the open-source culture, new tools for managing distributed software development on the net, and global connectivity) has emerged as a powerful new mechanism of software creation (*12*). It has even extended beyond code creation (e.g., Wikipedia). In contrast to commercially developed, proprietary software, open-source development regularly involves users—not necessarily in writing code, but for reporting bugs, flagging areas of improvement, or partaking in online design discussions (*13*). Decisions are often driven by the need to establish a rough consensus of those participating (*14*, *15*). Because peer production of software is organized through social networks, the Internet functions as both the technical infrastructure to diffuse code and the tool to maintain a social network, enabling communication and information-sharing among code writers and users. However, reliance on social networks may make open-source development just as conservative as commercial software production.

Many open-source projects consist of a small number of active coders and a larger number of bug reporters and commentators, all connected with each other through the Net (*13*). This thicket of connections within the community of a particular project facilitates coordination and information exchange among its members, but, as a social network topology, it is not conducive to radical innovation. Burt has suggested that an individual node's value is not proportional to the number of its links, but whether these links are within one's existing community or connect two disparate groups (*16*). In the latter case, the two connecting nodes are valuable information brokers, spanning what Burt terms a "structural hole" (see figure, left) (*17*). Brokerage opportunities between different communities, and the value gained from these, require the existence of such structural holes. Because of the way in which we have organized the development of software code through the Internet—in relatively well-connected online groups—open-source communities may suffer from a lack of such structural holes. An overabundance of connections over which information can travel too cheaply can reduce diversity, foster groupthink, and keep radical ideas from taking hold. This may explain, at least in part, why much peer-produced code rarely is altered in more than an incremental manner (*18*).

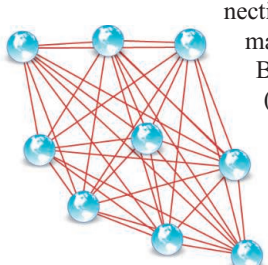

Groupthink
Many or all nodes linked to each other

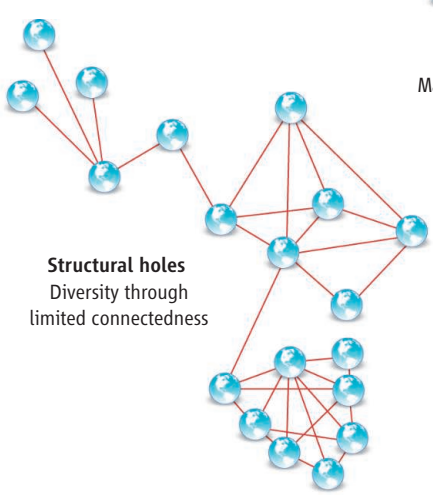

Structural holes
Diversity through limited connectedness

This is less problematic in a competitive, profit-driven setup. If a software ven-

Lee Kuan Yew School of Public Policy, National University of Singapore 259772, Singapore. E-mail: Viktor_MS@nus.edu.sg

Published by AAAS

dor falls too far behind the innovation curve because of too-conservative incremental changes, a competitor can mount a successful challenge. Such a competitive setup, in essence, creates two disconnected communities of development. It may require significant initial capital expenditure and time to build momentum. But the prospect of future (if temporary) market dominance fuels risk-takers, as well as a sufficient inflow of venture capital.

The situation becomes problematic, however, when there is insufficient economic incentive for multiple products. The most prominent example is not commercial software code, but the Internet, or more precisely the protocols underlying this dominant network infrastructure. It is too costly and risky for a commercial competitor to create and market a set of radically improved, but incompatible protocols. This is true for the peer-producing, open-source community, as well.

The National Science Foundation supports the Network Science and Engineering (NetSE) program and the Global Environment for Network Innovations (GENI), two mechanisms aimed at enabling more radical network innovations (*19*, *20*). Their work could be improved by incorporating the social network perspective on code creation I have outlined above. Given that they already have a social science component, such integration may not be too difficult. We need to create incentives to form network structures that stimulate and enable innovation.

Overcoming Connectedness

How should policy-makers respond, especially when wanting to facilitate the creation and growth of the next-generation Internet?

If densely connected social networks, although they permit incremental innovation, are hampering radical innovation, two potential responses come to mind. The first focuses on the physical network, implying that it may be necessary to build a next-generation Internet outside of the existing infrastructure. This could free development of the legacy constraints that may hamper radical innovative changes. Any government money to build out the backbone of this future network could mandate that more radical innovations be implemented, with interoperability achieved through defined gateways rather than built right into the system.

This option, however, may be of limited value, if development of the next iteration of Internet breakthroughs, or even the next-generation network itself, is organized through the Internet. Unlike their brethren during the Manhattan Project, today's coders stay connected through their social networks and remain tethered to the context of the existing structures. Project requirements may permit them to consider radical solutions, but their connectedness to the thinking of the status quo through their social networks holds them back.

The second policy option, therefore, focuses less on the physical than the social networks among the research and coding community. When offering public funding for development, government could mandate that the mechanism for allocating funding breaks loose of existing social networks. For example, funding proposals could be encouraged to involve smaller, but competing, groups and for longer periods of time, reintroducing limited separation, somewhat akin to what in the business literature is referred to as modularity (*21*, *22*). Proposals could be reviewed not by peers, as is traditional (who are likely from the same social network as the grant writer, which impedes heterogeneity of ideas), but through a panel of experts one step removed from the research community. Adding reviewers from more risky commercial startups could induce review panels to fund more radical and diverse proposals. The European Institute of Innovation and Technology, a funding initiative of the European Commission, has adopted a variant of this suggestion. Eight of its 18-member grant-awarding board come from the private sector (*23*). Announced well in advance, such measures signal to the research community that risky and radical proposals are particularly welcome.

Much of commercial development, owing to trade-secrecy concerns, is already less densely linked into a social network, with the result that less policy intervention may be required. Among the available policy tools for government are direct and indirect financial incentives for smaller startups. Government may also want to offer incentives for "skunkwork" projects—deliberately removed from the corporate structure and the connectedness this entails—within larger companies. The creation of the original IBM personal computer (PC), as well as the Apple Macintosh, are good examples of the kind of commercial behavior to incentivize.

Most of the deployment of the next-generation Internet—from the infrastructure all the way up to the application running on the network—will likely be privately funded. However, in areas where government steps in to fund network deployment—to overcome the digital divide, and/or to stimulate the economy—such funding could similarly shift from using efficient, but less innovative, mid-life-cycle mass-produced infrastructure equipment to more cutting edge technologies.

Conclusion

Connectedness of the current Internet constrains the ability of software coders to innovate and to build the code we need: messaging that is more resistant to spam, code to enable innovative controls of the personal information we share through social networking sites like Facebook, and measures to take open online collaboration to the next level, or to help us focus and tackle our society's most pressing problems. To enable innovations, especially nonincremental, discontinuous, and radical ones—which are needed, among other things, to launch successfully the next-generation Internet—may require unique policy intervention: reducing the social ties that link its coders.

References and Notes

1. W. Baumol *et al.*, "Economists' statement on network neutrality policy" (AEI-Brookings Joint Center Working Paper No. RP07-08, American Enterprise Institute for Public Policy Research–Brookings Institution, Washington, DC, 2007).
2. B. Van Schewick, *J. Telecommun. High Technol. Law* **5**, 329 (2007).
3. J. Saltzer, D. Reed, D. D. Clark, *ACM Trans. Comput. Syst.* **2**, 277 (1984).
4. MoveOn, *Huffington Post*, 29 October 2007; www.huffingtonpost.com/2007/10/29/obama-promises-to-reinsta_n_70317.html.
5. Editor, *Seattle Times*, 8 June 2009; http://seattletimes.nwsource.com/html/editorials/2009315207_edita09neutrality.html.
6. D. Meyer, ZDNet, 6 May 2009; http://news.zdnet.com/2100-9595_22-299414.html.
7. J. L. Zittrain, *Harv. Law Rev.* **119**, 1974 (2006).
8. J. Dalrymple, CNet, 12 June 2009; http://news.cnet.com/8301-13579_3-10263494-37.html.
9. H. Varian, C. Shapiro, *Information Rules: A Strategic Guide to the Network Economy* (Harvard Business School Press, Boston, 1998).
10. C. H. Loch, B. A. Huberman, *Manage. Sci.* **45**, 160 (1999).
11. A. Ely, *Information Week*, 20 December 2008; www.informationweek.com/news/infrastructure/ipv6/showArticle.jhtml?articleID=212501014.
12. Y. Benkler, *The Wealth of Networks: How Social Production Transforms Markets and Freedom* (Yale Univ. Press, New Haven, CT, 2006).
13. J. Lerner, J. Tirole, *J. Ind. Econ.* **50**, 197 (2002).
14. K. R. Lakhani, E. von Hippel, *Res. Policy* **32**, 923 (2003).
15. Steven Weber, *The Success of Open Source* (Harvard Univ. Press, Cambridge, MA, 2004).
16. R. Burt, *Brokerage and Closure* (Oxford Univ. Press, New York, 2005).
17. R. Burt, *Structural Holes: The Social Structure of Competition* (Harvard Univ. Press, Cambridge, MA, 1992).
18. S. E. Page, *The Difference: How the Power of Diversity Creates Better Groups, Firms, Schools, and Societies* (Princeton Univ. Press, Princeton, NJ, 2007).
19. NetSE, www.nsf.gov/funding/pgm_summ.jsp?pims_id=503325.
20. GENI, www.geni.net.
21. C. Baldwin, K. Clark, *Design Rules: The Power of Modularity* (MIT Press, Cambridge, 2000).
22. P. Evans, B. Wolf, *Harv. Bus. Rev.* **83**, 96 (2005).
23. European Institute of Innovation and Technology, http://eit.europa.eu/about-eit/governing-board.html.

10.1126/science.1178418

MATERIALS SCIENCE

Evolutionary Photonics with a Twist

The iridescent appearance of the hard forewings of scarab beetles can be caused by complex helical nanostructures.

Pete Vukusic

Iridescence with a difference. What appears to human eyes as green iridescence from certain scarab beetles, such as *Plusiotis alphabarrerai* shown here, mostly constitutes circularly polarized color.

The visual appearance of many animals is determined not by pigments but by structural processes that allow the animals to manipulate electromagnetic radiation—mostly visible light and color—in courtship, to find prey, or to escape predators. Studies of fish scales (*1*), insect coatings (*2*), and bird feathers (*3*) have revealed a wealth of complex biological structural designs and optical effects that mirror many technological photonic system designs. These photonic technologies are beginning to draw inspiration from the natural world for new generations of devices and products (*4*). On page 449 of this issue, Sharma *et al*. (*5*) add knowledge to this area by elucidating the processes through which the scarab beetle, *Plusiotis gloriosa*, reflects structural color from its external surfaces (elytra) in the form of left-handed circularly polarized light.

Left-handed circularly polarized reflection means that from the perspective of the observer, the electric field vector of the light reflected from the beetle describes a left-handed corkscrew, or helix, along its direction of propagation. Circularly polarized reflection from specific beetles was first observed nearly a century ago (*6*). *P. gloriosa*'s tendency to do this is thus not an isolated example, but the attribute is nonetheless rare. It requires a distinct azimuthally twisted—or helical—character in the nanostructure that forms the first few micrometers of its elytra. In these beetles, the spatial pitch of this helix creates the intrinsic periodicity that, to human vision, produces bright iridescent color (an example of this is shown in the figure).

Synthetic systems that exhibit strongly circularly polarized color reflections include certain layered mesophases, specifically those associated with cholesteric liquid crystals (also known as chiral nematic liquid crystals). Their circularly polarized optical properties arise because their constituent molecules lack inversion symmetry. This produces intermolecular forces that favor a specific small azimuthal twist through the whole system. In this way, an intrinsic physical helicity is generated that is right-handed or left-handed depending on molecule geometry, yielding right- or left-handed circularly polarized reflection, respectively (*7*).

Previous studies of circularly polarized colored reflections from beetle elytra revealed the presence of helicity and described the strong analogy with cholesteric liquid crystals (*8*). Electron micrographs of sections through these beetle elytra revealed "Bouligand structures" (*9*)—the characteristic series of curves within periodically contrasted layers that indicate the presence of helical symmetry in the constituent material.

In *P. gloriosa* and several other Rutelinae (*10*), however, the structural complexity goes beyond mere helically ordered layering. The elytral surfaces of these beetles consist of arrangements of mostly hexagonal micrometer-scale multicolored cells. The different colors are a result of nested close-packed surface concavities that shape the underlying structure, creating a set of color properties that depend on the nature of the illumination.

Using confocal microcopy, Sharma *et al*. now infer that in cross section, the form and geometry of these surface structures and subsurface features are analogous to the focal conic domains that spontaneously form at the free surface of a cholesteric liquid crystal (*11*). Given that the dynamics and formation processes of liquid crystals are generally well understood, this association provides new insight, beyond that of earlier cholesteric liquid crystal analogies (*8*), for the set of variables that may advance our understanding of the self-assembly pathways of this structurally colored insect cuticle. With a few noteworthy exceptions (*12*), the formation processes of these insect systems are not as well understood as are their photonics.

Helical nanostructure may have different biological functions. Where such helicity is present without accompanying circularly polarized reflection—for example, in some plant epidermi (*13*)—it may serve to add mechanical strength. This is mimicked effectively at the millimeter scale by processed plywood. However, the beetle helical ultrastructure is arguably too complex and too costly to produce without the benefit of a suitable optical selection advantage, such as effective signaling. The strong circularly polarized reflection observed in the beetles may, for example, play a role in intraspecific communication. This is especially the case for another scarab, *Plusiotis resplendens*. It exhibits strong broadband reflection of both left- and right-handed circularly polarized light due to the presence of two chirped helical layered regions separated by a half-wave plate (*14*).

Despite some initial behavioral studies, it remains unknown whether the circularly polarized reflection from these special beetles provides a channel of communication. However, Chiou *et al*. recently showed that such communication is possible for a marine

School of Physics, University of Exeter, Exeter EX4 4QL, UK. E-mail: p.vukusic@ex.ac.uk

CREDIT: P. VUKUSIC/UNIVERSITY OF EXETER

Published by AAAS

crustacean: the stomatopod *Odontodactylus* sp. Not only does this species signal brightly using circularly polarized colored light reflected from two posterior abdominal appendages, but it also responds behaviorally to circularly polarized stimuli (*15*). Its method for doing so is elegant. Chiou *et al*. revealed that incident circularly polarized light is converted to linearly polarized light when it is transmitted through a quarter-wave plate in specific cells of the eyes' mid-band region. Upon conversion to linearly polarized light, alignments of conventional microvilli (the basic elements that construct the photoreceptive region of the eye) are used for its photoreception.

This apparently adapted coupling between a circularly polarized light source and a circularly polarized light detection system in stomatopods is unlikely to be the only one in biological systems. Whether circularly polarized reflection in beetles such as *P. gloriosa* also has such an intraspecific communication purpose remains to be seen.

References

1. E. J. Denton, *Sci. Am.* **224**, 64 (January 1971).
2. P. Vukusic, J. R. Sambles, *Nature* **424**, 852 (2003).
3. G. E. Hill, K. J. McGraw, *Bird Coloration, Vol. I: Mechanisms and Measurements* (Harvard Univ. Press, Boston, 2006).
4. A. R. Parker, H. E. Townley, *Nat. Nanotechnol.* **2**, 347 (2007).
5. V. Sharma, M. Crne, J. O. Park, M. Srinivasarao, *Science* **325**, 449 (2009).
6. A. A. Michelson, *Philos. Mag.* **21**, 554 (1911).
7. F. Pedrotti, L. Pedrotti, *Introduction to Optics* (Prentice Hall, Englewood Cliffs, NJ, 1993).
8. A. C. Neville, S. Caveney, *Biol. Rev. Camb. Philos. Soc.* **44**, 531 (1969).
9. Y. Bouligand, *J. Phys. Colloque C4* **30**, 90 (1969).
10. S. A. Jewell, P. Vukusic, N. W. Roberts, *N. J. Phys.* **9**, 99 (2007).
11. R. Meister, M. A. Halle, H. Dumoulin, P. Pieranski, *Phys. Rev. E* **54**, 3771 (1996).
12. H. Ghiradella, *J. Morphol.* **202**, 69 (1989).
13. A. C. Neville, S. Levy, in *Biochemistry of Plant Cell Walls*, C. T. Brett, J. R. Hillman, Eds. (Cambridge Univ. Press, Cambridge, 1985), pp. 99–124.
14. S. Caveney, *Proc. R. Soc. London Ser. B* **178**, 205 (1971).
15. T. Chiou *et al.*, *Curr. Biol.* **18**, 429 (2008).

10.1126/science.1177729

ASTRONOMY

A Flare for Acceleration

Radio and gamma-ray observations show that particles are accelerated to extremely high energies very close to a black hole.

Mitchell Begelman

As black holes swallow matter, they often expel jets of plasma that can reach speeds very close to the speed of light. In the giant elliptical galaxy M87, 50 million light-years away, radio observations have traced such jets down to the immediate surroundings of the black hole, to less than 100 event horizon radii (*1*, *2*). However, radio observations alone cannot provide a complete picture of the power carried by these jets, their speed, or their composition. Gamma-rays, first detected from jets more than a decade ago, provide crucial evidence that particles are being accelerated to very high energies. But the relatively poor angular resolution of gamma-ray telescopes has prevented direct determination of where these particles are coming from. That uncertainty has now been resolved, at least for M87. On page 444 of this issue, Acciari *et al*. (*3*) report the first radio imaging of the site of a gamma-ray flare—and it is very close to the black hole.

Acciari *et al*. tracked changes in the jet's brightness and structure at radio, x-ray, and gamma-ray wavelengths. Jets are unsteady, with relatively quiet periods punctuated by sharp upswings in luminosity, called "flares." Over a period of a few days in early 2008, three independent arrays of very-high-energy (VHE) gamma-ray detectors noticed a sudden increase in radiation from M87. The VHE band, corresponding to photon energies of around a teraelectron volt (TeV), is readily observed from the ground by detecting the streak of blue Cherenkov radiation emitted as the photon passes through the atmosphere. At the same time, the Very Long Baseline Array (VLBA) mapped an increase in the radio emission near the black hole, in the form of a bright patch that moved outward during the ensuing months. The coincidence of the gamma-ray flare and the sudden appearance of a new patch of radio emission is strong evidence that the two phenomena are connected.

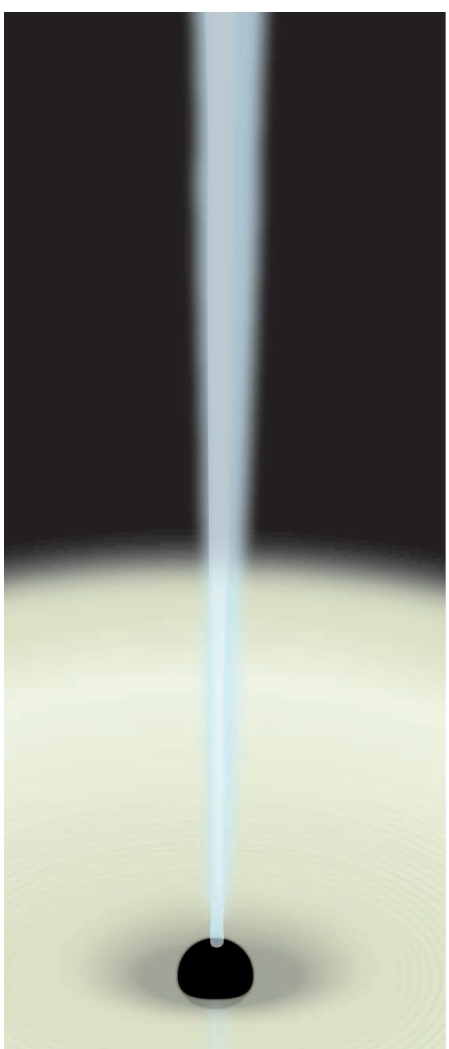

CREDIT: P. HUEY/*SCIENCE*

Flares and jets. M87's jets are thought to form just outside the region where a swirling disk of gas makes its final plunge into the black hole, as shown in this artist's conception. Gamma-rays from jets have long been regarded as evidence of particle acceleration to very high energies, but it was not known whether this acceleration occurs far from the black hole or close in. The new results by Acciari *et al*. show that this acceleration occurs right at the base of the jet.

The detection of gamma-rays from so close to the black hole is slightly surprising. VHE gamma-rays can be absorbed by infrared and visible-light photons to create electron-positron pairs. If the intensity of long-wavelength radiation is high enough, the gamma-rays will be completely extinguished. This is thought to be the situation close to the black holes in luminous objects such as quasars. When some quasars were first shown to be gamma-ray emitters in the early 1990s (*4*), most theorists concluded that the radiation had to be produced far from the black hole—hundreds or thousands of event horizon radii—where the long-wavelength radiation background is weaker (*5*–*7*). Compared to other gamma-ray sources,

JILA, University of Colorado, Boulder, CO 80309–0440, USA. E-mail: mitch@jila.colorado.edu

however, the luminosity of M87 is low, making it plausible that we can see gamma-rays coming from close in (see the figure).

Another curious feature of the M87 detection is that it comes from a jet that is not pointing at us—the jet is at an angle of ~15° to 30° relative to our line of sight. For most other gamma-ray–emitting jets, we appear to be looking straight "down the barrel." For observers with such a vantage point, effects predicted by the special theory of relativity would conspire to aid the escape of gamma-rays, increase their apparent luminosity, and make the onset of flares appear more sudden. We have no such advantage in our view of M87—that is, unless the flaring material is somehow moving toward us, rather than following the general track of the jet (*8*).

Jets produce radiation not only at radio and gamma-ray wavelengths, but at all wavelengths in between. In sources where gamma-rays are detected, they seem to dominate the total output, but there is usually a second broad peak of radiation at longer wavelengths. How that radiation is produced remains unclear. The longer wavelengths may arise from the gyration of electrons in the jet's magnetic field (synchrotron radiation), whereas the shorter wavelengths probably result from the scattering of radiation by energetic electrons (Compton scattering). But it is not known whether the supply of photons for the scattering process comes from the synchrotron radiation or from some other source (for example, an accretion disk) external to the jet (*5*, *6*). By correlating the time dependence of flares at different wavelengths, astronomers hope not only to pin down the details of the emission process, but also to answer broader questions about how jets are powered, accelerated, and focused into narrow streams.

With the region for acceleration now identified by Acciari *et al*. as being closer than expected to the black hole, other questions regarding the source of power for the jets can be addressed: Is it the energy contained in the swirling gas about to be swallowed, or is it rotational energy stored in the black hole itself (*9*)? We also do not know whether the jets are made of ordinary plasma consisting of protons and electrons, or of an exotic mix of electrons and positrons. And the importance of magnetic fields in jet dynamics and energetics, though strongly suspected, has yet to be proven. Gamma-ray astronomy will likely play a key role in resolving these questions, not only via the ground-based TeV arrays but also through the Fermi Gamma-Ray Space Telescope, launched in 2008 and expected to release its first data later this year.

References and Notes

1. W. Junor, J. A. Biretta, M. Livio, *Nature* **401**, 891 (1999).
2. With a mass estimated at between 3 and 6 billion solar masses, the black hole in M87 has an event horizon (the Schwarzschild radius) of 60 to 120 times the radius of the Earth's orbit, or 8 to 16 light-hours. The radio observations resolve the jet down to scales of several light-weeks.
3. V. A. Acciari *et al.*, *Science* **325**, 444 (2009); published online 2 July 2009 (10.1126/science.1175406).
4. R. C. Hartman *et al.*, *Astrophys. J.* **385**, L1 (1992).
5. C. D. Dermer, R. Schlickeiser, *Astrophys. J.* **416**, 458 (1993).
6. M. Sikora, M. C. Begelman, M. J. Rees, *Astrophys. J.* **421**, 153 (1994).
7. A. P. Marscher *et al.*, *Nature* **452**, 966 (2008).
8. D. Giannios, D. A. Uzdensky, M. C. Begelman, *Mon. Not. R. Astron. Soc.* **395**, L29 (2009).
9. R. D. Blandford, R. L. Znajek, *Mon. Not. R. Astron. Soc.* **179**, 433 (1977).

10.1126/science.1176908

MICROBIOLOGY

Tumbling for Stealth?

A green alga changes its flagellar beating patterns to create a run-and-tumble motion that may help it escape predation.

Roman Stocker and William M. Durham

Department of Civil and Environmental Engineering, Massachusetts Institute of Technology, Cambridge, MA 02139, USA. E-mail: romans@mit.edu

One of the most remarkable and pervasive feats in the microscopic world is the coordination of flagella, the slender, whiplike structures that protrude from many types of cells. The collective motion of flagella (also known as cilia when they occur in large numbers in eukaryotes) drives fluid transport (*1*), and permits individuals to save energy through cooperation (*2*). Because the internal structure of cilia is highly conserved among eukaryotes from algae to humans, free-swimming organisms like *Chlamydomonas* (see the first figure, panel A) have long been powerful model systems (*3*). On page 487 of this issue, Polin *et al*. (*4*) show how synchronization of the flagella in *Chlamydomonas reinhardtii* governs the movement of this green alga through water, a key determinant of its ecological fitness.

Polin *et al*. found that *C. reinhardtii* actively switches between synchronized and asynchronous flagellar beating. When the

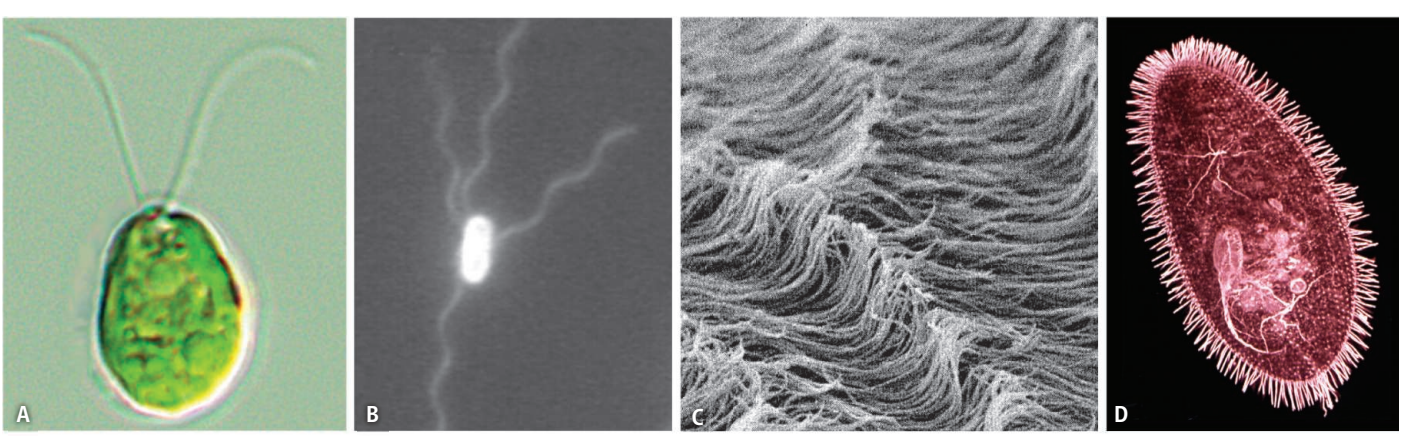

Cilia and flagella. The alga *Chlamydomonas reinhardtii* (body size 7 μm by 10 μm) (**A**) swims with two flagella. The bacterium *E. coli* (body size 1 μm by 2 μm) (**B**) swims by coordinating several helical flagella (*12*). The coordinated motion of thousands of cilia produces metachronal waves (wavelength 5 μm) (*13*) (**C**); these waves propel microorganisms like *Paramecium* (body size 50 μm by 100 μm) (**D**).

CREDIT: (PANEL A) BRIAN P. PIASECKI AND CAROLYN D. SILFLOW/UNIV. OF MINNESOTA. (PANEL B) FROM (*14*). (PANEL C) FROM (*13*). (PANEL D) ANNE FLEURY, MICHEL LAURENT, AND ANDRÉ ADOUTTE/UNIVERSITÉ PARIS-SUD

flagella beat in synchrony, they perform a "breaststroke" that propels the cell forward. Every 11 s on average, the cell desynchronizes its flagella, triggering a sharp change in direction. This behavior resembles the run-and-tumble motion of the bacterium *Escherichia coli* (see the first figure, panel B). When *E. coli* bundles its 4 to 10 flagella, rotation of the flagella within a bundle provides propulsion in a nearly straight path (the "run"). When one or more of the motors driving the flagella reverse direction, those flagella leave the bundle, causing a change in direction (the "tumble") (*5*). Polin *et al*. find that *C. reinhardtii* switches between the synchronous and asynchronous states by modulating the difference in the beat frequencies of its two flagella. When the frequency difference is small, the flagella synchronize, whereas when it is large, disarray prevails and the motion of the flagella decouples, causing the cell to turn sharply.

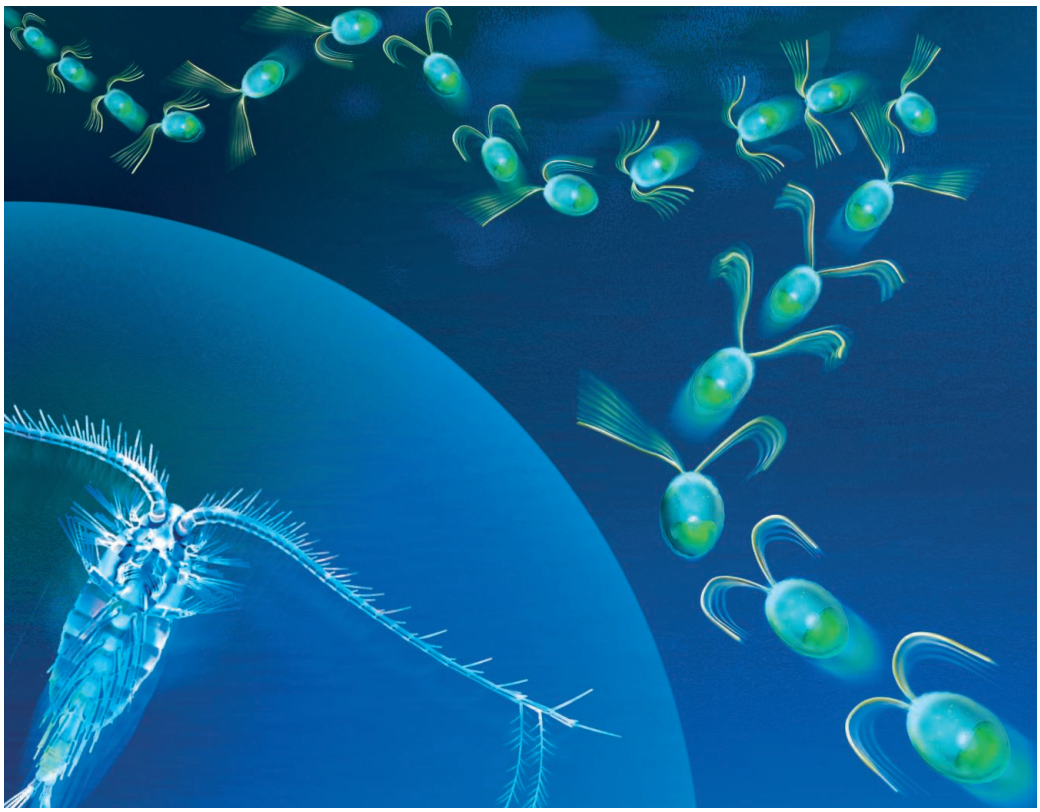

Run-and-tumble swimming. The swimming pattern of *Chlamydomonas* discovered by Polin *et al*. could be a stealthy tactic to avoid encounters with predators such as copepods. Straight runs occur when the alga's two flagella beat in unison, whereas tumbles are triggered when their motion is not synchronized. To minimize predation risk, the run length must be smaller than the predator's capture radius, represented by the spherical surface (*9*, *11*).

Synchronization arises in many biophysical processes, including cardiac pacemakers, clapping crowds, flashing fireflies, croaking frogs, and firing neurons. The classic example dates back to Huygens (*6*), who observed that the pendula of two clocks suspended from the same beam slowly vary in frequency until their swings are perfectly out of phase. This synchrony is achieved via forces transmitted through the beam. The results of Polin *et al*. indicate that, in a similar fashion, the two flagella of *C. reinhardtii* synchronize via forces transmitted through the fluid. Fluid forces have been known to synchronize the motion of microorganisms swimming near each other, including spirochetes and spermatozoa (*2*), and to induce the bundling of *E. coli*'s flagella during a run (*7*).

Passive synchronization through hydrodynamic coupling is also widely believed to be responsible for metachronal waves (*8*), (see the first figure, panel C), in which thousands of cilia undulate like "the wave" performed by crowds at stadiums. These patterns are responsible for a wide range of functions, from the flushing of the human respiratory system to the propulsion of microorganisms (see the first figure, panel D). The passive synchronization liberates a ciliated organism from the need to control each cilium with high accuracy.

Polin *et al*. show that the hydrodynamic coupling of *C. reinhardtii*'s flagella is periodically interrupted. By comparing the flagellar beating statistics of tethered cells with the statistics of turning events of free-swimming cells, they conclude that flagellar desynchronization results in a sharp, random change in direction. Their results suggest that the increase in the frequency difference between the flagella, and the ensuing tumble, are under the control of the cell.

The best strategy to explore new space is to swim straight, because a tumbling cell partially retraces its path (*9*). So why would *Chlamydomonas* choose to tumble? *E. coli* tumbles to perform chemotaxis: Each tumble is a random reorientation, but by selectively delaying tumbles, the cell can move to more favorable conditions in a chemical gradient. The mean time between tumbles (1 s) is dictated by Brownian rotational diffusion, which prevents *E. coli* from swimming straight for more than a second. But *Chlamydomonas* is 10 times as large and thus 1000 times less susceptible to rotational diffusion: It could swim straight to its target, but chooses not to.

The explanation may lie in a trade-off between the quest for resources and the avoidance of predators. Tumbling reduces predator encounters when the run length is smaller than the predator's capture radius (*9*). The resulting diffusive swimming can confer an evolutionary advantage over straight swimming (*10*) and is common among microorganisms (*9*). The tumbles reported by Polin *et al*. could thus be a stealthy strategy to avoid predators (see the second figure). Consistent with this idea, the capture radius of small predatory copepods, 4 to 8 mm (*11*), is larger than the mean run length of ~1 mm reported by Polin *et al*.

The global importance of the microscopic world often stems from its huge number of inhabitants: A myriad of tiny algae like *Chlamydomonas* produce a substantial fraction of the world's oxygen, and millions of microscopic cilia help us breath it. Yet, as Polin *et al*. show, a fundamental understanding of their collective effects hinges on a thorough characterization of microscopic processes on the level of an individual.

References and Notes

1. G. L. Baum, Z. Priel, Y. Roth, N. Liron, E. J. Ostfeld, Eds., *Cilia, Mucus, and Mucociliary Interactions* (Dekker, New York, 1998).
2. G. I. Taylor, *Proc. R. Soc. London A* **209**, 447 (1951).
3. G. Vogel, *Science* **310**, 216 (2005).
4. M. Polin, I. Tuval, K. Drescher, J. P. Gollub, R. E. Gold-

stein, *Science* **325**, 487 (2009).
5. H. C. Berg, *E. coli in Motion* (Springer, New York, 2004).
6. C. Huygens, Horologium Oscillatorium (Apud F. Muguet, Parisiis, France, 1673); English transl., *The Pendulum Clock* (Iowa State Univ. Press, Ames, 1986).
7. H. Flores, E. Lobaton, S. Mendez-Diez, S. Tlupova, R. Cortez, *Bull. Math. Biol.* **67**, 137 (2005).
8. S. L. Tamm, *J. Exp. Biol.* **113**, 401 (1984).
9. A. W. Visser, T. Kiørboe, *Oecologia* **148**, 538 (2006).
10. A. W. Visser, *J. Plankt. Res.* **29**, 447 (2007).
11. The feeding current, u, produced by a hovering predator of radius a, can be modeled in the far field by a stokeslet, which yields $u \approx Ua/r$ to leading order, where U is the near field feeding velocity and r is the distance from the predator. The capture radius is the distance r at which u is equal to the prey swimming speed (100 μm/s). For small copepods, $a \approx 100$ μm and $U = 4$ to 8 mm/s, yielding $r =$ 4 to 8 mm.
12. L. Turner, W. S. Ryu, H. C. Berg, *J. Bacteriol.* **182**, 2793 (2000).
13. S. L. Tamm, G. A. Horridge, *Proc. R. Soc. London B Biol. Sci.* **175**, 219 (1970).
14. We thank H. Berg, K. Foster, T. Kiørboe, T. Powers, and S. Tamm for insightful comments. R.S. acknowledges support from NSF (OCE CAREER 0744641) and W.M.D. acknowledges a National Defense Science and Engineering Graduate Fellowship.

10.1126/science.1177269

CHEMISTRY

How Deformation Can Lend a Hand to Molecular Ordering

Liquid crystal phases of molecules with no inherent handedness undergo subtle deformations that create unusual chiral fluids and nanostructures.

David B. Amabilino

The spontaneous separation of mirror-image molecules—enantiomers—into distinct crystals, first seen by Louis Pasteur (*1*), played a key role in the development of the basic principles of stereochemistry and is widely used to separate chiral compounds (*2*). Such "spontaneous resolution" has since been observed in many different molecular systems, such as monolayers and clusters (*3*), but it seemed highly unlikely to occur in an isotropic fluid phase, given the random motions that take place in the liquid state. Yet Hough *et al*. report on page 452 of this issue (*4*) that achiral molecules with a "boomerang" shape spontaneously resolve into right- and left-handed domains in an isotropic liquid. In related work on page 456, Hough *et al*. (*5*) show that members of this class of molecules can assemble into helical nanofilaments that lead to a new type of supramolecular ordering.

The fluids in question are liquid crystals based on so-called bent-core (boomerang-shaped core) molecules (see the figure, panel A). Liquid crystal molecules commonly organize themselves so that the cores of the molecules are aligned to some extent; in smectic liquid crystals, the molecules move within well-defined layers. The cores bear flexible side chains that disrupt crystal-packing interactions and promote formation of fluid phases. Typically, a liquid crystal phase is a mosaic of relatively large domains. Within each domain, the cores are ordered along one direction, but this direction varies between domains, so the material is anisotropic. This anisotropy causes the materials to be birefringent, exhibiting light and dark domains when viewed with crossed polarizing filters.

Institut de Ciència de Materials de Barcelona (CSIC), Campus Universitari, Esfera UAB, 08193 Bellaterra (Catalonia), Spain. E-mail: amabilino@icmab.es

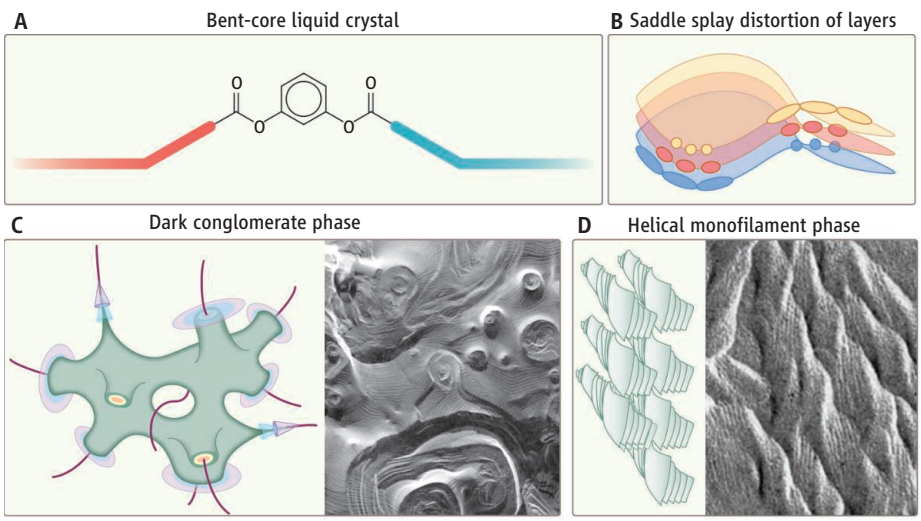

How chiral phases shape up. (**A**) Bent-core molecules consist of an aromatic center, linked (in the case shown) with ester groups, to other rigid aromatic groups (red and blue). These groups bear flexible side chains at their extremes. (**B**) The layers of the smectic liquid crystal phase undergo splay distortions, which cause right- and left-handed chiral domains to form. Here, the colors represent different layers. Depending on the particular molecules used, this process can create (**C**) a chiral isotropic liquid in a sponge-like "dark conglomerate" phase, or (**D**) helical nanofilaments, which are shown both schematically and as freeze-fracture micrographs.

In most cases, achiral molecules create a material with achiral domains. However, the bent-core liquid crystals can undergo spontaneous resolution (*6*, *7*) in their fluid form, resulting in chiral domains. The core of these molecules does not stay flat but twists along the bonds between the aromatic ring and the adjoining ester or imine groups (see the figure, panel A). The twisting creates either left- or right-handed helices, which undergo further packing to create chiral superstructures that are also polar in terms of the directionality of the cores.

Up to now, the phases formed by the bent-core molecules were like other liquid crystals in that they displayed anisotropy over large areas: The chirality of the different domains leads to light and dark regions when viewed with a polarizing optical microscope. However, the system described by Hough *et al*. (*4*) is different. The authors find that the phase that forms upon cooling the ordinary isotropic liquid, where the molecules move freely, still appears to be isotropic, at least at the macroscopic level. This "dark conglomerate" (DC) phase displays no long-range order and appears very dark when viewed with crossed polarizing filters. It is termed a conglomerate because the sample resolves spontaneously into domains (*8*–*10*)—in this case, homochiral domains up to hundreds of micrometers in width. The chirality of these domains manifests itself in remarkable optical activity: the ability to rotate plane-polarized light.

How can a liquid of achiral molecules that is isotropic at the macroscopic level exhibit signatures of chirality? In the layered DC phase, the molecules have short-range order (over

distances less than 100 nm), but this ordering is averaged at larger length scales because of strains that deform the layers. This "saddle splay deformation" is rather like the warping of a potato chip when it is cooked (*11*) (see the figure, panel B). Continuous sheets appear to twist and turn randomly across large areas to create an interpenetrating, sponge-like morphology (see the figure, panel C).

Indeed, this kind of morphology has also been seen in other liquid crystals (*12*), as well as in lyotropic (*13*) systems, where solvent molecules are also present. The deformation occurs in a continuous way, which in the case of the bent-core molecules allows for the chiral structure to be propagated within the layer while preventing long-range order. The ability of the bent-core molecules to couple their tilt between layers means that neighboring sheets have identical handedness. It has been estimated that for optical studies with green light, there are about 100 domains per cubic wavelength (~500 nm), so local birefringence is reduced by the random orientations to create a bulk isotropic phase.

In a related type of bent-core molecule, when the liquid crystal phase is more ordered, the saddle splay deformation leads to the development of helical nanofilaments (*5*) (see the figure, panel D). The achiral molecules again resolve spontaneously into differently handed conformations and arrangements, but their local chiral structure creates twisted layers that subsequently organize into arrays of helically packed layers. This non-optimum packing, which leaves much space between the fibers, is a result of the chiral twisting force generated by the molecules when they pack.

This structure is completely new and is different from the previously accepted structure of these liquid crystalline phases, called B4 (*14*). The order of the layers, which is ~40 nm (eight layers) within these nanofilaments, leads to weak x-ray diffraction, an effect that previously confused the assignment of the structure. Hough *et al*. (*5*) surmised that the flat layers are not a thermodynamic minimum for these molecules because of the structure in the strata, which must bend in order to match an optimum packing scenario. The transfer of chirality is extremely efficient in that single nucleation sites yield homochiral domains of nanofilaments. TEM measurements, which reveal details of the helices at different length scales, reveal the hierarchical nature of the chiral structure-forming process.

The observation of chirality in an isotropic liquid (*4*) is remarkable, given the many competing effects that should destabilize the ordering. The realization that certain liquid crystalline phases are composed of nanofilaments (*5*) is also groundbreaking. Both results go against intuition and are noteworthy advances in the area of spontaneous resolution (*15*). The implications of these supramolecular effects observed in fluid media could provide important insight into the transfer of chirality in soft materials. There may also be ways to use the layers in these materials as the basis of switches, as in liquid crystal displays. The use of these systems requires delicate control of the competition between layering and twist of the chiral system, and the concepts are sure to be useful in the explanation of chiral transfer in other systems with nanoscale features.

References

1. L. Pasteur, *Ann. Chim. Phys.* **24**, 442 (1848).
2. R. G. Kostyanovsky, *Mendeleev Commun.* **13**, 85 (2003).
3. L. Pérez-García, D. B. Amabilino, *Chem. Soc. Rev.* **31**, 342 (2002).
4. L. E. Hough *et al.*, *Science* **325**, 452 (2009).
5. L. E. Hough *et al.*, *Science* **325**, 456 (2009).
6. D. M. Walba *et al.*, *J. Phys. Org. Chem.* **13**, 830 (2000).
7. R. A. Reddy, C. Tchierske, *J. Mater. Chem.* **16**, 907 (2006).
8. J. Thisayukta, Y. Nakayama, S. Kawauchi, H. Takezoe, J. Watanabe, *J. Am. Chem. Soc.* **122**, 7441 (2000).
9. W. Weissflog, M. W. Schröder, S. Diele, G. Pelzl, *Adv. Mater.* **15**, 630 (2003).
10. G. Dantlgraber, C. Keith, U. Baumeister, C. Tschierske, *J. Mater. Chem.* **17**, 3419 (2007).
11. R. D. Kamien, *Science* **315**, 1083 (2007).
12. B. A. DiDonna, R. D. Kamien, *Phys. Rev. Lett.* **89**, 215504 (2002).
13. A. V. Gaikwad, P. Verschuren, T. van der Loop, G. Rothenberg, E. Eiser, *Soft Matter* **5**, 1994 (2009).
14. T. Sekine *et al.*, *J. Mater. Chem.* **7**, 1307 (1997).
15. L. Pérez-García, D. B. Amabilino, *Chem. Soc. Rev.* **36**, 941 (2007).

10.1126/science.1177315

CELL BIOLOGY

Connecting Organelles

Protein contacts between mitochondria and the endoplasmic reticulum allow metabolic exchange and communication.

Nils Wiedemann, Chris Meisinger, Nikolaus Pfanner

Mitochondria are organelles that form a dynamic network in most eukaryotic cell types. Although originally considered to be semi-autonomous powerhouses, they are intimately connected to the rest of the cell through metabolic and signaling pathways, and play a central role in programmed cell death (apoptosis). Sites of close proximity between mitochondria and the tubular network of the endoplasmic reticulum have long been known from electron micrographs, yet their molecular nature remained elusive. On page 477 in this issue, Kornmann *et al*. (*1*) show that a complex of proteins that controls mitochondrial shape and protein biogenesis (*2*–*4*) bridge these two organelles.

Institut für Biochemie und Molekularbiologie, Zentrum für Biochemie und Molekulare Zellforschung and Centre for Biological Signalling Studies, Universität Freiburg, 79104 Freiburg, Germany. E-mail: nikolaus.pfanner@biochemie.uni-freiburg.de

Proteins that connect the endoplasmic reticulum and mitochondria were previously suggested by interaction between the mitochondrial outer membrane and the mitochondria-associated membrane, a fraction of the endoplasmic reticulum membrane that can be biochemically isolated with mitochondria (*5*, *6*). Recently, mitofusin proteins were reported to connect both organelles to control the transport of Ca^{2+} ions between them (*7*, *8*). Inositol-1,4,5-trisphosphate (IP_3) receptors, which act as Ca^{2+} channels, are enriched in the mitochondria-associated membrane, and the close proximity of both organelles is thought to enhance mitochondrial uptake of Ca^{2+} that is released by the endoplasmic reticulum through IP_3 receptors (*7*). However, the mitochondria–endoplasmic reticulum interface was reduced by only ~40% in cells lacking mitofusin 2, indicating that redundant bridges between endoplasmic reticulum and mitochondria exist. Several additional proteins, including IP_3 receptors and the multifunctional phosphofurin acidic cluster sorting protein 2 have also been implicated in linking both organelles, but their relevance for forming such junctions has not been clear (*1*, *9*).

Kornmann *et al*. developed an elegant genetic screen to search for proteins that connect the endoplasmic reticulum and mitochondria. Their approach involved a fusion protein containing targeting and membrane anchor sequences for the endoplasmic reticulum and mitochondrial outer membrane (*9*). When this synthetic linker was expressed in yeast, it induced artificial contact sites between both organelles. The authors screened for yeast mutants that were unable to grow in the absence of this linker, and identified the mitochondrial distribution and morphology protein 12 (Mdm12), previously implicated in the processes it is named for (*10*). Mdm12

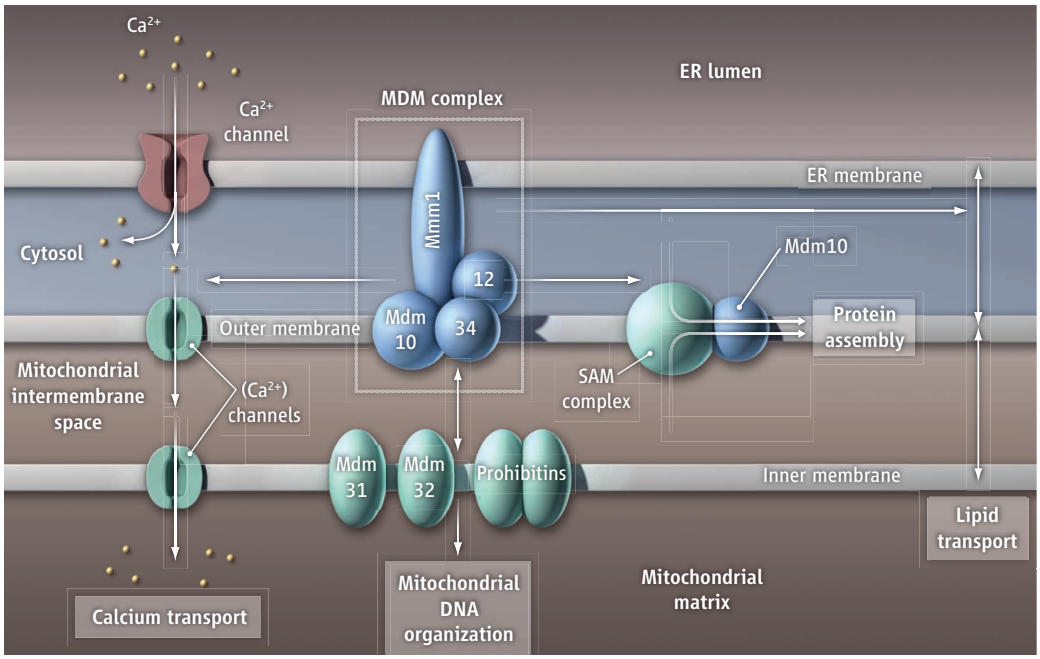

Junction functions. The MDM complex bridges the endoplasmic reticulum and mitochondrial outer membrane and forms a structural framework for interaction with inner-membrane proteins and the organization of mitochondrial DNA. Mitochondria–endoplasmic reticulum junctions are associated with transfer of lipids and Ca^{2+}, protein biogenesis, and membrane dynamics.

interacts with other proteins that affect mitochondrial morphology—collectively called the MDM complex [also called the mitochore (*3*) or endoplasmic reticulum–mitochondria encounter structure (*1*)]—including Mdm10, maintenance of mitochondrial morphology protein 1 (Mmm1), and Mdm34 (also called Mmm2) (*1*, *3*, *4*). Expression of the synthetic linker suppressed the growth defect of cells lacking Mdm34 and in part also the growth defect of cells lacking Mdm10 or Mmm1, indicating that the MDM complex connects endoplasmic reticulum and mitochondria. Kornmann *et al*. also show that the amino terminus of Mmm1 is anchored in the endoplasmic reticulum membrane, thereby providing a tether for attaching mitochondria to the endoplasmic reticulum (see the figure). Mmm1 was originally identified in mitochondrial membranes, and Mmm1 lacking its cytosolic carboxyl-terminal domain (which contacts other proteins of the MDM complex) had been localized to the endoplasmic reticulum (*11*).

Mitochondria–endoplasmic reticulum junctions localize to discrete foci, and a single yeast cell may contain ~10 mitochondria–endoplasmic reticulum junctions, although the number may vary from 2 to 100 (*1*, *6*). An individual junction may contain roughly 100 MDM complexes that form a structural framework to connect both organelles. These physical bridges may create membrane microdomains that recruit additional components for performing junction-localized functions. Indeed, genetic studies revealed a functional relationship of MDM components to lipid biosynthesis and Ca^{2+} signaling components (*1*, *12*). Mitochondria not only import about 1000 different proteins (*13*), but also many lipids; whereas the machinery for protein transport into mitochondria has been characterized in detail, little has been known about the mechanism of lipid transport into the mitochondria. Importantly, components of the MDM complex functionally interact with mitochondrial inner-membrane proteins, such as Md31 and Mdm32, and prohibitin ring complexes, to affect mitochondrial shape and the organization of mitochondrial DNA into nucleoids (*12*, *14*). Thus, as well as transferring lipids and Ca^{2+} ions from endoplasmic reticulum to the mitochondrial outer membrane, the mitochondria–endoplasmic reticulum junctions may also influence the structural organization of the mitochondrial inner membrane and DNA (*2*). Moreover, the MDM complex may have a role in connecting mitochondria to the cytoskeleton, either through adaptor proteins or through its association with the endoplasmic reticulum (*1*, *3*).

MDM complex proteins probably not only play structural roles but are likely functionally active. For example, Mdm10 is also part of the sorting and assembly machinery (SAM complex) of the outer membrane (*4*). The SAM complex is responsible for biogenesis and assembly of the translocase of the outer membrane (TOM complex), the central protein entry gate of mitochondria. Components of the MDM complex may function in both protein transport and lipid biogenesis.

The remarkable variety of functions associated with MDM complexes suggests that they represent the main organizing center for mitochondrial communication with the rest of the eukaryotic cell. Whereas Kornmann *et al*. define the role of MDM complexes for mitochondria–endoplasmic reticulum junctions in yeast, the role of mitofusins and IP_3 receptors was characterized in mammalian cells (*7*). It is likely that a number of different molecules are involved in forming the junctions in each species and thus provide a redundant system, reflecting the importance of the junctions for mitochondrial communication. Electron tomography revealed junctions with different distances between endoplasmic reticulum and mitochondrial outer membrane, ranging from approximately 10 to 25 nm in the same cell type (*9*). Different bridging molecules likely form tethers of different length, and conceivably, different functions of mitochondria–endoplasmic reticulum communication may be associated with them.

The molecular mechanisms underlying the dynamics of mitochondria–endoplasmic reticulum junctions are only partly understood and will thus represent a major field for future studies. Intriguing questions include how various lipids are extracted from one membrane, transferred by proteinaceous carriers, and then inserted into another membrane; how MDM complex proteins form membrane microdomains (*12*); and whether mitochondria–endoplasmic reticulum junctions are involved in protein biogenesis or targeting of messenger RNA to mitochondria (*4*, *15*).

References

1. B. Kornmann *et al.*, *Science* **325**, 477 (2009).
2. A. E. Aiken Hobbs, M. Srinivasan, J. M. McCaffery, R. E. Jensen, *J. Cell Biol.* **152**, 401 (2001).
3. I. R. Boldogh *et al.*, *Mol. Biol. Cell* **14**, 4618 (2003).
4. C. Meisinger *et al.*, *Dev. Cell* **7**, 61 (2004).
5. J. E. Vance, *J. Biol. Chem.* **265**, 7248 (1990).
6. G. Achleitner *et al.*, *Eur. J. Biochem.* **264**, 545 (1999).
7. O. M. de Brito, L. Scorrano, *Nature* **456**, 605 (2008).
8. R. Rizzuto *et al.*, *Science* **280**, 1763 (1998).
9. G. Csordás *et al.*, *J. Cell Biol.* **174**, 915 (2006).
10. K. H. Berger, L. F. Sogo, M. P. Yaffe, *J. Cell Biol.* **136**, 545 (1997).
11. N. Kondo-Okamoto, J. M. Shaw, K. Okamoto, *J. Biol. Chem.* **278**, 48997 (2003).
12. C. Osman *et al.*, *J. Cell Biol.* **184**, 583 (2009).
13. A. Sickmann *et al.*, *Proc. Natl. Acad. Sci. U.S.A.* **100**, 13207 (2003).
14. K. S. Dimmer, S. Jakobs, F. Vogel, K. Altmann, B. Westermann, *J. Cell Biol.* **168**, 103 (2005).
15. R. P. Zahedi *et al.*, *Mol. Biol. Cell* **17**, 1436 (2006).

10.1126/science.1178016

CREDIT: C. BICKEL/*SCIENCE*

INTRODUCTION

Connections

We are caught in an inescapable network of mutuality. ... Whatever affects one directly, affects all indirectly. —Martin Luther King Jr.

FROM CHAOS COMES COMPLEXITY. FROM THE MOVEMENT OF MOLECULES WITHIN our cells to communication across an entire planet, we are part of networks. This special section shows how scientists are pushing network analysis to its limits across disciplinary fields.

Barabási published his seminal paper on scale-free networks a decade ago, and he starts us off by looking both at the past and the future (p. 412). The dramatic progress of researchers from disparate fields plunging into network analysis needs to be tempered by awareness of the potential dangers of misapplying fundamental assumptions (Butts, p. 414). Network analyses are also providing insights that will help us deal with our largest societal challenges. Bascompte (p. 416) confronts the effects of climate change on ecosystems and Ostrom (p. 419) examines organizing to maintain sustainability.

Physicists have taken up the challenge, too, as Adrian Cho reports (p. 406), aiming to use quantitative methods to forecast ethnic strife in Somalia, monitor surges of emotion in Internet users, and track the emergence of behavioral norms. Additionally, John Bohannon (p. 409) looks into one of the most controversial uses of network analysis: to identify key figures in terrorist organizations and eliminate them. Furthermore, networks can teach us about underlying mechanisms that affect us individually and as a society, such as monetary exchanges (Schweitzer *et al.*, p. 422) or transportation systems that promote viral transmission (Vespignani, p. 425).

At a microscopic level, molecular biologists are using networks to analyze basic cellular circuitry (Kim *et al.*, p. 429) to describe how interactions within a cell can be measured or modeled to generate predictions of responses to perturbation. Additionally, *Science Signaling* focuses on dynamics in signaling networks.

We need more and better data in many disciplines. It is not enough to look at patterns; we need to study how they evolve and change. The magnitude of the challenges we are facing shows how much we still need to learn. How can we move between levels of a complex system—to understand the transition from DNA sequence to disease symptoms or to predict the next economic recession? Network analysis is allowing us to understand how the world works from new vantage points, and it is exciting to think about what we will learn in the next 10 years.

– BARBARA R. JASNY, LAURA M. ZAHN, ELIOT MARSHALL

Complex Systems and Networks

CONTENTS

News

Perspectives

Review

See also related Policy Forum on p. 396 and go to http://www.sciencemag.org/complexity/ for additional online material from Science Signaling *and http://sciencecareers.sciencemag.org/career_magazine/previous_issues/articles/2009_07_24/caredit.a0900091 for a look at Science Careers in Network Sciences.*

CREDIT: CESAR HIDALGO

Science

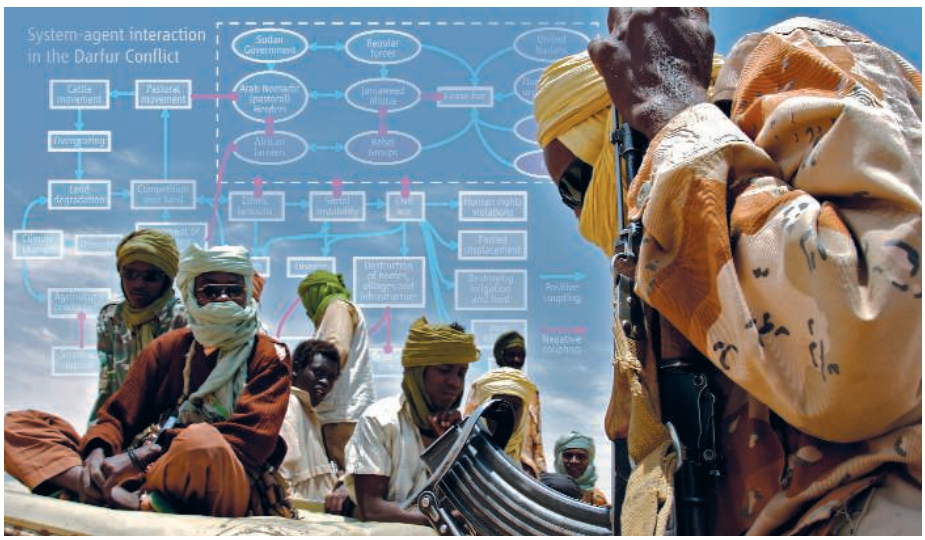

New model army. Janjaweed fighters interact with many other groups in a model of the Darfur conflict.

NEWS

Ourselves and Our Interactions: The Ultimate Physics Problem?

In the field of complex socioeconomic systems, physicists and others analyze people almost as if they were interchangeable electrons. Can that approach decipher society and what ails it?

ZÜRICH, SWITZERLAND—Janusz Holyst sounds frustrated. "When I look to the textbooks on emotion, there are no numbers, there are no equations," laments the theoretical physicist from the Warsaw University of Technology. Holyst hopes to supply what the books are lacking, however. He aims to develop the tools to analyze emotions quantitatively. Then he intends to use them to literally read your feelings.

With €3.6 million of support from the European Commission, Holyst and eight collaborators aim to develop a computer program that can analyze dialogue from Internet chat rooms and tell when people are growing excited, angry, and so on. Flagging key words isn't enough, he says, because people use language differently. Some, for example, curse regardless of their mood. Ultimately, Holyst hopes to decipher group emotion, such as the euphoria that pervades a stadium full of sports fans when the home team wins. "There are tens of models of opinion formation," he says, "but there are no models of emotion."

Holyst is one of a small but growing number of physicists who are turning from atoms and electrons to study social phenomena such as terrorism, the growth of cities, and the popularity of Internet videos. Joining with social scientists, they treat groups of people as "complex socioeconomic systems" of many interacting individuals and analyze them using conceptual tools borrowed from physics, mathematics, and computer science. Last month, 130 researchers of various stripes gathered here to discuss such work.*

Forays into "sociophysics" began in the early 1970s. Physicists proposed, for example, that individuals interact to form public opinion much as neighboring atoms make a crystal magnetic by aligning their magnetic fields; researchers analyzed the social phenomenon by adapting the Ising model used to describe such magnetic interactions. In the 1990s, many physicists turned to economics in the controversial subfield of econophysics (see sidebar, p. 408). Now, the movement seems to be gathering momentum, as complex-systems researchers have made solid contributions in the study of traffic, epidemiology, and economics. Some are now tackling more-daunting problems, such as the emergence of social norms.

"The problems are more complicated than most natural scientists assume, but less hopeless than most social scientists think," says Dirk Helbing, a physicist-turned-sociologist at the Swiss Federal Institute of Technology Zürich (ETHZ). Oversimplification is a risk. "In some fields, physicists have a bad reputation for applying the Ising model directly" to cases in which it may not fit the facts, says Stephen Eubank, a physicist at Virginia Polytechnic Institute and State University (Virginia Tech) in Blacksburg who models epidemics.

Nevertheless, physicists and social scientists are working together on increasingly nuanced and realistic models, Helbing says. The complex-systems approach could help avert—or at least explain—systemic crises such as the current global economic meltdown, he says. "We spend billions of dollars trying to understand the origins of the universe," Helbing says, "while we still don't understand the conditions for a stable society, a functioning economy, or peace."

Complex is as complex does

Scientists can't say exactly what a complex system is in the same way they can define an atom or a gene. Rather, they tend to describe how a complex system looks and behaves. "If you ask a biologist, 'What is life?' he will give you a list of characteristics. He probably won't give you a strict definition," says Ingve Simonsen, a physicist at the Norwegian University of Science and Technology in Trondheim. "It's similar with complex systems."

First off, a complex system consists of many elements that interact so strongly that they tend to organize themselves in one way or another. This "emergent behavior" makes the group more than the sum of its parts. A car may be complicated, but it is not a complex system, as each of its parts interacts with a few others in a predictable way. But cars in traffic form a complex system, as drivers' jockeying for position can lead to surprises such as "phantom" traffic jams that arise for no obvious reason.

Complex systems also tend to be persnickety. A tiny change among the pieces may lead to a big swing in the behavior of the whole

Online
sciencemag.org
Podcast interview with author Adrian Cho.

*International Workshop on Coping with Crises in Complex Socio-Economic Systems, 8–12 June 2009.

CREDITS (TOP TO BOTTOM): SHANE BAUER/NEWSCOM; (INSET GRAPHIC) ADAPTED FROM JÜRGEN SCHEFFRAN, MODELING CLIMATE-INDUCED INSTABILITIES AND CONFLICTS

Published by AAAS

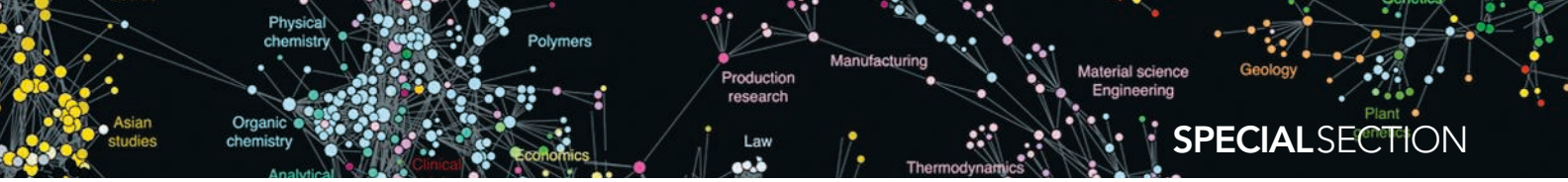

system—as when, on 4 November 2006, the disconnection of a single power cable in northern Germany triggered regional blackouts as far away as Portugal.

The systems are often hard to control and may be impossible to "tune" for optimal behavior. At the same time, "there are so many ways for a complex system to fail that it's impossible to prepare for them all," says Eubank.

Like the riveter's trade, the field is defined largely by its tools. Researchers borrow from statistical physics the theories that describe phase transitions—in which interactions among many atoms lead to dramatic changes in a material as a whole, such as the freezing of water into ice and the emergence of magnetism as hot iron cools—to probe how, say, public sentiment can suddenly turn against a once-popular war.

Much work also relies on networks that represent individuals—such as victims of an epidemic—as points or "nodes" and the social ties between them as lines or "edges." Researchers often use "agent-based models": computer simulations in which myriad virtual agents interact like robots following predefined rules. Such models might help reveal, for example, how interactions between investors, hedge funds, and banks trigger market swings.

Behind it all lies the assumption that, at least within distinct types, people are like subatomic particles: basically the same. "We like to think that we are unique," says Alessandro Vespignani, a physicist at Indiana University, Bloomington, who works on networks. "But probably for 90% of our social interactions, we are not so unique." The approach appeals to a physicist's penchant for divining the simple mechanisms that underlie complex phenomena, Vespignani says: "Physicists bring a special balance between mathematical rigor and computational approaches and intuition for the problem. We are artists of the approximation."

Germs and traffic jams

Over the past decade, complex-systems researchers have made some signal advances. For example, they have developed a deeper understanding of traffic, which, to a physicist, resembles a fluid flowing through a tube. There are key differences, however. Because the atoms in a fluid bounce off one another, a fluid typically speeds up when it flows through a constriction. Drivers avoid collisions at all costs, so when a highway narrows, traffic inevitably slows down.

To capture the essence of traffic, scientists have to include the "forces" between vehicles—actually, drivers' reactions to one another. In the 1990s, physicists and others developed mathematical models that do that and can accurately simulate highway and city traffic, and those models are now built into commercial software used by municipal planners and others. Researchers can also explain surprising effects, such as how pedestrians passing in a hallway spontaneously form two opposing lanes and how putting an obstacle in their path can actually speed the flow.

Complex-systems experts have also made contributions in epidemiology. In 2001, Vespignani and colleagues showed that in certain types of highly connected networks called "scale-free," it's impossible to stop the spread of an epidemic no matter how many people are inoculated. Conversely, in 2003, Shlomo Havlin, a physicist at Bar-Ilan University in Ramat Gan, Israel, and colleagues found a simple strategy for inoculating against a disease that beats picking random individuals. By going a step further and picking randomly chosen *friends* of those individuals, health officials can, on average, inoculate people with more social ties through which to spread the disease.

What's the holdup? Researchers can explain how traffic flow breaks down—although they can't necessarily prevent it from happening.

Some of the work is timely—even urgent. At the meeting, Vespignani presented a detailed model of the spread of the swine flu, H1N1, which includes the network of all the world's airline routes and detailed transit maps of major metropolitan areas. Such input allows researchers to predict not only the prevalence of a disease but also the geographical path of its spread, Vespignani says. His preliminary results suggest that 30% to 60% of Australians may catch H1N1 by October.

Such efforts are working their way into mainstream epidemiology. Vespignani's work is funded by the U.S. National Institutes of Health, as is modeling by Eubank, and federal officials have sought the modelers' input on problems such as the spread of H1N1. "Some of this is an ongoing effort by midlevel people to convince higher-level people to let science play more of a role" in responding to epidemics, Eubank says.

The hard social sciences

Traffic and epidemics may look like physics problems, but researchers are also tackling phenomena that seem purely social. To probe the emergence of social norms—the unwritten rules that keep us from, say, asking others how much they earn—some are turning to the computer simulations of evolutionary game theory, in which myriad virtual players engage in logical contests. In one classic setup, neighbors on a grid face the "prisoners' dilemma": Both are rewarded if they cooperate, and both are punished if they betray each other, or "defect." But each reaps a bigger reward for being the only defector and a stiffer penalty for being the sole cooperator. The logic of the situation drives both to defect.

To make the games more interesting, however, players' strategies can evolve. Players might imitate their most successful neighbor, or they might move closer to more-successful players. In either case, defectors dominate the field, Helbing finds. But imitation and migration together lead to the growth of colonies of cooperators.

More intriguing, Helbing has set two populations playing the same game with different reward schemes and, hence, different dominant strategies. However, interactions can cause players from one group to adopt the other's strategy. That resembles the emergence of a norm, Helbing says, as the interactions cause the players to change their behavior. The result may seem remote from the proscription of nose picking, but norms are often arbitrary, Helbing notes, "and for that reason we think it's okay to abstract them from their content."

Other researchers are analyzing historical movements. Europe in the Middle Ages con-

CREDITS (TOP TO BOTTOM): (BANNER) ADAPTED FROM J. BOLLEN *ET AL.* 2009 CLICKSTREAM DATA YIELDS HIGH-RESOLUTION MAPS OF SCIENCE. *PLOS ONE* 4(3): E4803. DOI:10.1371/JOURNAL.PONE.0004803; © PIYAL ADHIKARY/EPA/CORBIS

Econophysics: Still Controversial After All These Years

In 1997, physicists Imre Kondor of the Collegium Budapest and János Kertész of the Budapest University of Technology and Economics organized a conference on the budding field of econophysics, which has since enjoyed a mixed reputation. It is the biggest branch of complex-systems research, and physicists have flocked into finance. But many economists view econophysicists as dilettantes. "Shortly after this conference, I went to work in a bank, and I never met any animosity at all," Kondor says. "The reaction of the academic community has been markedly different than that of the practitioners."

Traditional economic theory is fundamentally flawed, econophysicists say. It relies on "representative agent models" in which a hypothetical average Joe interacts with monolithic economic forces. Such models ignore correlations that lead to, say, booms and busts. To prove rigorous theorems, economists assume that market fluctuations follow a bell-shaped "Gaussian distribution," which underestimates the probability of big swings. "Traditional economics is about creating mathematical models that are well-defined, tractable, and have nothing to do with reality," Kertész says.

Econophysicists claim to take a more data-driven approach. They have yet to score a major breakthrough, but they say their contributions are gaining wider acceptance. For example, econophysicists have introduced new tools to analyze correlations among stocks and more efficiently optimize a portfolio, Kertész says. They have also exploited new types of data, he says, such as high-resolution records of the smallest movements in a market and a market's limit order book, which records every offer to buy or sell a stock regardless of whether it leads to a transaction.

Uh-oh. Big market swings are inevitable, econophysicists warn.

Physicists are also helping to change the emphasis in research, Kondor says. Economists have long known that, for example, the returns on stocks do not fluctuate up and down as mildly as their models assume. The real distribution of returns has "fat tails" at its extremes, which means very large gains and losses are far more likely than assumed. But most economists continue to view such events as flukes instead of game-changing inevitabilities. "The physicists were the ones who started to systematically work through the consequences of the fat tails," Kondor says.

Still, econophysics does not impress some economists. "In my opinion, it is without influence and will continue to be without influence," says Ernst Fehr of the University of Zürich in Switzerland. Physicists apply their models to problems without grasping the details, he says. "I employed a physicist once, and I was really disappointed."

But Thomas Lux, an economist at the University of Kiel in Germany, says that, especially in Europe and Japan, growing numbers of economists are searching for alternatives to standard economic theory. "Interactions are what produce the economy, but economics ignores interactions," he says. In contrast, the multiple-agent models favored by econophysicists are ideal for scrutinizing interactions, Lux says.

With droves of physicists in finance, some critics have blamed them for the current global economic meltdown. That is unfair, econophysicists say: Most physicists working in finance were asked to devise and evaluate instruments—such as the notorious credit default swaps—with the tools they were given, not to invent better tools. Moreover, says Didier Sornette of the Swiss Federal Institute of Technology Zürich, "physicists have been the most critical of the axioms underlying the pricing, hedging, and risk analysis associated with these instruments." **–A.C.**

sisted of kingdoms, each ruled by a hierarchy of lords who collected taxes from those below them and passed them to those above. That system of indirect rule gradually gave way to one in which sovereigns ruled their countries directly, and Lars-Erik Cederman, a political scientist at ETHZ, has modeled that process.

Cederman represents each lord by a spot on a map and a node in a network resembling tree roots that can rearrange to funnel money upward most efficiently. Indirect rule won't arise at all, Cederman finds, if a lord's might begins to wane at the manor doorstep. But as the lords' influence spreads further into the countryside—presumably because of technological progress—the network of lords simplifies and eventually disappears. "The model, we claim, is the first to capture this historical trend," Cederman says.

Even more ambitiously, Jürgen Scheffran, a political scientist at the University of Hamburg in Germany, hopes to model the impact of climate change on regional conflicts. He and his colleagues are modeling the ethnic conflict in the Darfur region of Sudan, where the southward expansion of the desert has driven Arab herders onto the land of sub-Saharan farmers. "This may be one of the first cases where climate change has already affected a conflict," he says.

Over the next 5 years, Scheffran and colleagues aim to reproduce the conflict in a detailed agent-based computer model. That daunting task requires quantifying the interactions between numerous actors, including farmers, herders, rebels fighting on behalf of the farmers, the Janjaweed militiamen who oppose them, the Sudanese government, aid organizations, and others. "Hopefully, we would get better strategies for limiting the violence," Scheffran says.

How the field of complex systems will evolve remains to be seen. It appears to be growing faster in Europe, where the European Commission has recently committed €20 million to such research in the next 4 years. Researchers in the United States face tougher funding prospects, says Neil Johnson, a physicist at the University of Miami in Florida, who fits modeling of terrorist networks in with work on the mathematical ecology of fish, a strong suit at the university.

Still, with successes to build on and creative scientists tackling new problems, researchers are confident that further important results will come—even if they can't predict exactly where this network of idiosyncratic efforts will pay off most handsomely.

–ADRIAN CHO

NEWS

Counterterrorism's New Tool: 'Metanetwork' Analysis

Researchers have created sophisticated new programs to probe beneath the surface of social interactions. How well do they work against terrorists?

PALO ALTO, CALIFORNIA—In a comfortable Silicon Valley boardroom, a world away from the hellish violence of Iraq, Shyam Sankar projects a satellite map of Baghdad on a screen. "Now let's look at the geospatial distribution of significant acts," says the software engineer.

With a few clicks of his computer mouse, he creates a timeline below the map. What looks like a city skyline rises up over April and May 2008. But rather than skyscrapers, each bar represents a daily tally of carnage: suicide bombings, shootings, mortar attacks, and improvised explosive device (IED) detonations. The data come from a collaboration of researchers at Princeton University and the U.S. Military Academy at West Point in New York state. They are looking behind these known events to a shadowy network of insurgents. As Sankar slowly sweeps his cursor across the timeline, Baghdad's Sadr City district explodes with splotches of color—a heat map of violence. "The attacks turn out to be correlated over time and space with the construction of this security wall," says Asher Sinensky, tracing a line across the district.

Insights like these are crucial for U.S. and Iraqi forces trying to predict the insurgents' next moves. Sankar, 27, and Sinensky, 29, are "forward-deployed engineers" here at Palantir Technologies, the software company behind this data analysis platform. Business is booming.

"Here's work we're doing with the Naval Postgraduate School," says Sinensky. A blizzard of tiny boxes appears, all interconnected by a web of lines. "This is the network of people connected to Noordin Mohammed Top," a recruiter for the group Jemaah Islamiyah and Southeast Asia's most wanted terrorist. The graph represents the suspects' known communications and relationships, as well as their known involvement with terrorist plots, distilled from unclassified data provided by the International Crisis Group headquartered in Brussels. "You have this huge ball and it's somewhat meaningless," Sinensky says. He selects a command from a drop-down menu.

"So the postgraduates built these plug-ins to apply classic social network analysis techniques, like betweenness, centrality, and eigenvector centrality." He executes a command and names appear, ranked by a calculation of their importance as nodes in the network. "It's no surprise that Noordin is first," says Sinensky. "But what about these next two? Maybe these are people I should focus some resources on."

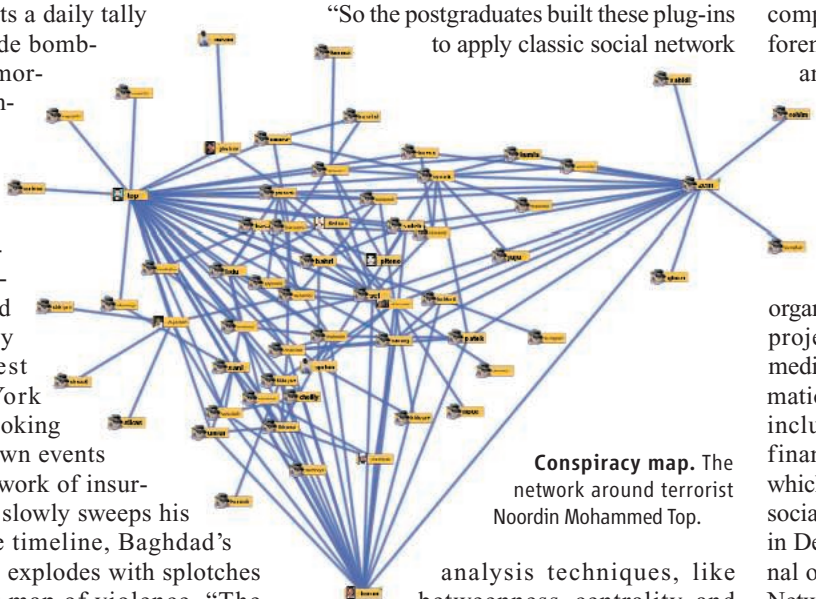

Conspiracy map. The network around terrorist Noordin Mohammed Top.

CREDIT: STEFFEN MERTEN COURTESY OF PALANTIR

A decade ago, most research on social networks was abstract and academic. But in the wake of the 11 September 2001 attacks, "there was an explosion of interest" in applying this research to warfare, says Kathleen Carley, a computer scientist at Carnegie Mellon University in Pittsburgh, Pennsylvania. Palantir is just one of many companies vying for a piece of the military funding. Academic network scientists such as Carley are also diving in, competing for lucrative U.S. military contracts and grants.

In spite of the boom, there is sharp disagreement about how effective social network analysis has been for counterterrorism. Some worry that in the rush to catch terrorists, the U.S. military has put too much faith in social network analysis. One former U.S. official even claims that applying these methods in war zones has led to unethical practices (see sidebar, p. 410).

Tangled webs

Just weeks after the 2001 plane hijackings in the United States that killed some 3000 people, it emerged that the attacks were not the work of a government but a team of international terrorists: 19 hijackers and dozens of people providing funding and logistical support. "The intelligence community was in a complete hysteria," says Marc Sageman, a forensic psychiatrist who has analyzed this and other militant networks for the U.S. government since the 1980s. U.S. government officials "turned to anyone" who could help assess this new threat and prevent another attack.

Among the first to be tapped was Valdis Krebs, a management consultant who studies social networks within organizations. "A terrorist cell is essentially a project team like any other," he says. The media provided a "nonstop stream" of information about the 11 September network—including their meetings, residences, and financial transactions around the world—which Krebs used to map a "quick and dirty" social network. Krebs published his analysis in December 2001 in *Connections*, the journal of the International Network for Social Network Analysis. One node in particular—Mohamed Atta—stood out in his network graph. "Atta scores the highest on all network centrality metrics—Degrees, Closeness, and Betweenness," Krebs concluded in his paper. "Degrees reveals [the intensity of] Atta's activity in the network. Closeness measures his ability to access others in the network and monitor what is happening. Betweenness shows his control over the flow in the network—he plays the role of a broker." Atta was indeed the ringleader and a member of al-Qaeda, the terrorist organization that claimed responsibility for the 11 September attacks through its spokesman, Osama bin Laden. Soon after, says Krebs, he and other

Published by AAAS

Investigating Networks: The Dark Side

A few months ago, Lawrence Wilkerson, a former U.S. State Department official and Army colonel, issued a scathing criticism of how the United States has conducted war in recent years. He also painted a nightmare scenario of how social network science can be applied in a battle zone. Describing how U.S. forces gathered intelligence to identify networks of insurgents after the 2003 invasion of Iraq, Wilkerson outlined something he called "the mosaic philosophy." The strategy, he claims, was similar to sequencing a genome. But instead of assembling millions of strands of DNA, investigators worked with data from interrogations of thousands of civilian prisoners.

Wilkerson wrote in a 17 March 2009 article at The Washington Note—a political commentary Web site—that the U.S. military relied on network analysis "computer programs" so that "dots could be connected and terrorists or their plots could be identified." Now based at the New America Foundation, a think tank in Washington, D.C., Wilkerson wrote that "it did not matter if a detainee were innocent." According to Wilkerson, the objective of the mosaic approach was to "extract everything possible … to have sufficient information about a village, a region, or a group of individuals. … Thus, as many people as possible had to be kept in detention for as long as possible to allow this … to work."

Wilkerson told *Science* that his allegation is based on "classified documents to which I had access from 2000 to 2005" as chief of staff for former U.S. Secretary of State Colin Powell. He puts the total number of people detained in Iraq and Afghanistan at 50,000. He says he does not know which computer program or researchers were involved. The U.S. Department of Defense declined to comment. The allegation could not be independently verified.

The general strategy of casting a wide net for intelligence gathering was familiar to all network researchers contacted by *Science* (see main text), but many expressed disbelief that it was carried out on such a grand scale in Iraq and Afghanistan. "Very scary if true," says Marc Sageman, a network researcher and longtime U.S. military contractor, but it would be "incredible." He adds that it would never work, even if it were tried.

Researchers who create network analysis computer programs have had similar reactions. Software engineers at one of the industry leaders, Palantir Technology in Palo Alto, California, say they had never heard of such abuses. And Wilkerson's "computer program" could not have been theirs, says Palantir CEO Alexander Karp, because the company only recently started courting the U.S. military for contracts. "If we ever learned that something like this was going on, we would immediately pull out," he adds.

Only one researcher contacted by *Science* had heard of the mosaic philosophy. "It's not a

network researchers were "invited to many meetings and briefings in Washington, D.C."

By 2003, U.S. defense officials had expanded the web of threats beyond the 11 September terrorists to include networks of "insurgents" in Afghanistan and Iraq. In October of that year, the U.S. Army created a research task force devoted to countering IEDs, which the U.S. Department of Defense described as "the weapon of choice for adaptive and resilient networks of insurgents and terrorists." Part of the strategy was to apply network analysis to the available data—from types of devices to people funding, building, and deploying them.

According to Sageman, the results were disappointing. "The network approach didn't really work to catch bad guys," he says. It was limited partly by the rigidity of the underlying field of mathematics, graph theory. "We are good at modeling static networks," he says, "but networks like these change over time. And we don't yet have a dynamic graph theory." When one terrorist is caught or killed, for example, "he is replaced by a cousin" with different social links. "Changing a single link can completely change the graph," he says, but the theory doesn't accommodate this. It's even harder to accommodate growth. "We don't have a decay function that can reliably remove the noise," says Sageman. As a result, the bigger your network model grows, the noisier its gets—and "the less you see."

Deadly clues. Researchers have struggled to model the Iraqi insurgent networks behind IED attacks.

The flaws of counterterrorism network analysis, according to Krebs, run deeper than math. "It is also about understanding sociology," he says. No matter how good a network model is, it can't provide insights if researchers aren't "paying attention to the right things and therefore collecting the right data." Without accounting for the content of communication, social network analysis runs into the "pizza delivery guy problem": confusing regular contact with significant contact.

As an illustration of the problem, Sageman points to a report on the 7 July 2005 bombing of the London Underground, issued in May by the U.K. Intelligence and Security Committee, titled *Could 7/7 Have Been Prevented?* Using network analysis, the researchers traced the relations between plotters, yielding a chaotic tangle of links. "They couldn't learn anything from this graph," says Sageman. "It's a hairball!" (U.K. government officials declined to provide *Science* with a publishable high-resolution version, citing "security reasons.")

Going meta

According to Ian McCulloh, a U.S. Army major who teaches network analysis at the Military Academy, the way forward is a tech-

CREDITS: AP IMAGES

term used in academia. It's used in the military," says Kathleen Carley, a computer scientist at Carnegie Mellon University in Pittsburgh, Pennsylvania, who does network analysis research for the U.S. military. "I am not part of the mosaic thing." Carley does not dismiss the strategy as ineffective. Without knowing exactly how the interrogations and data analysis were carried out, she says, "I don't think you can decide whether it's unworkable or not."

Asked if the mosaic philosophy is actively applied by U.S. military or intelligence agencies, Wilkerson says emphatically that it is not. Revelations about the torture of prisoners by U.S. forces have "caused the pendulum to swing the other way," he says. "The only place I still hear about its applicability and possible use is at the [National Security Agency]. … There, its use is to mine huge databases comprised of information gained from e-mails and telephone calls."

"Is this the dark side of networks? … I think it probably is," says Brian Uzzi, a network scientist at Northwestern University in Evanston, Illinois. "All powerful methods grow a dark side. Their power is eventually used irresponsibly. I think the real fear here is that a method that has a reputation for finding new insights is falsely used." **–J.B.**

Analytical fodder? A former U.S. official alleges that innocent people in Iraq and Afghanistan were interrogated to feed data into terrorist network models.

nique called "dynamic metanetwork analysis." McCulloh learned the technique from Carley, his adviser for a Ph.D. he completed at Carnegie Mellon last year. Carley and McCulloh say their models can deal with change in terrorist networks over time. And whereas classic social network analysis deals only with the question of "who" in networks, says Carley, "metanetworks include the who, when, what, where, why." By capturing these layers, metanetworks "begin to get at culture," she says. "You have to go beyond the communication network to consider the distribution of norms, attitudes, and beliefs, … the distribution of roles across gender, ages, and subgroups," she says. "But the programs to do that go way beyond general social network analysis."

Carley has developed computer programs of her own to do that. She says that one of them, the Organizational Risk Analyzer (ORA), helps analysts "use information about people to 'connect the dots.' Then, ORA examines this network and finds those dots, those people, who represent a threat to the overall system." The program uses both network theory and social psychology to calculate people's "cognitive demand," which Carley defines as a measure of things such as "how many others they need to interact with, how many activities they are involved with, how complex those activities are, [and] how many resources they need to handle." In the case of a business, an analyst can use ORA to identify employees who are crucial for a company's survival. The same applies for a network of insurgents.

McCulloh and Carley used metanetwork analysis to analyze 1500 videos made by insurgents in Iraq. "The insurgents would videotape most of their attacks as propaganda," says McCulloh. "As of March 2006, we had something like almost three out of every four U.S. deaths [on tape]." Carley extracted data from these videos, he says, "made a big network out of it, and ran a fragmentation algorithm which clustered them into little groups. And when you go back and look at the videos in those groups, you see forensic clues that identify who some of the insurgent cells were." The details extracted from the videos are classified, "because we worry that the insurgents will learn what we're using," McCulloh says. He and Carley worked with the U.S. military to "operationalize" the technique in Iraq. U.S. commanders there are faced with too much information and too little time to act on it. McCulloh says that Carley's metanetwork software helps them find clues and patterns—boosting the chances of catching or killing insurgents.

McCulloh claims that the technique has yielded dramatic results. "Sniper activity in Iraq is down by 70%," he says, and he's confident that IED deaths also dropped because of the insights provided by Carley's programs, although he can't cite data. "It's a simple application of metanetwork analysis," he says.

But Sageman is skeptical that military progress in Iraq can be chalked up to network analysis. "I'm not convinced [metanetworks] have helped at all," he says. "An easier explanation [for the drop in sniper attacks] might be the tribal uprising" against the insurgency in Iraq. "There's no way to know, and that's a big problem with this field in general." Carley counters that Sageman "doesn't understand the methods."

If not all researchers are sold on counterterrorism network analysis, the U.S. military certainly is. The Army established a network science center in Aberdeen, Maryland, 2 years ago. This year, the U.S. Army Research Lab is committing $162 million to a new program, the Network Science Collaborative Technology Alliance, to get academic, industry, and military researchers working on "network-centric warfare."

Carley is one of the academics applying for military funding. She says that network analysis is ready for war. A decade ago, models could handle only simple information about "hundreds" of people at once. But now, she says, "network analysis tools can handle millions or tens of millions of nodes." **–JOHN BOHANNON**

CREDIT: AP IMAGES

Published by AAAS

PERSPECTIVE

Scale-Free Networks: A Decade and Beyond

Albert-László Barabási

For decades, we tacitly assumed that the components of such complex systems as the cell, the society, or the Internet are randomly wired together. In the past decade, an avalanche of research has shown that many real networks, independent of their age, function, and scope, converge to similar architectures, a universality that allowed researchers from different disciplines to embrace network theory as a common paradigm. The decade-old discovery of scale-free networks was one of those events that had helped catalyze the emergence of network science, a new research field with its distinct set of challenges and accomplishments.

Nature, society, and many technologies are sustained by numerous networks that are not only too important to fail but paradoxically for decades have also proved too complicated to understand. Simple models, like the one introduced in 1959 by mathematicians Pál Erdős and Alfréd Rényi (*1*), drove much of our thinking about interconnected systems. They assumed that complex systems are wired randomly together, a hypothesis that was adopted by sociology, biology, and computer science. It had considerable predictive power, explaining for example why everybody is only six handshakes from anybody else (*2*–*5*), a phenomenon observed as early as 1929 (*2*) but which resonated in physical sciences only after Duncan Watts and Stephen Strogatz extended its reach beyond sociology (*5*). Yet, the undeniable success of the random hypothesis did pose a fundamental question: Are real networks truly random? That is, could systems such as the cell or a society function seamlessly if their nodes, molecules, or people were wired randomly together? This question motivated our work as well, leading 10 years ago to the discovery of the scale-free property (*6*, *7*).

Our first clue that real networks may show manifestly nonrandom features also came 10 years ago from a map of the World Wide Web (WWW) (*8*), finding that the probability that a Web page has exactly k links (in other words, degree k) follows a power law distribution

$$P(k) \sim k^{-\gamma} \qquad (1)$$

a stunning departure from the Poisson distribution predicted by random network theory (*1*). Yet, it was not until we realized that Eq. 1 characterizes the network of actors linked by movies and scientific papers linked by citations (*9*) that we suspected that the scale-free property (*6*) might not be unique to the WWW. The main purpose of the 1999 *Science* paper was to report this unexpected similarity between networks of quite different nature and to show that two mechanisms, growth and preferential attachment, are the underlying causes (Fig. 1).

When we concluded in 1999 that we "expect that the scale invariant state […] is a generic property of many complex networks" (*7*), it was more of a prediction than a fact, because nature could have chosen as many different architectures as there are networks. Yet, probably the most surprising discovery of modern network theory is the universality of the network topology: Many real networks, from the cell to the Internet, independent of their age, function, and scope, converge to similar architectures. It is this universality that allowed researchers from different disciplines to embrace network theory as a common paradigm.

Today, the scale-free nature of networks of key scientific interest, from protein interactions to social networks and from the network of interlinked documents that make up the WWW to the interconnected hardware behind the Internet, has been established beyond doubt. The evidence comes not only from better maps and data sets but also from the agreement between empirical data and analytical models that predict the network structure (*10*, *11*). Yet, the early euphoria was not without negative side effects, prompting some researchers to label many systems scale-free, even when the evidence was scarce at best. However, the net result was to force us to better understand the factors that shape network structure. For ex-

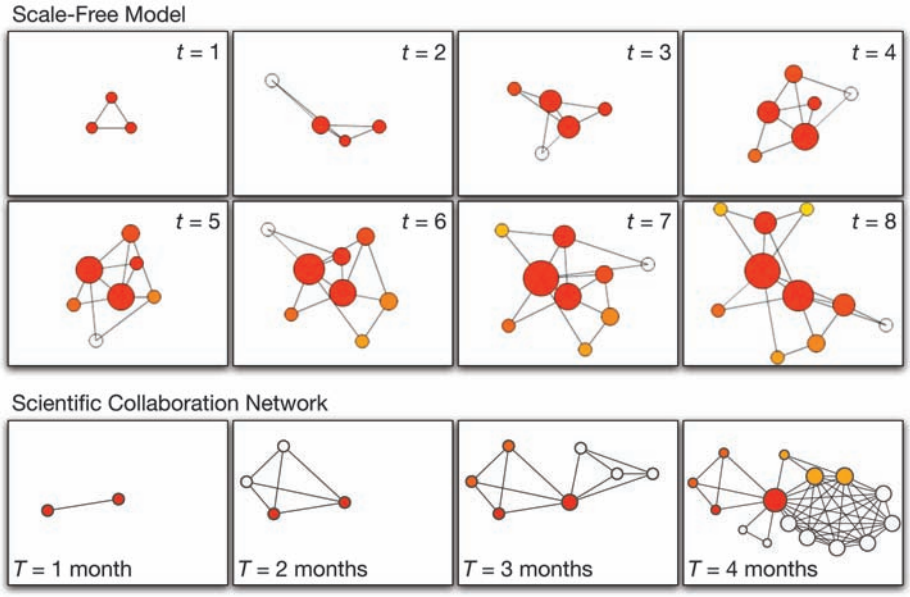

Fig. 1. The birth of a scale-free network. (**Top** and **Middle**) The simplest process that can produce a scale-free topology was introduced a decade ago in (*6*), and it is illustrated in the top two rows. Starting from three connected nodes (top left), in each image a new node (shown as an empty circle) is added to the network. When deciding where to link, new nodes prefer to attach to the more connected nodes, a process known as preferential attachment. Thanks to growth and preferential attachment, a rich-gets-richer process is observed, which means that the highly connected nodes acquire more links than those that are less connected, leading to the natural emergence of a few highly connected hubs. The node size, which was chosen to be proportional to the node's degree, illustrates the natural emergence of hubs as the largest nodes. The degree distribution of the resulting network follows the power law (Eq. 1) with exponent $\gamma = 3$. See also movies S1 to S3. (**Bottom**) Illustration of the growth process in the co-authorship network of physicists. Each node corresponds to an individual author, and two nodes are connected if they co-authored a paper together. The four images show the network's growth at 1-month time intervals, indicating how the network expands in time, leading to the emergence of a clear hub. Once again, the node size was chosen to be proportional to the node's degree. [Credit: D. Wang and G. Palla]

Center for Complex Network Research, Department of Physics, Biology, and Computer Science, Northeastern University, Boston, MA 02115, USA. Department of Medicine, Harvard Medical School and Center for Cancer Systems Biology, Dana Farber Cancer Institute, Boston, MA 02115, USA. E-mail: alb@neu.edu

ample, although the randomly bonded atoms in amorphous materials form a fascinating network, we now know that it does not display either the small-world (*12*) or the scale-free property, thanks to the chemical constraints the bonds must obey (*13*). Lastly, the topologies of several networks of considerable interest, like the neural-level map of a mammalian brain, remain to be elucidated, representing an area where we need both data and generative models (*14*).

A legacy of the scale-free property is the realization that the structure and the evolution of networks are inseparable (*6*). Indeed, traditional network models aimed to connect a fixed number of nodes with cleverly placed links. The scale-free property forced us to acknowledge that networks constantly change because of the arrival of nodes and links (Fig. 1). In other words, to explain a system's topology we first need to describe how it came into being.

The impact of network theory could have been limited if not for a series of findings that underlined the perils of ignoring network topology. Take, for example, the discovery of Romualdo Pastor-Satorras and Alessandro Vespignani that on a scale-free network the epidemic threshold converges to zero (*15*). It has long been known that only viruses whose spreading rate exceeds a critical threshold can survive in the population. Whereas the spreading rate captures the transmission dynamics, the threshold is determined by the topology of the network on which the virus spreads. Therefore, the vanishing threshold means that in scale-free networks even weakly virulent viruses can spread unopposed, a finding that affects all spreading processes, from AIDS to computer viruses. Similarly, the finding of Shlomo Havlin and collaborators (*16*) that in scale-free networks the overall network connectivity does not vanish under random node removal explained the exceptional robustness of real networks to random node failures (*17*). As a proof of the coherency of the emerging theory, both of these discoveries (*15*, *16*) were reduced to the same mathematical property, the diverging second moment of the degree distribution (Eq. 1), a unique feature of scale-free networks (*6*). Lately these features are of great interest, given the increasing concern about the vulnerability of real networks (such as power grids and the Internet) to attack and the realization that targeting hubs can be massively disruptive (*17*, *18*).

It is clear that no networks seen in nature or technology are completely random—that is, mechanisms beyond randomness shape their evolution. The universality of various topological characteristics, from degree distributions (*6*) to degree correlations (*19*–*21*), motifs (*22*), and communities (*23*–*25*), is used as a springboard to study diverse phenomena and to make predictions. With that, network theory has fundamentally reshaped our understanding of complexity. Indeed, although we continue to lack a universally agreed-on definition of complexity, the role of networks in this area is obvious: All systems perceived to be complex, from the cell to the Internet and from social to economic systems, consist of an extraordinarily large number of components that interact via intricate networks. To be sure, we were aware of these networks before. Yet, only recently have we acquired the data and tools to probe their topology, helping us realize that the underlying connectivity has such a strong impact on a system's behavior that no approach to complex systems can succeed unless it exploits the network topology.

In many ways, the demands of a future theory of complexity are obvious: We need to understand the behavior of the systems that we perceive as being complex. We need to be able to predict how the Internet responds to attacks and traffic jams or how the cell reacts to changes in its environment. To make progress in this direction, we need to tackle the next frontier, which is to understand the dynamics of the processes that take place on networks. The problem is that we have almost as many dynamical phenomena as there are complex systems. For example, biologists study reaction kinetics on metabolic networks; computer scientists monitor the flow of information on computer networks; and epidemiologists, sociologists, and economists explore the spread of viruses and ideas on social networks. Is there a chance that, despite their diversity, these dynamical processes share some common characteristics? I suspect that such commonalities do exist; we just have not yet found the framework to unveil their universality. If we do, combined with the universality of the network topology, we may soon have something that could form the foundation of a theory of complexity.

Can we keep the momentum and achieve this in the next decade or so? Perhaps—in my view the bottlenecks are mainly data driven. Indeed, the sudden emergence of large and reliable network maps drove the development of network theory during the past decade. If data of similar detail capturing the dynamics of processes taking place on networks were to emerge in the coming years, our imagination will be the only limitation to progress. If I dare to make a prediction for the next decade, it is this: Thanks to the proliferation of the many electronic devices that we use on a daily basis, from cell phones to Global Positioning Systems and the Internet, that capture everything from our communications to our whereabouts (*26*, *27*), the complex system that we are most likely to tackle first in a truly quantitative fashion may not be the cell or the Internet but rather society itself.

Today the understanding of networks is a common goal of an unprecedented array of traditional disciplines: Cell biologists use networks to make sense of signal transduction cascades and metabolism, to name a few applications in this area; computer scientists are mapping the Internet and the WWW; epidemiologists follow transmission networks through which viruses spread; and brain researchers are after the connectome, a neural-level connectivity map of the brain. Although many fads have come and gone in complexity, one thing is increasingly clear: Interconnectivity is so fundamental to the behavior of complex systems that networks are here to stay.

References and Notes

1. P. Erdős, A. Rényi, *Publ. Math. (Debrecen)* **6**, 290 (1959).
2. F. Karinthy, in *The Structure and Dynamics of Networks*, M. Newman, A.-L. Barabasi, D. Watts, Eds. (Princeton Univ. Press, Princeton, NJ, 2006).
3. S. Milgram, *Psychol. Today* **2**, 60 (1967).
4. I. Pool, M. Kochen, *Soc. Networks* **1**, 1 (1978).
5. D. J. Watts, S. H. Strogatz, *Nature* **393**, 440 (1998).
6. A.-L. Barabási, R. Albert, *Science* **286**, 509 (1999).
7. In a random network, the average node sets the scale of the network, which means that most nodes have about the same number of links as the average node. For networks that follow Eq. 1, for $\gamma < 3$ the second moment of the distribution diverges, which means that the average is not characteristic because the error bars characterizing our uncertainty about its value are infinite. These networks lack a characteristic scale; hence, they are called scale-free. Formally, networks whose degree distribution follows Eq. 1 are called scale-free networks.
8. R. Albert, H. Jeong, A.-L. Barabási, *Nature* **401**, 130 (1999).
9. S. Redner, *Eur. Phys. J. B* **4**, 131 (1998).
10. G. Caldarelli, *Scale-Free Networks* (Oxford Univ. Press, Oxford, 2007).
11. S. N. Dorogovtsev, J. F. F. Mendes, *Evolution of Networks: From Biological Networks to the Internet and WWW* (Oxford Univ. Press, Oxford, 2003).
12. The small-world property refers to the fact that in many networks the average node to node distance is rather small, of the order of log N, where N is the number of nodes in the network.
13. L. A. N. Amaral, A. Scala, M. Barthelemy, H. E. Stanley, *Proc. Natl. Acad. Sci. U.S.A.* **97**, 11149 (2000).
14. E. T. Bullmore, O. Sporns, *Nat. Rev. Neurosci.* **10**, 186 (2009).
15. R. Pastor-Satorras, A. Vespignani, *Phys. Rev. Lett.* **86**, 3200 (2001).
16. R. Cohen, K. Reez, D. Ben-Avraham, S. Havlin, *Phys. Rev. Lett.* **85**, 4626 (2000).
17. R. Albert, H. Jeong, A.-L. Barabási, *Nature* **406**, 378 (2000).
18. A. E. Motter, *Phys. Rev. Lett.* **93**, 098701 (2004).
19. M. E. J. Newman, *Phys. Rev. Lett.* **89**, 208701 (2002).
20. R. Pastor-Satorras, A. Vázquez, A. Vespignani, *Phys. Rev. Lett.* **87**, 258701 (2001).
21. S. Maslov, K. Sneppen, *Science* **296**, 910 (2002).
22. R. Milo *et al.*, *Science* **298**, 824 (2002).
23. M. E. J. Newman, *Phys. Today* **61**, 33 (2008).
24. G. Palla, I. Derényi, I. Farkas, T. Vicsek, *Nature* **435**, 814 (2005).
25. J. Reichardt, S. Bornholdt, *Phys. Rev. E* **74**, 016110 (2006).
26. A. Vespignani, *Science* **325**, 425 (2009).
27. M. C. González, C. A. Hidalgo, A.-L. Barabási, *Nature* **453**, 779 (2008).

Supporting Online Material

www.sciencemag.org/cgi/content/full/325/5939/412/DC1
Movies S1 to S3

10.1126/science.1173299

PERSPECTIVE

Revisiting the Foundations of Network Analysis

Carter T. Butts

Network analysis has emerged as a powerful way of studying phenomena as diverse as interpersonal interaction, connections among neurons, and the structure of the Internet. Appropriate use of network analysis depends, however, on choosing the right network representation for the problem at hand.

The past decade has seen a dramatic surge of interest in the study of networks, with much of it in fields outside the "traditional" areas of mathematics, computer science, and the social sciences (*1*, *2*). By providing a formal mechanism for representation, measurement, and modeling of relational structure, the use of network analytic methods in these new domains (including physics, biology, and medicine) has arguably paved the way for a range of advances. On the other hand, this rapid expansion creates the risk that existing methods may be misapplied or misinterpreted, leading to inappropriate conclusions and generally poor results.

Standard Framework and Core Assumptions

Most network research is based on a representational formalism borrowed from graph theory. Researchers begin with a finite set of identifiable entities, which are represented via a vertex set. Each element of this set, commonly called a node, represents a single entity that potentially may take part in the relation under study. Relationships themselves are represented via edges, which conventionally are either unordered pairs of nodes (in which case the relation is said to be undirected) or ordered pairs of nodes (in which case the relation is said to be directed). The network is represented by a graph, which is defined as the set of nodes together with the set of pairwise relationships among them (Fig. 1A).

This representational framework is quite restrictive. To represent a system in this way, we must be able to reduce it to a well-defined set of discrete components whose interactions are strictly dyadic in nature. For any given (possibly ordered) pair of such components, the relationship is dichotomous, either present or absent; although such a framework may seem so restrictive as to be useless, its typical purpose is to serve as an approximation to the structure of a more complex system, for purposes of studying a particular property (such as the diffusion of a disease in a community over a specific time scale). Moreover, it is precisely the reductive nature of graphical structure that has facilitated its rich mathematical development (*3*) and associated scientific applications (*4*, *5*).

Extensions and relaxations of this basic framework designed to accommodate more complex situations are many and varied. We may avoid the assumption of dichotomous relationships by allowing edges to carry different weights [such as the differing connection strengths among neurons in *Caenorhabditis elegans* (Fig. 1B) (*6*)]. Multilateral relationships (such as group memberships) may be represented by means of "hyperedges," which can involve arbitrarily many nodes (*7*). Temporal aspects of relationships may be handled by treating them as time series (*8*), such as with repeated cross-sectional sampling of group structure or Internet topology; as time intervals (*9*), such as with life history data on marital and employment relationships; or as effectively instantaneous events (*10*), such as with e-mail exchange or radio communications (Fig. 1C).

Many measurement, analysis, and modeling techniques are rooted within the standard framework. However, when assumptions of this framework do not serve as reasonable approximations of the system of interest, alternative representations and techniques may be necessary. What factors should be considered when choosing a network representation, and what are the consequences when this choice is poorly made?

When Is a Node a Node?

Consider a biologist who wishes to examine the structure of animal parasite–plant interactions and so undertakes a network study. Given sufficient time, technology, and resources, he or she might sample some designated area and document all such interactions, perhaps constructing a network of ties between each animal within the area and the sites on which it feeds. But what should count as a potential feeding site? Treating each plant as a single site may seem reasonable for relatively small plants but would obviously obscure the potentially complex interactions associated with even a single tree. Additional detail could be accommodated by distinguishing between classes of anatomical units (such as bark versus trunk versus leaves) or within classes, but here too judgment must be applied in determining which distinctions to make. The biologist's method of defining potential feeding sites will greatly influence the structure of the interaction network.

The basic problem is the definition of the class of distinct entities on which one's relation of interest will be defined. The mere act of positing such a class, of course, smuggles in the tacit assumption that such a class can be defined (and moreover, that it is scientifically useful to do so). The choice of individual humans as nodes in studies of friendship (*11*) or kinship (*12*) networks and the use of individual publications in citation studies (*13*) are examples in which this assumption is well-justified. On the other hand, studies of interactions between aggregates such as groups (*14*), households (*15*), or organizations may encounter problems due to the fluidity of the interacting units and the fact that subunits of a larger unit may themselves interact with others both within and without the "parent."

As in the biological example, collapsing all potentially interacting elements into a single unit may be a very poor approximation of reality. For example, my research group has studied networks formed during organizational responses to disasters. If we pooled all the groups operating under the aegis of one national government, then we would obscure the difference between small units such as urban search-and-rescue teams and large government ministries or departments, and also would incorrectly suggest that the resources or collaborators of one are necessarily available to the other. Other systems that also would be obscured by pooling include the molecular architecture of protein-protein binding sites (*16*) and hierarchical structures in the topology of the Internet (*17*).

Changing the node set can substantially influence the size and density of the resulting network, with considerable implications for subsequent analysis. For instance, the behavior of basic network properties such as degree centralization (a measure of the extent to which ties are concentrated on a small number of nodes) are known to change both qualitatively and quantitatively with size (*18*), as do the properties of even fairly simple models of network formation (*19*, *20*). In hierarchical contexts, different aggregation decisions can produce networks with very different structural features (Fig. 1A). To avoid misleading conclusions, the set of nodes should be defined so as to include all distinct entities that are capable of participating in the relationship under study; this definition should be used consistently across networks. Where no such set of entities can be uniquely identified [as is sometimes true in geographic analysis in which a continuous space is modeled as a partition (*21*)], it is possible that a finite network representation will be inappropriate. An alternative framework (such as a continuous spatial representation) may prove more fruitful. In other cases [such as multilevel processes (*22*)], simultaneous analysis of the same

Department of Sociology and Institute for Mathematical Behavioral Sciences, University of California at Irvine, 3151 Social Science Plaza, Irvine, CA 92697–5100, USA. E-mail: buttsc@uci.edu

system at multiple levels of aggregation may be appropriate.

When Is an Edge an Edge?

Many legal institutions (such as marriage) are dichotomous, and few if any societies allow one to be one-third someone's mother. Even for relations with quantitative aspects, one can often usefully identify relationships as present or absent. We do or do not regard another as a friend; a given neuron does or does not connect to another. When a relationship reflects either a general tendency toward or potential for interaction, the use of a binary representation can greatly simplify both theory and measurement. It is much simpler, for instance, to study sexual relationships than to enumerate sexual encounters, and indeed the mere potential for interaction can have behavioral consequences, even when specific relationships go unused [as in the case of potential trading partners in exchange networks (*23*) or third-party observers in dominance relations (*24*)].

Dichotomous distinctions can sometimes be misleading. Many forms of interaction are inherently episodic and occur at variable rates (*25*). Dichotomization of such data not only obscures such variation but also requires selecting a threshold level, the choice of which can substantially alter the properties of the resulting network, both directly through selective tie removal (*26*) and indirectly through changes in network density (*27*). The range of structures present at different connection strengths can vary greatly (Fig. 1B). This cannot be resolved solely with better data collection or more elaborate statistical techniques. Rather, one must determine whether the relationship under study is sufficiently stable to be well-approximated by a constant function over the period of interest and whether the values taken by this function across pairs are sufficiently constrained to be approximately dichotomous. For relationships known to be highly heterogeneous (such as trade or migration rates), no single threshold may suffice; a weighted graph representation will frequently be more appropriate. More studies that assess the effectiveness of such approximations—and provide concrete, empirically validated guidelines for practice within particular problem domains—would be a welcome addition to the literature.

Time Scales and Network Processes

In determining appropriate node and edge representations, it is vital to consider the time scales on

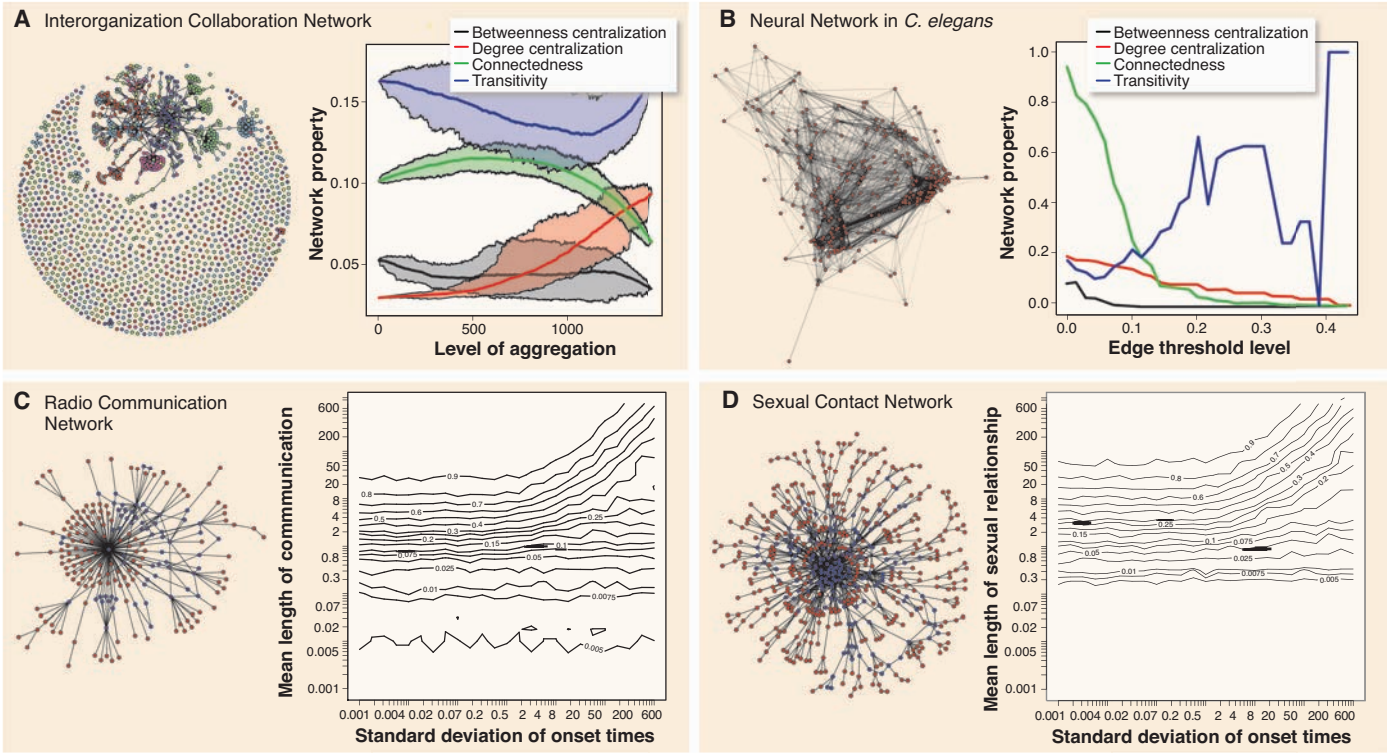

Fig. 1. Effects of changing definitions of "node" and "edge." (**A**) Network of interorganizational collaboration in the first 13 days of the Hurricane Katrina response (*39*) illustrates potential consequences of node aggregation; edges represent collaborations. Depending on the level of aggregation, each subordinate organization could be considered a node or a parent organization (containing subordinate nodes). (Left) The finest level of disaggregation, with all subordinates of a given organization having the same color. (Right) Iteratively merging randomly chosen organizations in the original network with their "parents" produces a series of increasingly aggregated structures. Shaded regions show the central 90% range of aggregated values on the basis of 100 series, and lines represent their means. The extent of aggregation affects fundamental network properties, as does the sequence of aggregation steps (indicated by width of the simulation intervals). (**B**) Neural network of *C. elegans* [based on (*6*)] shows differences in connection strength among neurons indicated as line (edge) shading in the figure at left. Nodes represent neurons, and edges reflect direct connections (arrows indicate directionality). All possible connections are shown regardless of their strength (threshold level = 0). Taking different thresholds for the edges (from 0 to 50% of maximum observed edge strength) leads to networks with different structural properties (right). (**C**) and (**D**) show the effects of edge timing, depicted as contour plots (right), in systems in which the edges are not static; each line represents the fraction of the population reached by the diffusion process. (Left) Time aggregates for the network being studied, including all relationships occurring during the observation period. (C) A radio communication network from the World Trade Center disaster, containing the largest set of people described in (*29*) from Port Authority Trans-Hudson channel 26 that were connected to each other by any chain of calls (left). Numbers within each contour line (right) indicate the mean fraction of the network that could receive information from a randomly chosen individual through an exponential diffusion process with the indicated edge parameters over 250 simulation runs. Static properties have not changed, but edge-timing variation (how long communication lasts and/or when it starts relative to the observation period) leads to variation in diffusion potential. (D) Diffusion simulation on the largest component of a sexual contact network described in (*40*) produces similar results (right) as in (C), although the degree distribution and cohesion properties (proportion of people connected by multiple common paths) differ. Each line indicates the proportion ultimately infected by a random individual (averaged over 250 trials) given the parameters of the diffusion process.

which the processes of interest unfold. For processes such as information diffusion, which unfold over hours or days, stable relationships such as kinship or friendship ties [with turnover times on the order of years (*28*)] may be approximated as essentially static. Such networks cannot be fixed in a life-cycle context, however, in which one's time scale of interest may span several decades. Likewise, the dynamics of rapidly evolving networks [such as radio communications during emergencies (Fig. 1C) (*29*)] are of potential importance even for fast-moving processes, such as information exchange. Failure to consider dynamics can lead to extremely misleading results.

A useful example of where static representations can go awry is provided by the case of HIV diffusion. Studies of sexual behavior generally find that the number of sexual partners possessed by a given individual over a fixed period of time is skewed (the mean is farther out in the long tail of the distribution than is the median) (*30*). Early studies of the behavior of simple diffusion processes on networks with extremely skewed [specifically, power-law (*31*)] degree distributions strongly suggested that epidemic potentials for HIV and similar sexually transmitted diseases were primarily governed by the behavior of a small number of individuals with large numbers of sexual contacts (*32*, *33*). This conclusion was of considerable practical import because it implied that only hub-targeted strategies were likely to prove efficacious in reducing epidemic thresholds (*31*, *32*). Although the applicability of the power-law degree model to these networks has since been questioned (*30*, *34*), equally important is the assumption that the time-aggregated network of sexual contacts was an effective model for HIV diffusion. The timing and duration of relationships are critical factors in the susceptibility of the dynamic network to disease transmission (*35*), factors that are hidden by the time-aggregated representation. This can be seen in Fig. 1D; for a given network, everyone may become infected or no one may be infected, depending on the edge duration and time of onset.

Studies of diffusion on dynamic networks suggest that partnership concurrency is also an important predictor of epidemic potential; uniformly low-degree networks potentially support epidemics when relationships are long and coterminous, and networks with high-degree nodes often fail to support epidemics when relationships are short and sequential (*35*–*37*). Interventions aimed at minimizing concurrent links are not necessarily the same as hub-targeted strategies, and thus the public health recommendations that follow from a dynamic network analysis may differ from those that would seem reasonable based on the assumption of a static, time-aggregated network.

Although HIV diffusion is a compelling example, it should be emphasized that similar issues can arise in systems as apparently different as radio communication (Fig. 1C) and peer-to-peer networks. Recent work in the latter area, for instance, has emphasized the impact of the entry and exit of network members (or "churn") on system performance (*38*); in this case, edge dynamics (potential and actual data transfers) can be understood only by taking into account the dynamic nature of the set of nodes.

Conclusion

To represent an empirical phenomenon as a network is a theoretical act. It commits one to assumptions about what is interacting, the nature of that interaction, and the time scale on which that interaction takes place. Such assumptions are not "free," and indeed they can be wrong. Whether studying protein interactions, sexual networks, or computer systems, the appropriate choice of representation is key to getting the correct result.

References and Notes

1. S. P. Borgatti, A. Mehra, D. J. Brass, G. Labianca, *Science* **323**, 892 (2009).
2. M. Newman, A. Barabasi, D. J. Watts, Eds., *The Structure and Dynamics of Networks* (Princeton Univ. Press, Princeton, NJ, 2006).
3. B. Bollobás, *Modern Graph Theory* (Springer, New York, 1998).
4. M. E. J. Newman, *SIAM Rev.* **45**, 167 (2003).
5. U. Brandes, T. Erlebach, Eds., *Network Analysis: Methodological Foundations* (Springer-Verlag, Berlin, 2005).
6. D. J. Watts, S. H. Strogatz, *Nature* **393**, 440 (1998).
7. S. Wasserman, K. Faust, *Social Network Analysis: Methods and Applications* (Cambridge Univ. Press, Cambridge, 1994).
8. T. A. B. Snijders, *J. Math. Sociol.* **23**, 149 (1996).
9. C. T. Butts, J. E. Pixley, *J. Math. Sociol.* **28**, 81 (2004).
10. C. T. Butts, *Sociol. Methodol.* **38**, 155 (2008).
11. K. M. Carley, D. Krackhardt, *Soc. Networks* **18**, 1 (1996).
12. J. P. Boyd, *J. Math. Psychol.* **6**, 139 (1969).
13. N. P. Hummon, P. Doreian, *Soc. Networks* **11**, 39 (1989).
14. R. L. Breiger, *Soc. Forces* **53**, 181 (1974).
15. M. Murphy, *Eur. J. Popul.* **12**, 363 (1996).
16. D. Reichmann, O. Rahat, M. Cohen, H. Neuvirth, G. Schreiber, *Curr. Opin. Sys. Biol.* **17**, 67 (2007).
17. L. Subramanian, S. Agarwal, J. Rexford, R. H. Katz, *Proceedings of IEEE INFOCOM* (2002).
18. C. T. Butts, *Soc. Networks* **28**, 283 (2006).
19. D. Strauss, *SIAM Rev.* **28**, 513 (1986).
20. M. S. Handcock, *Dynamic Social Network Modeling and Analysis*, R. Breiger, K. M. Carley, P. Pattison, Eds. (National Academies, Washington, DC, 2003), pp. 229–240.
21. S. Openshaw, *The Modifiable Areal Unit Problem* (Geo Books, Norwich, 1984).
22. P. R. Monge, N. S. Contractor, *Theories of Communication Networks*. (Oxford Univ. Press, Oxford, 2003).
23. D. Willer, Ed., *Network Exchange Theory* (Praeger, Westport, CN, 1999).
24. I. D. Chase, C. Tovey, D. Spangler, M. Manfredonia, *Proc. Natl. Acad. Sci. U.S.A.* **99**, 5744 (2002).
25. H. Whitehead, S. Dufault, *Adv. Stud. Behav.* **28**, 33 (1999).
26. J. P. Onnela *et al.*, *Proc. Natl. Acad. Sci. U.S.A.* **104**, 7332 (2007).
27. K. Faust, *Sociol. Methodol.* **37**, 209 (2007).
28. D. L. Morgan, M. B. Neal, P. Carder, *Soc. Networks* **19**, 9 (1997).
29. C. T. Butts, M. Petrescu-Prahova, B. R. Cross, *J. Math. Sociol.* **31**, 121 (2007).
30. D. Hamilton, M. S. Handcock, M. Morris, *Sex. Transm. Dis.* **35**, 30 (2008).
31. F. Liljeros, C. R. Edling, L. A. N. Amaral, H. E. Stanley, Y. Aberg, *Nature* **411**, 907 (2001).
32. Z. Dezso, A. Barabási, *Phys. Rev. E Stat. Nonlin. Soft Matter Phys.* **65**, 055103 (2002).
33. R. Pastor-Satorras, A. Vespignani, *Phys. Rev. Lett.* **86**, 3200 (2001).
34. J. H. Jones, M. S. Handcock, *Proc. R. Soc. London Ser. B* **270**, 1123 (2003).
35. J. Moody, *Soc. Forces* **81**, 25 (2002).
36. M. Morris, M. Kretzschmar, *AIDS* **11**, 641 (1997).
37. M. Morris, S. Goodreau, J. Moody, *Sexually Transmitted Diseases*, K. K. Holmes, *et al.*, Eds. (McGraw-Hill, New York, ed. 4, 2007), chap. 7.
38. D. Stutzbach, R. Rejaie, *Proceedings of ACM SIGCOMM* (2006).
39. C. T. Butts *et al.*, *31st Annual Hazards Research and Applications Workshop, Boulder, CO* (2006).
40. J. J. Potterat *et al.*, *Sex. Transm. Infect.* **78** (suppl. 1), i152 (2002).

41. The author would like to thank K. Faust, M. Morris, J. Moody, C. Marcum, A. Markopoulou, and R. Martin for helpful comments, and J. Potterat and S. Muth for making their data available. Supported in part by NSF awards BCS-0827027 and CMS-0624257 and by Office of Naval Research award N00014-08-1-1015.

10.1126/science.1171022

PERSPECTIVE

Disentangling the Web of Life

Jordi Bascompte

Biodiversity research typically focuses on species richness and has often neglected interactions, either by assuming that such interactions are homogeneously distributed or by addressing only the interactions between a pair of species or a few species at a time. In contrast, a network approach provides a powerful representation of the ecological interactions among species and highlights their global interdependence. Understanding how the responses of pairwise interactions scale to entire assemblages remains one of the great challenges that must be met as society faces global ecosystem change.

Network approaches to ecological research emphasize the pattern of interactions among species (the way links are arranged within the network) rather than the identity of the species composing a community (the nodes of the network of interactions). The idea of a complex network of interactions among species is as old as Darwin's contemplation of the tangled bank, showing the importance of networks in ecology (*1*). Despite this early realization, however, networks have only recently been incorporated into mainstream ecological theories. The "web of life"

Integrative Ecology Group, Estación Biológica de Doñana, Consejo Superior de Investigaciones Científicas, Calle Américo Vespucio s/n, E-41092 Sevilla, Spain. E-mail: bascompte@ebd.csic.es

model depicts the global interdependence among species (Fig. 1A) and, from a basic point of view, complements theories on biodiversity that have either neglected species interactions or assumed that they are homogeneously distributed across species.

The network approach benefits from tools and concepts imported from other fields such as physics and sociology. This flow of ideas has allowed us to compare ecological networks with protein interaction networks or connectivity within Internet communities. A comparative framework is useful because it suggests that there are very general mechanisms underlying network formation. Furthermore, the identification of common architectures, robust in the face of perturbations regardless of specific details, may also emerge from such studies.

The Architecture of Biodiversity

Food webs are central to ecology, as a way to describe and quantify the complexity of ecosystems (*2*–*7*) by connecting the trophic interactions among species in a community. Large networks are built from combinations of smaller motifs; a motif is a pattern of overrepresented interrelations among nodes relative to equivalent randomizations of the network (*8*) (Fig. 2). Empirical food webs, for example, show a consistent overrepresentation of tri-trophic food chains (in which a predator eats a consumer which in turn eats a resource; Fig. 2A), whereas omnivory (the predator eats both the consumer and the resource; Fig. 2B) is overrepresented in a majority of food webs but underrepresented in some (*9*). How these motifs combine into larger networks (Fig. 2C) may influence the stability of the overall network, as suggested by Robert May on theoretical grounds (*5*). The search for empirical evidence of this theory is a currently active area of research (*10*). Analyses of food web motifs have also been extended to include quantitative information such as the strength of the interactions (*11*) and body mass ratios (*12*) between predators and their prey.

More recently, ecologists have studied interactions beyond predator-prey webs to include mutually beneficial interactions, such as those between plants and their animal pollinators or seed dispersers. These interactions play a major role in the generation and maintenance of biodiversity on Earth (*13*) and organize communities around a network of mutual dependences (Fig. 1A). Such mutualistic networks are (i) heterogeneous, in which the bulk of species interact with a few species, and a few species have a much higher number of interactions than would be expected from chance alone; (ii) nested, in which specialists interact with a subset of the group of species that generalists interact with; and (iii) built on weak and asymmetric links among species (for example, in some cases when a plant interacts strongly with an animal, the animal tends to depend less on the plant) (*14*). Therefore, mutualistic networks are neither randomly organized nor organized in isolated compartments, but built cohesively around a core of generalist species.

Groups of species coevolve in time and space (*13*), and the study of this phenomenon has been facilitated by a network approach. If these groups of species and their interactions are overrepresented in the network, they can be considered to be motifs, in which case they are the basic building blocks from which we can scale up to full networks. These motifs often vary and develop in predictable ways among ecosystems, resulting in a well-defined geographic mosaic of coevolution (*13*). Two frequently assumed misconceptions arose from non-network analysis of coevolution: first, that coevolution leads toward highly specific, direct one-on-one interactions; and second, that coevolution within species-rich communities generates diffuse assemblages that are intractable to generalization. The documentation of geographically varying network motifs and the determination of well-defined structures of large networks are dispelling these assumptions.

Architecture Influences Robustness

Without an understanding of the structure of ecological networks, we cannot assess the robustness of networks to species extinctions, habitat loss, or other anthropogenic influences. Models of such networks have led to the prediction that the random extinction of species will result in coextinction cascades among remaining species because of a loss of resources. In such simulations, food webs are found to be robust to the random extinction of species, but rely on a few well-connected species that act as glue keeping the whole network together. If these key species disappear, it is expected that the entire network will collapse very rapidly (*7*, *15*, *16*).

Such simulations have looked specifically at the number of species, but not at their identity. The next step was to superimpose the phylogenies of the plants and animals on the network of interactions. Phylogenetic relatedness (for example, species belonging to the same genera) partly explains the patterns of interactions between species (*17*). As a consequence, coextinction avalanches tend to involve taxonomically related species, which may lead to a nonrandom pruning of the evolutionary tree and a faster erosion of taxonomic diversity (*17*). Related to this, coex-

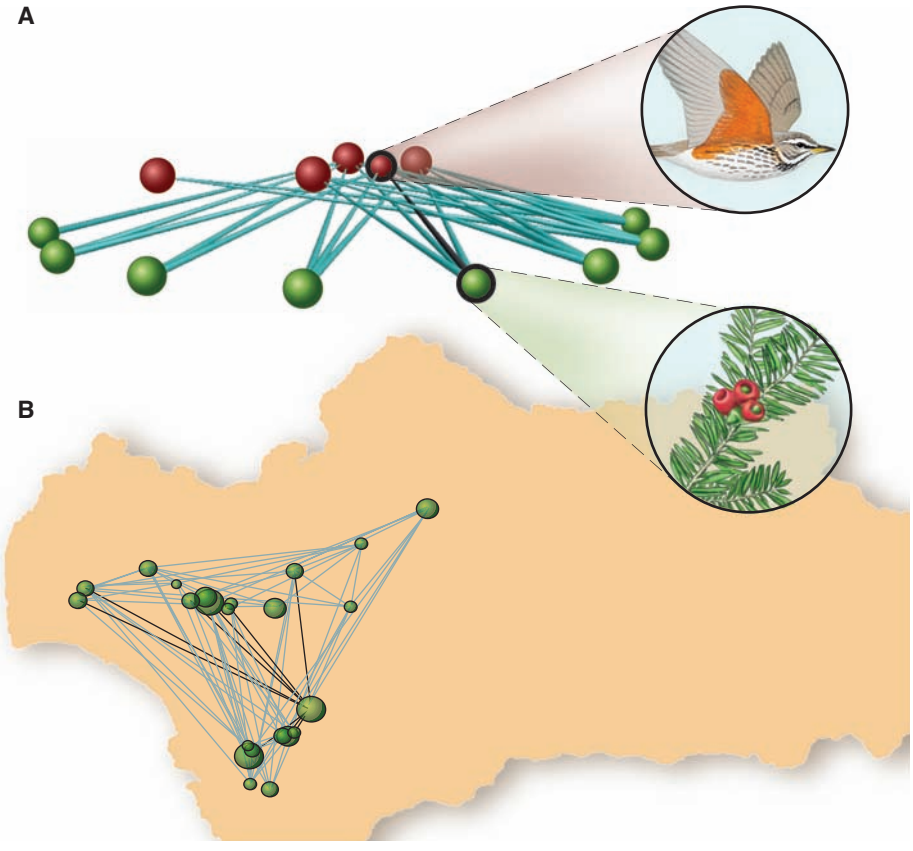

Fig. 1. The web of life is a powerful representation encapsulating ecological connectivity among elements. Examples of ecological networks illustrate how to scale from pairwise interactions to the entire assembly: (**A**) a plant-animal mutualistic network depicting the interactions of mutual benefit between plants and their seed dispersers and (**B**) a network of spatial genetic variation across habitat patches in a heterogeneous landscape inhabited by a Mediterranean plant. Studies such as (A) focus on coevolution at a community scale and set the foundation for predicting how global change will propagate through such networks. Studies such as (B) provide a framework to address the simultaneous influence of all patches on gene flow and quantify the importance of a single patch for the persistence of the entire metapopulation.

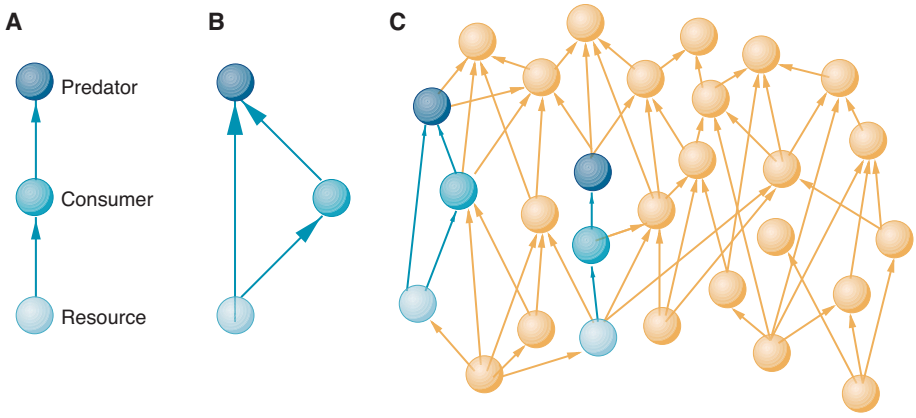

Fig. 2. The basic building blocks of ecological networks. (**A** and **B**) Two trophic modules: a tritrophic food chain (A) and an omnivory chain (B), which have been the subject of dynamical analyses. Some of these modules can be overrepresented in entire networks, in which case they are considered network motifs (**C**). Future studies hopefully will assess to what extent the stability of an entire network is explained by the stability of its basic blocks.

tinction cascades in food webs tend to involve species that are trophically unique; that is, that tend to be eaten by a set of predators and/or eat a set of prey with little overlap with other species in the community (*18*). Therefore, trophic diversity—the range of trophic roles played by species—decreases faster than would be expected on the basis of looking only at the number of coextinct species (*18*). Future studies should now complement these simulations of coextinction cascades by mapping the loss of ecosystem services that a species performs (*19*), such as pollination or biological control.

One topological way of simulating the consequences of species extinction assumes that species are fixed nodes without dynamics. The alternative is to use population dynamic models for each species. Traditionally, the dynamic approach has been performed with the most basic descriptions of trophic interactions, such as a tritrophic food chain (Fig. 2A). These basic descriptors of trophic interactions, known by theoreticians as trophic modules, provide a bridge between the complexity of entire communities and the simplicity of pairwise interactions (*20*). Indeed, trophic modules can be represented mathematically on the basis of the abundance of each species and how each is affected by the abundance of other species, which may be predators or prey. However, there is still a wide gap between the stability of these simple models of trophic interactions and that of the entire food web.

To reduce such gaps, network motifs provide a means by which to assess the most important trophic modules on the basis of their relative frequency within a food web. Modules that are overrepresented (motifs) tend to be most relevant to understanding food web dynamics (*9*–*11*). However, we cannot assume that the stability of the entire network can be deduced from the stability of its component parts, because the sum of the parts does not add up to a complete network. Thus, we need studies to add to our comprehension of the stability of entire food webs.

Recently, ecologists have analyzed the dynamics of large food web models. Two ingredients characterize these models. First, they incorporate realistic interaction networks among dozens of species occupying several trophic levels (*6*, *7*). Second, they use realistic estimates of species body sizes and metabolic rates (*21*), in contrast with traditional Lotka-Volterra models, in which parameters are assigned randomly. With these models, researchers have explored the stabilizing role of network properties, such as the observed body size ratios between predators and their prey (*12*), and predicted the effects of species removal on the abundance of the remaining species (*22*). The accuracy of these predictions increases with the size of the food web, so that the more complex the food web, the simpler the prediction of the consequences of species extinctions (*22*).

Architecture Influences Network Size

Network structure can affect not only the robustness of a given network (at what rate biodiversity will be lost) but its original size (how many species can be supported to begin with). Extensions of theory testing the roles of competition and mutualistic interactions in determining the maximum number of species that can stably coexist (*23*) showed the potential increase in species richness resulting from the architecture of mutualistic networks. For any given number of interactions, the nested structure of mutualistic networks maximizes the number of coexisting species (*23*). For example, two plant species that compete to attract shared pollinators gain when they coexist because more pollinators are attracted to the area by the total number of available flowers. In such cases, there is a balance between the opposing forces of competition and facilitation, which depends on the structure of the mutualistic network (*23*).

To properly study the relationship of network architecture to function, three challenges need to be faced. First, models need to be developed incorporating both how population dynamics affect network topology and how topology affects dynamics (*6*). Second, analyses of networks need to incorporate multiple interaction types, because it is probable that stability is related to how multiple interaction types function in combination (*23*). This may be particularly relevant if mutualistic and antagonistic effects are nonadditive, because until now networks have primarily been studied independently (*24*). Third, species invasions, climate change, and other current challenges to ecological and environmental systems will require a network focus because multiple species are likely to be perturbed in face of the many ongoing changes at both the local and global scales (*25*). For example, mutualistic pollination networks have demonstrated that such networks appear to facilitate the integration of invasive plant species and that the structure of the network also seems to buffer the consequences of such invasions (*26*).

Beyond Species Interactions

The application of networks in ecology is not restricted to species interactions but can also be applied to population dispersal across heterogeneous landscapes. For example, a node can be a patch of available habitat, and a link connecting two such patches can indicate the movement of individuals or genes. As habitat modification transforms continuous habitat into islands of disjointed patches (Fig. 1B), the regional persistence of a species inhabiting such a fragmented landscape will be determined by the balance between local extinction and migration among local patches (*27*). Indeed, networks may be a simplified representation of heterogeneous landscapes even in cases where parametrizing demographic data is not possible. The topology of these networks provides information about the relative importance of individual patches to the overall landscape connectivity. For example, network theory has been applied to the endangered Mexican spotted owl by mapping the discrete patches of original habitat as the nodes and using information on maximum dispersal distances to assess whether two such patches are potentially linked. This representation leads to the prediction that this species will survive even if substantial habitat transformation occurs, as long as a subset of the network of habitat patches is preserved (*28*).

Additionally, such methods can be used to visualize and analyze networks of genetic variation in space (Fig. 1B). Traditional approaches use the summary of pairwise effects of one population on another, but the network approach makes it possible to fully address the simultaneous influence of multiple local populations in shaping genetic variability (*29*). Finally, when network theory is applied to population biology,

it can address the inherent heterogeneity in who meets whom. This application can be extended to social networks as a way to estimate the spread of disease (*30*) and the evolution of cooperation (*31*) in heterogeneous societies.

Conclusions

Networks are useful descriptors of ecological systems that can show the composition of and interactions between multiple elements. The application of networks to ecosystems provides a conceptual framework to assess the consequences of perturbations at the community level. This may serve as a first step toward a more predictive ecology in the face of global environmental change. Networks are also able to introduce heterogeneity into our previously homogeneous theories of populations, diseases, and societies. Finally, networks have allowed us to find generalities among seemingly different systems that, despite their disparate nature, may have similar processes of formation and/or similar forces acting on their architecture in order to be functional. Although we have only begun to understand how changes in the environment affect species interactions and ecosystem dynamics through analyses of simple pairwise interactions, network thinking can provide a means by which to assess key questions such as how overfishing can cause trophic cascades, or how the disruption of mutualisms may reduce the entire pollination service within a community (*25*). As the flow of ideas among seemingly unrelated fields increases (a characteristic attribute of research on complex systems), we envision the creation of more powerful models that are able to more accurately predict the responses to perturbations of food webs, a major challenge for today's ecologist.

References and Notes

1. C. Darwin, *On the Origin of Species by Means of Natural Selection* (John Murray, London, 1859).
2. J. E. Cohen, *Food Webs and Niche Space* (Princeton Univ. Press, Princeton, NJ, 1978).
3. S. L. Pimm, *Food Webs* (Chapman & Hall, London, 1982).
4. G. Sugihara, thesis, Princeton University, Princeton, NJ, 1982.
5. R. M. May, *Nature* **238**, 413 (1972).
6. M. Pascual, J. A. Dunne, *Ecological Networks. Linking Structure to Dynamics in Food Webs* (Oxford Univ. Press, Oxford, 2006).
7. J. M. Montoya, S. L. Pimm, R. V. Solé, *Nature* **442**, 259 (2006).
8. R. Milo *et al.*, *Science* **298**, 824 (2002).
9. D. B. Stouffer, J. Camacho, W. Jiang, L. A. N. Amaral, *Proc. R. Soc. London Ser. B* **274**, 1931 (2007).
10. M. Kondoh, *Proc. Natl. Acad. Sci. U.S.A.* **105**, 16631 (2008).
11. J. Bascompte, C. J. Melián, E. Sala, *Proc. Natl. Acad. Sci. U.S.A.* **102**, 5443 (2005).
12. S. B. Otto, B. C. Rall, U. Brose, *Nature* **450**, 1226 (2007).
13. J. N. Thompson, *The Geographic Mosaic of Coevolution* (Univ. of Chicago Press, Chicago, 2005).
14. J. Bascompte, P. Jordano, *Annu. Rev. Ecol. Evol. Syst.* **38**, 567 (2007).
15. J. A. Dunne, R. Williams, N. Martinez, *Ecol. Lett.* **5**, 558 (2002).
16. J. Memmott, N. M. Waser, M. V. Price, *Proc. R. Soc. London Ser. B* **271**, 2605 (2004).
17. E. L. Rezende, J. E. Lavabre, P. R. Guimarães Jr., P. Jordano, J. Bascompte, *Nature* **448**, 925 (2007).
18. O. L. Petchey, A. Eklof, C. Borrvall, B. Ebenman, *Am. Nat.* **171**, 568 (2008).
19. A. Dobson *et al.*, *Ecology* **87**, 1915 (2006).
20. R. D. Holt, in *Multitrophic Interactions in Terrestrial Ecosystems*, A. C. Gange, V. K. Brown, Eds. (Blackwell Science, Oxford, 1997), pp. 333–349.
21. U. Brose, R. J. Williams, N. D. Martinez, *Ecol. Lett.* **9**, 1228 (2006).
22. E. L. Berlow *et al.*, *Proc. Natl. Acad. Sci. U.S.A.* **106**, 187 (2009).
23. U. Bastolla *et al.*, *Nature* **458**, 1018 (2009).
24. C. J. Melián, J. Bascompte, P. Jordano, V. Křivan, *Oikos* **118**, 122 (2009).
25. J. M. Tylianakis, R. K. Didham, J. Bascompte, D. A. Wardle, *Ecol. Lett.* **11**, 1351 (2008).
26. M. A. Aizen, C. L. Morales, J. M. Morales, *PLoS Biol.* **6**, e31 (2008).
27. I. Hanski, O. Ovaskainen, *Nature* **404**, 755 (2000).
28. D. Urban, T. H. Keitt, *Ecology* **82**, 1205 (2001).
29. R. J. Dyer, J. D. Nason, *Mol. Ecol.* **13**, 1713 (2004).
30. J. P. Aparicio, M. Pascual, *Proc. R. Soc. London Ser. B* **274**, 505 (2007).
31. H. Ohtsuki, C. Hauert, E. Lieberman, M. A. Nowak, *Nature* **441**, 502 (2006).

32. I thank L.-F. Bersier, P. Buston, J. E. Cohen, J. Dunne, M. A. Fortuna, R. D. Holt, P. Jordano, T. Keitt, J. Lavabre, R. M. May, J. Olesen, D. Stouffer, G. Sugihara, J. N. Thompson, J. Tylianakis, and two anonymous reviewers for comments on a previous draft. P. Jordano, A. Aparicio, and M. A. Fortuna provided material for Fig. 1. Funded by the European Heads of Research Councils, the European Science Foundation, and the European Community Sixth Framework Programme through a European Young Investigator Award.

10.1126/science.1170749

PERSPECTIVE

A General Framework for Analyzing Sustainability of Social-Ecological Systems

Elinor Ostrom[1,2]*

A major problem worldwide is the potential loss of fisheries, forests, and water resources. Understanding of the processes that lead to improvements in or deterioration of natural resources is limited, because scientific disciplines use different concepts and languages to describe and explain complex social-ecological systems (SESs). Without a common framework to organize findings, isolated knowledge does not cumulate. Until recently, accepted theory has assumed that resource users will never self-organize to maintain their resources and that governments must impose solutions. Research in multiple disciplines, however, has found that some government policies accelerate resource destruction, whereas some resource users have invested their time and energy to achieve sustainability. A general framework is used to identify 10 subsystem variables that affect the likelihood of self-organization in efforts to achieve a sustainable SES.

The world is currently threatened by considerable damage to or losses of many natural resources, including fisheries, lakes, and forests, as well as experiencing major reductions in biodiversity and the threat of massive climatic change. All humanly used resources are embedded in complex, social-ecological systems (SESs). SESs are composed of multiple subsystems and internal variables within these subsystems at multiple levels analogous to organisms composed of organs, organs of tissues, tissues of cells, cells of proteins, etc. (*1*). In a complex SES, subsystems such as a resource system (e.g., a coastal fishery), resource units (lobsters), users (fishers), and governance systems (organizations and rules that govern fishing on that coast) are relatively separable but interact to produce outcomes at the SES level, which in turn feed back to affect these subsystems and their components, as well other larger or smaller SESs.

Scientific knowledge is needed to enhance efforts to sustain SESs, but the ecological and social sciences have developed independently and do not combine easily (*2*). Furthermore, scholars have tended to develop simple theoretical models to analyze aspects of resource problems and to prescribe universal solutions. For example, theoretical predictions of the destruction of natural resources due to the lack of recognized property systems have led to one-size-fits-all recommendations to impose particular policy solutions that frequently fail (*3*, *4*).

The prediction of resource collapse is supported in very large, highly valuable, open-access systems when the resource harvesters are diverse, do not communicate, and fail to develop rules and norms for managing the resource (*5*) The dire predictions, however, are not supported under conditions that enable harvesters and local leaders to self-organize effective rules to manage a resource

[1]Workshop in Political Theory and Policy Analysis, Indiana University, Bloomington, IN 47408, USA. [2]Center for the Study of Institutional Diversity, Arizona State University, Tempe, AZ 85287, USA.

*E-mail: ostrom@indiana.edu

or in rigorous laboratory experiments when subjects can discuss options to avoid overharvesting (*3*, *6*).

A core challenge in diagnosing why some SESs are sustainable whereas others collapse is the identification and analysis of relationships among multiple levels of these complex systems at different spatial and temporal scales (*7*–*9*). Understanding a complex whole requires knowledge about specific variables and how their component parts are related (*10*). Thus, we must learn how to dissect and harness complexity, rather than eliminate it from such systems (*11*). This process is complicated, however, because entirely different frameworks, theories, and models are used by different disciplines to analyze their parts of the complex multilevel whole. A common, classificatory framework is needed to facilitate multidisciplinary efforts toward a better understanding of complex SESs.

I present an updated version of a multilevel, nested framework for analyzing outcomes achieved in SESs (*12*). Figure 1 provides an overview of the framework, showing the relationships among four first-level core subsystems of an SES that affect each other as well as linked social, economic, and political settings and related ecosystems. The subsystems are (i) resource systems (e.g., a designated protected park encompassing a specified territory containing forested areas, wildlife, and water systems); (ii) resource units (e.g., trees, shrubs, and plants contained in the park, types of wildlife, and amount and flow of water); (iii) governance systems (e.g., the government and other organizations that manage the park, the specific rules related to the use of the park, and how these rules are made); and (iv) users (e.g., individuals who use the park in diverse ways for sustenance, recreation, or commercial purposes). Each core subsystem is made up of multiple second-level variables (e.g., size of a resource system, mobility of a resource unit, level of governance, users' knowledge of the resource system) (Table 1), which are further composed of deeper-level variables .

This framework helps to identify relevant variables for studying a single focal SES, such as the lobster fishery on the Maine coast and the fishers who rely on it (*13*). It also provides a common set of variables for organizing studies of similar SESs such as the lakes in northern Wisconsin (e.g., why are the pollution levels in some lakes worse than in others?) (*14*), forests around the world (e.g., why do some locally managed forests thrive better than government-protected forests?) (*15*), or water institutions (e.g., what factors affect the likelihood that farmers will effectively manage irrigation systems?) (*16*). Without a framework to organize relevant variables identified in theories and empirical research, isolated knowledge acquired from studies of diverse resource systems in different countries by biophysical and social scientists is not likely to cumulate.

A framework is thus useful in providing a common set of potentially relevant variables and their subcomponents to use in the design of data collection instruments, the conduct of fieldwork, and the analysis of findings about the sustainability of complex SESs. It helps identify factors that may affect the likelihood of particular policies enhancing sustainability in one type and size of resource system and not in others. Table 1 lists the second-level variables identified in many empirical studies as affecting interactions and outcomes. The choice of relevant second or deeper levels of variables for analysis (from the large set of variables at multiple levels) depends on the particular questions under study, the type of SES, and the spatial and temporal scales of analysis.

To illustrate one use of the SES framework, I will focus on the question: When will the users of a resource invest time and energy to avert "a tragedy of the commons"? Garrett Hardin (*17*) earlier argued that users were trapped in accelerated overuse and would never invest time and energy to extract themselves. If that answer were supported by research, the SES framework would not be needed to analyze this question. Extensive empirical studies by scholars in diverse disciplines have found that the users of many (but not all) resources have invested in designing and implementing costly governance systems to increase the likelihood of sustaining them (*3*, *6*, *7*, *18*).

A theoretical answer to this question is that when expected benefits of managing a resource exceed the perceived costs of investing in better rules and norms for most users and their leaders, the probability of users' self-organizing is high (supporting online material text). Although joint benefits may be created, self-organizing to sustain a resource costs time, and effort can result in a loss of short-term economic gains. These costs, as well as the fear that some users will cheat on rules related to when, where, and how to harvest, can lead users to avoid costly changes and continue to overharvest (*6*). Accurate and reliable measures of users' perceived benefits and costs are difficult and costly to obtain, making it hard to test theories based on users' expected net benefits.

Multiple variables that have been observed and measured by field researchers are posited to affect the likelihood of users' engaging in collective action to self-organize. Ten second-level variables (indicated by asterisks in Table 1) are frequently identified as positively or negatively affecting the likelihood of users' self-organizing to manage a resource (*3*, *6*, *19*, *20*). To explain why these variables are potentially important for understanding sustainability and, in particular, for addressing the question of when self-organization activities will occur, I briefly discuss how they affect perceived benefits and costs.

Size of resource system (RS3). For land-related resource systems, such as forests, very large territories are unlikely to be self-organized given the high costs of defining boundaries (e.g., surrounding with markers or fences), monitoring use patterns, and gaining ecological knowledge. Very small territories do not generate substantial flows of valuable products. Thus, moderate territorial size is most conducive to self-organization (*15*). Fishers who consistently harvest from moderately sized coastal zones, lakes, or rivers are also more likely to organize (*13*) than fishers who travel the ocean in search of valuable fish (*5*).

Productivity of system (RS5). A resource system's current productivity has a curvilinear effect on self-organization across all sectors. If a water source or a fishery is already exhausted or apparently very abundant, users will not see a need to manage for the future. Users need to observe some

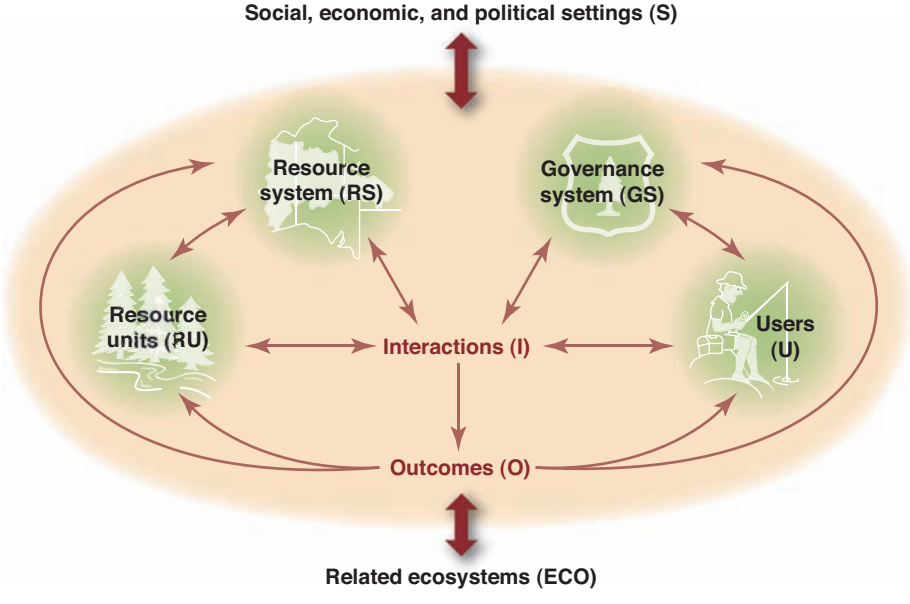

Fig. 1. The core subsystems in a framework for analyzing social-ecological systems.

scarcity before they invest in self-organization (*19*).

Predictability of system dynamics (RS7). System dynamics need to be sufficiently predictable that users can estimate what would happen if they were to establish particular harvesting rules or no-entry territories. Forests tend to be more predictable than water systems. Some fishery systems approach mathematical chaos and are particularly challenging for users or government officials (*21*). Unpredictability at a small scale may lead users of pastoral systems to organize at larger scales to increase overall predictability (*22*, *23*).

Resource unit mobility (RU1). Due to the costs of observing and managing a system, self-organization is less likely with mobile resource units, such as wildlife or water in an unregulated river, than with stationary units such as trees and plants or water in a lake (*24*).

Number of users (U1). The impact of group size on the transaction costs of self-organizing tends to be negative given the higher costs of getting users together and agreeing on changes (*19*, *20*). If the tasks of managing a resource, however, such as monitoring extensive community forests in India, are very costly, larger groups are more able to mobilize necessary labor and other resources (*25*). Thus, group size is always relevant, but its effect on self-organization depends on other SES variables and the types of management tasks envisioned.

Leadership (U5). When some users of any type of resource system have entrepreneurial skills and are respected as local leaders as a result of prior organization for other purposes, self-organization is more likely (*19*, *20*). The presence of college graduates and influential elders, for example, had a strong positive effect on the establishment of irrigation organization in a stratified sample of 48 irrigation systems in Karnataka and Rajasthan, India (*16*).

Norms/social capital (U6). Users of all types of resource systems who share moral and ethical standards regarding how to behave in groups they form, and thus the norms of reciprocity, and have sufficient trust in one another to keep agreements will face lower transaction costs in reaching agreements and lower costs of monitoring (*20*, *26*, *27*).

Knowledge of the SES (U7). When users share common knowledge of relevant SES attributes, how their actions affect each other, and rules used in other SESs, they will perceive lower costs of organizing (*7*). If the resource system regenerates slowly while the population grows rapidly, such as on Easter Island, users may not understand the carrying capacity of the resource, fail to organize, and destroy the resource (*28*).

Importance of resource to users (U8). In successful cases of self-organization, users are either dependent on the RS for a substantial portion of their livelihoods or attach high value to the sustainability of the resource. Otherwise, the costs of organizing and maintaining a self-governing system may not be worth the effort (*3*, *7*, *15*).

Collective-choice rules (GS6). When users, such as the Seri fishers in Mexico (*29*) and forest user groups in Nepal (*30*), have full autonomy at the collective-choice level to craft and enforce some of their own rules, they face lower transaction costs as well as lower costs in defending a resource against invasion by others (*5*).

Obtaining measures for these 10 variables is the first step in analyzing whether the users of one or more SESs would self-organize. Data analysis of these relationships is challenging, because the impact of any one variable depends on the values of other SES variables. As in most complex systems, the variables interact in a nonlinear fashion (*8*–*10*). Furthermore, although the long-term sustainability of SESs is initially dependent on users or a government to establish rules, these rules may not be sufficient over the long run (*7*, *18*).

If the initial set of rules established by the users, or by a government, are not congruent with local conditions, long-term sustainability may not be achieved (*8*, *9*, *18*). Studies of irrigation systems (*16*, *26*), forests (*25*, *31*), and coastal fisheries (*13*) suggest that long-term sustainability depends on rules matching the attributes of the resource system, resource units, and users. Rules forbidding the harvest of pregnant female fish are easy to monitor and enforce in the case of lobster, where eggs are visibly attached to the belly, and have been important in sustaining lobster fisheries (*13*). However, monitoring and enforcing these rules have proven more difficult in the case of gravid fish, where the presence of internal eggs is harder to assess.

Comparative studies of rules used in long-surviving resource systems governed by traditional societies document the wide diversity of rules used across sectors and regions of the world (*21*). Simple blueprint policies do not work. For example, the total allowable catch quotas established by the Canadian government for the west coast of Canada led to widespread dumping of unwanted fish, misrepresentation of catches, and the closure of the groundfishery in 1995 (*32*). To

Table 1. Examples of second-level variables under first-level core subsystems (S, RS, GS, RU, U, I, O and ECO) in a framework for analyzing social-ecological systems. The framework does not list variables in an order of importance, because their importance varies in different studies. [Adapted from (*12*)]

Social, economic, and political settings (S)	
S1 Economic development. S2 Demographic trends. S3 Political stability. S4 Government resource policies. S5 Market incentives. S6 Media organization.	
Resource systems (RS)	*Governance systems (GS)*
RS1 Sector (e.g., water, forests, pasture, fish)	GS1 Government organizations
RS2 Clarity of system boundaries	GS2 Nongovernment organizations
RS3 Size of resource system*	GS3 Network structure
RS4 Human-constructed facilities	GS4 Property-rights systems
RS5 Productivity of system*	GS5 Operational rules
RS6 Equilibrium properties	GS6 Collective-choice rules*
RS7 Predictability of system dynamics*	GS7 Constitutional rules
RS8 Storage characteristics	GS8 Monitoring and sanctioning processes
RS9 Location	
Resource units (RU)	*Users (U)*
RU1 Resource unit mobility*	U1 Number of users*
RU2 Growth or replacement rate	U2 Socioeconomic attributes of users
RU3 Interaction among resource units	U3 History of use
RU4 Economic value	U4 Location
RU5 Number of units	U5 Leadership/entrepreneurship*
RU6 Distinctive markings	U6 Norms/social capital*
RU7 Spatial and temporal distribution	U7 Knowledge of SES/mental models*
	U8 Importance of resource*
	U9 Technology used
Interactions (I) → outcomes (O)	
I1 Harvesting levels of diverse users	O1 Social performance measures (e.g., efficiency, equity, accountability, sustainability)
I2 Information sharing among users	
I3 Deliberation processes	
I4 Conflicts among users	O2 Ecological performance measures (e.g., overharvested, resilience, bio-diversity, sustainability)
I5 Investment activities	
I6 Lobbying activities	
I7 Self-organizing activities	O3 Externalities to other SESs
I8 Networking activities	
Related ecosystems (ECO)	
ECO1 Climate patterns. ECO2 Pollution patterns. ECO3 Flows into and out of focal SES.	

*Subset of variables found to be associated with self-organization.

remedy this initial failure, the government reopened the fishery but divided the coastal area into more than 50 sectors, assigned transferable quotas, and required that all ships have neutral observers onboard to record all catches (*32*).

Furthermore, the long-term sustainability of rules devised at a focal SES level depends on monitoring and enforcement as well their not being overruled by larger government policies. The long-term effectiveness of rules has been shown in recent studies of forests in multiple countries to depend on users' willingness to monitor one another's harvesting practices (*15*, *31*, *33*, *34*). Larger-scale governance systems may either facilitate or destroy governance systems at a focal SES level. The colonial powers in Africa, Asia, and Latin America, for example, did not recognize local resource institutions that had been developed over centuries and imposed their own rules, which frequently led to overuse if not destruction (*3*, *7*, *23*).

Efforts are currently under way to revise and further develop the SES framework presented here with the goal of establishing comparable databases to enhance the gathering of research findings about processes affecting the sustainability of forests, pastures, coastal zones, and water systems around the world. Research across disciplines and questions will thus cumulate more rapidly and increase the knowledge needed to enhance the sustainability of complex SESs. Quantitative and qualitative data about the core set of SES variables across resource systems are needed to enable scholars to build and test theoretical models of heterogeneous costs and benefits between governments, communities, and individuals and to lead to improved policies.

References and Notes

1. E. Pennisi, *Science* **302**, 1646 (2003).
2. R. B. Norgaard, *Conserv. Biol.* **22**, 862 (2008).
3. National Research Council, *The Drama of the Commons* (National Academies Press, Washington, DC, 2002).
4. L. Pritchett, M. Woolcock, *World Dev.* **32**, 191 (2004).
5. F. Berkes *et al.*, *Science* **311**, 1557 (2006).
6. E. Ostrom, R. Gardner, J. Walker, *Rules, Games, and Common-Pool Resources* (Univ. of Michigan Press, Ann Arbor, MI, 1994).
7. F. Berkes, C. Folke, Eds., *Linking Social and Ecological Systems* (Cambridge Univ. Press, Cambridge, 1998).
8. M. A. Janssen, *Complexity and Ecosystem Management* (Edward Elgar, Cheltenham, UK, 2002).
9. J. Norberg, G. Cumming, Eds., *Complexity Theory for a Sustainable Future* (Columbia Univ. Press, New York, 2008).
10. S. A. Levin, *Ecology* **73**, 1943 (1992).
11. R. Axelrod, M. D. Cohen, *Harnessing Complexity* (Free Press, New York, 2001).
12. E. Ostrom, *Proc. Natl. Acad. Sci. U.S.A.* **104**, 15181 (2007).
13. J. Wilson, L. Yan, C. Wilson, *Proc. Natl. Acad. Sci. U.S.A.* **104**, 15212 (2007).
14. W. A. Brock, S. R. Carpenter, *Proc. Natl. Acad. Sci. U.S.A.* **104**, 15206 (2007).
15. A. Chhatre, A. Agrawal, *Proc. Natl. Acad. Sci. U.S.A.* **105**, 13286 (2008).
16. R. Meinzen-Dick, *Proc. Natl. Acad. Sci. U.S.A.* **104**, 15200 (2007).
17. G. Hardin, *Science* **162**, 1243 (1968).
18. T. Dietz, E. Ostrom, P. Stern, *Science* **302**, 1907 (2003).
19. R. Wade, *Village Republics: Economic Conditions for Collective Action in South India* (ICS, San Francisco, CA, 1994).
20. J.-M. Baland, J.-P. Platteau, *Halting Degradation of Natural Resources* (Oxford Univ. Press, New York, 2000).
21. J. M. Acheson, J. A. Wilson, R. S. Steneck, in *Linking Social and Ecological Systems*, F. Berkes, C. Folke, Eds. (Cambridge Univ. Press, Cambridge, 1998), pp. 390–413.
22. P. N. Wilson, G. D. Thompson, *Econ. Dev. Cult. Change* **41**, 299 (1993).
23. E. Mwangi, *Socioeconomic Change and Land Use in Africa* (Palgrave MacMillan, New York, 2007).
24. E. Schlager, W. Blomquist, S. Y. Tang, *Land Econ.* **70**, 294 (1994).
25. A. Agrawal, in *People and Forests: Communities, Institutions, and Governance*, C. C. Gibson, M. A. McKean, E. Ostrom, Eds. (MIT Press, Cambridge, MA, 2000), pp. 57–86.
26. P. B. Trawick, *Hum. Ecol.* **29**, 1 (2001).
27. E. Ostrom, *Understanding Institutional Diversity* (Princeton Univ. Press, Princeton, NJ, 2005).
28. J. A. Brander, M. S. Taylor, *Am. Econ. Rev.* **88**, 119 (1998).
29. X. Basurto, *J. Soc. Nat. Resour.* **18**, 643 (2005).
30. H. Nagendra, *Proc. Natl. Acad. Sci. U.S.A.* **104**, 15218 (2007).
31. E. Ostrom, H. Nagendra, *Proc. Natl. Acad. Sci. U.S.A.* **103**, 19224 (2006).
32. C. W. Clark, *The Worldwide Crisis in Fisheries: Economic Models and Human Behavior* (Cambridge Univ. Press, Cambridge, 2006).
33. G. C. Gibson, J. T. Williams, E. Ostrom, *World Dev.* **33**, 273 (2005).
34. E. Coleman, B. Steed, *Ecol. Econ.* **68**, 2106 (2009).

35. Supported in part by NSF grants BCS-0624178 and BCS-0601320. I thank T. K. Ahn, R. Axtell, X. Basurto, J. Broderick, E. Coleman, C. Eavey, B. Fischer, C. A. González, E. Jameson, B. de Leon, D. Porter, M. Schlueter, D. Sprinz, and J. Walker for comments and suggestions.

10.1126/science.1172133

PERSPECTIVE

Economic Networks: The New Challenges

Frank Schweitzer,[1]* Giorgio Fagiolo,[2] Didier Sornette,[1,3] Fernando Vega-Redondo,[4,5] Alessandro Vespignani,[6,7] Douglas R. White[8]

The current economic crisis illustrates a critical need for new and fundamental understanding of the structure and dynamics of economic networks. Economic systems are increasingly built on interdependencies, implemented through trans-national credit and investment networks, trade relations, or supply chains that have proven difficult to predict and control. We need, therefore, an approach that stresses the systemic complexity of economic networks and that can be used to revise and extend established paradigms in economic theory. This will facilitate the design of policies that reduce conflicts between individual interests and global efficiency, as well as reduce the risk of global failure by making economic networks more robust.

The economy, as any other complex system, reflects a dynamic interaction of a large number of different agents, not just a few key players. The resulting systemic behavior, observable on the aggregate level, often shows consequences that are hard to predict, as illustrated by the current crisis, which cannot be simply explained by the failure of a few major agents. Thus, we need a more fundamental insight into the system's dynamics and how they can be traced back to the structural properties of the underlying interaction network.

Research examining economic networks has been studied from two perspectives; one view comes from economics and sociology; the other originated in research on complex systems in physics and computer science. In both, nodes represent the different individual agents, which can represent firms, banks, or even countries, and where links between the nodes represent their mutual interactions, be it trade, ownership, R&D alliances, or credit-debt relationships. Different agents may have different behaviors under the same conditions and have strategic interactions (*1*). These evolving interactions can be represented by network dynamics that are bound in space and time and can change with the environment and coevolve with the agents (*2*). Networks are formed or devolve on the basis of the addition or deletion of either agents or the links between them.

The socioeconomic perspective has emphasized understanding how the strategic behavior of the interacting agents is influenced by—and reciprocally shapes—relatively simple network architectures. One common example is that of a star-spoke network, like a very centralized or-

[1]ETH Zurich, D-MTEC, Kreuzplatz 5, 8032 Zurich, Switzerland. [2]Laboratorio di Economia e Management (LEM), Scuola Superiore Sant'Anna, Piazza Martiri della Liberta 33, 56127 Pisa, Italy. [3]Swiss Finance Institute, c/o University of Geneva, 40 Boulevard Du Pont d'Arve, 1211 Geneva 4, Switzerland. [4]Economics Department, European University Institute, Via della Piazzuola 43, 50133 Firenze, Italy. [5]Instituto Valenciano de Investigaciones Economicas, Calle Guardia Civil, 22 esc. 2 no 1, 46020 Valencia, Spain. [6]School of Informatics and Pervasive Technology Institute, Indiana University, 919 East 10th Street, Bloomington, IN 47408, USA. [7]Institute for Scientific Interchange, 10133 Torino, Italy. [8]Institute of Mathematical Behavioral Sciences, University of California, 3151 Social Science Plaza, Irvine, CA 92697, USA.

*To whom correspondence should be addressed. E-mail: fschweitzer@ethz.ch

ganization, in which a central "hub" channels all communication among agents. In this "micro" perspective we focus on the individual system elements and their detailed network of relations. In contrast, for large setups, one adopts a "macro" perspective that focuses on the statistical regularities of the network as a whole. Each approach has its advantages and disadvantages. Previous work on the micro perspective was strongly rooted in oversimplifying assumptions on both the structure of the network and on agents' behaviors (*3*). For example, the micro approach may have emphasized agent incentives in the development of informal links within firms and may have failed to successfully predict realistic dynamic outcomes. The macro approach better accounts for the large-scale system properties, but fails in linking these to the economic motivation of individual agents (*4*).

In recent micro approaches, economic networks were often viewed as the result of a network-formation game among competing and cooperating agents. In this regard, agents include firms that collaborate in joint R&D projects (*5*) or workers who share information on job opportunities (*6*); their links are added or deleted as the consequence of purposeful decisions attempting to maximize their payoffs. In this context, agents must rely on (and be able to) anticipate what others may do (in a generally imperfect and asymmetric manner); use information about their environment (which may be limited); frame the problem within some necessarily bounded time horizon; and learn from the past, which may create a biased experience if similar situations are encountered later.

These considerations tended to result in a dramatically large number of options that agents must choose from on the basis of limited information. The micro analysis of economic networks relies on game theory, which aims at identifying Nash equilibria (i.e., situations that are strategically stable in the sense that no agent has an incentive to deviate). It can also rely on operations research, where algorithms for searching and optimizing have been developed. As the number of nodes and possible links scales up, however, such problems become very difficult to solve, and classical approaches are unsatisfactory.

The game-theoretic literature has highlighted the crucial role of incentives in the endogenous and induced behavior of socioeconomic networks (*3*, *7*, *8*). However, this micro approach has not typically been integrated with macro approaches that can identify the complex systemic forces at work. Without this information, we cannot fully understand important issues, such as the conflict between individual incentives and aggregate welfare, or their impact on the overall efficiency in the performance of the network at large. Furthermore, this problem is exacerbated if the underlying environment is subject to persistent volatility, which may, for example, be due to the intrinsic ephemerality of innovation (*9*), and if agents are out of equilibrium, as in most real-world situations. If this is the case, it is reasonable to posit that agents follow simple bounded-rational rules that are modified in light of their experiences. However, under such conditions, agents are unable to attain efficient configurations, despite their continuous efforts to adapt to an ever-changing situation. Additionally, even small changes in environmental volatility can have drastic consequences in the overall configuration of the system [e.g., (Fig. 1)].

The inability of previous approaches to reproduce statistical regularities that have been observed empirically in network structures justifies our pursuit of a complex-systems approach that may provide predictions for large-scale networks. These predictions are made from the testing of stochastic rules that affect link formation and that take into account, in addition to some sort of randomness, the characteristic features of the agents, such as their degree of connectivity (number of links) or their centrality, as measured on the basis of the importance of a node—which, in turn, can be affected by its links to other nodes.

However, the complex-systems approach postulates rules exogenously and does not explicitly examine how these rules might be grounded on the basis of the economic incentives of the agents. Thus, instead of focusing on understanding the endogenous behavior of individual agents, the complex-systems approach centers on understanding how the network-formation rules systematically affect the emerging link structure (*4*).

Networks generated with different stochastic algorithms, such as random, scale-free or small-world networks, have been compared with real complex networks including those in biology, i.e., metabolic and genetic networks; infrastructure, i.e., road networks and power grids; communication, i.e., internet and mobile phone; and social interaction, i.e., collaborations (*1*, *2*, *10*). Comparing network structures across these different disciplines suggests that economic networks may also reflect a similar universality (*11*). Indeed, the connections of banks in an interbank network (*12*, *13*), show the fat tail, characteristic of a scale-free system, that indicates that only a few banks interact with many others. In this example, banks with similar investment behavior will cluster in the network. Similar regularities also can be traced for many examples including the international trade network (ITN) (*14*, *15*) and regional investment or ownership networks (*16*).

In the complex-network context, "links" are not binary (existing or not existing), but are weighted according to the economic interaction under consideration [for example, in a network of major financial institutions worldwide shown in (Fig. 2)]. Furthermore, links represent traded volumes, invested capital, and so on, and their weight can change over time. Distinguishing networks at different levels where we consider directed or undirected and weighted or unweighted links helps illuminate the evolution of their topological properties.

When the foreign direct investments (FDI) among European firms are presented as a directed network, power-law scaling is observed. This scaling depends on the number of employees in both the investing and the firm invested in, and on the number of incoming and outgoing investments of both firms (*16*) This allows single time-point predictions about the investments that regions will receive or make, on the basis of the activity and connectivity of their firms.

Similar structural transitions can also be detected in the ITN. By weighting a country's centrality in terms of the likelihood that any given additional dollar traded in the world reaches that country by following existing links with a probability proportional to its weight, the relative changes in centrality over time show trends for different countries that predict divergence in

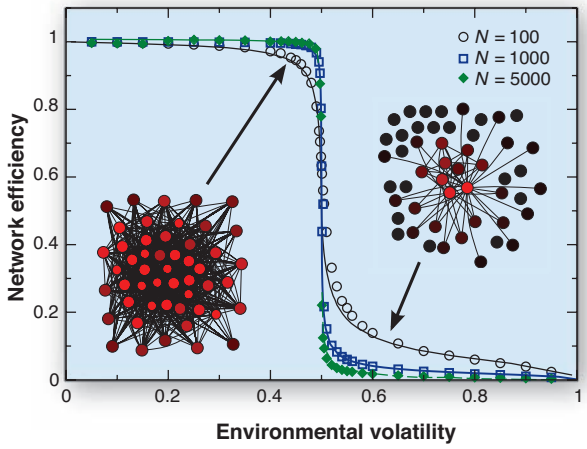

Fig. 1. The structure and efficiency of an equilibrium network strongly depend on the conditions under which myopic agents can form links. We show computer simulations that assume that agents prefer to connect to the neighbors of their neighbors that have a higher centrality, which creates local shortcuts. Network efficiency is measured on the basis of the aggregate centrality of agents. Environmental volatility measures the risk that if any single agent is exposed to an exogeneous shock, it will force the deletion of one link. If the loss of links pushes the network efficiency down and environmental volatility up past some critical level, the strongly homogeneous network structure will break down into a sparse, hierarchical structure, similar to a core-periphery structure and is accompanied with a breakdown in network efficiency.

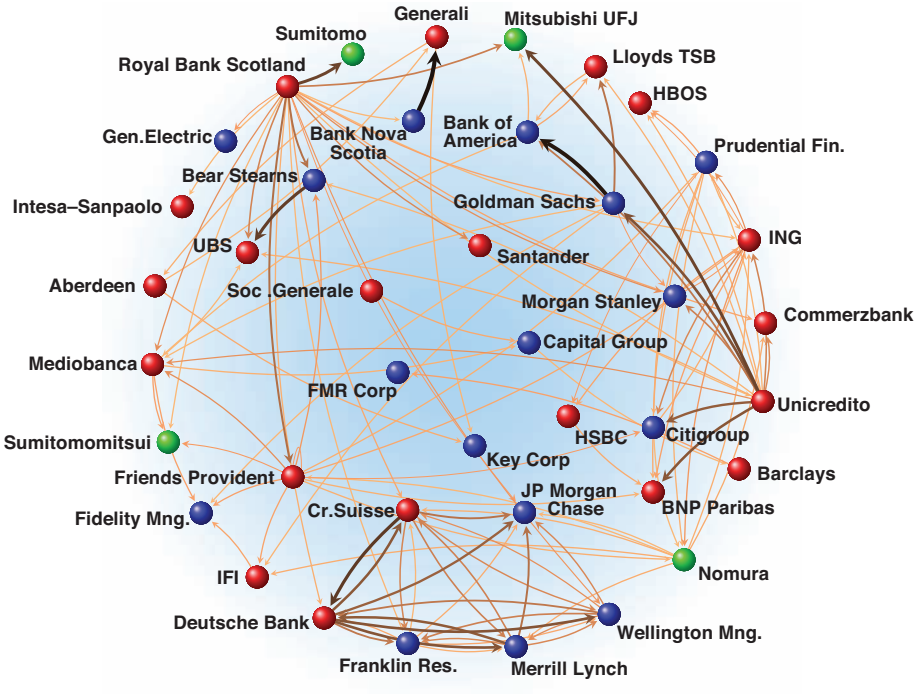

Fig. 2. A sample of the international financial network, where the nodes represent major financial institutions and the links are both directed and weighted and represent the strongest existing relations among them. Node colors express different geographical areas: European Union members (red), North America (blue), other countries (green). Even with the reduced number of links displayed in the figure, relative to the true world economy, the network shows a high connectivity among the financial institutions that have mutual share-holdings and closed loops involving several nodes. This indicates that the financial sector is strongly interdependent, which may affect market competition and systemic risk and make the network vulnerable to instability.

regional integration within the global economy and do so better than traditional international trade and macroeconomic statistics (*17*). This is also because the latter do not account for the entire network topology but only consider bilateral direct trade links. For example, between 1980 and 2005 East Asian countries experienced huge increases in their centrality scores, but the centrality ranking of most Latin American countries fell. The trade statistics of these regions, however, displayed similar patterns. In other words, these astonishingly different development records were not well tracked by international trade and macroeconomics statistics. Thus, network-based approaches may provide a more powerful way to manage, monitor, and govern complex economics systems.

However, a focus on centrality or other such properties of networks can only provide a first-order classification that emphasizes the role of fluctuations and randomness and cannot predict the underlying dynamics of the agents, whether they are firms or countries. We anticipate that the next generation of research will be able to measure any deviations from universality and will allow us to identify the idiosyncrasies associated with individual agent dynamics and their decision-making processes. This new wave of research should begin to merge the description of individual agents strategies with their coevolving networks of interactions. We should then be able to predict and propose economic policies that favor networks structures that are more robust to economic shocks and that can facilitate integration or trade. Below, we briefly describe what is needed to tackle this endeavor.

Massive data analysis. Our ability to obtain more and better quality data will foster the transition from a qualitative to a quantitative and evidence-based science. As computational power increases, large-scale network data can be gathered for different levels of the economy (e.g., firms, industries, and countries), and models can be tested through the generation of large, synthetic, data sets. New processing methods should open a wide range of business data and internet communication that can be exploited. It will then be possible to gather individualized data on specific interactions over time such as employee flows, R&D collaborations, and so on within a business or firm-bank credit market interactions. These large data streams require more powerful tools to digest and manipulate the huge scale of available information reflecting agent interactions and network properties. Databases containing this information may therefore complement both theoretical economic network experiments (*18*, *19*) and empirical economic network studies (*20*, *21*) and provide large-scale observations in real-time (*22*).

Time and space. By allowing a time-dependent resolution of the properties of economic networks, we will be able to move beyond a single-snapshot approach. This will allow the researcher to identify the evolutionary path of networks through the combination of complementary information sources. A good illustration of this is provided by the R&D networks in the field of human biotechnology (*20*), which follow a predictable life cycle related to the timing of the exchange and integration of knowledge.

Structure identification. Extracting network topology from reported data, in particular for aggregated economic data, is very difficult. This is particularly true for the banking sector, where detailed accounts of debt-credit relations are not publicly available, although theoretical decompositions of aggregated data have been studied (*13*). Even then, analyses may resemble reading tea leaves and reveal only previously known or predicted information. Statistical regularities in economic networks can be identified through large-scale data sets, but difficulties in assessing the relevance of the various measures remain. In an evolving economic network, we require information about agents' roles, their function and their influence (*23*). New methods are needed to identify patterns, and new concepts are needed to quantify both direct and indirect influence (e.g., through ownership). The identification in the ITN of such roles based on similar positions in the network suggests that promising steps have begun to identify functional roles played by interactive agents that relate to specific patterns in the link structure of their multirelational interaction network (*24*). Mapping a large network as a homologous small one, with statistically optimal sets of distinctive roles, gives a statistical correspondence in the case of the ITN world alignments for New World–Afro–East Asian versus North and Central Eurasia alignments by cross-cutting each of their interconnected cores, semiperipheries, and peripheries, as in world system models, but with much greater precision.

Beyond simplicity. All economic networks are heterogeneous with respect to both their agents and interaction strength and can also strongly vary in time (*25*). Previous studies of efficient (i.e., not wasteful) and equilibrium (or strategically stable) networks assumed homogeneity. However, as the differences between weighted and unweighted network properties indicate for the ITN case (*14*), any prediction of phase transitions may fail under these simplified assumptions. In fact, heterogeneities of agents can turn out to prevent phase transitions, i.e., become a source of stability.

Systemic feedbacks. Simple amplification mechanisms (such as herding) can dominate the network dynamics at large, despite the best intentions of the agents. Economic networks are subject to amplifications that may result from the redistribution of the load if one node fails (e.g., electricity in a power grid or credit debt in a banking network). If a single node fails, it may force

other nodes to fail as well, which may eventually lead to failure cascades and the breakdown of the system, denoted as systemic risk. This applies in particular to financial networks where links represent standing debts and claims between connected financial institutions. However, it is not well understood how the structure of a financial network affects the probability of a systemic failure. Although a topical subject, most theoretical and empirical methods are not suited to predicting cascading network effects. The mainstream view assumes that a denser network allows for a better diversification of the individual failure risk (*26*). However, systemic risk has been shown to increase, depending on the coupling strength between nodes (*27*). Furthermore, most stable dynamic network models account for only the addition or removal of a single agent to or from the network at each instance of time. However, the addition or removal of whole groups of agents to or from the network (e.g., as part of a systemic failure) may result in a larger, less predictable, and less stable system.

In summary, we anticipate a challenging research agenda in economic networks, built upon a methodology that strives to capture the rich process resulting from the interplay between agents' behavior and the dynamic interactions among them. To be effective, however, empirical studies providing insights into economic networks from massive data analysis, theory encompassing the appropriate description of economic agents and their interactions, and a systemic perspective bestowing a new understanding of global effects as coming from varying network interactions are needed. We predict that such studies will create a more unified field of economic networks that advances our understanding and leads to further insight. We are still far from a satisfactory identification and integration of the many components, but the recent advances outlined suggest a promising start.

References and Notes

1. F. Vega-Redondo, *Complex Social Networks* (Econometric Society Monographs, Cambridge Univ. Press, Cambridge, 2007).
2. A. Barrat, M. Barthelemy, A. Vespignani, *Dynamical Processes on Complex Networks* (Cambridge Univ. Press, Cambridge, 2008).
3. M. O. Jackson, A. Wolinsky, *J. Econ. Theory* **71**, 44 (1996).
4. R. Albert, A.-L. Barabasi, *Rev. Mod. Phys.* **74**, 47 (2002).
5. J. Hagedoorn, *Res. Policy* **31**, 477 (2002).
6. M. Granovetter, *Getting a Job: A Study of Contacts and Careers* (Univ. of Chicago Press, Chicago, 1995)
7. V. Bala, S. Goyal, *Econometrica* **68**, 1181 (2000).
8. M. D. König, S. Battiston, M. Napoletano, F. Schweitzer, *Netw. Heterog. Media* **3**, 201 (2008).
9. M. Marsili, F. Vega-Redondo, F. Slanina, *Proc. Natl. Acad. Sci. U.S.A.* **101**, 1439 (2004).
10. S. P. Borgatti, A. Mehra, D. J. Brass, G. Labianca, *Science* **323**, 892 (2009).
11. R. M. May, S. A. Levin, G. Sugihara, *Nature* **451**, 893 (2008).
12. G. Iori, G. De Masi, O. Precup, G. Gabbi, G. Caldarelli, *J. Econ. Dyn. Control* **32**, 259 (2008).
13. M. Boss, H. Elsinger, M. Summer, S. Thurner, *Quant. Finance* **4**, 677 (2004).
14. G. Fagiolo, S. Schiavo, J. Reyes, *Phys. Rev. E Stat. Nonlin. Soft Matter Phys.* **79**, 036115 (2009).
15. D. Garlaschelli, M. I. Loffredo, *Phys. Rev. Lett.* **93**, 188701 (2004).
16. S. Battiston, J. F. Rodrigues, H. Zeytinoglu, *Adv. Complex Syst.* **10**, 29 (2007).
17. J. Reyes, S. Schiavo, G. Fagiolo, *Adv. Complex Syst.* **11**, 685 (2008).
18. M. Kosfeld, *Rev. Netw. Econ.* **3**, 20 (2004).
19. S. Callander, C. Plott, *J. Public Econ.* **89**, 1469 (2005).
20. W. Powell, D. White, K. Koput, J. Owen-Smith, *Am. J. Sociol.* **110**, 1132 (2005).
21. B. Kogut, G. Walker, *Am. Sociol. Rev.* **66**, 317 (2001).
22. D. Sornette, F. Deschatres, T. Gilbert, Y. Ageon, *Phys. Rev. Lett.* **93**, 228701 (2004).
23. T. A. Snijders, G. G. van de Bunt, C. E. Steglich, *Soc. Networks*, in press; published online 26 March 2009 (10.1016/j.socnet.2009.02.004).
24. J. Reichardt, D. White, *Eur. Phys. J. B* **60**, 217 (2007).
25. A. Kirman, *J. Evol. Econ.* **7**, 339 (1997).
26. F. Allen, D. Gale, *J. Polit. Econ.* **108**, 1 (2000).
27. S. Battiston, D. Delli Gatti, M. Gallegati, B. Greenwald, J. Stiglitz, *J. Econ. Dyn. Control* **31**, 2061 (2007).

28. We would like to thank M. König, C. J. Tessone, S. Battiston, and S. Vitali (ETH Zurich) for aid with figures and S. White for commentary on the text. Data for Fig. 2 were provided by Orbis Database (end of 2007), Bureau Van Dijk. F.S. and D.S. acknowledge financial support from the ETH Competence Center, "Coping with Crises in Complex Socio-Economic Systems" (CCSS), through ETH Research Grant CH1-01-08-2. F.V-R. gratefully acknowledges financial support from the Spanish Ministry of Education under grant SEJ2007-62656. A.V. acknowledges funding from NIH, DTRA, the EC-FET program and the Lilly Foundation. D.W.'s work is supported by external faculty funding at the Santa Fe Institute and anonymous nonprofit contributions to the University of California at Irvine faculty group in Social Dynamics and Complexity.

10.1126/science.1173644

PERSPECTIVE

Predicting the Behavior of Techno-Social Systems

Alessandro Vespignani

We live in an increasingly interconnected world of techno-social systems, in which infrastructures composed of different technological layers are interoperating within the social component that drives their use and development. Examples are provided by the Internet, the World Wide Web, WiFi communication technologies, and transportation and mobility infrastructures. The multiscale nature and complexity of these networks are crucial features in understanding and managing the networks. The accessibility of new data and the advances in the theory and modeling of complex networks are providing an integrated framework that brings us closer to achieving true predictive power of the behavior of techno-social systems.

Modern techno-social systems consist of large-scale physical infrastructures (such as transportation systems and power distribution grids) embedded in a dense web of communication and computing infrastructures whose dynamics and evolution are defined and driven by human behavior. To predict the behavior of such systems, it is necessary to start with the mathematical description of patterns found in real-world data. These descriptions form the basis of models that can be used to anticipate trends, evaluate risks, and eventually manage future events. If fed with the right data, computational modeling approaches can provide the requested level of predictability in very complex settings. The most successful example is weather forecasting, in which sophisticated supercomputer infrastructures are used to integrate current data and huge libraries of historical meteorological patterns into large-scale computational simulations. Although we often complain about the accuracy of daily weather forecasts, we must remember that numerical weather models and predictions allow us to project the path and intensity of hurricanes, storms, and other severe meteorological occurrences and, in many cases, to save thousand of lives by anticipating and preparing for these events.

Given the success that has been achieved in weather forecasting for decades, why haven't we achieved the same success in the quantitative prediction of the next pandemic spatio-temporal pattern or the effects over the next decade of connecting billions of people from China and India on Internet growth and stability? The basic difference is that forecasting phenomena in techno-social systems starts with our limited knowledge of society and human behavior rather than with the physical laws governing fluid and gas masses. In other words, though it is possible to produce satellite images of atmospheric turbulence, we do not yet have large-scale worldwide, quantitative knowledge of human mobility, the progression of risk perception in a population, or the tendency to adopt certain social behaviors. In recent years, however, tremendous progress has been made in data gathering, the development of new informatics tools, and increases in computational power. A huge flow of quantitative data that combine the demographic and behavioral

Center for Complex Networks and Systems Research, School of Informatics and Computing, and Pervasive Technology Institute, Indiana University, Bloomington, IN 47408, USA; and Institute for Scientific Interchange, Turin, Italy. E-mail: alexv@indiana.edu

aspects of society with the infrastructural substrate is becoming available (*1*–*6*). Analogously to what happened in physics, we are finally in the position to move from the analysis of the "social atom" or "social molecules" (i.e., small social groups) to the quantitative analysis of social aggregate states, as envisioned by social scientists at the beginning of the past century (*7*). Here, I refer to "social aggregate states" as large-scale social systems consisting of millions of individuals that can be characterized in space (geographic and social) and time. The shift from the study of a small number of elements to the study of the behavior of large-scale aggregates is equivalent to the shift from atomic and molecular physics to the physics of matter. The understanding of how the same elements assembled in large number can give rise, according to the various forces and elements at play, to different macroscopic and dynamical behaviors opens the path to quantitative computational approaches and forecasting power. Yet at the same time, the study of social aggregate states present us with all the challenges already faced in the physics of matter, from turbulence to multiscale behavior.

Reality Mining and Proxy Networks

The level of information flow regarding technosocial systems is not just due to advances in number crunching power of modern computer processors. Insights into the nature of the interlinks between people and technology and the dissolution of boundaries between the cyberworld and our real-world social activities are changing our accessibility to data, leading to "reality-mining," which has been defined as the collection of machine-sensed environmental data that are related to human social behavior (*2*). A prime example of the people/technology interlinkage can be found in the analysis of human mobility. In the past, approaches to human interactions and mobility have mostly relied on census and survey data, which were often incomplete and/or limited to a specific context. Despite advances in the study of human transport (*8*, *9*), this lack of data has hindered the construction of a general framework of human mobility based on dynamical principles at the individual level with the ability to bridge spatial scales, from small communities to large urban areas and countries, in a bottom-up perspective. However, in pioneering work, Brockmann *et al*. (*4*) showed that popular Web sites for currency tracking (such as http://en.eurobilltracker.com and www.wheresgeorge.com) collect a massive number of records on money dispersal that can be used as a proxy for human mobility. This work opened the path to the general exploitation of proxy data for human interaction and mobility (*10*). Analogously, modern mobile phones and personal digital assistants combine sophisticated technologies such as Bluetooth, Global Positioning System, and WiFi, constantly producing detailed traces on our daily activities (*2*, *11*). For instance, in a recent study, Gonzalez *et al*. (*6*) used mobile phone data to track the movements of 100,000 people over a 6-month time span. Furthermore, it is now possible to use sensors and tags that produce data at the microscale of one-to-one interactions (*1*, *2*).

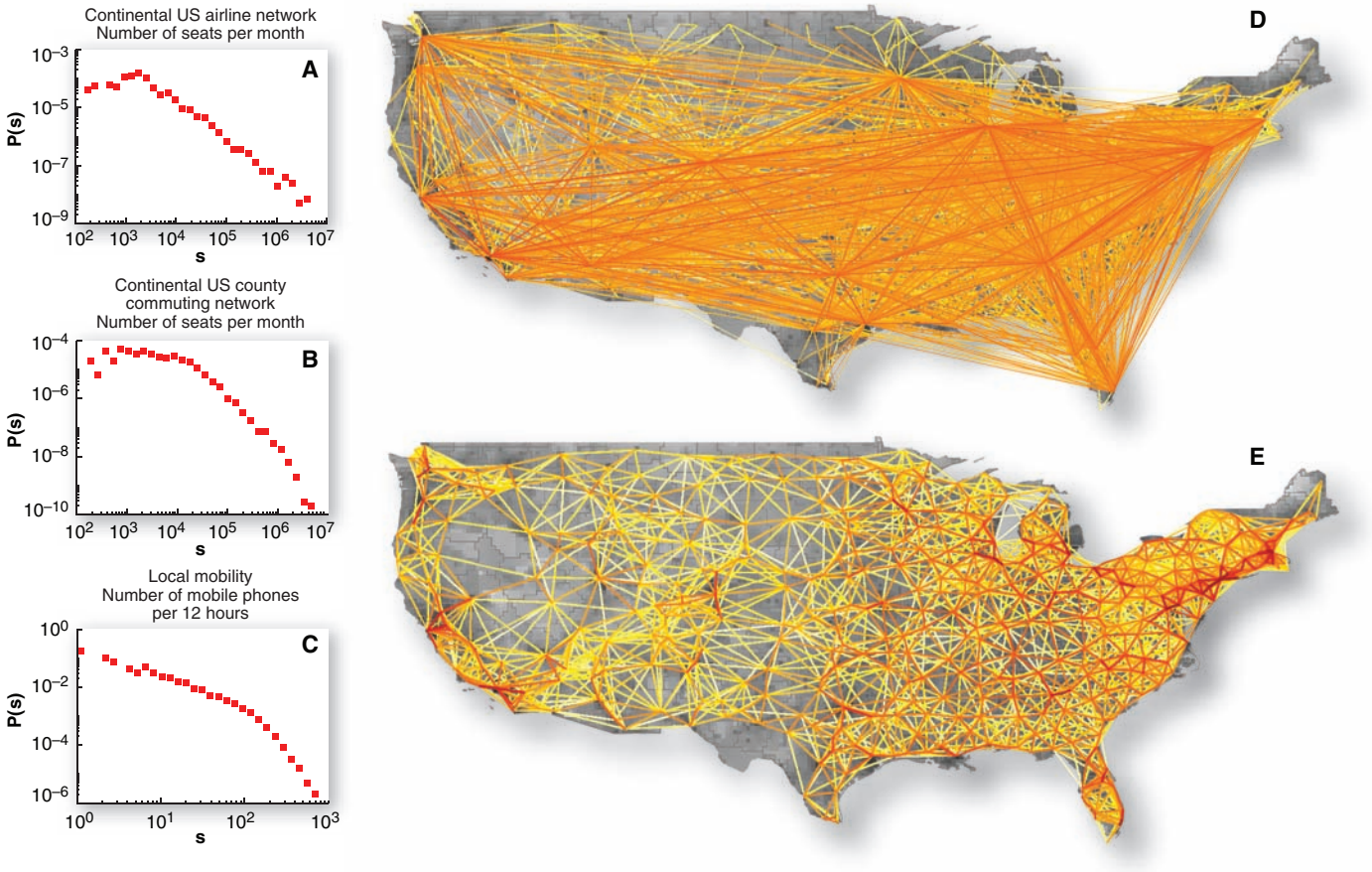

Fig. 1. Multiscale properties of mobility networks. On the left, we report the probability distribution $P(s)$ for the traffic, measured as the number of traveling individuals, on any given connection, of three different networks: (**A**) the continental U.S. airline network, (**B**) the continental U.S. county commuting network, and (**C**) the mobility among telephone tower cells in a major urban area. In all cases, the distributions are highly skewed and span from three to seven orders of magnitude. On the right, we show the illustration of the continental U.S. airline network (**D**) and the commuting network (**E**) among major census areas. The color scale from yellow to dark red identifies the traffic flow magnitude in logarithmic scale. The airline network is made mostly by long-range connections as compared with a gridlike ordering of the commuting network. The daily average flow of the commuting network is one order of magnitude larger than that of the airline network.

Through confronting us with serious ethical and privacy questions, these kinds of data and the reduced cost of producing, accessing, and communicating information on techno-social systems are changing our understanding of a wide range of phenomena (*12*–*17*). The spatial dynamics of human infectious diseases are determined by the mobility of individuals who carry a disease into previously uninfected populations. Analogously, human migration and mobility mediate a large number of bioinvasions, defined as the introduction of previously unknown organisms in ecosystems. The evolution of languages and dialects is also driven by the mixing of populations and the merging and/or isolation of communities. Finally, the daily mobility of humans in Internet space defines our exploitation and foraging of information.

Network Thinking

The Internet and virtual worlds are networks that we navigate and explore every day (*17*–*19*). Human-interaction models are based on social networks in which nodes represent individual interacting agents and the links are potential interactions (*20*). Mobility, ecological, and epidemiological models rely on metapopulation networks that consist of entire populations interlinked by virtue of the exchanges between groups of individuals (*21*). A large body of work has shown that most real-world networks exhibit dynamic self-organization (that is, they become more complicated over time without the intervention of outside forces) and are statistically very heterogeneous; these characteristics are typical hallmarks of complex systems (*22*–*24*). The various statistical distributions characterizing these networks (including the probabilities of node connection and the intensities of the connecting links) are generally heavy tailed and skewed, and they vary over several orders of magnitude (*25*). The foremost challenge offered by complex networks therefore resides in their interconnectedness (networks of networks) and multiscale nature. Figure 1 depicts three networks that exemplify human mobility at different scales, ranging from cross-continental airline travel to within-city mobility among mobile phone cell towers. Ideally, to make predictions about the processes driven by human mobility, we need to integrate this data, with its wide-ranging granularities (from a few hundred meters and a few hours to thousands of kilometers and several days), into a huge multiscale network.

Thus, the complexity of techno-social systems calls for a "network" mindset. A simple example is provided by the large-scale description of epidemic spreading. The spread of the plague epidemic in the 14th century (the Black Death) (*26*) was mainly a spatial diffusion phenomenon. Historical studies have established that the disease propagation followed a simple pattern that can be adequately described mathematically within the framework of continuous differential equations with terms that describe diffusion. As anticipated in 1933 (*27*), the large-scale and geographical impact of infectious diseases [such as the SARS epidemic (*28*) or the current swine flu epidemic] on populations in the modern world is mainly due to commercial air travel. An epidemic that starts in Southeast Asia will rapidly reach North America and Europe (Fig. 2). This picture, therefore, cannot be simply described in terms of diffusive phenomena; rather, it must incorporate the spatial structure of modern transportation networks. For instance, it is the heavy-tailed nature of the airline traffic network that explains why travel restrictions alone are ineffective in containing a global epidemic unless the global mobility rate is reduced at least by one order of magnitude (*29*–*31*).

Another crucial aspect of modern network thinking is the dynamical self-organization that gives rise to large-scale infrastructure patterns independent of human planning and engineering of the system. The prime example of a dynamical self-organizing system may be the Internet, but most communication infrastructures, road and transportation systems, supply networks, and power distribution grids are also dynamically growing networks. Road construction, for instance, is obviously planned, and it is not surprising that considerations of optimization of cost, efficiency, and utility inform the planning effort. As a consequence, one could generally expect road networks to exhibit a high degree of regularity. Yet everyday experience suggests that this is not the case, especially in towns that have grown over a long period of time. For this reason, researchers have formulated simple road-formation models (*32*) that try to capture the tension between the notion of optimality that inspires planners and the limited time and spatial horizons that inform their decisions.

However, the biggest challenge in providing a holistic description of multiscale networks is the necessity of simultaneously dealing with multiple time and length scales. The final system's dynamical behavior at any scale is the product of the events taking place on all scales. The single agent spreading a disease or single node of the Internet that fails are apparently not affected by

Fig. 2. Epidemic invasion tree obtained from the simulations of a pandemic originating in Hanoi, Vietnam. The nodes identify 3200 populations worldwide, and the directed links indicate the path along which the epidemic has moved from one population to the other. The color map from dark red to dark blue is according to the time ordering of the epidemic invasion. Simulations obtained with the worldwide epidemic and mobility model from (*38*).

the multiscale nature of the network, just as single molecules do not care about the multiscale nature of turbulent fluids. However, the collective dynamical behavior and our ability to conduct mathematical and/or computational analyses of techno-social systems are constrained by the multiscale characteristic of the system. In the context of networks and techno-social systems, the multiscale challenge is making its appearance now because of the availability of large-scale data sets. Thus, we have to develop appropriate formalisms and techniques, as researchers studying multiscale physical systems (fluids, solids, distribution of masses in the universe, etc.) have done in the past (*33*). To achieve analytical understanding of techno-social systems and approach them computationally, we must find different strategies to deal with dynamical behavior and/or equations that work at very different characteristic scales but still influence each other. Such methods will finally allow the definition of layered computational approaches in which different modeling assumptions and granularities can be used consistently in the context of a general multiscale framework.

Taking Advantage of Multiscale Networks

Knowledge of network characteristics opens the path to the discovery and understanding of new statistical and dynamical laws governing large infrastructural systems coupled to social systems. Furthermore, the massive interconnectivity of spatially distributed populations and the complexity and strong heterogeneity of multiscale networks are the keys to the construction of ab-initio computational models, in which the behavior of the system can be understood in a bottom-up perspective, as opposed to the traditional mean-field or top-down strategies. This happens in a wide array of contexts ranging from urban planning (*34*) to epidemic modeling (*35*–*38*). Notable examples are the TRANSIM and EPISIMS projects (*35*), in which agent-based models, including millions of individuals, are used to simulate the dynamics and traffic of entire cities and the spread of biological agents, respectively.

In some cases, the understanding of complex networks provides counterintuitive and surprising approaches to the engineering and management of complex techno-social systems. For example, in power grids and other flow-carrying networks, the failure of a single node or line can trigger a domino effect ("cascading failure"), in which the overload induced by the flow redistribution may generate a global failure of the network. By taking advantage of the heterogeneity of the flow carried on the links of multiscale networks, A. E. Motter (*39*) has proposed an adaptive defense mechanism that is actually based on the removal of a certain number of nodes to induce intentional failures. Although this mechanism might appear counterintuitive, the intentional failure of appropriately chosen nodes does not amplify the cascade process and, on the contrary, is able to mitigate the final damage. In other words, we now can provide a rationale for understanding the emerging tipping points and nonlinear properties that often underpin the most interesting characteristics of a techno-social system's behavior.

The Toughest Challenge

Although many basic conceptual questions remain unresolved, the major roadblock in defining the fundamental predictability limits for techno-social systems is their sensitivity and dependence on social adaptive behavior. In the absence of a stress on the system, a stationary state is reached in which the feedback between the social behavior and the physical infrastructure determines the details of how the network behavior and the dynamical process of interest play out. We can imagine using steady-state data to forecast system behavior under such "normal" conditions. However, in the case of catastrophic events (for instance, the disruption of social order during emergencies such as pandemics or major natural disasters), the behavior of techno-social networks is driven out of equilibrium into unknown territory.

An interesting and ethically challenging aspect of predicting and managing the unfolding of catastrophic events in techno-social networks is the system's adaptation to predictions when they are made publicly available. Social behaviors react and adapt to knowledge of predictions. Contrary to what happens in physical systems, the predictions themselves are part of the system dynamic. In addition, predictions may point to unethical control and anticipation strategies favoring specific demographic sectors of the society. Finally, the risk of erroneous predictions may lead to costly or unethical social control mechanisms with no actual benefits. Whereas some of the above issues may find a partial solution through improvements in the accuracy and reliability of models, it is clear that social adaptation to predictions presents us with new methodological and ethical problems.

Addressing these problems involves tackling three major scientific challenges. The first is the gathering of large-scale data on information spread and social reactions that occur during periods of crisis. This is not presently out of reach, via large-scale mobile communication databases (such as mobile telephones, Twitter logs, and social Web tools) operating at the moment of specific disaster or crisis events. The second challenge is the formulation of formal models that make it possible to quantify the effect of risk perception and awareness phenomena of individuals on the techno-social network structure and dynamics. The third challenge concerns the deployment of monitoring infrastructures capable of informing computational models in real time. Complex systems and networks theory, mathematical biology, statistics, nonequilibrium statistical physics, and computer science all play a key role in the effort to meet these challenges. Although such an integrated approach might still be in its infancy, it now seems possible to imagine the creation of computational forecasting infrastructures that will help us design better energy-distribution systems, plan for traffic-free cities, anticipate the demands of Internet connectivity, or manage the deployment of resources during health emergencies.

References and Notes

1. D. Lazer *et al.*, *Science* **323**, 721 (2009).
2. A. Pentland, in *The Global Information Technology Report 2008-2009* (World Economic Forum, Geneva, 2009), p. 75.
3. J. P. Onnela *et al.*, *Proc. Natl. Acad. Sci. U.S.A.* **104**, 7332 (2007).
4. D. Brockmann, L. Hufnagel, T. Geisel, *Nature* **439**, 462 (2006).
5. D. J. Watts, *Nature* **445**, 489 (2007).
6. M. C. Gonzalez, C. A. Hidalgo, A.-L. Barabasi, *Nature* **453**, 779 (2008).
7. G. A. Lundberg, M. Lawsing, *Am. Sociol. Rev.* **2**, 318 (1937).
8. S. Erlander, N. F. Stewart, *The Gravity Model in Transportation Analysis* (VSP, Utrecht, Netherlands, 1990).
9. J. de Dios Ortuzar, L. G. Willumsen, *Modelling Transport* (Wiley, New York, 2001).
10. D. Brockmann, F. Theis, *Pervasive Comput.* **7**, 28 (2008).
11. F. Giannotti, D. Pedretti, *Mobility Data, Mining and Privacy* (Springer, Berlin, 2008).
12. S. Riley, *Science* **316**, 1298 (2007).
13. C. Viboud *et al.*, *Science* **312**, 447 (2006); published online 29 March 2006 (10.1126/science.1125237).
14. L. Hufnagel, D. Brockmann, T. Geisel, *Proc. Natl. Acad. Sci. U.S.A.* **101**, 15124 (2004).
15. V. Colizza *et al.*, *Proc. Natl. Acad. Sci. U.S.A.* **103**, 2015 (2006).
16. G. M. Ruiz *et al.*, *Nature* **408**, 49 (2000).
17. B. A. Huberman, L. Adamic, *Lecture Notes in Physics* (Springer, Heidelberg, Germany, 2003).
18. R. Pastor-Satorras, A. Vespignani, *Evolution and Structure of the Internet* (Cambridge Univ. Press, Cambridge, 2004).
19. M. E. Crovella, B. Krishnamurthy, *Internet Measurements: Infrastructure, Traffic and Applications* (Wiley, Chichester, UK, 2006).
20. S. Wasserman, K. Faust, *Social Network Analysis* (Cambridge Univ. Press, Cambridge, 1994).
21. I. A. Hanski, O. E. Gaggiotti, *Ecology, Genetics and Evolution of Metapopulations* (Academic Press, San Diego, CA, 2004).
22. A.-L. Barábasi, R. Albert, *Science* **286**, 509 (1999).
23. M. E. J. Newman, *SIAM Rev.* **45**, 167 (2003).
24. A. Barrat, M. Barthelemy, A. Vespignani, *Dynamical Processes on Complex Networks* (Cambridge Univ. Press, Cambridge, 2008).
25. A. Barrat *et al.*, *Proc. Natl. Acad. Sci. U.S.A.* **101**, 3747 (2004).
26. J. D. Murray, *Mathematical Biology* (Springer, New York, 1993).
27. A. Massey, *Epidemiology in Relation to Air Travel* (H. K. Lewis, London, 1933).
28. J. S. M. Peiris, K. Y. Yuen, K. Stohr, *N. Engl. J. Med.* **349**, 2431 (2003).
29. T. D. Hollingsworth, N. M. Ferguson, R. M. Anderson, *Nat. Med.* **12**, 497 (2006).
30. J. M. Epstein *et al.*, *PLoS One* **2**, e401 (2007).
31. V. Colizza, A. Vespignani, *J. Theor. Biol.* **251**, 450 (2008).
32. M. Barthelemy, A. Flammini, *Phys. Rev. Lett.* **100**, 138702 (2008).
33. G. I. Pavliotis, A. M. Stuart, *Multiscale Methods: Averaging and Homogenization* (Springer, Heidelberg, Germany, 2008).
34. M. Batty, *Science* **319**, 769 (2008).
35. S. Eubank *et al.*, *Nature* **429**, 180 (2004).
36. N. M. Ferguson *et al.*, *Nature* **442**, 448 (2006).
37. T. C. Germann *et al.*, *Proc. Natl. Acad. Sci. U.S.A.* **103**, 5935 (2006).
38. V. Colizza *et al.*, *PLoS Med.* **4**, e95 (2007).
39. A. E. Motter, *Phys. Rev. Lett.* **93**, 098701 (2004).

40. I thank V. Colizza, D. Balcan, B. Goncalves, M. Gonzalez, and H. Hu for help with the figures and M. Gonzalez for the data used in Fig. 1C. I am partially supported by NIH, NSF, the Defense Threat Reduction Agency, the Lilly Endowment Foundation, and the Future Emerging Technologies projects Epiwork and Dynanets.

10.1126/science.1171990

REVIEW

Transcriptional Regulatory Circuits: Predicting Numbers from Alphabets

Harold D. Kim,[1]* Tal Shay,[2]* Erin K. O'Shea,[1] Aviv Regev[2]†

Transcriptional regulatory circuits govern how cis and trans factors transform signals into messenger RNA (mRNA) expression levels. With advances in quantitative and high-throughput technologies that allow measurement of gene expression state in different conditions, data that can be used to build and test models of transcriptional regulation is being generated at a rapid pace. Here, we review experimental and computational methods used to derive detailed quantitative circuit models on a small scale and cruder, genome-wide models on a large scale. We discuss the potential of combining small- and large-scale approaches to understand the working and wiring of transcriptional regulatory circuits.

The next frontier in genomics is to assemble systematically the functional components of genomes and cells into the circuits that transform signals into cellular responses. These circuits include signal transduction, metabolic, and transcriptional pathways. One major challenge is to predict, in a given cell type and under a given condition, the expression level of every gene. This view focuses on regulatory circuits that take trans regulators and cis sequence determinants as input and yield gene expression level as output (Fig. 1A).

Small-scale approaches have been used to develop detailed quantitative models of the regulatory circuits controlling one or very few genes. Complementary large-scale approaches used computational algorithms to reconstruct genome-scale circuits; these methods typically result in comprehensive, albeit less-detailed, models. These two strategies already inform and influence each other (*1*, *2*) and are likely to merge and deliver quantitative and biochemically interpretable genome-wide models of circuit wiring (*3*).

Small-Scale Approaches: Success Stories from Prokaryotes

Small-scale measurements focus on a single circuit and its cis regulation, typically by using thermodynamics or kinetic models as a framework for interpreting data. Inputs and outputs for several regulatory circuits have been measured in vivo on a small scale in prokaryotes (*4*–*7*). Inputs include inducers that modulate the activity of the trans factor (*6*, *7*), or the trans factor itself (*4*, *8*, *9*). Such studies rely on the availability of a transcription factor (TF) that binds a well-characterized promoter, with activity that can be continuously tuned in a controlled manner. The output is typically represented by the rate of protein production (*4*, *6*), protein activity (*6*, *7*), or steady-state protein level (*8*, *9*) and is measured by means of a reporter, such as a fluorescent protein gene or gene encoding an enzyme (whose activity serves as the reporter) that is placed under the control of the promoter of interest (*4*, *10*). The input-output relation, termed the gene-regulation function (*4*), is generally measured from a population of cells, although the same approaches apply to single-cell measurements.

Direct measurements, along with prior knowledge about the molecular system, are used to infer a quantitative model of gene regulation (*5*). The gene-regulation function is often approximated by the Hill function (Fig. 1B) which summarizes threshold, sensitivity, and maximum expression level. To understand the relation between phenomenological Hill parameters and the actual biochemical parameters of gene regulation, one needs to know whether TFs oligomerize, how strongly they interact with cis elements in the promoter region, whether they interact cooperatively with themselves or other factors when binding to the promoter, and how they interact with RNA polymerase (*5*). Numerous studies of prokaryotic systems, such as the *lac* and lambda promoters (*11*, *12*), have provided insights into the biochemical basis for the Hill parameters of single-input gene-regulation functions (*7*).

Quantitative models have been built for more complex circuits as well, such as a circuit based on the *lac* promoter that can perform simple computations such as AND and OR logic (*6*, *10*). Circuit models can be used in a bottom-up approach to predict the behavior of more-complex regulatory networks, as demonstrated in synthetic gene networks in *Escherichia coli* (*3*). Overall, the agreement between data and models for prokaryotic gene expression can be attributed to the tractability of the system and the accumulated knowledge of the relevant biochemistry and biophysics.

There are several ways to validate and refine such models. Researchers can compare a biochemical parameter extracted from the model (e.g., the equilibrium dissociation constant between a TF and the DNA) with a corresponding in vitro measurement. Another approach requires perturbing the TF binding equilibrium, by varying the DNA sequence of cis elements and observing whether the data fit the model. Such measurements also offer insights into the plasticity and evolution of the regulatory circuit (*10*). The model can be further constrained by measuring additional variables, such as noise in gene expression (*13*).

When a model fails to be validated by the data, we can discover previously unknown events or components that likely are associated with the regulatory circuit, thus correctly identifying the circuit's wiring. For example, a smaller-than-expected maximal expression level suggests the existence of another pathway or factor (*7*) that can limit binding of the TF to the promoter or modulate its activity post binding. A higher-than-expected sensitivity might point to hidden mechanisms of cooperativity, such as physical interactions between TFs, or to indirect interactions that are mediated by other factors (*7*, *14*). Circuits connected in series can also lead to a higher overall sensitivity (*15*). Moreover, hidden feedback loops can dramatically influence the shape of the gene-regulation function (*16*).

Small-Scale Approaches to Eukaryotic Gene-Regulation Functions

Eukaryotic systems have regulatory circuits that are more complex than those of prokaryotes. For example, eukaryotic cis elements are not equally accessible to TFs because nucleosomes generally hinder binding of TFs. Moreover, nucleosomes are not passive inhibitors of TFs but are removed from the DNA by adenosine triphosphate–dependent chromatin-remodeling factors. Furthermore, nucleosomes are bound with a different affinity to the DNA, depending on their chemical modification and underlying DNA sequence (*17*).

The eukaryotic cis regulatory code is also more diverse and has many types of binding sites for multiple TFs (*18*). Additionally, complexities on the trans side can affect the activity of a TF as a function of location and posttranslational modification, posing both measurement and modeling challenges. Moreover, sequence-specific TFs interact with various chromatin-remodeling factors and histone-modifying complexes, but we have limited knowledge about the identity of these factors and their quantitative effect on gene regulation. Thus, even for well-studied model eukaryotic promoters, we lack a full understanding of the components, wiring, and biochemical interactions in the circuit.

Gene expression levels have been modeled according to promoter architecture in yeast (*8*, *19*–*21*), worms (*22*), and sea urchins (*23*). Yeast gene expression levels were measured from both synthetic and genomic promoters varying in composition and organization of TF-binding sites among different environments and could be successfully modeled on the basis of the equilibrium binding of TFs to

[1]Howard Hughes Medical Institute, Harvard University Faculty of Arts and Sciences Center for Systems Biology, Departments of Molecular and Cellular Biology and Chemistry and Chemical Biology, Cambridge, MA 02138, USA. [2]Department of Biology, Massachusetts Institute of Technology, and Broad Institute of MIT and Harvard, Cambridge, MA 02142, USA.

*These authors contributed equally to this work.
†To whom correspondence should be addressed. E-mail: aregev@broad.mit.edu

DNA and to each other (*19*, *20*). Other studies underscore the importance of nucleosomes in determining the level of gene expression (*24*). For example, a study testing the gene-regulation functions of phosphate-regulated promoters in yeast, by using different combinations of cis elements, identified a role for nucleosomes in decoupling threshold and maximum expression levels of the gene-regulation function (*8*).

Large Scale: From Single Gene to Genome-Wide Models

Small-scale models focus on deciphering regulatory functions for circuits where the key components and wiring were previously known. In contrast, large-scale approaches tend to have less precision but can be used to infer circuit components and wiring. Such efforts are particularly critical when studying gene regulation in higher organisms, with largely uncharacterized circuits.

The emergence of large-scale approaches that aim for genome-wide prediction of output has been tightly coupled to an improved ability to measure circuit input, output, and wiring on a genomic scale. For example, output such as mRNA levels can be measured by microarrays or sequencing (*25*). Also, as an example of cis input, we now can more easily detect promoter sequences because of advances in computation and the availability of whole-genome sequences (*26*). Trans inputs can be measured as direct interactions of DNA with proteins, including TFs (*18*, *27*), histone-modification states (*28*), and nucleosome positions in vivo (*29*). TF-promoter interactions also can be inferred from in vitro assays, such as protein-binding microarrays (*30*).

Large-scale genomic studies of regulatory circuits are still limited, most notably in measurements of the abundance and activity of trans input, as is direct manipulation of cis and trans inputs. As a result, most large-scale models do not incorporate detailed regulatory functions and either address cis inputs or trans inputs but not both. Furthermore, the generalizing of the circuit model across the promoters and expression levels of multiple genes comes at the cost of limited power to explain the observed expression of any individual gene (*31*).

Genome-Wide Reconstruction of Cis Regulatory Functions

Genome-wide sequencing and profiling efforts have spurred the development of numerous approaches to reconstruct cis regulatory functions that explain observed expression levels by the type, number, and organization of cis regulatory elements in promoters. Linear, Bayesian, and thermodynamic approaches have been used and each reflects a different set of assumptions on the biochemical basis of transcriptional regulation (Fig. 1B). Linear models assume that the expression output is a linear combination of cis-element inputs (*32*–*34*). Probabilistic Bayesian approaches can handle the noisy nature of large-scale data and are able to capture the combinatorial logic and organization of promoters by modeling combinations of motifs, as well as their relative distance and orientation (*35*). Some studies cast a linear model in a probabilistic setting, combining the benefit of both approaches (*31*). More realistic thermodynamic models have recently emerged. For example, expression patterns in *Drosophila* segmentation were predicted by calculating the probabilities of all possible configurations of trans factors on the cis regulatory sequence and summing their contributions to expression (*36*). Sequence preferences for nucleosomes and transcription factors were used to predict expression in yeast (*37*). However, thermodynamic models have not yet been applied on a genomic scale to test their general power. Genome-wide inference of cis regulatory functions critically depends on accurate and comprehensive detection of cis elements in DNA sequences—this is a notoriously difficult problem, especially in higher organisms.

Estimating the success of the models in predicting gene expression is a challenging task. Ideally, large-scale models should be trained on one data set and then tested for their ability to generalize to unseen data. However, most data sets are of limited scale, and systematic experimental follow-up is lacking. Indeed, many studies do not report such objective success rates, whereas others use various

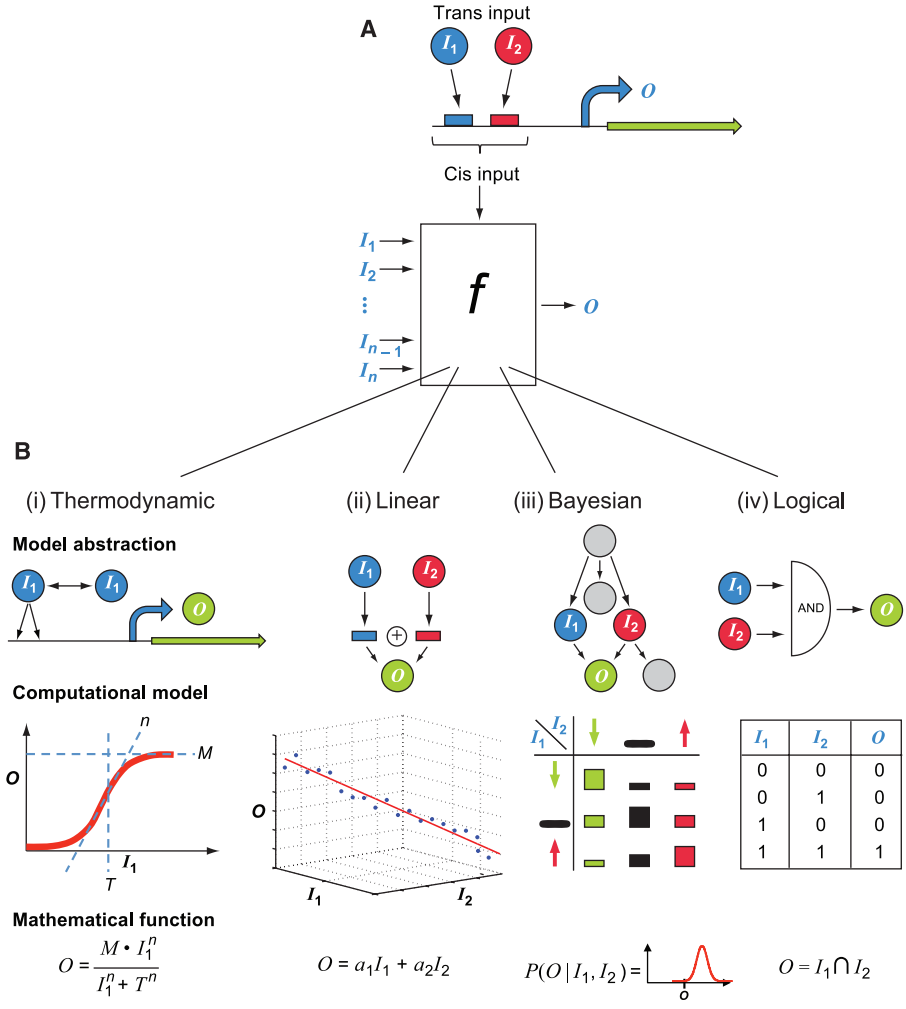

I_1	I_2	O
0	0	0
0	1	0
1	0	0
1	1	1

Fig. 1. Gene-regulation functions. (**A**) A gene-regulation function describes how trans inputs, such as transcription factors (I_1, I_2, ... I_n), and cis inputs, such as regulatory elements, are transformed into a gene's mRNA level (O). (**B**) Different functions describe distinct scenarios, using distinct mathematical approaches. Most small-scale approaches rely on a thermodynamically motivated model (i), which explains the dependency on a single tunable trans input and fits the response to a Hill function. The extracted Hill parameters, maximum expression level (M), threshold (T), and sensitivity (n), become functions of the remaining trans- and cis-input variables. Large-scale approaches utilize a host of approaches. (ii) Linear models assume that the output is a linear combination of the cis or trans inputs. (iii) Bayesian networks give the probability distribution of the output given the input values. (iv) Logical (Boolean) circuits consider the output as a result of applying logical operations on the inputs. (Top) The assumption underlying each modeling approach; (middle) the gene-regulation function in this modeling approach; and (bottom) an equivalent mathematical formulation. All modeling approaches are applicable in both small- and large-scale studies.

measures to assess the quality of their prediction. For example, models that predict module assignment for each gene typically report the percentage of correct assignment of coregulated genes or genes that share the same function with success rate reported from ~30% (*38*) to 73% (*35*) in studies in yeast. Other works report the likelihood of the data given the model (*39*, *40*), but this measure is hard to compare between models of different complexity. The most quantifiable success level to date is reported for models that predict the actual expression of each gene; they typically report the percentage of the variance in gene expression that is accounted for by the model. Both Bayesian and linear models that predict gene expression from cis regulatory sequences have reported high rates of success in yeast [e.g., 51% in (*35*), 52 to 72% in (*33*)]. However, the success of similar approaches in mammalian cells has been much more modest [e.g., 6% in (*31*), 11 to 24% in (*32*)]. It is important to consider the amount of expression that we can expect to explain with a particular model. A recent study with synthetic promoter libraries in yeast estimated that cis regulation can explain at most 65% of the variance in expression and that a thermodynamic small-scale model explains 44 to 59% (*19*). Similar work in the urochordate *Ciona* explains 30 to 89% of the variance at the cis level (*22*). Establishing standard approaches and data sets on which we can compare the performance of different models is an important goal. The DREAM project aims to achieve such a fair comparison by posting challenges for the community (*42*).

Discovering Arrows: Inferring Trans Regulation on a Genomic Scale

Cis input alone cannot predict expression, because dynamic expression patterns change with environmental conditions, cell type, and cell cycle stage. These changes are accompanied by corresponding changes in trans factors, which have been studied by three genome-scale strategies.

Genome-scale measurement of physical interactions allows direct incorporation of trans factors into circuit models. For example, TF-DNA interactions, measured either in vivo (*18*, *41*) or in vitro (*43*), were used to derive a detailed map of TF binding in yeast. Such maps can then be coupled with measurements of expression output to build a model of regulatory circuits (*44*). Discrepancies between the conditions in which binding and expression are measured can limit such efforts. Conversely, measurement of TF binding before and after a stimulus can help distinguish between direct and indirect targets (*1*, *18*, *45*). Notably, the scale and quality of measurements of trans inputs are still limited by the required effort and cost associated with generating the needed reagents and data (e.g., generating an epitope-tagged version of every TF and using it in chromatin immunoprecipitation across many conditions).

Alternatively, the level, activity, and wiring of trans factors can be inferred from mRNA levels because many trans regulators are embedded within transcriptional feedback regulatory loops (*46*, *47*); this results in detectable changes in their mRNA levels. Such inference is needed because we currently cannot assay the activities of a large number of regulators in parallel. Translational and post-translational regulations can create a substantial gap between the mRNA level of a trans factor and the level of active protein, but nonetheless, such approaches have been successful in *E. coli*, yeast, mouse, and human (*40*, *48*–*50*). In one approach, temporal expression data were collected to characterize processes such as cell differentiation and responses to environmental stimuli in mammalian systems (*46*, *51*), which showed that the transcriptional program was propagated by sequential waves of transcription controlled by different TFs. However, inferring regulatory activity from output levels limits the model's ability to distinguish between causality and correlation.

The perturbation of regulators can also be used to decipher and validate trans-regulation function. For example, 263 TFs were systematically deleted in yeast, and each deletion strain was compared with the wild type for genome-wide expression (*52*). RNA interference technology, which can target expression of specific genes and RNAs, has enabled similar approaches in mammalian cells, albeit at a more limited scale (*31*). Furthermore, epistasis analysis can be used to infer fine details of a multi-input circuit, as demonstrated by comparing strains from which one, two, or three trans regulators were deleted for their genome-wide effect on the yeast osmotic stress response (*1*).

Integrating Cis and Trans Models at a Genomic Scale

The obvious next direction is to systematically measure and model both trans factors and cis regulatory components simultaneously in different conditions (*51*). However, we are limited in our ability to finely perturb or measure cis and trans inputs to the circuits because of cost, a relative paucity of genetic tools in higher organisms, and the lack of synthetic approaches required to generate promoter-sequence variants (*19*).

An alternative strategy to engineered perturbations is to focus on the natural genetic polymorphisms underlying variation in gene expression between strains and species. Regulatory circuits that explain expression differences between natural genetic variants in a population or expression quantitative trait loci have been reconstructed on the basis of genetic variation in cis and trans factors (*53*, *54*). This approach is particularly appealing as it incorporates the collective effects of subtle perturbations to multiple circuit components and uses the power of genetic linkage and association to determine causality. Probabilistic and linear methods, in combination with linkage analysis, have incorporated genotypes as predictors to infer trans factors and regulatory networks in yeast, mouse, and human (*55*–*57*).

Similarly, studying expression in hybrids can exploit the genetic differences between two related species to estimate the relative cis and trans contributions to regulation as observed in yeast and fly (*54*, *58*). In yeast, basal differences in expression between species are explained by cis changes, whereas changes in expression regulation between different environmental conditions are associated with trans changes (*58*). Related studies have also been performed in mouse cells into which a human chromosome was introduced, showing that cis effects are stronger than trans effects (*59*).

Validation poses a particular challenge for all large-scale studies. Specific predictions can be tested by small-scale approaches, such as manipulation of individual trans factors or cis elements followed by genome-wide profiling [e.g., (*31*, *47*)]. However, these strategies are typically used to validate only a small portion of the model ("cherry picks") and focus on the system's wiring rather than its quantitative aspects. In rare examples, large-scale validation is conducted by comparing a model's prediction (e.g., inferred regulation from cis data) with independent genome-wide data [e.g., TF-DNA binding for all TFs (*18*)]. In most cases, however, model validation is modest, and few of the model's components are tested. The two key challenges are, thus, how to experimentally test predictions on a genomic scale and how to incorporate the results of these experiments once collected. One immediate use is as test data, on which to check how well the model generalizes. A more ambitious goal is to use the data for the iterative refinement of the model.

The detailed genetic and molecular manipulation needed to study circuits by small-scale approaches is extremely challenging in higher organisms. For example, genetic deletion of trans factors is about 100 times as expensive and time-consuming in mammals as in yeast and bacteria, and promoter manipulation is similarly challenging. Because many trans factors are pleiotropic, their deletion is lethal, and hence, requires more sophisticated approaches. Small interfering RNA has opened the possibility of manipulation by silencing (knockdown), but it is prone to nonspecific off-target effects that are not yet fully understood. Future characterization of these nonspecific effects will greatly promote the study of mammalian transcriptional circuits. The ability to perturb multiple proteins (combinatorial knockdown) is limited in mammalian cells. The introduction of morpholino oligonucleotides microinjection in developing embryos of zebrafish, sea urchin, and *Xenopus* (*60*) has been very successful, but this approach has not been established in mammalian systems.

The most comprehensive and successful model in animals, thus far, has been reconstructed in the sea urchin, including a complete model of the gene regulatory network that specifies the skeletogenic micromere lineage (*61*). In this model organism, systematic manipulation and measurement of trans factors, cis elements in promoters, and mRNA output measures were combined to devise a detailed validated model of gene regulation. The abil-

ity to use morpholine-based knockdown, promoter engineering methods, and mRNA in situ measurements substantially contributed to this success.

Combining Lessons from Small- and Large-Scale Approaches

Despite advances from small-scale and large-scale analysis of gene regulation, most studies do not yet bridge the gap between these approaches. As previously noted, small-scale approaches can generate fine, realistic details and extensive validation, but are limited to a few genes (often one). However, large-scale approaches examine many genes, but often rely on regulation functions that are biologically unrealistic (e.g., Boolean logic or linearity) and lack validation.

Recent studies highlight the promise of combining the power of both approaches. For example, genetic approaches typical of smaller-scale studies combined with linear modeling and mRNA profiling have allowed detailed quantitative reconstruction of the regulatory circuits controlling the response to high osmolarity in yeast (*1*). In addition, findings from large-scale studies can be followed up in detail with small-scale approaches. For instance, the behavior of a yeast regulon observed in mRNA profiles was explained by small-scale studies on a single input circuit controlling a representative target gene (*2*). Bayesian network approaches, originally developed to study mRNA profiles (*48*), have been successfully applied to single-cell measurements of signaling pathways (*62*).

Indeed, the distinction between small- and large-scale approaches is rapidly blurring, with recent technological advances enabling the experimental toolbox of small-scale approaches to be applied to the genomic level. These include the ability to profile multiple genes in single cells even during multicellular organism development (*63*), large-scale manipulation of sequences (allowing engineering and perturbation of promoters and TFs), and large-scale tunable trans perturbation, including that in higher organisms (*31*). As such large-scale perturbations of cellular components become increasingly feasible, the number of samples that need to be genomically profiled becomes exceptionally high. This raises the need for genome-scale profiling methods that are at least two orders of magnitude cheaper and faster and require substantially lower cell numbers and per-sample effort than, for example, a microarray. In this respect, application of very recent advances in assays for measurement of smaller gene signatures (of several hundred genes) at low cost and high scale (*64*, *65*) will be essential for both the generation and validation of large-scale models of gene regulation. Overall, such improved methods will allow construction of large-scale models of gene-regulation functions that are closer to the realistic models used in small-scale systems.

Another direction for a major advance is coupling such approaches with time-series experiments, which will allow the study of dynamic gene-regulation functions. Many current studies rely on steady-state measurements, but transcriptional responses unfold over time in response to environmental changes, during differentiation, and in disease. Furthermore, temporal relations can help distinguish correlation from causality. Most computational methods have not leveraged this power, but recent studies (*31*, *51*) have demonstrated its potential. A useful stepping stone will be to construct well-defined subnetworks ("toy-models"), and then to study their regulation and dynamics (*20*, *66*) as benchmarks to compare models' performance.

The fundamental challenge for all approaches may be building models that truly generalize to novel states. Almost all current models predict expression in the studied conditions or very similar ones. As the space of possible states may be very large, how successful we can be may depend on our understanding of the underlying features of nonlinearity and combinatorial effects in gene-regulation functions.

In this review we only considered the circuits regulating transcript levels, where the inputs are cis sequences and trans factors that affect transcription directly (e.g., TFs, nucleosomes, or chromatin modifications), and the output is transcript level. However, these circuits are part of a much larger and more complex cellular network composed of many other interacting components. For example, transcripts alone are directly affected by editing, chemical modification, RNA binding proteins, and other noncoding RNAs, which affect their rate of degradation, accessibility for translation, and rate of translation to proteins. More generally, the transcriptional circuits are tightly coupled to signaling, metabolic, and localization systems that are part of the complex three-dimensional organization of cells and organisms. It is the way in which this complex system processes information and executes functions that ultimately determines the phenotype.

References and Notes

1. A. P. Capaldi *et al.*, *Nat. Genet.* **40**, 1300 (2008).
2. L. Cai, C. K. Dalal, M. B. Elowitz, *Nature* **455**, 485 (2008).
3. N. J. Guido *et al.*, *Nature* **439**, 856 (2006).
4. N. Rosenfeld, J. W. Young, U. Alon, P. S. Swain, M. B. Elowitz, *Science* **307**, 1962 (2005).
5. L. Bintu *et al.*, *Curr. Opin. Genet. Dev.* **15**, 125 (2005).
6. Y. Setty, A. E. Mayo, M. G. Surette, U. Alon, *Proc. Natl. Acad. Sci. U.S.A.* **100**, 7702 (2003).
7. T. Kuhlman, Z. G. Zhang, M. H. Saier, T. Hwa, *Proc. Natl. Acad. Sci. U.S.A.* **104**, 6043 (2007).
8. H. D. Kim, E. K. O'Shea, *Nat. Struct. Mol. Biol.* **15**, 1192 (2008).
9. A. Becskei, B. B. Kaufmann, A. van Oudenaarden, *Nat. Genet.* **37**, 937 (2005).
10. A. E. Mayo, Y. Setty, S. Shavit, A. Zaslaver, U. Alon, *PLoS Biol.* **4**, 555 (2006).
11. M. E. Wall, W. S. Hlavacek, M. A. Savageau, *Nat. Rev. Genet.* **5**, 34 (2004).
12. A. D. Johnson *et al.*, *Nature* **294**, 217 (1981).
13. M. Thattai, A. van Oudenaarden, *Proc. Natl. Acad. Sci. U.S.A.* **98**, 8614 (2001).
14. J. T. Wade, T. A. Belyaeva, E. I. Hyde, S. J. W. Busby, *EMBO J.* **20**, 7160 (2001).
15. S. Hooshangi, S. Thiberge, R. Weiss, *Proc. Natl. Acad. Sci. U.S.A.* **102**, 3581 (2005).
16. U. Alon, *Nat. Rev. Genet.* **8**, 450 (2007).
17. S. D. Taverna, H. Li, A. J. Ruthenburg, C. D. Allis, D. J. Patel, *Nat. Struct. Mol. Biol.* **14**, 1025 (2007).
18. C. T. Harbison *et al.*, *Nature* **431**, 99 (2004).
19. J. Gertz, E. D. Siggia, B. A. Cohen, *Nature* **457**, 215 (2009).
20. T. Ellis, X. Wang, J. J. Collins, *Nat. Biotechnol.* **27**, 465 (2009).
21. J. Gertz, B. A. Cohen, *Mol. Syst. Biol.* **5**, 244 (2009).
22. C. D. Brown, D. S. Johnson, A. Sidow, *Science* **317**, 1557 (2007).
23. C. H. Yuh, H. Bolouri, E. H. Davidson, *Science* **279**, 1896 (1998).
24. F. H. Lam, D. J. Steger, E. K. O'Shea, *Nature* **453**, 246 (2008).
25. A. Mortazavi, B. A. Williams, K. McCue, L. Schaeffer, B. Wold, *Nat. Methods* **5**, 621 (2008).
26. P. D'haeseleer, *Nat. Biotechnol.* **24**, 959 (2006).
27. D. S. Johnson, A. Mortazavi, R. M. Myers, B. Wold, *Science* **316**, 1497 (2007).
28. T. S. Mikkelsen *et al.*, *Nature* **448**, 553 (2007).
29. N. Kaplan *et al.*, *Nature* **458**, 362 (2009).
30. M. F. Berger, M. L. Bulyk, *Methods Mol. Biol.* **338**, 245 (2006).
31. The FANTOM Consortium and Riken Omics Science Center, *Nat. Genet.* **41**, 553 (2009).
32. D. Das, Z. Nahlé, M. Q. Zhang, *Mol. Syst. Biol.* **2**, 2006.0029 (2006).
33. D. H. Nguyen, P. D'haeseleer, *Mol. Syst. Biol.* **2**, 2006.0012 (2006).
34. T. S. Gardner, D. di Bernardo, D. Lorenz, J. J. Collins, *Science* **301**, 102 (2003).
35. M. A. Beer, S. Tavazoie, *Cell* **117**, 185 (2004).
36. E. Segal, T. Raveh-Sadka, M. Schroeder, U. Unnerstall, U. Gaul, *Nature* **451**, 535 (2008).
37. T. Raveh-Sadka, M. Levo, E. Segal, *Genome Res.*, published online 18 May 2009, 10.1101/gr.088260.108, in press.
38. E. Segal, R. Yelensky, D. Koller, *Bioinformatics* **19**, i273 (2003).
39. E. Segal, Y. Barash, I. Simon, N. Friedman, D. Koller, *RECOMB '02: Proceedings of the Sixth Annual International Conference on Computational Biology*, Washington, DC, 18 to 21 April 2002 (Association for Computing Machinery, New York, 2002), pp. 263–272.
40. D. Pe'er, A. Tanay, A. Regev, *J. Mach. Learn. Res.* **7**, 167 (2006).
41. F. Gao, B. Foat, H. Bussemaker, *BMC Bioinformatics* **5**, 31 (2004).
42. G. Stolovitzky, D. Monroe, A. Califano, *Ann. N. Y. Acad. Sci.* **1115**, 1 (2007).
43. C. Zhu *et al.*, *Genome Res.* **19**, 556 (2009).
44. C. Ye, S. J. Galbraith, J. C. Liao, E. Eskin, *PLOS Comput. Biol.* **5**, e1000311 (2009).
45. C. T. Workman *et al.*, *Science* **312**, 1054 (2006).
46. I. Amit *et al.*, *Nat. Genet.* **39**, 503 (2007).
47. E. Segal *et al.*, *Nat. Genet.* **34**, 166 (2003).
48. D. Pe'er, A. Regev, G. Elidan, N. Friedman, *Bioinformatics* **17**, S215 (2001).
49. J. J. Faith *et al.*, *PLoS Biol.* **5**, e8 (2007).
50. K. Basso *et al.*, *Nat. Genet.* **37**, 382 (2005).
51. S. A. Ramsey *et al.*, *PLOS Comput. Biol.* **4**, e1000021 (2008).
52. Z. Hu, P. J. Killion, V. R. Iyer, *Nat. Genet.* **39**, 683 (2007).
53. R. B. Brem, G. Yvert, R. Clinton, L. Kruglyak, *Science* **296**, 752 (2002).
54. P. J. Wittkopp, B. K. Haerum, A. G. Clark, *Nat. Genet.* **40**, 346 (2008).
55. S. I. Lee *et al.*, *PLoS Genet.* **5**, e1000358 (2009).
56. V. Emilsson *et al.*, *Nature* **452**, 423 (2008).
57. Y. Chen *et al.*, *Nature* **452**, 429 (2008).
58. I. Tirosh, S. Reikhav, A. A. Levy, N. Barkai, *Science* **324**, 659 (2009).
59. M. D. Wilson *et al.*, *Science* **322**, 434 (2008).
60. D. R. Corey, J. M. Abrams, *Genome Biol.* **2**, reviews1015.1 (2001).
61. P. Oliveri, Q. Tu, E. H. Davidson, *Proc. Natl. Acad. Sci. U.S.A.* **105**, 5955 (2008).
62. K. Sachs, O. Perez, D. Pe'er, D. A. Lauffenburger, G. P. Nolan, *Science* **308**, 523 (2005).
63. D. Dupuy *et al.*, *Nat. Biotechnol.* **25**, 663 (2007).
64. J. Du *et al.*, *Nat. Biotechnol.* **27**, 77 (2009).
65. G. K. Geiss *et al.*, *Nat. Biotechnol.* **26**, 317 (2008).
66. I. Cantone *et al.*, *Cell* **137**, 172 (2009).

67. We gratefully acknowledge the assistance of I. Amit. H.D.K. was supported by the Burroughs Wellcome Fund Career Award at the Scientific Interface. E.K.O. was supported by HHMI and NIH GM51377. A.R. was supported by the Burroughs Wellcome Fund Career Award at the Scientific Interface and by NIH DP1-OD003958-01.

10.1126/science.1171347

Knockout Rats via Embryo Microinjection of Zinc-Finger Nucleases

Aron M. Geurts,[1,2]* Gregory J. Cost,[3]* Yevgeniy Freyvert,[3] Bryan Zeitler,[3] Jeffrey C. Miller,[3] Vivian M. Choi,[3] Shirin S. Jenkins,[3] Adam Wood,[4] Xiaoxia Cui,[4] Xiangdong Meng,[3] Anna Vincent,[3] Stephen Lam,[3] Mieczyslaw Michalkiewicz,[1,2] Rebecca Schilling,[1,2] Jamie Foeckler,[3] Shawn Kalloway,[3] Hartmut Weiler,[1,2] Séverine Ménoret,[5] Ignacio Anegon,[5] Gregory D. Davis,[4] Lei Zhang,[3] Edward J. Rebar,[3] Philip D. Gregory,[3] Fyodor D. Urnov,[3] Howard J. Jacob,[1,2,6]† Roland Buelow[7]†

The laboratory rat is a well-established model for the genetic dissection of human disease-related traits (*1*) despite the fact that targeted modification of its genome is largely intractable. We investigated the application of engineered zinc-finger nucleases [ZFNs (*2*)] for the elimination of specific rat gene functions and generation of knockout rats. ZFNs induce site-specific, double-strand DNA breaks that can be repaired by the error-prone nonhomologous end-joining DNA repair pathway to result in a targeted mutation (Fig. 1A). In the fruit fly and zebrafish, direct embryo injection of ZFN-encoding mRNA has been used to generate heritable knockout mutations at specific loci (*2*).

The design and validation of three sets of ZFN reagents that target the green fluorescent protein (GFP) gene and two endogenous rat genes, *Immunoglobulin M* (*IgM*) and *Rab38*, were performed as described (*3*) and are detailed in (*4*). To take advantage of the potential for greater specificity of action afforded by longer (and therefore rarer) targets, we used five- and six-finger ZFNs.

We delivered these ZFNs to 36 hemizygous GFP-transgenic (*5*) inbred SS (Dahl S; GFP ZFNs), 91 inbred FHH (Fawn-hooded hypertensive; Rab38 ZFNs), and 2793 outbred SD (Sprague Dawley; IgM ZFNs) embryos by pronuclear or intracytoplasmic injection of ZFN-encoding DNA or mRNA at different concentrations (table S1). Screening 295 founder animals yielded 35 (12%) that harbored targeted mutations.

Full knockout of the GFP transgene was achieved because mutant animals lacked both GFP expression and wild-type GFP sequence (Fig. 1, B and C). Thirty-two IgM mutants and the single Rab38 mutant carried 25 to 100% disrupted target chromosomes (fig. S1). Sequence analysis of 18 founders revealed deletion alleles ranging from 3 to 187 base pairs; of note, one animal carried biallelic mutations in *IgM* (table S1). Furthermore, ZFN-mediated gene disruption demonstrated high fidelity for each target sequence because no ZFN-induced mutations were detected in target gene–disrupted animals at any of 20 predicted ZFN off-target sites (figs. S2 and S3). After breeding to wild-type animals, one out of one GFP and three out of four *IgM* mutations were transmitted through the germline, one of which was subsequently bred to homozygosity (table S1 and fig. S4).

The high percentage of disrupted chromosomes demonstrates that ZFNs are active in early rat embryos from three strains, leading to both mono- and biallelic gene disruption. Although we observed no cleavage at predicted off-target sites, such events could be segregated away from the desired mutation by backcrossing to the parental strain. ZFN-driven gene disruption and germline transmission can be accomplished in 4 months' time, and ZFNs can be engineered against a broad range of sequences (*6*, *7*); this strategy adds a valuable tool to an increasingly powerful rat genetic toolbox, opening up a range of new experiments and models of human disease.

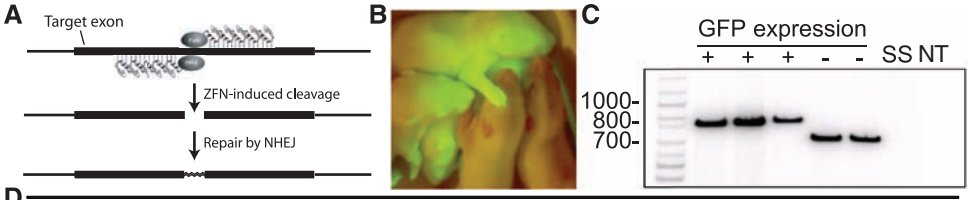

D

Strain	Target/ Construct	Route/ Dose (ng/ul)	Injected/ Transferred (%)	Founders (%)*	Mutants (%)†	Bred/ F1 inheritance
SS	GFP/mRNA	PNI/1.5	36/25 (69)	5 (20)	2 (40)	1/1
SD	IgM/Plasmid	PNI/10	609/493 (81)	54 (11)	6 (11)	4/3
SD	IgM/Plasmid	PNI/2	605/468 (77)	82 (18)	8 (10)	ND
SD	IgM/Plasmid	PNI/0.4	511/423 (83)	62 (15)	4 (6)	ND
SD	IgM/mRNA	PNI/10	186/104 (56)	14 (13)	4 (29)	ND
SD	IgM/mRNA	PNI/2	230/142 (62)	21 (15)	4 (19)	ND
SD	IgM/mRNA	PNI/0.4	183/118 (64)	19 (16)	1 (5)	ND
SD	IgM/mRNA	IC/10	272/197 (72)	4 (2)	3 (75)	ND
SD	IgM/mRNA	IC/2	197/134 (68)	17 (13)	2 (12)	ND
FHH	Rab38/mRNA	IC/2	91/83 (91)	17 (20)	1 (6)	ND

PNI - pronuclear injection; IC - intracytoplasmic; * - of transferred; † - of liveborn founders; ND - not determined

Fig. 1. ZFN-mediated gene disruption in rat embryos. (**A**) ZFNs containing five or six fingers were designed to target coding sequences of interest (gray lines) for site-specific cleavage. (**B**) Two of five pups born after microinjection of GFP-targeted ZFNs were devoid of GFP expression. (**C**) Polymerase chain reaction using GFP-specific primers revealed truncated but no wild-type sequence in each of the GFP negative pups compared with positive littermates. SS indicates Dahl S control DNA; NT indicates no template. (**D**) Table of injection data revealing successful mutagenesis of the three gene targets after multiple delivery methods and doses in three rat strains.

References and Notes

1. T. J. Aitman *et al.*, *Nat. Genet.* **40**, 516 (2008).
2. D. Carroll, *Gene Ther.* **15**, 1463 (2008).
3. Y. Doyon *et al.*, *Nat. Biotechnol.* **26**, 702 (2008).
4. Materials and methods are available as supporting material on *Science* Online.
5. M. Michalkiewicz *et al.*, *Am. J. Physiol. Heart Circ. Physiol.* **293**, H881 (2007).
6. C. O. Pabo, E. Peisach, R. A. Grant, *Annu. Rev. Biochem.* **70**, 313 (2001).
7. A. Klug, *Proc. Jpn. Acad.* **81**, 87 (2005).
8. We thank R. Jaenisch, R. Hammer, P. Sullivan, and three anonymous referees for helpful suggestions; D. Smoller and E. Lanphier for support; E. Eastlund for the Rab38 ZFN mRNA; R. DeKelver and R. Amora for technical assistance; and Caliper Life Sciences, Incorporated for excellent service. Supported by NIH grants 5U01HL066579-08 and 5P01HL082798-03, a sponsored research agreement between the Medical College of Wisconsin and Sigma-Aldrich, and the American Physiological Society Fellowship in Physiological Genomics to A.M.G. The authors are filing patents based on the results reported in this paper.

Supporting Online Material

www.sciencemag.org/cgi/content/full/325/5939/433/DC1
Materials and Methods
Figs. S1 to S5
Tables S1 and S2
References

18 February 2009; accepted 1 May 2009
10.1126/science.1172447

[1]Human and Molecular Genetics Center, Medical College of Wisconsin, Milwaukee, WI 52336, USA. [2]Department of Physiology, Medical College of Wisconsin, Milwaukee, WI 52336, USA. [3]Sangamo BioSciences, Incorporated, Richmond, CA 94804, USA. [4]Sigma-Aldrich Biotechnology, St. Louis, MO 63103, USA. [5]INSERM, UMR 643, CHU, Nantes, Université de Nantes, 44322 Nantes, France. [6]Department of Pediatrics, Medical College of Wisconsin, Milwaukee, WI 52336, USA. [7]Open Monoclonal Technology, Incorporated, Palo Alto, CA 94303, USA.

*These authors contributed equally to this work.
†To whom correspondence should be addressed. E-mail: jacob@mcw.edu (H.J.J.); rbuelow@omtinc.net (R.B.)

Dependence of Mouse Embryonic Stem Cells on Threonine Catabolism

Jian Wang,[1] Peter Alexander,[1] Leeju Wu,[1] Robert Hammer,[1] Ondine Cleaver,[2] Steven L. McKnight[1]*

Measurements of the abundance of common metabolites in cultured embryonic stem (ES) cells revealed an unusual state with respect to one-carbon metabolism. These findings led to the discovery of copious expression of the gene encoding threonine dehydrogenase (TDH) in ES cells. TDH-mediated catabolism of threonine takes place in mitochondria to generate glycine and acetyl–coenzyme A (CoA), with glycine facilitating one-carbon metabolism via the glycine cleavage system and acetyl-CoA feeding the tricarboxylic acid cycle. Culture media individually deprived of each of the 20 amino acids were applied to ES cells, leading to the discovery that ES cells are critically dependent on one amino acid—threonine. These observations show that ES cells exist in a high-flux backbone metabolic state comparable to that of rapidly growing bacterial cells.

Embryonic stem (ES) cells are small, rapidly dividing cells with the pluripotent capacity to form any and all cells present in the adult body. Cultured mouse ES cells measure only several micrometers in diameter, as compared to the 10- to 30-μm range typical of cultured somatic cells (*1*). The cell division cycle of ES cells under the standard culture conditions used in our studies lasts only 5 hours. This rate of cell division matches that measured for ICM (inner cell mass) cells of the early mouse embryo (*2*). This doubling time is shorter than that of even the most rapidly dividing cancer cells and approaches that of single-celled microbial organisms. When deprived of leukemia inhibiting factor (LIF), mouse ES cells slow their growth rate, increase in size, form embryoid bodies, and enter pathways leading to differentiation (*3*).

Mouse ES cells exist in a high-flux metabolic state. To investigate whether ES cells might exist in a metabolic state that facilitates rapid growth, we surveyed the abundance of numerous common metabolites. Mouse ES cells (line E14) grown without feeder cells were exposed to organic solvents that allow soluble extracts to be subjected to liquid chromatography–mass spectrometry (LC-MS/MS), enabling multiple reaction monitoring of scores of metabolites (*4*). Parameters necessary for the detection of the two most abundant daughter ions for each metabolite upon collision-induced fragmentation were optimized so that metabolite identity and abundance could be simultaneously assessed.

The relative amounts of individual metabolites prepared from ES cells were compared with those of embryoid body cells deprived of LIF for 3, 5, or 7 days (Fig. 1A and fig. S1). Three patterns of fluctuation in metabolite abundance were observed. One class consisted of metabolites that changed little as a function of the transition of ES cells into the differentiating cells present in embryoid bodies. Included in this class were many essential and nonessential amino acids. The second class consisted of metabolites present at a higher abundance in ES cells relative to differentiating cells. 5-Aminoimidazolecarboxamide-R (AICAR), an intermediate in purine biosynthesis, was the most abundant member of this class,

[1]Department of Biochemistry, University of Texas Southwestern Medical Center, 5323 Harry Hines Boulevard, Dallas, TX 75390–9152, USA. [2]Department of Molecular Biology, University of Texas Southwestern Medical Center, 5323 Harry Hines Boulevard, Dallas, TX 75390–9152, USA.

*To whom correspondence should be addressed. E-mail: steven.mcknight@utsouthwestern.edu

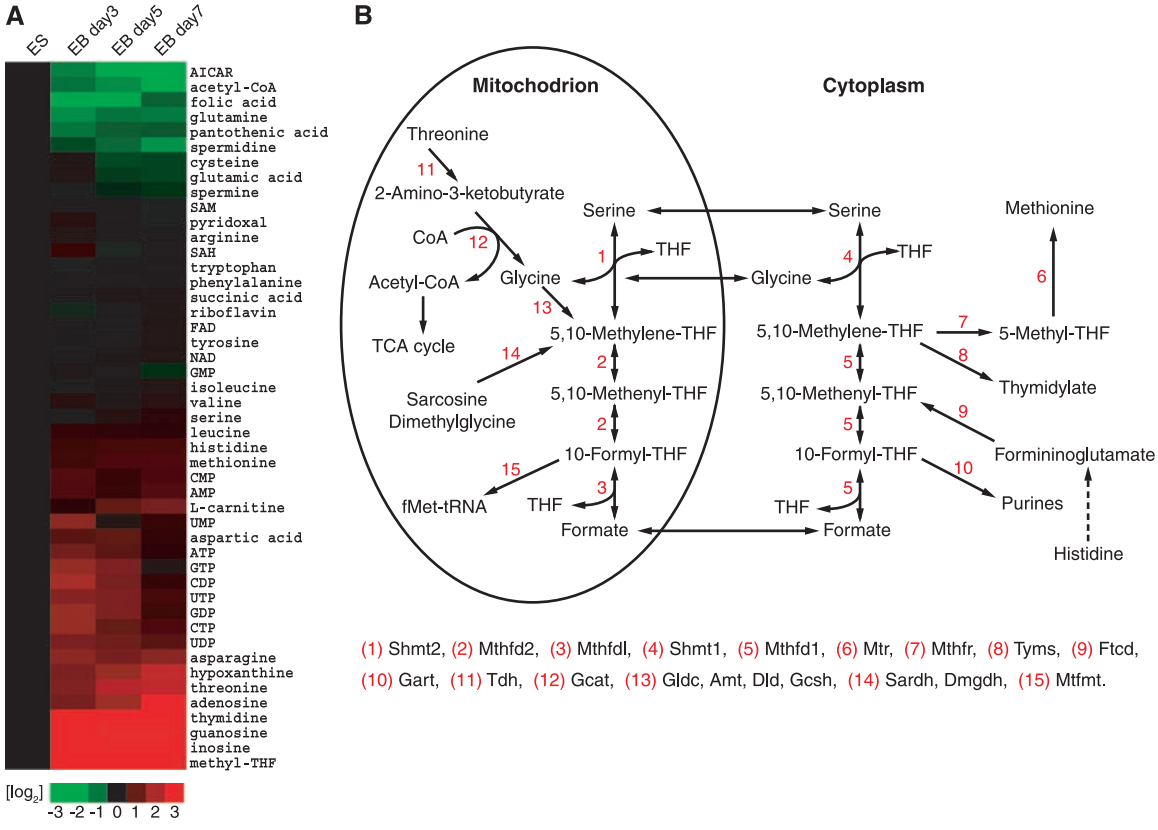

(1) Shmt2, (2) Mthfd2, (3) Mthfdl, (4) Shmt1, (5) Mthfd1, (6) Mtr, (7) Mthfr, (8) Tyms, (9) Ftcd, (10) Gart, (11) Tdh, (12) Gcat, (13) Gldc, Amt, Dld, Gcsh, (14) Sardh, Dmgdh, (15) Mtfmt.

Fig. 1. Coordinated changes in metabolite abundance during ES cell differentiation. Metabolites extracted from cells in 50% aqueous methanol were subjected to LC-MS/MS analysis (*4*). (**A**) Heat map showing the relative levels of metabolites in ES cells as a function of 3, 5, and 7 days after withdrawal of LIF and differentiation into embryoid bodies. Metabolite levels are expressed as $\log_2$ transformation of the fold change at days 3, 5, and 7 relative to the same measurement in undifferentiated ES cells; green indicates metabolites that decrease in abundance as a function of differentiation and red, metabolites that increase as ES cells differentiate. (**B**) Schematic diagram of the pathways facilitating folate-mediated, one-carbon metabolism.

followed by acetyl–coenzyme A (CoA) and folic acid. The third class included metabolites that increased in abundance as a function of differentiation. Methyl-tetrahydrofolate (mTHF) was the most prominent member of this class, being nearly undetectable in ES cells, yet normalizing considerably in differentiating cells. A similar pattern of differentiation-associated increase in abundance was observed for guanosine, adenosine, inosine, and threonine.

Knowing that ES cells must replicate the genome at a prolific rate, it was not surprising to observe that six of the metabolites changing most markedly in abundance as a function of ES cell differentiation are involved in the purine biosynthetic pathway (folic acid, mTHF, AICAR, guanosine, adenosine, and inosine). The de novo synthesis of purine nucleotides requires that each purine base receive carbon atoms at two different steps along the pathway. The source of one-carbon metabolism for purine synthesis is formyl-tetrahydrofolate (*5*). This and the other two "charged" forms of tetrahydrofolate, methylene-tetrahydrofolate and methyl-tetrahydrofolate, are the sole sources of one-carbon metabolism (*6*, *7*). Notably, the AICAR intermediate in purine synthesis is located immediately downstream of one of the two single-carbon donating steps in the pathway. Because AICAR was present at increased abundance in rapidly growing ES cells, and because folic acid and mTHF levels fluctuated substantially as a function of conversion of ES cells into embryoid bodies, we hypothesized that the demand for metabolic flux via one-carbon metabolism might be unusually high in undifferentiated ES cells.

The threonine dehydrogenase gene and enzyme are expressed copiously in mouse ES cells. Quantitative polymerase chain reaction (qPCR) assays were performed on samples prepared from ES cells and seven tissues of the adult mouse to measure the levels of mRNAs specifying the 15 enzymes most proximal to the pathway of one-carbon metabolism (Fig. 1B). Such measurements revealed unusually accentuated, ES cell–specific expression of the gene encoding threonine dehydrogenase (TDH). The level of mRNA specifying synthesis of the TDH enzyme in ES cells was roughly 1000 times as high as that in any of the seven tissues that were assayed (fig. S2). In only one other case did the ES mRNA level of a folate-associated metabolic enzyme exceed that of other tissues (the level of thymidylate synthase mRNA in ES cells was roughly twice as high as the levels observed in lung, intestine, and testis).

The TDH enzyme performs the initial, rate-limiting step in an atypical form of threonine catabolism, wherein threonine is converted to glycine and acetyl-CoA. In eukaryotic cells, the TDH enzyme is located within mitochondria. There it supplies acetyl-CoA for direct entry into the tricarboxylic (TCA) cycle, and likewise passes glycine to tetrahydrofolate charging via the glycine cleavage system (*8*). If the TDH enzyme is selectively active in undifferentiated ES cells, this might explain why threonine abundance was reduced in ES cells compared with differentiating cells associated with embryoid bodies (Fig. 1A). High TDH enzyme activity might also explain why ES cells contained increased amounts of acetyl-CoA relative to embryoid body cells. To test this hypothesis, mitochondria were isolated from ES cells, assayed for the threonine-dependent conversion of NAD (nicotinamide adenine dinucleotide) to NADH, and found to contain much higher TDH activity than human 293T cells tailored to express an exogenous form of the TDH gene (Fig. 2, A and B). Similarly, TDH enzyme activity, TDH mRNA levels, and immunoreactivity to TDH-specific antibodies as detected by Western blotting all declined sharply as a function of differentiation of ES cells into embryoid bodies (Fig. 2, C to E). The availability of TDH-specific antibodies (see Materials and Methods) allowed immunohistochemical staining of ES cell colonies as a function of differentiation. Before LIF withdrawal–induced differentiation, all cells in each ES colony stained positive for mitochondria-associated TDH (Fig. 3). One day after LIF withdrawal, TDH immunoreactivity was lost in differentiating cells located around the periphery of each colony, yet maintained in the small, centrally located cells. After prolonged LIF-withdrawal, all TDH-specific immunoreactivity was lost. Together, these observations suggest that threonine catabolism via the TDH enzyme might be important to the growth and metabolic state of mouse ES cells.

Elegant studies of metabolic flux in rapidly growing bacterial cells have defined reaction pathways that flow at rates more than three to four orders of magnitude higher than those of other pathways of intermediary metabolism (*9*). The core circuitry of what has been termed the high-flux backbone (HFB) of metabolism includes the TDH enzyme. Whereas most amino acids are processed into biomass via translation during HFB metabolism, TDH converts most threonine into glycine and acetyl-CoA. Because most microbial organisms, including yeast (*10*), can synthesize threonine de novo, the HFB pathway allows synthesis of sufficient amounts of threonine to satisfy the demands of both threonine catabolism to glycine and acetyl-CoA, as well its requirement for protein synthesis.

Mouse ES cells critically depend on threonine. Mammalian cells, unlike bacteria or yeast, require threonine as an essential amino acid. To test whether ES cells might deploy the TDH enzyme to adopt a metabolic state comparable to the HFB of bacterial cells, we prepared culture media that were individually deprived of each of the 20 amino acids. ES cells of the E14 line were plated and exposed to each of the "drop-out" culture media. After 36 hours of exposure, nor-

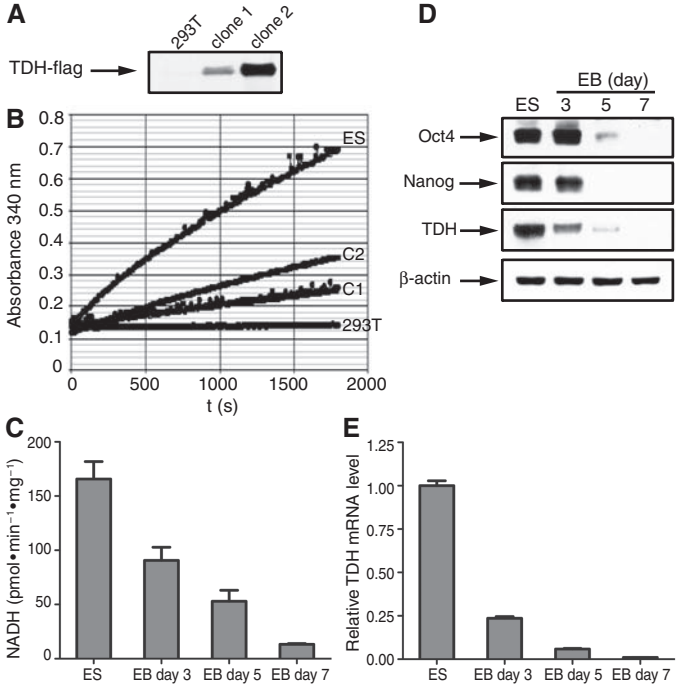

Fig. 2. Measurements of TDH enzyme activity, mRNA abundance, and protein abundance as a function of ES cell differentiation. (**A**) Western blotting assays of 293T cells stably transformed with an expression vector encoding a Flag-tagged version of TDH. Western blotting revealed no TDH signal in parental 293T cells, an intermediate signal in transformed clone 1, and a higher signal in transformed clone 2. (**B**) TDH enzyme activity assays for ES cells (ES), untransformed 293T cells (293T), transformed 293T clone 1 cells (C1), and transformed 293T clone 2 cells (C2). Mitochondria were isolated from ES cells and the three 293T clones by differential centrifugation (see Materials and Methods). Equal amounts (10 μg) of mitochondrial protein were subjected to an assay reaction containing 100 mM tris–HCl (pH 8.0), 50 mM NaCl, 25 mM threonine, and 5 mM NAD^+ at 25°C. Absorbance at 340 nm was recorded over time on a microplate reader to monitor conversion of NAD^+ to NADH. (**C**) TDH enzyme activity present in mitochondrial extracts from undifferentiated ES cells and day 3, 5, and 7 embryoid body cells as determined under the same reaction conditions as in (B). Experiments were performed in triplicate; error bars indicate ±SD. (**D**) Western blotting signals for Oct4, Nanog, TDH, and actin in protein samples prepared from undifferentiated ES cells and day 3, 5, and 7 embryoid body cells. (**E**) shows TDH mRNA levels as monitored by qPCR in ES cells and day 3, 5, and 7 embryoid body cells. Experiments were performed in triplicate; error bars indicate ±SD.

mal ES colonies were observed to grow in all culture media except that deprived of threonine (Fig. 4A and fig. S3A). Colonies grown from either control media, or media individually lacking all amino acids except threonine, stained positively with the alkaline phosphatase marker prototypical of undifferentiated ES cells. Light microscopic inspection of ES cell colonies showed little or no difference in colony morphology, cell size, or cell number as a function of media type. All of the media samples tested contained 10% fetal bovine serum. The serum component provides cells with residual amounts of amino acids, as well as with serum proteins that can be hydrolyzed by cells to salvage amino acids for protein synthesis and other metabolic needs. These residual amounts of amino acids are sufficient for the growth of ES cells in all cases except threonine deprivation. Almost indistinguishable observations of acute threonine dependence were obtained on the CCE line of mouse ES cells, as well as the AOK-5P line of mouse embryonic fibroblast (MEF)–derived induced pluripotent stem (iPS) cells (fig. S3, B and C). Moreover, as with the E14 line of ES cells, the CCE and AOK-5P lines were observed by immunofluorescence staining to express copious amounts of mitochondrial TDH enzyme (fig. S4).

When the same samples of drop-out media were tested for colony formation assays using human cancer (HeLa) cells, only leucine-deficient culture medium impeded cell growth (fig. S5A). Threonine-deficient medium supported HeLa colony formation as well as fully supplemented culture medium. Similar studies on MEF cells and mouse NIH 3T3 cells also failed to reveal differential sensitivity to threonine deprivation. MEF and 3T3 cell growth was instead exceptionally sensitive to cysteine deprivation (fig. S5, B and C). MEF cells grew indistinguishably in the presence of the 19 other drop-out media, including that lacking threonine. 3T3 cells grew at a slower rate in culture medium deprived of either arginine or leucine. Mildly reduced growth was also observed for culture medium lacking methionine, glutamine, lysine, threonine, tryptophan, phenylalanine, or valine. Finally, media samples deprived of serine, alanine, glycine, asparagine, histidine, tyrosine, aspartic acid, isoleucine, or proline supported 3T3 cell growth to a level equivalent to that of fully supplemented culture medium. The unusual sensitivity to cysteine deprivation may indicate that some aspect of sulfur metabolism, perhaps relating to the production of glutathione, is critical to the growth or survival of these partially differentiated, embryo-derived cell types. It can be concluded, however, that the growth properties of HeLa, MEF, and 3T3 cells are not uniquely sensitive to threonine deprivation, as was observed for mouse ES cells.

If TDH-mediated threonine breakdown in ES cells indeed supplies glycine to fuel one-carbon metabolism for enhanced purine biosynthesis, one might anticipate that deprivation of threonine would impede DNA synthesis. To test this hypothesis, we cultured ES cells in the presence of varying levels of threonine and exposed the cells to brief labeling with [^{3}H]thymidine. The incorporation of [^{3}H]thymidine into DNA was substantially reduced as a function of threonine concentration in the culture medium (Fig. 4C). Reduction of threonine supplementation to 30 μM partially inhibited [^{3}H]thymidine incorporation into DNA. When threonine concentrations were reduced to 10 μM, DNA synthesis was impeded to a level similar to that observed by complete elimination of threonine from culture medium (except for residual amounts present in serum). By contrast, when HeLa cells were grown in culture medium supplemented with varying concentrations of threonine, DNA synthesis was unimpeded even under conditions of complete threonine deprivation (Fig. 4C).

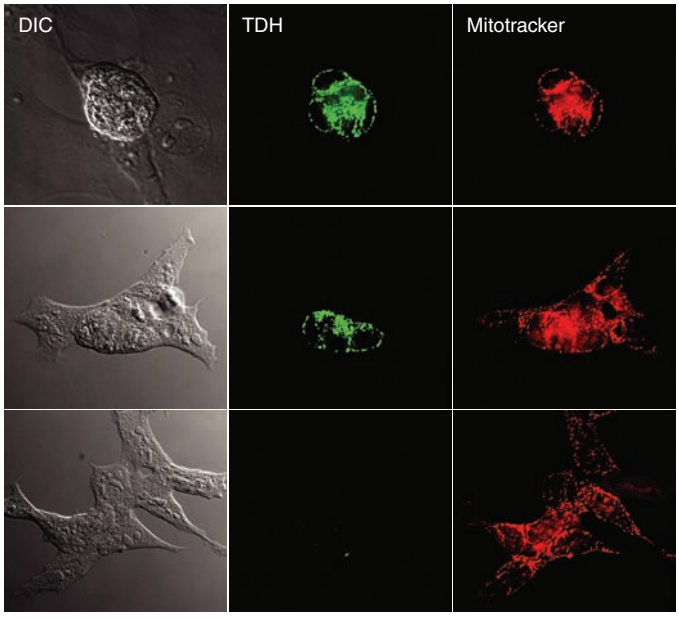

Fig. 3. Immunohistochemical staining of TDH in mouse ES cells as a function of differentiation. Mouse ES cells were grown in chamber slides and subjected to LIF withdrawal–mediated differentiation. Shown are images of an undifferentiated ES colony (top), a partially differentiated colony (middle), and an extensively differentiated colony (bottom). Cells were fixed and stained with antibodies specific to the mouse TDH enzyme. TDH immunoreactivity was visualized with Alexa488-labeled goat antibody to rabbit secondary antibodies (green). Before fixation, cells were incubated with Mitotracker dye, allowing visual localization of mitochondria (red).

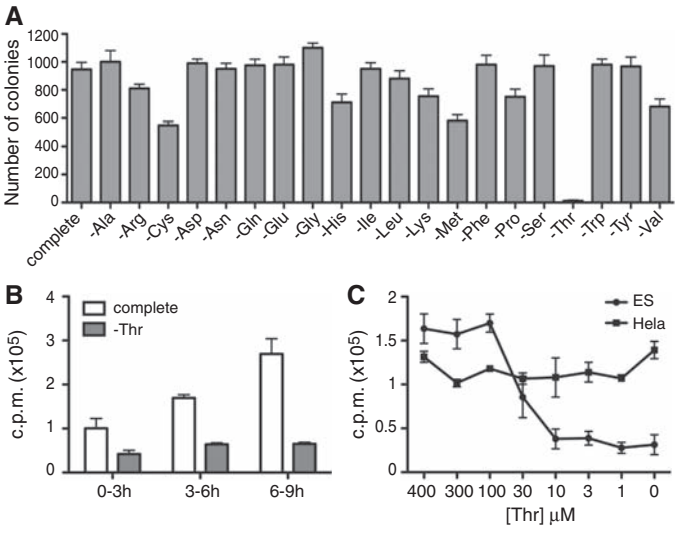

Fig. 4. Inhibition of cell growth and DNA synthesis in ES cells deprived of threonine. (**A**) Growth dependence of ES cells on threonine supplementation to culture media. After plating at single-cell density and growth on gelatinized dishes for 6 hours, E14Tg2A mouse ES cells were exposed for 36 hours to complete culture medium or to medium missing a single amino acid. The numbers of alkaline phosphatase–positive colonies were counted and plotted. The experiments were performed in triplicate; error bars indicate ±SD. (**B**) Time-dependent effects of threonine deprivation on DNA synthesis in cultured ES cells. After growth of undifferentiated ES cells in complete culture medium for 1 day, 2×10^5 cells were exposed to complete (white bar) or threonine-deprived (gray bar) medium for 3, 6, or 9 hours. Cells were metabolically labeled with 2 μCi of [^{3}H]thymidine at 3-hour intervals as indicated (see Materials and Methods). Progressively increased amounts of label incorporation at 6 and 9 hours were observed for cells grown in complete culture medium, reflective of increased cell number owing to a 5-hour doubling time. Experiments were performed in triplicate; error bars indicate ±SD. (**C**) Dose-dependent effects of threonine deprivation on DNA synthesis in cultured ES cells. ES cells (2×10^5) (closed circle) or HeLa cells (5×10^5) (closed square) were exposed for 3 hours to culture medim containing the indicated concentrations of threonine, and then metabolically labeled for 3 hours with [^{3}H]thymidine. DNA was purified from each sample and the amount of radioactivity incorporated was measured by scintillation counting. Experiments were performed in triplicate; error bars indicate ±SD.

Assuming that the TDH enzyme might allow ES cells to convert threonine into glycine as an alternative and theoretically enhanced mode of one-carbon metabolism, we supplemented culture medium deprived of threonine by increased concentrations of glycine. Instead of the normal, 400 μM concentration of glycine, threonine-deficient medium was supplemented with 4 mM glycine. ES cells subjected to this threonine-deficient, glycine-enriched medium grew no better than those subjected to the threonine drop-out medium itself. It is possible that ES cells cannot deliver the supplemented glycine to mitochondria to feed the glycine cleavage system and folate charging. Alternatively, TDH-mediated production of acetyl-CoA could be equally important to the HFB-like metabolic state. This alternative interpretation is consistent with the observation that among all metabolites that decline in abundance most precipitously as a function of the conversion of ES cells into differentiating embryoid bodies, acetyl-CoA was second only to the purine intermediate AICAR (Fig. 1). To investigate these alternatives, we used 3-hydroxynorvaline (3-HNV), a synthetic variant of threonine containing an extra carbon atom. The TDH enzyme can hydrolyze this threonine analog, yet instead of producing glycine and acetyl-CoA, catabolism of 3-HNV yields glycine and propionyl-CoA (*11*). Compared with the 3.56 mM K_m (Michaelis constant) for threonine, the TDH enzyme catabolizes 3-HNV with a K_m of 11.48 mM. ES cells were cultured in either normal or threonine-deficient medium supplemented with varying amounts of 3-HNV. Not only did the analog fail to complement the absence of threonine, but it instead inhibited ES cell colony formation in the presence of normal culture medium (fig. S6A). The inhibitory effect of 3-HNV was not observed on the growth of HeLa, MEF, or 3T3 cells (fig. S6B). These data are consistent with the interpretation that mouse ES cells critically rely on TDH-mediated production of both glycine and acetyl-CoA. Because 3-HNV is a known TDH enzyme substrate, we hypothesize that it competes with the TDH enzyme in mitochondria of ES cells, yielding only one of the two metabolites required of HFB metabolism.

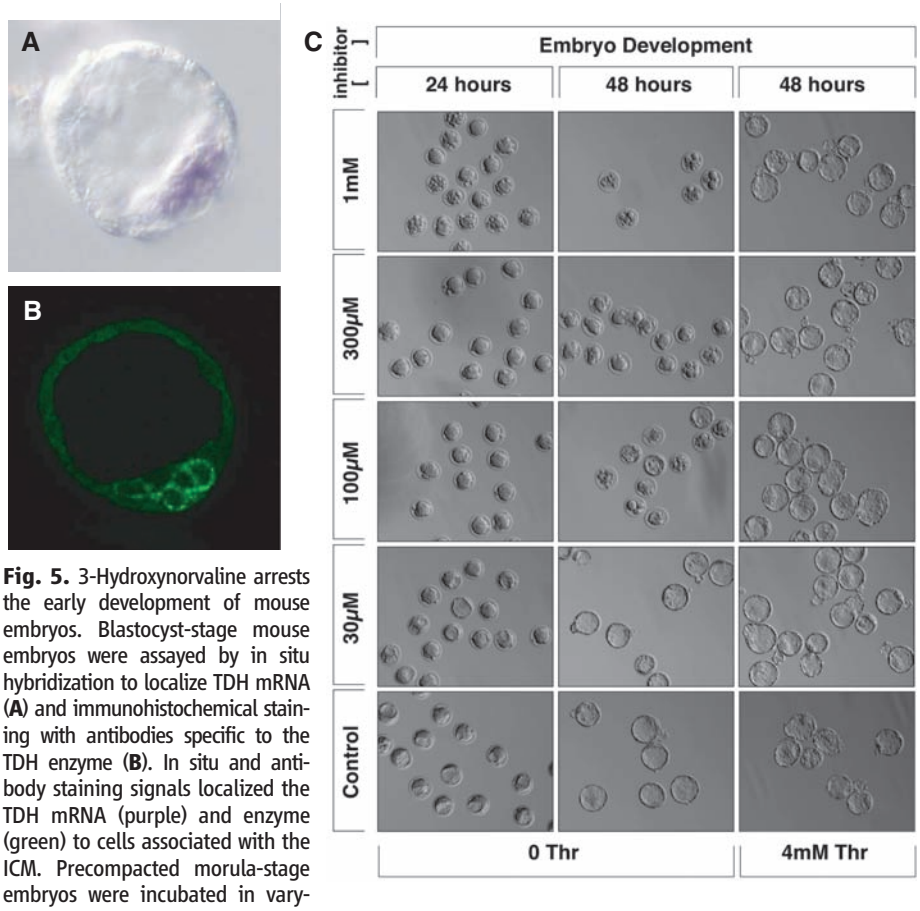

Fig. 5. 3-Hydroxynorvaline arrests the early development of mouse embryos. Blastocyst-stage mouse embryos were assayed by in situ hybridization to localize TDH mRNA (**A**) and immunohistochemical staining with antibodies specific to the TDH enzyme (**B**). In situ and antibody staining signals localized the TDH mRNA (purple) and enzyme (green) to cells associated with the ICM. Precompacted morula-stage embryos were incubated in varying concentrations of the threonine analog 3-HNV. Embryos exposed to 1 mM and 300 μM 3-HNV were blocked from forming cavitated blastocysts (**C**). Incubation with 4 mM threonine resulted in complete rescue of embryonic development even at the highest concentration (1 mM) of 3-HNV.

Growth of mouse embryos is critically dependent on threonine. The availability of 3-HNV as a cell-permeable threonine analog facilitated experiments using living mouse embryos. Before testing the effects of 3-HNV on early mouse embryo development, we performed in situ hybridization and immunohistochemical staining assays to investigate the expression pattern of both TDH mRNA and TDH enzyme. Both assays revealed staining patterns within the inner cell mass (ICM) of blastocyst embryos (Fig. 5, A and B). Knowing that the ICM represents the in vivo source of ES cells (*12*), we hypothesized that the early development of mouse embryos might be inhibited by 3-HNV. When administered at doses of 1 mM and 300 μM, 3-HNV blocked the conversion of morula-staged embryos into cavitated blastocysts. Less inhibition was observed when embryos were incubated with 100 μM concentrations of the threonine analog, and no inhibition was observed at 30 μM. Complete rescue of normal development was effected, even at 1 mM 3-HNV, when embryos were incubated in culture medium supplemented by 4 mM threonine (Fig. 5C). These studies provide evidence that ICM cells of the early mouse embryo, like cultured mouse ES cells, are critically dependent on threonine catabolism.

Neither MEF nor 3T3 cell growth was selectively sensitive to threonine deprivation. Threonine-low (Tl) culture medium could thus be anticipated to selectively favor the growth of embryonic fibroblasts over ES cells. Unlike the threonine dependence of ES cells, it was instead observed that both MEF and 3T3 cells failed to grow in cysteine-deprived medium (fig. S5, B and C). Thus, threonine-high:cysteine-low (ThCl) culture media could rationally be predicted to selectively support ES cell growth relative to that of differentiating or differentiated cells of the early mouse embryo. As an initial test of this hypothesis, small numbers of ES cells were mixed and cultured with a vast excess of either MEF or 3T3 cells and exposed to culture media supplemented with varying amounts of either threonine or cysteine. As expected, threonine deprivation severely limited the retrieval of ES clones from the mixed cultures under conditions in which both MEF and 3T3 cell growth was unimpeded (fig. S7). By contrast, deprivation of cysteine in the presence of 4 mM threonine favored the growth of ES cells relative to either MEF or 3T3 cells (Fig. 6).

Mouse ES cells grow well in culture medium supplemented with standard amounts of essential and nonessential amino acids, remaining continuously in a state of rapid, symmetric, self-renewing division in which all cells are maintained in the ES state. ES cells derived from other species, even rodents as closely related as rats, have a strong tendency toward differentiation. So profound is the difference between mouse ES cells and ES cells derived from other organisms that there has not been a single reported incidence of success in the use of ES cells from any other species for homologous recombination and subsequent generation of an animal bearing targeted changes in the genome. It is hoped that forced expression of the TDH gene, proper choice of ThCl culture medium, or both might favor the establishment of improved ES cell lines from species other than mice.

Humans are deficient in the threonine dehydrogenase enzyme. The human gene encoding TDH appears to be nonfunctional by virtue

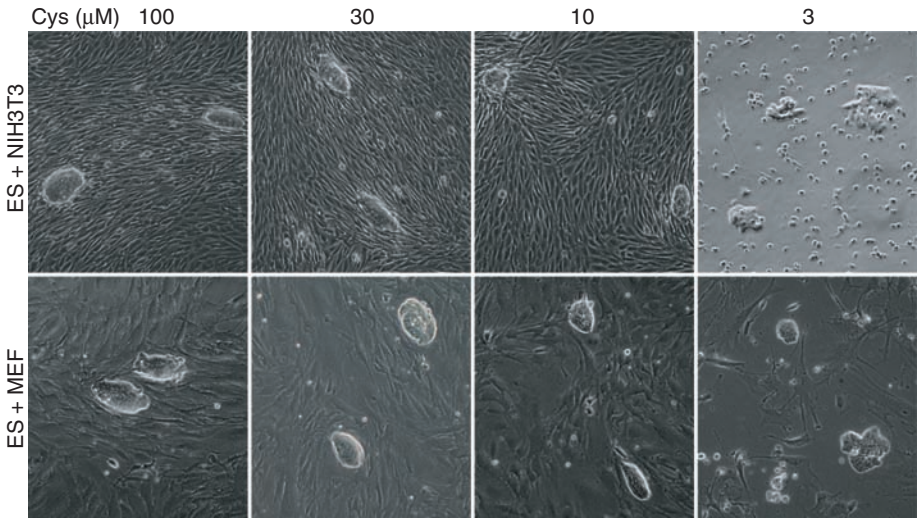

Fig. 6. Effects of cysteine deprivation on the growth of ES, MEF, and 3T3 cells. Cocultures of ES/MEF or ES/3T3 cells were subjected for 2 days to media containing varying amounts of supplemented cysteine. Cysteine deprivation severely impeded MEF cell growth at 10 and 3 μM and 3T3 growth at 3 μM (see also fig. S5). Although colony morphology was altered under the most severe conditions of cysteine deprivation, ES cell colonies were observed under all culture conditions tested.

of three inactivating mutations (*13*). Although highly conserved in gene organization, as well as primary amino acid sequence of the predicted TDH open reading frame, the human TDH gene carries AG-to-GG splice acceptor mutations in exons 4 and 6, as well as a nonsense mutation within exon 6 wherein arginine codon 214 is replaced by a translational stop codon. Whereas polymorphic variation within the human population has been observed for the exon 4 splice acceptor mutation, with some individuals carrying the normal AG splice acceptor dinucleotide and others carrying the GG variant, all individuals genotyped to date carry both the splice acceptor and nonsense mutations in exon 6. Reverse transcriptase–PCR analysis of TDH transcripts expressed in human fetal liver tissue showed complete skipping of exon 4 and either complete skipping or aberrant splicing of exon 6 (fig. S8). Given that exons 4 and 6 encode segments of the enzyme critical to its function and that truncation via the nonsense codon at amino acid 214 would also be predicted to yield an inactive variant, it appears that the human gene is incapable of producing an active TDH enzyme. Remarkably, all metazoans whose genomes have been sequenced to date, including chimpanzees, appear to contain an intact TDH gene (*14*). Unless humans evolved adaptive capabilities sufficient to overcome three mutational lesions, it would appear they are TDH deficient.

Human ES cells grow at a far slower rate than mouse ES cells, with a doubling time of 35 hours (*15*). Whether the slower growth rate of human ES cells reflects the absence of a functional TDH enzyme can perhaps be tested by introducing, into human ES cells, either a repaired human TDH gene or the intact TDH gene of a closely related mammal. That this strategy might work is supported by the expression in human cells of a functional form of the 2-amino-3-ketobutyrate-CoA ligase enzyme that converts the short-lived product of TDH-mediated catabolism of threonine into acetyl-CoA and glycine (Fig. 1B). It is possible that the culture conditions used to grow human ES cells do not match the ICM environment of the human embryo, in which the cell division cycle is more rapid than the 35-hour doubling time of cultured human ES cells (*16*). If human ES cells do not use the TDH enzyme to acquire an advantageous metabolic state for rapid growth, and if conditions can be adapted to facilitate the rapid proliferation of human ES cells in culture, the tools and approaches that we describe here may prove useful. As often happens in science, findings made in one experimental system can open avenues of investigation useful for other matters of inquiry. Finally, it is important to consider whether humans benefit from some form of selective advantage as a consequence of mutational inactivation of the TDH gene.

References and Notes

1. B. Alberts *et al.*, in *Molecular Biology of the Cell* (Garland, New York, ed. 5, 2007), p. 1.
2. M. H. L. Snow, *J. Embryol. Exp. Morphol.* **42**, 293 (1977).
3. A. G. Smith, *Annu. Rev. Cell Dev. Biol.* **17**, 435 (2001).
4. B. P. Tu *et al.*, *Proc. Natl. Acad. Sci. U.S.A.* **104**, 16886 (2007).
5. L. Warren, J. M. Buchanan, *J. Biol. Chem.* **229**, 613 (1957).
6. H. Weissbach, A. Peterkofsky, B. G. Redfield, H. Dickerman, *J. Biol. Chem.* **238**, 3318 (1963).
7. E. A. Phear, D. M. Greenberg, *J. Am. Chem. Soc.* **79**, 3737 (1957).
8. R. A. Dale, *Biochim. Biophys. Acta* **544**, 496 (1978).
9. E. Almaas, B. Kovacs, T. Vicsek, Z. N. Oltvai, A. L. Barabasi, *Nature* **427**, 839 (2004).
10. J. L. Hartman, *Proc. Natl. Acad. Sci. U.S.A.* **104**, 11,700 (2007).
11. T. Kazuoka *et al.*, *J. Bacteriol.* **185**, 4483 (2003).
12. F. A. Brook, R. L. Gardner, *Proc. Natl. Acad. Sci. U.S.A.* **94**, 5709 (1997).
13. A. J. Edgar, *BMC Genet.* **3**, 18 (2002).
14. K. D. Pruitt, T. Tatusova, D. R. Maglott, *Nucleic Acids Res.* **35**, D61 (2007).
15. M. Amit *et al.*, *Dev. Biol.* **227**, 271 (2000).
16. K. Hardy, A. H. Handyside, R. M. T. Winston, *Development* **107**, 597 (1989).

17. We thank B. Tu for the help with LC-MS/MS analysis; J. De Brabander and J. Ready for guidance on the chemical properties of threonine analogs; E. Olson for providing the AOK-5P line of iPS cells; D. Chong for technical assistance with in situ hybridization assays; and J. Goldstein, M. Rosen, and W. Neaves for helpful scientific input. This work was funded by an NIH Directors Pioneer Award, and unrestricted funds provided to S.L.M. by an anonymous donor.

Supporting Online Material

www.sciencemag.org/cgi/content/full/1173288/DC1
Materials and Methods
Figs. S1 to S8

9 March 2009; accepted 17 June 2009
Published online 9 July 2009;
10.1126/science.1173288
Include this information when citing this paper.

String Theory, Quantum Phase Transitions, and the Emergent Fermi Liquid

Mihailo Čubrović, Jan Zaanen, Koenraad Schalm*

A central problem in quantum condensed matter physics is the critical theory governing the zero-temperature quantum phase transition between strongly renormalized Fermi liquids as found in heavy fermion intermetallics and possibly in high–critical temperature superconductors. We found that the mathematics of string theory is capable of describing such fermionic quantum critical states. Using the anti–de Sitter/conformal field theory correspondence to relate fermionic quantum critical fields to a gravitational problem, we computed the spectral functions of fermions in the field theory. By increasing the fermion density away from the relativistic quantum critical point, a state emerges with all the features of the Fermi liquid.

Quantum many-particle physics lacks a general mathematical theory to deal with fermions at finite density. This is known as the "fermion sign problem": There is no recourse to brute-force lattice models because the statistical path-integral methods that work for any bosonic quantum field theory do not work for finite-density Fermi systems.

The nonprobabilistic fermion problem is known to be of exponential complexity (*1*), and in the absence of a general mathematical framework, all that remains is phenomenological guesswork in the form of the Fermi-liquid theory describing the state of electrons in normal metals and the mean-field theories describing superconductivity and other manifestations of spontaneous symmetry breaking. This problem has become particularly manifest in quantum condensed matter physics with the discovery of electron systems undergoing quantum phase transitions that are reminiscent of the bosonic quantum critical systems (*2*) but are governed by fermion statistics. Empirically well-documented examples are found in the "heavy fermion" intermetallics, where the zero-temperature transition occurs between different Fermi liquids with quasi-particle masses that diverge at the quantum critical point [(*3*) and references therein]. Such fermionic quantum critical states are believed to have a direct bearing on the problem of high–critical temperature (high-T_c) superconductivity because of the observation of quantum critical features in the normal state of optimally doped cuprate high-T_c superconductors [(*4*); (*5*) and references therein].

A large part of the fermion sign problem is to understand this strongly coupled fermionic quantum critical state. The emergent scale invariance and conformal symmetry at critical points is a benefit in isolating deep questions of principle. The fundamental problem is: How does the system get rid of the scales of Fermi energy and Fermi momentum that are intrinsically rooted in the workings of Fermi-Dirac statistics (*6*, *7*)? From another perspective, how can one construct a renormalization group with a relevant "operator" that describes the emergence of a statistics-controlled (heavy) Fermi liquid from the critical state (*3*), or perhaps the emergence of a high-T_c superconductor? Here, we show that a mathematical method developed in string theory has the capacity to answer at least some of these questions.

String theory for condensed matter. Our analysis makes use of the AdS/CFT correspondence: a duality relation between classical gravitational physics in a $d + 1$–dimensional "bulk" space-time with an anti–de Sitter (AdS) geometry and a strongly coupled conformal (quantum critical) field theory (CFT), with a large number of degrees of freedom, that occupies a flat or spherical d-dimensional "boundary" space-time. Applications of AdS/CFT to quantum critical systems have already been studied in the context of the quark-gluon plasma (*8*, *9*), superconductor-insulator transitions (*10*–*14*), and cold atom systems at the Feshbach resonance (*15*–*17*), but so far the focus has been on bosonic currents [see (*18*, *19*) and references therein]. Although AdS/CFT is convenient, in principle the ground state or any response of a bosonic statistical field theory can also be computed directly by averaging on a lattice. For fermions, statistical averaging is not possible because of the sign problem. There are, however, indications that AdS/CFT should be able to capture finite-density Fermi systems as well. Ensembles described through AdS/CFT can exhibit a specific heat that scales linearly with the temperature characteristic of Fermi systems (*20*), zero sound (*20*–*22*), and a minimum energy for fermionic excitations (*23*, *24*).

To address the question of whether AdS/CFT can describe finite-density Fermi systems and the Fermi liquid in particular, we compute the single charged fermion propagators and the associated spectral functions that are measured experimentally by angle-resolved photoemission spectroscopy ("AdS-to-ARPES") and indirectly by scanning tunneling microscopy. The spectral functions contain the crucial information regarding the nature of the fermion states. These are computed on the AdS side by solving for the on-shell (classical) Dirac equation in the curved AdS space-time background with sources at the boundary. A temperature T and finite $U(1)$ chemical potential μ_0 for electric charge is imposed in the field theory by studying the Dirac equation in the background of an AdS Reissner-Nordstrom black hole. We do so with the expectation that the $U(1)$ chemical potential induces a finite density of the charged fermions. The procedure to compute the retarded CFT propagator from the dual AdS description is then well established (*8*, *19*). Relative to the algorithm for computing bosonic responses, the treatment of Dirac waves in AdS is more delicate but straightforward; details are provided in (*25*). The equations obtained this way are solved numerically and the output is the retarded single fermion propagator $G_R(\omega, k)$ at finite T. Its imaginary part is the single fermion spectral function $A(\omega, k) = -(1/\pi)\ \mathrm{Im}\ \mathrm{Tr}[i\gamma^0 G_R(\omega, k)]$ that can be directly compared with ARPES experiments (*26*).

The reference point for this comparison is the quantum critical point described by a zero chemical potential ($\mu_0 = 0$), zero temperature ($T = 0$), and conformal and Lorentz invariant field theory. (Below, we use relativistic notation where $c = 1$.) Here the fermion propagators $\langle\overline{\Psi}\Psi\rangle \equiv G(\omega, k)$ are completely fixed by symmetry to be of the form

$$G^{\mathrm{CFT}}_{\Delta_\Psi}(\omega, k) \sim \frac{1}{(\sqrt{-\omega^2 + k^2})^{d-2\Delta_\Psi}} \quad (1)$$

where Δ_Ψ is the scaling dimension of the fermion field. Through the $\mathrm{AdS}_{d+1}/\mathrm{CFT}_d$ dictionary, Δ_Ψ is related to the mass parameter in the $d + 1$–dimensional AdS Dirac equation. Unitarity bounds this mass from below in units of the AdS radius $mL = \Delta_\Psi - d/2 > -1/2$ (we set $L = 1$ in the remainder). The choice of which value to use for m will prove essential to show the emergence of the Fermi liquid. The lower end of the unitarity-bound $m = -1/2 + \delta$, $\delta << 1$, corresponds to introducing a fermionic conformal operator with weight $\Delta_\Psi = [(d - 1)/2] + \delta$. This equals the scaling dimension of a nearly free fermion. Even though the underlying CFT is strongly coupled, the absence of a large anomalous dimension for a fermion with mass $m = -1/2 + \delta$ argues that such an operator fulfills a spectator role and is only weakly coupled to this CFT. We therefore use such values in our calculations. Our expectation is that the Fermi liquid, as a system with well-defined quasi-particle excitations, can be described in terms of weakly interacting long-range fields. As we increase m from $m = -1/2 + \delta$, the interactions increase and we can expect the quasi-particle description to cease to be valid beyond $m = 0$. For that value $m = 0$, and beyond $m > 0$, the naïve scaling dimension Δ_O of the fermion-bilinear $O_{\Delta_O} = \Psi\Psi$ is marginal or irrelevant, and it is hard to see how the ultraviolet conformal theory can flow to a Fermi-liquid state, assuming that all vacuum state changes are caused by the condensation of bosonic oper-

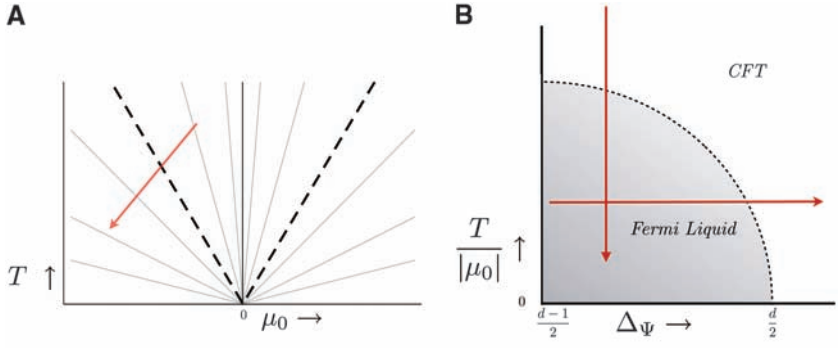

Fig. 1. (**A**) The phase diagram near a quantum critical point. Gray lines depict lines of constant μ_0/T; the spectral function of fermions is unchanged along each line if the momenta are appropriately rescaled. As we increase μ_0/T we cross over from the quantum critical regime to the Fermi liquid. (**B**) The trajectories in parameter space (μ_0/T, Δ_Ψ) studied here. We show the crossover from the quantum critical regime to the Fermi liquid by varying μ_0/T while keeping Δ_Ψ fixed; we cross back to the critical regime varying $\Delta_\Psi \to d/2$ for μ_0/T fixed. The boundary region is not an exact curve but only a qualitative indication.

Institute-Lorentz for Theoretical Physics, Leiden University, P.O. Box 9506, Leiden, Netherlands.

*To whom correspondence should be addressed. E-mail: kschalm@lorentz.leidenuniv.nl

ators. This intuition is borne out by our results: When $m \geq 0$, the standard Fermi liquid disappears. A similar approach to describing fermionic quantum criticality (*27*) discusses the special case $m = 0$ or $\Delta_\Psi = d/2$ in detail; an early attempt to describe the $m = 0$ system is (*28*).

The emergent Fermi liquid. With an eye toward experiment, we consider the AdS_4 dual to a relativistic CFT_3 in $d = 2 + 1$ dimensions (*25*). We do not know the detailed microscopic CFT, nor do we know whether a dual AdS with fermions as the sole $U(1)$ charged field exists as a fully quantum-consistent theory for all values of $m = \Delta_\Psi - d/2$, but the behavior of fermion spectral functions at a strongly coupled quantum critical point can be deduced nonetheless. Aside from Δ_Ψ, the spectral function will depend on the dimensionless ratio μ_0/T as well as the $U(1)$ charge g of the fermion; we set $g = 1$ from here on, as we expect that only large changes away from $g = 1$ will change our results qualitatively. We therefore study the system as a function of μ_0/T and Δ_Ψ. Our approach is sketched in Fig. 1B. We first study the spectral behavior as a function of μ_0/T for fixed $\Delta_\Psi < 3/2$; then we study the spectral behavior as we vary the scaling dimension Δ_Ψ from 1 to $3/2$ for fixed μ_0/T coding for an increasingly interacting fermion. Note that our setup and numerical calculations necessitate a finite value of μ_0/T; all our results are at nonzero T.

Our analysis starts near the reference point $\mu_0/T \to 0$, where the long-range behavior of the system is controlled by the quantum critical point (Fig. 1A). Here we expect to recover conformal invariance, as the system forgets about any well-defined scales, and the spectral function should be controlled by the branchcut at $\omega = k$ in the Green's function (Eq. 1): (i) For $\omega < k$ it should vanish. (ii) At $\omega = k$ we expect a sharp peak, which for $\omega >> k$ scales as $\omega^{2\Delta_\Psi - d}$. Figure 2A shows this expected behavior of spectral function for three different values of the momentum for a fermionic operator with weight $\Delta_\Psi = 5/4$ computed from AdS_4 following the setup in (*25*).

Turning on μ_0/T while holding $\Delta_\Psi = 5/4$ fixed shifts the center location of the two branchcuts to an effective chemical potential $\omega = \mu_{\text{eff}}$; this bears out our expectation that the $U(1)$ chemical potential induces a finite fermion density. Although the peak at the location of the negative branchcut $\omega \sim \mu_{\text{eff}} - k$ stays broad, the peak at the other branchcut $\omega \sim \mu_{\text{eff}} + k$ sharpens distinctly as the size of μ_0/T is increased (Fig. 2B). We identify this peak with the quasi-particle of the Fermi liquid and its appearance as the crossover between the quantum critical regime and the Fermi-liquid regime. The spectral properties of the Fermi liquid are very well known and display a number of uniquely identifying characteristics (*29*, *30*). If this identification is correct, all these characteristics must be present in our spectra as well.

1) The quasi-particle peak should approach a delta function at the Fermi momentum $k = k_F$. In Fig. 2B we see the peak narrow as we increase k, then peak and broaden back out as we pass $k \sim k_F$ (recall that $T = 0$ is outside our numerical control and the peak always has some broadening). In addition, the spectrum should vanish identically at the Fermi energy $A(\omega = E_F, k) = 0$, independent of k (Fig. 2C).

2) The quasi-particle should have linear dispersion relation near the Fermi energy with a renormalized Fermi velocity v_F different from the underlying relativistic speed $c = 1$. In Fig. 3 we plot the maximum of the peak ω_{max} as a function of k. At high k we recover the linear dispersion relation $\omega = |k|$ underlying the Lorentz invariant branchcut in Eq. 1. Near the Fermi energy and Fermi momentum, however, this dispersion relation changes to a slope $v_F \equiv \lim_{\omega \to E_F, k \to k_F} (\omega - E_F)/(k - k_F)$ clearly less than unity.

Note that the Fermi energy E_F is not located at zero frequency. Recall, however, that the AdS chemical potential μ_0 is the bare $U(1)$ chemical potential in the CFT. This is confirmed in Fig. 3 from the high-k behavior: Its Dirac point is μ_0. On the other hand, the chemical potential felt by the IR fermionic degrees of freedom is renormalized to the value $\mu_F = \mu_0 - E_F$. As is standard, the effective energy $\tilde{\omega} = \omega - E_F$ of the quasi-particle is measured with respect to E_F.

3) At low temperatures, Fermi-liquid theory predicts the width of the quasi-particle peak to

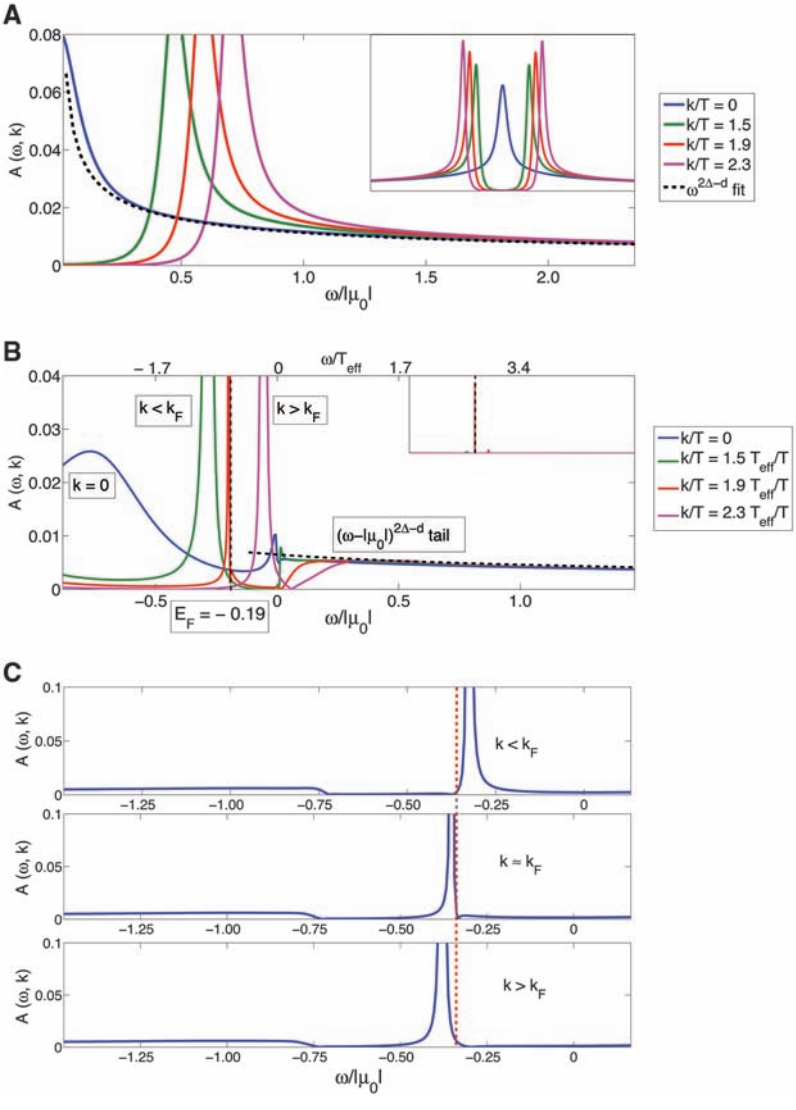

Fig. 2. (**A**) The spectral function $A(\omega,k)$ for $\mu_0/T = 0.01$ and $m = -1/4$. The spectral function has the asymptotic branchcut behavior of a conformal field of dimension $\Delta_\Psi = d/2 + m = 5/4$: It vanishes for $\omega < k$, save for a finite T tail, and for large ω it scales as $\omega^{2\Delta_\Psi - d}$. (**B**) The emergence of the quasi-particle peak as we change the chemical potential to $\mu_0/T = -30.9$ for the same value $\Delta_\Psi = 5/4$. The three displayed momenta k/T are rescaled by a factor T_{eff}/T for the most meaningful comparison with those in (A) (*25*). The insets show the full scales of the peak heights and the dominance of the quasi-particle peak for $k \sim k_F$. (**C**) Vanishing of the spectral function at E_F for $\Delta_\Psi = 1.05$ and $\mu_0/T = -30.9$. The deviation of the dip location from E_F is a finite temperature effect; it decreases with increasing μ_0/T.

grow quadratically with temperature. Figure 4, A and B, shows this distinctive behavior up to a critical temperature, $T_c/\mu_0 \sim 0.16$. This temperature behavior directly follows from the fact that the imaginary part of the self-energy $\Sigma(\omega, k) = \omega - k - [\mathrm{Tr}\, i\gamma^0 G(\omega, k)]^{-1}$ should have no linear term when expanded around E_F: $\mathrm{Im}\,\Sigma(\omega, k) \sim (\omega - E_F)^2 + \ldots$ This is shown in Fig. 4, C and D.

These results give us confidence that we have identified the characteristic quasi-particles at the Fermi surface of the Fermi liquid emerging from the quantum critical point.

We now discuss how this Fermi liquid evolves when we increase the bare μ_0 (Fig. 5). Similar to the fermion chemical potential μ_F, the fundamental control parameter of the Fermi liquid, the fermion density ρ_F, is not directly related to the AdS μ_0. We can, however, infer it from the Fermi momentum k_F that is set by the quasi-particle pole via Luttinger's theorem $\rho_F \sim k_F^{d-1}$. The more illustrative figure is therefore Fig. 5B, which shows the quasi-particle characteristics as a function of k_F/T. We find that the quasi-particle velocities decrease slightly with increasing k_F, rapidly leveling off to a finite constant less than the relativistic speed. Thus, the quasi-particles become increasingly heavy as their mass $m_F \equiv k_F/v_F$ approaches linear growth with k_F. The Fermi energy E_F also shows linear growth. Suppose the heavy Fermi–quasi-particle system has the underlying canonical nonrelativistic dispersion relation $E = k^2/(2m_F) = k_F^2/(2m_F) + v_F(k - k_F) + \ldots$; in that case, the observed Fermi energy E_F should equal the renormalized Fermi energy $E_F^{(ren)} \equiv k_F^2/(2m_F)$. Figure 5B shows that these energies E_F and $E_F^{(ren)}$

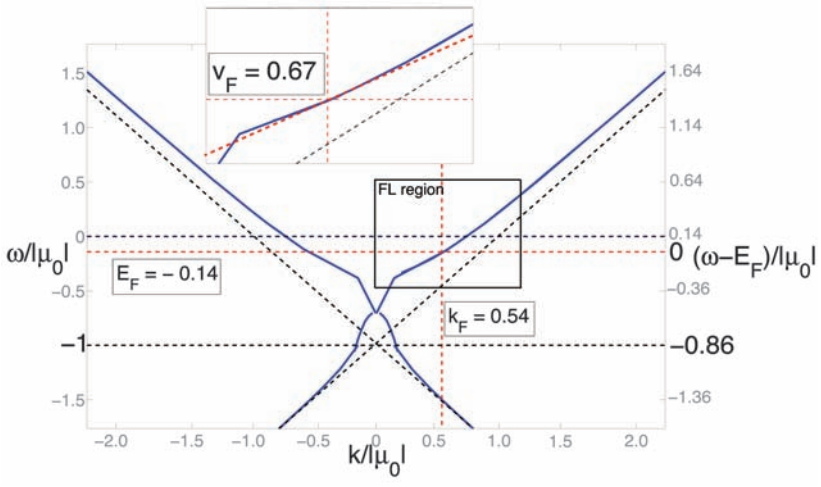

Fig. 3. Maxima in the spectral function as a function of k/μ_0 for $\Delta_\Psi = 1.35$ and $\mu_0/T = -30.9$. Asymptotically for large k the negative-k branchcut recovers the Lorentz-invariant linear dispersion with unit velocity, but with the zero shifted to $-\mu_0$. The peak location of the positive-k branchcut that changes into the quasi-particle peak changes noticeably. It gives the dispersion relation of the quasi-particle near (E_F, k_F). The change of the slope from unity shows renormalization of the Fermi velocity. This is highlighted in the inset. Note that the Fermi energy E_F is not located at $\omega_{AdS} = 0$. The AdS calculation visualizes the renormalization of the bare chemical potential $\mu_0 = \mu_{AdS}$ to the effective chemical potential $\mu_F = \mu_0 - E_F$ felt by the low-frequency fermions.

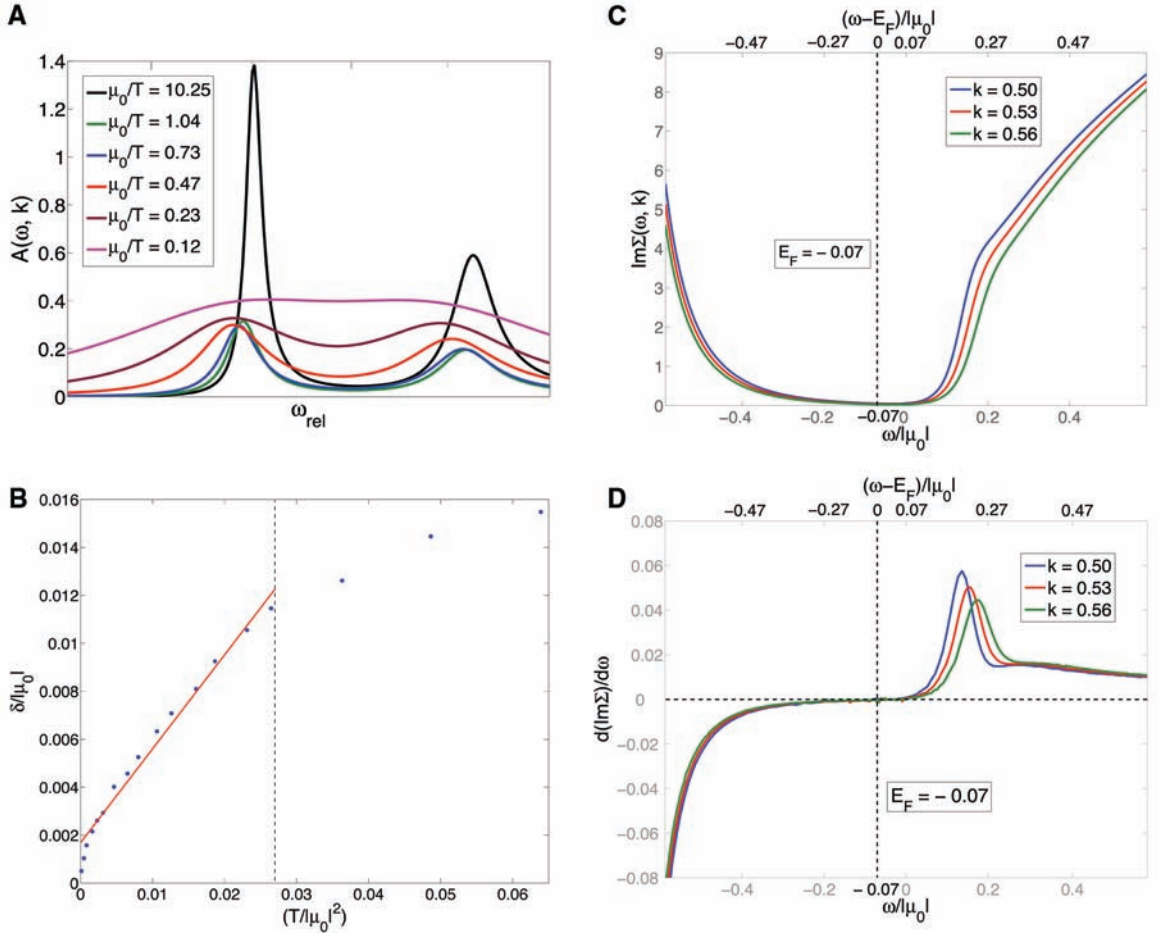

Fig. 4. (**A**) Temperature dependence of the quasi-particle peak for $\Delta_\Psi = 5/4$ and $k/k_F \approx 0.5$; all curves have been shifted to a common peak center. (**B**) The quasi-particle peak width $\delta \sim \mathrm{Re}\,\Sigma(\omega, k = k_F)$ for $\Delta_\Psi = 5/4$ as a function of T^2; it reflects the expected behavior $\delta \sim T^2$ up to a critical temperature T_c/μ_0, beyond which the notion of a quasi-particle becomes untenable. (**C** and **D**) The imaginary part of the self-energy $\Sigma(\omega, k)$ near E_F, k_F for $\Delta_\Psi = 1.4$, $\mu_0/T = -30.9$. The defining $\mathrm{Im}\,\Sigma(\omega, k) \sim (\omega - E_F)^2 + \ldots$ dependence for Fermi-liquid quasi-particles is faint in (C) but obvious in (D). It shows that the intercept of $\partial_\omega\,\mathrm{Im}\,\Sigma(\omega, k)$ vanishes at E_F, k_F.

track each other remarkably well. We therefore infer that the true zero of energy of the Fermi quasi-particle is set by the renormalized Fermi energy as deduced from the Fermi velocity and Fermi momentum.

Although the true quasi-particle behavior disappears at $T > T_c$, Fig. 5A indicates that in the limit $k_F/T \to 0$ the quasi-particle pole strength vanishes, $Z_k \to 0$, while the Fermi velocity v_F remains finite; v_F approaches the bare velocity $v_F = 1$. This is seemingly at odds with the heavy Fermi liquid relation $Z_k \sim m_{micro}/m_F = m_{micro}v_F/k_F$. The resolution is the restoration of Lorentz invariance at zero density. From general Fermi liquid considerations it follows that $v_F = Z_k\,(1 + \partial_k \mathrm{Re}\,\Sigma|_{E_F,k_F})$ and $Z_k = 1/(1 - \partial_\omega \mathrm{Re}\,\Sigma|_{E_F,k_F})$, where $\partial_{k,\omega}$ Re Σ refers to the momentum and energy derivatives of the real part of the fermion self-energy $\Sigma(\omega, k)$ at k_F, E_F. Lorentz invariance imposes $\partial_\omega\Sigma' = -\partial_k\Sigma'$, which allows for vanishing Z_k with $v_F \to 1$. Interestingly, the case has been made that such a relativistic fermionic behavior might be underlying the physics of cuprate high-T_c superconductors (*31*).

Finally, we address the important question of what happens when we vary the conformal dimension Δ_Ψ of the fermionic operator. Figure 6 shows that the Fermi momentum k_F stays constant as we increase Δ_Ψ. This completes our identification of the new phase as the Fermi liquid: It indicates that the AdS dual obeys Luttinger's theorem, if we can interpret the conformal dimension of the fermionic operator as a proxy for the interaction strength. We find furthermore that the quasi-particle pole strength vanishes as we approach $\Delta_\Psi = {}^3/_2$. This confirms our earlier assumption that it is essential to study the system for $\Delta_\Psi < d/2$ and that the point $\Delta_\Psi = d/2$, where the naïve fermion bilinear becomes marginal, signals the onset of a new regime. Because the fermion bilinear is marginal at that point, this ought to be an interesting regime in its own right, and we refer to (*27*) for a discussion thereof (*32*). Highly remarkable is that the pole strength vanishes in an exponential fashion rather than the anticipated algebraic behavior (*6*, *7*). This could indicate that an essential singularity governs the critical point at $\Delta_\Psi = d/2$, and we note that such a type of behavior was identified by Lawler *et al.* in their analysis of the Pomeranchuk instability in $d = 2 + 1$ dimensions using the Haldane patching bosonization procedure (*33*). Note that this finite μ_0/T transition as we vary Δ_Ψ has no clear symmetry change, similar to (*7*). However, this may be an artifact of the fact that our theory is not quantum mechanically complete (*25*). Note also that the quasi-particle velocity and the renormalized Fermi energy $E_F = v_F(k - k_F) - E$ stay finite at the $\Delta_\Psi = {}^3/_2$ transition with $Z \to 0$, which could indicate an emergent Lorentz invariance for the reasons discussed above.

Concluding remarks. We have presented evidence that the AdS dual description of strongly coupled field theories can describe the emergence of the Fermi liquid from a quantum critical state, as a function of both density and interaction strength, as encoded in the conformal dimension of the fermionic operators. From the AdS gravity perspective, it was unclear whether this would happen. Sharp peaks in the CFT spectral function correspond to so-called quasi-normal modes of black holes (*34*), but Dirac quasi-normal modes have received little study [see, e.g., (*35*)]. It is remarkable that the AdS calculation processes the Fermi-Dirac statistics essential to the Fermi liquid correctly. This is manifested by the emergent renormalized Fermi energy and the validity of Luttinger's theorem. The AdS gravity computation, however, is completely classical without explicit quantum statistics, although we do probe the system with a fermion. It would therefore be interesting to fully understand the AdS description of what is happening, in particular how the emergent scales

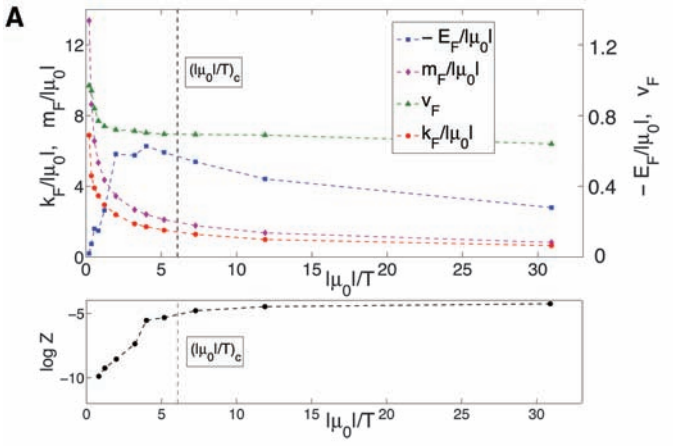

Fig. 5. The quasi-particle characteristics as a function of μ_0/T for $\Delta_\Psi = 5/4$. (**A**) The change of k_F, v_F, m_F, E_F, and the pole strength Z (the total weight between half-maxima) as we change μ_0/T. Beyond a critical value $(\mu_0/T)_c$ we lose the characteristic T^2 broadening of the peak and there is no longer a real quasi-particle, although the peak is still present. For the Fermi liquid, k_F/T rather than μ_0/T is the defining parameter. (**B**) We can invert this relation, and (B) shows the quasi-particle characteristics as a function of k_F/T. Note the linear relationships of m_F and E_F to k_F and that the renormalized Fermi energy $E^{(ren)} \equiv k_F^2/(2m_F)$ matches the empirical value E_F remarkably well.

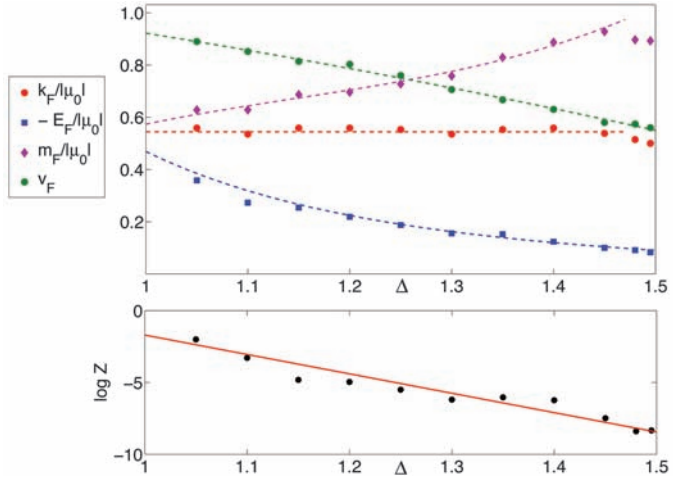

Fig. 6. The quasi-particle characteristics as a function of the Dirac fermion mass $-{}^1/_2 < m < 0$ corresponding to $1 < \Delta_\Psi < {}^3/_2$ for $\mu_0/T = -30.9$. The upper panel shows the independence of k_F of the mass. This indicates Luttinger's theorem if the anomalous dimension Δ_Ψ is taken as an indicator of the interaction strength. Note that v_F and E_F both approach finite values as $\Delta_\Psi \to {}^3/_2$. The lower panel shows the exponential vanishing pole strength Z (the integral between the half-maxima) as $m \to 0$.

E_F and k_F feature in the geometry. An early indication of such scales was seen in (*24*, *36*) in a variant of the story that geometry is not universal in string theory: The geometry depends on the probe used, and different probes experience different geometric backgrounds. The absence of these scales in the general relativistic description of the AdS black hole could thus be an artifact of the Riemannian metric description of space-time.

Regardless of these questions, AdS/CFT has shown itself to be a powerful tool to describe finite-density Fermi systems. The description of the emergent Fermi liquid presented here argues that AdS/CFT is uniquely suited as a computational device for field theory problems suffering from fermion sign problems. AdS/CFT represents a rich mathematical environment and a new approach to qualitatively and quantitatively investigate important questions in quantum many-body theory at finite fermion density.

References and Notes

1. M. Troyer, U. J. Wiese, *Phys. Rev. Lett.* **94**, 170201 (2005).
2. S. Sachdev, *Quantum Phase Transitions* (Cambridge Univ. Press, Cambridge, 1999).
3. J. Zaanen, *Science* **319**, 1295 (2008).
4. D. van der Marel *et al*., *Nature* **425**, 271 (2003).
5. J. Zaanen, *Nature* **430**, 512 (2004).
6. T. Senthil, *Phys. Rev. B* **78**, 035103 (2008).
7. F. Krüger, J. Zaanen, *Phys. Rev. B* **78**, 035104 (2008).
8. D. T. Son, A. O. Starinets, *Annu. Rev. Nucl. Part. Sci.* **57**, 95 (2007).
9. S. S. Gubser, A. Karch, http://arxiv.org/abs/0901.0935 (2009).
10. C. P. Herzog, P. Kovtun, S. Sachdev, D. T. Son, *Phys. Rev. D* **75**, 085020 (2007).
11. S. A. Hartnoll, P. K. Kovtun, M. Muller, S. Sachdev, *Phys. Rev. B* **76**, 144502 (2007).
12. S. S. Gubser, *Phys. Rev. D* **78**, 065034 (2008).
13. S. A. Hartnoll, C. P. Herzog, G. T. Horowitz, *Phys. Rev. Lett.* **101**, 031601 (2008).
14. S. A. Hartnoll, C. P. Herzog, G. T. Horowitz, *J. High Energy Phys.* **0812**, 015 (2008).
15. D. T. Son, *Phys. Rev. D* **78**, 046003 (2008).
16. K. Balasubramanian, J. McGreevy, *Phys. Rev. Lett.* **101**, 061601 (2008).
17. A. Adams, K. Balasubramanian, J. McGreevy, *J. High Energy Phys.* **0811**, 059 (2008).
18. S. A. Hartnoll, *Science* **322**, 1639 (2008).
19. S. A. Hartnoll, http://arxiv.org/abs/0903.3246 (2009).
20. M. Kulaxizi, A. Parnachev, *Nucl. Phys. B* **815**, 125 (2009).
21. A. Karch, D. T. Son, A. O. Starinets, *Phys. Rev. Lett.* **102**, 051602 (2009).
22. M. Kulaxizi, A. Parnachev, *Phys. Rev. D* **78**, 086004 (2008).
23. L. Brits, M. Rozali, http://arxiv.org/abs/0810.5321 (2008).
24. H. H. Shieh, G. van Anders, *J. High Energy Phys.* **0903**, 019 (2009).
25. See supporting material on *Science* Online.
26. ARPES Fermi-surface measurements assume that electrons are the only relevant charged objects. If this is so, then it measures the electron (i.e., fermion) spectral function. This spectral function is what we compute here, even though in our AdS setup the fermions are almost certainly not the only charged objects.
27. H. Liu, J. McGreevy, D. Vegh, http://arxiv.org/abs/0903.2477 (2009).
28. S. S. Lee, *Phys. Rev. D* **79**, 086006 (2009).
29. E. M. Lifshitz, L. P. Pitaevskii, *Statistical Physics, Part 2* (Pergamon, Oxford, 1980).
30. H. J. Schulz, G. Cuniberti, P. Pieri, in *Field Theories for Low-Dimensional Condensed Matter Systems*, G. Morandi, P. Sodano, A. Tagliacozzo, V. Tognetti, Eds. (Springer, Berlin, 2000), chap. 2.
31. M. Randeria, A. Paramekanti, N. Trivedi, *Phys. Rev. B* **69**, 144509 (2004).
32. Note that the $m = 0$ spectral peak discussed in (*27*) is therefore not the peak we identified with the quasi-particle state. See (*25*).
33. M. J. Lawler, V. Fernandez, D. G. Barci, E. Fradkin, L. Oxman, *Phys. Rev. B* **73**, 085101 (2006).
34. P. K. Kovtun, A. O. Starinets, *Phys. Rev. D* **72**, 086009 (2005).
35. H. T. Cho, A. S. Cornell, J. Doukas, W. Naylor, *Phys. Rev. D* **77**, 016004 (2008).
36. M. Rozali, H. H. Shieh, M. Van Raamsdonk, J. Wu, *J. High Energy Phys.* **0801**, 053 (2008).

37. We thank F. Denef, S. Hartnoll, H. Liu, J. McGreevy, S. Sachdev, D. Sadri, and D. Vegh for discussions. Supported by a VIDI Innovative Research Incentive Grant (K.S.) from the Netherlands Organization for Scientific Research (NWO) and by a Spinoza Award (J.Z.) from NWO and the Dutch Foundation for Fundamental Research on Matter (FOM).

Supporting Online Material

www.sciencemag.org/cgi/content/full/1174962/DC1
SOM Text
Fig. S1
References

14 April 2009; accepted 16 June 2009
Published online 25 June 2009;
10.1126/science.1174962
Include this information when citing this paper.

REPORTS

Radio Imaging of the Very-High-Energy γ-Ray Emission Region in the Central Engine of a Radio Galaxy

The VERITAS Collaboration, the VLBA 43 GHz M87 Monitoring Team, the H.E.S.S. Collaboration, the MAGIC Collaboration*

The accretion of matter onto a massive black hole is believed to feed the relativistic plasma jets found in many active galactic nuclei (AGN). Although some AGN accelerate particles to energies exceeding 10^{12} electron volts and are bright sources of very-high-energy (VHE) γ-ray emission, it is not yet known where the VHE emission originates. Here we report on radio and VHE observations of the radio galaxy Messier 87, revealing a period of extremely strong VHE γ-ray flares accompanied by a strong increase of the radio flux from its nucleus. These results imply that charged particles are accelerated to very high energies in the immediate vicinity of the black hole.

Active galactic nuclei (AGN) are extragalactic objects thought to be powered by massive black holes in their centers. They can show strong emission from the core, which is often dominated by broadband continuum radiation ranging from radio to x-rays and by substantial flux variability on different time scales. More than 20 AGN have been established as very-high-energy (VHE) γ-ray emitters with measured energies above 0.1 TeV; the jets of most of these sources are believed to be aligned with the line of sight to within a few degrees. The size of the VHE γ-ray emission region can generally be constrained by the time scale of the observed flux variability (*1*, *2*), but its location remains unknown.

We studied the inner structure of the jet of the giant radio galaxy Messier 87 (M87), a known VHE γ-ray–emitting AGN (*2*–*5*) with a $(6.0 \pm 0.5) \times 10^9$ solar mass black hole (*6*) (scaled by distance), located 16.7 Mpc (54 million light years) away in the Virgo cluster of galaxies. The angle between its plasma jet and the line of sight is estimated to lie between 15° and 25° [see supporting online material (SOM) text]. The substructures of the jet, which are expected to scale with the Schwarzschild radius R_s of the black hole (*7*), are resolved in the x-ray, optical, and radio wave bands (*8*) (Fig. 1). High-frequency radio very-long-baseline interferometry (VLBI) observations with resolution under a milli–arc second (milli–arc sec) are starting to probe the collimation region of the jet (*9*). With its proximity, bright and well-resolved jet, and very massive black hole, M87 provides a unique laboratory in which to study relativistic jet physics in connection with the mechanisms of VHE γ-ray emission in AGN.

VLBI observations of the M87 inner jet show a well-resolved, edge-brightened structure extending to within 0.5 milli–arc sec (0.04 pc or 70 R_s) of the core. Closer to the core, the jet has a wide opening angle, suggesting that this is the collimation region (*9*). Generally, the core can be offset from the actual location of the black hole by an unknown amount (*10*), in which case it could mark the location of a shock structure or the region where the jet becomes optically thin. However, in the case of M87, a weak structure

*The full list of authors and affiliations is presented at the end of this paper.

is seen on the opposite side of the core from the main jet, which may be the counter-jet, based on its morphology and length (*11*, *12*). Together with the observed pattern in opening angles, this suggests that the black hole of M87 is located within the central resolution element of the VLBI images, at most a few tens of R_s from the radio core (see SOM text). Along the jet, previous monitoring observations show both near-stationary components (*12*) (parsec scale) and features that move at apparent superluminal speeds (*13*, *14*) (100 pc scale). The presence of superluminal motions and the strong asymmetry of the jet brightness indicate that the jet flow is relativistic. The near-stationary components could be related to shocks or instabilities that can be either stationary (for example, if they are the result of interaction with the external medium) or slowly moving (if they are the result of instabilities in the flow).

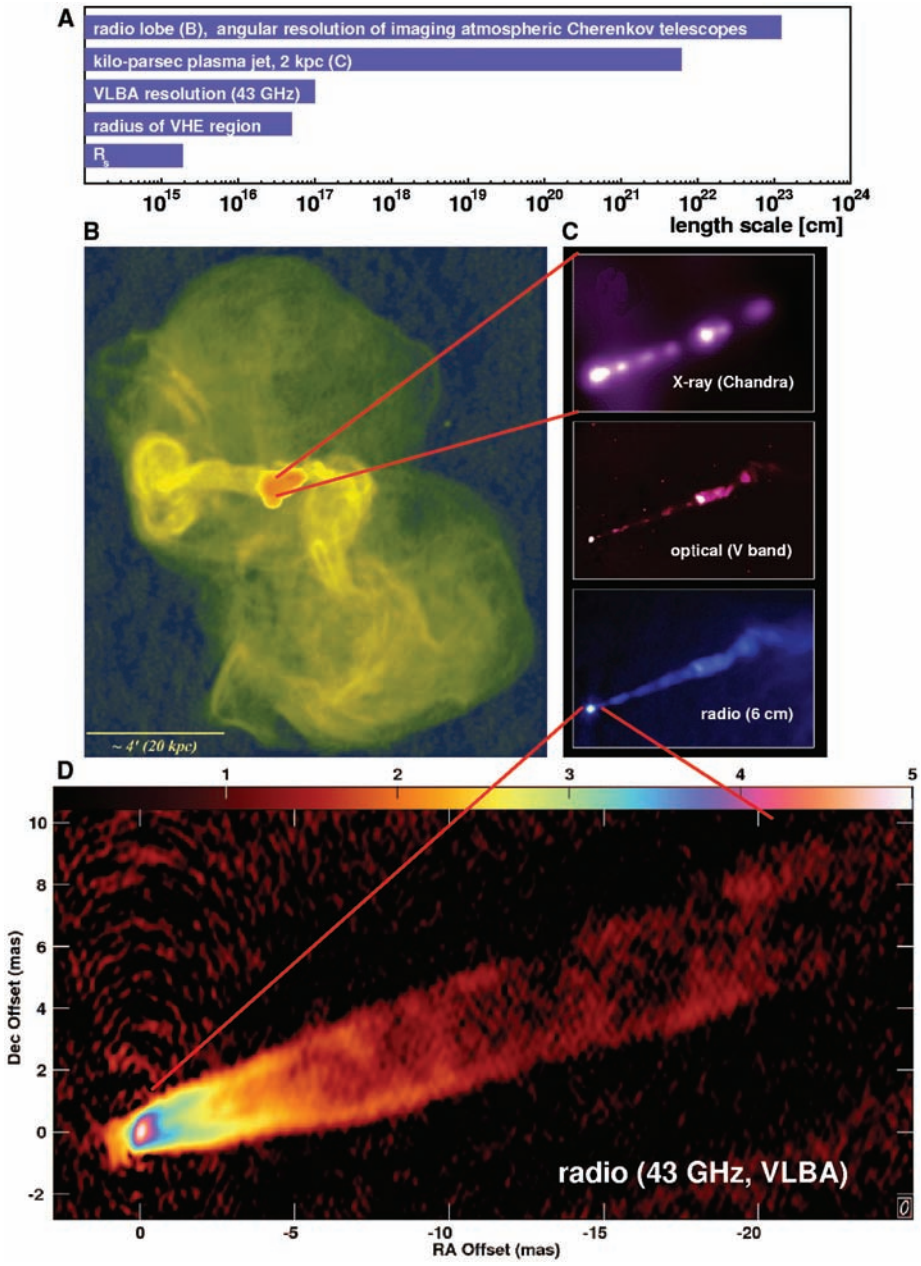

Fig. 1. M87 at different photon frequencies and length scales. (**A**) Comparison of the different length scales. (**B**) 90-cm radio emission measured with the VLA. The jet outflows terminate in a halo that has a diameter of ~80 kpc (15′). The radio emission in the central region is saturated in this image. [Credit: F. N. Owen, J. A. Eilek, and N. E. Kassim (*32*), NRAO/Associated Universities Incorporated/NSF] (**C**) Zoomed image of the plasma jet with an extension of 2 kpc (20″), seen in different frequency bands: x-rays (Chandra, top), optical (V band, middle), and radio (6 cm, bottom). Individual knots in the jet and the nucleus can be seen in all three frequency bands. The innermost knot HST-1 is located at a projected distance of 0.86 arc sec (60 pc, $\approx 10^5 R_s$) from the nucleus. [Credit: x-ray, NASA/Chandra X-Ray Observatory Science Center/Massachusetts Institute of Technology/H. Marshall *et al.*; radio, F. Zhou, F. Owen (NRAO), J. Biretta (Space Telescope Science Institute); optical, NASA/STScI/University of Maryland Baltimore County/E. Perlman *et al.* (*8*)] (**D**) An averaged, and hence smoothed, radio image based on 23 images from the VLBA monitoring project at 43 GHz. The color scale gives the logarithm of the flux density in units of 0.01 millijansky per beam. The indication of a counter-jet can be seen, emerging from the core toward the lower left side. mas, milli–arc seconds.

A first indication of VHE γ-ray emission from M87 was reported by the High Energy Gamma-Ray Astronomy (HEGRA) Collaboration in 1998/1999 (*3*). The emission was confirmed by the High Energy Stereoscopic System (H.E.S.S.) in 2003 to 2006 (*2*), with γ-ray flux variability on time scales of days. M87 was detected again with the Very Energetic Radiation Imaging Telescope Array System (VERITAS) in 2007 (*4*) and, recently, the short-term variability was confirmed with the Major Atmospheric Gamma-Ray Imaging Cherenkov (MAGIC) telescope during a strong VHE γ-ray outburst (*5*) in February 2008. Causality arguments imply that the emission region should have a spatial extent of less than $\approx 5\delta R_s$, where δ is the relativistic Doppler factor. This rules out explanations for the VHE γ-ray emission on the basis of (i) dark matter annihilation (*15*), (ii) cosmic-ray interactions with the matter in M87 (*16*), or (iii) the knots in the plasma jet (Fig. 1C). Leptonic (*17*, *18*) and hadronic (*19*) VHE γ-ray jet emission models have been proposed. However, the location of the emission region is still unknown. The nucleus (*20*, *21*), the inner jet (*22*), or larger structures in the jet, such as the knot HST-1 (Fig. 1C), have been discussed as possible sites (*14*). Because the angular resolution of VHE experiments is of the order of 0.1°, the key to identifying the location of the VHE γ-ray emission lies in connecting it to measurements at other wave bands with considerably higher spatial resolutions. An angular resolution more than six orders of magnitude better (less than 6×10^{-8} degrees, corresponding to approximately $30R_s$ in the case of M87) can be achieved with radio observations (Fig. 1).

We used the H.E.S.S. (*23*), MAGIC (*24*), and VERITAS (*25*) instruments to observe M87 during 50 nights between January and May 2008, accumulating over 95 hours of data (corrected for the detector dead times) in the energy range between 0.1 TeV and several 10s of TeV. Simultaneously, we monitored M87 with the Very Long Baseline Array (*26*) (VLBA) at 43 GHz with a resolution of 0.21 × 0.43 milli–arc sec (*27*), corresponding to about 30 × 60 R_s. During the first half of 2008, three x-ray pointings were performed with the Chandra satellite (*28*). Our light curves are shown in Fig. 2.

We detected multiple flares at VHE in February 2008 with denser sampling, following a trigger sent by MAGIC [~23 hours of the data published in (*5*)]. The short-term VHE variability, first observed in 2005 (*2*), is clearly confirmed and the flux reached the highest level observed

so far from M87, amounting to more than 10% of that of the Crab Nebula. At x-ray frequencies the innermost knot in the jet (HST-1) is found in a low state, whereas in mid-February 2008, the nucleus was found in its highest x-ray flux state since 2000 (*28*). This is in contrast to the 2005 VHE γ-ray flares (*2*), which happened after an increase of the x-ray flux of HST-1 over several years (*29*), allowing speculation that HST-1 might be the source of the VHE γ-ray emission (*14*); no 43 GHz radio observations were obtained at that time. Given its low x-ray flux in 2008, HST-1 is an unlikely site of the 2008 VHE flaring activity.

Over at least the following two months, until the VLBA monitoring project ended, the 43-GHz radio flux density from the region within 1.2 milli–arc sec of the core rose by 30%, as compared with its level at the time of the start of the VHE flare, and by 57%, as compared with the average level in 2007 (Fig. 2). The resolution of the 43-GHz images corresponds to 30 × 60 R_s, and the initial radio flux density increase was located in the unresolved core. The region around the core brightened as the flare progressed (Fig. 3), suggesting that new components were emerging from the core. At the end of the observations, the brightened region extended about 0.77 milli–arc sec from the peak of the core, implying an average apparent velocity of 1.1c (where c is the speed of light), well under the approximately 2.3c seen just beyond that distance in the first half of 2007. Astrometric results obtained as part of the VLBA monitoring program show that the position of the M87 radio peak, relative to M84, did not move by more than ~6R_s during the flare, suggesting that the peak emission corresponds to the nucleus of M87.

Because VHE, x-ray, and radio flares of the observed magnitude are uncommon, the fact that they happen together (chance probability of $P < 0.5\%$, SOM text) is good evidence that they are connected. This is supported by our joint modeling of the VHE and radio light curves: The observed pattern can be explained by an event in the central region causing the VHE flare. The plasma travels down the jet, and the effect of synchrotron self-absorption causes a delay of the observed peak in radio emission because the region is not transparent at radio energies at the beginning of the injection (SOM text, section 3). The VLBI structure of the flare, along with the timing of the VHE activity, imply that the VHE emission occurred in a region that is small when compared with the VLBA resolution. Unless a source of infrared radiation is located very close to the central black hole, which is not supported by current observations (*30*), teraelectron volt γ-ray photons can escape the central region of M87 without being heavily absorbed through e^+e^- pair production (*20*, *21*).

The light curve might indicate a rise in radio flux above the range of variations observed in the past, starting before the first VHE flare was detected. This could imply that the radio emission is coming from portions of the jet launched from further out in the accretion disk than that responsible for the VHE emission. However, it is difficult to derive a quantitive statement on this, because no VHE data were taken in the week previous to the flaring. Thus, an earlier start of the VHE activity cannot be excluded either.

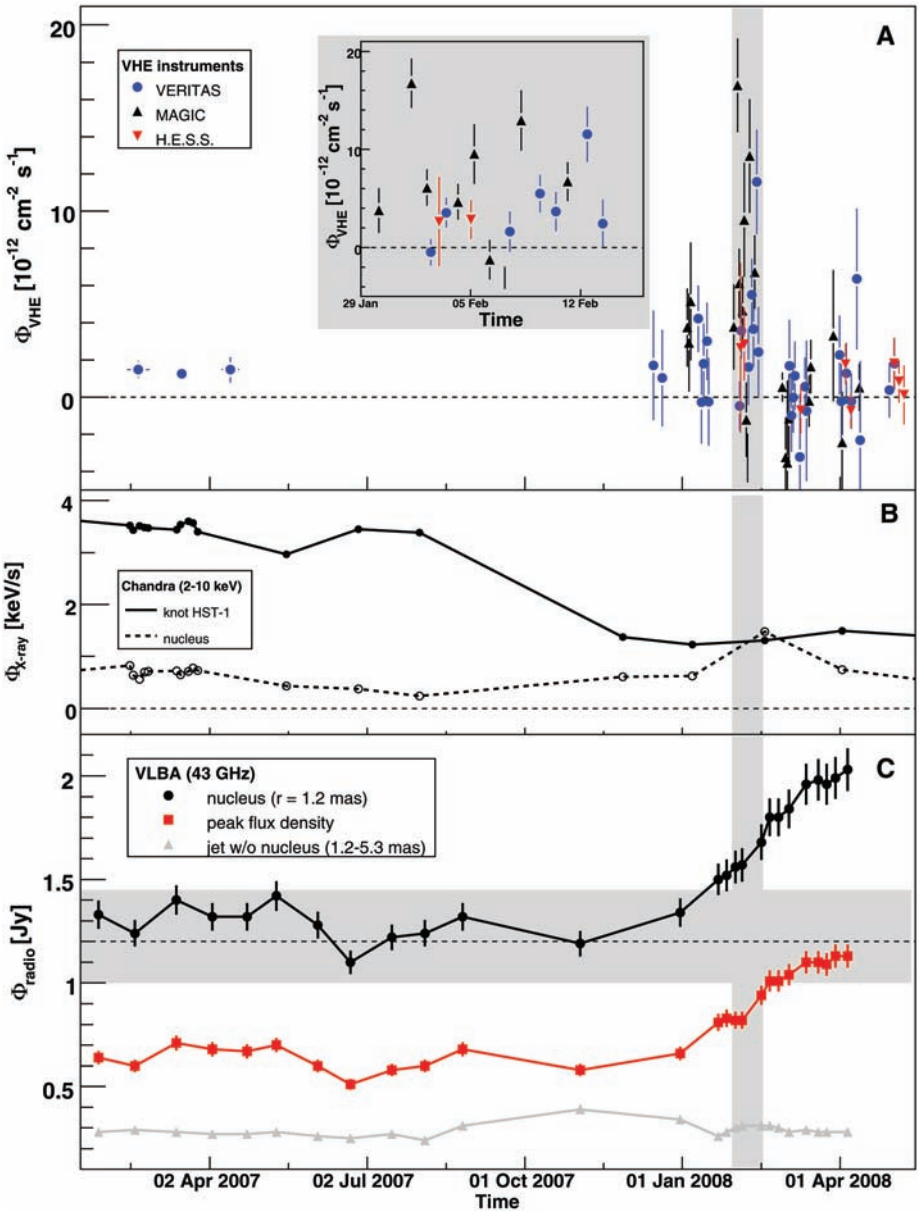

Fig. 2. Combined M87 light curves from 2007 to 2008. (**A**) VHE γ-ray fluxes ($E > 0.35$ TeV, nightly average), showing the H.E.S.S., MAGIC, and VERITAS data. The fluxes with statistical errors (1 SD) were calculated assuming a power-law spectral shape of $dN/dE \propto E^{-2.3}$. Monthly binned archival VERITAS data taken in 2007 are also shown (*4*). The systematic uncertainty in the flux calibration between the experiments was estimated to be on the order of 20%, based on Crab Nebula data. The regular gaps in the light curve correspond to phases of full moon during which no observations were possible. The inlay shows a zoomed version of the flaring activity in February 2008; the time span is indicated by the gray vertical box in all panels. (**B**) Chandra x-ray measurements (2 to 10 keV) of the nucleus and the knot HST-1 (*28*). (**C**) Flux densities from the 43-GHz VLBA observations are shown for (i) the nucleus (circular region with radius r = 1.2 milli–arc sec = 170R_s centered on the peak flux), (ii) the peak flux (VLBA resolution element), and (iii) the flux integrated along the jet between distances of r = 1.2 to 5.3 milli–arc sec (compare with Fig. 3). The error bars correspond to 5% of the flux. The shaded horizontal area indicates the range of fluxes from the nucleus before the 2008 flare. Whereas the flux of the outer regions of the jet does not change substantially, most of the flux increase results from the region around the nucleus.

A possible injection of plasma at the base of the jet observed at optical and x-ray energies, with a delayed passage through the radio core ~10^4R_s further down the jet—interpreted as a standing shock and accompanied by an increase in radio emission—has been discussed in the case of BL Lac (*10*) (with evidence for VHE emission,

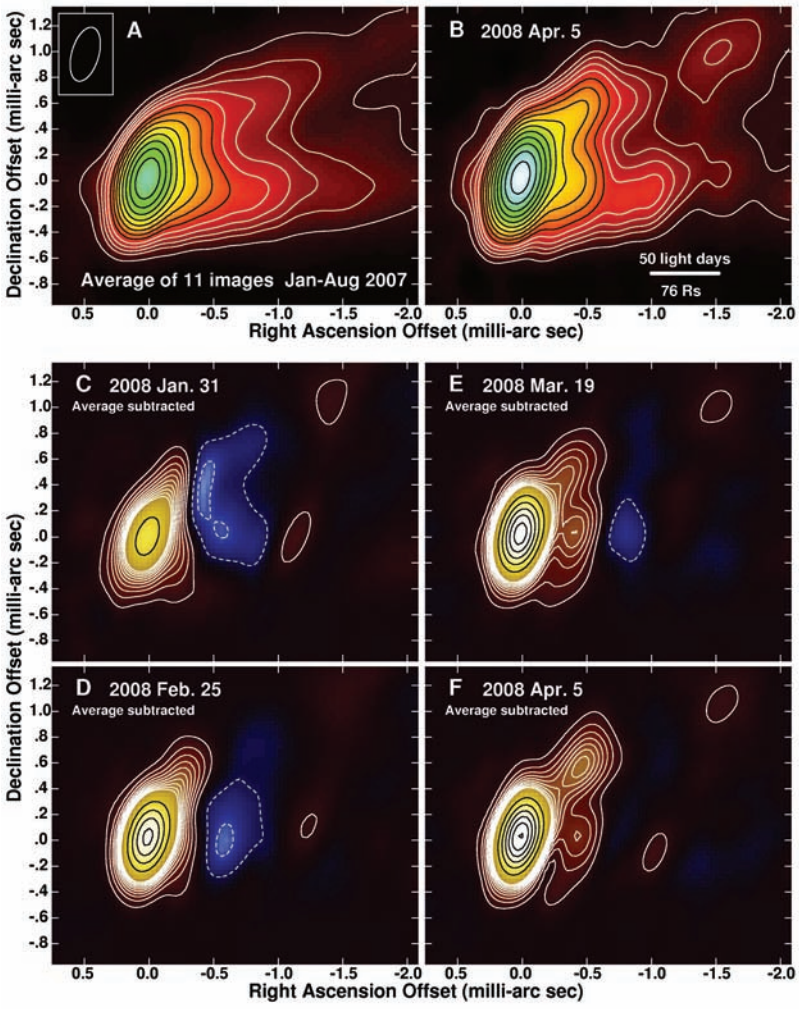

Fig. 3. VLBA images of M87 at 43 GHz. (**A**) Average (hence smoothed) of 11 images from data taken between January and August 2007, well before the VHE and radio flare. The contour levels start at 5, 10, 14.3, and 20 mJy per beam and increase from there by factors of $\sqrt{2}$. The restoring beam used for all of the images is 0.21 × 0.43 milli–arc sec (30 × 60 R_s) elongated in position angle −16°, as shown by the ellipse in the upper left corner. (**B**) Image from 5 April 2008, with the same contours and colors as in (A). The linear scale in light days and Schwarzschild radii is also shown. (**C** to **F**) Difference images for observations during the period of the radio flare, showing its effects. These were made by subtracting the average image (A) from the individual epoch images. The contours are linear with 10 (white) at intervals of 7 mJy per beam, followed by the rest (black) at intervals of 70 mJy per beam; negative contours are indicated by dashed lines. At the time of the VHE flare, the core flux density was already above the average, but the region of the jet between −0.5 and −1.0 milli–arc sec RA offset was below average, suggesting that there had been a period of below-normal activity leading up to the flare and that the radio flare may have begun before the VHE flare. The sequence shows the substantial rise in the core flux density and the appearance of enhanced emission along the inner jet.

see SOM text for more details). M87 is much closer than BL Lac and has a much more massive black hole, allowing the VLBA to start resolving the jet collimation region whose size, from general relativistic magnetohydrodynamic simulations (*31*), is thought to extend over ~1000R_s. In the case of M87, the radio core does not appear to be offset by more than the VLBA resolution of ~50R_s from the black hole (see SOM text), and the jet has a larger angle to the line of sight than in BL Lac. Thus, the coincidence of the VHE and radio flares (separated in photon frequency by 16 orders of magnitude), constrains the VHE emission to occur well within the jet collimation region.

References and Notes

1. J. A. Gaidos *et al.*, *Nature* **383**, 319 (1996).
2. F. Aharonian *et al.*, *Science* **314**, 1424 (2006); published online 26 October 2006 (10.1126/science.1134408).
3. F. Aharonian *et al.*, *Astron. Astrophys.* **403**, L1 (2003).
4. V. A. Acciari *et al.*, *Astrophys. J.* **679**, 397 (2008).
5. J. Albert *et al.*, *Astrophys. J.* **685**, L23 (2008).
6. K. Gebhardt, J. Thomas, *Astrophys. J.*, in press; preprint available at http://arxiv.org/abs/0906.1492 (2009).
7. The Schwarzschild radius of a black hole with the mass m is defined as $R_s = 2Gm/c^2$, where G is the gravitational constant. The Schwarzschild radius defines the event horizon of the black hole.
8. A. S. Wilson, Y. Yang, *Astrophys. J.* **568**, 133 (2002).
9. W. Junor, J. A. Biretta, M. Livio, *Nature* **401**, 891 (1999).
10. A. P. Marscher *et al.*, *Nature* **452**, 966 (2008).
11. C. Ly, R. C. Walker, W. Junor, *Astrophys. J.* **660**, 200 (2007).
12. Y. Y. Kovalev, M. L. Lister, D. C. Homan, K. I. Kellermann, *Astrophys. J.* **668**, L27 (2007).
13. J. A. Biretta, W. B. Sparks, F. Macchetto, *Astrophys. J.* **520**, 621 (1999).
14. C. C. Cheung, D. E. Harris, L. Stawarz, *Astrophys. J.* **663**, L65 (2007).
15. E. A. Baltz *et al.*, *Phys. Rev. D* **61**, 023514 (2000).
16. C. Pfrommer, T. A. Enßlin, *Astron. Astrophys.* **407**, L73 (2003).
17. M. Georganopoulos, E. S. Perlman, D. Kazanas, *Astrophys. J.* **634**, L33 (2005).
18. J.-P. Lenain *et al.*, *Astron. Astrophys.* **478**, 111 (2008).
19. A. Reimer, R. J. Protheroe, A.-C. Donea, *Astron. Astrophys.* **419**, 89 (2004).
20. A. Neronov, F. A. Aharonian, *Astrophys. J.* **671**, 85 (2007).
21. F. M. Rieger, F. A. Aharonian, *Int. J. Mod. Phys. D* **17**, 1569 (2008).
22. F. Tavecchio, G. Ghisellini, *Mon. Not. R. Astron. Soc.* **385**, L98 (2008).
23. F. Aharonian *et al.*, *Astron. Astrophys.* **457**, 899 (2006).
24. J. Albert *et al.*, *Astrophys. J.* **674**, 1037 (2008).
25. V. A. Acciari *et al.*, *Astrophys. J.* **679**, 1427 (2008).
26. P. J. Napier *et al.*, *Proc. IEEE* **82**, 658 (1994).
27. R. C. Walker, C. Ly, W. Junor, P. E. Hardee, *J. Phys. Conf. Ser.* **131**, 012053 (2008).
28. D. E. Harris, C. C. Cheung, L. Stawarz, J. A. Biretta, E. S. Perlman, *Astrophys. J.* **699**, 305 (2009).
29. D. E. Harris *et al.*, *Astrophys. J.* **640**, 211 (2006).
30. E. S. Perlman *et al.*, *Astrophys. J.* **663**, 808 (2007).
31. J. C. McKinney, *Mon. Not. R. Astron. Soc.* **368**, 1561 (2006).
32. F. N. Owen, J. A. Eilek, N. E. Kassim, *Astrophys. J.* **543**, 611 (2000).

33. H.E.S.S.: We thank the Namibian authorities and the University of Namibia for support in facilitating the construction and operation of H.E.S.S. We also thank the German Ministry for Education and Research (BMBF), the Max Planck Society, the French Ministry for Research, CNRS-IN2P3 and the Astroparticle Interdisciplinary Programme of CNRS, the U.K. Science and Technology Facilities Council (STFC), the Institute of Particle and Nuclear Physics of the Charles University, the Polish Ministry of Science and Higher Education, and the South African Department of Science and Technology and National Research Foundation for support. We appreciate the excellent work of the technical support staff in Berlin, Durham, Hamburg, Heidelberg, Palaiseau, Paris, and Saclay and also in Namibia in the construction and operation of the equipment. MAGIC: We thank the Instituto de Astrofísica de Canarias for the excellent working conditions at the Observatorio del Roque de los Muchachos in La Palma, as well as the German BMBF and MPG, the Italian INFN and Spanish Ministerio de Ciencia e Innovación. This work was also supported by ETH research grant TH 34/043, the Polish MniSzW grant N N203 390834, and the Young Investigators Program of the Helmholtz Gemeinschaft. VERITAS: This research is supported by grants from the U.S. Department of Energy, NSF, the Smithsonian Institution, the Natural Sciences and Engineering Research Council of Canada, Science Foundation Ireland, and the STFC in the U.K. We acknowledge the excellent work of the technical support staff at the Fred Lawrence Whipple Observatory and the collaborating institutions in the construction and operation of the instrument. VLBA: The Very Long Baseline Array is operated by the National Radio Astronomy Observatory, a facility of NSF, operated under cooperative agreement by Associated Universities, Inc.

***The VERITAS Collaboration:** V. A. Acciari,[1] E. Aliu,[2] T. Arlen,[3] M. Bautista,[4] M. Beilicke,[5]† W. Benbow,[1] S. M. Bradbury,[6] J. H. Buckley,[5] V. Bugaev,[5] Y. Butt,[7] K. Byrum,[8] A. Cannon,[9] O. Celik,[3] A. Cesarini,[10] Y. C. Chow,[3] L. Ciupik,[11] P. Cogan,[4] W. Cui,[12] R. Dickherber,[5] S. J. Fegan,[3] J. P. Finley,[12] P. Fortin,[13] L. Fortson,[11] A.

Furniss,[14] D. Gall,[12] G. H. Gillanders,[10] J. Grube,[9] R. Guenette,[4] G. Gyuk,[11] D. Hanna,[4] J. Holder,[2] D. Horan,[15] C. M. Hui,[16] T. B. Humensky,[17] A. Imran,[18] P. Kaaret,[19] N. Karlsson,[11] D. Kieda,[16] J. Kildea,[1] A. Konopelko,[20] H. Krawczynski,[5]† F. Krennrich,[18] M. J. Lang,[10] S. LeBohec,[16] G. Maier,[4] A. McCann,[4] M. McCutcheon,[4] J. Millis,[21] P. Moriarty,[22] R. A. Ong,[3] A. N. Otte,[14] D. Pandel,[19] J. S. Perkins,[1] D. Petry,[23] M. Pohl,[18] J. Quinn,[9] K. Ragan,[4] L. C. Reyes,[24] P. T. Reynolds,[25] E. Roache,[1] E. Roache,[1] H. J. Rose,[6] M. Schroedter,[18] G. H. Sembroski,[12] A. W. Smith,[8] S. P. Swordy,[17] M. Theiling,[1] J. A. Toner,[10] A. Varlotta,[12] S. Vincent,[16] S. P. Wakely,[17] J. E. Ward,[9] T. C. Weekes,[1] A. Weinstein,[3] D. A. Williams,[14] S. Wissel,[17] M. Wood[3]

The VLBA 43 GHz M87 Monitoring Team: R. C. Walker,[26]† F. Davies,[26,27] P. E. Hardee,[28]† W. Junor,[29] C. Ly[30]

The H.E.S.S. Collaboration: F. Aharonian,[31,43] A. G. Akhperjanian,[32] G. Anton,[46] U. Barres de Almeida,[38]‡ A. R. Bazer-Bachi,[33] Y. Becherini,[42] B. Behera,[44] K. Bernlöhr,[31,35] A. Bochow,[31] C. Boisson,[36] J. Bolmont,[49] V. Borrel,[33] J. Brucker,[46] F. Brun,[49] P. Brun,[37] R. Bühler,[31] T. Bulik,[54] I. Büsching,[39] T. Boutelier,[47] P. M. Chadwick,[38] A. Charbonnier,[49] R. C. G. Chaves,[31] A. Cheesebrough,[38] L.-M. Chounet,[40] A. C. Clapson,[31] G. Coignet,[41] M. Dalton,[35] M. K. Daniel,[38] I. D. Davids,[39,52] B. Degrange,[40] C. Deil,[31] H. J. Dickinson,[38] A. Djannati-Ataï,[42] W. Domainko,[31] L. O'C. Drury,[43] F. Dubois,[41] G. Dubus,[47] J. Dyks,[54] M. Dyrda,[58] K. Egberts,[31] D. Emmanoulopoulos,[44] P. Espigat,[42] C. Farnier,[45] F. Feinstein,[45] A. Fiasson,[45] A. Förster,[31] G. Fontaine,[40] M. Füßling,[35] S. Gabici,[43] Y. A. Gallant,[45] L. Gérard,[42] D. Gerbig,[51] B. Giebels,[40] J. F. Glicenstein,[37] B. Glück,[46] P. Goret,[37] D. Göhring,[46] D. Hauser,[44] M. Hauser,[44] S. Heinz,[46] G. Heinzelmann,[34] G. Henri,[47] G. Hermann,[31] J. A. Hinton,[55] A. Hoffmann,[48] W. Hofmann,[31] M. Holleran,[39] S. Hoppe,[31] D. Horns,[34] A. Jacholkowska,[49] O. C. de Jager,[39] C. Jahn,[46] I. Jung,[46] K. Katarzyński,[57] U. Katz,[46] S. Kaufmann,[44] E. Kendziorra,[48] M. Kerschhaggl,[35] D. Khangulyan,[31] B. Khélifi,[40] D. Keogh,[38] W. Kluźniak,[54] T. Kneiske,[34] Nu. Komin,[37] K. Kosack,[31] G. Lamanna,[41] J.-P. Lenain,[36] T. Lohse,[35] V. Marandon,[42] J. M. Martin,[36] O. Martineau-Huynh,[49] A. Marcowith,[45] D. Maurin,[49] T. J. L. McComb,[38] M. C. Medina,[36] R. Moderski,[54] E. Moulin,[37] M. Naumann-Godo,[40] M. de Naurois,[49] D. Nedbal,[50] D. Nekrassov,[31] B. Nicholas,[56] J. Niemiec,[58] S. J. Nolan,[38] S. Ohm,[31] J.-F. Olive,[33] E. de Oña Wilhelmi,[42,59] K. J. Orford,[38] M. Ostrowski,[53] M. Panter,[31] M. Paz Arribas,[35] G. Pedaletti,[44] G. Pelletier,[47] P.-O. Petrucci,[47] S. Pita,[42] G. Pühlhofer,[44] M. Punch,[42] A. Quirrenbach,[44] B. C. Raubenheimer,[39] M. Raue,[31,59]† S. M. Rayner,[38] M. Renaud,[42,31] F. Rieger,[31,59] J. Ripken,[34] L. Rob,[50] S. Rosier-Lees,[41] G. Rowell,[56] B. Rudak,[54] C. B. Rulten,[38] J. Ruppel,[51] V. Sahakian,[32] A. Santangelo,[48] R. Schlickeiser,[51] F. M. Schöck,[46] R. Schröder,[51] U. Schwanke,[35] S. Schwarzburg,[48] S. Schwemmer,[44] A. Shalchi,[51] M. Sikora,[54] J. L. Skilton,[55] H. Sol,[36] D. Spangler,[38] Ł. Stawarz,[53] R. Steenkamp,[52] C. Stegmann,[46] F. Stinzing,[46] G. Superina,[40] A. Szostek,[53,47] P. H. Tam,[44] J.-P. Tavernet,[49] R. Terrier,[42] O. Tibolla,[31,44] M. Tluczykont,[34] C. van Eldik,[31] G. Vasileiadis,[45] C. Venter,[39] L. Venter,[36] J. P. Vialle,[41] P. Vincent,[49] M. Vivier,[37] H. J. Völk,[31] F. Volpe,[31,40,59] S. J. Wagner,[44] M. Ward,[38] A. A. Zdziarski,[54] A. Zech[36]

The MAGIC Collaboration: H. Anderhub,[60] L. A. Antonelli,[61] P. Antoranz,[62] M. Backes,[63] C. Baixeras,[64] S. Balestra,[62] J. A. Barrio,[62] D. Bastieri,[65] J. Becerra González,[66] J. K. Becker,[63] W. Bednarek,[67] K. Berger,[67] E. Bernardini,[68] A. Biland,[60] R. K. Bock,[65,69] G. Bonnoli,[70] P. Bordas,[71] D. Borla Tridon,[69] V. Bosch-Ramon,[71] D. Bose,[62] I. Braun,[60] T. Bretz,[72] I. Britvitch,[60] M. Camara,[62] E. Carmona,[69] S. Commichau,[60] J. L. Contreras,[62] J. Cortina,[73] M. T. Costado,[66,74] S. Covino,[61] V. Curtef,[63] F. Dazzi,[75]§ A. De Angelis,[75] E. De Cea del Pozo,[76] C. Delgado Mendez,[66] R. De los Reyes,[62] B. De Lotto,[75] M. De Maria,[75] F. De Sabata,[75] A. Dominguez,[77] D. Dorner,[60] M. Doro,[65] D. Elsaesser,[72] M. Errando,[73] D. Ferenc,[78] E. Fernández,[73] R. Firpo,[73] M. V. Fonseca,[62] L. Font,[64] N. Galante,[69] R. J. García López,[66,74] M. Garczarczyk,[73] M. Gaug,[66] F. Goebel,[69]|| D. Hadasch,[64] M. Hayashida,[69] A. Herrero,[66,74] D. Hildebrand,[60] D. Höhne-Mönch,[72] J. Hose,[69] C. C. Hsu,[69] T. Jogler,[69] D. Kranich,[60] A. La Barbera,[61] A. Laille,[78] E. Leonardo,[70] E. Lindfors,[79] S. Lombardi,[65] F. Longo,[75] M. López,[65] E. Lorenz,[60,69] P. Majumdar,[68] G. Maneva,[80] N. Mankuzhiyil,[75] K. Mannheim,[72] L. Maraschi,[61] M. Mariotti,[65] M. Martínez,[73] D. Mazin,[73]† M. Meucci,[70] J. M. Miranda,[62] R. Mirzoyan,[69] H. Miyamoto,[69] J. Moldón,[71] M. Moles,[77] A. Moralejo,[73] D. Nieto,[62] K. Nilsson,[79] J. Ninkovic,[69] I. Oya,[62] R. Paoletti,[70] J. M. Paredes,[71] M. Pasanen,[79] D. Pascoli,[65] F. Pauss,[60] R. G. Pegna,[70] M. A. Perez-Torres,[77] M. Persic,[75,81] L. Peruzzo,[65] F. Prada,[77] E. Prandini,[65] N. Puchades,[73] I. Reichardt,[73] W. Rhode,[63] M. Ribó,[71] J. Rico,[73,82] M. Rissi,[60] A. Robert,[64] S. Rügamer,[72] A. Saggion,[65] T. Y. Saito,[69] M. Salvati,[61] M. Sanchez-Conde,[77] K. Satalecka,[68] V. Scalzotto,[65] V. Scapin,[75] T. Schweizer,[69] M. Shayduk,[69] S. N. Shore,[83] N. Sidro,[73] A. Sierpowska-Bartosik,[76] A. Sillanpää,[79] J. Sitarek,[67,69] D. Sobczynska,[67] F. Spanier,[72] A. Stamerra,[70] L. S. Stark,[60] L. Takalo,[79] F. Tavecchio,[61] P. Temnikov,[80] D. Tescaro,[73] M. Teshima,[69] D. F. Torres,[76,82] N. Turini,[70] H. Vankov,[80] R. M. Wagner,[69]† V. Zabalza,[71] F. Zandanel,[77] R. Zanin,[73] J. Zapatero[64]

[1]Fred Lawrence Whipple Observatory, Harvard-Smithsonian Center for Astrophysics, Amado, AZ 85645, USA. [2]Department of Physics and Astronomy and the Bartol Research Institute, University of Delaware, Newark, DE 19716, USA. [3]Department of Physics and Astronomy, University of California, Los Angeles, CA 90095, USA. [4]Physics Department, McGill University, Montreal, Quebec H3A 2T8, Canada. [5]Department of Physics, Washington University, St. Louis, MO 63130, USA. [6]School of Physics and Astronomy, University of Leeds, Leeds, LS2 9JT, UK. [7]Harvard-Smithsonian Center for Astrophysics, 60 Garden Street, Cambridge, MA 02138, USA. [8]Argonne National Laboratory, 9700 South Cass Avenue, Argonne, IL 60439, USA. [9]School of Physics, University College Dublin, Belfield, Dublin 4, Ireland. [10]School of Physics, National University of Ireland, Galway, Ireland. [11]Astronomy Department, Adler Planetarium and Astronomy Museum, Chicago, IL 60605, USA. [12]Department of Physics, Purdue University, West Lafayette, IN 47907, USA. [13]Department of Physics and Astronomy, Barnard College, Columbia University, NY 10027, USA. [14]Santa Cruz Institute for Particle Physics and Department of Physics, University of California, Santa Cruz, CA 95064, USA. [15]Laboratoire Leprince-Ringuet, Ecole Polytechnique, CNRS/IN2P3, F-91128 Palaiseau, France. [16]Department of Physics and Astronomy, University of Utah, Salt Lake City, UT 84112, USA. [17]Enrico Fermi Institute, University of Chicago, Chicago, IL 60637, USA. [18]Department of Physics and Astronomy, Iowa State University, Ames, IA 50011, USA. [19]Department of Physics and Astronomy, University of Iowa, Van Allen Hall, Iowa City, IA 52242, USA. [20]Department of Physics, Pittsburg State University, 1701 South Broadway, Pittsburg, KS 66762, USA. [21]Department of Physics, Anderson University, 1100 East 5th Street, Anderson, IN 46012. [22]Department of Life and Physical Sciences, Galway-Mayo Institute of Technology, Dublin Road, Galway, Ireland. [23]European Southern Observatory, Karl-Schwarzschild-Strasse 2, 85748 Garching, Germany. [24]Kavli Institute for Cosmological Physics, University of Chicago, Chicago, IL 60637, USA. [25]Department of Applied Physics and Instrumentation, Cork Institute of Technology, Bishopstown, Cork, Ireland. [26]National Radio Astronomy Observatory (NRAO), Socorro, NM 87801, USA. [27]Physics Department, 333 Workman Center, New Mexico Institute of Mining and Technology, 801 Leroy Place, Socorro, NM 87801, USA. [28]Department of Physics and Astronomy, University of Alabama, Tuscaloosa, AL 35487, USA. [29]ISR-2, MS-D436, Los Alamos National Laboratory, Los Alamos, NM 87545, USA. [30]Department of Astronomy, University of California, Los Angeles, CA 90095–1547, USA. [31]Max-Planck-Institut für Kernphysik, Post Office Box 103980, D-69029 Heidelberg, Germany. [32]Yerevan Physics Institute, 2 Alikhanian Brothers Street, 375036 Yerevan, Armenia. [33]Centre d'Etude Spatiale des Rayonnements, CNRS/UPS, 9 Avenue du Colonel Roche, BP 4346, F-31029 Toulouse Cedex 4, France. [34]Universität Hamburg, Institut für Experimentalphysik, Luruper Chaussee 149, D-22761 Hamburg, Germany. [35]Institut für Physik, Humboldt-Universität zu Berlin, Newtonstrasse. 15, D-12489 Berlin, Germany. [36]Laboratoire Univers et Théories, Observatoire de Paris, CNRS, Université Paris Diderot, 5 Place Jules Janssen, 92190 Meudon, France. [37]Institut de Recherche sur les lois Fondamentales de l'Univers/La Direction des Sciences de la Matière/Commissariat a l'Energie Atomique CE Saclay, F-91191 Gif-sur-Yvette, Cedex, France. [38]University of Durham, Department of Physics, South Road, Durham DH1 3LE, UK. [39]Unit for Space Physics, North-West University, Potchefstroom 2520, South Africa. [40]Laboratoire Leprince-Ringuet, Ecole Polytechnique, CNRS/IN2P3, F-91128 Palaiseau, France. [41]Laboratoire d'Annecy-le-Vieux de Physique des Particules, CNRS/IN2P3, 9 Chemin de Bellevue, BP 110 F-74941 Annecy-le-Vieux Cedex, France. [42]UMR 7164 (CNRS, Université Paris VII, CEA, Observatoire de Paris); Astroparticule et Cosmologie, CNRS; Universite Paris 7 Denis Diderot, 10, rue Alice Domon et Leonie Duquet, F-75205 Paris Cedex 13, France. [43]Dublin Institute for Advanced Studies, 5 Merrion Square, Dublin 2, Ireland. [44]Landessternwarte, Universität Heidelberg, Königstuhl, D-69117 Heidelberg, Germany. [45]Laboratoire de Physique Théorique et Astroparticules, Université Montpellier 2, CNRS/IN2P3, CC 70, Place Eugène Bataillon, F-34095 Montpellier Cedex 5, France. [46]Universität Erlangen-Nürnberg, Physikalisches Institut, Erwin-Rommel-Strasse 1, D-91058 Erlangen, Germany. [47]Laboratoire d'Astrophysique de Grenoble, Institut National des Sciences de l'Univers/CNRS, Université Joseph Fourier, BP 53, F-38041 Grenoble Cedex 9, France. [48]Institut für Astronomie und Astrophysik, Universität Tübingen, Sand 1, D-72076 Tübingen, Germany. [49]Laboratoire de Physique Nucléaire et des Hautes, Université Pierre et Marie Curie Paris 6, Université Denis Diderot Paris 7, CNRS/IN2P3, 4 Place Jussieu, F-75252, Paris Cedex 5, France. [50]Charles University, Faculty of Mathematics and Physics, Institute of Particle and Nuclear Physics, V Holesovickách 2, 180 00, Prague, Czech Republic. [51]Institut für Theoretische Physik, Lehrstuhl IV: Weltraum und Astrophysik, Ruhr-Universität Bochum, D-44780 Bochum, Germany. [52]University of Namibia, Private Bag 13301, Windhoek, Namibia. [53]Obserwatorium Astronomiczne, Uniwersytet Jagielloński, ulica Orla 171, 30-244 Kraków, Poland. [54]Nicolaus Copernicus Astronomical Center, ulica Bartycka 18, 00-716 Warsaw, Poland. [55]School of Physics and Astronomy, University of Leeds, Leeds LS2 9JT, UK. [56]School of Chemistry and Physics, University of Adelaide, Adelaide 5005, Australia. [57]Toruń Centre for Astronomy, Nicolaus Copernicus University, ulica Gagarina 11, 87-100 Toruń, Poland. [58]Instytut Fizyki Jadrowej PAN, ulica Radzikowskiego 152, 31-342 Kraków, Poland. [59]European Associated Laboratory for Gamma-Ray Astronomy, jointly supported by CNRS and Max-Planck-Gessellschaft. [60]ETH Zurich, CH-8093 Switzerland. [61]Istituto Nazionale di Astrofisica (INAF) National Institute for Astrophysics, I-00136 Rome, Italy. [62]Universidad Complutense, E-28040 Madrid, Spain. [63]Technische Universität Dortmund, D-44221 Dortmund, Germany. [64]Universitat Autònoma de Barcelona, E-08193 Bellaterra, Spain. [65]Università di Padova and Istituto Nazionale di Fisica Nucleare (INFN), I-35131 Padova, Italy. [66]Instituto de Astrofísica de Canarias, E-38200 La Laguna, Tenerife, Spain. [67]University of Łódź, PL-90236 Lodz, Poland. [68]Deutsches Elektronen-Synchrotron, D-15738 Zeuthen, Germany. [69]Max-Planck-Institut für Physik, D-80805 München, Germany. [70]Università di Siena, and INFN Pisa, I-53100 Siena, Italy. [71]Universitat de Barcelona [Institut de Ciencias del Cosmos/Institut d'Estudis Espacials de Catalunya (IEEC)], E-08028 Barcelona, Spain. [72]Universität Würzburg, D-97074 Würzburg, Germany. [73]Institut de Física d'Altes Energies, Edifici Cn, Campus Universitat Autònoma de Barcelona, E-08193 Bellaterra, Spain. [74]Departamento de Astrofísica, Universidad, E-38206 La Laguna, Tenerife, Spain. [75]Università di Udine, and INFN Trieste, I-33100 Udine, Italy. [76]Institut de Cienciès de l'Espai [IEEC–Consejo Superior de Investigaciones Científicas (CSIC)], E-08193 Bellaterra, Spain. [77]Institut de Astrofísica de Andalucia (CSIC), E-18080 Granada, Spain. [78]University of California, Davis, CA 95616–8677, USA. [79]Tuorla Observatory, Turku University, FI-21500 Piikkiö, Finland. [80]Institute for Nuclear Research and Nuclear Energy, BG-1784 Sofia, Bulgaria. [81]INAF/Osservatorio Astronomico and INFN, I-34143 Trieste, Italy. [82]Institució Catalana de Recerca i Estudis Avançats, E-08010 Barcelona, Spain. [83]Università di Pisa, and INFN Pisa, I-56126 Pisa, Italy.

†To whom correspondence should be addressed. E-mail: beilicke@physics.wustl.edu (M.B.); krawcz@wuphys.wustl.edu (H.K.); cwalker@aoc.nrao.edu (R.C.W.); phardee@bama.ua.edu (P.E.H.); martin.raue@mpi-hd.mpg.de (M.R.); mazin@ifae.es (D.M.); robert.wagner@mpp.mpg.de (R.M.W.)

‡Supported by Coordenacao de Aperfeicoamento de Pessoal de Nivel Superior Foundation, Ministry of Education of Brazil.
§Supported by INFN Padova.

||Deceased.

Supporting Online Material

www.sciencemag.org/cgi/content/full/1175406/DC1
SOM Text
Figs. S1 and S2
References

24 April 2009; accepted 24 June 2009
Published online 2 July 2009;
10.1126/science.1175406
Include this information when citing this paper.

Structural Origin of Circularly Polarized Iridescence in Jeweled Beetles

Vivek Sharma,[1,2] Matija Crne,[2,3] Jung Ok Park,[1,2] Mohan Srinivasarao[1,2,3]

The iridescent metallic green beetle, *Chrysina gloriosa*, which selectively reflects left circularly polarized light, possesses an exoskeleton decorated by hexagonal cells (~10 μm) that coexist with pentagons and heptagons. The fraction of hexagons decreases with an increase in curvature. In bright field microscopy, each cell contains a bright yellow core, placed in a greenish cell with yellowish border, but the core disappears in dark field. With use of confocal microscopy, we observe that these cells consist of nearly concentric nested arcs that lie on the surface of a shallow cone. We infer that the patterns are structurally and optically analogous to the focal conic domains formed spontaneously on the free surface of a cholesteric liquid crystal. These textures provide the basis for the morphogenesis as well as key insights for emulating the intricate optical response of the exoskeleton of scarab beetles.

Iridescent beetles, butterflies, certain sea organisms, and many birds derive their color from the interaction of light with the structure or morphology that is imprinted on their exoskeletons (*1*–*5*). The bright and varied colors of beetles have been of interest to scientists (*2*, *6*–*8*), but they also have a long and interesting history as "jewel beetles," which were used in textiles or ornaments (*9*) in many Asian countries. The study of photonics in nature reveals beautiful and diverse examples of subwavelength structural features that create observed colors through thin layered or multilayered interference, diffraction, zero order diffraction, and light scattering (*1*–*5*) and often with contributions from pigmentation as well. The complexity of the patterns is in part determined genetically, but the final development and control is related to the conditions during the formation of the pattern (*10*, *11*). The physical and chemical aspects of morphogenesis can be unraveled by studying the patterns in nature and analyzing their analogs in equilibrium and nonequilibrium patterns formed in condensed matter (*12*–*15*). The quest for miniature optical devices and photonics is most likely to benefit from the study of bioengineered organs and organelles of the biological world. Rational design requires one to understand how basic structural units interact with light and how they can be fabricated by either self-assembly or a top-down approach.

In this context, we have been examining the structure on the exocuticle of the beetle *Chrysina gloriosa* (or *Plusiotis gloriosa*), which selectively reflects left circularly polarized light and possesses a brilliant metallic appearance (Fig. 1). If left circularly polarized light is blocked by the use of a quarter wave plate and a polarizer, as shown in Fig. 1B, the beetle loses its characteristic bright green reflection. The ability of certain species of beetles to reflect circularly polarized light has been investigated for nearly a century (*16*–*20*), since it was first reported by Michelson (*6*). Recently Goldstein (*7*) summarized the history of optical measurements made in scarab beetles and performed ellipsometric studies confirming their polarizing behavior. The reflectance of the *C. gloriosa* beetle has a broad halo from 500 to 600 nm with two peaks at 530 (green) and 580 nm (yellow), respectively.

When the exoskeleton of the beetle is observed under an optical microscope, the body appears as a richly decorated mosaic of cusps and color, consisting of a regularly spaced lattice of features that distinguish one species of beetle from the other. In bright field microscopy (Fig. 2), the structure of *C. gloriosa* seems to consist of hexagonal cells (~10 μm), where each cell appears to be green with a bright yellow core or nucleus. We characterized the extent of hexagonal order in patterns by using Voronoi analysis, which is a versatile method for pattern recognition and for modeling the properties of spatial structures (*21*). Although the population of six-sided polygons is the highest, there exist large numbers of five- and seven-sided polygons. If we define P_n to represent the fraction of n-sided polygons, we find that P_5 decreased from 0.34 at the highly curved head to about 0.19 at the flattest region on the beetles' back, whereas P_7 is typically close to 0.13 everywhere else. Although most of the pentagons and heptagons occur in clusters, there are finite numbers of pentagons that occur individually. The number and spatial distribution of polygons characterizes the spatial order. Entropy, $S = -\Sigma P_n \ln P_n$, of the structure was determined for each image. Whereas for perfectly ordered hexagons $P_6 = 1$ and $S = 0$, the value of the entropy on beetle exoskeleton varies between 0.85 and 0.95. Both P_5 and entropy are higher in the regions of greater curvature, revealing packing issues on curved surfaces.

The head, thorax, and abdomen of a beetle are all curved, although the radius of curvature, R, is large compared with the size of individual cells, a, or $R/a >> 1$. Although hexagonal packing provides the most efficient utilization of space on a plane, defects in coordination number are essential for wrapping such tessellations on a sphere (*22*). For example, soccer balls and C60 (fullerenes) contain 12 pentagons in addition to the hexagons that template the curved structure. Because the beetle has a curved body, a certain number of pentagons is expected, but the analysis reveals much higher disorder. According to Nelson (*22*), the energetic cost associated with creating these 12 defects scales as YR^2, where Y is the two-dimensional (2D) Young's modulus. Because the cost becomes substantial for systems with large R/a, the system creates minimum-energy configurations for the curved substrates by incorporating grain boundaries and defects (*22*–*24*). This results in the faceted morphology of viruses (*22*) and grain boundary scars in colloidosomes (particles packed on a spherical droplet) (*23*). We can infer that the exoskeleton of the beetle possesses imperfect hexagonal, cellular pattern because sixfold triangulations or hexagons are not energetically favored everywhere.

We examined the beetle exoskeleton with use of a laser scanning confocal microscope [Leica TCS SP DMR XE (Leica Microsystems GmbH, Wetzlar, Germany)] and reconstructed a 3D map of the underlying structure by using the auto-

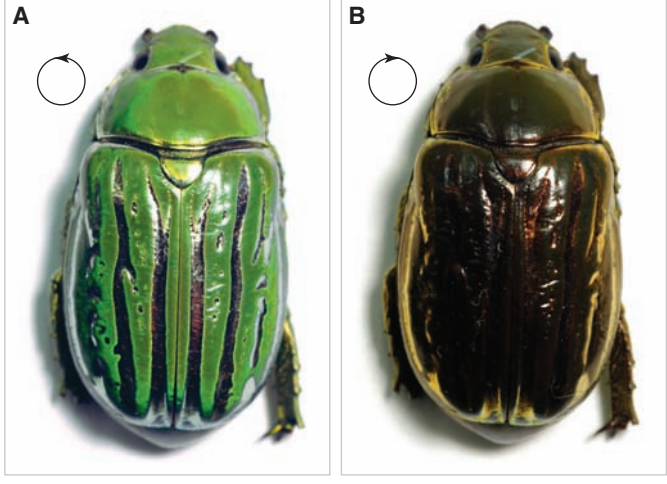

Fig. 1. Photographs of the beetle *C. gloriosa*. (**A**) The bright green color, with silver stripes as seen in unpolarized light or with a left circular polarizer. (**B**) The green color is mostly lost when seen with a right circular polarizer.

[1]School of Polymer, Textile, and Fiber Engineering, Georgia Institute of Technology, Atlanta, GA 30332, USA. [2]Center for Advanced Research on Optical Microscopy (CAROM), Georgia Institute of Technology, Atlanta, GA 30332, USA. [3]School of Chemistry and Biochemisty, Georgia Institute of Technology, Atlanta, GA 30332, USA.

fluorescence of the beetle under the excitation of a 488-nm laser. The relief of the cells, when observed under high magnification, consists of bright and dark nearly concentric regions, as shown in Fig. 3, A to C. The fluorescence response from the unidentified fluorophore present in the elytra is dependent on the polarization state and intensity of light that excites it. Hence, the darker regions could point to either changing fluorophore orientation or to a change in the fluorophore concentration. The 3D reconstruction of the images suggests the former: It shows the existence of a microstructure of nested arcs, and the cells seem to have a conical protrusion at the center.

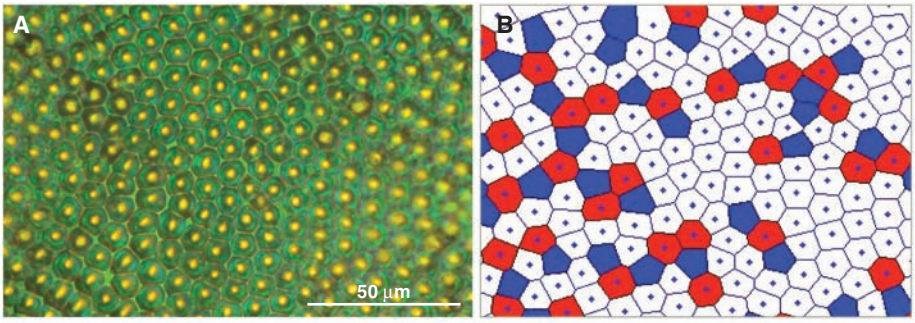

Fig. 2. (**A**) An optical micrograph of the exoskeleton of beetle *C. gloriosa* showing bright yellow reflections from the core of each cell (~10 μm in size) and greenish reflection from the edges. (**B**) Voronoi analysis of a section from the corresponding image. Pentagons are colored blue, heptagons are red, and hexagons are white.

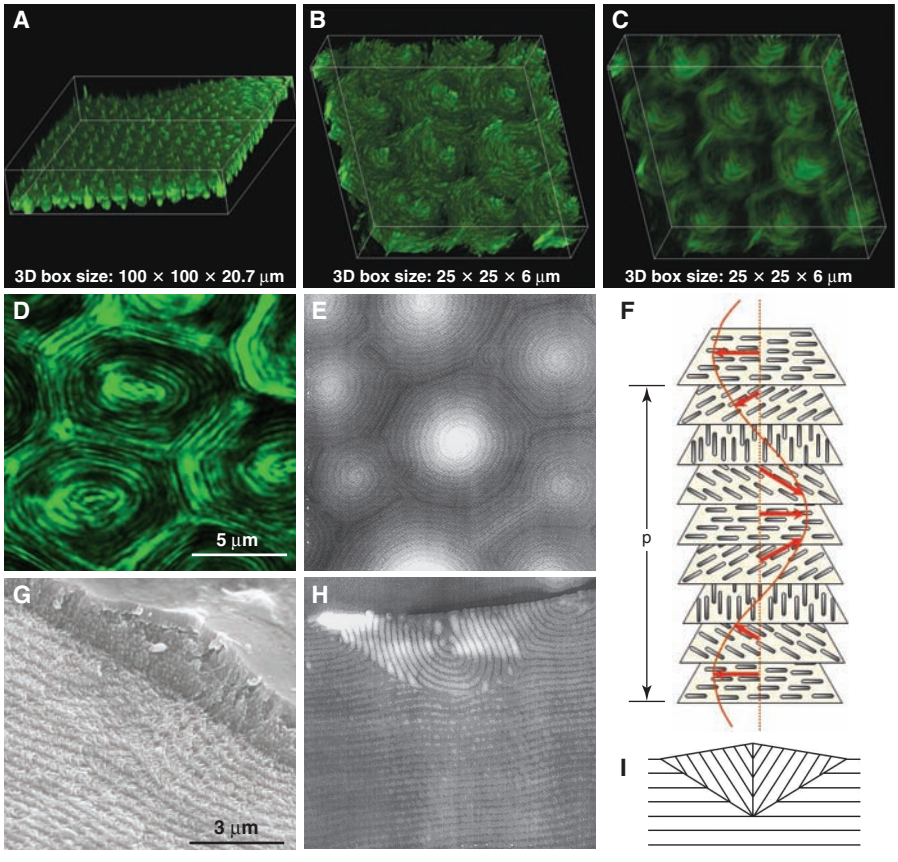

Fig. 3. Morphology and microstructure of cellular pattern of *C. gloriosa*. (**A**) An angled view of 3D image at a low magnification reveals upward cones at the center of each cell. (**B** and **C**) Three-dimensional images at higher magnification for limited thickness range in different viewing modes, which may imply that the concentric bright/dark regions are spiraled. (**D**) A typical *x-y* section, showing a relief feature with concentric rings that is resolved only at a high magnification and present only near the free surface. (**E**) An AFM image of the cholesteric focal conic domains at the free surface, showing double spirals that form a shallow cone [from (*25*)]. (**F**) Schematic representation of relative arrangement of chiral mesogens in a cholesteric liquid crystal, stacked in a single twist structure (layers are for illustration purposes only, no lamellar ordering in the *z* direction). (**G**) SEM image shows the nested arcs and a waxy layer on top. (**H**) AFM image of the microtome cut perpendicular to free surface [from (*25*)]. (**I**) Model of focal conic domain adopted from (*25*), showing a cut along the center of the cone, neglecting the exact structure at the center.

The microstructure of the beetle surface (Fig. 3D) resembles the atomic force microscopy (AFM) image of the focal conic domains (Fig. 3E) that spontaneously arise on the free surface of a siloxane oligomer–based cholesteric liquid crystal (*25*). The spiral structure (Fig. 3, A to C) observed in each cell on the beetle exoskeleton also correlates nicely with the conical form observed by Meister *et al*. (*25*) with use of AFM, where the periodic structure resulting from the cholesteric pitch is superimposed on a fat cone (height/maximum diameter ~ 0.01). Likewise the focal conic cholesteric domains are organized in a near-hexagonal packing. Furthermore, our scanning electron microscopy (SEM) image (Fig. 3G) of the beetle exoskeleton bears similarity to the corresponding AFM image (Fig. 3H) obtained for a section microtomed perpendicular to the free surface (*25*), where the underlying layers can be seen clearly.

The selective reflection of circularly polarized light of one-handedness by exocuticle of many beetles has been noted to be similar to the optical response of cholesteric liquid crystals (*16*–*20*). The cholesteric liquid crystal possesses a long-range orientational order described by a unit vector **n**, known as the director, and the equilibrium director structure is a helicoid (*20*, *26*–*28*). The director advances uniformly, tracing a helix of pitch *p* as sketched in Fig. 3F. The presence of helicoidal structure in beetles and other organisms (*2*, *5*, *16*–*20*) is well recognized. Pace (*29*) noticed the helicoid in transmission electron microscopy (TEM) micrographs from of the exoskeleton of *C. gloriosa* and called it a Bouligand structure. Bouligand (*19*, *20*) had carried out an extensive study on the similarity of textures observed in crabs and other organisms to cholesteric liquid crystals and explored their role in morphogenesis. The surfaces produced by the freeze fracture process can possess a relief resulting from the anisotropic propagation of fracture, and the action of a microtome knife produces a topography (studied by using TEM) that depends on the texture of the cut material (*19*, *25*, *30*). But in this study, because we imaged the 3D microstructure of the beetle elytra in a nondestructive fashion with confocal microscopy, the similarity to the cholesteric focal conic texture at the free surface is unmistakable. Interestingly, the confocal image (3D) has a remarkable similarity to the TEM images of *C. gloriosa* by Pace (*29*). Although the helicoidal structure and resulting optical response has been investigated before (*2*, *5*, *18*, *29*), the observed disorder in hexagonal pattern (Fig. 2); details related to microstructure, including resemblance to focal conic domains at the free surface of a cholesterics (Fig. 3); and the

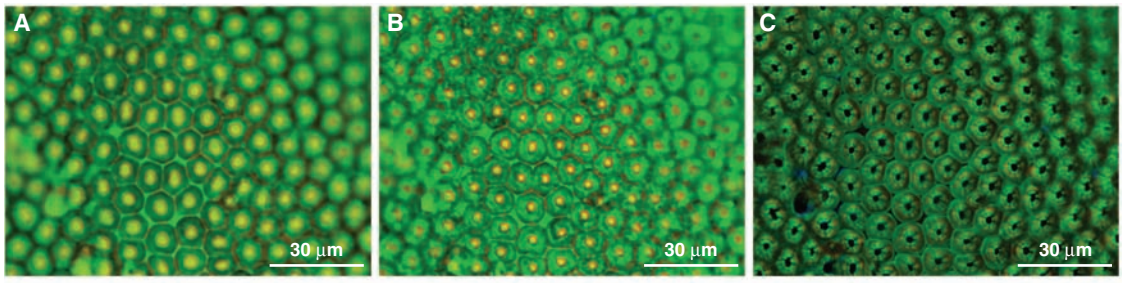

Fig. 4. Optical micrographs of the exoskeleton of *C. gloriosa.* Because the surfaces are curved, only the central parts of the images are in focus. (**A**) In bright field, with microscope aperture wide open, to allow a bigger cone of white light. (**B**) In bright field, near-normal incidence obtained by decreasing the aperture. (**C**) In dark field, where near-normal incidence is not present.

intricate optical response of cells (Fig. 4) presented here have not been reported.

Lastly, let us return to the question of the iridescence or angle-dependent color of the beetles (Fig. 4). Because we have limited knowledge of all of the optical and structural parameters necessary for determining the optical response by ray tracing, we can put forward only phenomenological arguments. Because of its chiral and periodic helicoidal structure, the cholesteric phase with a pitch comparable to the wavelength of visible light shows Bragg-like reflection for normal incidence, peaked at wavelength, λ_0, given by $\lambda_0 = np$, where n is the average refractive index (*26*, *28*, *31*). The spectral width of the reflection peak for a pure cholesteric phase is related to birefringence ($\Delta n = n_e - n_o$) by $\Delta\lambda = p\Delta n$ (*26*, *28*, *31*), where n_o and n_e are the refractive indices for polarizations perpendicular (ordinary) and parallel (extraordinary) to the axis of anisotropy, respectively. For oblique incidence at an angle ϕ, the reflection for a helical axis oriented at some angle θ with respect to surface normal, the condition for first-order Bragg reflection is modified to $\lambda = np\cos(\phi - \theta)$, and additional effects appear (*31*). When we look at the beetle structure in the white light in a reflection microscope, the Bragg-like reflection is yellow at the center of the cell and green elsewhere. When the range of incidence angles is increased by increasing the aperture size (Fig. 4A), the locus of the yellow reflection expands (in comparison to Fig. 4B), implying that, by increasing the angle of incidence of beams over the beetle, $(\phi - \theta)$ becomes smaller; hence, $\cos(\phi - \theta)$ increases, and thus a longer wavelength (yellow as opposed to green) satisfies the condition. In the dark field, when only large angles of incidence are possible, $\phi - \theta$ is large; hence, the $\cos(\phi - \theta)$ term near the center gets even smaller, leading to extinction of color at the center (Fig. 4C). This red shift in wavelength on increasing angle of incidence is also discernible in spectral analysis from the green region, where the peak wavelength increases from 525 nm at normal incidence to 556 nm in dark field illumination. In this analysis, we have neglected the change in incident angle at the helix resulting from refraction at wax-air interface. However, this does not perturb the arguments for the optics presented here.

In the optical studies by Jewell *et al*. (*32*) on *P. boucardi* beetles, similar hexagonal cells are observed to show dark centers in dark field and to turn yellow in bright field. For *P. resplendens* (*17*), *P. boucardi* (*32*), and the New Zealand manuka beetle (*33*), the presence of chiral reflectors with two different pitches satisfying Bragg reflection was cited as responsible for color. Similarly, Brink *et al*. (*34*) simulated the reflected spectrum of the red and green scarabaeid beetle *Gymnopleurus virens* by using a perturbed cholesteric structure that has an abrupt jump in pitch and in rotation of the cholesteric structure. We propose that the focal conic domains formed at the free surface of a cholesteric liquid crystal can create the perturbed cholesteric relief that can account for the color and the morphology of the exocuticle of the scarabaeid beetles. The selective reflection of the cholesteric phases can be modified by a change in pitch, birefringence, cell thickness, angle of incidence, and polarization as well as by the orientation of helical axis (*26*–*28*, *31*, *35*), and the scarabeid beetles, examples of photonic structures in biology, have used a multiplicity of these possibilities (*17*, *19*, *32*–*34*). Although the details of morphogenesis will influence the exact nature of the microstructure and observed color for a particular beetle, we infer that each of these mechanisms provides us with inspiration to the design of chiro-optical devices. In fact, inorganic analogs that mimic optical effects of scarabeid beetles are already being developed (*8*). The desired optical response can be achieved from self-assembly akin to biological systems either by incorporating a bistable cholesteric phase formed because of free surface, by using controlled anchoring, or by using structures with variable pitch [say by having a concentration gradient of nematic blended into a cholesteric fluid (*36*)].

References and Notes

1. H. Ghiradella, *Appl. Opt.* **30**, 3492 (1991).
2. M. Srinivasarao, *Chem. Rev.* **99**, 1935 (1999).
3. P. Vukusic, J. R. Sambles, *Nature* **424**, 852 (2003).
4. A. R. Parker, *J. Opt. A Pure Appl. Opt.* **2**, R15 (2000).
5. S. Bertheier, *Iridescences: The Physical Color of Insects* (Springer, New York, 2007).
6. A. A. Michelson, *Studies in Optics* (Univ. of Chicago Press, Chicago, IL, 1927).
7. D. H. Goldstein, *Appl. Opt.* **45**, 7944 (2006).
8. S. Lowrey, L. De Silva, I. Hodgkinson, J. Leader, *J. Opt. Soc. Am. A Opt. Image Sci. Vis.* **24**, 2418 (2007).
9. V. Z. Rivers, in *Les Insectes Dans la Tradition Orale/Insects in Oral Literature and Traditions*, E. Motte-Florac, J. M. C. Thomas, Eds., SELAF 407, Ethnosciences 11 (Peeters, Walpole, MA, 2003), pp. 163–174.
10. D. A. Thompson, *On Growth and Form* (Cambridge Univ. Press, Cambridge, 1961).
11. P. S. Stevens, *Patterns in Nature* (Little, Boston, MA, 1974).
12. A. M. Turing, *Philos. Trans. R. Soc. London Ser. B* **237**, 37 (1953).
13. P. Ball, *The Self-Made Tapestry: Pattern Formation in Nature* (Oxford Univ. Press, Oxford, 1999).
14. M. C. Cross, P. C. Hohenberg, *Rev. Mod. Phys.* **65**, 851 (1993).
15. A. J. Koch, H. Meinhardt, *Rev. Mod. Phys.* **66**, 1481 (1994).
16. A. C. Neville, S. Caveney, *Biol. Rev. Cambridge Philos. Soc.* **44**, 531 (1969).
17. S. Caveney, *Proc. R. Soc. London Ser. B* **178**, 205 (1971).
18. A. C. Neville, *Biology of Fibrous Composites: Development Beyond the Cell Membrane* (Cambridge Univ. Press, Cambridge, 1993).
19. Y. Bouligand, *C. R. Chim.* **11**, 281 (2008).
20. Y. Bouligand, in *Bifurcation Theory, Mechanics, and Physics*, C. P. Bruter, A. Arangol, A. Lichenrowicz, Eds. (Riedel, Dordecht, Netherlands, 1983).
21. A. Okabe, B. Boots, K. Sugihara, S. N. Chiu, *Spatial Tessellations: Concepts and Applications of Voronoi Diagrams* (Wiley, New York, 2000).
22. D. R. Nelson, *Proc. Int. Sch. Phys. Enrico Fermi* **155**, 365 (2004).
23. A. R. Bausch *et al*., *Science* **299**, 1716 (2003).
24. V. Vitelli, J. B. Lucks, D. R. Nelson, *Proc. Natl. Acad. Sci. U.S.A.* **103**, 12323 (2006).
25. R. Meister, M. A. Halle, H. Dumoulin, P. Pieranski, *Phys. Rev. E Fluids Relat. Interdiscip. Topics* **54**, 3771 (1996).
26. P. G. de Gennes, J. Prost, *Int. Ser. Monogr. Phys* **83**, 263 (1995).
27. M. Kleman, O. D. Lavrentovich, *Soft Matter Physics: An Introduction* (Springer-Verlag, New York, 2003).
28. P. Oswald, P. Pieranski, in *Nematic and Cholesteric Liquid Crystals*, G. W. Gray, J. W. Goodby, A. Fukuda, Eds. (Taylor and Francis, Boca Raton, FL, 2005), pp. 415–492.
29. A. Pace Jr., *Science* **176**, 678 (1972).
30. D. W. Berreman, S. Meiboom, J. A. Zasadzinski, M. J. Sammon, *Phys. Rev. Lett.* **57**, 1737 (1986).
31. V. A. Belyakov, V. E. Dmitrienko, *Optics of Chiral Liquid Crystals* (Harwood, New York, 1989).
32. S. A. Jewell, P. Vukusic, N. W. Roberts, *N. J. Phys.* **9**, 99 (2007).
33. L. De Silva *et al*., *Electromagnetics* **25**, 391 (2005).
34. D. J. Brink, N. G. van der Berg, L. C. Prinsloo, I. J. Hodgkinson, *J. Phys. D* **40**, 2189 (2007).
35. W. D. St. John, W. J. Fritz, Z. J. Lu, D. K. Yang, *Phys. Rev. E* **51**, 1191 (1995).
36. D. J. Broer, J. Lub, G. N. Mol, *Nature* **378**, 467 (1995).
37. M.S. acknowledges support from NSF (DMR-0706235) and useful discussions with L. Tolbert, A. Rey, P. Collings, and H. Ghiradella.

Supporting Online Material

www.sciencemag.org/cgi/content/full/325/5939/449/DC1
Materials and Methods
SOM Text
References

9 February 2009; accepted 5 June 2009
10.1126/science.1172051

Chiral Isotropic Liquids from Achiral Molecules

L. E. Hough,[1]* M. Spannuth,[1] M. Nakata,[1]† D. A. Coleman,[1] C. D. Jones,[1] G. Dantlgraber,[2] C. Tschierske,[2] J. Watanabe,[3] E. Körblova,[4] D. M. Walba,[4] J. E. Maclennan,[1] M. A. Glaser,[1] N. A. Clark[1]*

A variety of simple bent-core molecules exhibit smectic liquid crystal phases of planar fluid layers that are spontaneously both polar and chiral in the absence of crystalline order. We found that because of intralayer structural mismatch, such layers are also only marginally stable against spontaneous saddle splay deformation, which is incompatible with long-range order. This results in macroscopically isotropic fluids that possess only short-range orientational and positional order, in which the only macroscopically broken symmetry is chirality—even though the phases are formed from achiral molecules. Their conglomerate domains exhibit optical rotatory powers comparable to the highest ever found for isotropic fluids of chiral molecules.

Pasteur discovered molecular chirality in sodium ammonium tartrate by showing that molecular species of opposite handedness phase-separated into distinct crystals upon growth from solution (*1*). Such an appearance of macroscopic chiral domains is now a commonly observed feature of the crystallization of both chiral and achiral molecules, and serves as the basis for a broad range of chemical and medical technology (*2*). Spontaneous resolution of chiral molecules or conglomerate domain formation of achiral molecules requires intermolecular interactions that are specific and strong enough to collectively expel or rearrange molecules of the wrong handedness. This situation is most readily achieved in the phases with the lowest translational symmetry—the packed periodic environments of crystals—but was recently found in more symmetric phases, where stacked fluid layers of achiral bent-core molecules having a single broken translational symmetry in the form of the smectic layering were shown to exhibit macroscopic chiral conglomerate domains (*3*). Here we extend the exploration of macroscopic spontaneous chirality to fluids that are fully translationally symmetric and isotropic. We show that even in a liquid with only short-range translational and orientational order, it is possible to preserve local structural specificity sufficient to enable the long-range propagation of chirality. The resulting phases are strongly optically active, exhibiting optical rotations of ~1°/μm for visible light; such values are exceeded only by macroscopically helixed liquid crystal phases (*4*).

Banana-shaped molecules with bent cores and one or two flexible tails exhibit a wide variety of novel structural phenomena involving the interplay of chiral, polar, and liquid crystalline (LC) order (*5*–*7*). The strong local preference for layering, coupled with the bent shape of the molecules, promotes molecular packing that is both polar [with the arrows of the molecular bows aligning in a direction **p** in the layer plane (*7*)] and tilted (*3*) (with the molecular plane rotated about **p**) to drive the formation of chiral layered phases such as the B2 and B7 phases (Fig. 1, A and B), (*8*, *9*). One of the striking and mysterious properties of many of these bent-core systems is the presence of layered phases that we have termed "dark conglomerates" (DCs), which (as with the B2 phase) appear via first-order transitions from the high-temperature isotropic phase (*10*–*18*). The DCs, unlike the B2 smectics, have little or no birefringence and thus are nearly dark between crossed polarizers. However, they exhibit spontaneous macroscopic chirality more robustly than does the B2 phase, manifested by conglomerate domains up to hundreds of micrometers in size. We show that such DC phases are macroscopically isotropic fluids, with handedness as the only macroscopic ordering: a chiral coupling of local tilt, polarization, and layer deformation that limits the orientational and translational order.

We combined freeze-fracture transmission electron microscopy (TEM), x-ray diffraction

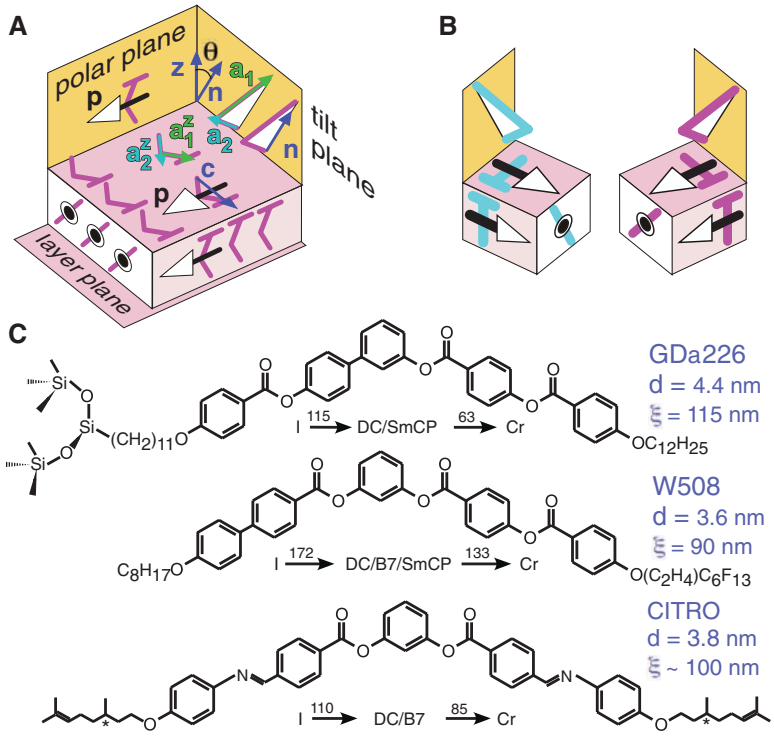

Fig. 1. Simultaneous tilt and polar ordering is a common feature of phases formed from bent-core molecules. (**A**) The B2 phase is formed from the stacking of fluid layers of bent-core molecules, where the molecular long axis (**n**) is tilted (by angle θ) relative to the layer normal (**z**). In addition, polar order of the molecules leads to a macroscopic polarization (**p**) orthogonal to **n** and **z**, and in the molecular plane—the plane that contains both of the half-molecular arms ($\mathbf{a}_1$ and $\mathbf{a}_2$). The projections of the half-molecular arms onto the layer plane ($\mathbf{a}_1^z$ and $\mathbf{a}_2^z$) are nearly perpendicular for most bent-core molecules. (**B**) The left- and right-handed layer structures. The B2 subphases consist of the four possible bilayer alternations of direction of **p** and **c**. (**C**) The chemical structures, phase sequences, and layer spacing and correlation lengths (as measured by XRD and freeze-fracture TEM) of the three compounds studied here. The notation DC/B7 indicates that either the DC or B7 structure may be present, depending on sample thermal history or field application; similar notations have similar meanings.

[1]Department of Physics and Liquid Crystal Materials Research Center, University of Colorado, Boulder, CO 80309, USA. [2]Institute of Organic Chemistry, University of Halle-Wittenberg, D-06120 Halle (Saale), Germany. [3]Department of Organic and Polymeric Materials, Tokyo Institute of Technology, O-okayama 2-12-1, Meguro-Ku, Tokyo 152-8552, Japan. [4]Department of Chemistry and Biochemistry and Liquid Crystal Materials Research Center, University of Colorado, Boulder, CO 80309, USA.

*To whom correspondence should be addressed. E-mail: hough@colorado.edu (L.E.H.); noel.clark@colorado.edu (N.A.C.)

†Deceased.

(XRD), and depolarized transmission light microscopy (DTLM) to establish the molecular organization of the DC phase in the materials W508, GDa226 (*13*), and racemic CITRO (*19*) (Fig. 1C), all of which transformed to chiral B2 phases under application of sufficiently large electric field (*20*), indicating that the inherent local layer structure is fluid, polar, and chiral (Fig. 1, A and B). The local chirality is maintained in this type of transition (*21*). We performed freeze-fracture TEM (*20*, *22*), which enables visualization of the layer structure of smectic phases (*9*, *23*) and, in the case of the DCs, shows the local layering as well as the layer curvature and distortion on larger length scales (Fig. 2, A, B, C, and F, Fig. 3A, and figs. S3 to S5). These images reveal the well-defined local smectic layering and its interfacial topography, showing a strong tendency for saddle splay layer deformation, as seen in GDa226 in Fig. 2, A and D, and Fig. 3A. The layer topography for CITRO appears more broken, although distinct saddle-shaped domains can still be seen and are decorated with undulations of the polarization splay stripes of the B7 phase (Fig. 2, C and F), which have a short wavelength in CITRO (*9*).

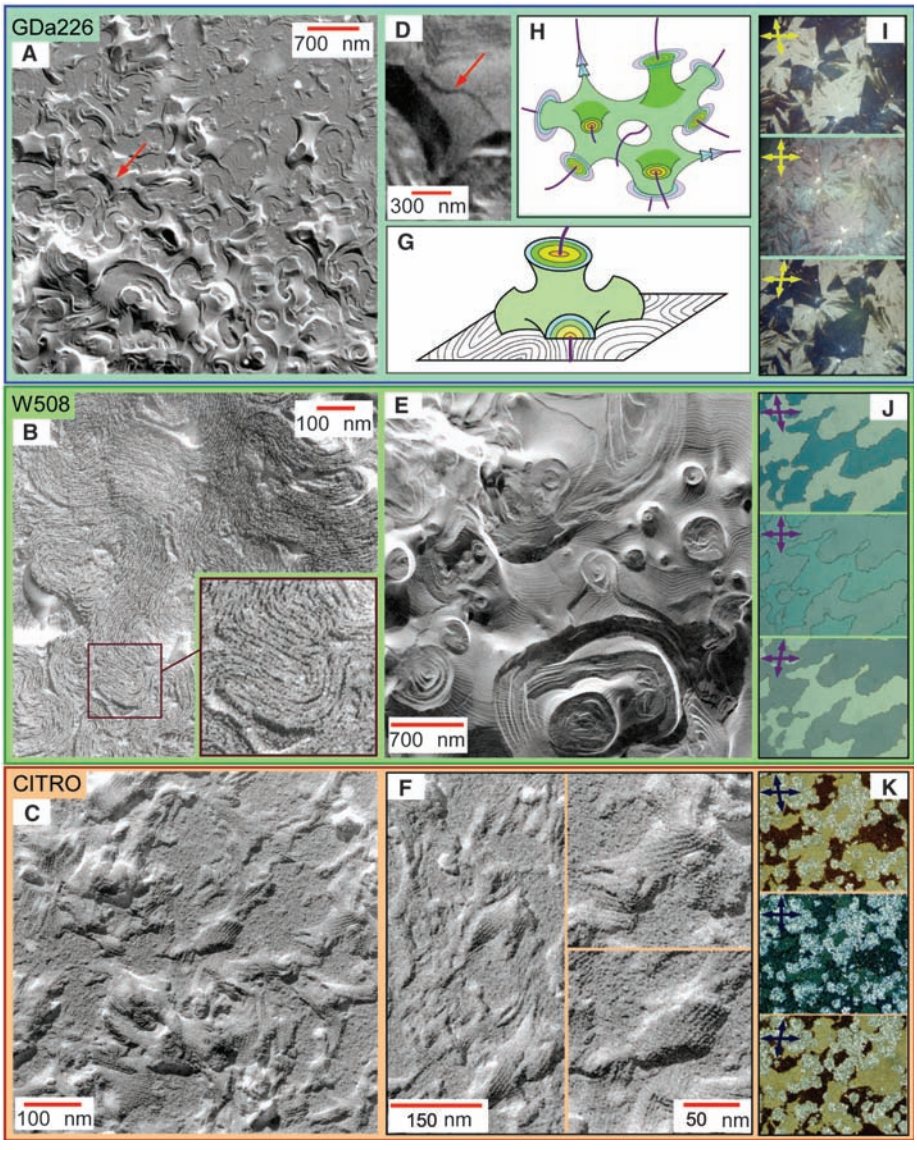

Fig. 2. Freeze-fracture TEM (**A** to **F**) and DTLM (**I** to **K**) images of the DC phase [(A) to (D), (F), and (I) to (K)] and B7 phase [(E) and (K)] of GDa226 [(A), (D), and (I)], W508 [(B), (E), and (J)], and CITRO [(C), (F), and (K)]. The freeze-fracture TEM images reveal that in the DC, although the local layering is well defined, the layer topography is highly curved, forming saddle-shaped domains. Occasional layer steps in the freeze-fracture TEM [red arrow, (A); magnified in (D)] identify the saddle-shaped domains as the surfaces of individual layers. When the fracture occurs at the nylon-coated glass surface [(B) and upper half of (A)], the layer orientation is preferentially perpendicular to the surface, and the ends of individual layers are apparent as faint lines whose measured spacing is consistent with that measured by XRD (see also figs. S3 to S5). As is particularly apparent in (B), the layers, although highly curved, are continuous over long distances (see also figs. S3 to S5). These two features, layer curvature and layer continuity, are characteristic of the lyotropic sponge phase [(**H**), from (*38*)], with the empty volume filled with smectic layers (**G**). The layer topography of CITRO [(C) and (F)], in addition to showing a distinct saddle shape, is decorated with the undulations of its B7 phase. W508 shows B7 undulations in the focal conic texture of (E), but not in the DC phase. The orientation of the layer undulations is governed by the layer curvature, with the polarization direction between the two principal curvature directions. In (I) to (K), the DC phase appears dark between crossed polarizers (center images), and domains of opposite-handed optical activity become apparent upon decrossing of the analyzer relative to the polarizer (top and bottom images). Coexisting B7 domains in CITRO are bright because of their birefringence (K). Image widths in (I) to (K) are 300 μm.

Occasionally, fracture occurs at the LC-glass interface, where the layers have a tendency to terminate normal to the surface. This partially constrains the DC texture, but enables excellent visualization of the disorder characterizing the DC in the surface plane [Fig. 2A (upper half), Fig. 2B, and figs. S3 to S5]. Individual smectic layers are visible and form a periodic structure with layer spacing of ~5 nm, consistent with the layer spacing measured by XRD (Fig. 1C). Unlike smectic lamellar phases, the layers of the DC are planar over only very short distances (<100 nm), as a result of the layer folding, bending, and twisting, although (as in bulk smectics) the layer spacing appears to be uniform throughout. The layer disorder of the phase was further confirmed by XRD, where diffuse Bragg lamellar reflections are indicative of only short-range layer ordering (Fig. 1C and figs. S1, S2, and S6). Additionally, despite their substantial curvature, the layers intersecting the fracture plane are continuous over long distances, with edge dislocations marking the end of a layer only occasionally visible (Fig. 2B and figs. S4 and S5). The DC layer structure is characterized by sets of nested curved layers with defects localized to lines where the radius of layer curvature approaches the layer spacing.

In the DC structure, the layer surfaces are largely continuous, enabling a local field (e.g., the handedness) to percolate through space and attain long-range order. In particular, the DC optical texture exhibits chiral conglomerate domains—macroscopic patches of highly uniform optical activity of opposite handedness, 10 to 100 μm in size (Fig. 2, I to K). The optical rotation is clearly visible because of the low birefringence, which is the result of the isotropy of the DC phase and its having an orientational correlation length that is small relative to the wavelength of visible light. Typically there are ~100 independently oriented domains per cubic wavelength of green light, so that although the local birefringence is large, it is reduced by orientational averaging. The optical activity of the DC phases of W508 and GDa226 was characterized by measuring the optical rotation as a function of wavelength (fig. S8), which

was found to be well described by models typically used to account for the dispersion of the optical anisotropy of LC materials (*24*). This finding is consistent with the view that there is no chiral organization on a length scale larger than the wavelength and that the optical rotation is a result of the chiral organization of the local molecular optical anisotropy (*25*, *26*). A local structure of flat synclinic or anticlinic chiral layers does not appear to generate enough optical rotation to account for the DC data (*27*, *28*), indicating that saddle splay layer curvature may have to be introduced into the optical modeling of the optical rotation.

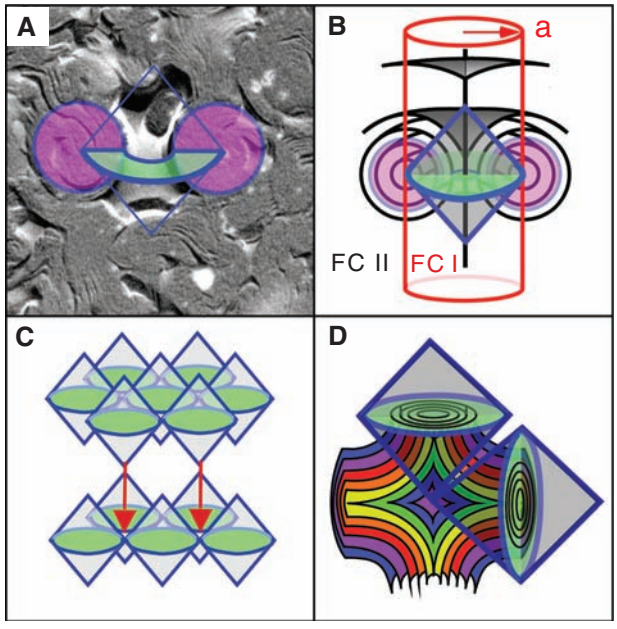

Fig. 3. (**A**) The layer structure of the DC phase is characterized by sets of nested curved layers with defects localized to lines where the radius of layer curvature approaches the layer spacing. (**B**) This overall organization is analogous to that of focal conic (FC) defects, particularly those of type I (characterized by negative Gaussian curvature) rather than of type II (characterized by mean curvature). We consider the toric focal conic defect in (B) to be a good model for the spatial organization of the DC phase. (**C**) Space can be filled with predominantly FC I and little contribution from FC II—for example, to form (**D**), the cubic bicontinuous (P-surface) plumber's-nightmare structure (*30*).

The topography of individual layers in the DC phase resembles that of the layers of the lyotropic sponge phase (Fig. 2H and Fig. 3D) (*29*, *30*), an isotropic phase of bilayer sheets of amphiphiles characterized by well-defined interfaces and layer deformation. These phases are produced in systems with sufficiently low membrane rigidity (*31*) or an inherent preference for membrane curvature (*32*). Such phases are not typically seen in lyotropics at high surfactant concentration or in thermotropic smectics because in these systems the layers are in more intimate contact and cannot act independently; rather, they are constrained to more definite layer spacing everywhere. Under this constraint, layer curvature is possible but is limited to the familiar focal conic-like structures observed as defects of lamellar smectics (*29*) (Fig. 3). Several reports of isotropic phases with observable layering correlations suggest that this type of behavior might be possible in thermotropic smectics (*33*, *34*).

The freeze-fracture TEM images show that the DC layer system is locally lamellar but globally disordered. Disorder must arise either from thermally generated fluctuations (as in the case of the lyotropic sponge phase) or enthalpically, from an energetic preference for local saddle splay of the layers—the dominant motif of disorder in the freeze-fracture TEM images. The local lamellar structure does not exhibit any features consistent with enhanced fluctuations; the layers are smooth

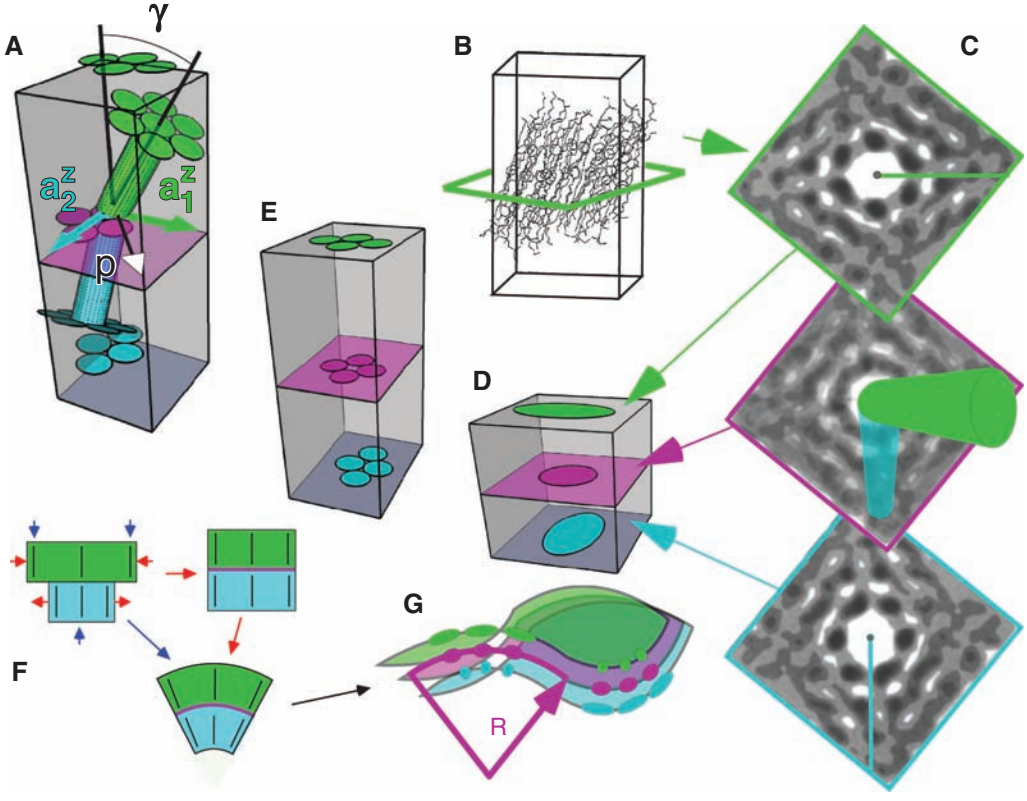

Fig. 4. Frustration between molecular fragments in a tilted bent-core molecule can be relieved by saddle splay curvature of the layers. (**A**) The projections of the two half-molecular arms (green and blue cylinders) onto the layer plane ($\mathbf{a}_1^z$ and $\mathbf{a}_2^z$) are nearly orthogonal (the case shown here) for most tilted bent-core molecules. (**B**) Simulation of the SmC phase of rod-shaped molecules shows an elongation of the in-plane pair correlation function, g(**r**) in the direction of the molecular tilt. The bent-core molecular arms, each tilted by γ relative to the layer normal, will also have oblong preferred in-plane correlations (**C** to **E**), which costs energy to deform into a circularly symmetric organization required for the formation of flat layers with tilted molecules. This energy cost can be relieved by layer curvature. (**F**) For example, consider the case of two elastic sheets of different length; if the longer (green) is compressed and the shorter (blue) is dilated, they can be made to match. If they are then attached at the interface and left to relax, the structure will curve, partially relieving the compressional and dilational stresses imposed on the sheets. (**G**) Similarly, the orthogonal tilt directions of the two half-molecular arms produces in each direction a dilation in one half-layer and compression in the other half; saddle splay curvature can reduce this frustration. Upon passing from one sublayer to the other, opposite pairs of molecules in groups of four exchange their nearest-neighbor status, as shown in (E).

and of nearly constant thickness, with variations in spacing suppressed by the layer compressional elasticity. We therefore explored the possibility of an energetic preference for layer saddle splay, specifically related to the bent molecular shape and polar order.

The fluid bent-core smectics possess structural frustration not present in other layered LCs or crystals. The molecular length (larger than for typical calamitic LCs) and molecular bend reduce out-of-layer fluctuations, strongly stratifying the layers. For molecules with flexible tails at either end, the areal confinement of the tails results in an entropic pressure tending to increase the in-plane area per tail, a response that can be achieved by the tilting of the molecular planes defined by the half-molecular arm directors $\mathbf{a}_1$ and $\mathbf{a}_2$ (Fig. 1A) through an angle θ with respect to the layer normal **z**. Because of the molecular bend (i.e., the finite angle ψ between $\mathbf{a}_1$ and $\mathbf{a}_2$), the tilting of the $\mathbf{a}_1$ and $\mathbf{a}_2$ molecular planes leads to different in-plane azimuthal orientations of the tilt planes of the individual molecular arms about **z**, given by the half-molecular arm tilt directors $\mathbf{a}_1^z$ and $\mathbf{a}_2^z$ (Fig. 1A and Fig. 4A). For the geometry typical of bent-core fluid smectics ($\psi \approx 120°$ and $\theta \approx 30°$), $\mathbf{a}_1^z$ and $\mathbf{a}_2^z$ are nearly perpendicular.

This situation produces a strong tendency for negative Gaussian curvature of the layers via the coupling of the tilt of the molecular arms to molecular positional correlations in the two-dimensional (2D) molecular liquid that is the layer. Figure 4C shows a computer simulation of the molecular positional pair correlation function $g(\mathbf{r})$ (the average distribution of molecules about a given molecule) of a fluid, tilted, smectic layer, in this case a smectic C (SmC) of rod-shaped molecules, which should serve as a good model of the half-layer of half-molecular arms of a bent-core system (*35*). We assume a half-molecular arm tilt from the layer normal, **z**, of $\gamma \approx 30°$. The molecular 2D fluid is characterized by a local stretched hexagonal lattice, evident from the ellipsoidal ring of six peaks about the origin, with a correlation length of only a few intermolecular spacings, as indicated by the weakness of the second and third rings. The correlation function, although nearly circular in the plane perpendicular to the molecule, shows a pronounced stretch in the layer plane: $r_t(\gamma)/r_t(0) = 1/(\cos\gamma) \approx 1.15$, where r_t is the radius of the ring of nearest neighbors in the tilt direction.

If we now imagine a bent-core smectic layer in which the molecules are cut into two independent arms at the layer midplane, then each sublayer would tend to have a pair correlation function, $g(\mathbf{r})$, like that of Fig. 4C, elongated along its tilt direction. If for simplicity we take the half-molecular arm tilt directors $\mathbf{a}_1^z$ and $\mathbf{a}_2^z$ to be orthogonal, then the situation shown in Fig. 4D develops, in which, because the sublayer $g(\mathbf{r})$s are stretched in different directions, their correlation peaks fail to overlap for flat layers. In an actual bent-core layer, however, the molecules are connected across the layer midplane and the sublayer correlation functions therefore must overlap, a condition that can be achieved by deforming the sublayer $g(\mathbf{r})$s. Thus, in a flat layer this must be accomplished by forcing each group of four molecules from their preferred local hexagonal arrangement into a local square lattice (Fig. 4E, magenta) in both the upper and lower sublayers. Such a local deformation of $g(\mathbf{r})$ costs energy, but this cost can be reduced by allowing the layer to make a saddle splay deformation (Fig. 4G), enabling $g(\mathbf{r})$ in each sublayer to have its preferred stretch along the tilt direction while connecting the molecules in the layer midplane (Fig. 4G, magenta). A similar situation is sketched for a 1D case in Fig. 4F; flat plates of different lengths can be matched by relative stretch and compression. If the plates are attached and left to deform into the **z** direction, the bilayer will bend to relieve the internal strain of the flat geometry.

The situation depicted in Fig. 4, F and G—where the sublayers are subjected to compression in order to match their pair correlations, laminated together, and then left to relax to a curved state—can be quantitatively modeled (*20*) by regarding the sublayers as elastic sheets of thickness $d/2$, in which there is in-plane dilation and shear under a condition of zero stress along the layer normal. For simplicity we assume that the half-layer sheets are of isotropic elastic material, characterized by compressional and shear moduli M and μ, respectively. The upper and lower sheets are subjected to a pure in-plane shear strain of opposite sign, $\partial u_x/\partial x = -\partial u_y/\partial y = \pm\beta$, laminated together, and then allowed to relax to reduce elastic energy, which can be calculated by integration through the thickness of the two half-layers (*20*). The resultant net elastic energy per unit volume for the composite of the upper and lower half-layers depends on its principal curvatures σ′ and σ″:

$$f_b = f_0 + (K/2)(\sigma' + \sigma'')^2 + \bar{K}\ (\sigma'\sigma'') + G(\sigma' + \sigma'') \quad (1)$$

where $f_o = 4\mu\beta^2$, $K = (\frac{2}{3}\mu + \frac{1}{2}M)(d^2/24)$, $\bar{K} = -(d^2/6)\mu$, and $G = \mu\beta(d/2)$. The second and third terms are the energy of mean and Gaussian curvature, respectively, and will yield flat layers for any reasonable value of the ratio M/μ. The last term, which depends linearly on the stretch β, drives negative Gaussian curvature. For the case of pure negative Gaussian curvature $\sigma = \sigma' = -\sigma''$, f_b is minimized versus σ for $\sigma = \sigma_p$, where $\sigma_p \equiv 1/R_p \equiv G/\bar{K}$. Taking $\beta = [(1/\cos\gamma) - 1]/2 = 0.075$ from the half-layer simulation and layer thickness $d = 4$ nm, we find $R_p = 20$ nm. Note that $G(\sigma' + \sigma'')$ is just the $\mathbf{p}\cdot\mathbf{L}\cdot\mathbf{c}$ term proposed by de Gennes for the chiral coupling between polarization **p**, tilt direction **c**, and layer curvature tensor **L**, present in the free energy expansion of a chiral smectic layer (*4*, *20*).

To understand the global response to such an internal strain, it is necessary to account for the fact that in a thermotropic smectic, where the layer deformation is under the constraint of constant spacing, the preferred local saddle splay condition cannot be achieved everywhere. Thus, the local energy density $f_b[\sigma'(\mathbf{r}), \sigma''(\mathbf{r})]$ of all three terms of Eq. 1 must be integrated over the volume of interest. The images of Fig. 2 are dominated by layer curvature motifs of focal conic domains, the dominant layer organization seen in smectic phases (*20*, *29*). As a result we chose as a representative volume a focal conic domain dominated by negative Gaussian curvature (FC I, Fig. 3) and found that the free energy is minimized for domain size of ~200 nm, consistent with the observed structures (Fig. 3).

A striking feature of these DC isotropic fluids is their spontaneous macroscopic chirality, making them the sole known materials that have only handedness as a macroscopic broken symmetry. Our results reveal the two key elements that make such a state possible. First, saddle splay deformation of a tilted chiral smectic is itself inherently chiral, as expressed by the $\mathbf{p}\cdot\mathbf{L}\cdot\mathbf{c}$ coupling (*4*) leading to Eq. 1, meaning that of the B2 subphases, the four possible bilayer alternations of **c** and **p** (Figs. 1 and 4), only the homochiral SmC_SP_S and SmC_AP_A give a tendency for homogeneous saddle splay [i.e., have the same sign of saddle splay in adjacent layers (*20*)], with the racemic SmC_SP_A and SmC_AP_F cases producing alternating sign and thus remaining flat. Because **L** is symmetric under combined mirror reflection and 90° rotation about **z**, racemic alternations with longer pitch (e.g., a four-layer 90° clock; fig. S9) will also produce homogeneous saddle splay, which may explain the observation of achiral DCs (*36*). Second, the freeze-fracture TEM images reveal a layer organization that, although disordered on length scales longer than ~100 nm, exhibits distinctly focal conic-like structures locally. In space-filling focal conic arrays, neighboring defects share continuous layers, a feature also exhibited by the DC disordered focal conic arrays shown in Fig. 2 and figs. S3 to S5, and illustrated by the paths in figs. S4 and S5. Changes in chirality between adjacent layers in the planar layered B2 phases are much more prevalent than intralayer chirality changes (*5*, *37*); as a result, layer continuity becomes an effective means of propagating layer chirality in the DC phases and constitutes a basic reason why such isotropic chiral fluids can be formed from achiral molecules (*20*).

References and Notes

1. L. Pasteur, *C. R. Acad. Sci* **26**, 535 (1848).
2. J. Jacques, A. Collet, S. H. Wilen, *Enantiomers, Racemates, and Resolutions* (Wiley Interscience, New York, 1981).
3. D. R. Link *et al.*, *Science* **278**, 1924 (1997).
4. P. G. de Gennes, J. Prost, *The Physics of Liquid Crystals* (Oxford, New York, ed. 2, 1993).
5. H. Takezoe, Y. Takanishi, *Jpn. J. Appl. Phys.* **45**, 597 (2006).
6. R. A. Reddy, C. Tschierske, *J. Mater. Chem.* **16**, 907 (2006).
7. T. Niori, T. Sekine, J. Watanabe, T. Furukawa, H. Takezoe, *J. Mater. Chem.* **6**, 1231 (1996).
8. D. M. Walba *et al.*, *Science* **288**, 2181 (2000).
9. D. A. Coleman *et al.*, *Science* **301**, 1204 (2003).
10. J. Thisayukta, Y. Nakayama, S. Kawauchi, H. Takezoe, J. Watanabe, *J. Am. Chem. Soc.* **122**, 7441 (2000).

11. G. Heppke, D. D. Parghi, H. Sawade, *Liq. Cryst.* **27**, 313 (2000).
12. H. N. S. Murthy, B. K. Sadashiva, *Liq. Cryst.* **29**, 1223 (2002).
13. G. Dantlgraber *et al.*, *Angew. Chem. Int. Ed.* **41**, 2408 (2002).
14. A. Eremin, S. Deile, G. Pelzl, W. Weissflog, *Phys. Rev. Lett.* **67**, 020702 (2003).
15. R. A. Reddy, B. K. Sadashiva, *Liq. Cryst.* **30**, 1031 (2003).
16. J. Etxebarria, C. L. Folcia, J. Ortega, B. Ros, *Phys. Rev. E* **67**, 042702 (2003).
17. W. Weissflog, M. W. Schroder, S. Diele, G. Pelzl, *Adv. Mater.* **15**, 630 (2003).
18. G. Liao *et al.*, *Phys. Rev. E* **72**, 021710 (2005).
19. M. Nakata *et al.*, *Phys. Rev. E* **71**, 011705 (2005).
20. See supporting material on *Science* Online.
21. S. K. Lee, L. Shi, M. Tokita, H. Takezoe, J. Watanabe, *J. Phys. Chem. B* **111**, 8698 (2007).
22. M. J. Costello, R. Fetter, M. Hochli, *J. Microsc.* **125**, 125 (1982).
23. J. A. Zasadzinski, *J. Phys.* **51**, 747 (1990).
24. S. T. Wu, *Phys. Rev. A* **33**, 1270 (1986).
25. L. E. Hough, N. A. Clark, *Phys. Rev. Lett.* **95**, 107802 (2005).
26. J. Ortega, C. L. Folcia, J. Etxebarria, N. Gimeno, M. B. Ros, *Phys. Rev. E* **68**, 011707 (2003).
27. J. Etxebarria, C. L. Folcia, J. Ortega, *Phys. Rev. Lett.* **101**, 079801 (2008).
28. L. E. Hough *et al.*, *Phys. Rev. Lett.* **101**, 079802 (2008).
29. M. Kléman, O. Lavrentovich, *Soft Matter Physics: An Introduction* (Springer-Verlag, New York, 2003).
30. B. A. DiDonna, R. D. Kamien, *Phys. Rev. Lett.* **89**, 215504 (2002).
31. D. A. Huse, S. Leibler, *J. Phys.* **49**, 605 (1988).
32. G. Porte *et al.*, *Physica A* **176**, 168 (1991).
33. L. Navailles, C. W. Garland, H. T. Nguyen, *J. Phys.* **6**, 1243 (1996).
34. J. Yamamoto, I. Nishiyama, M. Inoue, H. Yokoyama, *Nature* **437**, 525 (2005).
35. M. A. Glaser, R. Malzbender, N. A. Clark, D. M. Walba, *J. Phys. Condens. Matter* **6**, A261 (1994).
36. C. Keith *et al.*, *J. Mater. Chem.* **17**, 3796 (2007).
37. M. Nakata *et al.*, *J. Mater. Chem.* **11**, 2694 (2001).
38. G. Porte, *J. Phys. Condens. Matter* **4**, 8649 (1992).
39. Supported by NSF grant DMR 0606528 (N.A.C.), NSF Materials Research Science and Engineering Center grant DMR 0820579 (N.A.C.), and an NSF Graduate Research Fellowship (L.E.H.). Use of the National Synchrotron Light Source was supported by the U.S. Department of Energy, Divisions of Materials and Chemical Sciences. We thank T. Giddings for technical assistance with the freeze-fracture TEM.

Supporting Online Material

www.sciencemag.org/cgi/content/full/325/5939/452/DC1
Materials and Methods
SOM Text
Figs. S1 to S9
References

19 December 2008; accepted 4 June 2009
10.1126/science.1170028

Helical Nanofilament Phases

L. E. Hough,[1]* H. T. Jung,[2] D. Krüerke,[3] M. S. Heberling,[1] M. Nakata,[1]† C. D. Jones,[1] D. Chen,[1] D. R. Link,[1] J. Zasadzinski,[4] G. Heppke,[3] J. P. Rabe,[5] W. Stocker,[5] E. Körblova,[6] D. M. Walba,[6] M. A. Glaser,[1] N. A. Clark[1]*

In the formation of chiral crystals, the tendency for twist in the orientation of neighboring molecules is incompatible with ordering into a lattice: Twist is expelled from planar layers at the expense of local strain. We report the ordered state of a neat material in which a local chiral structure is expressed as twisted layers, a state made possible by spatial limitation of layering to a periodic array of nanoscale filaments. Although made of achiral molecules, the layers in these filaments are twisted and rigorously homochiral—a broken symmetry. The precise structural definition achieved in filament self-assembly enables collective organization into arrays in which an additional broken symmetry—the appearance of macroscopic coherence of the filament twist—produces a liquid crystal phase of helically precessing layers.

The principal ordering motif of materials at low temperature is crystallization, the organization of atoms or molecules into layers. However, some species—for example, pear-shaped molecules with mutually adhesive stems—prefer to assemble into aggregates that do not pack very well into layers. With such frustration, crystallization can take place at the expense of local strain or may be suppressed entirely. In addition to these homogeneous possibilities, ordering into inhomogeneous states can occur in which the local preference is manifest only in some places, leading to order that is spatially modulated on the mesoscopic scale. Interesting and useful phenomena result, including vortex lattice (*1*) and magnetic stripe phases (*2*), lipid bilayer ripples (*3*), and polarization splay modulation (*4*).

A particularly noteworthy instance of competition between local preference and global ordering is that between chirality and layering, present in all chiral crystals and layered chiral liquid crystals. The chiral packing of molecules induces local molecular twist, but macroscopic ordering into layers expels twist, leaving the local organization strained. In fluid layered (smectic) liquid crystals of rod-shaped molecules, this competition produces inhomogeneous phases in which molecular and layer twist coexist, the latter enabled by periodic arrays of (twist) grain boundaries (*5*, *6*) or melted sheets (*7*). Here, we studied a system of simple bent-core molecules in which a particularly strong coupling between chirality and layering originates in the requirement to accommodate the size and shape of molecular subfragments in the presence of a robust tendency for layering. The bent-core molecules are achiral, but spontaneous polar order and chirality appear as broken symmetries, coupling to drive local Gaussian curvature (saddle splay deformation) of the layers—a local solution that cannot fill space. This frustration leads to a spectacular hierarchical structure in which layering can appear only if twisted, doing so in the form of nanofilaments of twisted layers. The nanofilaments in turn collectively organize into a homochiral liquid crystalline array with coherent twist. Such macroscopic nanoporous assemblies of helically precessing layers are unanticipated solutions to the problem of obtaining coexisting layering and twist in a condensed phase, and may be useful in applications requiring chiral nanoporous media.

The helical nanofilament (HNF) phase, heretofore known as the B4 phase, was one of the first new phases to be observed once the directed exploration of thermotropic smectics of bent-core molecules commenced (*8*–*10*). However, its structure and origin have remained obscure and controversial despite extensive study (*11*–*13*). The observation of strong optical activity (*14*) (fig. S11), indicating twist of molecular orientation, as well as x-ray diffraction (XRD) evidence for smectic layering (*9*, *15*) led to the proposal that the B4 phase was some kind of smectic phase with twisted layers (*9*). However, both the presence of in-plane two-dimensional (2D) positional ordering (*15*) and XRD evidence showing that the layer ordering in the B4 phase was only short-range (Fig. 1C) were inconsistent with the available models of twisted smectics of chiral molecules—long-range ordered smectic blocks separated by twist grain boundaries (TGBs) (*16*). Here, we present the structure and origin of a quite distinct way of accommodating twist and layering, which suggests the existence of alternative modes of accommodation of tendencies for local and long-range ordering in a variety of modulated materials systems.

We studied the B4 phase of bent-core compounds in the phenylene bis(alkoxyphenylimiinomethyl) benzoate (PnOPIMB) series (*9*) with the use of atomic force microscopy (AFM), freeze-fracture transmission electron microscopy (FFTEM), x-ray and electron diffraction (XRD, ED), and depolarized transmission light microscopy (DTLM) (Fig. 1A) (*16*). The B4 phase appears upon cooling from the isotropic phase or from the B2 or B3 phases, smectics in which the achiral bent-core molecules have spontaneously developed polar order and tilt to form chiral planar layers with long-range lamellar order (*17*, *18*). The transition to the B4 phase is marked by the in-plane hexatic

[1]Department of Physics and Liquid Crystal Materials Research Center, University of Colorado, Boulder, CO 80309, USA. [2]Department of Chemical and Biomolecular Engineering (BK-21), Korea Advanced Institute of Science and Technology, Daejeon 305-701, Korea. [3]Institute of Inorganic and Analytical Chemistry, Technical University of Berlin, 10623 Berlin, Germany. [4]Department of Chemical Engineering, University of California, Santa Barbara, CA 93106, USA. [5]Department of Physics, Humboldt University Berlin, 10099 Berlin, Germany. [6]Department of Chemistry and Biochemistry and Liquid Crystal Materials Research Center, University of Colorado, Boulder, CO 80309, USA.

*To whom correspondence should be addressed. E-mail: hough@colorado.edu (L.E.H.); noel.clark@colorado.edu (N.A.C.)

positional ordering of the layers (*15*, *16*) (Fig. 1C and fig. S4), as might be expected for a lower-temperature phase. Surprisingly, the B4 layering x-ray reflections appear as diffuse peaks (Fig. 1C and fig. S6), indicating the loss of long-range lamellar smectic order of the B2, and giving layer ordering over scales of only <40 nm (~8 layers). Nonetheless, this B4 local layering, although only short-range, is robust, yielding several harmonic reflections (fig. S5).

FFTEM (n = 9, 12) and AFM (n = 12) were used to reveal details of the B4 local layer structure, resulting in images of the layer organization of the B4 phase (Fig. 2, Fig. 3, and figs. S1, S7, and S8). The key evidence revealing the essential structural basis of the B4 phase came from FFTEM of samples that were cooled into the B4 phase from the higher-temperature phase to near room temperature, either rapidly cooled neat samples or slowly cooled samples diluted by isotropic solvent (*16*). The resulting images (Fig. 2, D to F, and fig. S1, D and F) reveal independently growing nanofilaments of twisted layers (Fig. 2C) similar to structures observed in the self-assembly of chiral biomolecules (*19*, *20*) and organic gelation (*21*). The nested smectic layers within each nanofilament exhibit strong saddle splay curvature with a radius comparable to only a few layers (e.g., Fig. 2, Fig. 3, and fig. S1). The FFTEM images show that the filaments are characterized by features at three distinct length scales, which we can identify as the smectic layer spacing d, the filament width w, and the half-pitch h of the layer twist in the filament. In regions of the images where the layers intersect the fracture plane at right angles, they appear as distinct periodic lines of spacing $d \approx 5$ nm (e.g., Fig. 2D), consistent with the x-ray spacing (Fig. 1C). An intermediate length scale is the width w of individual NFs, which we measured on isolated NFs to be 25 nm < w < 30 nm (Fig. 2, Fig. 3, and fig. S1). At longer length scale is the NF half-pitch, $h \approx 100$ nm, the distance over which the layer normal **z** makes a π rotation about the filament axis (Fig. 3, A to D). These lengths, although independently established in individually grown NFs, are highly uniform over scales of many micrometers (Fig. 2, D to G, and fig. S1), indicating that they are an inherent property of the local NF structure and formation. Each individual NF is clearly chiral in structure (Fig. 2, D to F), a spontaneously broken symmetry because the molecules are achiral; in addition, the filament assemblies are homogeneously chiral, with all filaments in each FFTEM image found to have the same handedness over micrometer length scales (Fig. 1B, Fig. 2, D to G, Fig. 3, and fig. S1) to form macroscopic (~100 μm) chiral conglomerate domains (Fig. 1B) (*22*). Because the filaments appear to grow independently, this macroscopic chirality indicates the presence of some effective chiral interaction between them, such as occurs in the homochiralization of stirred solutions (*23*), as otherwise they would appear locally in both left- and right-handed variants.

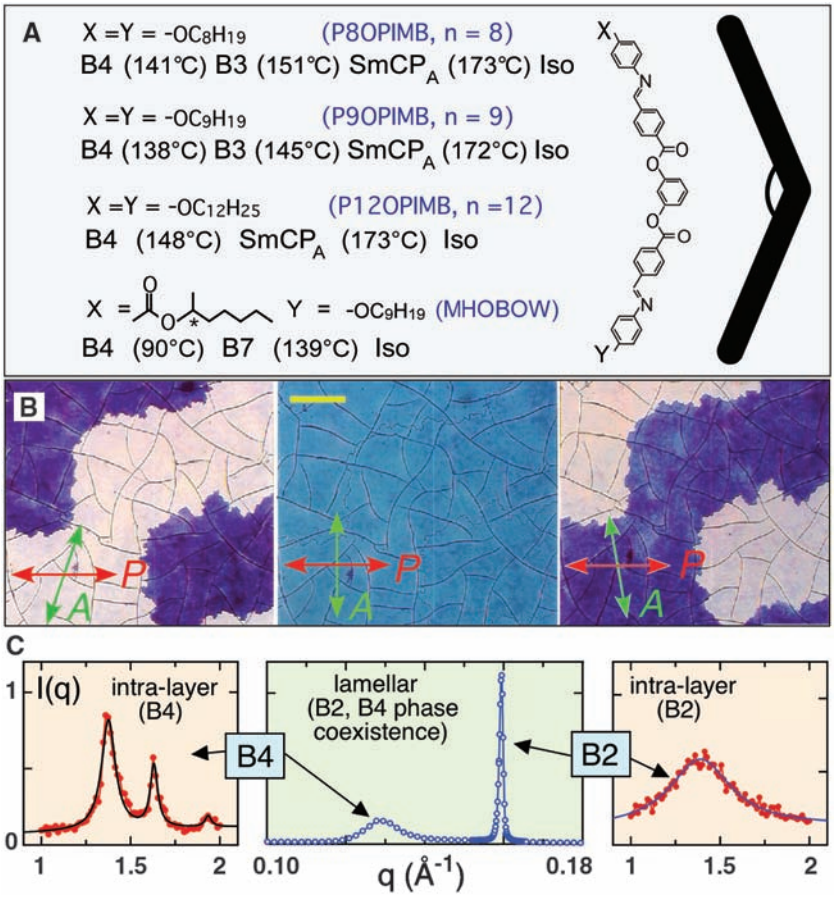

Fig. 1. (**A**) The structure and phase sequence upon cooling of the four B4 phase–forming compounds studied. (**B**) DTLM images of a 12-μm layer of the B4 phase of P12OPIMB between glass plates at T = 25°C. Scale bar, 100 μm. These materials are fluid at higher T in the B4 range and have become glassy at T = 25°C. With crossed polarizer (*P*) and analyzer (*A*), the sample transmits only weakly because of its low birefringence. Uncrossing the analyzer by 5° reveals areas of uniform but opposite optical activity, several hundred micrometers in width, indicating the formation of chiral conglomerate domains. (**C**) High-resolution powder x-ray diffraction of P9OPIMB shows that the resolution-limited peaks of the high-T fluid smectic B2 phase give way at the B2-B4 transition to a diffuse reflection indicating short-range local layering only in the B4 phase. At the same time, the broad wide-angle peak indicative of liquid-like in-plane order of the B2 phase is replaced by several diffuse peaks, indicating hexatic in-plane order within the layers in the B4 phase.

FFTEM and AFM of samples cooled slowly into the B4 phase show that the equilibrium bulk B4 structure is the ordered packing of NFs with little distortion of the filament structure (Fig. 2G, Fig. 3, and fig. S1), also characterized by the length scales d, w, and h. The smectic layering is apparent in both AFM and FFTEM images (Fig. 2, Fig. 3, and fig. S1), giving $d \approx$ 5 nm. The filament width w, which can be identified in the bulk images as the spacing between the distinct saddle domains (Fig. 3 and fig. S1), is approximately the same in the bulk structure as in the images of individual filaments (25 nm < w < 30 nm). Finally, the apparent periodicity appears as a range of values, $h(\theta) = h \sec(\theta) \geq 100$ nm, made longer by oblique cuts at angle θ to the helix axis (*16*).

The twisted nanofilament growth motif suggests that layer flatness becomes thermodynamically unfavorable in the HNF phase, which we now try to understand in terms of the layer structure. Transmission ED study of ultrathin B4 films, shear-aligned between polished NaCl crystals to have single or few domains of the in-layer ordering, produced a definitive determination of the in-plane structure in both flat layers and the twisted layers of nanofilaments (Fig. 4 and fig. S4). Because each of the four sublayers j [either tail (t) or core arm (ca)] of a given layer (t-ca-ca-t) is composed of parallel rod-like molecular elements tilted from the layer normal by angle β_j, the scattering from sublayer j is weak unless the scattering vector **q** lies within its form-factor sheet (i.e., is in the plane normal to $\mathbf{n}_j$) (*16*) (fig. S4B). As shown by powder x-ray diffraction measurement of $d(n)$, the B4 layer spacing versus carbon number n shows that d varies linearly with n (fig. S2), with a slope that indicates that $\beta_t = 24° \pm 2°$. An extrapolation to $n = 0$ yields a core (c) $d_c = 2.47$ nm (fig. S2), which, when combined with quantum chemical

calculations of the alkoxy O-O separation (L_{OO}, fig. S3), gives $\beta_{ca} = 38° \pm 2°$ (*16*). Thus, the core arms and tails have different tilts, making it possible to orient the layer to obtain substantial ED from only a single sublayer.

ED patterns of single domains of in-plane order showed distinct patterns for the flat and twisted layers, shown respectively in red and green in Fig. 4A. The red lattice is centered rectangular (index 0,1 and 1,0 peaks very weak) with herringbone order [(1,2) peak observed], as shown in fig. S4. The rectangular symmetry of this scattering indicates that the tilt direction of the scattering sublayer must be along either the 01 or 10 lattice symmetry directions. Radial scans through the (1,1), (0,2), and (1,2) peaks [Fig. 4A (red) and fig. S4A] yield an in-plane coherence length for in-plane order of ~6 nm in the flattened layers (*16*). The green lattice exhibits two distinct lattice spacings: (0,2) and (1,2) reflections that overlap with the red lattice, adding to give yellow in the overlaid image of Fig. 4A; and diffuse (1,1) peaks that are nonoverlapping and thus appear green, shifted out to higher q in the 01 direction, indicative of contributions from a distinct sublayer. Because a core arm tilt that is larger than the tail tilt requires a smaller spacing of the core arms and thus scattering at larger q, we assign the (green) diffuse $q_{(1,1)}$ peaks to be scattering from the cores, with the (0,2) and (1,2) reflections dominated by the tail layer. The resulting reciprocal space structure of each half-layer is sketched in fig. S4B.

Remarkably, the core arm (1,1) scattering is also rotated through ~5° relative to the tail scattering—a situation impossible for scattering from extended in-plane 2D ordering. This provides unambiguous evidence that this scattering is coming from a single tail sublayer and adjacent core arm sublayer within twisted layering of limited extent. This rotation is a consequence of the layer twist along the filaments [$180°/(h \approx 100$ nm) $\approx 2°$/nm], producing a comparable twist about the local **z** of a tail sublayer relative to its neighboring core arm layer, ~2 nm away ($2°/\text{nm} \times 2$ nm $\approx 4°$). An additional key observation is that the core arm lattice is sheared to be slightly oblique, with the lattice diagonals differing in length by ~2%. If the sublayer tilts were coplanar through the molecule, as in the untilted polar hexatic ($HexAP_F$) structure, this lattice of (1,1) core arm peaks would be rotated but at the corners of a square. The shear deformation indicates that the tilts of the upper and lower molecular halves are not coplanar, and because the tail lattice is rectangular, these halves must be in mutually orthogonal planes. In this geometry (Fig. 2B and fig. S4, B and F), connecting the molecular arms across the layer midplane to make complete molecules renders the structure macroscopically polar, with polarization **p** at 45° from the half-molecular tilt planes, t, singling out one of the (1,1) directions (cyan arrow, Fig. 4, C to H, and fig. S4, F to M). The structure is also chiral because of the tilt of the core planes (Fig. 4F and fig. S4F).

The geometry of the real-space tail and core arm lattices is sketched in fig. S4E, and the projections of the lattices from either side of the layer midplane onto the midplane (yellow and violet) are shown in fig. S4, E and G. Because of the anisotropy of the yellow and violet in-plane lattices (Fig. 4C and fig. S4G), the corresponding molecular halves cannot connect across the layer midplane if the layer is flat. However, they can be made to do so by bending the layers with saddle splay curvature (Fig. 4, D and E, blue arrows) such that the lattices match in the layer midplane; in this case, the molecular midpoints necessarily lie on a centered square lattice (orange, Fig. 4, C to H, and fig. S4M).

This lattice mismatch–driven layer curvature was modeled quantitatively, using the process indicated by the red arrows in Fig. 4D. The half-layers were represented by elastic slabs of the unit cell shape (Fig. 4C), taken to be isotropic for simplicity and thus characterized by compressional and shear elastic moduli, M and μ, respectively. The yellow half-layer of Fig. 4C was compressed in the t direction by a factor $1 - \beta$ ($\approx 7.3/8.4 = 0.87$, Fig. 4C), dilated by $1 + \beta$ in the $\perp$ direction (making it square), and adhered to the violet layer, which had been given the

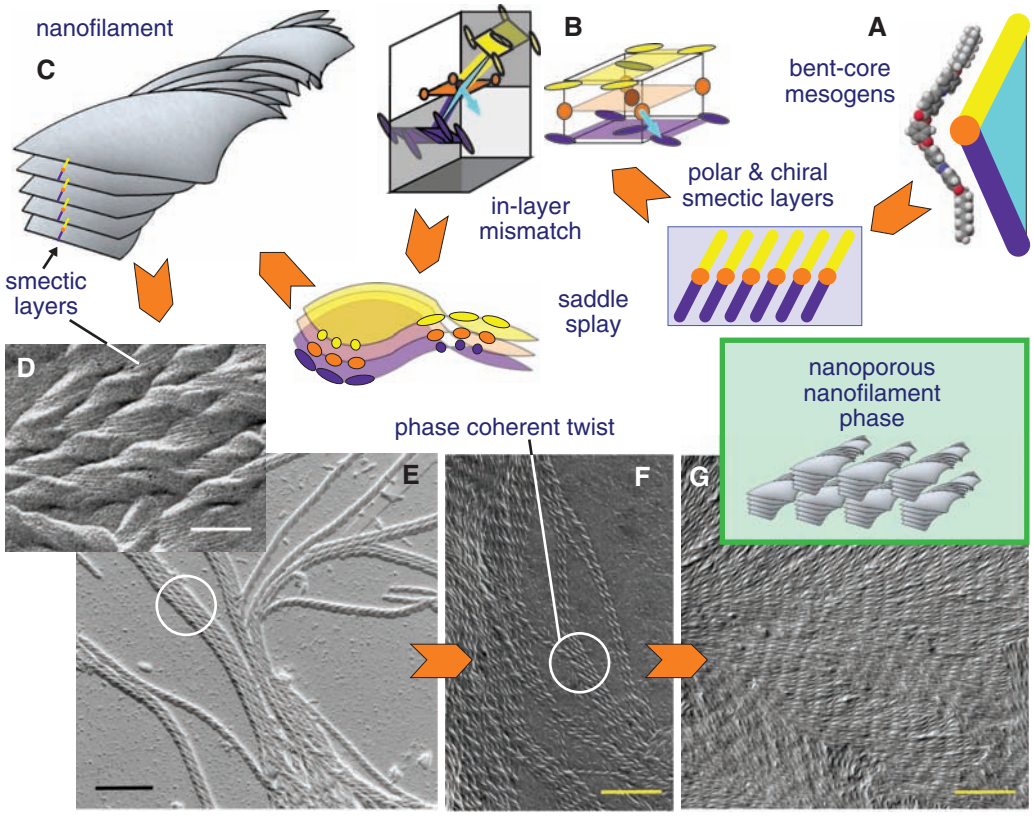

Fig. 2. (**A**) Hierarchical self-assembly of the nanofilament (NF) phase starts with bent-core mesogenic molecules, which form well-defined smectic layers with in-plane crystal or hexatic order, macroscopic polarization, and tilt of the molecular planes, making them chiral. (**B**) In this state, the half-molecular tilt directions on either side of the layer midplane are nearly orthogonal. (**C** to **F**) The projections onto the layer midplane of the lattices formed by the core arms (yellow and violet) do not match, resulting in a local preference for saddle splay layer curvature and driving the formation of nanofilaments. These nanofilaments grow independently [(E) and (F)] or collectively in packs that order in the bulk into a nanoporous nanofilament structure (F) having macroscopic coherence of the phase of the NF twist. (D) FFTEM image of NFs of P12OPIMB (T = 25°C). The smectic layers are visible, with a spacing $d \approx 5$ nm. (E) FFTEM image of NFs of P9OPIMB grown from a mixture with the calamitic LC 8CB (cooled from the isotropic phase and quenched from T = 37°C). (F) FFTEM image of individual NFs obtained by fast cooling of P12OPIMB from the isotropic to T = 25°C (quenched from T = 25°C). (**G**) FFTEM image of the bulk B4 phase of P9OPIMB at T = 25°C exhibiting large domains of parallel, coherently twisting NFs (quenched from T = 25°C). Note the phase coherence of the NF twist in independently grown but contacting filaments in (E) to (G) [circles in (E) and (F)], indicative of the phase fluidity and lubrication of the filaments enabling sliding along one another into preferred positions. Scale bars, 60 nm (D), 400 nm [(E) and (G)], 370 nm (F).

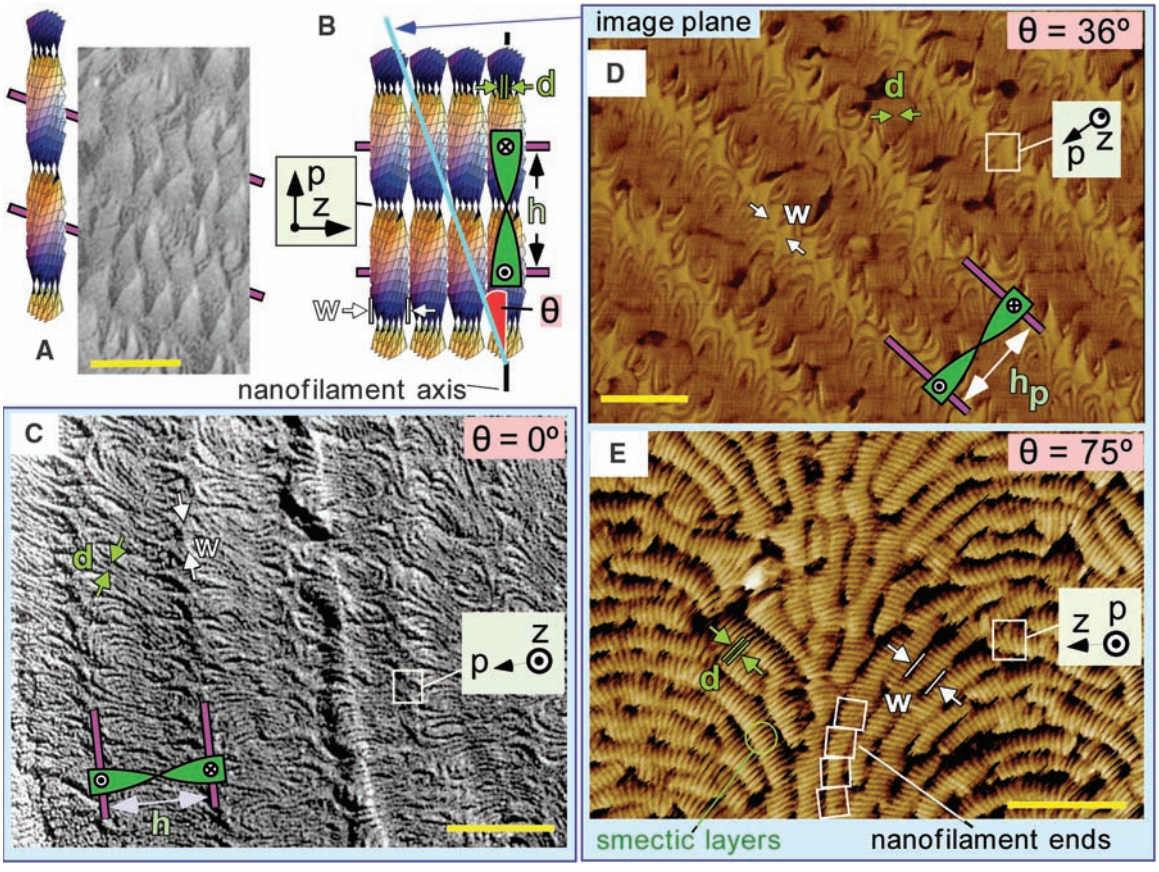

Fig. 3. (**A** and **C**) FFTEM images of P9OPIMB. (**D** and **E**) AFM images of P12OPIMB. These images show the three characteristic length scales of the bulk NF phase at T = 25°C [sketched in (**B**)]: individual layers as the thin dark lines spaced by $d \approx 5$ nm, the NF width $w \approx 25$ nm, and the NF twist half-pitch $h \approx 100$ nm. In (A), (C), and (D), image planes nearly parallel to the helix axis **p** reveal the distinct saddle structure of the layers. In (E), an AFM image of a plane nearly normal to **p** exhibits the Bouligand texture (*16*, *26*), showing the macroscopic helical precession of the smectic layers in the NF array, propagated by NFs (white squares) contacting with the layers face-to-face. In this image the NFs anneal at the surface into the "loaf-of-bread" structure, whereas in other images the NF terminations are more prominent (*16*) (figs. S7 and S8). Scale bars, 100 nm.

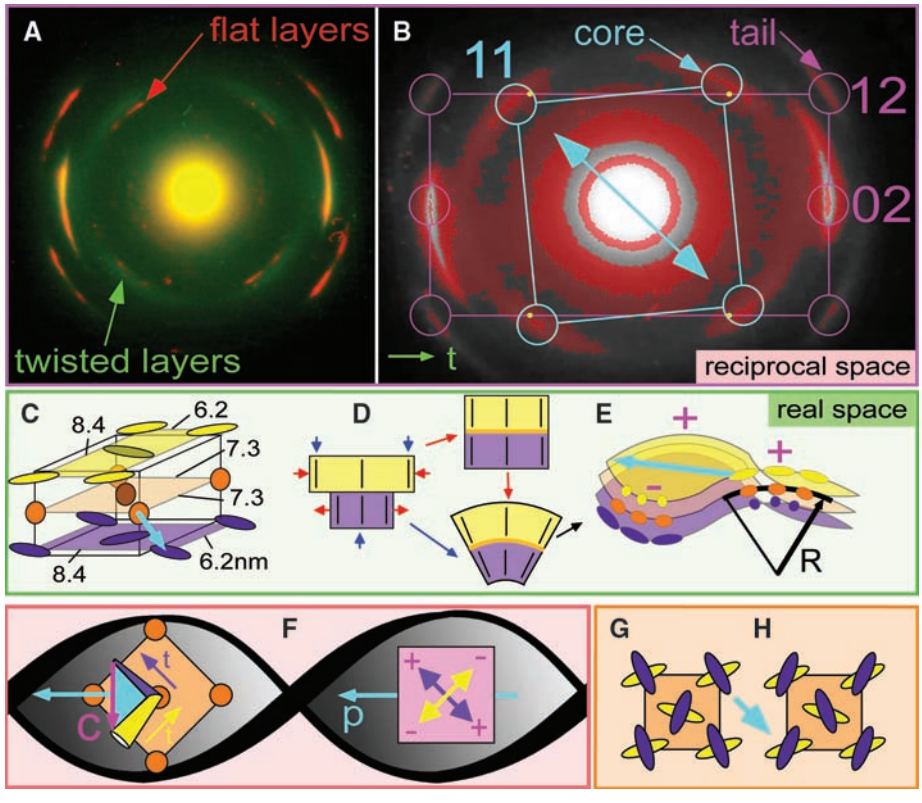

Fig. 4. Details of the molecular organization within the layer structure obtainable from the ED patterns of thin films of P9OPIMB. (**A** and **B**) Two different patterns, false-colored in red and green, are scattering from flattened layers and twisted layers within a single filament, respectively. The (1,1) peaks are diffuse but strong from the twisted layer sample and appear at larger q than expected on the basis of the (2,0) and (2,1) positions [yellow dots in (B)], indicating that there are two different lattices contributing to the ED of the twisted layers. The (1,1) peaks in (B) are due to the core domains and are rotated relative to the (2,0) and (2,1) peaks from the tail domains as a result of the twist of the layer within a filament. The (1,1) peak lattice is also sheared as a result of the chiral symmetry of polarization **p**, oriented along one of the square diagonals (cyan arrow). (**C**) The tilt of the tails relative to the cores is such that both lattices project onto the same centered rectangular herringbone lattice (yellow and purple layers). The rectangular lattices from the two half-layers (top, yellow; bottom, purple) are orthogonal. The two half-layers are covalently linked in the layer midplane (orange). (**D**) The elastic strain required to join the two half-layers can be partially relieved by layer curvature. (**E**) In the 3D case, this elastic strain leads to the formation of saddles, with elastic strain determined by the polarization (teal arrow) between the two principal curvature directions and the radius of curvature R. (**F**) This phase is SHG-active, and thus polar, and so the polarization direction must lie along the helix axis giving the molecular geometry shown. (**G** and **H**) The herringbone ordering and polarization create inequivalent sublattices that generate split peaks in the cross-polarization/magic angle spinning ^{13}C nuclear magnetic resonance of the B4 phase (*11*).

deformation of opposite sign until square. The elastic energy $f_E(\sigma', \sigma'')$ of the resulting laminate of half-layers in a given state of curvature was then calculated to quadratic order in the principal curvatures σ' and σ''. The layer elastic energy per volume obtained is $f_E = K/2(\sigma' + \sigma'')^2 - \bar{K}(\sigma'\sigma'') + G(\sigma'' - \sigma')$, where K is the Frank elastic constant for mean curvature $(\sigma' + \sigma'')$, $\bar{K}$ is the Frank constant for Gaussian curvature $(-\sigma'\sigma'')$, and $G \propto \beta$ drives curvature in response to the frustrated internal in-plane layer strain β (*16*). For a minimal surface ($\sigma = \sigma' = -\sigma''$), the free energy is particularly simple: $f_E^m = \bar{K}\sigma^2 - 2G\sigma$, making $R_p \equiv \bar{K}/G$ the preferred radius of curvature. The energy $f = f_E(\sigma', \sigma'') + \Delta u$, where Δu is the Gibbs potential per volume of the in-plane freezing, can be used to predict the structure of a filament, viewed as a set of ribbon-like layers twisted with a half-pitch $h \equiv \pi/q$ (*16*). The central layer is a minimal surface of curvature $\sigma = q$ along its centerline, so that for a very narrow ribbon ($w << h$), minimizing f_E^m gives $q = G/\bar{K}$ and therefore $h = \pi/\sigma_p = \pi R_p \sim 20$ nm. However, as T is lowered into the B4 range, the ribbon can further lower its free energy by growing wider, gaining Δu in a larger volume. Overall energy minimization yields finite-width filaments with the layer ordering suppressed (melted) outside, as the increase in w is ultimately limited by the energy cost of reduced (and thus less favorable) curvature away from the centerline in a wider ribbon. Predicted values of w and h are consistent with $R_p \sim 200$ nm, about 4 times the estimate from the in-layer structure (*16*).

The orientation of the in-plane structure within the nanofilaments is shown in Fig. 4, F to H, and fig. S4M. The lattice diagonal (polarization **p**) must be either along or normal to the NF axis for the saddle splay curvature to give the required NF twist (Fig. 4, E and F). The choice of **p** to be along the NF axis is clearly indicated by second harmonic generation (SHG) evidence for local C_∞ rather than D_∞ symmetry of the phase (*16*, *24*). With this orientation, the filament edges are (1,1) rows of molecules (fig. S4M); the result is a crystal face with a low Miller index that resists the addition of new material upon cooling, thereby promoting the highly anisotropic growth of the needle-like filaments.

Upon slow cooling into the B4 phase, the filaments appear via heterogeneous nucleation at dilute sites. Each nucleation site is homochiral; FFTEM and AFM show that once a handedness is chosen, single-handed domains are formed, out to distances of 10 to 100 μm. This leads to the observed strong "sergeants and soldiers" enantioselection of B4 chirality by weak chiral doping (*18*), chiral surface treatment (*25*), or nucleation from a chiral phase (*14*). At higher temperatures the NF phase is fluid, likely a consequence of lubrication of the filaments by the B2 or isotropic phase that is suppressed from hexatic ordering by the requirement for layer curvature. This fluidity enables the filaments to anneal in their orientation and twist phase into the coherent helical structures seen in Fig. 2G, Fig. 3, and fig. S1. Such coherence shows that the filaments must interact, but this interaction is weak in that it does not noticeably influence the structure of contacting filaments (Fig. 2, E and F). The AFM textures like that in Fig. 3E, visualizing the planes nearly normal to **p**, suggest that this interaction is strongest when layers in adjacent filaments are face-to-face and provide unambiguous evidence for the coherent macroscopic helical twist of the layering.

The B4 or HNF phase appears in a simple bent-core molecular system as a response to the competition between layering and twist inherent in chiral media. The inability of the best local solution to fill space selectively suppresses layering to produce a nanophase segregation of different degrees of order in a structural hierarchy that enables both macroscopic chirality and layering in an exotic liquid crystal phase.

References and Notes

1. J. F. Annett, *Superconductivity, Superfluids, and Condensates* (Oxford Univ. Press, Oxford, 2004).
2. M. Seul, D. Andelman, *Science* **267**, 476 (1995).
3. A. H. de Vries, S. Yefimov, A. E. Mark, S. J. Marrink, *Proc. Natl. Acad. Sci. U.S.A.* **102**, 5392 (2005).
4. D. A. Coleman *et al.*, *Science* **301**, 1204 (2003).
5. P. G. deGennes, *Solid State Commun.* **10**, 753 (1972).
6. S. R. Renn, T. C. Lubensky, *Phys. Rev. A* **38**, 2132 (1988).
7. J. Fernsler *et al.*, *Proc. Natl. Acad. Sci. U.S.A.* **102**, 14191 (2005).
8. T. Sekine *et al.*, *J. Mater. Chem.* **7**, 1307 (1997).
9. T. Sekine *et al.*, *Jpn. J. Appl. Phys.* **36**, 6455 (1997).
10. P. Collings *et al.*, *Abstracts of the First International Workshop on Banana-Shaped Liquid Crystals*, Berlin (1997) (www2.tu-berlin.de/~insi/ag_heppke/banana).
11. D. M. Walba, L. Eshdat, E. Korblova, R. K. Shoemaker, *Cryst. Growth Des.* **5**, 2091 (2005).
12. H. Takezoe, Y. Takanishi, *Jpn. J. Appl. Phys.* **45**, 597 (2006).
13. R. A. Reddy, C. Tschierske, *J. Mater. Chem.* **16**, 907 (2006).
14. H. Niwano *et al.*, *J. Phys. Chem. B* **108**, 14889 (2004).
15. J. Thisayukta, H. Takezoe, J. Watanabe, *Jpn. J. Appl. Phys.* **40**, 3277 (2001).
16. See supporting material on *Science* Online.
17. T. Niori, T. Sekine, J. Watanabe, T. Furukawa, H. Takezoe, *J. Mater. Chem.* **6**, 1231 (1996).
18. D. R. Link *et al.*, *Science* **278**, 1924 (1997).
19. A. Aggeli *et al.*, *Proc. Natl. Acad. Sci. U.S.A.* **98**, 11857 (2001).
20. M. S. Spector, J. M. Schnur, J. V. Selinger, in *Materials Chirality: A Special Volume in the Topics in Stereochemistry Series*, M. M. Green, R. J. M. Nolte, E. W. Meijer, Eds. (Wiley-VCH, Weinheim, Germany, 2002), pp. 281–372.
21. R. G. Weiss, P. Terech, *Molecular Gels: Materials with Self-Assembled Fibrillar Networks* (Springer, Dordrecht, Netherlands, 2005).
22. J. Thisayukta *et al.*, *J. Am. Chem. Soc.* **122**, 7441 (2000).
23. W. L. Noorduin *et al.*, *J. Am. Chem. Soc.* **130**, 1158 (2008).
24. F. Araoka *et al.*, *Phys. Rev. Lett.* **94**, 137801 (2005).
25. S.-W. Choi *et al.*, *Angew. Chem. Int. Ed.* **45**, 6503 (2006).
26. Y. Bouligand, F. Livolant, *J. Phys.* **45**, 1899 (1984).

27. Supported by NSF grant DMR 0606528 (N.A.C.), NSF Materials Research Science and Engineering Center grant DMR 0820579 (N.A.C.), an NSF Graduate Research Fellowship (L.H.), Deutsche Forschungsgemeinschaft grant Sfb 448 (J.P.R.), and NIH grant HL-51177 (J.Z.). Use of the National Synchrotron Light Source was supported by the U.S. Department of Energy, Divisions of Materials and Chemical Sciences.

Supporting Online Material

www.sciencemag.org/cgi/content/full/325/5939/456/DC1
Materials and Methods
SOM Text
Figs. S1 to S8
References

19 December 2008; accepted 4 June 2009
10.1126/science.1170027

Observational and Model Evidence for Positive Low-Level Cloud Feedback

Amy C. Clement,[1]* Robert Burgman,[1] Joel R. Norris[2]

Feedbacks involving low-level clouds remain a primary cause of uncertainty in global climate model projections. This issue was addressed by examining changes in low-level clouds over the Northeast Pacific in observations and climate models. Decadal fluctuations were identified in multiple, independent cloud data sets, and changes in cloud cover appeared to be linked to changes in both local temperature structure and large-scale circulation. This observational analysis further indicated that clouds act as a positive feedback in this region on decadal time scales. The observed relationships between cloud cover and regional meteorological conditions provide a more complete way of testing the realism of the cloud simulation in current-generation climate models. The only model that passed this test simulated a reduction in cloud cover over much of the Pacific when greenhouse gases were increased, providing modeling evidence for a positive low-level cloud feedback.

Low-level clouds are of great climatic importance because of their net cooling effect on the global climate (*1*). If the coverage of this type of cloud were to change as the climate warms, it could lead to either an enhancement or a reduction in the warming (i.e., as either a positive or negative feedback, depending on whether cloud cover decreases or increases). At

present, the sign of the low-level cloud feedback in climate change is unknown (*2*–*5*).

Previous research on the subtropical stratocumulus decks in the Northeast (NE) Pacific has laid the groundwork for our current understanding of environmental controls on this cloud type (*6*–*10*). These studies have shown that changes in local meteorological conditions can explain much of the variability in low-level cloud cover occurring on daily to interannual time scales. The longer-term variability of these clouds, however, has received much less attention, partly because long-term fluctuations in any particular cloud data set would rightly be regarded with some skepticism. Surface-based cloud observations, for instance, can be problematic due to the subjective nature of the measurement and sparse sampling for large regions of the ocean (*11*, *12*). Satellite-based cloud observations have spurious trends related to instrument drift and calibration (*13*, *14*) and are available for only the past 25 years. Here we examine long-term cloud variations in independent cloud data sets and analyze meteorological data to provide a physical framework for interpreting these variations.

Our principal source of data is monthly mean gridded surface-based observations of total cloud cover from the Comprehensive Ocean Atmosphere Data Set (*15*) (COADS) during 1952 to 2007. We supplement this with cloud-type information from COADS that has been compiled by Hahn and Warren (*16*) for the period 1952 to 1997, and in particular, we examine the category of marine stratiform clouds (comprising ordinary stratocumulus, cumulus under stratocumulus, fair-weather stratus, and bad-weather stratus). Additional independent information on total cloud amount, low-level cloud amount, and surface radiative fluxes is provided by the International Satellite Cloud Climatology Project (*17*, *18*) (ISCCP). Before using ISCCP data, we applied some adjustments to remove spurious long-term variability caused by satellite artifacts and to account for erroneous retrievals of low-level cloud-top height (*19*). Other climate variables used in the analysis are sea surface temperature (SST) (*20*), sea-level pressure (SLP) from the Hadley center reanalysis (*21*), and vertical velocity, surface winds, and lower tropospheric static stability (potential temperature at 700 mb minus surface temperature) from the ERA-40 reanalysis (*22*).

The time series of total and low-level cloud cover averaged over the NE Pacific (115° to 145°W, 15° to 25°N) are displayed in Fig. 1, A and B. Both COADS and adjusted ISCCP data sets show a shift toward more total cloud cover in the late 1990s, and the shift is dominated by low-level cloud cover in the adjusted ISCCP data (bars, in Fig. 1B). The longer COADS total cloud time series indicates that a similar-magnitude shift toward reduced cloud cover occurred in the mid-1970s, and this earlier shift was also dominated by marine stratiform clouds (bars, Fig. 1A). PATMOS-X, a next-generation version (*23*) of the Advanced Very High Resolution Radiometer Pathfinder Atmosphere (PATMOS) data set with improved algorithms (*24*), shows similar signals over the 1982 to 2007 period (fig. S1). These cloud changes appear throughout the year, and the shifts are also apparent in SST and SLP time series (Fig. 1, C and D).

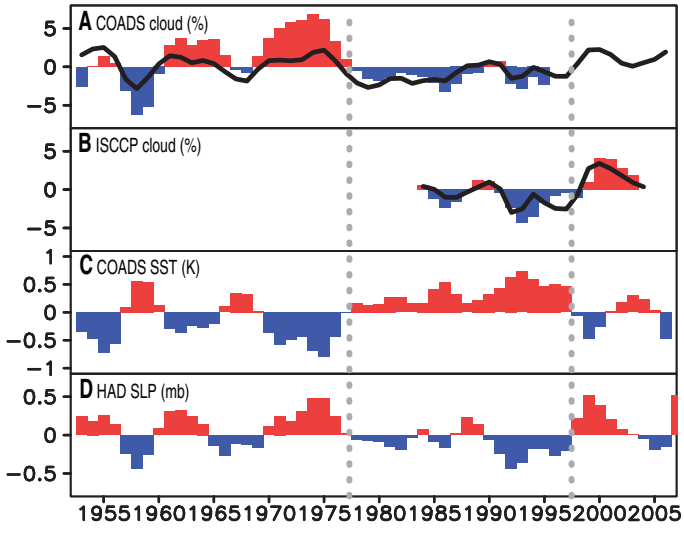

Fig. 1. Time series of annual mean values of cloud and climate quantities averaged over the NE Pacific (115° to 145°W, 15° to 25°N). The time mean of each field is removed, and a 1-2-1 smoothing is applied. (**A**) COADS total cloud cover (black line) and marine stratiform cloud cover (bars). Units are percent cloud cover. (**B**) Adjusted ISCCP total cloud cover (black line) and adjusted ISCCP low- plus mid-level cloud cover (bars). Units are percent cloud cover. (**C**) COADS SST. Units are K. (**D**) Hadley center SLP. Units are hPa. The vertical dashed lines indicate the approximate mid-point of the 1976 and 1990s climate shifts that have been previously identified in the literature. We use low- plus mid-level cloud cover from ISCCP rather than low-level only because low-level clouds can be mistakenly identified as mid-level clouds. This does not appear to be as much of an issue in the NE Pacific as it is for the SE Pacific (*19*).

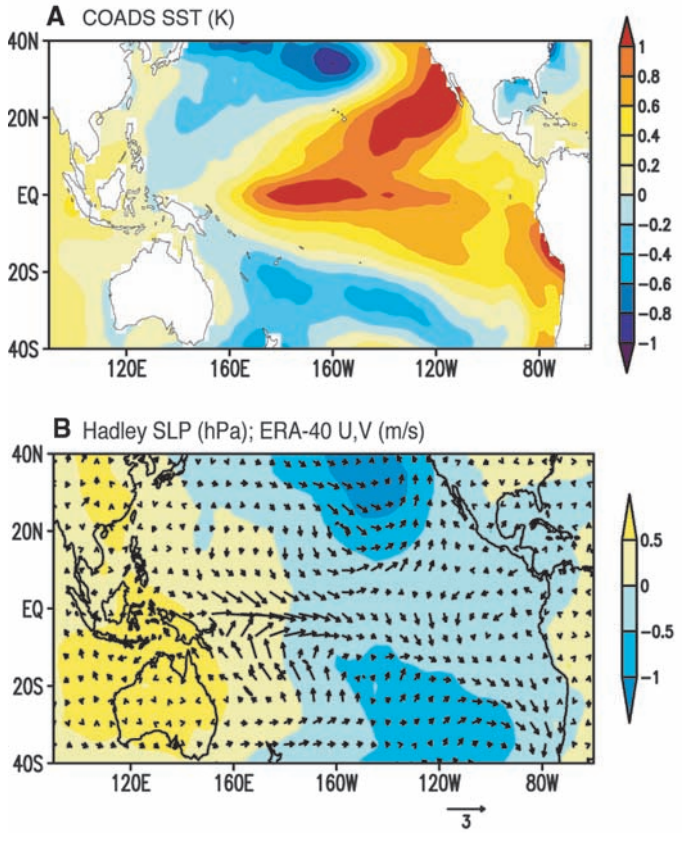

Fig. 2. Regression of climate variables on the time series of NE Pacific SST (from Fig. 1C). Values are shown per degree change in the NE Pacific index. (**A**) SST (in K). (**B**) SLP (colors, units of hPa), surface winds from ERA-40 (arrows, units of m/s).

[1]Rosenstiel School of Marine and Atmospheric Sciences, University of Miami, Division of Meteorology and Physical Oceanography, MSC 362, 4600 Rickenbacker Causeway, Miami, FL 33149, USA. [2]Scripps Institution of Oceanography, University of California-San Diego, La Jolla, CA 92093–0224, USA.

*To whom correspondence should be addressed. E-mail: aclement@rsmas.miami.edu

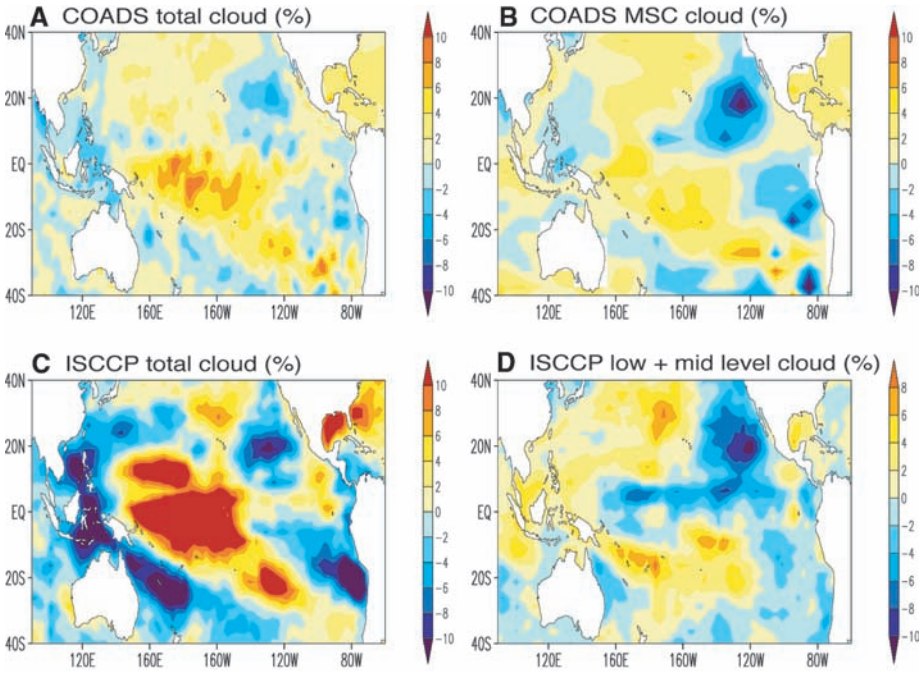

Fig. 3. Regression of cloud data on the time series of NE Pacific SST (from Fig. 1C). All panels are in units of percent cloud cover per degree change in the SST index. (**A**) COADS total cloud cover (for the period 1952 to 2006). (**B**) COADS marine stratiform cloud (MSC) cover (for the period 1952 to 1997). (**C**) Adjusted ISCCP total cloud and (**D**) adjusted ISCCP low- plus mid-level cloud cover [both (C) and (D) are for the period 1984 to 2005].

Table 1. Correlation between cloud and various meteorological quantities in the NE Pacific for observations and climate models. For the observations, the ISCCP-corrected and COADS cloud fraction (both total and low-level cloud values are shown) are correlated with observed SST (first column), lower tropospheric stability (LTS, second column), sea-level pressure (SLP, third column), and mid-tropospheric pressure vertical velocity (fourth column). For the models, the total cloud cover is used because the separate low-level cloud cover is not made available in this archive for most models. Models are grouped according to the sign of the correlation (*r*) relative to observations. We only include models for which all diagnostics are available. Statistical significance of the correlation values is calculated with a one-tailed *t* test. Degrees of freedom are derived with the lag-1 autocorrelation. Values that are significant at the 99% level are shown in bold.

	SST	LTS	SLP	ω 500
Observations				
ISSCP-corrected total	**-0.75**	0.44	**0.80**	0.30
ISCCP-corrected low + mid	**-0.91**	**0.81**	**0.89**	**0.70**
COADS total	**-0.74**	0.35	**0.73**	0.53
COADS MSC	**-0.82**	0.42	**0.74**	**0.70**
Models with the correct cloud-meteorology relationships				
ukmo_hadgem1	**-0.81**	**0.84**	**0.65**	**0.39**
inmcm3_0	**-0.77**	**0.37**	**0.58**	0.14
Models that simulate the wrong sign r(cloud, ω 500)				
mri_cgcm2_3_2a	**-0.60**	0.21	**0.35**	**-0.58**
gfdl_cm2_0	**-0.69**	0.06	**0.52**	**-0.42**
ncar_ccsm3_0	**-0.66**	**0.48**	**0.63**	-0.18
Models that simulate the wrong sign r(cloud, SLP)				
miroc3_2_hires	**-0.91**	**0.54**	-0.03	-0.10
Models that simulate the wrong sign (or close to zero) r(cloud, LTS)				
cccma_cgcm3_1_t63	**-0.86**	0.01	**0.52**	0.20
cccma_cgcm3_1	**-0.80**	-0.08	**0.35**	-0.14
cnrm_cm3	**-0.73**	-0.24	**0.54**	**-0.54**
ipsl_cm4	**-0.53**	-0.16	0.25	**-0.32**
ukmo_hadcm3	**-0.44**	-0.17	**0.33**	**-0.43**
gfdl_cm2_1	**-0.31**	**-0.38**	0.05	**-0.56**
mpi_echam5	-0.23	**-0.44**	0.06	**-0.70**
miroc3_2_medres	-0.13	-0.08	-0.04	**-0.67**
Models that simulate the wrong sign r(cloud, SST)				
giss_aom	0.12	**-0.63**	**-0.39**	**-0.67**
iap_fgoals1_0_g	0.22	**-0.43**	-0.24	**-0.89**
giss_model_e_h	0.34	0.10	0.10	**-0.81**
giss_model_e_r	**0.39**	-0.04	0.003	**-0.58**

The decadal changes in NE Pacific clouds and climate are linked to well-known basin-wide climate shifts (*25*–*30*). This is illustrated in Fig. 2, A and B, which shows that the regression patterns of SST, SLP, and ERA-40 surface winds on the NE Pacific SST time series resemble the now familiar pattern of Pacific Decadal Variability. The SST signal spans the entire Pacific basin and persists throughout the year, and the SLP pattern comprises a weaker Walker circulation in the equatorial region and a deeper Aleutian low in the North Pacific (Fig. 2B). The extension of the North Pacific SLP low anomaly into the stratocumulus region constitutes a weakening of the climatological high, and trade winds around the high are weakened (hence the anomalous southerly and westerly flow shown in Fig. 2B). The subsidence and lower tropospheric stability (LTS) in the NE Pacific are both weaker when SST is warm there (fig. S2).

The spatial patterns of cloud-cover change (Fig. 3) are physically consistent with the local meteorological changes displayed in Fig. 2 and fig. S2, with reduced cloud cover in the NE Pacific when SST is warm, SLP is low, and subsidence, equatorward advection, and static stability are weak (*6*–*10*). For COADS total cloud, we calculate the regression over the entire time period (Fig. 3A), which includes both the 1976 and late-1990s shifts. The regression for marine stratiform cloud (Fig. 3B), however, includes only the 1976 shift due to lack of the Hahn and Warren data compilation after 1997. A comparison of the patterns in Fig. 3, A and B, indicates that marine stratiform cloudiness dominates the total cloud cover change and that the climate shifts in 1976 and the late 1990s were analogous but of opposite sign (i.e., the

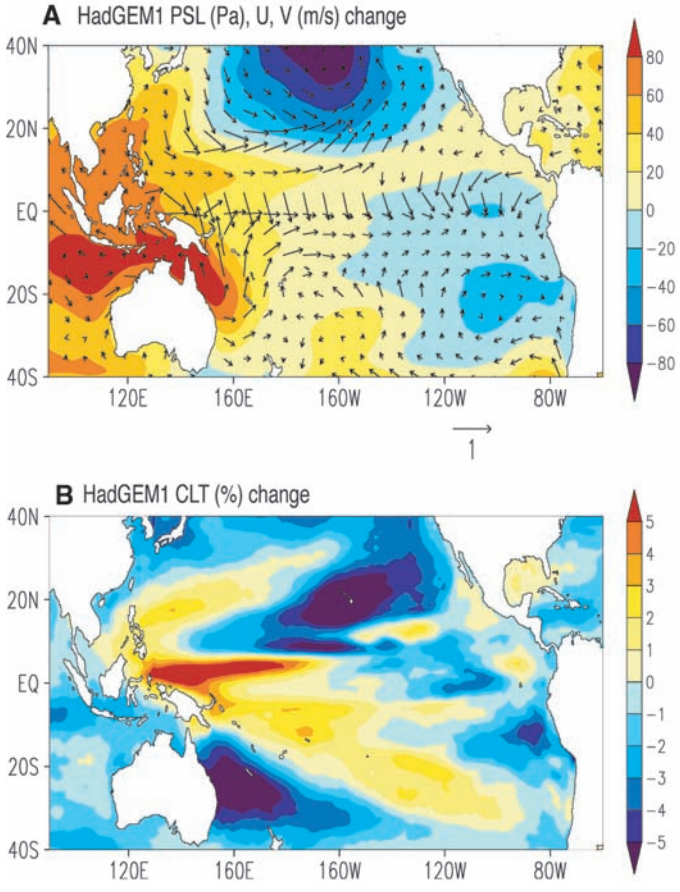

Fig. 4. (**A**) UKMO-HadGEM1 sea-level pressure change in 2 × CO_2 – present climate (in Pa). (**B**) Total cloud cover (CLT) change (%) in UKMO-HadGEM1 for 2 × CO_2 – present climate. These data are taken from the 1pctto2x experiment, which was initialized from year 410 of the PIcntrl experiment. CO_2 was increased by 1% per year, compounded until doubling (year 480), and then held fixed [at 710 parts per million (ppm)] for another 150 years. The differences shown in this figure were calculated by taking the last 50 years of the simulation with CO_2 held at 710 ppm and subtracting years 1 to 70 of the simulation.

earlier shift was a warming and reduction in clouds and the latter a cooling and increase in clouds). The adjusted ISCCP regressions for total and low-level cloud (Fig. 3, C and D) are in agreement with both total and marine stratiform cloudiness from COADS. This concurrence is surprising given the fundamentally different measurement methods (human eye versus satellite retrieval and algorithm). Furthermore, the similarity in pattern and magnitude between adjusted ISCCP low-level cloud cover and the COADS marine stratiform cloud cover is especially impressive considering that they do not occur over the same climate shifts (adjusted ISCCP captures only the late-1990s shift, whereas COADS marine stratiform captures only the 1976 shift). The larger size of both COADS and adjusted ISCCP low-level cloud signals relative to the total cloud signals in the NE Pacific indicates that upper-level clouds increase when low-level clouds decrease. Enhanced upper-level cloud cover is consistent with the weakening of subsidence over the NE Pacific (fig. S2).

We emphasize that the NE Pacific cloud changes described above are tied to cloud changes that span the Pacific basin. Despite much less surface sampling in the Southeast (SE) Pacific, cloud and meteorological changes in that region generally occur in parallel with those in the NE Pacific (Figs. 2 and 3). Also, we find that the leading mode in an empirical orthogonal function analysis (15% of the variance) of global cloud cover (fig. S3) has a spatial pattern similar to that in Fig. 3 and the time series shows the same decadal shifts as in Fig. 1, indicating that the changes in the NE Pacific are part of a dominant mode of global cloud variability.

The regression of adjusted shortwave and longwave cloud radiative effects from the ISCCP Flux Dataset on NE Pacific SST reveals that the change in net cloud radiative effect warms the ocean by about 6 W m^{-2} K^{-1} (fig. S4). Despite the weaker winds, latent heat flux anomalies still act to cool the ocean when SST is warmer (*31*). Model studies have shown a negligible simulated SST response when forced with a wind pattern like that displayed in Fig. 2B (*32*), suggesting that ocean dynamics play little role in NE Pacific decadal SST variability. Hence, we conclude that a change in solar heating of the ocean due to a change in stratocumulus cloud cover is the principal factor maintaining decadal SST anomalies in the NE Pacific. Previous studies have shown that decreased cloud cover and warm SST additionally promote weaker circulation (*33*–*37*). This response is caused by a decrease in longwave radiative cooling of the boundary layer by clouds that reduces large-scale horizontal temperature and pressure gradients. The existence of these same relationships among SST, cloud, and circulation on decadal time scales implies that changes in subtropical stratocumulus act as a positive feedback on climate in the region.

Is this feedback present in climate models? To address this question, we analyze the 20th-century climate simulation in 18 coupled ocean-atmosphere general circulation models with comprehensive output available from the World Climate Research Programme's (WCRP's) Coupled Model Intercomparison Project phase 3 (CMIP3) multimodel archive (*38*, *39*). Correlations between cloud cover in the NE Pacific and the local thermal structure (SST and LTS) and circulation (SLP and mid-tropospheric vertical velocity) are computed for each model and compared with observations in Table 1. Models are grouped according to whether they have the wrong sign correlation relative to observations. By eliminating models successively on this basis, we are left with only two that simulate the correct sign correlations for all variables, the INM-CM3.0 and the HadGEM1. Because these two models represent opposite ends of the range of values of equilibrium climate sensitivity (INM-CM3.0 has the lowest value and HadGEM1 has the highest) (*5*), the cloud-meteorology correlation test alone is not a sufficient metric for global climate sensitivity.

These models are distinct in other ways that are relevant for the simulation of low-level clouds. The INM-CM3.0 adopts a more empirical approach that parameterizes low-level cloud cover as a linear function of relative humidity with coefficients that depend on temperature, altitude, land/ocean, and stratification (*40*), whereas the HadGEM1 has higher spatial resolution, more explicit cloud microphysics, interactive parameterization of cloudiness as a function of local variability in humidity, and a sophisticated planetary boundary-layer mixing scheme (*41*, *42*). Moreover, the HadGEM1 produces doubled carbon dioxide (2 × CO_2) changes in SST, LTS, and circulation that are consistent with the multimodel mean, but the INM-CM3.0 does not (fig. S5). Unlike the INM-CM3.0, most models simulate a weakening of tropical atmospheric circulation under increased greenhouse gases (*43*)—a phenomenon that appears in 20th-century observations as well (*43*, *44*).

Our observational analysis indicates that increased SST and weaker subtropical highs (Fig. 4A) will act to reduce NE Pacific cloud cover, as indeed occurs in HadGEM1 under increased greenhouse gases (Fig. 4B). Although one might expect an increase in low-level cloud cover from the increase in LTS simulated by all models for 2 × CO_2 (*45*, *46*), the resemblance of the spatial structures of the HadGEM1 2 × CO_2 cloud change and SLP change (Fig. 4) to observed decadal cloud and SLP variability suggests that LTS does not play a dominant role. Although we cannot evaluate the exact causes of these cloud changes without additional experiments, the decreased cloud cover in subtropical stratocumulus regions appears to

result from warmer SST and a weakening of the large-scale atmospheric circulation in the Pacific in this model.

The question of whether low-level clouds act as a positive or negative feedback to climate change has been an issue for decades. The analysis presented here provides observational evidence that this feedback is positive in the NE Pacific on decadal time scales. The only model in the CMIP3 archive that properly simulates clouds in the NE Pacific and exhibits $2 \times CO_2$ circulation changes that are consistent with multimodel mean produces a reduction in cloud throughout much of the Pacific in response to greenhouse gas forcing (i.e., a positive feedback). Evaluating cloud feedback with one model is, however, far from ideal. This presents a clear challenge to develop a larger number of climate models that can pass these and other tests so that we may have greater confidence in the sign of the low-cloud feedback under future changes in greenhouse gas concentrations.

References and Notes

1. D. L. Hartmann, M. E. Ockert-Bell, M. L. Michelsen, *J. Clim.* **5**, 1281 (1992).
2. S. Bony, J.-L. Dufresne, *Geophys. Res. Lett.* **32**, L20806 (2005).
3. B. J. Soden, I. M. Held, *J. Clim.* **19**, 3354 (2006).
4. M. J. Webb *et al*., *Clim. Dyn.* **27**, 17 (2006).
5. Intergovernmental Panel on Climate Change, *Climate Change 2007: The Physical Science Basis,* Contribution of Working Group I to the Fourth Assessment Report of the IPCC, S. Solomon *et al*., Eds. (Cambridge Univ. Press, Cambridge, 2007).
6. S. A. Klein, D. L. Hartmann, *J. Clim.* **6**, 1587 (1993).
7. S. A. Klein, D. L. Hartmann, J. R. Norris, *J. Clim.* **8**, 1140 (1995).
8. J. R. Norris, S. A. Klein, *J. Clim.* **13**, 245 (2000).
9. B. Stevens *et al*., *Mon. Weather Rev.* **135**, 985 (2007).
10. J. R. Norris, C. B. Leovy, *J. Clim.* **7**, 1915 (1994).
11. J. R. Norris, *J. Clim.* **12**, 1864 (1999).
12. J. R. Norris, *J. Geophys. Res.* **110**, D08206 (2005).
13. A. T. Evan, A. K. Heidinger, D. J. Vimont, *Geophys. Res. Lett.* **34**, L04701 (2007).
14. J. R. Norris, *Space Sci. Rev.* **94**, 375 (2000).
15. S. J. Worley, S. D. Woodruff, R. W. Reynolds, S. J. Lubker, N. Lott, *Int. J. Climatol.* **25**, 823 (2005).
16. C. J. Hahn, S. G. Warren, "Extended edited synoptic cloud reports from ships and land stations over the globe, 1952-1996," NDP-026C (Carbon Dioxide Information Analysis Center, Oak Ridge National Laboratory, Oak Ridge, TN, 1999); available at http://cdiac.esd.ornl.gov/epubs/ndp/ndp026c/ndp026c.html.
17. W. B. Rossow, R. A. Schiffer, *Bull. Am. Meteorol. Soc.* **80**, 2261 (1999).
18. Y. Zhang, W. B. Rossow, A. A. Lacis, V. Oinas, M. I. Mishchenko, *J. Geophys. Res.* **109**, D19105 (2004).
19. Supporting material is available at *Science* Online.
20. T. M. Smith, R. W. Reynolds, *J. Clim.* **16**, 1495 (2003).
21. R. Allan, T. Ansell, *J. Clim.* **19**, 5816 (2006).
22. S. M. Uppala *et al*., *Q. J. R. Meteorol. Soc.* **131**, 2961 (2006).
23. M. J. Pavolonis, A. K. Heidinger, T. Uttal, *J. Appl. Meteorol.* **44**, 804 (2005).
24. H. Jacobowitz *et al*., *Bull. Am. Meteorol. Soc.* **84**, 785 (2003).
25. C. Deser, A. S. Phillips, J. W. Hurrell, *J. Clim.* **17**, 3109 (2004).
26. N. J. Mantua, S. R. Hare, Y. Zhang, J. M. Wallace, R. C. Francis, *Bull. Am. Meteorol. Soc.* **78**, 1069 (1997).
27. W. T. Peterson, F. B. Schwing, *Geophys. Res. Lett.* **30**, 1896 (2003).
28. J. Chen, A. D. Del Genio, B. E. Carlson, M. G. Bosilovich, *J. Clim.* **21**, 2634 (2008).
29. R. J. Burgman, A. C. Clement, C. M. Mitas, J. Chen, K. Esslinger, *Geophys. Res. Lett.* **35**, L01704 (2008).
30. Y. Zhang, J. M. Wallace, D. S. Battisti, *J. Clim.* **10**, 10041020 (1997).
31. R. Seager, M. Benno Blumenthal, Y. Kushnir, *J. Clim.* **8**, 1951 (1995).
32. W. Hazeleger, R. Seager, M. Cane, N. Naik, *J. Phys. Oceanogr.* **34**, 320 (2004).
33. J. R. Norris, *J. Geophys. Res. Atmos.* **110**, D21110 (2005).
34. C.-C. Ma, C. R. Mechoso, A. W. Robertson, A. Arakawa, *J. Clim.* **9**, 1635 (1996).
35. Y. Wang, S.-P. Xie, B. Wang, H. Xu, *J. Clim.* **18**, 934 (2005).
36. S. Nigam, *J. Clim.* **10**, 2447 (1997).
37. V. Misra, L. Marx, *J. Geophys. Res.* **112**, D20105 (2007).
38. G. A. Meehl *et al*., *Bull. Am. Meteorol. Soc.* **88**, 1383 (2007).
39. We only include the 18 (of 23) models for which all of the diagnostics used in this study are available.
40. E. M. Volodin, N. A. Dianskii, *Russ. Meteorol. Hydrol.* **12**, 1 (2004).
41. T. C. Johns *et al*., *J. Clim.* **19**, 1327 (2006).
42. A. P. Lock, A. R. Brown, M. R. Bush, G. M. Martin, R. N. B. Smith, *Mon. Weather Rev.* **128**, 3187 (2000).
43. G. A. Vecchi, B. J. Soden, *J. Clim.* **20**, 4316 (2007).
44. M. Zhang, H. Song, *Geophys. Res. Lett.* **33**, L12701 (2006).
45. R. L. Miller, *J. Clim.* **10**, 409 (1997).
46. B. Medeiros *et al*., *J. Clim.* **21**, 4974 (2008).

47. We gratefully acknowledge comments from B. Stevens and two anonymous reviewers. We also acknowledge the various international modeling groups participating in IPCC/AR4, the Program for Climate Model Diagnosis and Intercomparison (PCMDI), and the IPCC Data Archive at Lawrence Livermore National Laboratory (supported by the Office of Science, U.S. Department of Energy) for providing the data that made this analysis possible. Funding for this work was provided by the National Oceanic and Atmospheric Administration Office of Global Programs (grant NA06OAR4310142). An NSF CAREER award (ATM02-38527) supported the work by J.R.N.

Supporting Online Material

www.sciencemag.org/cgi/content/full/325/5939/460/DC1
SOM Text
Figs. S1 to S5
References

22 January 2009; accepted 11 June 2009
10.1126/science.1171255

The Dynamics of Phenotypic Change and the Shrinking Sheep of St. Kilda

Arpat Ozgul,[1] Shripad Tuljapurkar,[2] Tim G. Benton,[3] Josephine M. Pemberton,[4] Tim H. Clutton-Brock,[5] Tim Coulson[1]*

Environmental change, including climate change, can cause rapid phenotypic change via both ecological and evolutionary processes. Because ecological and evolutionary dynamics are intimately linked, a major challenge is to identify their relative roles. We exactly decomposed the change in mean body weight in a free-living population of Soay sheep into all the processes that contribute to change. Ecological processes contribute most, with selection—the underpinning of adaptive evolution—explaining little of the observed phenotypic trend. Our results enable us to explain why selection has so little effect even though weight is heritable, and why environmental change has caused a decline in the body size of Soay sheep.

A major goal of population biology is to understand how environmental change generates a rapid phenotypic response (*1*, *2*). Recently, it has been recognized that evolution can occur on ecological time scales (*2*), and the new challenge is to differentiate trait dynamics driven by evolution from those driven by ecological responses to environmental change (*3*). This is difficult because ecological and evolutionary effects are intimately intertwined (*2*, *4*), and available analytical methods do not allow the quantification of different sources of change. For example, evolutionary models of phenotypic change (*5*, *6*) focus on selection and the genetic response to it (*7*). However, when applied in well-studied, pedigreed, wild animal populations, they often fail to explain phenotypic outcome, leading many authors to speculate that plastic responses to environmental variation play a large role in phenotypic dynamics (*1*, *8*–*11*). Conversely, some phenotypic trends are interpreted as evolutionary change without any evolutionary analysis. An exact method to decompose phenotypic change into contributing processes would aid in identifying the roles of selection (the underpinning of adaptive evolution) and ecology in generating phenotypic trends.

In 1970, Price developed an equation that describes change in the mean value of a phenotypic

[1]Department of Life Sciences, Imperial College London, Silwood Park, Ascot, Berkshire SL5 7PY, UK. [2]Department of Biology, Stanford University, Stanford, CA 94305-5020, USA. [3]Faculty of Biological Sciences, University of Leeds, Leeds LS2 9JT, UK. [4]Institute for Evolutionary Biology, University of Edinburgh, Kings Buildings, West Mains Road, Edinburgh EH9 3JT, UK. [5]Department of Zoology, University of Cambridge, Downing Street, Cambridge CB2 3EJ, UK.

*To whom correspondence should be addressed. E-mail: t.coulson@imperial.ac.uk

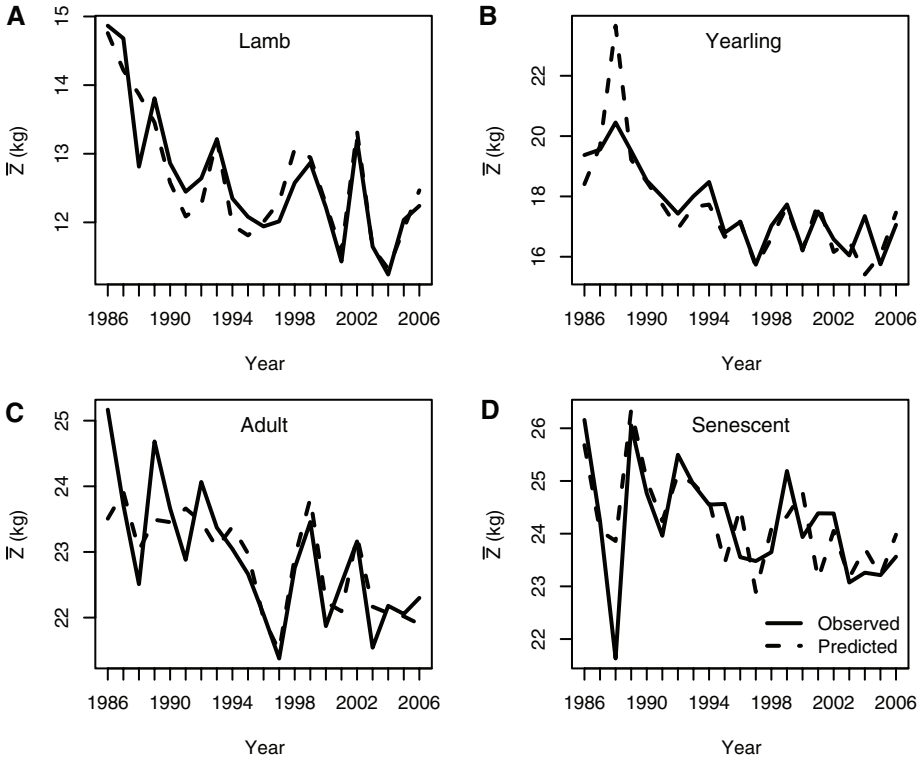

Fig. 1. Mean annual August weights for (**A**) lambs, (**B**) yearlings, (**C**) adults, and (**D**) senescent female Soay sheep. The solid lines show the observed fluctuations in $\Delta\bar{Z}$, and the dashed lines show those obtained from the application of the age-structured Price equation. Lambs declined on average (±SE) by 90 ± 30 g/year, yearlings by 170 ± 30 g/year, adults by 120 ± 30 g/year, and senescent sheep by 80 ± 60 g/year. This pattern of decline suggests some compensatory growth at later ages. The majority of the decline in body size occurred in the first decade of the study, when population size increased and the North Atlantic Oscillation was predominantly positive. The solid and dashed lines do not match perfectly because several of the terms require information on animals caught in successive catches—a constraint that is not required when estimating observed mean body weight.

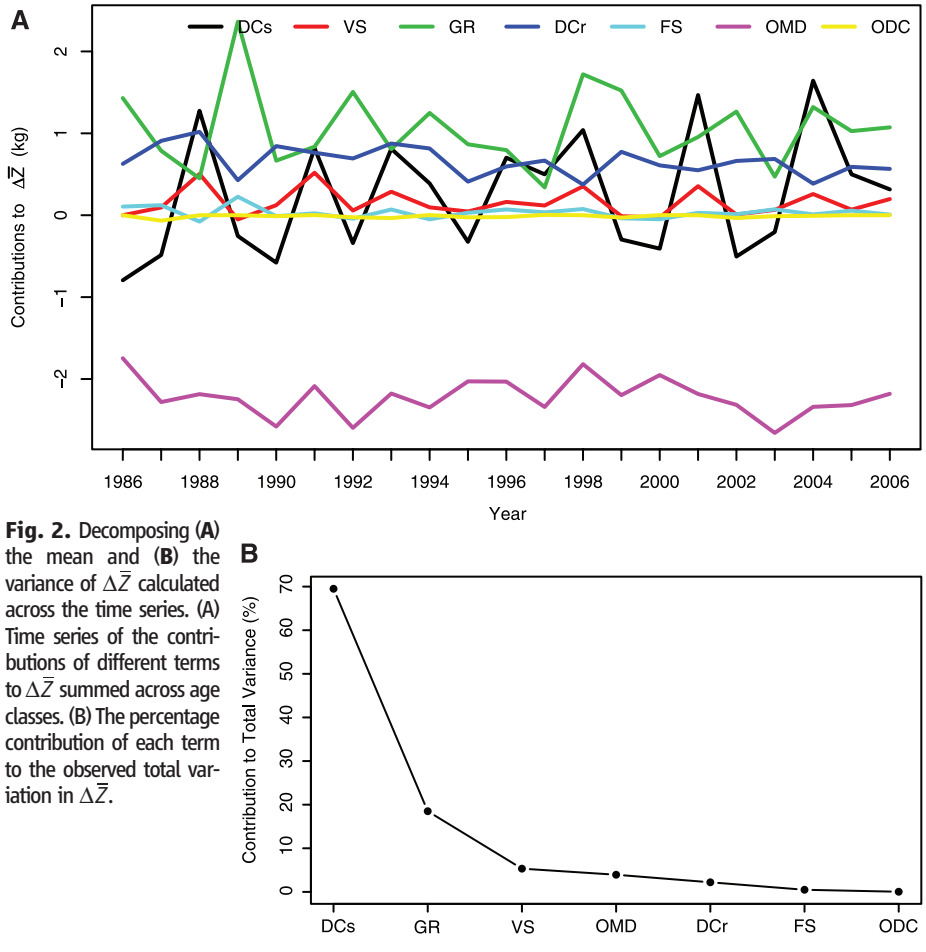

Fig. 2. Decomposing (**A**) the mean and (**B**) the variance of $\Delta\bar{Z}$ calculated across the time series. (A) Time series of the contributions of different terms to $\Delta\bar{Z}$ summed across age classes. (B) The percentage contribution of each term to the observed total variation in $\Delta\bar{Z}$.

trait, $\Delta\bar{Z}$, with time (*12*). Coulson and Tuljapurkar (*13*) derived an age-structured version of this equation, which separates fitness into its survival and fertility components. This equation permits an exact retrospective decomposition of $\Delta\bar{Z}$ into contributions from selection and other processes in a variable environment. Survival-related terms are (i) changes in demographic structure (DCs) caused by age-specific survival rates (*14*); (ii) age-specific viability selection (VS) differentials, which describe change resulting from differential survival associated with the trait (*15*); and (iii) age-specific trait development, which describes how the average trait value changes among surviving individuals as they age [growth rate (GR)]. Reproduction-related terms are (i) changes in demographic structure caused by age-specific reproduction (DCr) (*14*); (ii) age-specific fertility selection (FS) differentials, which describe the difference in mean trait value between selected parents and the unselected population (*16*); (iii) the mean age-specific difference between offspring and parental trait values [offspring-mother difference (OMD)] (*12*); and (iv) the covariation between litter size and the difference between offspring and parental trait values [offspring difference covariance (ODC)] (*13*).

Using the age-structured Price equation and data from an ungulate population, we decomposed the observed change in a heritable phenotypic trait into the different contributing processes. We used detailed individual-based life history data and August body weights from the female component of a population of Soay sheep living on the island of Hirta in the St. Kilda archipelago, Scotland (*7*). We focused on this heritable trait

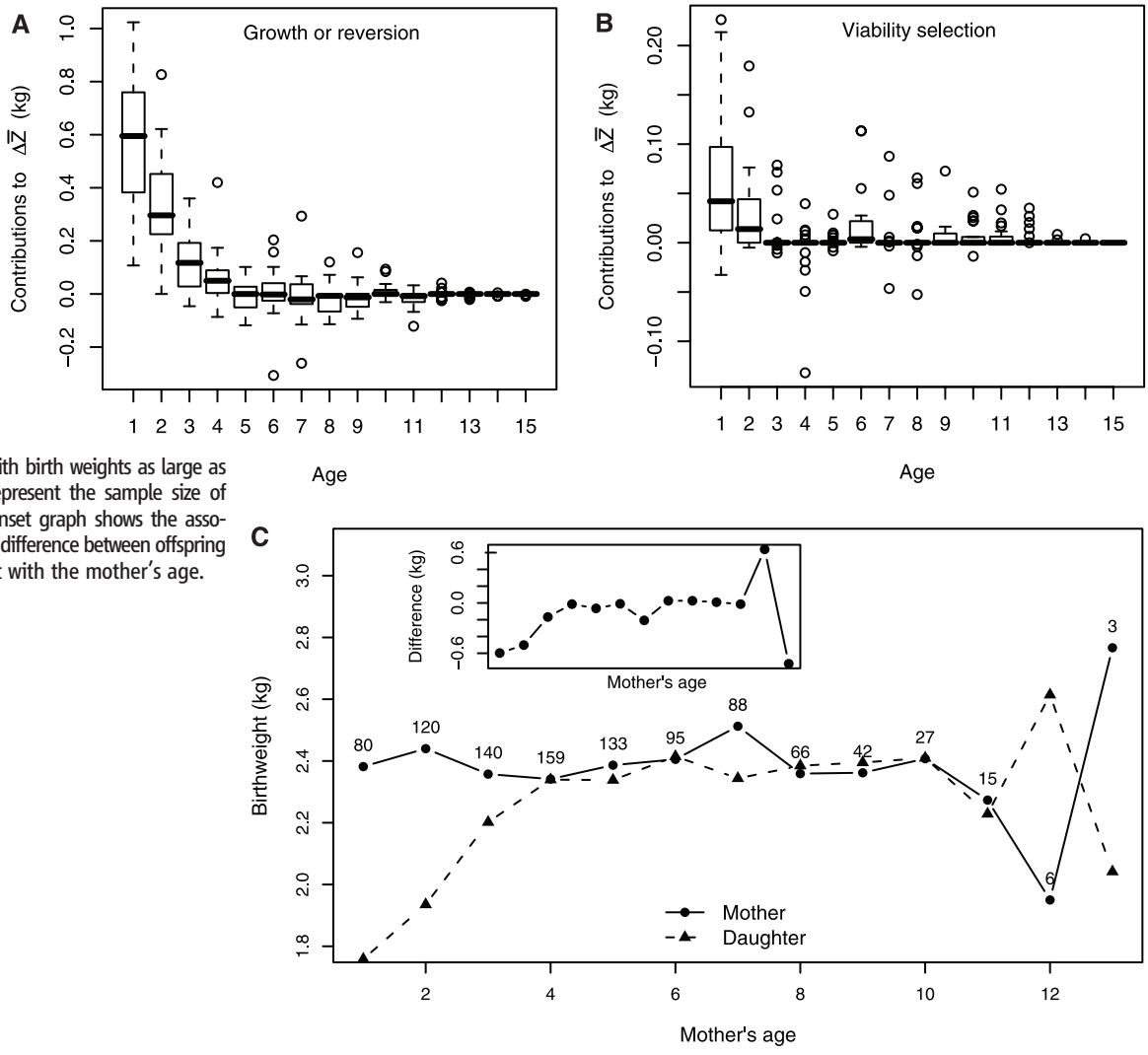

Fig. 3. Distributions of age-specific contributions to $\Delta\bar{Z}$ from (**A**) growth or reversion (GR) and (**B**) VS over time. Box plots show the median contribution (heavy horizontal lines), interquartile range (bars), non-outlier limits (dotted lines), and outliers (circles) for each age group. (**C**) Mean maternal and female offspring birth weights as a function of maternal age. On average, mothers less than 4 years old are unable to produce female offspring with birth weights as large as their own. The numbers represent the sample size of mothers at each age; the inset graph shows the association between the average difference between offspring and maternal birth weight with the mother's age.

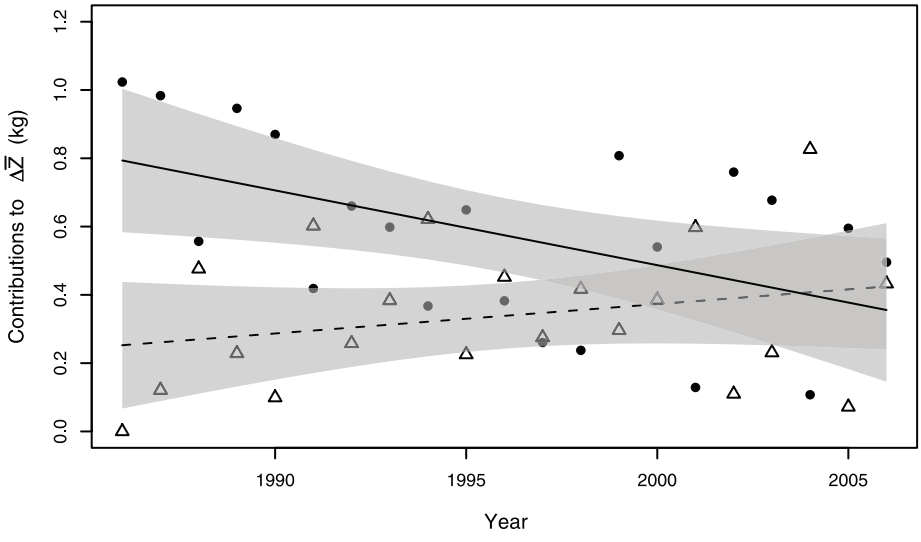

Fig. 4. Temporal trend in the contributions of GRs to $\Delta\bar{Z}$ from the first to the second (circles) and the second to the third (triangles) August of life. Trends in these contributions occur because of a decrease in the GRs of individuals in the first year of life [$\bar{G}_+(1,t)$] rather than a change in the proportion of lambs within the population. The significant decline in the contribution of growth in the first year of life (solid line, $F_{1,19} = 6.50$, $P = 0.02$) is partly compensated for by a nonsignificant increase in the contribution from growth in the second year of life (dashed line, $F_{1,19} = 1.29$, $P = 0.27$). Shaded regions indicate the 95% confidence limits.

because mean body weight has fluctuated substantially around a declining trend over 20 years (*17*). Previous research has reported this declining trend despite positive selection for larger body size; it has been speculated that these counterintuitive findings result from environmental deterioration obscuring evolutionary change (*18*).

We grouped individuals into four age classes (*19*): lambs (<1 year), yearlings, prime-aged adults (2 to 6 years), and senescent individuals (>6 years). Mean weights fluctuated around a declining trend in all age classes (Fig. 1), with declines representing a loss of between ~0.3% (senescents) and ~0.8% (yearlings) of mean body weight/year. This decline is mirrored by a decrease in hindleg length (*7*), suggesting that the body weight decline reflects sheep getting smaller rather than a decline in body condition.

We decomposed $\Delta\bar{Z}$ for body weight to generate a time series of each term of the age-structured Price equation (Fig. 2A). These terms sum to produce $\Delta\bar{Z}$. On average, the growth of surviving individuals contributed positively to $\Delta\bar{Z}$ [GR (mean ± SE), 1056 ± 105 g/year), followed by change in the demographic struc-

ture due to reproduction (DCr, 659 ± 39 g/year) and survival (DCs, 251 ± 161 g/year). Viability and fertility selection contributed less (VS, 153 ± 36; FS, 32 ± 15 g/year). These positive contributions were offset by the negative contribution from the difference between offspring and parental weights (OMD, −2220 ± 51 g/year). The positive terms increased mean body weight by +2151 g/year; the negative terms decreased it by −2232 g/year, giving an average decrease in weight of 81 g/year.

The above analysis pools contributions across age classes. We next investigated age-related variation in $\Delta\overline{Z}$. On average, the positive contributions of VS and GR (Fig. 3) occurred in the first 2 years of life, dropping to close to zero by the time individuals reached adult body size; heavy individuals were more likely to survive than light individuals when young (*20*). These results raise an intriguing question: Given positive viability selection on size (Fig. 2A) and the heritable nature of the trait (*20*), why have sheep not increased in size? The answer must be found in the OMD term, which is the only term that contributes negatively to $\Delta\overline{Z}$. Examination of this term showed that, on average, younger females produce lambs that are smaller than they themselves were at birth, probably because of physiological or morphological constraints caused by not having reached full adult body size (Fig. 3C) (*21*). Consequently, the mean birth weight of parents is greater than that of their offspring, counteracting much of the effect of selection. By the first August of life, when we collected weight data, daughters weigh, on average, ~150 g less than their mothers did at the same age. Given that the mean contribution of selection was +185 g, this suggests an upper limit for the contribution of a response to selection (*22*) of 35 g/year, corresponding to ~100 g per generation, or <0.8% of August lamb weight.

The difference between parental and offspring birth weights cannot alone explain the decline in body weight. We next examined trends in each component of the age-structured Price equation. The contribution of GR between the first and second August of life has declined over the course of the study (Fig. 4). During this period, sheep are growing more slowly than they used to (on average by 93 ± 36 g/year). The contribution of slower growth between the first and second year of life has partly been compensated for by an increase in the contribution of GRs in the second year of life, but not sufficiently to prevent the observed decline in adult body mass (Fig. 1).

Why are sheep growing more slowly than they used to? We next analyzed individual GRs within each age class (*7*). The growth of lambs was significantly negatively influenced by August body weight and population density, operating additively and via an interaction with the preceding winter's North Atlantic Oscillation (NAO) index (*23*). Lambs grew more slowly in years of high density after a bad winter: Over the course of the study, the NAO has steadily decreased, meaning that long harsh winters occur less frequently than they used to. Changing winter conditions have extended the season of grass growth while reducing the length of time that individuals depend on stored fat reserves. A consequence of this is that an increasing proportion of small slow-growing individuals are surviving through the winter than used to be the case. The survival of these individuals has acted to reduce average growth rates and to increase population size (*24*). This suggests that the form of density dependence has changed with the climate (*24*) and that this has had phenotypic consequences. These results suggest that climate change has the potential to generate rapid change in phenotypic traits, providing contemporary support for observations from the fossil record of phenotypic change accompanying climate change (*25*).

We next identified how each term contributed to the temporal dynamics of mean body size by analyzing temporal variation in $\Delta\overline{Z}$ (*7*). Fluctuations in the population structure (DCs and DCr) caused by density dependence and climatic variation (*24*), followed by the growth terms (GR), contributed most. These terms accounted for 88% of the observed variance. VS and FS accounted for 5.8%, and OMD and ODC explained 4% (Fig. 2B). An individual-based analysis of annual growth rates suggests that climate and population density explain substantial amounts of variation, particularly for lambs (*7*). Although the OMD and ODC terms contribute little to the dynamics, we also conducted an individual-based analysis of the difference between offspring and maternal weights. Population density and maternal body weight (which is determined by the birth weight of the mother and her growth since birth) explain significant amounts of variation, suggesting that any response to selection contributes substantially less than 4% to the phenotypic dynamics, which in turn suggests that the recent dynamics of body weight have not been strongly influenced by selection and adaptive evolution.

Our approach has provided several insights. First, the dynamics of body size—both the trend and variation around the trend—are primarily a consequence of environmental variation and not evolution. Second, we determined that positive viability selection on size early in life is countered by young mothers being unable to produce offspring that are as heavy as they themselves were at birth. Finally, we report that environmental change has resulted in a reduction in lamb growth rates, and this explains why sheep are smaller than they used to be. There are two general conclusions from this analysis. First, the recent focus on evolutionary explanations for changes in heritable phenotypic traits (*26*, *27*) could fruitfully be complemented with research identifying the role of environmental variation. Second, individuals and populations respond to environmental change in complex ways, and there should be no expectation of simple linear associations between environment, phenotype, genotype, and population dynamics. These results reinforce the need for a theory linking genetic, phenotypic, and population dynamics in age-structured populations in variable environments.

References and Notes

1. D. Reale, A. G. McAdam, S. Boutin, D. Berteaux, *Proc. R. Soc. London Ser. B* **270**, 591 (2003).
2. N. G. Hairston, S. P. Ellner, M. A. Geber, T. Yoshida, J. A. Fox, *Ecol. Lett.* **8**, 1114 (2005).
3. M. D. Rausher, *Evolution* **46**, 616 (1992).
4. T. Coulson, T. G. Benton, P. Lundberg, S. R. X. Dall, B. E. Kendall, *Evol. Ecol. Res.* **8**, 1155 (2006).
5. D. Falconer, *Introduction to Quantitative Genetics* (Longman, London, 1960).
6. R. Lande, *Evolution* **33**, 402 (1979).
7. See supporting material on *Science* Online for additional details on the theory and methods.
8. A. Charmantier *et al*., *Science* **320**, 800 (2008).
9. D. Garant, L. E. B. Kruuk, R. H. McCleery, B. C. Sheldon, *Am. Nat.* **164**, E115 (2004).
10. P. Gienapp, C. Teplitsky, J. S. Alho, J. A. Mills, J. Merila, *Mol. Ecol.* **17**, 167 (2008).
11. L. E. B. Kruuk, J. Merila, B. C. Sheldon, *Trends Ecol. Evol.* **18**, 207 (2003).
12. G. R. Price, *Nature* **227**, 520 (1970).
13. T. Coulson, S. Tuljapurkar, *Am. Nat.* **172**, 599 (2008).
14. S. Tuljapurkar, *Population Dynamics in Variable Environments* (Springer-Verlag, New York, 1990).
15. J. W. Vaupel, K. G. Manton, E. Stallard, *Demography* **16**, 439 (1979).
16. R. Lande, S. J. Arnold, *Evolution* **37**, 1210 (1983).
17. J. Gratten *et al*., *Science* **319**, 318 (2008).
18. A. J. Wilson *et al*., *Evol. Ecol.* **21**, 337 (2007).
19. E. A. Catchpole, B. J. T. Morgan, T. N. Coulson, S. N. Freeman, S. D. Albon, *J. R. Stat. Soc. Ser. C Appl. Stat.* **49**, 453 (2000).
20. F. Pelletier, T. Clutton-Brock, J. Pemberton, S. Tuljapurkar, T. Coulson, *Science* **315**, 1571 (2007).
21. T. H. Clutton-Brock, J. M. Pemberton, *Soay Sheep: Dynamics and Selection in an Island Population* (Cambridge Univ. Press, Cambridge, 2004).
22. J. S. Heywood, *Evolution* **59**, 2287 (2005).
23. J. W. Hurrell, *Science* **269**, 676 (1995).
24. T. Coulson *et al*., *Ecology* **89**, 1661 (2008).
25. G. Hunt, K. Roy, *Proc. Natl. Acad. Sci. U.S.A.* **103**, 1347 (2006).
26. D. W. Coltman *et al*., *Nature* **426**, 655 (2003).
27. E. M. Olsen *et al*., *Nature* **428**, 932 (2004).

28. Thanks to the National Trust for Scotland Scottish and National Heritage for permission to work on St. Kilda and the Ministry of Defense, QinetiQ, Amey, and ESS staff on St. Kilda and Benbecula for logistical support. J. Pilkington, previous field assistants, and many volunteers collected the data. L.-M. Chevin, M. Crawley, T. Ezard, J. Hostetler, O. Jones, L. Kruuk, R. Lande, A. Malo, F. Pelletier, M. Oli, J. Slate, I. Smallegange, and A. Wilson provided comments. This work was funded by Natural Environment Research Council grant NE/E015921/1 and National Institute of Aging grant P01/AG/22500.

Supporting Online Material

www.sciencemag.org/cgi/content/full/1173668/DC1
Materials and Methods
SOM Text
Fig. S1
Tables S1 and S2
References

17 March 2009; accepted 19 June 2009
Published online 2 July 2009;
10.1126/science.1173668
Include this information when citing this paper.

Heat Exchange from the Toucan Bill Reveals a Controllable Vascular Thermal Radiator

Glenn J. Tattersall,[1,3] Denis V. Andrade,[2,3] Augusto S. Abe[2,3]

The toco toucan (*Ramphastos toco*), the largest member of the toucan family, possesses the largest beak relative to body size of all birds. This exaggerated feature has received various interpretations, from serving as a sexual ornament to being a refined adaptation for feeding. However, it is also a significant surface area for heat exchange. Here we show the remarkable capacity of the toco toucan to regulate heat distribution by modifying blood flow, using the bill as a transient thermal radiator. Our results indicate that the toucan's bill is, relative to its size, one of the largest thermal windows in the animal kingdom, rivaling elephants' ears in its ability to radiate body heat.

In the hall of animal oddities, the toucan's enlarged bill is the avian example of exaggeration, being a source of debate since Buffon labeled it a "grossly monstrous" appendage (*1*). Even Darwin was intrigued, stating that "toucans may owe the enormous size of their beaks to sexual selection, for the sake of displaying the diversified and vivid stripes of colour with which these organs are ornamented" (*2*). More recent explanations for the oversized bill include fruit peeling (*3*), nest predation (*4–6*), social selection in the context of territorial defense (*7*), and, finally, serving as a visual warning (*6*). Although the selective forces that led to the large bills of present-day toucans remain elusive, the current use, costs, and proximal consequences can be examined. We investigated the role of the toucan bill in thermoregulation. As must any endothermic organism, toucans regulate their body temperature primarily by balancing metabolic heat production with heat exchange with the environment. Therefore, a large and uninsulated appendage, such as the bill, may be an important avenue for heat exchange (*8–11*).

We focused on the toco toucan (*Ramphastos toco* Muller, 1776), which has the largest bill of all the toucans (*12*). The bill has a network of superficial blood vessels supporting the horny ramphotheca (*13*, *14*) (Fig. 1). Therefore, the toucan's bill combines all the important features of a candidate thermal radiator: It is enlarged, uninsulated, and well vascularized (*8*, *9*, *11*, *15*). It is, however, crucial that blood flow be adjustable in order to control heat exchange from the bill. We examined whether the toucan's bill can operate as a thermal window for heat loss, capable of being "opened" within and above the thermal neutral zone and "closed" to conserve metabolic heat at lower temperatures. We used infrared thermography (*15*) to examine the effects of changing ambient temperature (T_a) on the heat exchange profile of different regions of the bird's body (*16*).

The bill of the toucan attains its remarkable size through a steep ontogenetic growth (Fig. 1), leading to a bill surface area 25 to 40 times larger than that predicted from scaling relationships (*17*). Changes in bill length follow a moderate trajectory during the first 4 to 5 weeks of life, scaling with positive allometry, relative to body mass (bill length = 0.33 body mass$^{0.598}$). Thereafter, when the juvenile attains nearly 80% of its adult mass, the bill exhibits more rapid allometric growth, with the scaling exponent (b) increasing to 0.845, nearly three times predictions from isometry. This positive allometry in bill growth led us to examine whether juvenile toucans (n = 2, mass = 503 g, bill length = 10.7 cm) with actively growing bills would have the same ability to modify heat exchange as adults (n = 4, mass = 676 ± 42 g, bill length = 18.7 ± 0.4 cm; table S1).

As T_a changed, significant alterations were detected in the superficial temperature of the birds' backs (a feather-covered area with no practical ability to adjust heat exchange, $F_{21,105}$ = 5.56, $P = 1 \times 10^{-14}$), the eye/peripalpebral region ($F_{21,105}$ = 78.5, $P = 1.7 \times 10^{-54}$), and the proximal ($F_{23,69}$ = 2.12, P = 0.0087; adults only) and distal ($F_{23,69}$ = 12.1, $P = 4\times10^{-16}$; adults only) regions of the bill (Fig. 2 and fig. S1). As expected, the temperature of the feather-

[1]Department of Biological Sciences, Brock University, St. Catharines, Ontario, Canada. [2]Departamento de Zoologia, Universidade Estadual Paulista, Campus Rio Claro, São Paulo, Brazil. [3]Instituto Nacional de Ciência e Tecnologia em Fisiologia Comparada.

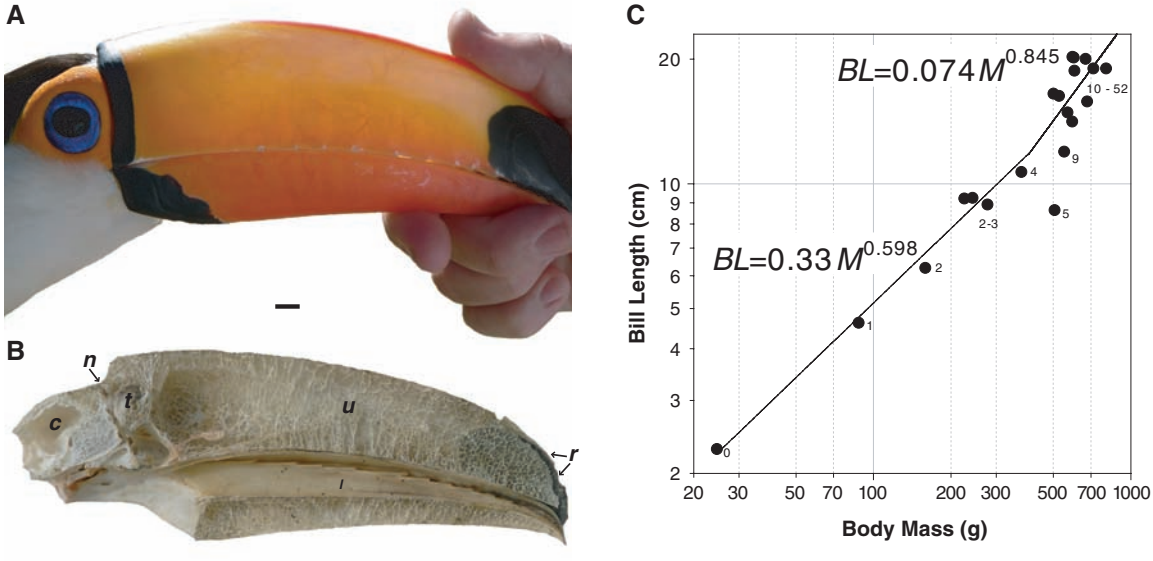

Fig. 1. (**A**) Side view of an adult toco toucan bill with visible blood vessels. (**B**) A sagittal section of a museum specimen demonstrating the lightweight bone (c, cranium; n, nares; t, turbinates; u, upper bill; l, lower bill, r, ramphotheca). Horizontal scale bar = 1 cm. (**C**) Bill length in toco toucans scales with positive allometry. Values are derived from digital photographs and measurements of toucans of known mass and age (numbers adjacent to data points indicate age in weeks). Equations describe the scaling relationship for the first 5 weeks [b = 0.598 ± 0.055; 95% confidence interval (CI), correlation coefficient (r) = 0.993] separately from that for toucans older than 5 weeks (b = 0.845 ± 0.503; 95% CI, r = 0.634). Both exponents were significantly greater than isometry [$t_{df\text{-}7}$ (t_7) = 9.1, $P = 2 \times 10^{-5}$, and t_{17} = 1.8, P = 0.045, respectively].

covered areas was only slightly above ambient temperature and varied significantly only at the lowest temperatures (Fig. 2). Temperature in the eye region was kept nearly constant [30° to 36°C; compare to toucan body temperature of ~38° to 39°C (*18*)] at all T_a, indicating continuous blood flow to the naked skin around the eye regardless of T_a. Proximal and distal bill regions were more variable, but the prevailing trend was for larger gradients to occur between 20° and 25°C in the proximal region (in adults), with the distal region not exhibiting sustained dilation until T_a was above 25°C (Figs. 2 and 3). Thus, the proximal region of the bill was used mainly to dump heat at lower T_a (>16° to 25°C), and as temperature rose, the distal region began to receive increased blood flow, becoming warmer, helping the bird cope with the extra heat load. The greatest variance in bill surface temperatures occurs within the toucan's thermal neutral zone (~18° to 30°C) (*18*), according to the expectations of a thermal window. These results show that vasomotory adjustments to the bill's surface in toco toucans serve a thermoregulatory function. Furthermore, breathing frequency and expired air temperatures changed suddenly at air temperatures below ~21°C, paralleling the thresholds for bill vasodilation (fig. S2).

Heat loss from the bill is highly variable, and, depending on air speed and T_a, could account for as little as 25% (minimum) to as much as 400% (maximum) of resting heat production in adults (Fig. 4), the largest reported for an animal. It is, therefore, remarkable that the toucan bill, which represents ~30 to 50% of body surface area (table S1), is capable of playing such a critical role in heat transfer, whereas other species' thermal windows, such as the duck's bill and the elephant's ear, have been estimated to account for 9 to 91% of resting heat production (*19*, *20*). This capacity for heat loss might become a liability at low temperatures. However, toucans and toucanets are well known for tucking their bills beneath their wings and orienting their tail feathers rostrally during sleep (*12*) (movie S1); this posture increases insulation of the bill and mitigates heat loss incurred during sleep.

The remarkable heat exchange capacity of the bill may also be instrumental when metabolic heat production is increased, as would occur during flight [when heat production is 10 to 12 times that at rest (*21*)]. For one bird (fig. S3), bill temperatures (T_{bill}) started at ~30° to 31°C and began to rise within 4 min of flight, until eventually reaching a maximum of 37°C by the 10th minute, after which the bird voluntarily terminated its flight. Thus, the heat loss from the bill could prove essential for maintaining adequate thermal balance when heat production increases.

As a proportion of total heat loss, the bill routinely accounted for 30 to 60% of heat loss in adults and juveniles. However, adults could adjust heat loss from the bill to account for as little as 5% ($T_{bill} - T_a \sim 0$), and, for short periods, up to 100% of total body heat loss (Fig. 4). In contrast, juvenile toucans were unable to adjust circulation to the bill to any great extent (Fig. 4), even at very low T_a (<15°C), when such a response would confer considerable heat conservation. Therefore, even 2-month-old toucans exhibit high obligatory heat loss from the bill, which cannot be down-regulated in the cold. As young, toucans remain blind and naked for the first 3 weeks, begin plumage growth at 4 weeks, and fledge only after 6 weeks of age (*5*, *22*), at which point the bill is less than half the adult size. During this period, the young are not brooded by the adults during the day (*5*) and shiver at temperatures as high as 26° to 27°C (*5*). Thus, even in subtropical climates, young toucans would incur thermoregulatory costs, made more challenging by their poor ability to control bill heat exchange. The need for substrate delivery to the rapidly growing bill must demand high and steady blood flow, conflicting with the vasoconstriction required for heat conservation. Furthermore, the complexities of the vasculature and controlling mechanisms needed to adjust the blood flow to the bill may not be completely developed until adulthood.

Temporal changes in the adult bill's surface temperatures are rapid and reversible, occurring within minutes (fig. S1), which was most evident when we observed the birds while they were sleeping. As the birds begin to sleep, a transient bill vasodilation occurs (movie S1). Because birds, like most endotherms, reduce body temperature during their nocturnal sleep, our results show that toucans have the ability to use their bill to rapidly dump body heat as the thermal set-point declines (*23*). Furthermore, we found that sleeping birds show transient changes in bill surface temperature without evidence of awakening, indicative of sleep-state transitions associated with changes in thermoregulatory state (*24*) (movie S2).

Ultimately, the changes in heat loss from the bill derive from the underlying vasculature. Little is known about the vascular anatomy of the toucan bill; however, a fine network of vessels ramifies within the dermis between the horny and bony parts of the bill (Fig. 1) (*14*, *19*). Because surface temperatures in the distal and proximal regions often follow distinct and unique patterns, separate vessels must supply the distal and proximal regions; indeed, arteriovenous anastomoses (AVAs) are found in abundance in the tip of the duck's bill (*14*, *15*). Nevertheless, because of the steepness of the temperature gradient profile along the bill and the fact that distal regions approach T_a in the cold (Fig. 3), countercurrent mechanisms of heat conservation might be at play at low temperatures. At high T_a, however, the distal region of the bill can exhibit surface temperatures equal to or in excess of the proximal region (fig. S1F), indicating that counter-

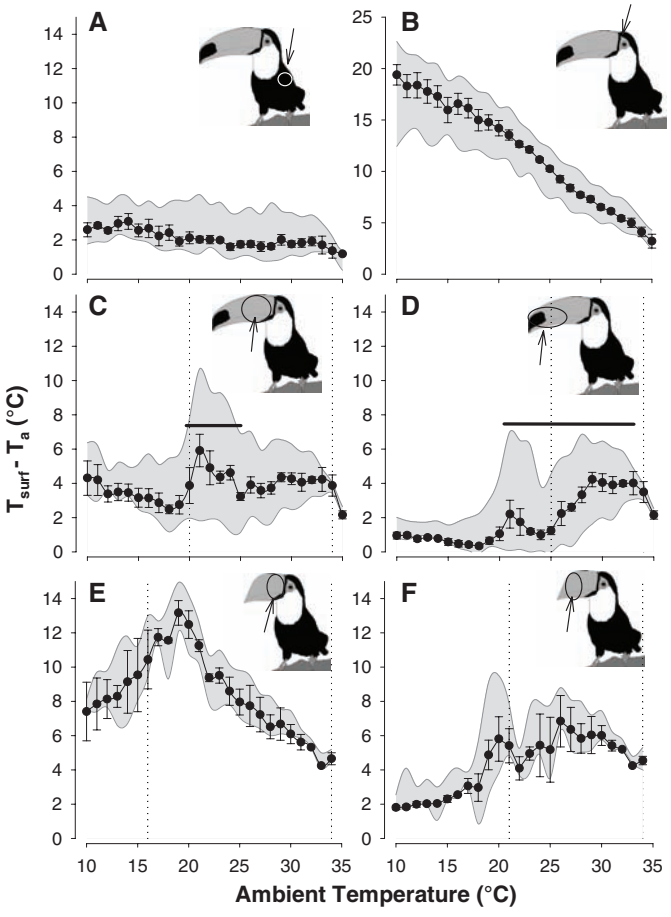

Fig. 2. Bill surface temperatures (T_{surf}) (mean ± SE) obtained from toco toucans exposed to a range of T_a (10° to 35°C), expressed as differential values ($T_{surf} - T_a$). (**A**) T_{surf} of the external back feathers (n = 6 toucans). (**B**) T_{surf} of the eye (n = 6). (**C**) and (**D**) The differential values for the proximal and distal bill regions of adult toucans (n = 4). (**E**) and (**F**) Bill surface temperature differentials from juveniles (n = 2, no statistics reported). Solid horizontal lines in (C) and (D) denote the range of statistically significant differences from values assessed at T_a = 32°C.

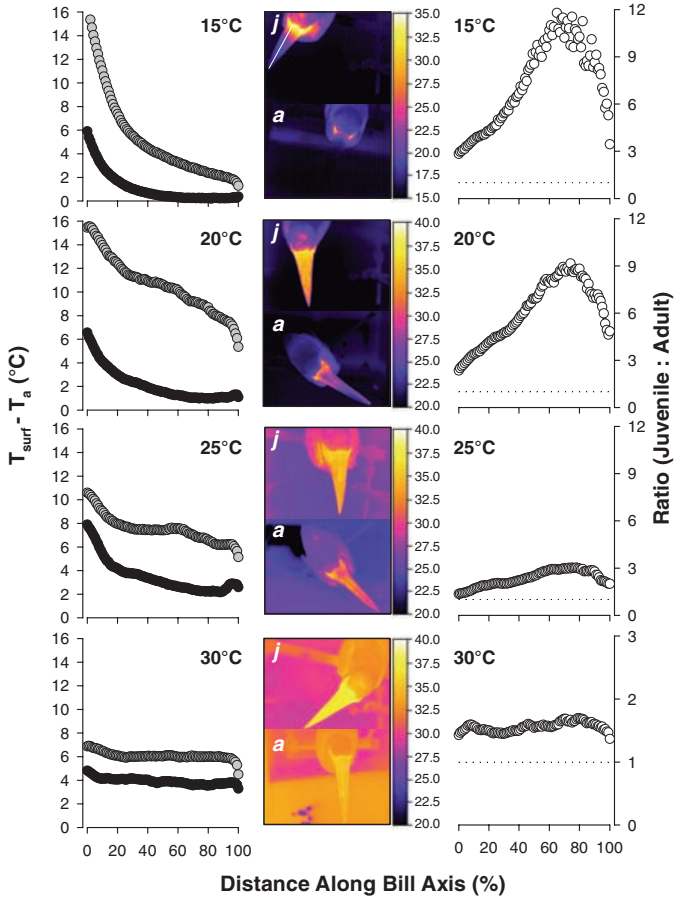

Fig. 3. Temperature profiles of surface temperature differentials of the toucan bill at four different T_a (15°, 20°, 20°, and 35°C). The lefthand plots depict the average $T_{surf} - T_a$ differences for adults (n = 4, black circles) and juveniles (n = 2, gray circles), expressed against the relative distance along the bill (white line in top middle panel; 0 = proximal end; 100 = distal tip). The middle column depicts thermographic images from adult (a) and juvenile (j) toucans at the respective T_a. The ratio of the juvenile:adult values for the $T_{surf} - T_a$ differences is shown in the righthand panels. The horizontal dotted line indicates the line of equality, where the ratio = 1.

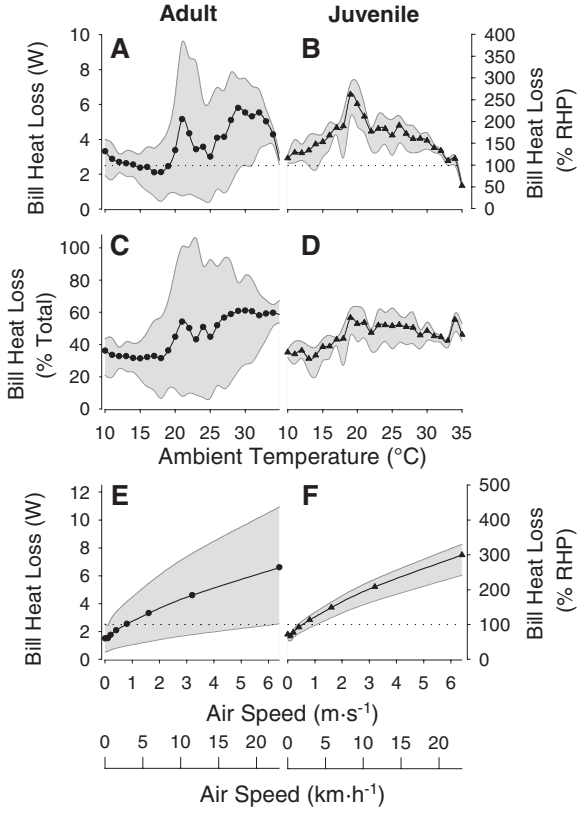

Fig. 4. Estimated rates of heat loss from toco toucans (average values are depicted as symbols and minimum and maximum values as gray shading). (**A** and **B**) Estimated bill heat loss for adults (circles) and juvenile (triangles) toucans at an air speed of 5 m s^{-1}. The horizontal dotted line indicates resting heat production (RHP) (*18*). (**C** and **D**) Bill heat loss expressed as a percentage of total heat body loss from all sources. (**E** and **F**) The summarized influence of air speed at T_a = 21°C on heat loss from the bill in adult and juvenile toucans.

current arrangements can be bypassed through AVAs when needed.

Our results demonstrate that the constraints of heat exchange and the bill's potential use as a thermoregulatory organ should be considered in understanding the distribution, ecology, and behavior of toucans. Furthermore, given the rapid radiation of bill structures and diversity of beak morphologies of birds (*3*, *25*), thermal constraints from bill heat loss may prove to be a common feature among many avian fauna.

References and Notes

1. G. L. L. Buffon, *Histoire Naturelle, Générale et Particulièire avec la Description du Cabinet du Roi* (L'Impreimerie Royale, Paris, 1780).
2. C. Darwin, *The Descent of Man: And Selection in Relation to Sex* (J. Murray, London, 1871).
3. J. S. Jones, *Nature* **315**, 182 (1985).
4. H. Sick, *Ornitologia Brasileira* (Editor Nova Fronteira, Rio de Janeiro, Brazil, 1997).
5. J. Van Tyne, *The Life History of the Toucan* Ramphastos brevicarinatus (Museum of Zoology, Univ. of Michigan, Ann Arbor, MI, 1929).
6. P. Buhler, in *Tropical Biodiversity and Systematics*, H. Ulrich, Ed. (Zoologishes Forschung Institut und Museum, Bonn, Germany, 1997), pp. 305–310.
7. M. J. West-Eberhard, *Q. Rev. Biol.* **58**, 155 (1983).
8. P. K. Phillips, A. F. Sanborn, *J. Therm. Biol.* **19**, 423 (1994).
9. G. J. Tattersall, W. K. Milsom, *J. Exp. Biol.* **206**, 33 (2003).
10. W. C. Lancaster, S. C. Thomson, J. R. Speakman, *J. Therm. Biol.* **22**, 109 (1997).
11. J. J. Klir, J. E. Heath, N. Bennani, *Comp. Biochem. Physiol. A* **96**, 141 (1990).
12. H. Alvarenga, *Toucans of the Americas* (M. Pontual Edições e Arte, Rio de Janeiro, Brazil, 2004).
13. T. S. Traill, *Trans. Linn. Soc. London* **11**, 288 (1815).
14. U. Midtgard, *Zoomorphology* **104**, 323 (1984).
15. G. R. Scott, V. Cadena, G. J. Tattersall, W. K. Milsom, *J. Exp. Biol.* **211**, 1326 (2008).
16. See supporting material on *Science* Online.
17. G. E. Walsberg, J. R. King, *J. Exp. Biol.* **76**, 185 (1978).
18. B. K. McNab, *Auk* **118**, 916 (2001).
19. A. A. Hagan, J. E. Heath, *J. Therm. Biol.* **5**, 95 (1980).
20. P. K. Phillips, J. E. Heath, *Comp. Biochem. Physiol. A Mol. Integr. Physiol.* **101**, 693 (1992).
21. V. A. Tucker, *J. Exp. Biol.* **48**, 67 (1968).
22. A. F. Skutch, *Condor* **60**, 201 (1958).
23. H. C. Heller, *Can. J. Zool.* **66**, 61 (1988).
24. P. Alfoldi, G. Rubicsek, G. Cserni, F. Obal, *Pflügers Arch.* **417**, 336 (1990).
25. A. Abzhanov *et al.*, *Nature* **442**, 563 (2006).

26. This research was supported by grants from the Conselho Nacional de Desenvolvimento Científico e Tecnológico (CNPq) to A.S.A. and D.V.A., from the Fundação de Amparo a Pesquisa do Estado de São Paulo (FAPESP) and Fundação para o Desenvolvimento da Unesp (FUNDUNESP) to D.V.A., and the Natural Sciences and Engineering Research Council of Canada to G.J.T. M. Symonds kindly commented on the manuscript, and D. Skandalis, V. Cadena, and M. da Silva assisted with experiments.

Supporting Online Material

www.sciencemag.org/cgi/content/full/325/5939/468/DC1
Materials and Methods
Figs. S1 to S3
Table S1
References
Movies S1 and S2

29 April 2009; accepted 2 June 2009
10.1126/science.1175553

Synchronous and Stochastic Patterns of Gene Activation in the *Drosophila* Embryo

Alistair N. Boettiger[1] and Michael Levine[2]*

Drosophila embryogenesis is characterized by rapid transitions in gene activity, whereby crudely distributed gradients of regulatory proteins give way to precise on/off patterns of gene expression. To explore the underlying mechanisms, a partially automated, quantitative in situ hybridization method was used to visualize expression profiles of 14 developmental control genes in hundreds of embryos. These studies revealed two distinct patterns of gene activation: synchronous and stochastic. Synchronous genes display essentially uniform expression of nascent transcripts in all cells of an embryonic tissue, whereas stochastic genes display erratic patterns of de novo activation. RNA polymerase II is "pre-loaded" (stalled) in the promoter regions of synchronous genes, but not stochastic genes. Transcriptional synchrony might ensure the orderly deployment of the complex gene regulatory networks that control embryogenesis.

Eukaryotic transcription is an intrinsically stochastic process due to variability in the recruitment and subsequent assembly of the RNA polymerase II (Pol II) complex and associated coactivator complexes such as Mediator, TFIID, and TFIIH (*1*–*4*). Consequently, not all cells that receive the same inducing signal would be expected to respond at precisely the same time. Recent studies have shown that many of the developmental control genes governing *Drosophila* embryogenesis are bound by Pol II before their induction (*5*, *6*). This "pre-loaded" (or stalled) Pol II accelerates the induction of transcription of the *Drosophila* heat shock genes upon stress. In principle, any cell-to-cell variation in the onset of transcription might be diminished for genes containing stalled Pol II.

The early *Drosophila* embryo is an ideal system to examine variability in the onset of de novo transcription within a developmental field of coordinately induced cells. However, most previous studies examined relatively few embryos (*7*–*11*). To distinguish subtle differences in the patterns of transcriptional induction, we used computational methods to process hundreds of staged embryos in a quantitative and unbiased fashion. This procedure employs in situ hybridization with a battery of fluorescent probes against large intronic regions of the target genes, high-resolution confocal microscopy, and semi-automated image segmentation algorithms [see methods section in the supporting online material (SOM)]. This method can detect most nascent transcripts at the onset of transcription (Fig. 1).

We began the analysis with six genes that are activated at approximately the same stage (early nuclear cleavage cycle 14) in the presumptive mesoderm. Three of the genes, Mes4 (*12*) [or NF-Yc (*13*)], *Myocyte Enhancing Factor 2* (*Mef2*) (*14*), and *heartbroken* (*hbr*) (*15*) [or *downstream of FGF* (*16*) or *stumps* (*17*)], lack stalled Pol II in tissues where the genes are inactive but display Pol II binding across the length of the transcription unit in the mesoderm when expressed (see diagrams above embryos in Fig. 1B and fig. S2). At the time of induction, all three genes display stochastic patterns of expression, as judged by the nuclear hybridization "dots" representing de novo transcripts. However, within 30 min after induction, hybridization dots are detected in most mesodermal nuclei of most embryos (fig. S4).

Very different results were obtained with *heartless (htl)* (*18*) (FGF receptor), Mes2 (a SANT-domain transcription factor) (*16*), and *Mdr49* [a membrane adenosine triphosphatase, also called Mes5 (*19*)], which contain stalled Pol II in tissues where the genes are inactive (top diagrams, orange and red Pol II traces, Fig. 1A and fig. S2). These genes display synchronous patterns of activation, with clear hybridization signals detected in most nuclei of most embryos (Fig. 1A).

Distinct patterns of gene activation, synchronous and stochastic, are also seen for genes expressed in the other primary embryonic tissues, the neurogenic ectoderm and dorsal ectoderm (Fig. 1, C and D, and fig. S2). *thisbe* (*ths*, encoding FGF8) (*20*, *21*) lacks stalled Pol II and exhibits stochastic activation within the neurogenic ectoderm (Fig. 1D), whereas Neu3 (*12*) contains stalled Pol II and exhibits nearly uniform induction profiles in the same region (Fig. 1C). *pannier* (*pnr*) (*22*) and *u-shaped (ush)* (*23*) display stochastic and synchronous patterns of induction, respectively, in the dorsal ectoderm (fig. S2).

The degree of synchrony in expression for a given gene is inferred from the frequency of early

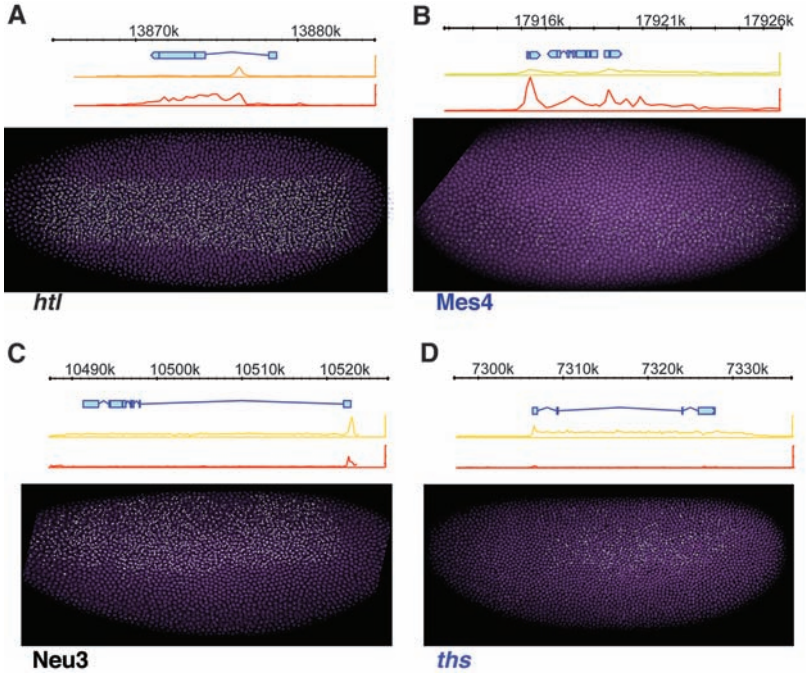

Fig. 1. Assaying asynchrony of gene expression. (**A** to **D**) Nascent transcripts tagged with fluorescent probes (green) in whole-mount embryos allow for the activation state of each nucleus (purple) to be determined. All embryos are oriented anterior to the left, dorsal side to the top. The diagram above each image shows the gene prediction models (blue) and Pol II ChIP-chip binding data in dorsal-ectoderm (orange), neural-ectoderm (yellow), or mesodermal (red) tissue (*37*). *htl* and Mes4 are simultaneously expressed in the mesoderm [(A) and (B)]. Neu3 and *ths* are simultaneously expressed in the neural-ectoderm [(C) and (D)]. Genes that show a peak Pol II binding in the ChIP-chip data at the promoter in all tissues regulate transcriptional elongation via stalled polymerase [(A) and (C)]. Genes that lack promoter proximal Pol II binding in inactive tissue are nonstalled [(B) and (D)]. Gene names shown in black are stalled; purple are nonstalled.

[1]Biophysics Program, University of California, Berkeley, CA 94720, USA. [2]Department of Molecular and Cell Biology, University of California, Berkeley, CA 94720, USA.

*To whom correspondence should be addressed. E-mail: mlevine@berkeley.edu

cleavage cycle 14 embryos showing partial expression (summarized in Fig. 2). The population statistics include the analysis of an average of ~50 embryos for each gene. Colored blocks represent embryos in which only a fraction of nuclei in the tissue exhibit nascent transcripts. Black blocks represent embryos where all nuclei exhibit active transcription. The genes are sorted from least synchronous (high frequency of partial activation) to most synchronous. Following this analysis, we see that all of the genes lacking stalled Pol II (Mes4, *hbr*, *pnr*, *ths*, and *Mef2*) segregate from the synchronous genes, which contain stalled Pol II (*sog*, *htl*, Neu3, *tup*, Mdr49, *vnd*, *ush*, *rho*, and Mes2) [see fig. S2 for embryo stains and chromatin immunoprecipitation (ChIP)–chip results]. All of the nonstalled genes show a higher degree of asynchronous activation than any of the stalled genes. The window of time between the detection of the first nuclei with hybridization signals until the detection of the last-activated nuclei is very short for stalled genes (2 to 3 min or less). In contrast, the variation in activation times for genes lacking stalled Pol II is much larger (15 to 20 min or more), resulting in the observed stochastic expression profiles. Times were inferred from morphological staging and population statistics (see SOM).

We next examined the activation of seven different genes in embryos containing an ectopic anterior-posterior Dorsal nuclear gradient (*24*) (Fig. 3). This gradient arises from the localized expression of an activated Toll receptor at the anterior pole of transgenic embryos using the bicoid 3′ untranslated region (UTR) (*25*). The resulting gradient induces ectopic patterns of gene expression, including the activation of mesodermal genes in the presumptive head. Nonetheless, the trend observed for stalled and nonstalled genes in wild-type (WT) embryos is also seen in these highly abnormal mutants.

The stalled Mes2 gene exhibits uniform ectopic activation in head regions, whereas the nonstalled Mes4 gene displays stochastic induction (Fig. 3C and fig. S3). Similarly, Neu3 (stalled) is uniformly activated in middle-body regions (Fig. 3A), whereas *ths* (nonstalled) exhibits stochastic activation profiles in the same region (Fig. 3B). The quantitative analysis of 95 different embryos suggests that all three nonstalled genes (*pnr*, *ths*, and Mes4) display stochastic activation by the ectopic Dorsal gradient. In contrast, the four stalled genes (*ush*, *rho*, Neu3, and Mes2) all display synchronous activation patterns (Fig. 3C). These results suggest that synchronous induction is an autonomous property of stalled Dorsal target genes and does not depend on unknown factors that are independently localized across the dorsal-ventral (DV) axis.

To determine how stalled genes respond to genetic perturbation, we examined the expression of four stalled genes in embryos derived from *dorsal* heterozgyotes (*dl*/+). A nuclear gradient of Dorsal establishes the DV patterning of the early *Drosophila* embryo. Dorsal works in concert with Twist and Snail, sequence-specific transcription factors encoded by immediate early target genes of the Dorsal gradient. Embryos derived from *dl*/+ females contain half the normal dose of the Dorsal nuclear gradient (*26*, *27*). Two of the dorsal target genes that were examined, *vnd* (Fig. 4A) and *sog* (fig. S3), display normal patterns of synchronous induction (summarized in Fig. 4C), whereas the other two genes, *rho* (Fig. 4B) and Neu3 (fig. S3), display stochastic patterns of activation, whereby nuclei exhibiting nascent transcripts are adjacent to those lacking detectable expression. It is possible that some of the mild patterning defects previously reported in *dl*/+ embryos arise from these perturbations in synchrony (*28*).

Both of the genes that display normal activation in *dl*/+ embryos, *vnd* and *sog*, contain "shadow enhancers," secondary enhancers for

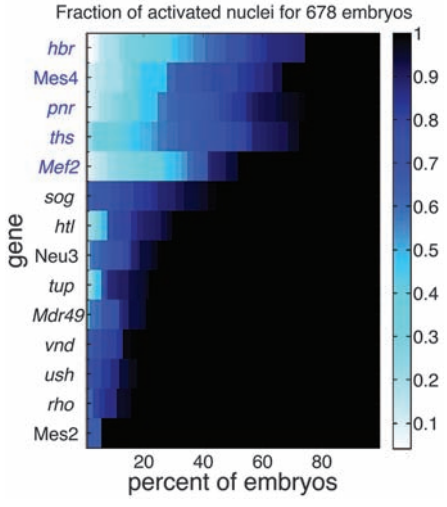

Fig. 2. Asynchronous expression among paused and unpaused ectodermal. Heat map summarizing synchrony results for each gene. The color indicates the fraction of activated nuclei in the region of expression. The *x* axis shows the proportion of similarly staged embryos with a fractional activation of at least *n* [0,1]. The results are sorted from top to bottom by the sum along the row, putting the most asynchronous genes at the top and the most synchronous at the bottom.

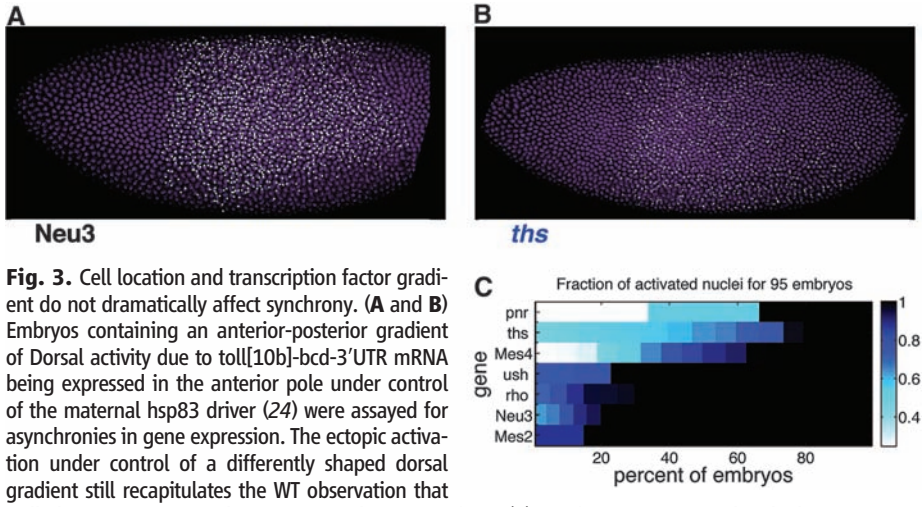

Fig. 3. Cell location and transcription factor gradient do not dramatically affect synchrony. (**A** and **B**) Embryos containing an anterior-posterior gradient of Dorsal activity due to toll[10b]-bcd-3′UTR mRNA being expressed in the anterior pole under control of the maternal hsp83 driver (*24*) were assayed for asynchronies in gene expression. The ectopic activation under control of a differently shaped dorsal gradient still recapitulates the WT observation that stalled genes are activated in a more synchronous fashion. (**C**) Results are summarized in the heat map as in Fig. 2.

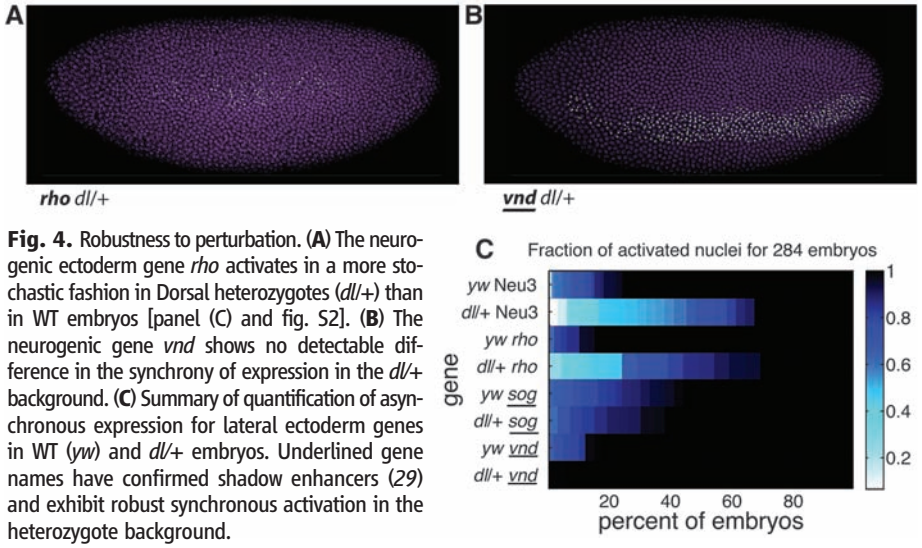

Fig. 4. Robustness to perturbation. (**A**) The neurogenic ectoderm gene *rho* activates in a more stochastic fashion in Dorsal heterozygotes (*dl*/+) than in WT embryos [panel (C) and fig. S2]. (**B**) The neurogenic gene *vnd* shows no detectable difference in the synchrony of expression in the *dl*/+ background. (**C**) Summary of quantification of asynchronous expression for lateral ectoderm genes in WT (*yw*) and *dl*/+ embryos. Underlined gene names have confirmed shadow enhancers (*29*) and exhibit robust synchronous activation in the heterozygote background.

activation in the presumptive neurogenic ectoderm (*29*), identified by ChIP-chip assays for the DV regulatory genes Dorsal, Twist, and Snail (*30*). Shadow enhancers might compensate for fluctuations in Dorsal concentrations by increasing the probability of occupancy of critical Dorsal binding sites (*10*, *29*–*33*). In contrast, neither of the genes that display stochastic activation in *dl*/+ embryos (*rho* and Neu3) appear to contain shadow enhancers (Fig. 4C). However, these results are preliminary, and definitive evidence that shadow enhancers provide an adaptive response to genetic perturbations will require additional study.

Previous visualization studies failed to distinguish synchronous and stochastic modes of gene activation (*12*–*18*, *20*, *21*, *23*, *27*, *30*, *34*–*36*). This finding was made possible by the use of a quantitative method that examines gene expression in many embryos rather than just a few individual embryos. Most DV patterning genes contain stalled Pol II (*37*), and we predict that most of these genes exhibit synchronous patterns of induction.

Pol II stalling and transcriptional synchrony may help to ensure the orderly unfolding of the complex genetic programs that control development. It is likely that any given gene, or even small sets of genes, can be activated in a stochastic fashion without causing severe patterning defects. However, the reproducible and reliable development of large populations of embryos might be incrementally augmented by the acquisition of stalled Pol II on critical developmental control genes.

References and Notes

1. A. Raj, C. S. Peskin, D. Tranchina, D. Y. Vargas, S. Tyagi, *PLoS Biol.* **4**, e309 (2006).
2. A. Raj, A. van Oudenaarden, *Cell* **135**, 216 (2008).
3. J. M. Raser, E. K. O'Shea, *Science* **304**, 1811 (2004); published online 27 May 2004 (10.1126/science.1098641).
4. J. M. Raser, E. K. O'Shea, *Science* **309**, 2010 (2005).
5. D. A. Hendrix, J. W. Hong, J. Zeitlinger, D. S. Rokhsar, M. S. Levine, *Proc. Natl. Acad. Sci. U.S.A.* **105**, 7762 (2008).
6. J. T. Lis, *Nature* **450**, 198 (2007).
7. S. Bergmann *et al.*, *PLoS Biol.* **5**, e46 (2007).
8. M. Coppey, A. N. Boettiger, A. M. Berezhkovskii, S. Y. Shvartsman, *Curr. Biol.* **18**, 915 (2008).
9. T. Gregor, W. Bialek, R. R. d. R. van Steveninck, D. W. Tank, E. F. Wieschaus, *Proc. Natl. Acad. Sci. U.S.A.* **102**, 18403 (2005).
10. T. Gregor, D. W. Tank, E. F. Wieschaus, W. Bialek, *Cell* **130**, 153 (2007).
11. T. Gregor, E. F. Wieschaus, A. P. McGregor, W. Bialek, D. W. Tank, *Cell* **130**, 141 (2007).
12. A. Stathopoulos, M. Van Drenth, A. Erives, M. Markstein, M. Levine, *Cell* **111**, 687 (2002).
13. S. N. Maity, B. de Crombrugghe, *Trends Biochem. Sci.* **23**, 174 (1998).
14. M. K. Baylies, A. M. Michelson, *Curr. Opin. Genet. Dev.* **11**, 431 (2001).
15. A. M. Michelson, S. Gisselbrecht, E. Buff, J. B. Skeath, *Development* **125**, 4379 (1998).
16. M. Y. Zhu, R. Wilson, M. Leptin, *Genetics* **170**, 767 (2005).
17. F. Imam, D. Sutherland, W. Huang, M. A. Krasnow, *Genetics* **152**, 307 (1999).
18. M. Leptin, M. Affolter, *Curr. Biol.* **14**, R480 (2004).
19. S. Ricardo, R. Lehmann, *Science* **323**, 943 (2009).
20. T. Gryzik, H. A. Muller, *Curr. Biol.* **14**, 659 (2004).
21. A. Stathopoulos, B. Tam, M. Ronshaugen, M. Frasch, M. Levine, *Genes Dev.* **18**, 687 (2004).
22. P. Ramain, P. Heitzler, M. Haenlin, P. Simpson, *Development* **119**, 1277 (1993).
23. L. H. Frank, C. Ruschlow, *Development* **122**, 1343 (1996).
24. A. M. Huang, J. Rusch, M. Levine, *Genes Dev.* **11**, 1963 (1997).
25. P. M. Macdonald, G. Struhl, *Nature* **336**, 595 (1988).
26. Y. T. Ip, R. E. Park, D. Kosman, K. Yazdanbakhsh, M. Levine, *Genes Dev.* **6**, 1518 (1992).
27. R. P. Zinzen, K. Senger, M. Levine, D. Papatsenko, *Curr. Biol.* **16**, 1358 (2006).
28. S. Gonzalez-Crespo, M. Levine, *Genes Dev.* **7**, 1703 (1993).
29. J.-W. Hong, D. A. Hendrix, M. S. Levine, *Science* **321**, 1314 (2008).
30. J. Zeitlinger *et al.*, *Genes Dev.* **21**, 385 (2007).
31. H. C. Berg, E. M. Purcell, *Biophys. J.* **20**, 193 (1977).
32. W. Bialek, S. Setayeshgar, *Phys. Rev. Lett.* **100**, 258101 (2008).
33. G. Tkacik, T. Gregor, W. Bialek, *PLoS One* **3**, e2774 (2008).
34. E. Bier, L. Y. Jan, Y. N. Jan, *Genes Dev.* **4**, 190 (1990).
35. V. Francois, M. Solloway, J. W. O'Neill, J. Emery, E. Bier, *Genes Dev.* **8**, 2602 (1994).
36. J. B. Skeath, G. F. Panganiban, S. B. Carroll, *Development* **120**, 1517 (1994).
37. J. Zeitlinger *et al.*, *Nat. Genet.* **39**, 1512 (2007).

38. We thank P. Ralph and S. Evans for help with constructing and analyzing the mathematical models of Pol II elongation and initiation that motivated our hypothesis about the synchrony of gene expression. A.N.B. is supported by NSF Graduate Research Fellowship Program. This study was funded by a grant from NIH (GM34431).

Supporting Online Material

www.sciencemag.org/cgi/content/full/325/5939/471/DC1
SOM Text
Figs. S1 to S7
Table S1
References

24 March 2009; accepted 4 June 2009
10.1126/science.1173976

A Gene Network Regulating Lysosomal Biogenesis and Function

Marco Sardiello,[1] Michela Palmieri,[1] Alberto di Ronza,[1] Diego Luis Medina,[1] Marta Valenza,[2] Vincenzo Alessandro Gennarino,[1] Chiara Di Malta,[1] Francesca Donaudy,[1] Valerio Embrione,[1] Roman S. Polishchuk,[3] Sandro Banfi,[1] Giancarlo Parenti,[1,4] Elena Cattaneo,[2] Andrea Ballabio[1,4]*

Lysosomes are organelles central to degradation and recycling processes in animal cells. Whether lysosomal activity is coordinated to respond to cellular needs remains unclear. We found that most lysosomal genes exhibit coordinated transcriptional behavior and are regulated by the transcription factor EB (TFEB). Under aberrant lysosomal storage conditions, TFEB translocated from the cytoplasm to the nucleus, resulting in the activation of its target genes. TFEB overexpression in cultured cells induced lysosomal biogenesis and increased the degradation of complex molecules, such as glycosaminoglycans and the pathogenic protein that causes Huntington's disease. Thus, a genetic program controls lysosomal biogenesis and function, providing a potential therapeutic target to enhance cellular clearing in lysosomal storage disorders and neurodegenerative diseases.

Lysosomes are specialized to degrade macromolecules received from the secretory, endocytic, autophagic, and phagocytic pathways (*1*). Because degradation requirements of the cell may vary depending on tissue type, age, and environmental conditions, we postulated the presence of a cellular program coordinating lysosomal activity. By using the g:profiler (*2*) tool, we observed that genes encoding lysosomal proteins, hereafter referred to as lysosomal genes, tend to have coordinated expression (figs. S1 and S2). Pattern discovery analysis of the promoter regions of the 96 known lysosomal genes (*3*) resulted in the identification of a palindromic 10–base pair (bp) GTCACGTGAC motif highly enriched in this promoter set (68 genes out of 96; $P < 0.0001$) (fig. S3). This motif is preferentially located within 200 bp from the transcription start site (TSS), either as a single sequence or as tandem multiple copies (fig. S4 and table S1). The distribution of this motif was determined around all human gene TSSs (Fig. 1A), and gene ontology analysis of the genes with at least two motifs within 200 bp from the TSS—suggesting that they are probably in a promoter—showed a significant enrichment for functional categories related to lysosomal biogenesis and function (table S2). Thus, we named this motif Coordinated Lysosomal Expression and Regulation (CLEAR) element. A luciferase assay showed that the CLEAR element mediates transcriptional activation (Fig. 1B).

The CLEAR consensus sequence overlaps that of the E-box (CANNTG), a known target site for basic helix-loop-helix (bHLH) transcription factors (*4*). In particular, members of the microphthalmia–transcription factor E (MiT/TFE) subfamily of bHLH factors were found to bind sequences similar to the CLEAR consensus (*5*). The MiT/TFE subfamily is composed of four members in humans: MITF, TFE3, TFEB, and TFEC (*6*). To determine whether any of these proteins are able to modulate the expression of lysosomal genes, we transfected HeLa cells with plasmids carrying *MITF*, *TFE3*, *TFEB*, or *TFEC*

[1]Telethon Institute of Genetics and Medicine, Via P. Castellino 111, 80131 Naples, Italy. [2]Department of Pharmacological Sciences and Center for Stem Cell Research, University of Milan, Via Balzaretti 9, 20133 Milan, Italy. [3]Telethon Electron Microscopy Core Facility, Department of Cell Biology and Oncology, Consorzio Mario Negri Sud, I-66030 Santa Maria Imbaro, Chieti, Italy. [4]Department of Pediatrics, Federico II University, Via S. Pansini 5, 80131 Naples, Italy.

*To whom correspondence should be addressed. E-mail: ballabio@tigem.it

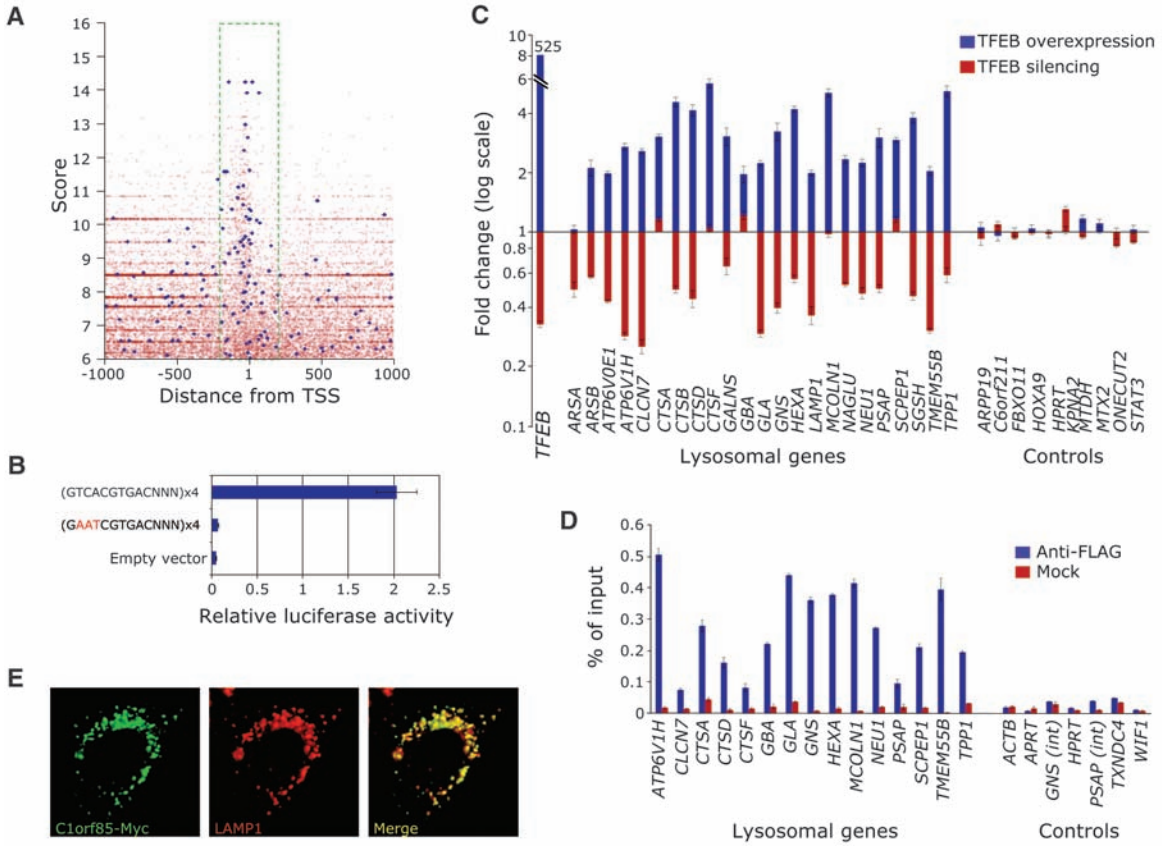

Fig. 1. A regulatory gene network controlling the expression of lysosomal genes. (**A**) Genomic distribution of CLEAR elements (red dots) at human gene promoters. Scores are assigned based on the CLEAR position weight matrix. Blue dots indicate CLEAR elements in the promoters of lysosomal genes. The dashed box contains all the elements corresponding to the genes that were used for Gene Ontology analysis. (**B**) Luciferase assay using constructs carrying four tandem copies of either intact (top) or mutated (middle; mutations in red) CLEAR elements. (**C**) Expression analysis of lysosomal genes after TFEB overexpression and silencing. Blue bars show the fold change of the mRNA levels of lysosomal genes in TFEB- versus pcDNA3-transfected cells. Red bars show the fold change of mRNA levels in mimic-miR-128–transfected cells versus cells transfected with a standard control miRNA (mimic-miR-cel-67). Randomly chosen nonlysosomal genes were used as controls. Gene expression was normalized relative to *glyceraldehyde-3-phosphate dehydrogenase* (*GAPDH*). (**D**) ChIP analysis. The histogram shows the amount of the immunoprecipitated DNA expressed as a percentage of the total input DNA. Controls include promoters of housekeeping genes (*ACTB*, *APRT*, and *HPRT*), random genes lacking CLEAR sites (*TXNDC4* and *WIF1*), and intronic sequences (int) of lysosomal genes. Lysosomal genes and controls were significantly different: Mann-Whitney-Wilcoxon test ($P < 10^{-4}$). All experiments in (B), (C), and (D) were performed in triplicates (data represent mean ± SD). (**E**) Confocal microscopy showing colocalization of C1orf85-Myc (green) with the lysosomal membrane marker LAMP1 (red) in HeLa cells.

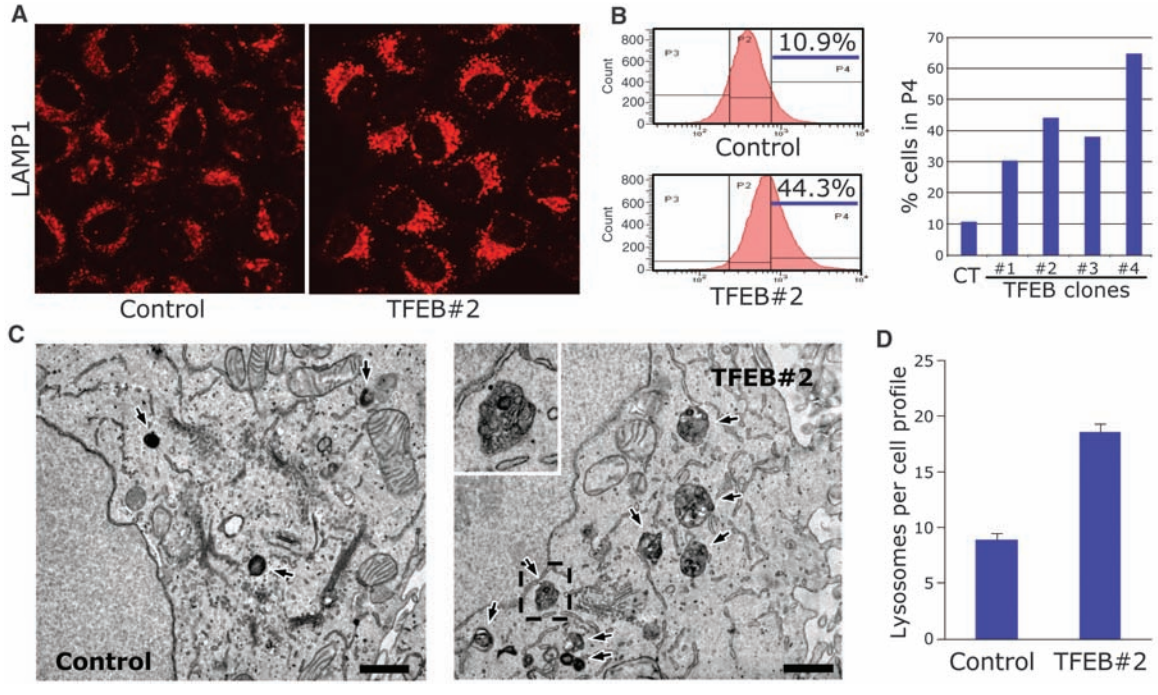

Fig. 2. TFEB overexpression induces lysosomal biogenesis. Comparison of HeLa stable transfectants of either *TFEB* or empty pcDNA3 vector (control). (**A**) Confocal microscopy after staining with an antibody against the lysosomal marker LAMP1. (**B**) Fluorescence-activated cell sorting (FACS) analysis after staining with lysosome-specific dye Lysotracker. The analysis was performed on four independent clones (TFEB#1 to -4) (fig. S12). Blue bars indicate the proportion of cells with fluorescence intensity greater than the indicated threshold (P4 gate). 30,000 cells per clone were analyzed. (**C**) Electron microscopy analysis. Thin sections exhibit more lysosome profiles (arrows) with typical ultrastructure (inset, details corresponding to dash boxed area) in *TFEB*–overexpressing transfectants over the control. Scale bar, 720 nm. (**D**) Number of lysosomes in thin sections (average ± SE, $n = 20$ cells).

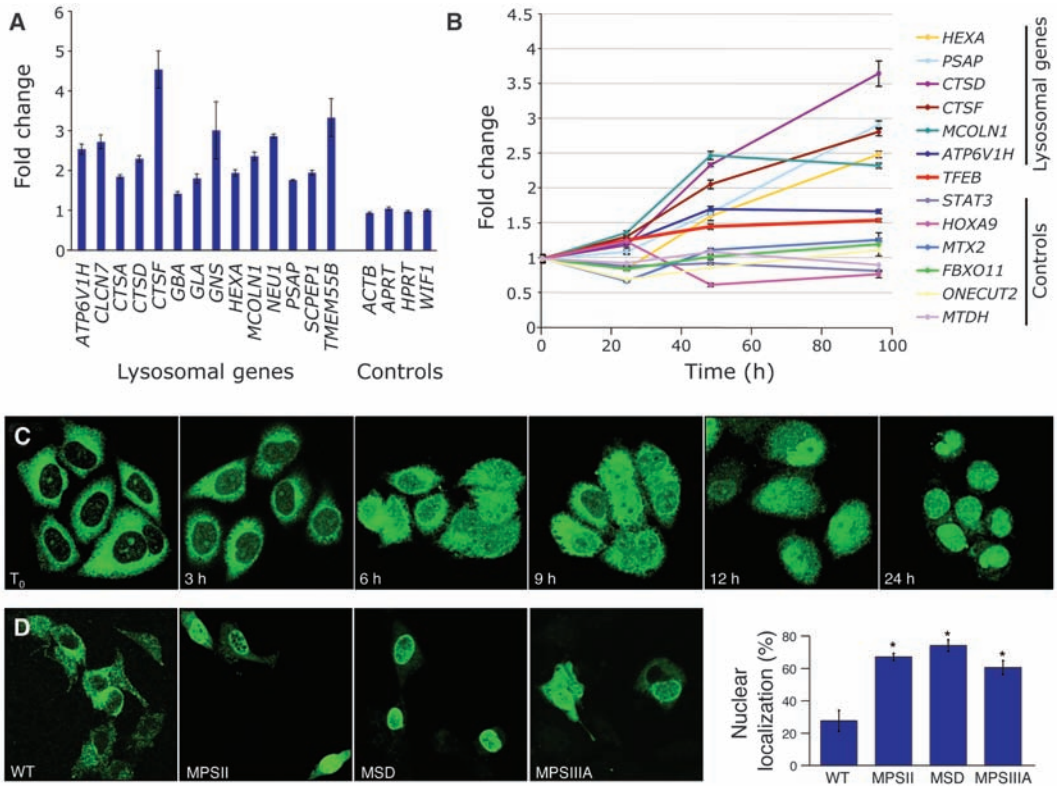

Fig. 3. The CLEAR network is activated by lysosomal storage. (**A**) ChIP analysis following lysosomal storage of sucrose. The histogram shows the ratio (expressed as fold change) between the amounts of FLAG-immunoprecipitated chromatin in sucrose-treated versus non-treated cells. Lysosomal genes show an average two- to three-fold increase of immunoprecipitated chromatin, whereas no significant changes are observed for control genes. (**B**) Expression analysis of lysosomal genes after sucrose supplementation. The diagram shows a time-course analysis of the mRNA levels of lysosomal genes and of *TFEB*. Gene expression was monitored by means of real-time quantitative polymerase chain reaction (PCR) and normalized relative to *GAPDH*. All experiments in (A) and (B) were performed at least in duplicates (data represent mean ± SD). (**C**) Immunofluorescence microscopy analysis of TFEB subcellular localization after sucrose supplementation. HeLa clones stably expressing TFEB-3xFLAG were stained with an antibody to FLAG at various time points after the addition of sucrose in culture medium. (**D**) Immunofluorescence microscopy analysis of TFEB localization in mouse embryonic fibroblasts (MEFs) from mouse models of three different types of LSDs. MEFs from LSD or wild-type (WT) mice were transiently transfected with a TFEB-3xFLAG construct and stained with an antibody to FLAG. The percentages of nuclei positive for FLAG staining were estimated by examining 100 cells per cell type in two different transfection experiments (data represent mean ± SD).

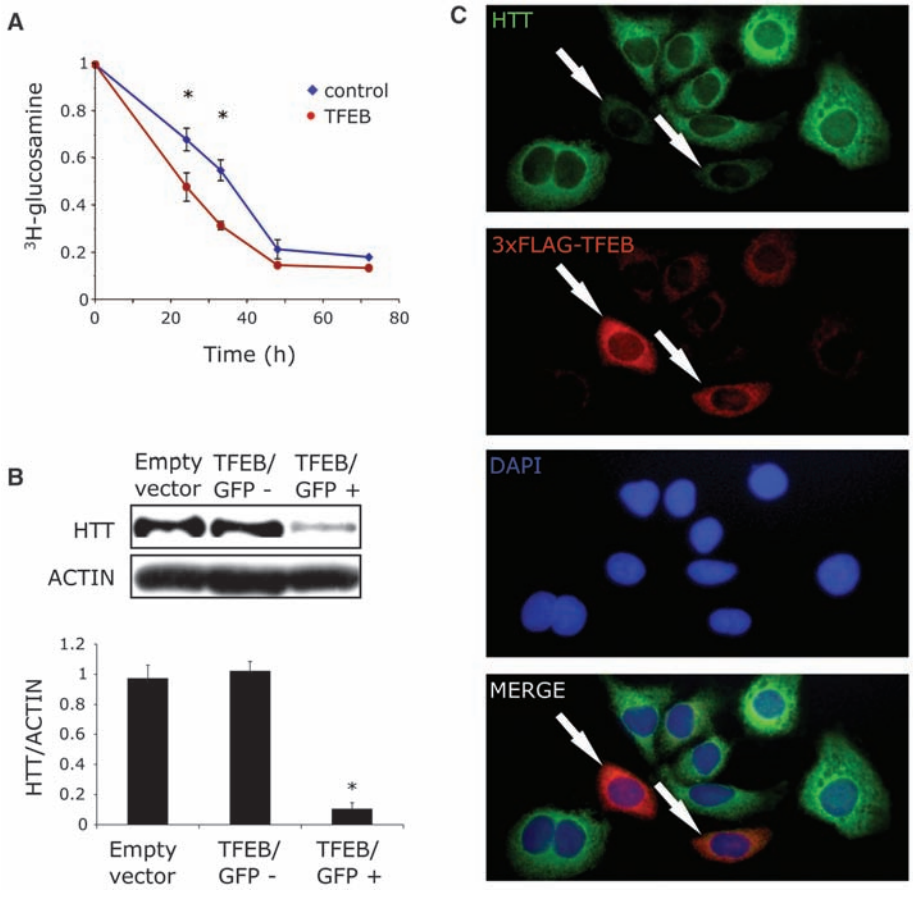

Fig. 4. TFEB enhances cellular clearance. (**A**) Comparison of the kinetics of GAG clearance in HeLa-stable clones of either *TFEB* or empty pcDNA3 vector (control). The graph shows relative amounts of ^{3}H-glucosamine incorporated into GAGs over time. 1 = ^{3}H-glucosamine levels at time zero. *$P < 0.05$. Experiments were performed in triplicates (data represent mean ± SD). (**B** and **C**) Clearance of polyQ-expanded huntingtin (HTT) after TFEB overexpression. (B) Immunoblot analysis of TFEB-EGFP–positive (+) and TFEB-EGFP–negative (–) HD43 cells separated by FACS 24 hours after electroporation. The graph of densitometric analysis shows a strong decrease of polyQ-expanded huntingtin in TFEB-EGFP–positive cells as compared with that in controls. (C) Immunocytochemical analysis of TFEB and HTT in HD43(Q105) cells transfected with 3xFLAG-TFEB construct showing little huntingtin staining in cells positive for 3xFLAG-TFEB staining.

cDNAs. We observed an increase in the mRNA levels of lysosomal genes (22 out of 23 genes tested) only after TFEB overexpression (Fig. 1C). Accordingly, we detected a significant increase in the activities of lysosomal enzymes β-glucosidase, Cathepsin D, and β-glucuronidase (fig. S5). Induction of lysosomal genes after TFEB overexpression was also observed in human embryonic kidney (HEK) 293 cells (fig. S6). We predicted that TFEB could be a target of the microRNA miR-128 (*7*), which was confirmed by luciferase experiments (fig. S7). TFEB silencing mediated by miRNA was associated with the downregulation of 18 out of the 23 lysosomal genes tested (Fig. 1C and fig. S8). Thus, TFEB regulates the expression of lysosomal genes.

To test whether lysosomal genes are direct targets of TFEB, we performed chromatin immunoprecipitation (ChIP) analysis on HeLa cells that stably express a TFEB 3xFLAG construct using an antibody to FLAG. The results demonstrated that TFEB binds to CLEAR sites (Fig. 1D). To identify genes responsive to TFEB on a genomic scale, we performed microarray analysis of the HeLa transcriptome after TFEB overexpression. We observed that 291 genes were upregulated and seven were down-regulated, at a false discovery rate of <0.1 (table S3). Upregulated genes were greatly enriched with lysosomal genes and genes related to lysosomal biogenesis and function (figs. S9 and S10 and table S4). Accordingly, gene set enrichment analysis (GSEA) showed a significant enrichment (enrichment score = 0.84; $P < 0.0001$) of lysosomal genes that contain CLEAR elements in their promoters among induced genes (fig. S11). Nonlysosomal genes involved in degradation pathways appear to be modulated by TFEB. These include *RRAGC* and *UVRAG*, which are key factors regulating autophagy (*8*, *9*); *CSTB*, which plays a role in protecting against the proteases leaking from lysosomes (*10*); and *M6PR* and *IGF2R*, which mediate the import of proteins into the lysosome (*11*). To illustrate the feasibility of using the CLEAR network as a tool to identify genes involved in lysosomal function and to provide candidate genes for orphan lysosomal diseases (*3*), we determined the subcellular distribution of two randomly chosen proteins of unknown function, *C1orf*85 and *C12orf*49. The uncharacterized TFEB target, *C1orf85*, was found localized to lysosomes (Fig. 1E).

An expansion of the lysosomal compartment was detected in HeLa transfectants that stably overexpress TFEB (Fig. 2, A and B, and fig. S12). Accordingly, ultrastructural analysis revealed a significant increase in the number of lysosomes per cell (Fig. 2, C and D), indicating the involvement of TFEB in lysosomal biogenesis. This is similar to MITF, another member of the MiT/TFE family, which is involved in a related cellular function, melanosomal biogenesis (*6*).

An increase of the expression levels of lysosomal genes and of genes involved in cholesterol biosynthesis and intracellular trafficking was previously reported in a sucrose-induced vacuolation model (*12*, *13*). We used this model to test whether the TFEB-CLEAR network responds to lysosomal storage of undegraded molecules. An increase of the binding events of TFEB to lysosomal promoters (Fig. 3A) and of the mRNA levels of lysosomal genes, and to a lesser extent of *TFEB*, was detected upon sucrose supplementation to the culture medium (Fig. 3B). The addition of sucrose also determined the progressive translocation of TFEB from a diffuse localization in the cytoplasm, where it predominantly resides in untreated cells, to the nucleus (Fig. 3C), suggesting that nuclear translocation is an important mechanism for TFEB activation.

Over 40 lysosomal storage disorders (LSDs) are characterized by the progressive accumulation of undigested macromolecules within the cell, resulting in cellular dysfunction that leads to diverse clinical manifestations (*1*, *14*, *15*). We investigated TFEB subcellular localization in embryonic fibroblasts obtained from mouse models of three different LSDs, Mucopolysaccharidoses types II and IIIA (MPSII and MPSIIIA) and Multiple Sulfatase Deficiency (MSD) (*16*–*18*). A predominant nuclear localization of TFEB was detected in cells from all three LSD mouse models (Fig. 3D), suggesting that the TFEB signaling pathway is activated after the intralysosomal storage of undegraded molecules. Such activation could be part of the cellular physiological response to lysosomal stress and could serve degradation needs by enhancing the lysosomal system.

To test the ability of TFEB to enhance lysosome-dependent degradation pathways, we analyzed the degradation of glycosaminoglycans (GAGs) in a pulse-chase experiment. TFEB stable transfectants displayed a faster rate of GAG clearance as compared with that in controls (Fig. 4A). We also investigated the ability of TFEB to induce the degradation of the polyglutamine (polyQ)–expanded huntingtin protein that is responsible for Huntington's disease using the rat striatal cell model HD43 that carries an inducible transgene for mutant huntingtin (*19*). Immunoblot analyses showed a strong decrease of mutant huntingtin in TFEB-overexpressing cells as compared with those in controls (Fig. 4B). In a parallel experiment, induced HD43 cells were electroporated with a 3xFLAG-TFEB construct. Immunofluorescence analyses showed that the cells that are positive for 3xFLAG-TFEB show little if any huntingtin accumulation (Fig. 4C).

We have discovered a cellular program that regulates lysosomal biogenesis and participates in macromolecule clearance. Lysosomal enhancement as a cellular response to pathogenic accumulation has been observed in neurodegenerative diseases (*20*–*22*). Cathepsin D (*23*, *24*), one of the key enzymes involved in the degradation of neurotoxic proteins, belongs to the CLEAR network and is induced by TFEB overexpression. Also, miR-128 (which we used for TFEB downregulation) is significantly upregulated in the brain of patients with Alzheimer's disease (*25*) and in both prion- and chemical-induced neurodegeneration (*26*, *27*). An appealing perspective would be the use of the CLEAR network as a therapeutic target to enhance cellular response to intracellular pathogenic accumulation in neurodegenerative diseases.

Note added in proof: While this study was in proof, a report was published by Schieweck *et al*. (*28*) in which was shown a lysosomal localization for NCU-G1, the mouse ortholog of Clorf85.

References and Notes

1. P. Saftig, *Medical Intelligence Unit: Lysosomes* (Springer, New York, 2003).
2. J. Reimand, M. Kull, H. Peterson, J. Hansen, J. Vilo, *Nucleic Acids Res.* **35**, W193 (2007).
3. T. Lubke, P. Lobel, D. E. Sleat, *Biochim. Biophys. Acta* **1793**, 625 (2008).
4. M. E. Massari, C. Murre, *Mol. Cell. Biol.* **20**, 429 (2000).
5. N. A. Meadows *et al*., *J. Biol. Chem.* **282**, 1891 (2007).
6. E. Steingrimsson, N. G. Copeland, N. A. Jenkins, *Annu. Rev. Genet.* **38**, 365 (2004).
7. V. A. Gennarino *et al*., *Genome Res.* **9**, 481 (2009).
8. Y. Sancak *et al*., *Science* **320**, 1496 (2008).
9. C. Liang *et al*., *Nat. Cell Biol.* **10**, 776 (2008).
10. Y. Shin, J. Klucken, C. Patterson, B. T. Hyman, P. J. McLean, *J. Biol. Chem.* **280**, 23727 (2005).
11. S. Kornfeld, W. S. Sly, in *The Metabolic and Molecular Basis of Inherited Disease*, vol. 2, C. R. Scriver, W. S. Sly, A. L. Beaudet, D. Valle, Eds. (McGraw-Hill, New York, 2001), pp. 3469–3482.
12. L. E. Karageorgos *et al*., *Exp. Cell Res.* **234**, 85 (1997).
13. A. Helip-Wooley, J. G. Thoene, *Exp. Cell Res.* **292**, 89 (2004).
14. E. F. Neufeld, J. Muenzer, in *The Metabolic and Molecular Basis of Inherited Disease*, C. R. Scriver, W. S. Sly, A. L. Beaudet, D. Valle, Eds. (McGraw-Hill, New York, 2001) pp. 3421–3454.
15. A. Ballabio, V. Gieselmann, *Biochim. Biophys. Acta* **1793**, 684 (2009).
16. J. Muenzer *et al*., *Acta Paediatr. Suppl.* **91**, 98 (2002).
17. K. M. Hemsley, J. J. Hopwood, *Behav. Brain Res.* **158**, 191 (2005).
18. C. Settembre *et al*., *Proc. Natl. Acad. Sci. U.S.A.* **104**, 4506 (2007).
19. S. Sipione *et al*., *Hum. Mol. Genet.* **11**, 1953 (2002).
20. A. M. Cataldo *et al*., *Neuron* **14**, 671 (1995).
21. A. M. Cataldo, J. L. Barnett, C. Pieroni, R. A. Nixon, *J. Neurosci.* **17**, 6142 (1997).
22. J. Bendiske, B. A. Bahr, *J. Neuropathol. Exp. Neurol.* **62**, 451 (2003).
23. U. S. Ladror, S. W. Snyder, G. T. Wang, T. F. Holzman, G. A. Krafft, *J. Biol. Chem.* **269**, 18422 (1994).
24. L. Qiao *et al*., *Mol. Brain* **1**, 17 (2008).
25. W. J. Lukiw, *Neuroreport* **18**, 297 (2007).
26. W. J. Lukiw, A. I. Pogue, *J. Inorg. Biochem.* **101**, 1265 (2007).
27. R. Saba, C. D. Goodman, R. L. Huzarewich, C. Robertson, S. A. Booth, *PLoS One* **3**, e3652 (2008).
28. Schieweck *et al*., *Biochem. J.* 10.1042/BJ20090567 (2009).

29. This paper is dedicated to the memory of Ms. Susanna Agnelli, President of the Italian Telethon Foundation. We thank S. Anand, M. V. Barone, L. Cutillo, M. Morleo, A. Pignata, R. M. Tuzzi, and S. Pepe for technical assistance. We also thank B. Amati, E. Guccione, and P. De Camilli for helpful suggestions and P. Di Fiore, G. Diez-Roux, A. Luini, and C. Missero for comments on the manuscript. This work was supported by the European Union, 7th Framework Program "Euclyd—a European Consortium for Lysosomal Storage Diseases" (health F2/2008 grant agreement 201678) and by the Italian Ministry of Research (PRIN 2006064337). The contributions of the Italian Telethon Foundation and

of the National MPS Society USA are gratefully acknowledged. The authors have no conflicts of interest. Expression microarray data are available at the Gene Expression Omnibus repository under accession number GSE16267. A patent application on the discovery of a gene network regulating lysosomal biogenesis and function has been filed to the European Patent Office (patent application EP 091527788). A.B. and M.S. are inventors on this patent.

Supporting Online Material
www.sciencemag.org/cgi/content/full/1174447/DC1
Materials and Methods
Figs. S1 to S12
Tables S1 to S5
References

2 April 2009; accepted 10 June 2009
Published online 25 June 2009;
10.1126/science.1174447
Include this information when citing this paper.

An ER-Mitochondria Tethering Complex Revealed by a Synthetic Biology Screen

Benoît Kornmann,[1]* Erin Currie,[1]† Sean R. Collins,[2,3]‡ Maya Schuldiner,[4] Jodi Nunnari,[5] Jonathan S. Weissman,[2,3] Peter Walter[1,3]

Communication between organelles is an important feature of all eukaryotic cells. To uncover components involved in mitochondria/endoplasmic reticulum (ER) junctions, we screened for mutants that could be complemented by a synthetic protein designed to artificially tether the two organelles. We identified the Mmm1/Mdm10/Mdm12/Mdm34 complex as a molecular tether between ER and mitochondria. The tethering complex was composed of proteins resident of both ER and mitochondria. With the use of genome-wide mapping of genetic interactions, we showed that the components of the tethering complex were functionally connected to phospholipid biosynthesis and calcium-signaling genes. In mutant cells, phospholipid biosynthesis was impaired. The tethering complex localized to discrete foci, suggesting that discrete sites of close apposition between ER and mitochondria facilitate interorganelle calcium and phospholipid exchange.

Eukaryotic cells evolved segregation of functions into separate organelles. Compartmentalization increases the efficiency of biochemical reactions by creating tailored chemical microenvironments, but also creates a need for communication and routes of metabolite exchange. Membrane lipids, for example, are primarily synthesized in the endoplasmic reticulum (ER) and distributed to other organelles. Many organelles exchange phospholipids with the ER via vesicular transport. In contrast, mitochondria are not connected to vesicular trafficking pathways, and many lipids of the inner and outer mitochondrial membranes (IMM and OMM) cannot be synthesized within mitochondria but are imported by unclear mechanisms. Phospholipids may transfer from the ER to the OMM at spatially restricted sites, which are frequently observed by electron microscopy and have been enriched by cell fractionation (*1*–*3*).

Other work has implicated ER-mitochondrial contact sites in Ca^{++} transport between the ER and mitochondria (*4*–*6*), suggesting a mechanism that may exploit the formation of an encapsulated space at the contact sites, akin to that formed at neuronal or immunological synapses. Such a connection between the ER and the mitochondria might buffer and control cytosolic and mitochondrial Ca^{++} concentrations (*7*). Several proteins have been implicated to participate in ER-mitochondria contacts, including the ER resident Ca^{++} channel IP3 receptor, the mitochondrial voltage-dependent anion channel, the chaperones grp75 and sigma-1R, the sorting protein PACS-2, and the mitofusin Mfn2 (*8*–*11*).

To explore a role for ER-mitochondrial junctions, we sought mutants in the yeast *Saccharomyces cerevisiae*, in which tethering between the two organelles was impaired. We reasoned that, if such contacts are important, defects in proteins that establish these interactions would be detrimental, yet perhaps could be suppressed by artificially tethering ER and mitochondria (Fig. 1A). We designed a synthetic ER-mitochondria tether ("ChiMERA" for construct helping in mitochondria-ER association) (Fig. 1B) consisting of an N-terminal mitochondrial signal sequence and transmembrane domain derived

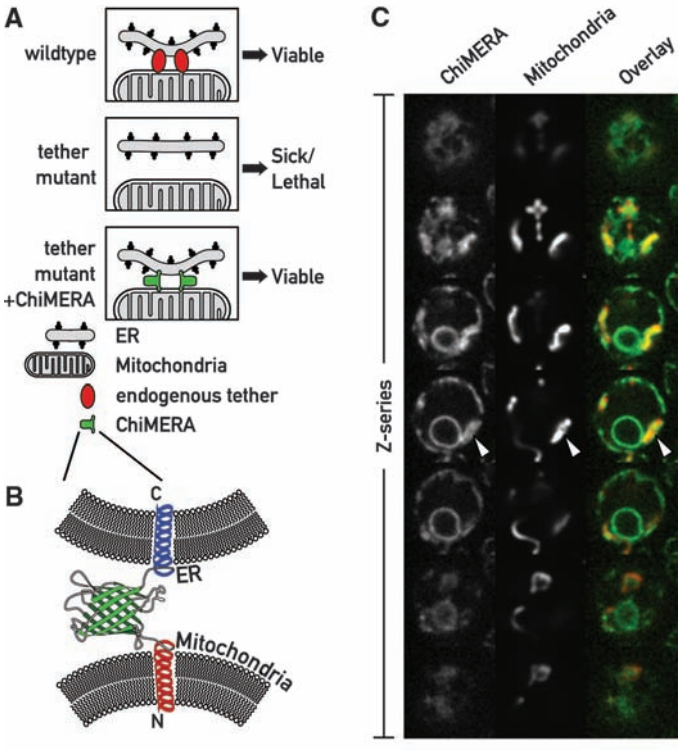

Fig. 1. A synthetic biology screen to uncover mutants of the ER-mitochondria connection. (**A**) Rationale of the screen. (Top) In WT cells a yet unknown endogenous complex tethers the ER to the mitochondria. (Middle) Mutations causing the loss of the endogenous complex are detrimental and cause slow growth or cell death. (Bottom) Artificial ER-mitochondria tethering by ChiMERA can suppress the defects associated with the loss of the endogenous tether. (**B**) Outline of the ChiMERA. A central GFP molecule (green) is flanked by the mitochondria-directed N-terminal Tom70 presequence and transmembrane sequence (red) and the ER-directed C-terminal Ubc6 tail anchor sequence (blue). (**C**) Confocal Z-series across a yeast cell expressing the ChiMERA and a mitochondrial marker (mt-dsRed). ChiMERA displays a characteristic ER staining with additional thicker structures (arrowheads), which colocalize with mitochondria and represent sites of artificial tethering.

[1]Department of Biochemistry and Biophysics, University of California at San Francisco, San Francisco, CA 94158, USA. [2]Department of Cellular and Molecular Pharmacology, University of California at San Francisco, San Francisco, CA 94158, USA. [3]Howard Hughes Medical Institute, University of California at San Francisco, San Francisco, CA 94158, USA. [4]Molecular Genetics, Weizmann Institute of Science, Rehovot, Israel. [5]Molecular and Cellular Biology, University of California at Davis, Davis, CA 95616, USA.

*To whom correspondence should be addressed. E-mail: benoit.kornmann@ucsf.edu
†Present address: Gladstone Institute of Cardiovascular Disease, San Francisco, CA 94158, USA.
‡Present address: Chemical and Systems Biology, Bio-X Program, Stanford University, Stanford, CA 94305, USA.

from Tom70, a central module composed of green fluorescent protein (GFP), and a C-terminal ER tail-anchor derived from Ubc6. The design was based on a similar chimeric protein that strengthened mitochondria-ER interactions (*12*). The GFP moiety allowed us to visualize its tethering activity directly (Fig. 1C and fig. S1A). ChiMERA localized mainly to ER membranes and stained both peripheral and perinuclear ER. In addition, ChiMERA localized to patches of contact with mitochondria (Fig. 1C). Mitochondria in untransformed wild-type (WT) cells showed the characteristic morphology of a uniformly tubular network (Fig. 2B and fig. S1B) and adopted a pronounced patchy structure at the artificial contact sites in cells expressing ChiMERA (Fig. 1C and fig. S1A; see also Fig. 2B). Thus, ChiMERA tethers mitochondria and ER as intended. The dominant ER staining probably reflects a partial dominance of the ER targeting sequence over the mitochondrial one. We also generated a second version of the artificial tether in which the yeast Tom70 presequence and transmembrane domain was replaced by the mouse AKAP1 presequence (*12*). This construct also localized predominantly to the ER but accumulated in only one to three discrete foci per cell (fig. S2). These foci colocalized with both ER (fig. S2A) and mitochondria (fig. S2B). This construct, however, did not create distortions in mitochondrial shape. It is likely that this synthetic protein does not exert a substantial tethering force and instead labels preexisting ER-mitochondrial interfaces. We refer to this construct as ChiMERA-ra (for ChiMERA with reduced affinity).

We next used a construct expressing ChiMERA from a centromeric expression plasmid in a classical sectoring screen (*13*). We screened ~100,000 ethylmethanesulfonate-treated colonies and retrieved two mutants that could not grow in the absence of the plasmid. Genetic complementation (*14*) indicated that the mutations are two different alleles of *MDM12*. Accordingly, a strain bearing a complete deletion of *MDM12* grew on respiration plates when it expressed the ChiMERA, but the strain failed to grow without it (Fig. 2A). Mdm12 is a peripheral OMM protein (*15*) (fig. S3). Mdm12 can be isolated from cell extracts as a complex with Mmm1 and Mdm10 and localizes in a few punctate structures along the mitochondrial network, together with a fourth protein, Mdm34 (*16*, *17*) (Fig. 3A). All four proteins are required for respiratory growth and for the maintenance of the proper tubular morphology of mitochondria. We deleted *MMM1*, *MDM10*, and *MDM34* and assessed the extent to which ChiMERA could rescue their phenotypes. ChiMERA expression partially suppressed growth defects, albeit to highly different extents (Fig. 2A). *mdm12Δ*, *mmm1Δ*, *mdm10Δ*, and *mdm34Δ* strains displayed enlarged and spherical mitochondria as compared with the tubular WT mitochondria (*18*). ChiMERA expression also restored the mitochondrial morphology of *mdm12Δ* and *mdm34Δ* strains (Fig. 2B and fig. S4), although it failed to do so in *mmm1Δ* and *mdm10Δ* strains, consistent with the lesser rescue of growth on respiration medium (Fig. 2A). An Mdm34-mCherry fusion protein colocalized with both the punctate structures labeled by ChiMERA-ra and the broad ER-mitochondria interfaces created by ChiMERA (fig. S5).

Thus, one core molecular function of the Mmm1/Mdm10/Mdm12/Mdm34 complex is to connect ER and mitochondria, which can be bypassed by expressing a synthetic tether. Henceforth, we refer to the complex as ERMES (ER-mitochondria encounter structure).

ERMES localizes into a few discrete foci (*16*, *17*), and mutations in any single component cause the puncta to disappear (*16*, *17*). We reasoned that ERMES components may be respectively localized to the ER and mitochondria, and they might serve to zipper the organelles together. ERMES disruption would then cause some of the components to partition with ER, whereas some others would partition with mitochondria.

To address this possibility, we replaced the gene encoding each ERMES component with that of a functional GFP fusion protein and imaged both WT and mutant cells (Fig. 3A). In WT cells, ERMES components displayed the expected punctate pattern, with the exception of Mdm10, which displayed a more widespread localization throughout the mitochondrial network. This is consistent with the observation that Mdm10 is not only a component of ERMES but is also a component of the sorting and assembly machinery (SAM) complex in the OMM (*19*). As expected from its assignment as an OMM protein, Mdm34-GFP relocalized uniformly to mitochondria in the absence of Mdm10, Mdm12, and Mmm1 (Fig. 3A; note the swollen morphology of mitochondria in the mutants). Likewise, Mdm10-GFP remained colocalized with mitochondria in all strains tested. In contrast, and contrary to expectation, Mmm1-GFP relocalized to the ER, showing a characteristic peripheral and perinuclear staining in the absence of Mdm10, Mdm12, or Mdm34. Mdm12-GFP, a membrane peripheral protein (fig. S3), relocalized to the ER in the absence of Mdm10 or Mdm34, and the mitochondria in the absence of Mmm1, suggesting that its localization depends on the availability of interaction partners at either organelle.

Mmm1 harbors a classical helical transmembrane domain, previously proposed to be inserted into either the outer or inner mitochondrial membrane (*20*), yet our localization data suggested that Mmm1 is instead inserted into the ER. Many integral ER membrane proteins are N-glycosylated within their lumenal domains, and four potential N-glycosylation sites lie in the N terminus of Mmm1 preceding the transmembrane domain. To address whether these sites were glycosylated, we replaced the *MMM1* gene with fully functional hemagglutinin (HA)–tagged *MMM1* and assessed the electrophoretic mobility of HA-Mmm1 from cell extracts with or without treatment with the glycosidase $Endo H_f$, which removes N-linked glycans. Treatment with $Endo H_f$ caused HA-Mmm1 to migrate faster (Fig. 3B and fig. S6A), indicating that Mmm1 is N-glycosylated and therefore is an integral ER membrane protein that was misannotated as a mitochondrial protein. The misannotation was partly due to the interpretation of a tobacco etch virus (TEV) protease cleavage accessibility assay (*20*). We used the same assay with an ER-targeted TEV protease and confirmed Mmm1 ER-membrane insertion (fig. S6B).

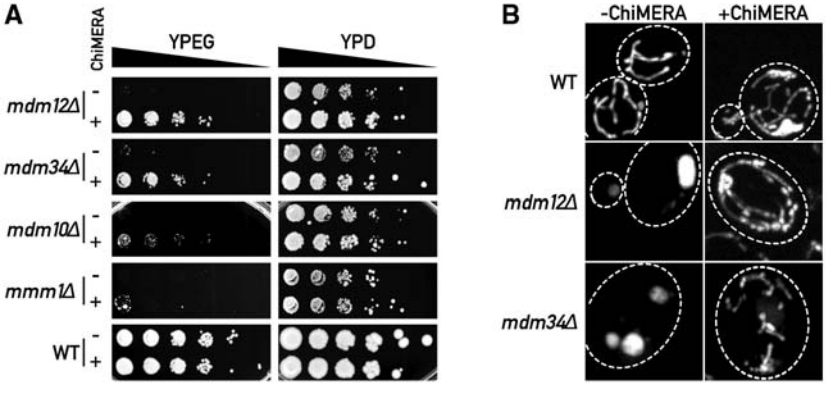

Fig. 2. ChiMERA expression suppresses phenotypes associated with deletions of ERMES complex components. (**A**) 10-fold serial dilutions of a saturated culture were spotted on YP + ethanol/glycerol medium (YPEG) that supports growth by respiration or YP + dextrose (YPD) that allows fermentation. ChiMERA expression rescues growth of *mdm12Δ*, *mdm34Δ*, *mdm10Δ*, and *mmm1Δ* strains to different extents on respiration medium. (**B**) The mitochondrial shape defect of *mdm12Δ* and *mdm34Δ* strains is partially suppressed by expression of the ChiMERA. Cells bearing a mitochondria-targeted dsRed were imaged with the use of confocal fluorescence microscopy. Z projections across the whole volume of the cells are shown. A broken white line outlines the perimeter of the cell. ChiMERA expression has no effect in WT cells, other than formation of artificial tethering structures. *mdm12Δ* and *mdm34Δ* strains display rounded and enlarged mitochondria. The mitochondrial tubular shape is substantially restored upon ChiMERA expression. A quantitation of this effect is shown in fig. S4.

Taken together, our results indicate that ERMES functions as a molecular zipper bridging between ER and mitochondria. ERMES consists of the ER-resident membrane protein Mmm1 and the OMM-resident β-barrel protein Mdm10 (*21*). The well-characterized interaction of these two proteins (*16*, *19*) requires Mdm12 and Mdm34. Defects in these latter proteins can be compensated by expressing ChiMERA, a synthetic protein that bridges ER and mitochondrial membranes, strongly suggesting that one primary physiological role of ERMES is that of a mechanical tether. Mutation of a single ERMES component causes complex disassembly but results in different growth phenotypes. Deletions of *MDM12* and *MDM34* are easily compensated for by ChiMERA expression, whereas deletions of *MMM1* and *MDM10* are less efficiently compensated. The variability in phenotypes indicates that Mmm1 and Mdm10 still provide useful activity in the absence of a functional complex, provided that an artificial tether is present. Mdm10 is a component of both ERMES and of the SAM complex (*19*) that imports β-barrel proteins in the OMM, and therefore, this latter activity would not be expected to be compensated for by ChiMERA expression.

From these results, it appeared plausible that impairing ER-mitochondrial tethering provided the molecular basis for the phenotypes associated with ERMES defects, thus offering a unique opportunity to investigate the physiology of ER-mitochondria communication. To evaluate systematically the phenotypic consequences of loss of ERMES, we analyzed a recently generated epistasis mini-array profile (E-MAP) (see supplement) (*22*). The E-MAP methodology identifies functionally related genes by comparing their profiles of genetic interaction. In the map, a set of 1493 null or hypomorphic alleles, including *mmm1Δ*, *mdm10Δ*, *mdm12Δ*, and *mdm34Δ* strains, was crossed to a set of 484 query null or hypomorphic strains selected primarily for their association with mitochondrial and ER biology. The phenotype of the ~700,000 double mutants was assessed by colony size and used to calculate quantitative genetic interactions. This analysis confirmed previously characterized genetic interactions. For instance, prohibitins (*PHB1* and *PHB2*), which have been shown to be synthetic lethal to ERMES component deletions (*23*), display some of the strongest synthetic phenotypes (Fig. 4A).

We used the interaction patterns of the 1493 genes in this analysis to calculate pairwise correlation coefficients. In this analysis, genes encoding ERMES components consistently showed strong correlation with each other (Fig. 4B), confirming that these genes are functionally related and that this analysis has the power to uncover this relation. Two genes, *GEM1* and *PSD1*, showed strong correlation to every ERMES gene. Gem1 is a calcium-binding rho-like GTPase inserted in the OMM and involved in calcium-dependent mitochondrial movement and inheritance (*24*, *25*). Psd1 is a phosphatidylserine (PS) decarboxylase involved in the de novo biosynthesis of aminoglycerophospholipids. ER-mitochondria connections have been previously shown to be important for interorganelle calcium and phospholipid exchange, further supporting a role for ERMES in mediating ER-mitochondrial junctions.

The phenotypic similarity between ERMES and *PSD1* was particularly notable because Psd1 is the only aminoglycerophospholipid biosynthetic enzyme in mitochondria (*1*) (fig. S7), implying that its substrate has to be transported from the ER and its product back to the ER. To assess a role of ER-mitochondrial junctions in lipid biosynthesis, we first analyzed mitochondrial phospholipid content in ERMES-disrupted (*mdm12Δ*) cells at steady-state conditions. All phospholipid classes were represented in ratios comparable to those of WT cells, with the notable exception of cardiolipin (CL), which was much reduced in its relative abundance (Fig. 4C). CL is a mitochondria-specific phospholipid essential for respiration. Deletion of any ERMES component, as well as of *PSD1*, is synthetically lethal with a deletion of *CRD1* (Fig. 4A) (*26*), which encodes the CL synthase (*27*). Moreover, *psd1Δ* cells also display reduced CL levels (*28*). Thus, similar to *psd1Δ* cells, ERMES mutant strains suffer from mitochondrial phospholipid abnormalities and cannot tolerate the absence of a functional CL biosynthesis pathway, even when grown in fermentable medium. In addition, an extensive cross talk has been observed between aminoglycerophospholipid and CL synthesis, along with a reduction in CL levels in *mmm1Δ*, *mdm10Δ*, and *mdm34Δ* strains (*23*).

The maintenance of a balance between most phospholipid species besides CL in *mdm12Δ* mutant cells suggests that ER-mitochondria connections might affect the rate of phospholipid biosynthesis but have little effect on steady-state levels because of compensatory mechanisms (*28*). To assess this possibility, we monitored the

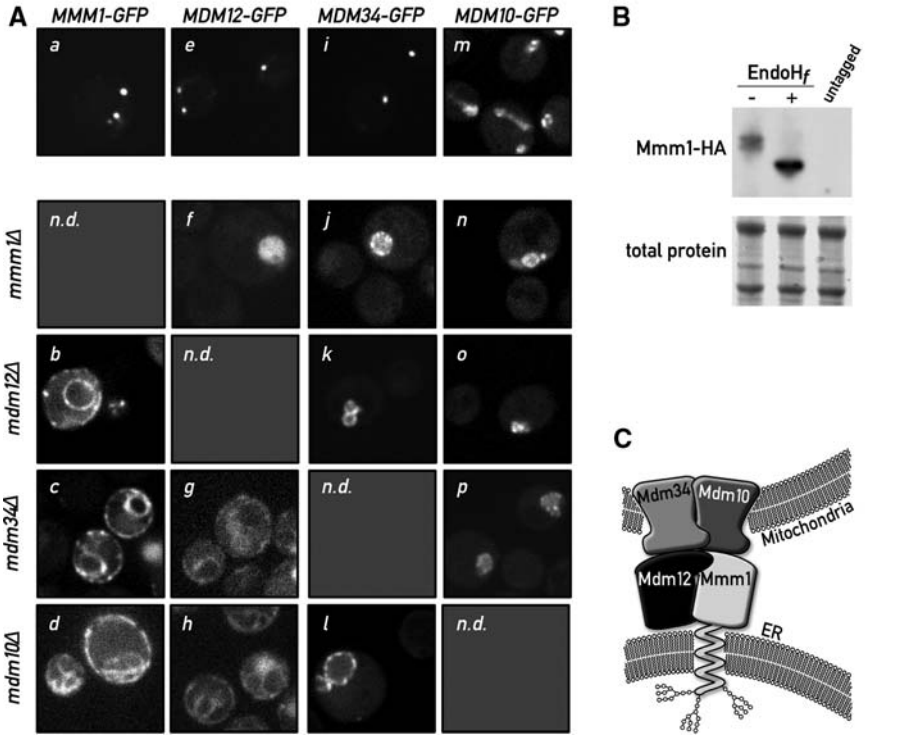

Fig. 3. Mmm1 is an integral ER protein. (**A**) Disruption of a single ERMES component causes disassembly of the complex. Mmm1-GFP is localized in punctate structures in WT cells (a). Upon deletion of *MDM12* (b), *MDM34* (c), or *MDM10* (d), Mmm1-GFP relocalizes to the ER. Mdm12-GFP displays a punctate pattern in WT cells (e). In the absence of Mmm1 (f), Mdm12-GFP displays a uniform mitochondrial localization (note the rounded swollen mitochondrial shape in *mmm1Δ* strains), but in the absence of *MDM34* (g) or *MDM10* (h), Mdm12-GFP relocalizes to the ER. Mdm34-GFP is also in punctate structures in WT cells (i). Upon mutation of any other complex member, Mdm34 relocalizes more uniformly to the mitochondrial membrane (j, k, l). Mdm10-GFP localizes to the whole surface of the mitochondria (m) and localizes to the rounded mitochondria after deletion of any other ERMES component (n, o, p). n.d., not determined. (**B**) Mmm1 is N-glycosylated. Whole-cell extract from a strain bearing a functional HA-tagged *MMM1* gene was subjected to SDS–polyacrylamide gel electrophoresis with or without pretreatment with the glycosidase *EndoH*$_f$. Detection was performed by Western blotting with an anti-HA antibody. The shift in electrophoretic mobility upon glycosidase treatment is indicative that Mmm1 is N-linked glycosylated. (**C**) Model of ERMES-mediated ER-mitochondria tethering. Mmm1 is an integral ER protein glycosylated on its N-terminal side. Mmm1 interacts with Mdm10, a OMM β-barrel protein. Mdm34 and Mdm12 promote this association, most probably via direct association.

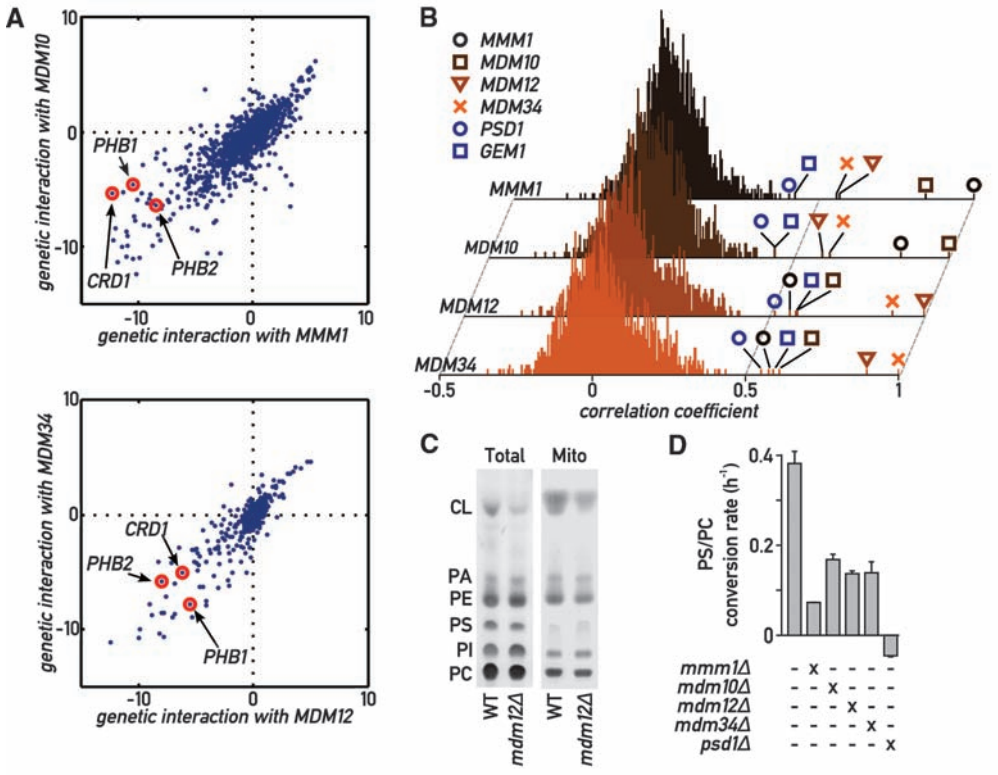

Fig. 4. Global analysis of ERMES genetic interactions. (**A**) Genetic interactions of *MMM1* and *MDM10* (top) and of *MDM12* and *MDM34* (bottom). Positive values indicate epistatic or suppressive interactions (i.e., double mutant grows better than expected from the combination of the phenotypes of each single mutant); negative values indicate a synthetic sick/lethal genetic interaction (i.e., double mutant grows worse than expected). (**B**) Histograms of correlation coefficients generated by comparing the profiles of genetic interaction for each ERMES component to all other 1493 profiles in the E-MAP analysis. ERMES components display strongest correlation to each other and to *GEM1* and *PSD1*. (**C**) Thin-layer chromatography (TLC) analysis of steady-state total and mitochondrial phospholipids in WT and *mdm12Δ* strains. PA, phosphatidic acid; PI, phosphatidylinositol. (**D**) The aminoglycerophospholipid biosynthesis pathway is slowed down in ERMES mutants. Cultures of the indicated genotypes were labeled with ^{14}C-serine, then chased with an excess cold serine. The variation of the PC/PS ratio was then measured over time by quantitative TLC, and its slope was estimated with linear regression. Error bars represent the SE of the linear regression.

conversion of PS to phosphatidylcholine (PC) in a ^{14}C-serine pulse-chase. This experiment was conducted in a *psd2Δ* background to exclude the contribution of the vacuolar PS decarboxylase Psd2 (*29*). An otherwise WT strain displayed a high rate of PS-to-PC conversion (Fig. 4E), whereas a *psd1Δ psd2Δ* strain failed to convert PS to PC. Mutants of ERMES showed a two- to fivefold reduction in PS-to-PC conversion rate (Fig. 4D), consistent with the notion that disruption of ERMES impairs phospholipid exchange between ER and mitochondria. This defect was partially reversed by ChiMERA expression in *mdm12Δ psd2Δ* and *mdm34Δ psd2Δ* strains (fig. S8). Contrary to *psd1Δ psd2Δ* strains, however, none of the *psd2Δ* ERMES mutants were auxotrophic for ethanolamine, showing that, consistent with the pulse-chase labeling data, Psd1 still displayed activity even in the absence of tethering.

Thus, ERMES-mediated ER-mitochondria connections are necessary for efficient interorganellar phospholipid exchange. A reduced rate of lipid exchange in turn slows down aminoglycerophospholipid turnover, which results in impaired CL synthesis (*28*). It is likely that part of the pronounced defects in ERMES mutant cells results from problems in mitochondrial membrane maintenance (*23*).

Our strategy of discovering unknown genes by encoding their function into artificial constructs may be applicable to other situations in which a synthetic protein can substitute for an endogenous gene(s).

Mmm1 and Mdm12 belong to the SMP-domain protein family that has multiple members across all eukaryotes (*30*), making it likely that complexes containing one or more of these SMP-domain–containing proteins perform similar functions in metazoan cells.

The organization of the ERMES complex into 2 to 10 foci per cell suggests that the number and extent of interorganelle exchange surfaces have been vastly overestimated (*2*), or that eukaryotes may have evolved multiple specialized and spatially restricted structures that perhaps are dedicated to particular tasks. Each ERMES punctum represents a large macromolecular assembly that is expected to contain, for example, ~250 molecules of Mmm1 (*31*). The mechanical tethering provided by ERMES might organize specialized membrane domains that serve as platforms to recruit other molecules, which, in turn, carry out the physiological roles of the junctions, such as lipid transport or calcium exchange. ERMES foci localize adjacent to actively replicating mitochondrial nucleoids, as part of a poorly characterized assembly spanning both OMM and IMM (*32*). Such structures would span a third membrane and thus could strategically connect the ER lumen and the mitochondrial genome. The purpose of such a link is unclear, but we can speculate that it might help coordinate mitochondrial growth by coupling mitochondrial genome replication and membrane upkeep. In this light, the presence of Mdm10 in both SAM and ERMES complexes provides the intriguing possibility that such a link includes regulation of mitochondrial protein import.

References and Notes

1. D. R. Voelker, *J. Lipid Res.* **44**, 441 (2003).
2. G. Achleitner *et al.*, *Eur. J. Biochem.* **264**, 545 (1999).
3. J. E. Vance, *J. Biol. Chem.* **266**, 89 (1991).
4. R. Rizzuto, A. W. Simpson, M. Brini, T. Pozzan, *Nature* **358**, 325 (1992).
5. R. Rizzuto, M. Brini, M. Murgia, T. Pozzan, *Science* **262**, 744 (1993).
6. R. Rizzuto *et al.*, *Science* **280**, 1763 (1998).
7. P. Pinton *et al.*, *Oncogene* **27**, 6407 (2008).
8. T. Simmen *et al.*, *EMBO J.* **24**, 717 (2005).
9. G. Szabadkai *et al.*, *J. Cell Biol.* **175**, 901 (2006).
10. T. Hayashi, T. Su, *Cell* **131**, 596 (2007).
11. O. M. de Brito, L. Scorrano, *Nature* **456**, 605 (2008).
12. G. Csordás *et al.*, *J. Cell Biol.* **174**, 915 (2006).
13. P. Hieter, C. Mann, M. Snyder, R. W. Davis, *Cell* **40**, 381 (1985).
14. M. D. Rose, J. R. Broach, *Methods Enzymol.* **194**, 195 (1991).
15. K. H. Berger, L. F. Sogo, M. P. Yaffe, *J. Cell Biol.* **136**, 545 (1997).
16. I. R. Boldogh *et al.*, *Mol. Biol. Cell* **14**, 4618 (2003).
17. M. J. Youngman *et al.*, *J. Cell Biol.* **164**, 677 (2004).
18. S. J. McConnell, L. C. Stewart, A. Talin, M. P. Yaffe, *J. Cell Biol.* **111**, 967 (1990).
19. C. Meisinger *et al.*, *EMBO J.* **26**, 2229 (2007).
20. N. Kondo-Okamoto, J. M. Shaw, K. Okamoto, *J. Biol. Chem.* **278**, 48997 (2003).
21. S. Kutik *et al.*, *Cell* **132**, 1011 (2008).
22. M. Schuldiner *et al.*, *Cell* **123**, 507 (2005).
23. C. Osman *et al.*, *J. Cell Biol.* **184**, 583 (2009).
24. X. Wang, T. L. Schwarz, *Cell* **136**, 163 (2009).
25. R. L. Frederick *et al.*, *J. Cell Biol.* **167**, 87 (2004).
26. V. M. Gohil, M. N. Thompson, M. L. Greenberg, *J. Biol. Chem.* **280**, 35410 (2005).
27. S. C. Chang *et al.*, *J. Biol. Chem.* **273**, 14933 (1998).
28. R. Birner, M. Bürgermeister, R. Schneiter, G. Daum, *Mol. Biol. Cell* **12**, 997 (2001).
29. P. J. Trotter, D. R. Voelker, *J. Biol. Chem.* **270**, 6062 (1995).
30. I. Lee, W. Hong, *FASEB J.* **20**, 202 (2006).
31. S. Ghaemmaghami *et al.*, *Nature* **425**, 737 (2003).

32. S. Meeusen, J. Nunnari, *J. Cell Biol.* **163**, 503 (2003).
33. We thank all members of the Walter lab for their support; N. Krogan, S. Wang, and N. Bajwa for their work creating the genetic interaction maps; and J. Shaw and K. Okamoto for their kind gift of plasmids and discussions. This work was supported by NIH. B.K. is a fellow of the Swiss National Science Foundation; M.S. is supported by a Human Frontiers Science Program Career Development Award; and P.W and J.S.W. are investigators at the Howard Hughes Medical Institute.

Supporting Online Material

www.sciencemag.org/cgi/content/full/1175088/DC1
Materials and Methods
Figs. S1 to S8
Tables S1 and S2
References
Database S1

17 April 2009; accepted 8 June 2009
Published online 25 June 2009;
10.1126/science.1175088
Include this information when citing this paper.

Pathogenesis and Transmission of Swine-Origin 2009 A(H1N1) Influenza Virus in Ferrets

Vincent J. Munster,[1]* Emmie de Wit,[1]* Judith M. A. van den Brand,[1] Sander Herfst,[1] Eefje J. A. Schrauwen,[1] Theo M. Bestebroer,[1] David van de Vijver,[1] Charles A. Boucher,[1] Marion Koopmans,[1,2] Guus F. Rimmelzwaan,[1] Thijs Kuiken,[1] Albert D. M. E. Osterhaus,[1] Ron A. M. Fouchier[1]†

The swine-origin A(H1N1) influenza virus that has emerged in humans in early 2009 has raised concerns about pandemic developments. In a ferret pathogenesis and transmission model, the 2009 A(H1N1) influenza virus was found to be more pathogenic than a seasonal A(H1N1) virus, with more extensive virus replication occurring in the respiratory tract. Replication of seasonal A(H1N1) virus was confined to the nasal cavity of ferrets, but the 2009 A(H1N1) influenza virus also replicated in the trachea, bronchi, and bronchioles. Virus shedding was more abundant from the upper respiratory tract for 2009 A(H1N1) influenza virus as compared with seasonal virus, and transmission via aerosol or respiratory droplets was equally efficient. These data suggest that the 2009 A(H1N1) influenza virus has the ability to persist in the human population, potentially with more severe clinical consequences.

In April 2009, swine-origin 2009 A(H1N1) influenza virus [2009 A(H1N1) influenza virus] was recognized as the causative agent of influenza-like illnesses in humans in North America (*1*–*3*). Since then, 76 countries have officially reported 35,928 cases of 2009 A(H1N1) influenza virus infection, including 163 deaths (*4*). The 2009 A(H1N1) influenza virus contains a previously unseen combination of gene segments from the North American and Eurasian swine influenza virus lineages (*1*, *5*). The virus has apparently circulated in the swine population without detection and recently crossed the species barrier into humans. The most recent common ancestor of the human 2009 A(H1N1) influenza viruses was estimated to have emerged between November 2008 and March 2009. One of the unusual characteristics of the 2009 A(H1N1) influenza virus as compared with other recent zoonotic influenza viruses is sustained human-to-human transmission, with basic reproduction ratio (R_0) estimates in the range of 1.2 to 1.6, which is higher than that reported for seasonal human influenza A viruses (*1*). In response to the available information on sustained human-to-human transmission in multiple parts of the world, the World Health Organization (WHO) raised the level of influenza pandemic alert to phase 6 on 11 June 2009 (*6*).

Currently available data indicate that the majority of laboratory-confirmed infections with the 2009 A(H1N1) influenza virus result in a self-limiting, uncomplicated influenza (*2*, *3*, *7*). Typical clinical symptoms include fever, rhinorrhea, cough, and sore throat, which are indistinguishable from the symptoms observed for seasonal A(H1N1) and A/H3N2 influenza virus infections. However, in addition to uncomplicated influenza, a variety of clinical symptoms unusual for seasonal influenza have been described, including vomiting and diarrhea in a relatively large proportion of cases. Moreover, some patients have required hospitalization because of severe pneumonia and respiratory failure, with a fatal outcome occurring in 0.5% of laboratory-confirmed cases. In contrast to seasonal influenza, a substantial proportion of the cases of severe illness and death have occurred among young and previously healthy adults. Severe illness and deaths have also been noted relatively frequently in adults with underlying disease and in pregnant women (*2*, *3*, *7*).

The distinct antigenic properties of the 2009 A(H1N1) influenza virus as compared with seasonal A(H1N1) virus suggests that population humoral immunity against pandemic 2009 A(H1N1) influenza virus is limited (*5*), although the age distribution of reported cases suggests some degree of protection in older age groups (*1*–*3*).

We used a ferret (*Mustela putorius furo*) model to study clinical signs, virus shedding, tissue distribution, pathology, and aerosol transmission

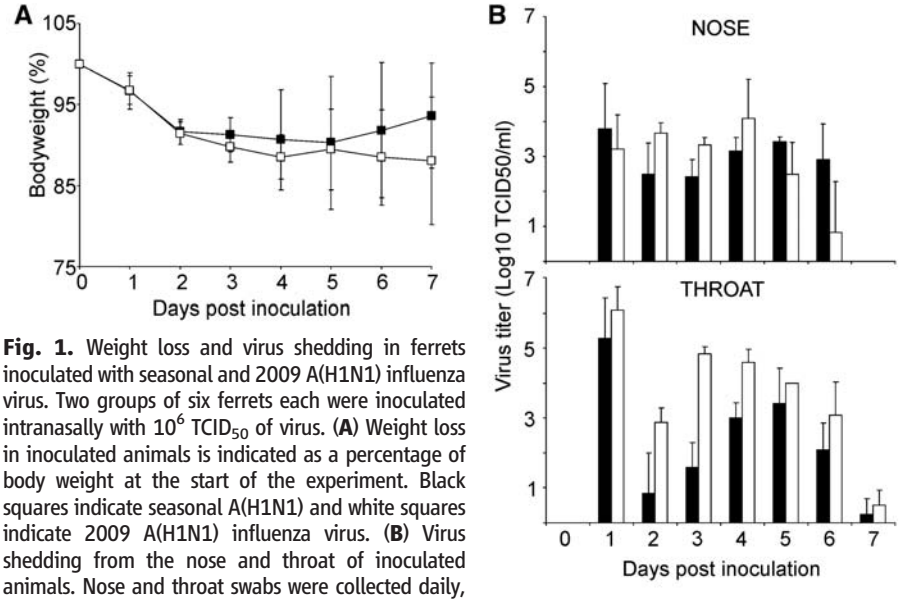

Fig. 1. Weight loss and virus shedding in ferrets inoculated with seasonal and 2009 A(H1N1) influenza virus. Two groups of six ferrets each were inoculated intranasally with 10^6 $TCID_{50}$ of virus. (**A**) Weight loss in inoculated animals is indicated as a percentage of body weight at the start of the experiment. Black squares indicate seasonal A(H1N1) and white squares indicate 2009 A(H1N1) influenza virus. (**B**) Virus shedding from the nose and throat of inoculated animals. Nose and throat swabs were collected daily, and virus titers in the swabs were determined by means of end-point titration in MDCK cells. Geometric mean titers are displayed; error bars indicate SD. Black bars indicate seasonal A(H1N1) and white bars indicate 2009 A(H1N1) influenza virus.

[1]National Influenza Center and Department of Virology, Erasmus Medical Center, 3015GE Rotterdam, Netherlands. [2]National Institute for Public Health and the Environment, 3720BA Bilthoven, Netherlands.

*These authors contributed equally to this work.
†To whom correspondence should be addressed. E-mail: r.fouchier@erasmusmc.nl

of the pandemic 2009 A(H1N1) influenza virus as compared with a seasonal 2007 A(H1N1) virus. Ferrets are a suitable animal model for influenza A virus infections in humans because they are susceptible to natural infection and develop respiratory disease and lung pathology similar to humans when suffering from seasonal, avian, or pandemic influenza virus infections (*8*). Patterns of influenza virus attachment to cells in the trachea and lower respiratory tract are similar in ferrets and humans (*9*). The ferret model has also been used successfully for studies on virus transmission via direct contact and aerosols or respiratory droplets (*10*). Influenza virus A/Netherlands/602/2009 was isolated from the first case of laboratory-confirmed 2009 A(H1N1) influenza virus infection in the Netherlands. The patient was a 3-year-old child that traveled with the family from Mexico to the Netherlands and developed fever (>39.5°C) and respiratory symptoms upon return (*11*). The patient was treated with oseltamivir and recovered uneventfully. A nasopharyngeal swab was collected before the start of treatment, and the virus was isolated in 11-day-old embryonated chicken eggs then passaged once in Madin-Darby canine kidney (MDCK) cells. The virus differs in eight amino acid positions from influenza virus A/California/4/2009 (*12*). Seasonal influenza virus A/Netherlands/26/2007 was isolated in MDCK cells from a patient infected during the 2006–2007 influenza season.

Two groups of six female ferrets each were inoculated intranasally with 10^6 50% tissue culture infectious dose ($TCID_{50}$) of virus. The animals were observed for clinical signs and weighed daily as an indicator of disease. Both viruses caused lethargy, sneezing, ruffled fur, decreased interest in food, and nasal discharge in the ferrets. The mean maximum weight loss was 10% for animals inoculated with the seasonal influenza virus and 12% for the 2009 A(H1N1) influenza virus–inoculated animals (Fig. 1A and fig. S1). Four days after inoculation onwards, the clinical condition of the animals infected with the seasonal influenza virus improved. In contrast, the recovery of the ferrets infected with the 2009 A(H1N1) influenza virus was delayed by ~2 days.

Nose and throat swabs were collected from inoculated animals daily, and virus titers were determined by means of end-point titration in MDCK cells. Virus shedding was observed to start at 1 day after inoculation for both viruses, with throat swabs generally containing higher virus titers than did nose swabs. Infectious virus shedding continued until 6 days after inoculation for the nose swabs and 7 days after inoculation for the throat swabs. On 2 and 3 days after inoculation, virus titers in both throat and nose swabs were significantly higher from animals inoculated with 2009 A(H1N1) influenza virus than from animals inoculated with seasonal influenza virus (Mann-Whitney test; 2 days after inoculation, nose $P = 0.034$, throat $P = 0.022$; 3 days after inoculation, nose $P = 0.005$, throat $P = 0.004$). The total virus shedding from the throat within the 7 days of the experiment (Fig. 1B) in animals inoculated with 2009 A(H1N1) influenza virus was ~1.5-fold higher as compared with shedding in animals inoculated with seasonal influenza virus (Mann Whitney test, $P = 0.004$). Virus shedding from the nose was comparable for both viruses (Fig. 1B).

At 3 and 7 days after inoculation, three animals from each group were euthanized and used for pathological and virological examination of the nasal turbinates, trachea, lungs, liver, spleen, kidney, and brain. At 3 days after inoculation, gross examination of the lungs revealed focal to multifocal mild consolidation in all ferrets from both groups. Upon gross examination of the lungs at 7 days after inoculation, 10, 20, and 40% of the lungs were affected in animals inoculated with seasonal influenza virus as compared with 20, 40, and 70% in animals inoculated with 2009 A(H1N1) influenza virus. Gross examination of the liver, spleen, kidney, and brain did not reveal lesions in the two ferret groups.

Parts of the nasal turbinates, trachea, lungs, liver, spleen, kidney, and brain were homogenized, and virus titers were determined by means of end-point titration in MDCK cells. Both the seasonal and 2009 A(H1N1) influenza viruses were detected in the nasal turbinates of inoculated ferrets at 3 days after inoculation, with 2009 A(H1N1) influenza virus yielding slightly higher virus titers ($10^{6.9}$ versus $10^{6.3}$ $TCID_{50}$/gram tissue and 95% confidence intervals of 6.34 to 7.47 and 5.63 to 7.04, respectively) (Table 1). The 2009 A(H1N1) influenza virus was also detected in the trachea and lungs ($10^{5.2}$ and $10^{4.6}$ $TCID_{50}$/gram tissue, respectively)

Table 1. Virus titers in the respiratory tract tissues of ferrets inoculated with seasonal and 2009 A(H1N1) influenza viruses. Three ferrets were euthanized at 3 and 7 days after inoculation. Virus titers in nasal turbinates, trachea, and lung were determined by means of end-point titration in MDCK cells. No virus was detected in liver, spleen, kidney, and brain tissue for either virus and were thus not included in the table. Geometric mean titer ± SD is indicated. ND, not detected. Cut-off value for trachea and lungs was <2 and <1.5 Log10 $TCID_{50}$/gram tissue, respectively.

Tissue	Virus titer (log10 $TCID_{50}$/gram tissue)			
	Day 3 after inoculation		Day 7 after inoculation	
	Seasonal A(H1N1)	2009 A(H1N1)	Seasonal A(H1N1)	2009 A(H1N1)
Nasal turbinates	6.3 (±0.6)	6.9 (±0.5)	4.6 (±1.2)	3.2 (±1.4)
Trachea	ND	5.2 (±1.3)	ND	ND
Lung	ND	4.6 (±1.5)	ND	ND

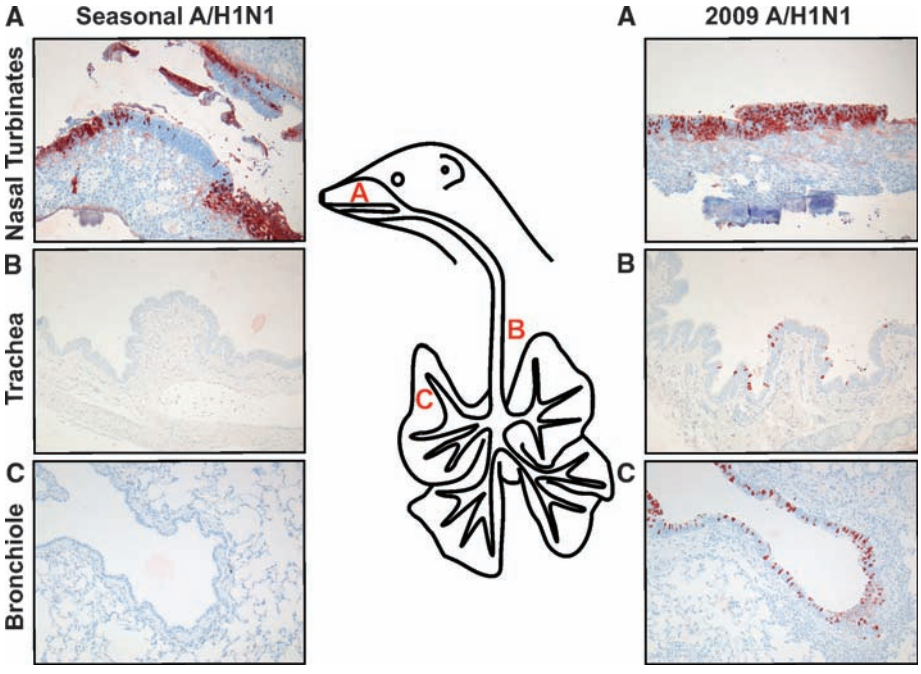

Fig. 2. Immunohistochemical analysis of respiratory tract tissues of ferrets inoculated with seasonal or 2009 A(H1N1) influenza virus, collected at 3 days after inoculation. Tissue sections of the nasal turbinates (**A**), trachea (**B**), and bronchi (**C**) were stained with a monoclonal antibody against influenza A virus nucleoprotein, which is visible as a red-brown staining. In animals inoculated with seasonal influenza virus, only cells in the nasal turbinates stained positive for nucleoprotein, whereas in animals inoculated with 2009 A(H1N1) influenza virus, cells in the nasal turbinates, trachea, and bronchi stained positive. See fig. S2 for data taken at 7 days after inoculation.

Table 2. Transmission of seasonal and 2009 A(H1N1) influenza virus via aerosol or respiratory droplets. Four ferrets each were inoculated intranasally with 10^6 $TCID_{50}$ of virus and placed in transmission cages. At 1 day after inoculation, one naïve ferret was added to each transmission cage. The transmission cages prevent direct contact of ferrets but allow airflow. Ferrets were observed daily for signs of disease, including sneezing. Nose and throat swabs were collected on 0, 1, 2, 3, 5, 7, and 9 days after inoculation (or days after exposure) to determine virus shedding by the inoculated animal and the contact ferret. Infection was confirmed with seroconversion in all inoculated and contact ferrets.

Virus	Infected ferrets			Aerosol contacts		
	Sneezing	Virus shedding	Onset of shedding (days after inoculation)*	Sneezing	Virus shedding	Onset of shedding (days after exposure)*
Seasonal A(H1N1)	4/4	4/4	1	3/4	4/4†	1,2
2009 A(H1N1)	4/4	4/4	1,2	4/4	4/4	1,2

*Virus titers in nose and throat swabs are shown in fig. S4. †One of four aerosol contacts was positive as detected by means of reverse transcription polymerase chain reaction but not virus isolation.

of inoculated ferrets, whereas the seasonal influenza virus was not. At 7 days after inoculation, both viruses were detected at relatively low titers in the nasal turbinates and not detected in other parts of the respiratory tract. The 2009 A(H1N1) influenza virus was cleared from the lungs and trachea by this time. No virus was detected in the liver, spleen, kidney, or brain of animals inoculated with either virus at 3 or 7 days after inoculation.

Histopathological analyses revealed that ferrets inoculated with the 2009 A(H1N1) influenza virus had a multifocal mild or moderate necrotizing rhinitis, tracheitis, bronchitis, and bronchiolitis, whereas the ferrets inoculated with seasonal influenza virus displayed only multifocal moderate necrotizing rhinitis. We performed immunohistochemistry in order to assess the presence of influenza A virus–infected cells in respiratory tissues obtained at 3 days after inoculation (Fig. 2). Infected cells were associated with superficial necrosis and inflammation. In ferrets inoculated with the 2009 A(H1N1) influenza virus, many infected cells were detected in the nasal cavity, trachea, bronchus, and bronchioles and rarely in the alveoli. In contrast, detection of virus-infected cells was limited to the nasal turbinates in ferrets inoculated with seasonal influenza virus. At 7 days after inoculation, most of the virus-infected cells were cleared from the respiratory tract of the animals in both groups, as determined with immunohistochemistry (fig. S2).

Transmission of the 2009 A(H1N1) and seasonal influenza viruses via aerosol or respiratory droplets was tested in ferrets. We conducted transmission experiments in cages designed to prevent direct contact between animals but allow airflow from an inoculated ferret to a neighboring naïve ferret (fig. S3). Four ferrets were inoculated, and each animal was housed individually with a naïve ferret in a transmission cage so as to test the transmission of both virus isolates. Inoculated ferrets started to shed virus from the nose and throat at 1 or 2 days after inoculation, with virus titers up to 10^6 $TCID_{50}$/ml (fig. S4). Both viruses were transmitted from the inoculated to naïve ferrets in four out of four transmission experiments (Table 2). Transmission was detected within the first 2 days after placing the naïve ferret in the cage adjacent to the inoculated ferret. Peak virus shedding in the naïve and inoculated ferrets was comparable in the 2009 A(H1N1) and seasonal influenza virus groups (fig. S4).

Our results indicated that the 2009 A(H1N1) influenza virus replicates efficiently in the upper and lower respiratory tract of ferrets, is associated with mild or moderate clinical signs and pathological changes, and is transmitted efficiently between ferrets via aerosols or respiratory droplets. These results are in agreement with observations in humans, in which generally mild disease but relatively efficient human-to-human transmission has been observed (*1*–*3*, *5*). Compared with other zoonotic influenza viruses such as highly pathogenic avian influenza viruses of the H5 and H7 subtypes and the 1918 Spanish H1N1 influenza virus, which are often fatal in ferret models (*13*–*17*), the 2009 A(H1N1) influenza virus is a relatively mild pathogen that did not replicate in the alveoli or tissues beyond the respiratory tract and did not cause any mortality in our ferret model. The 2009 A(H1N1) influenza virus may be a relatively mild pathogen in humans, but our data indicated that it is more pathogenic than seasonal influenza A(H1N1) virus in ferrets, with wider distribution of virus replication and associated lesions in the respiratory tract.

The 2009 A(H1N1) influenza virus used here was isolated from a mild case of disease. It is possible that other viruses could emerge that are intrinsically more pathogenic because of mutations in one or more of the viral gene segments. The ferret models described here will be useful to monitor such adaptive changes that affect pathogenicity or transmission of the circulating 2009 A(H1N1) influenza viruses.

Because the 2009 A(H1N1) influenza virus shares the predominant site of virus replication—the upper respiratory tract—with seasonal A(H1N1) and A/H3N2 influenza viruses in the ferret model, and displays comparable receptor-binding properties (fig. S6), the possibility of reassortment of 2009 A(H1N1) influenza virus with seasonal influenza viruses in humans is a serious concern (*18*, *19*). Because 2009 A(H1N1) influenza virus also replicates deeper down the airways, reassortment with A/H5N1 viruses could be an additional concern. Reassortment can facilitate the rapid emergence of viruses that are better adapted to humans (*20*) or are resistant to neuraminidase inhibitors after acquiring the N1 gene segment from the oseltamivir-resistant seasonal H1N1 viruses that have emerged recently (*21*).

The shedding and transmission data suggested that the 2009 A(H1N1) is sufficiently fit to compete with the seasonal A(H1N1) virus. Because serological cross-reactivity between 2009 A(H1N1) and seasonal H1N1 viruses was found to be negligible (*5*), and different antigenic variants of influenza B viruses have coexisted for extended periods of time (*22*), the 2009 A(H1N1) influenza virus should be considered capable of continued cocirculation in the human population with the existing seasonal influenza viruses.

References and Notes

1. C. Fraser *et al.*, *Science* **324**, 1557 (2009); published online 11 May 2009 (10.1126/science.1176062).
2. V. Shinde *et al.*, *N. Engl. J. Med.* **7**, 10.1056/NEJMoa0903812 (2009).
3. A. V. I. T. Novel Swine-Origin Influenza, *N. Engl. J. Med.* **360**, 2605 (2009).
4. WHO, www.who.int/csr/don/2009_05_29/en/index.html (2009).
5. R. J. Garten *et al.*, *Science* **22**, 10.1126/science.1176225 (2009).
6. WHO, www.who.int/csr/disease/swineflu/en (2009).
7. WHO, *Wkly. Epidemiol. Rec.* **21**, 185 (2009).
8. J. A. Maher, J. DeStefano, *Lab Anim. (NY)* **33**, 50 (2004).
9. D. van Riel *et al.*, *Am. J. Pathol.* **171**, 1215 (2007).
10. E. M. Sorrell, H. Wan, Y. Araya, H. Song, D. R. Perez, *Proc. Natl. Acad. Sci. U.S.A.* **106**, 7565 (2009).
11. ProMed, www.promedmail.org/pls/otn/f?p=2400:1202:6682247203355318::NO::F2400_P1202_CHECK_DISPLAY,F2400_P1202_PUB_MAIL_ID:X,77295 (2009).
12. Materials and methods are available as supporting material on *Science* Online.
13. T. M. Tumpey *et al.*, *Science* **315**, 655 (2007).
14. J. A. Belser *et al.*, *J. Virol.* **81**, 11139 (2007).
15. T. R. Maines *et al.*, *J. Virol.* **79**, 11788 (2005).
16. L. A. Zitzow *et al.*, *J. Virol.* **76**, 4420 (2002).
17. E. A. Govorkova *et al.*, *J. Virol.* **79**, 2191 (2005).
18. M. I. Nelson *et al.*, *PLoS Pathog.* **4**, e1000012 (2008).
19. A. Rambaut *et al.*, *Nature* **453**, 615 (2008).
20. R. B. Belshe, *N. Engl. J. Med.* **353**, 2209 (2005).
21. A. Lackenby *et al.*, *Euro Surveill.* **13**, 113 (2008).
22. K. Mizuta *et al.*, *Epidemiol. Infect.* **132**, 721 (2004).

23. We thank M. Schutten, J. Guldenmeester, G. Arron, S. Chutinimitkul, L. Leijten, P. van Run, R. Diaz-D'Ullois, and G. van Amerongen for technical assistance. V.M., E.d.W, and R.F. were financed through National Institute of Allergy and Infectious Diseases–NIH contract HHSN266200700010C.

Supporting Online Material

www.sciencemag.org/cgi/content/full/1177127/DC1
Materials and Methods
Figs. S1 to S6
References

1 June 2009; accepted 23 June 2009
Published online 2 July 2009;
10.1126/science.1177127
Include this information when citing this paper.

Transmission and Pathogenesis of Swine-Origin 2009 A(H1N1) Influenza Viruses in Ferrets and Mice

Taronna R. Maines,[1] Akila Jayaraman,[2] Jessica A. Belser,[1] Debra A. Wadford,[1] Claudia Pappas,[1] Hui Zeng,[1] Kortney M. Gustin,[1] Melissa B. Pearce,[1] Karthik Viswanathan,[2] Zachary H. Shriver,[2] Rahul Raman,[2] Nancy J. Cox,[1] Ram Sasisekharan,[2] Jacqueline M. Katz,[1] Terrence M. Tumpey[1]*

Recent reports of mild to severe influenza-like illness in humans caused by a novel swine-origin 2009 A(H1N1) influenza virus underscore the need to better understand the pathogenesis and transmission of these viruses in mammals. In this study, selected 2009 A(H1N1) influenza isolates were assessed for their ability to cause disease in mice and ferrets and compared with a contemporary seasonal H1N1 virus for their ability to transmit to naïve ferrets through respiratory droplets. In contrast to seasonal influenza H1N1 virus, 2009 A(H1N1) influenza viruses caused increased morbidity, replicated to higher titers in lung tissue, and were recovered from the intestinal tract of intranasally inoculated ferrets. The 2009 A(H1N1) influenza viruses exhibited less efficient respiratory droplet transmission in ferrets in comparison with the highly transmissible phenotype of a seasonal H1N1 virus. Transmission of the 2009 A(H1N1) influenza viruses was further corroborated by characterizing the binding specificity of the viral hemagglutinin to the sialylated glycan receptors (in the human host) by use of dose-dependent direct receptor-binding and human lung tissue–binding assays.

On 11 June 2009, the World Health Organization (WHO) raised the global pandemic alert level to phase 6, the pandemic phase, in response to the emergence and global spread of a novel influenza A(H1N1) virus that contains a previously unseen combination of genes of swine origin (*1*). Leading up to this event were reports of increased numbers of patients with influenza-like illness and associated hospitalizations and deaths in several areas of Mexico during March and April (*2*). On 15 and 17 April 2009, two unrelated cases of febrile respiratory illness in children who resided in adjacent counties in southern California were confirmed to be caused by infection with a swine-origin A(H1N1) influenza virus (*3*, *4*), hereafter referred to as 2009 A(H1N1) influenza viruses. In the period of March to 21 June 2009, there have been over 44,000 laboratory-confirmed human cases of 2009 A(H1N1) influenza virus infections reported in 85 countries on six continents (*5*). Although most confirmed cases have occurred among individuals with uncomplicated, febrile, upper respiratory tract illnesses with symptoms similar to those of seasonal influenza, there have been over 180 deaths, and approximately 40% of infected individuals have experienced symptoms that include gastrointestinal distress and vomiting, which is higher than that reported for seasonal influenza (*6*). The current case fatality rate of this global outbreak is uncertain, as is the total number of persons infected with the 2009 A(H1N1) influenza virus (*7*).

The factors that lead to the generation of pandemic viruses are complex and poorly understood; however, the ability of a novel influenza virus to cause substantial illness and transmit through the air are critical properties of pandemic influenza strains (*8*–*10*). Thus, knowing the inherent virulence and transmissibility of the 2009 A(H1N1) influenza viruses, relative to seasonal influenza viruses, is important for executing appropriate public health responses.

We have therefore characterized the pathogenesis and transmissibility of three 2009 A(H1N1) influenza viruses (isolated from nasopharyngeal swabs) in the ferret (*Mustela putorius furo*) model, which appears to recapitulate not only human disease severity but also efficient transmission of seasonal (H1N1 and H3N2) influenza viruses and the poor transmission of avian (H5 and H7) influenza viruses (*11*–*14*). A/California/04/2009 (CA/04) virus was isolated from a pediatric patient with uncomplicated, upper respiratory tract illness; A/Mexico/4482/2009 (MX/4482) virus was isolated from a 29-year-old female patient with severe respiratory disease; and Texas/15/2009 (TX/15) virus was isolated from a pediatric patient with fatal respiratory illness. The three 2009 A(H1N1) influenza viruses were compared with a representative seasonal H1N1 virus, A/Brisbane/59/2007 (Brisbane/07; H1N1) (*14*). To date, 2009 A(H1N1) influenza viruses exhibit high genome-sequence identity (99.9%) and lack previously identified molecular markers of influenza A virus virulence or transmissibility (*1*). Alignments of the deduced amino acid sequences between the three viruses that we studied revealed a few differences. These were observed in the hemagglutinin (HA), neuraminidase (NA), polymerase (PA), nucleoprotein (NP), and nonstructural proteins NS1 and NS2 (table S1). Viruses were propagated in Madin-Darby canine kidney (MDCK) cells or embryonated hens' eggs (*15*).

For respiratory droplet–transmission experiments, three ferrets were inoculated intranasally with 10^6 plaque-forming units (PFU) of virus (*15*). Approximately 24 hours later, inoculated-contact animal pairs were established by placing a naïve ferret in each of three adjacent cages with perforated side walls, allowing the exchange of respiratory droplets without direct or indirect contact (*11*). Direct-contact transmission experiments were performed similarly, except that naïve ferrets were

[1]Influenza Division, National Center for Immunization and Respiratory Diseases, Centers for Disease Control and Prevention, Atlanta, GA 30333, USA. [2]Harvard–Massachusetts Institute of Technology (MIT) Division of Health Sciences and Technology and Koch Institute for Integrative Cancer Research, Department of Biological Engineering, MIT, E25-519, Cambridge, MA 02139, USA.

*To whom correspondence should be addressed. E-mail: tft9@cdc.gov

Table 1. Replication and transmission of 2009 A(H1N1) influenza viruses and a seasonal H1N1 virus in ferrets.

Virus	Inoculated animals					DC contact animals*		RD contact animals*	
	Clinical signs			Virus detection					
	Weight loss (%)†	Sneezing‡	Lethality§	Lung (peak titer)‖	Intestinal tract¶	Virus detection	Seroconversion#	Virus detection	Seroconversion#
CA/04	6/6 (10.3)	2/6	0/6	3/3 (5.8)	5/9 (2.3)	3/3	3/3	2/3	2/3
TX/15	6/6 (9.1)	1/6	0/6	3/3 (6.0)	1/9 (1.3)	3/3	3/3	2/3	2/3
MX/4482	6/6 (17.5)	3/6	3/6	2/3 (4.1)	2/9 (2.7)	3/3**	3/3	2/3**	2/3
Brisbane/07	6/6 (4.9)	6/6	0/6	0/3	0/9	3/3	3/3	3/3	3/3

*DC, direct contact; RD, respiratory droplet. †The percentage mean maximum weight loss observed during the first 10 days after inoculation. ‡Number of animals in which sneezing was observed during the first 10 days after inoculation. §Number of animals euthanized before the end of the 14-day experimental period because of reaching a clinical end point. ‖Virus titers are expressed as mean $\log_{10}$ peak PFU/gram of tissue. ¶Virus titers in intestinal tissue or rectal swabs are expressed as the mean $\log_{10}$ peak PFU/ml or PFU/gram for the positive samples. #Hemagglutination inhibition antibody titers ranged from 640 to 1280 and were determined by use of homologous virus and serum collected at least 17 days after contact. **Virus was detected in intestinal tract as well as nasal wash for 1 of 3 DC and 2 of 3 RD contact animals.

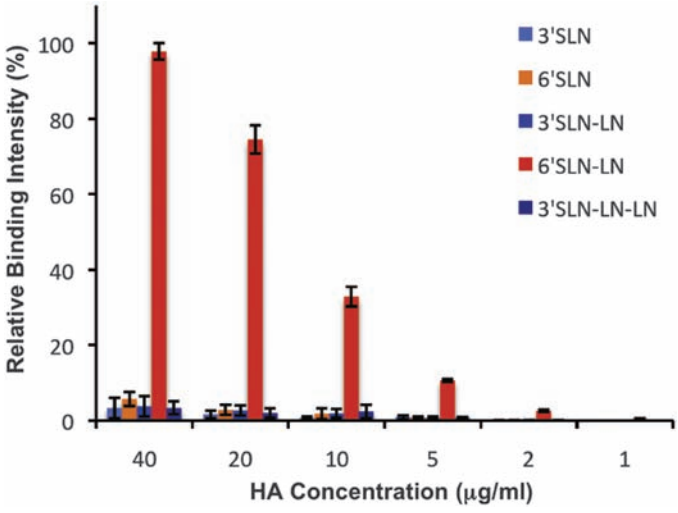

Fig. 1. Dose-dependent direct receptor-binding of CA/04 HA. A streptavidin plate array consisting of representative biotinylated α2-3– and α2-6–sialylated glycans were used for the assay. The biotinylated glycans include 3′SLN, 6′SLN, 3′SLN-LN, 6′SLN-LN, and 3′SLN-LN-LN. LN corresponds to lactosamine (Galβ1-4GlcNAc), and 3′SLN and 6′SLN correspond to Neu5Acα2-3 and Neu5Acα2-6 linked to LN, respectively. The assay was carried out as previously described (*18*) for an entire range of HA concentration from 0.01 to 40 μg/ml by precomplexing HA:primary antibody:secondary antibody in the ratio 4:2:1 in order to enhance the multivalent presentation of HA. The binding signals for HA concentrations below 1 μg/ml were at background level, and so their concentrations are not shown on the *x* axis. The *y* axis shows the normalized binding signal as a percentage of the maximum value.

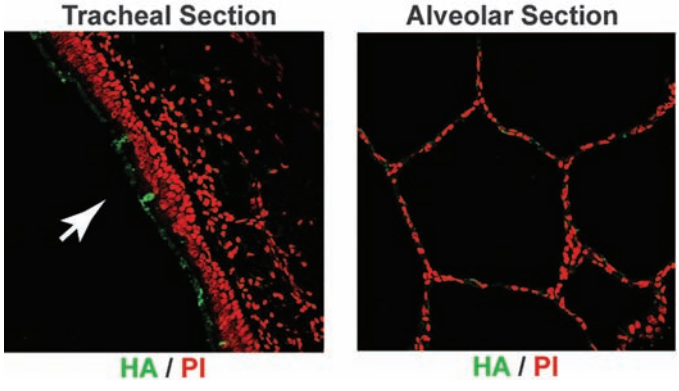

Fig. 2. Human tissue binding of CA/04 HA. Shown to the left is the binding of CA/04 HA at 20 μg/ml concentration to the apical surface (white arrow) of human tracheal tissue sections (green; propidium iodide staining is in red). The apical surface of tracheal tissue is known to predominantly express α2-6–sialylated glycans (*19*). The binding of the recombinantly expressed HA to the human tissues was carried out as previously described (*19*) by precomplexing HA:primary antibody:secondary antibody in the ratio 4:2:1 in order to enhance multivalent presentation of HA. Shown to the right is the minimal binding of HA at 20 μg/ml concentration to the alveolar tissue section. The sialic acid–specific binding of HA to the tracheal tissue section was confirmed by means of blocking HA binding to the tissue section pretreated with 0.2 U of sialidase (recombinant from *Arthrobacter ureafaciens*).

placed in the same cage as each of the inoculated ferrets, where they shared a common food and water source. Inoculated and contact animals were monitored for clinical signs over a 14-day period. Transmission was assessed by means of titration of infectious virus in nasal washes and detection of virus-specific antibodies in convalescent sera (*11*). Three additional inoculated ferrets from each virus-infected group were euthanized on day 3 after inoculation for assessment of infectious virus in tissues (*15*).

Ferrets inoculated with CA/04 virus showed no overt clinical signs but displayed mild signs of inactivity [relative inactivity index (RII) = 1.0]. TX/15 or MX/4482 virus infection resulted in more pronounced clinical features, including a slight increase in RII (1.2). Significantly greater weight loss was observed in all ferrets with the 2009 A(H1N1) influenza viruses than in those with the seasonal influenza virus, Brisbane/07 ($P < 0.05$) (Table 1). One ferret infected by means of direct-contact transmission from a TX/15-inoculated ferret was euthanized at 10 days after inoculation because of excessive weight loss, and three of six MX/4482-inoculated ferrets were euthanized before the end of the experimental period because of severe lethargy or excessive weight loss (Table 1). Ferrets inoculated with any of the 2009 A(H1N1) influenza virus isolates shed high peak mean titers of infectious virus in nasal washes as early as day 1 after inoculation ($10^{7.1–7.7}$ PFU/ml) (figs. S1 and S2) that were sustained at titers of $\geq 10^{4.4}$ PFU/ml for 5 days after inoculation. The 2009 A(H1N1) influenza virus–shedding showed kinetics similar to Brisbane/07 virus, which was also sustained for 5 days in ferrets at titers of $\geq 10^{4.7}$ PFU/ml. In contrast to Brisbane/07, the CA/04, TX/15, and MX/4482 viruses were detected in the lower respiratory tract at high titers ($10^{5.8–6.0}$ PFU/g lung tissue) and the intestinal tract. For the latter, viral titers were detected in rectal swabs or tissue samples collected throughout the intestinal tract (Table 1 and fig. S3). There was no evidence of viremia or infectious virus in the brain, kidney, liver, and spleen tissues with any of the viruses tested (fig. S3).

Table 2. Glycan-binding residues of H1N1 HAs. The residues are organized into network-forming clusters. The sugar unit (numbered as shown in Fig. 3), which makes contact with the clusters, is shown in the last row. The amino acids specific to 2009 H1N1 HAs are highlighted in red. SolIS_3_06, A/Solomon Islands/3/06; Bris_59_07, A/Brisbane/59/07; NewCal_20_99, A/New Caledonia/20/99; TX_36_91, A/Texas/36/91.

H1N1 Strains	Cluster 1									Cluster 2		Cluster 3							Cluster 4						Cluster 5				
	136	138	226	137	153	155	194	183	145	222	225	190	189	187	186	219	227	192	193	156	159	196
SolIs_3_06	S	S	Q	A	W	T	L	H	S	K	D	D	G	N	P	K	E	R	A	G	G	H
Bris_59_07	S	S	Q	A	W	T	L	H	S	K	D	D	G	N	P	K	E	K	A	G	G	H
NewCal_20_99	S	S	Q	A	W	T	L	H	S	K	D	N	G	N	P	K	E	R	A	G	G	H
TX_36_91	T	S	Q	T	W	T	I	H	S	K	D	D	R	N	S	K	E	R	A	E	G	H
SC18	T	A	Q	A	W	T	L	H	S	K	D	D	T	T	P	A	A	Q	S	K	S	Q
TX/15	T	A	Q	A	W	V	L	H	K	K	D	D	A	T	S	I	E	Q	S	K	N	Q
MX/4482	T	A	Q	A	W	V	L	H	K	K	D	D	A	T	S	I	E	Q	S	K	N	Q
CA/04	T	A	Q	A	W	V	L	H	K	K	D	D	A	T	S	I	E	Q	S	K	N	Q
	Neu5Ac-1									Gal-2		GlcNAc-3						Gal-4, Glc-5, …				

Consistent with the experimental transmission data obtained with contemporary human H1N1 and H3N2 viruses (*11*, *14*, *16*), the seasonal influenza H1N1 (Brisbane/07) virus efficiently transmitted via direct contact and respiratory droplets to all of the contact ferrets that shed virus as early as day 1 after contact (figs. S1 and S2). Direct contact transmission was observed between all animal pairs for CA/04, TX/15, and MX/4482 viruses; infectious virus was recovered from nasal washes, and seroconversion was detected in all contact animals (Table 1 and fig. S1). However, the 2009 A(H1N1) influenza viruses did not spread through respiratory droplet to every contact ferret, and transmission was delayed by 5 or more days after exposure in two of six infected ferret pairs (fig. S2). Respiratory droplet transmission of 2009 A(H1N1) influenza viruses was significantly reduced as compared with respiratory droplet transmission of the seasonal influenza virus ($P \leq 0.01$) (Table 1). Sneezing was frequently observed in Brisbane/07–inoculated ferrets but was rarely observed in the CA/04–, TX/15–, or MX/4482–inoculated ferrets during the study period, which is similar to the infrequent sneezing observed in ferrets infected with avian influenza viruses (*11*). Collectively, these findings demonstrate that 2009 A(H1N1) influenza viruses elicited elevated respiratory disease relative to seasonal H1N1 viruses in ferrets, yet despite efficient direct-contact transmission, the viruses exhibited less efficient respiratory droplet transmission as compared with that of contemporary seasonal human influenza viruses (*11*, *14*).

The binding of influenza viruses to their target cells is mediated by viral HA, and binding preference to specific sialylated glycan receptors is a critical determinant of H1N1 virus transmission efficiency in ferrets (*14*, *17*, *18*). We examined the glycan-binding properties of the 2009 A(H1N1) HA by means of dose-dependent direct receptor-binding (*18*) and human lung tissue–binding assays using recombinantly expressed soluble CA/04 HA (*19*). In the direct glycan receptor–binding assay, CA/04 HA exhibited a dose-dependent binding to only a single α2-6 glycan (6′SLN-LN) and only minimal binding to α2-3 glycans (Fig. 1). Although the binding pattern of CA/04 HA is similar to that of HA from the 1918 pandemic influenza A virus [A/South Carolina/1/1918 (SC18)], the binding affinity of CA/04 HA is considerably lower than that of SC18 HA (figs. S4 and S5). Examining the tissue binding of CA/04 HA indicates that it binds uniformly to the apical surface of the human tracheal (representative upper respiratory) tissue sections (Fig. 2). This binding pattern correlates with the predominant distribution of α2-6 sialylated glycans on the apical surface of the tracheal tissue (*19*) and the α2-6 binding of CA/04 HA in the direct binding assay. Although CA/04 shows some binding to alveolus, it is not as extensive as the tracheal binding that is consistent with the minimal α2-3 binding observed in the direct binding assay.

The receptor-binding site (RBS) of the 2009 A (H1N1) HAs (*20*), used in this study, were compared with those from SC18 and the recent seasonal influenza H1N1 viruses (Table 2). The similarity in the binding pattern between CA/04 HA and SC18 HA could potentially arise from the majority of the "similar or analogous" RBS residues between these HAs, including Asp190 and Asp225, which are "hallmark" amino acids of human-adapted H1N1 HAs that make optimal contacts with the α2-6 glycans. The main differences in RBS between SC18 and CA/04 HA are at positions 145, 186, 189, 219, and 227. The CA/04 HA has a Lys145 that provides an additional anchoring contact for the sialic acid (*20*). The residues at 186, 187, and 189 are positioned to form an interaction network with Asp190 (*18*, *20*). In the case of SC18 HA, this network involves oxygen atoms of Thr187, Thr189, and Asp190 (*18*). In a similar fashion, in the case of CA/04 HA this network could potentially be formed by the oxygen atoms of Ser186, Thr187, and Asp190. The residues 219 and 227 in turn influence the orientation of residue 186. Comparison of residues 219 and 227 (Table 2) reveals that either both amino acids are hydrophobic, such as Ala219 and Ala227 (as observed in SC18 HA), or they are charged residues, such as Lys219 and Glu227 (as observed in the seasonal influenza HAs). The 2009 A(H1N1) HAs have a combination of Ile219 and Glu227 that results in a set of interactions that is neither fully hydrophobic nor fully charged. This combination could destabilize the hydrophobic or ionic network of residues at 186, 219, and 227, disrupting optimal contacts with the α2-6 sialylated glycans (Fig. 3). Analysis of the RBS of the 2009 A(H1N1) HA offers an explanation for the lower α2-6–binding affinity of CA/04 HA as compared with that of SC18 HA, despite the similar binding pattern (fig. S4). Taken together, the differences in the glycan-binding property of the 2009 A(H1N1) HA when compared with that of SC18 and the recent seasonal influenza HAs correlate with the observed differences in the respiratory droplet transmission in ferrets.

To evaluate the pathogenicity of the novel H1N1 viruses in another mammalian species, we inoculated BALB/c mice intranasally with three 2009 A(H1N1) influenza virus isolates and then determined virus replication, morbidity (as measured by weight loss), 50% mouse infectious dose (MID_{50}), and 50% lethal dose (LD_{50}) titers. In addition to CA/04 and TX/15, A/Mexico/4108/2009 (Mx/4108; H1N1) virus, obtained from a hospitalized case of nonfatal infection, was included in the mouse pathotyping experiments. The 2009 A(H1N1) influenza viruses isolates did not kill mice [$LD_{50} > 10^6$ PFU or 50% egg infection dose (EID_{50})], which displayed only transient weight reduction (Table 3); however, all three 2009 A(H1N1) influenza viruses replicated efficiently in mouse lungs without prior host adaptation (Table 3). Typically, human influenza

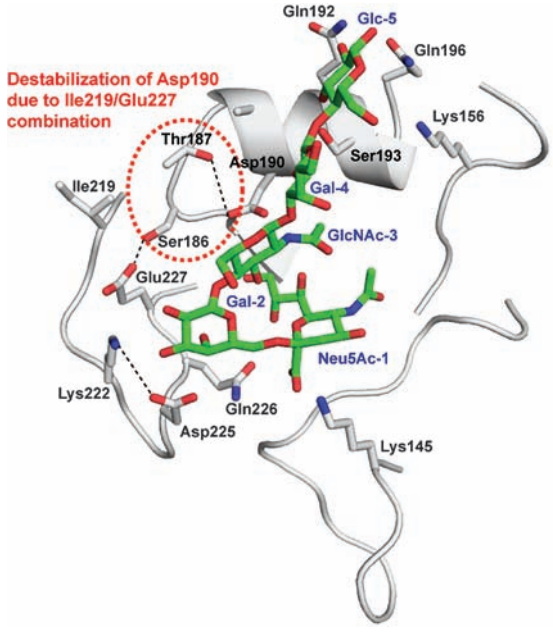

Fig. 3. Structural model of CA/04 HA bound to α2-6 oligosaccharide. The contacts of CA/04 HA with an α2-6 oligosaccharide (Neu5Acα2-6Galβ1-4GlcNAcβ1-3Galβ1-4Glc) were analyzed through the construction of a structural model as previously described (*20*). Shown in the figure is the illustrated representation of the glycan-binding site of CA/04 HA; the side chains of the key amino acids are shown in stick representation (carbon, gray; oxygen, red; nitrogen, blue). The α2-6 oligosaccharide is shown as a stick representation (carbon, green; oxygen, red; nitrogen, blue) and labeled blue starting from the nonreducing end Neu5Ac-1 to the reducing end Glc-5. The potential destabilization of the interaction network due to the Ile219/Glu227 combination is highlighted in the red dotted circle.

Table 3. Pathogenicity of 2009 A(H1N1) influenza viruses in BALB/c mice.

Virus	PFU/ml*	Weight loss†	Lung titers‡	MID_{50}§	LD_{50}§
CA/04	7.4	5.3	5.8 ± 1.2	1.5	>6
TX/15	7.7	1.5	5.4 ± 0.9	0.5	>6
MX/4108	7.8	3.5	6.8 ± 0.4	1.5	>6

*Titer of virus stocks prepared on MDCK cells or eggs expressed as $\log_{10}$ PFU/ml. †Maximum percent weight loss (5 mice per group) after inoculation with 10^5 PFU or EID_{50}. ‡Average lung titers of three mice on day 3 after inoculation, expressed as PFU/ml ± SD. § MID_{50} and LD_{50} are expressed as the $\log_{10}$ PFU or EID_{50} required to give one MID_{50} or one LD_{50}.

A strains of the H1N1 subtype replicate efficiently in mice only after they are adapted to growth in these animals (*21*). The MID_{50} titers, determined through the detection of virus in the lungs of mice 3 days after inoculation, were markedly low (MID_{50} = $10^{0.5–1.5}$ PFU or EID_{50}), indicating high infectivity in this model. We next determined whether 2009 A(H1N1) influenza viruses replicated systemically in the mouse after intranasal infection, a characteristic of virulent avian influenza (H5N1) viruses isolated from humans but not of 1918 (H1N1) virus (*17*, *22*). All mice infected with CA/04, TX/15, or MX/4108 viruses had undetectable levels (<10 PFU/ml) of virus in whole spleen, thymus, brain, and intestinal tissues, indicating that the 2009 A(H1N1) influenza viruses did not spread to extrapulmonary organs in the mouse.

The full clinical spectrum of disease caused by 2009 A(H1N1) influenza viruses and its transmissibility are not completely understood. The present study shows that overall morbidity and lung viral titers were higher in ferrets infected with 2009 A(H1N1) influenza virus isolates as compared with those infected with the seasonal H1N1 virus. Moreover, the detection of 2009 A(H1N1) influenza viruses in the intestinal tissue of ferrets is consistent with gastrointestinal involvement among some human 2009 A(H1N1) cases (*6*). Although the 2009 A(H1N1) influenza viruses demonstrated similar replication kinetics as the seasonal H1N1 virus in the upper respiratory tract of inoculated ferrets, the 2009 A(H1N1) influenza viruses did not spread to all naïve ferrets by means of respiratory droplets. This lack of efficient respiratory droplet transmission suggests that additional virus adaptation in mammals may be required to reach the high-transmissible phenotypes observed with seasonal H1N1 or the 1918 pandemic virus (*14*, *17*).

It was demonstrated previously (*17*) that the efficiency of respiratory droplet transmission in ferrets correlates with the α2-6–binding affinity of the viral HA. In fact, a single amino acid mutation in HA of the efficiently transmitting SC18 virus led to a virus (NY18) that transmitted inefficiently (fig. S5). The α2-6–binding affinity of NY18 HA was substantially lower than that of SC18 HA (fig. S5). In a similar fashion, the substantially lower α2-6–binding affinity of CA/04 HA than that of SC18 HA correlates with the less efficient 2009 A(H1N1) influenza virus respiratory droplet transmission (fig. S5).

Adaptation of the polymerase basic protein 2 (PB2) is also critical for efficient aerosolized respiratory transmission of an H1N1 influenza virus (*14*, *17*, *23*). A single amino acid substitution from glutamic acid to lysine at amino acid position 627 supports efficient influenza virus replication at the lower temperature (33°C) found in the mammalian airway and contributes to efficient transmission in mammals (*14*, *23*). All three of the 20th-century influenza pandemics were caused by viruses containing human adapted PB2 genes, and in general lysine is present at position 627 among the human influenza viruses, whereas a glutamic acid is found in this position among the avian influenza isolates that fail to transmit efficiently among ferrets (*14*). In contrast to the Brisbane/07 virus and other seasonal H1N1 viruses, all 2009 A(H1N1) influenza viruses to date with an avian influenza lineage PB2 gene possess a glutamic acid at residue 627 (*1*). The phenotype of PB2 is determined by the amino acid at position 627, which can arise by mutant selection or reassortment, and along with adaptive changes in the RBS should be closely monitored as markers for enhanced virus transmission.

References and Notes

1. R. J. Garten *et al.*, *Science* **325**, 5937 (2009); published online 22 May 2009 (10.1126/science.1176225).
2. *MMWR Morb. Mortal. Wkly. Rep.* **58**, 453 (2009).
3. *MMWR Morb. Mortal. Wkly. Rep.* **58**, 400 (2009).
4. *MMWR Morb. Mortal. Wkly. Rep.* **58**, 467 (2009).
5. http://www.who.int/en/
6. F. S. Dawood *et al.*, *J. Med.* **360**, 2605 (2009).
7. C. Fraser *et al.*, *Science* **324**, 1557 (2009); published online 11 May 2009 (10.1126/science.1176062).
8. T. M. Tumpey, J. A. Belser, *Annu. Rev. Microbiol.* **63**, 252 (2009).
9. R. J. Webby, R. G. Webster, *Science* **302**, 1519 (2003).
10. C. Viboud *et al.*, *Vaccine* **24**, 6701 (2006).
11. T. R. Maines *et al.*, *Proc. Natl. Acad. Sci. U.S.A.* **103**, 12121 (2006).
12. J. A. Belser *et al.*, *Proc. Natl. Acad. Sci. U.S.A.* **105**, 7558 (2008).
13. A. C. Lowen, P. Palese, *Infect. Disord. Drug Targets* **7**, 318 (2007).
14. N. Van Hoeven *et al.*, *Proc. Natl. Acad. Sci. U.S.A.* **106**, 3366 (2009).
15. Materials and methods are available as supporting material on *Science* Online.
16. H. L. Yen *et al.*, *J. Virol.* **81**, 6890 (2007).
17. T. M. Tumpey *et al.*, *Science* **315**, 655 (2007).
18. A. Srinivasan *et al.*, *Proc. Natl. Acad. Sci. U.S.A.* **105**, 2800 (2008).
19. A. Chandrasekaran *et al.*, *Nat. Biotechnol.* **26**, 107 (2008).
20. V. Soundararajan *et al.*, *Nat. Biotechnol.* **27**, 510 (2009).
21. C. A. Hartley, P. C. Reading, A. C. Ward, E. M. Anders, *Arch. Virol.* **142**, 75 (1997).
22. T. R. Maines *et al.*, *J. Virol.* **79**, 11788 (2005).
23. J. Steel, A. C. Lowen, S. Mubareka, P. Palese, *PLoS Pathog.* **5**, e1000252 (2009).

24. We thank P. Blair (Naval Health Research Center, San Diego), G. J. Demmler (Texas Children's Hospital, Houston), C. Alpuche-Aranda [Instituto de Diagnóstico y Referencia Epidemiológicos, Mexico], and the WHO Collaborating Centre for Reference and Research on Influenza (Melbourne) for facilitating access to viruses. We also thank X. Lu and A. Balish for preparation of viruses and V. Veguilla for statistical analysis. R.S. acknowledges the consortium for functional glycomics for providing glycan standards and support from the Singapore-MIT Alliance for Research and Technology and the National Institute of General Medical Sciences of the NIH (GM 57073 andU54 GM62116). Confocal microscopy of the human lung tissue sections was performed at the W. M. Keck Foundation Biological Imaging Facility at the Whitehead Institute. The findings and conclusions in this report are those of the authors and do not necessarily reflect the views of the funding agency.

Supporting Online Material

www.sciencemag.org/cgi/content/full/1177238/DC1
Materials and Methods
Figs. S1 to S5
Table S1
References

3 June 2009; accepted 23 June 2009
Published online 2 July 2009;
10.1126/science.1177238
Include this information when citing this paper.

Chlamydomonas Swims with Two "Gears" in a Eukaryotic Version of Run-and-Tumble Locomotion

Marco Polin,[1] Idan Tuval,[1] Knut Drescher,[1] J. P. Gollub,[1,2] Raymond E. Goldstein[1]*

The coordination of eukaryotic flagella is essential for many of the most basic processes of life (motility, sensing, and development), yet its emergence and regulation and its connection to locomotion are poorly understood. Previous studies show that the unicellular alga *Chlamydomonas*, widely regarded as an ideal system in which to study flagellar biology, swims forward by the synchronous action of its two flagella. Using high-speed imaging over long intervals, we found a richer behavior: A cell swimming in the dark stochastically switches between synchronous and asynchronous flagellar beating. Three-dimensional tracking shows that these regimes lead, respectively, to nearly straight swimming and to abrupt large reorientations, which yield a eukaryotic version of the "run-and-tumble" motion of peritrichously flagellated bacteria.

One of the most highly conserved structures among eukaryotes is the flagellum (*1*, *2*), whose composition in humans is nearly identical to that in unicellular algae (*3*). Because the coordinated motion of flagella is involved in fluid transport in the respiratory system (*4*), embryonic left-right asymmetry (*5*, *6*), intercellular communication (*7*), and possibly the evolution of multicellularity (*8*), it is important to understand the origin of flagellar synchronization. An emerging hypothesis (*9*–*12*) implicates hydrodynamic interactions, yet experimental proof is lacking. Flagellar synchronization is also important for prokaryotes, in which "run-and-tumble"

[1]Department of Applied Mathematics and Theoretical Physics, University of Cambridge, Wilberforce Road, Cambridge CB3 0WA, UK. [2]Department of Physics, Haverford College, Haverford, PA 19041, USA.

*To whom correspondence should be addressed. E-mail: R.E.Goldstein@damtp.cam.ac.uk

chemotaxis relies on the stochastic bundling and unbundling of flagella (*13*), resulting in individual random walks and the diffusion of populations (*14*).

Here, we ask whether eukaryotic locomotion has any relationship to the run-and-tumble paradigm, using the alga *Chlamydomonas reinhardtii* as a model (*15*, *16*). Its two flagella are termed cis and trans because of their positions relative to the eyespot, a rudimentary light-sensing organelle. Analysis of cells in the dark, over short (1- to 2-s) intervals (*17*, *18*), has shown two behaviors. Most cells (~95%) beat with a synchronous breaststroke interrupted occasionally by extra beats ("slips") of the trans flagellum, a phenomenon confirmed by later experiments over much longer periods (*19*). In this regime, cells swim in a tight helix along an almost straight center line. The remaining cells (~5%) beat asynchronously, with a large interflagellar frequency difference (10 to 30%), compatible with observations on demembranated cells (*20*), where trans flagella often beat with a higher frequency than cis flagella. These results have been interpreted as representative of distinct subpopulations. However, the underlying biochemical or physical processes that control synchronization remain unknown.

Previous studies tracking *C. reinhardtii* swimming (*21*–*23*) suggest that, like bacteria, entire populations display diffusive behavior. Existing interpretations (*22*) attribute diffusion to the accumulation of small deflections but lack explicit references to the actual beating dynamics of the flagella.

Here, we present three main experimental results on the beating of *C. reinhardtii* flagella and its relationship to swimming in the dark, where phototactic reorientations do not occur. First, we demonstrate that individual cells stochastically switch over the course of time between the two regimes: synchronous with slips and asynchronous. Second, we show that either the cis or the trans flagellum can be the faster one during asynchrony, so although their phototactic responses are intrinsically different (*17*, *18*, *20*), there is no absolute frequency asymmetry. Third, we present strong evidence that the diffusion of populations of *C. reinhardtii* is the result of localized events of large nonphototactic reorientations, corresponding to periods of asynchronous flagellar beating. Taken together, these results strongly suggest that the beating frequencies themselves are under the control of the cell. The stochastic movement back and forth between synchrony and asynchrony is reminiscent of the run-and-tumble motion of bacteria, with sharp turns taking the place of tumbles.

We first studied (*24*) the diffusion of a population of *C. reinhardtii* by gently centrifuging a dilute suspension of cells to the bottom of a plastic cuvette and analyzing the dynamics of the concentration profile as it spread upward (Fig. 1, A and B). In a region far from the bottom of the chamber, where cell-cell interactions are rare, the concentration flux is a linear function of the concentration gradient (Fig. 1C), and the slope of the fitted line gives then an estimate of the diffusion constant for an isolated individual: $D_{exp} = (0.68 \pm 0.11) \times 10^{-3}$ cm^2/s. A random walk of typical speed u and free-flight time τ gives a diffusion constant $D \sim u^2\tau$, implying a characteristic time on the order of 5 to 10 s for $u \sim 100$ μm/s.

To interpret this time and connect the macroscopic diffusive behavior to the dynamics of individual cells, we analyzed in a separate experiment high-speed movies of the flagella pairs of isolated *C. reinhardtii* cells held by micropipettes. The fact that a given cell moves back and forth between synchronous and asynchronous states is illustrated in Fig. 2. Figure 2A shows time series of the individual signals from the left and right flagella over a short (0.5-s) interval within a period of synchrony several seconds long, whereas Fig. 2B displays the asynchronous state in which the interflagellar phase difference drifts linearly in time

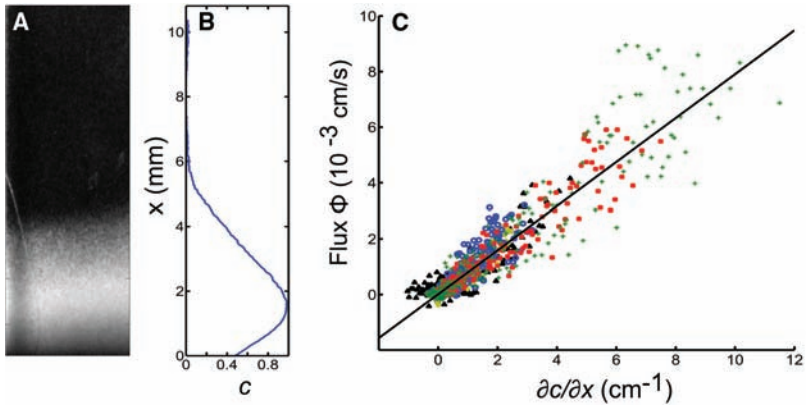

Fig. 1. Diffusive behavior of a population of *C. reinhardtii* containing thousands of individual cells. (**A**) Light scattered from the cells 1 min after being spun in a centrifuge. (**B**) Integrated light intensity as a function of height x. (**C**) Flux versus concentration gradient at various points in space and time; the linearity shows that cells spread according to Fick's law. Different-colored symbols correspond to independent trials.

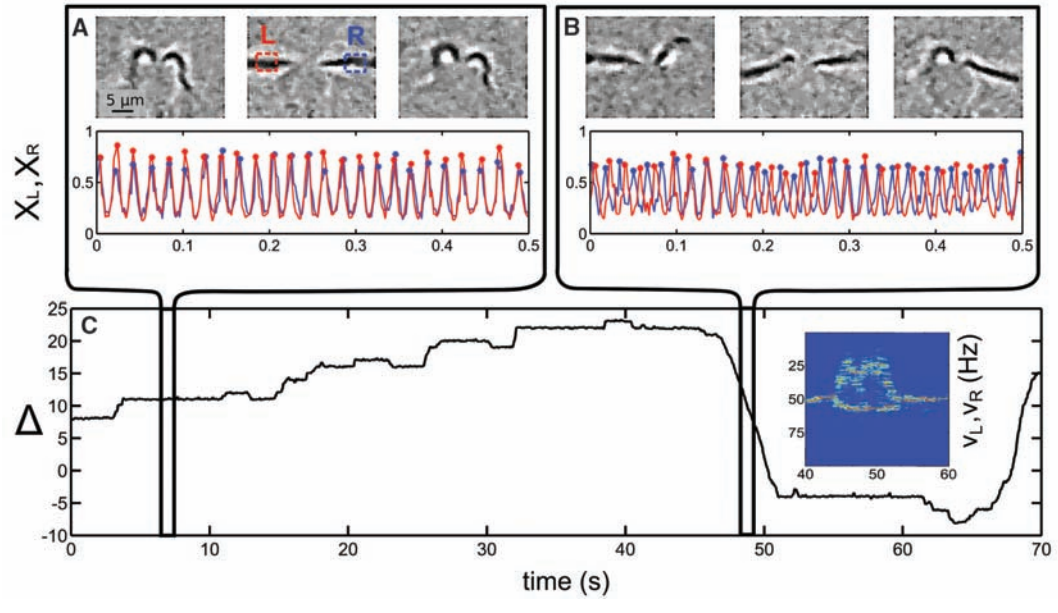

Fig. 2. A single *C. reinhardtii* cell moves back and forth between synchronous (**A**) and asynchronous (**B**) states. Movie frames showing a few cycles and the oscillatory intensity signals $X_{L,R}(t) = \Gamma_{L,R}(t)\sin[2\pi\theta_{L,R}(t)]$ (X, signal; L, left; R, right; Γ, amplitude; t, time; θ, phase), obtained by local sampling of the video light intensity near the two flagella, are shown for both cases. (**C**) A long (70-s) time series of the phase difference $\Delta(t) = \theta_L(t) - \theta_R(t)$ contains periods of synchrony interrupted by drifts of either sign. A windowed Fourier transform of the beating signals during the transition from synchronization to drifting and then back again to synchrony (inset) shows a large frequency difference in the asynchronous state. This behavior was characteristic of all 24 observed cells.

over tens of cycles. These short intervals are part of a much longer measurement window of 70 s (Fig. 2C). In this long time series, we see that drifts extend over periods of 1 to 3 s and can be of either sign. The interflagellar frequency difference during drifts is in the range from 10 to 30% of the mean (inset Fig. 2C). Synchronous intervals are more frequently interrupted by much shorter events (~0.2 s) resulting in a single extra beat of one flagellum: a phase slip. Slips can be of either sign, but are biased in one direction, constant throughout each experiment, and happen randomly in time. This behavior was characteristic of all the observed cells (*24*).

On a basic level, the two flagella of *C. reinhardtii* are oscillators, coupled through the fluid in which they move and possibly the cell wall through which they emerge, and subject to noise of both thermal and biochemical origin. Despite their complexity, the basic phenomenology can be captured by a simple mathematical model describing the dynamics of weakly coupled self-sustained noisy oscillators (*24*, *25*). Three parameters characterize this model: the interflagellar coupling strength ε, the flagellar noise intensity T_{eff}, and the intrinsic frequency difference between the two flagella $\delta\nu$, which can be determined even in the synchronized state and is responsible for the bias in the distribution of slips. The distribution of the measured coupling strengths ε (Fig. 3A) shows a well-defined peak at a value that compares very well with a rough estimate ε_m given by an idealized flagellar model with hydrodynamic coupling (*24*). This suggests that fluid flow is indeed the major contribution to the coupling responsible for flagellar synchronization.

Synchronous and asynchronous states cluster into two regions in parameter space, separated by nearly two orders of magnitude in the intrinsic interflagellar frequency difference (Fig. 3B), with no cells at intermediate values. These two distinct dynamical regimes are analogous to two distinct internal "gears." In the lower gear (a lower value of $\delta\nu$), the intrinsic interflagellar frequency difference is sufficiently small for the coupling to lead to robust synchronization. In the upper gear, the flagella beat with a high intrinsic frequency difference, and the coupling is too weak to cause significant frequency entrainment. Because individual cells alternate in time between these two regimes, we conclude that *C. reinhardtii* can control the state of synchronization of its flagella by actively changing their intrinsic frequency difference.

The stochastic switching between synchrony and asynchrony has clear effects on swimming trajectories. Figure 4A shows a portion of the

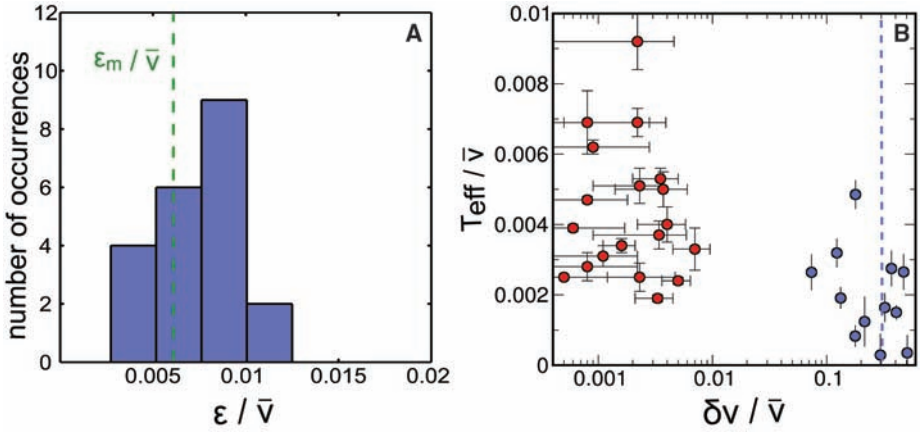

Fig. 3. Parameters of the phase synchronization model (*24*) extracted from high-speed imaging studies of flagellar dynamics, rescaled by the mean flagellar beating frequency $\bar{\upsilon}$. (**A**) The probability distribution of the coupling amplitude $\varepsilon/\bar{\upsilon}$ shows a well-defined peak at 0.0076, comparable to the estimate $\varepsilon_m/\bar{\upsilon}$ = 0.006 based on hydrodynamic interactions. (**B**) Data clustering in the parameter space defined by the intrinsic interflagellar frequency difference $\delta\nu$ and the flagellar noise intensity T_{eff} supports the existence of two distinct regimes. Although the noise differences are modest, the relative intrinsic frequency differences span two orders of magnitude, from 0.001–0.01 to 0.1–0.4. The dashed vertical line represents the intrinsic frequency difference observed in cell models (*20*).

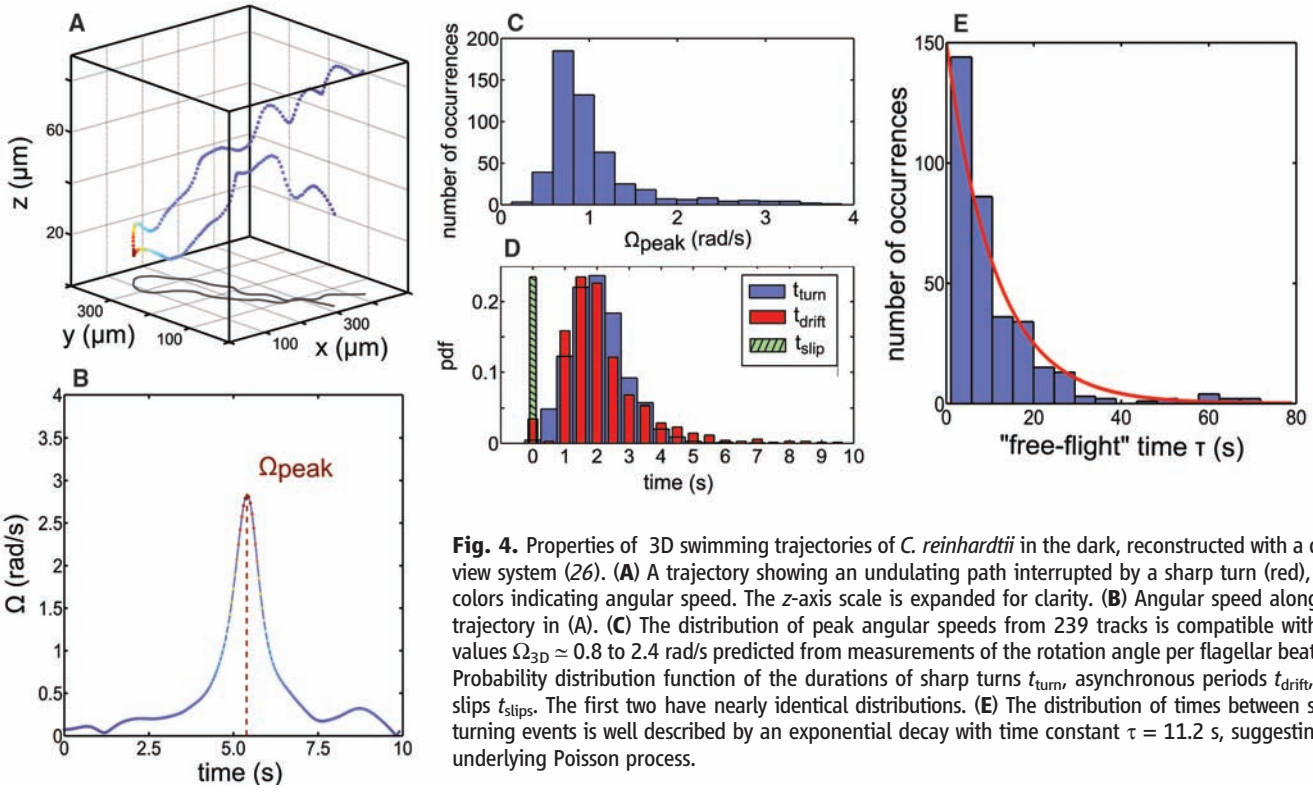

Fig. 4. Properties of 3D swimming trajectories of *C. reinhardtii* in the dark, reconstructed with a dual-view system (*26*). (**A**) A trajectory showing an undulating path interrupted by a sharp turn (red), with colors indicating angular speed. The *z*-axis scale is expanded for clarity. (**B**) Angular speed along the trajectory in (A). (**C**) The distribution of peak angular speeds from 239 tracks is compatible with the values $\Omega_{3D} \simeq 0.8$ to 2.4 rad/s predicted from measurements of the rotation angle per flagellar beat. (**D**) Probability distribution function of the durations of sharp turns t_{turn}, asynchronous periods t_{drift}, and slips t_{slips}. The first two have nearly identical distributions. (**E**) The distribution of times between sharp turning events is well described by an exponential decay with time constant τ = 11.2 s, suggesting an underlying Poisson process.

three-dimensional (3D) reconstruction (*26*) of a trajectory containing both helical swimming and a clearly recognizable sharp turning event (Fig. 4B). Analysis of hundreds of sharp turns from 3D trajectories (*24*) yields the probability distribution of their angular speeds (Fig. 4C) and duration (Fig. 4D). The range of angular speeds is consistent with an estimate derived from the average frequency difference during asynchronous beating periods and the average angular rotation of the cell body per flagellar beat (*24*). The distribution of durations of turns is nearly identical to that of drifts (Fig. 4D) and incompatible with that of slips, the only other observed behavior that could lead to turns in the dark. These results indicate that sharp turns are the direct consequence of periods of asynchronous flagellar beating. Because sharp turns are defined by angular speeds much higher than typical background rates (Fig. 4B), we choose to consider these as the only turning events, which separate straight-line free-flight segments. The probability distribution of the duration of such free flights, shown in Fig. 4E, decays exponentially with a mean of $\tau = 11.2$ s. This time scale is clearly the one inferred earlier from the macroscopic diffusion measurements. The diffusion constant D can be estimated more precisely with the well-known results from run-and-tumble random walk models (*14*). With the average parameters extracted from the 3D trajectories, we obtain (*24*) $D \cong (0.47 \pm 0.05) \times 10^{-3}$ cm^2/s, which is in very good agreement with the value estimated from the macroscopic measurements on large populations.

We have found that in the dark, *C. reinhardtii* can vary the intrinsic frequencies of its two flagella so that they alternate between synchronous and asynchronous beating, with synchrony realized though a mechanism consistent with hydrodynamic coupling. This leads to swimming trajectories with stochastically distributed sharp turns and ultimately to the diffusive behavior of a population. In contrast to previous observations on cell models (*20*), we showed that in each cell either flagellum can beat faster than the other. This approximate symmetry is a strong indication that the unknown regulatory system at work here is distinct from that governing phototaxis, which is based instead on opposite amplitude modulations of flagellar motion, and it shows that the idea of a well-defined intrinsic frequency difference between cis and trans flagella is incorrect. Such control mechanisms could also have a role in coordinating large numbers of cilia in simple multicellular organisms lacking a central nervous system (such as *Volvox*). Open issues include the origins of this regulation, the characteristic time scale between asynchronous intervals, and the noise of flagellar beats, along with the possible interplay of these processes with chemotaxis and phototaxis.

References and Notes

1. I. Ibañez-Tallon, N. Heintz, H. Omran, *Hum. Mol. Genet.* **12**, R27 (2003).
2. G. J. Pazour, N. Agrin, J. Leszyk, G. B. Witman, *J. Cell Biol.* **170**, 103 (2005).
3. D. R. Mitchell, *J. Phycol.* **36**, 261 (2000).
4. B. A. Afzelius, *Science* **193**, 317 (1976).
5. S. Nonaka *et al*., *Cell* **95**, 829 (1998).
6. J. H. E. Cartwright, O. Piro, I. Tuval, *Proc. Natl. Acad. Sci. U.S.A.* **101**, 7234 (2004).
7. Q. Wang, J. Pan, W. J. Snell, *Cell* **125**, 549 (2006).
8. C. A. Solari, S. Ganguly, J. O. Kessler, R. E. Michod, R. E. Goldstein, *Proc. Natl. Acad. Sci. U.S.A.* **103**, 1353 (2006).
9. S. Gueron, K. Levit-Gurevich, *Proc. Natl. Acad. Sci. U.S.A.* **96**, 12240 (1999).
10. B. Guirao, J. F. Joanny, *Biophys. J.* **92**, 1900 (2007).
11. A. Vilfan, F. Julicher, *Phys. Rev. Lett.* **96**, 058102 (2006).
12. T. Niedermayer, B. Eckhardt, P. Lenz, *Chaos* **18**, 037128 (2008).
13. H. C. Berg, D. A. Brown, *Nature* **239**, 500 (1972).
14. H. C. Berg, *Random Walks in Biology* (Princeton Univ. Press, Princeton, NJ, 1983).
15. C. Ainsworth, *Nature* **448**, 638 (2007).
16. *The Chlamydomonas Sourcebook*, E. H. Harris, D. Stern, G. Witman, Eds. (Elsevier, Oxford, ed. 2, 2009).
17. U. Rüffer, W. Nultsch, *Cell Motil.* **7**, 87 (1987).
18. U. Rüffer, W. Nultsch, *Cell Motil.* **41**, 297 (1998).
19. K. Josef, J. Saranak, K. W. Foster, *Cell Motil. Cytoskeleton* **61**, 83 (2005).
20. N. Okita, N. Isogai, M. Hirono, R. Kamiya, K. Yoshimura, *J. Cell Sci.* **118**, 529 (2005).
21. V. A. Vladimirov, M. S. C. Wu, T. J. Pedley, P. V. Denissenko, S. G. Zakhidova, *J. Exp. Biol.* **207**, 1203 (2004).
22. N. A. Hill, D.-P. Häder, *J. Theor. Biol.* **186**, 503 (1997).
23. P. Hegemann, B. Bruck, *Cell Motil.* **14**, 501 (1989).
24. Materials and methods are available as supporting material on *Science* Online.
25. A. Pikovsky, M. Rosenblum, J. Kurths, *Synchronization. A Universal Concept in Nonlinear Science* (Cambridge Univ. Press, Cambridge, 2001).
26. K. Drescher, K. Leptos, R. E. Goldstein, *Rev. Sci. Instrum.* **80**, 014301 (2009).

27. We thank K. Leptos, T. J. Pedley, C. A. Solari, K. Visscher, A. Nedelcu, D. Page-Croft, T. Parkin, and N. Price and acknowledge support from the Marie-Curie Program (M.P.), the Human Frontiers Science Program (I.T.), the Leverhulme Trust (J.P.G.), the Biotechnology and Biological Sciences Research Council, the Engineering and Physical Sciences Research Council, the U.S. Department of Energy, and the Schlumberger Chair Fund.

Supporting Online Material

www.sciencemag.org/cgi/content/full/325/5939/487/DC1
Materials and Methods
Figs. S1 to S3
References

23 February 2009; accepted 2 June 2009
10.1126/science.1172667

Translocator Protein (18 kD) as Target for Anxiolytics Without Benzodiazepine-Like Side Effects

Rainer Rupprecht,[1,2]* Gerhard Rammes,[2,3] Daniela Eser,[1] Thomas C. Baghai,[1] Cornelius Schüle,[1] Caroline Nothdurfter,[1,2] Thomas Troxler,[4] Conrad Gentsch,[4] Hans O. Kalkman,[4] Frederique Chaperon,[4] Veska Uzunov,[4] Kevin H. McAllister,[4] Valerie Bertaina-Anglade,[5] Christophe Drieu La Rochelle,[5] Dietrich Tuerck,[6] Annette Floesser,[4] Beate Kiese,[7] Michael Schumacher,[8] Rainer Landgraf,[2] Florian Holsboer,[2] Klaus Kucher[4]

Most antianxiety drugs (anxiolytics) work by modulating neurotransmitters in the brain. Benzodiazepines are fast and effective anxiolytic drugs; however, their long-term use is limited by the development of tolerance and withdrawal symptoms. Ligands of the translocator protein [18 kilodaltons (kD)] may promote the synthesis of endogenous neurosteroids, which also exert anxiolytic effects in animal models. Here, we found that the translocator protein (18 kD) ligand XBD173 enhanced γ-aminobutyric acid–mediated neurotransmission and counteracted induced panic attacks in rodents in the absence of sedation and tolerance development. XBD173 also exerted antipanic activity in humans and, in contrast to benzodiazepines, did not cause sedation or withdrawal symptoms. Thus, translocator protein (18 kD) ligands are promising candidates for fast-acting anxiolytic drugs with less severe side effects than benzodiazepines.

Anxiety disorders are highly prevalent disabling disorders (*1*) that frequently turn into chronic clinical conditions (*2*). Benzodiazepines such as diazepam are fast-acting and effective antianxiety agents (*3*–*5*) and the most commonly prescribed anxiolytics. However, their side effects such as sedation and, following chronic administration, development of tolerance, consecutive abuse liability, and withdrawal symptoms render their use problematic in the long-term treatment of anxiety disorders (*2*–*4*). Currently, antidepressants such as selective serotonin reuptake inhibitors are first-line treatment for most anxiety disorders. However, their anxiolytic effects occur only after several weeks of treatment (*2*–*4*). Thus, there is need for anxiolytic agents that retain the rapid anxiolytic potential of benzodiazepines but lack their unfavorable side effects.

Neurosteroids are synthesized from cholesterol or steroidal precursors and modulate neurotransmitter receptors (*6*–*8*). Ring A–reduced neurosteroids are endogenous metabolites of the hormone progesterone and potent positive allosteric modulators of γ-aminobutyric acid type A ($GABA_A$) receptors, which mediate the effects of the inhibitory neurotransmitter GABA in the mammalian nervous system (*6*–*8*). They exert pronounced anxiolytic effects in animal models (*9*–*11*), and their concentrations are reduced

during panic attacks in patients with panic disorder (*12*, *13*). Thus, neurosteroidogenic compounds might represent a previously undiscovered anxiolytic principle. The translocator protein (18 kD), formerly called peripheral or mitochondrial benzodiazepine receptor, is mainly located in the outer mitochondrial membrane and favors the transport of cholesterol to the inner mitochondrial membrane, ultimately promoting neurosteroid synthesis (*14*, *15*). Certain ligands of this protein have been shown to enhance neurosteroidogenesis in the brain (*16*–*18*) and to exert acute anxiolytic/anticonflict activity in rodent models (*17*–*20*). However, so far no data are available as to whether such compounds act as anxiolytics also in humans or whether they lack tolerance development and withdrawal effects.

XBD173 binds to the translocator protein (18 kD) with nanomolar affinity and shows negligible affinity to a broad range of neurotransmitter receptors, including $GABA_A$ receptors (*19*).

At the cellular level, we examined whether XBD173 modulates the GABA-induced response in human WSS1 cells expressing rat $\alpha_1\gamma_2$ and human β_3 $GABA_A$ receptor subunits. In contrast to diazepam, XBD173 did not enhance GABA-evoked chloride currents (fig. S1, A to C). However, in mouse neocortical slices XBD173 potentiated GABA-mediated (GABAergic) neurotransmission (Fig. 1A, fig. S2D, and table S1A), which was prevented by the 5α-reductase inhibitor finasteride (Fig. 1B). This is in line with the induction of neurosteroidogenesis after XBD173 administration (fig. S1D). Thus, the enhancement of GABAergic neurotransmission by XBD173 in vivo is mediated indirectly through the generation of GABAergic neurosteroids.

XBD173 exerted acute anxiolytic effects, which were prevented by the translocator protein (18 kD) antagonist PK11195 (fig. S3, A and B), in the social exploration test in rats and the elevated plus maze test (table S2). To address tolerance development, we administered XBD173 to rats twice daily for 5 days. Its anxiolytic activity in the social exploration test was fully retained with this subchronic administration (fig. S3A). Next, we explored whether XBD173 could counteract lactate- or cholecystokinin tetrapeptide (CCK4)–induced panic in rodent paradigms, because panic-like anxiety can be experimentally induced in humans through challenge with lactate or the neuropeptide fragment CCK4 (*12*, *21*). Both the benzodiazepine alprazolam and XBD173

[1]Department of Psychiatry and Psychotherapy, Ludwig Maximilian University, Nussbaumstrasse 7, Munich 80336, Germany. [2]Max-Planck-Institute of Psychiatry, Kraepelinstrasse 2, Munich 80804, Germany. [3]Department of Anaesthesiology, Technische Universität, Munich 81675, Germany. [4]Novartis Institute for Biomedical Research (NIBR), Neuroscience, 4056 Basel, Switzerland. [5]Biotrial, 3500 Rennes, France. [6]Drug Metabolism and Pharmacokinetics, F. Hoffmann-La Roche AG, 4070 Basel, Switzerland. [7]Biostatistics, Novartis Pharma AG, 4056 Basel, Switzerland. [8]INSERM UMR 788, and University Paris-Sud 11, 94274 Paris, France.

*To whom correspondence should be addressed. E-mail: rainer.rupprecht@med.uni-muenchen.de

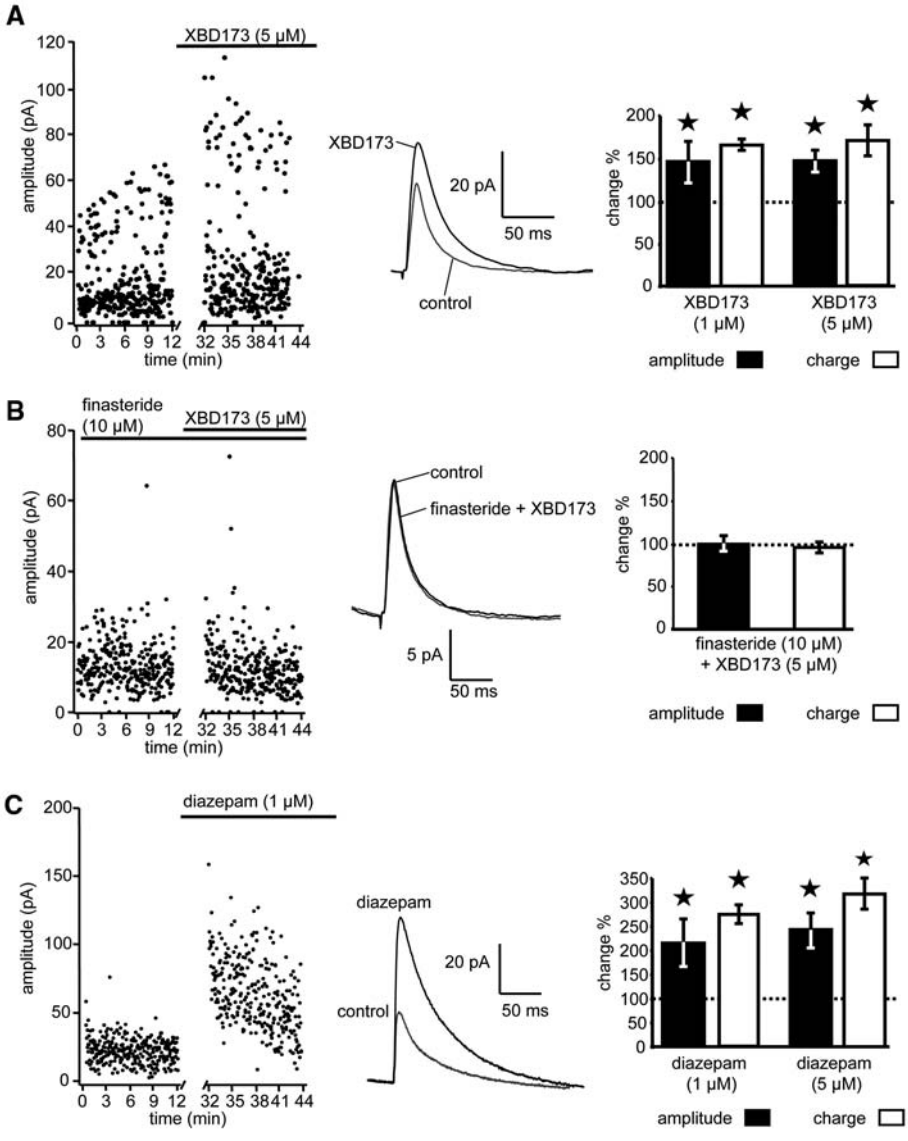

Fig. 1. Effects of XBD173 and diazepam on GABAergic neurotransmission in slices of the medial prefrontal cortex. The mean amplitude of all recorded inhibitory postsynaptic currents (IPSCs) in the absence of compounds was 26.0 ± 2.7 pA with a decay time constant (τ) of 27.8 ± 2.8 ms, and the mean charge was 1.5 ± 0.7 pC (mean ± SEM) (n = 54 neurons). (**A** to **C**) (Left) Individual response amplitudes during the course of a representative experiment. (Middle) Averaged traces from all consecutive IPSCs for the control experiments and in the presence of 5 μM XBD173, 10 μM finasteride and 5 μM XBD173, or 1 μM diazepam. Compounds were applied for at least 20 min at the indicated concentrations before IPSCs were recorded. (Right) Averaged data (mean ± SEM) of all experiments (n = 6 to 8 neurons). (A) Effects of XBD173. The effect of XBD173 was monitored with whole-cell recordings and minimal stimulation. XBD173 increases the amplitude and charge and prolongs the decay of $GABA_A$ receptor–mediated synaptic transmission (table S1A). (B) Antagonism of the effects of XBD173 by finasteride. (C) Effects of diazepam. Diazepam increases the amplitude and charge of $GABA_A$ receptor–mediated synaptic transmission. Electrophysiological data were analyzed by the t test for paired samples. *P < 0.05, as compared with control experiments.

effectively prevented panic behavior elicited by means of an infusion of sodium lactate in panic-prone rats (Fig. 2A). No sedation was observed after treatment with XBD173, whereas alprazolam caused a marked reduction in locomotor activity (fig. S4). Also, in the CCK4 challenge paradigm in rats both alprazolam (Fig. 2B) and XBD173 (Fig. 2C) clearly displayed antipanic properties. These preclinical studies suggest that XBD173 exerts rapid anxiolytic and antipanic effects with a more favorable side-effect profile than that of benzodiazepines.

Next, we investigated the anxiolytic potential of XBD173 in healthy male volunteers using the CCK4 challenge. Only subjects that showed a clear panic response to the initial CCK4 challenge entered one of the five treatment arms of the study (n = 14 subjects each). Out of 85 subjects, 71 healthy volunteers were randomized to treatment for 7 consecutive days with placebo, 10, 30, or 90 mg/day XBD173 or 2 mg/day alprazolam before undergoing a second CCK4 challenge. Seventy subjects completed the study (fig. S5). Both XBD173 and alprazolam were rapidly absorbed, with peak concentrations occurring within 2.5 hours after oral administration (fig. S6). For analysis of the anxiolytic potential of XBD173 and alprazolam, the difference in the acute panic inventory (API) [area under the time curve (AUC)] between the first and the second challenge with CCK4 relative to the effects of placebo served as an efficacy parameter in this exploratory analysis (Fig. 3 and fig. S5). One-way analysis of covariance (ANCOVA) revealed a significant difference from placebo in attenuating CCK4-induced anxiety after both alprazolam and the highest dose of XBD173 (Fig. 3). The number of side effects reported with XBD173 was comparable to the incidence in the placebo group. In contrast, a much higher incidence was reported by the alprazolam-treated group, in particular dizziness and somnolence (table S3A). Although 57% of the subjects treated with alprazolam complained of withdrawal symptoms such as sleep disturbances or restlessness, these were almost absent in the XBD173-treated groups (table S3B). No serious adverse event occurred during the entire study, and there was no need for treatment of withdrawal symptoms. Thus, this placebo-controlled parallel group study indicates that in humans XBD173 has both anxiolytic properties and clearly fewer side effects compared with benzodiazepines.

Ligands of the translocator protein (18 kD) such as XBD173 may represent a pharmacological mechanism for the treatment of anxiety disorders (*13*). XBD173 seems to be superior to benzodiazepines because a rapid anxiolytic activity is retained in the absence of their well-known side effects (*3*, *4*). This fast anxiolytic effect is also superior to antidepressants, which have a considerably slower onset of action (*2*–*4*). Surprisingly, withdrawal symptoms were reported after treatment with alprazolam for only 7 days. This is remarkable because prescription of benzodiazepines is recommended for up to 4 weeks (*3*, *4*). No withdrawal symptoms were noted in the XBD173-treated subjects in spite of an anxiolytic efficacy of the 90 mg/day dose comparable to that of alprazolam, which is in line with the lack of withdrawal-induced hypophagia after chronic administration of XBD173 in mice (*13*). A major challenge in the development of anxiolytic compounds is the failure rate in clinical trials, even for those compounds with proven preclinical anxiolytic properties in commonly used animal models. The possibility of the challenge with sodium lactate or CCK4 in rats and humans (*12*, *22*) may thus represent an advantage in a translational approach for evaluating anxiolytics. Although the CCK4 challenge was used as a surrogate marker, which does not allow us to draw firm conclusions on the efficacy of XBD173 in anxiety disorders, CCK4 fulfills the criteria for an ideal panicogenic agent (*21*, *23*, *24*), and the panic induction by CCK4 is sensitive to clinically effective anxiolytic agents, including benzodiazepines (*24*, *25*).

Translocator protein (18 kD) ligands promote the biosynthesis of endogenous neurosteroids (*17*, *18*, *26*). An enhancement of GABAergic neurotransmission by neurosteroids probably accounts for the anxiolytic effects of XBD173 because anxiolytic effects of translocator protein (18 kD) ligands can be prevented by finasteride (*26*) and neurosteroidogenesis is increased after XBD173 administration. Moreover, XBD173 potentiated GABAergic neurotransmission in neocortical slices, and its GABA-enhancing potential was prevented by finasteride (*13*). Neurosteroids modulate $GABA_A$ receptors via an allosteric site different from that targeted by benzodiazepines (*5*, *7*, *27*). These distinct sites of action at the $GABA_A$ receptor might explain the lack of tolerance development and withdrawal symptoms after XBD173-induced neurosteroidogenesis. There is considerable evidence for an involvement of neurosteroids in the etiology of anxiety

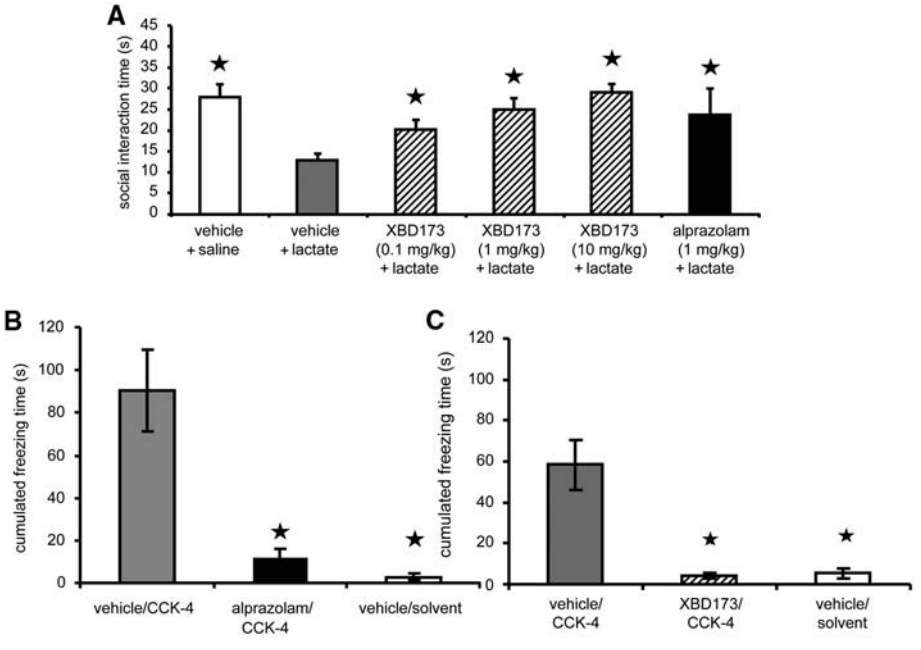

Fig. 2. Effects of XBD173 or alprazolam in models for pharmacologically induced panic in rats. (**A**) Effect of an acute pretreatment (–60 min) with XBD173 (0.1, 1, or 10 mg/kg per second orally) or alprazolam (1 mg/kg intraperitoneally) on the time spent in social interaction after an intravenous infusion of a 1 M sodium lactate solution in panic-prone rats. Bars represent the mean (±SEM) social interaction time during 5 min after the lactate challenge (n = 8 rats per group). Data were analyzed by means of restricted maximum-likelihood analysis of variance (ANOVA) followed by Student's t test. *P < 0.05, as compared with rats treated with vehicle and lactate. (**B**) Effects of alprazolam on the freezing response induced by 10 mg/kg subcutaneously CCK4. Bars represent the mean (±SEM) of the cumulated time spent freezing between 2 and 15 min after an injection of CCK4 or solvent (n = 11 rats per group). Rats were subcutaneously pretreated with either vehicle or alprazolam (0.1 mg/kg) 15 min before CCK4 or solvent injection. (**C**) Effects of XBD173 on the freezing response induced by 10 mg/kg subcutaneously CCK-4. Bars represent the mean (±SEM) of the cumulated time spent freezing between 2 and 10 min after an injection of CCK4 or solvent (n = 10 rats per group). Rats were orally pretreated with either vehicle or XBD173 (0.1 mg/kg) 60 min before CCK4 or solvent injection. Data were analyzed by means of Kruskal-Wallis one-way ANOVA followed by the Mann-Whitney U test. *P < 0.001, as compared with control rats treated with vehicle and CCK4.

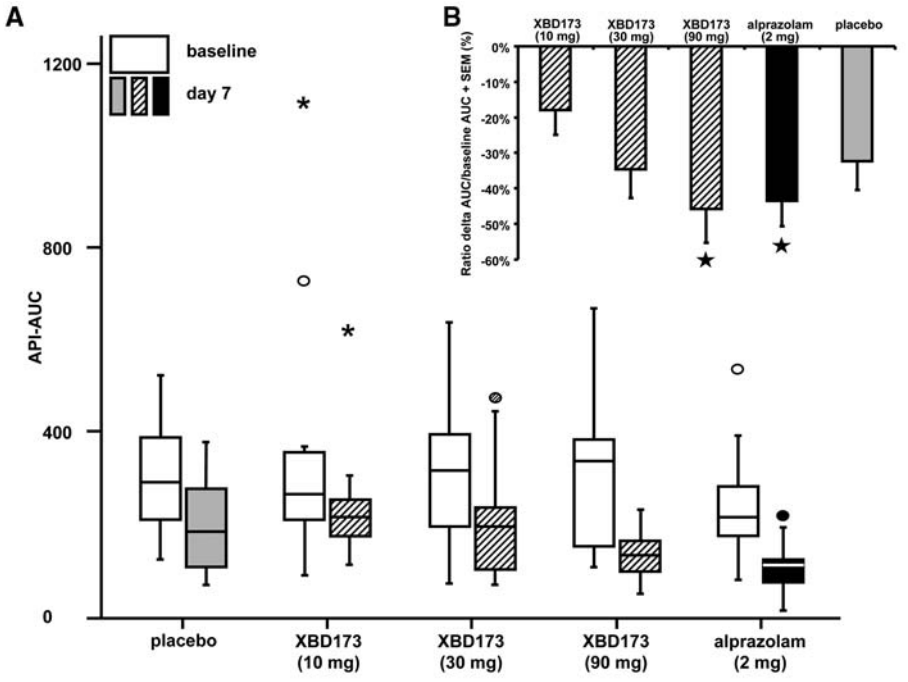

Fig. 3. Effects of XBD173 or alprazolam on CCK4-induced anxiety in healthy male volunteers. (**A**) AUC of the API score during the first and second CCK4 challenge. Boxplots represent the median equivalent to the 50th percentile (line within the boxes), the range containing all individual values above the 25th and below the 75th percentile (boxes), and the range of individual values within 150% above or below the difference between the 75th and the 25th percentile (error bars). Open circles indicate outliers located more than 150% and asterisks indicate extreme values located more than 300% of the box height above the 75th percentile. (**B**) Decrease in CCK4-induced anxiety (ΔAPI-AUC) after treatment with XBD173, alprazolam, or placebo in relation to baseline AUC (mean ± SEM). Asterisks indicate a significant difference against placebo for 90 mg XBD173 ($P < 0.036$) and alprazolam ($P < 0.019$) by way of ANCOVA.

disorders. Neurosteroid homeostasis is altered (*12*, *13*), and translocator protein (18 kD)–binding sites on platelets are reduced in panic disorder (*28*). Moreover, variations in the encoding gene may confer susceptibility to this disease (*29*).

XBD173 enhances GABAergic neurotransmission via induction of neurosteroidogenesis and shows anxiolytic efficacy in humans with a favorable side-effect profile, which suggests that the translocator protein (18 kD) represents a target for anxiolytic drug discovery.

References and Notes

1. R. C. Kessler *et al.*, *Arch. Gen. Psychiatry* **62**, 593 (2005).
2. D. Nutt, J. Ballenger, D. Sheehan, H. U. Wittchen, *Int. J. Neuropsychopharmacol.* **5**, 315 (2002).
3. B. Bandelow *et al.*, *World J. Biol. Psychiatry* **9**, 248 (2008).
4. D. S. Baldwin *et al.*, *J. Psychopharmacol.* **19**, 567 (2005).
5. U. Rudolph, H. Mohler, *Curr. Opin. Pharmacol.* **6**, 18 (2006).
6. R. Rupprecht, F. Holsboer, *Trends Neurosci.* **22**, 410 (1999).
7. D. Belelli, J. J. Lambert, *Nat. Rev. Neurosci.* **6**, 565 (2005).
8. R. Rupprecht *et al.*, *Neuron* **11**, 523 (1993).
9. E. Carboni, S. Wieland, N. C. Lan, K. W. Gee, *Psychopharmacology (Berl.)* **126**, 173 (1996).
10. D. Bitran, R. J. Hilvers, C. K. Kellogg, *Brain Res.* **561**, 157 (1991).
11. V. K. Patchev, M. Shoaib, F. Holsboer, O. F. X. Almeida, *Neuroscience* **62**, 265 (1994).
12. A. Ströhle *et al.*, *Arch. Gen. Psychiatry* **60**, 161 (2003).
13. Materials and methods, supplementary text, and supplementary data are available as supporting material on *Science* Online.
14. V. Papadopoulos, L. Lecanu, R. C. Brown, Z. Han, Z. X. Yao, *Neuroscience* **138**, 749 (2006).
15. V. Papadopoulos *et al.*, *Trends Pharmacol. Sci.* **27**, 402 (2006).
16. E. Romeo *et al.*, *J. Pharmacol. Exp. Ther.* **267**, 462 (1993).
17. M. Serra *et al.*, *Br. J. Pharmacol.* **127**, 177 (1999).
18. M. Verleye *et al.*, *Pharmacol. Biochem. Behav.* **82**, 712 (2005).
19. A. Kita *et al.*, *Br. J. Pharmacol.* **142**, 1059 (2004).
20. S. Okuyama *et al.*, *Life Sci.* **64**, 1455 (1999).
21. D. Eser *et al.*, *Psychopharmacology (Berl.)* **192**, 479 (2007).
22. A. Shekhar, S. R. Keim, J. R. Simon, W. J. McBride, *Pharmacol. Biochem. Behav.* **55**, 249 (1996).
23. J. Harro, E. Vasar, J. Bradwejn, *Trends Pharmacol. Sci.* **14**, 244 (1993).
24. P. Zwanzger, R. Rupprecht, *J. Psychiatry Neurosci.* **30**, 167 (2005).
25. P. Zwanzger *et al.*, *Neuropsychopharmacology* **28**, 979 (2003).
26. A. Kita, K. Furukawa, *Pharmacol. Biochem. Behav.* **89**, 171 (2008).
27. A. M. Hosie, M. E. Wilkins, H. da Silva, T. G. Smart, *Nature* **444**, 486 (2006).
28. S. Pini *et al.*, *Psychopharmacology (Berl.)* **181**, 407 (2005).
29. K. Nakamura *et al.*, *Am. J. Med. Genet. B. Neuropsychiatr. Genet.* **141**, 222 (2006).

30. The authors thank M. Enunwa and S. de la Motte for their help with the clinical proof of concept study, B. Müller-Myhsok for statistical advice, M. Nussbaumer for technical assistance, and P. Lière for help with the gas chromatography–mass spectrometry analysis. The clinical study has been sponsored by Novartis Pharma AG, Basel, Switzerland. Molecular and electrophysiological experiments were supported by a Max Planck Fellow grant to R.R. R.R. has been a paid consultant for Novartis and been on Novartis advisory boards.

Supporting Online Material

www.sciencemag.org/cgi/content/full/1175055/DC1
Materials and Methods
SOM Text
Figs. S1 to S6
Tables S1 to S3
References

16 April 2009; accepted 8 June 2009
Published online 18 June 2009;
10.1126/science.1175055
Include this information when citing this paper.

New Products

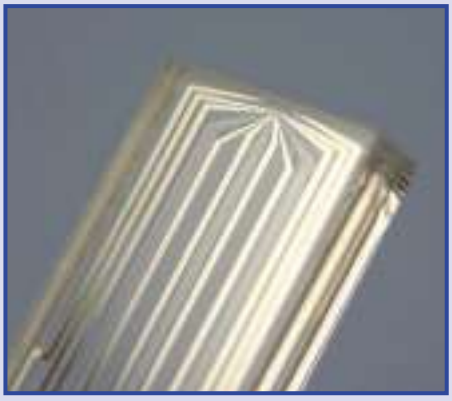

Microfluidics Chip Functionality

Dolomite now offers the ability to integrate metal electrodes into its range of glass and polymer microfluidic chips. A wide variety of geometries can be achieved, such as interdigitated electrodes, heaters, and temperature sensors. Applications include impedance detection, temperature control in microreactors, and generation of electrical fields for dielectrophoresis. With its excellent chemical-resistant and heat-resistant properties, platinum is most frequently used as an electrode material, but a wide range of metals can be deposited onto the microfluidic glass or polymer chips, including gold, copper, titanium, and chrome. Metal feature size can be as small as 2 μm. Metal layers can also be deposited on the inside surface of the microchannels.

Dolomite
For information +44-1763-242491
www.dolomite-microfluidics.com

Desktop Nanofabrication

The next generation Dip Pen Nanolithography (DPN) system, the DPN 5000, brings greater control and performance to desktop nanofabrication. The DPN 5000 offers versatile nanopatterning capabilities coupled with high-performance atomic force microscopy imaging for immediate characterization of the deposited patterns. System highlights include an ultralow-noise scanner with closed-loop flexure technology to produce accurate and repeatable nanoscale patterns. For subsequent imaging of substrates, a low-coherence laser with a reduced laser spot size ensures high-quality lateral-force imaging. Enhanced lithography software, InkCAD 4.0, includes improved control of tip-based patterning, along with nanoscale mapping and positioning, allowing users to precisely position multiple features, even those created from different materials.

NanoInk
For information 847-679-6266
www.nanoink.net

Sperm Freezing Kit

The JAX Sperm Cryo Kit provides a reliable and cost-effective method of cryopreserving the sperm of novel mouse models. Researchers can preserve the sperm in their own laboratories, while still enjoying the benefit of having The Jackson Laboratory perform quality control testing and provide long-term storage. The kit contains all the necessary items, including collection dishes, straws and cassettes, freezing apparatus, cryo-protective media, and a detailed instruction manual. It even includes extra reagents and plasticware to perform a practice run. The Jackson Laboratory will perform a quality control test on one sperm sample from each strain to assess fertility and report the results back.

The Jackson Laboratory
For information 800-422-6423
www.jax.org/jaxservices

Confocal FRAP Imaging

The VT-HAWK combines high precision point-scanning fluorescence recovery after photobleaching (FRAP) with multibeam confocal imaging. The instrument's ability to switch between imaging and photo-bleach modes in seconds enables accurate quantitation of fluorescence intensity dynamics in precise, user-defined regions of the image. VT-HAWK supports FRAP, fluorescence loss in photobleaching, photo-activation, and photo-conversion techniques with selectable pinhole sizes for confocal imaging. The instrument's optics deliver optimal laser beam quality at the sample without compromising the performance of either mode. Options include a laser-merge module that houses up to six solid-state lasers.

VisiTech International
For information +44-(0)-191-5166255
www.visitech.co.uk

Metabolite Database

The Symyx Metabolite database, a comprehensive collection of drug metabolism data, is now available to pharmaceutical, agrochemical, and biotechnology researchers via the Symyx Isentris data access, analysis, and decision support system, as well as the web-based DiscoveryGate content platform. The database can accelerate research and development productivity by making it possible for scientists to focus on the most therapeutically promising compounds (those with the right metabolic profile) early in the discovery process. Scientists can use Symyx Metabolite's structure-searchable metabolic schemes, biotransformation explorer, and easy-to-use query and browse tools to explore the fate of parent compounds, their metabolites, and properties by leveraging in-house and Symyx database information.

Symyx Technologies
For information +44-208-546-0869
www.symyx.com

Electrophoresis Software

Spresso is free, open-source software for electrophoresis that can ease experimental design and troubleshooting. The software provides a new tool for designing and optimizing complex electrophoresis problems. The designers say that the software is 75 times faster than current tools thanks to unique numerical algorithms. The speed can mean the difference between waiting overnight to get a result and getting it in a few minutes. Spresso allows scientists to iterate through experimental variations much faster than they could by going into the lab and relying on trial and error.

Stanford School of Engineering
For information 650-736-2245
microfluidics.stanford.edu/spresso/2008/09/introducing-spresso.html

Electronically submit your new product description or product literature information! Go to **www.sciencemag.org/products/newproducts.dtl** for more information.

Newly offered instrumentation, apparatus, and laboratory materials of interest to researchers in all disciplines in academic, industrial, and governmental organizations are featured in this space. Emphasis is given to purpose, chief characteristics, and availabilty of products and materials. Endorsement by *Science* or AAAS of any products or materials mentioned is not implied. Additional information may be obtained from the manufacturer or supplier.

POSITIONS OPEN

UNIVERSITY OF MARYLAND

TENURE-TRACK FACULTY POSITIONS
Cell Biology and Molecular Genetics

The Department of Cell Biology and Molecular Genetics at the University of Maryland, College Park is seeking junior and mid-career faculty with the demonstrated ability to develop high-impact research programs in cell biology and/or microbial pathogenesis. In cell biology, areas of interest include membrane traffic, signal transduction, and the regulation of gene expression, with emphasis on approaches that involve mammalian systems, genetics of model organisms, bioinformatics, functional genomics, and high-resolution microscopy. In microbial pathogenesis, areas of interest include viral, bacterial, and protozoan pathogens, their interactions with host plants or animals, and strategies for detection, prevention, and treatment of disease. These appointments will be part of an ongoing campus drive for enhancement in the life sciences.

Successful candidates will be expected to maintain a vigorous, externally funded research program and to participate in undergraduate and graduate teaching. Applicants must have a doctoral degree, relevant postdoctoral experience, an outstanding publication record, and a commitment to excellence in teaching. Additional information about the Department can be found at **website: http://www.life.umd.edu/CBMG.**

The University of Maryland, College Park is the flagship campus of the University System of Maryland and one of the most rapidly advancing public research universities in the country. The Department offers outstanding new research facilities and a highly interactive environment, with extensive opportunities to interact with scientists affiliated with other departments, centers, and institutes at the University of Maryland, including the Center for Bioinformatics and Computational Biology, the Maryland Pathogen Research Institute, the Maryland NanoCenter, and the Center for Biomolecular Structure and Organization. Additionally, close proximity to Washington, D.C., Baltimore, and the Maryland Biotechnology Corridor facilitates interactions with an extraordinary range of major research institutions, including the NIH, National Institute of Standards and Technology, U.S. Department of Agriculture, the Smithsonian Institution, and U.S. Food and Drug Administration.

Applicants should apply electronically by e-mailing a single PDF file containing (1) a letter of application, (2) curriculum vitae, (3) statement of research and teaching interests, and (4) the names and addresses of at least four references to: **Dr. Jonathan Dinman, Search Committee Chair, e-mail: mbarott@umd.edu.** For best consideration, applications should be received by September 30, 2009, but will be accepted until positions are filled.

The University of Maryland is an Affirmative Action/Equal Opportunity Employer. Women and members of underrepresented groups are especially encouraged to apply.

Tenure-track ASSISTANT/ASSOCIATE PROFESSOR, New York University School of Medicine. The Department of Environmental Medicine is seeking an individual to set up an independent research program in epigenetics and its regulation in relation to toxicological responses or to cancer development. An attractive startup package is available depending on qualifications. Laboratories are located 45 minutes outside Manhattan near Tuxedo, New York. Please send curriculum vitae and list of three references to: **Dr. Max Costa, Professor and Chairman, Department of Environmental Medicine, at e-mail: max.costa@nyumc.org.**

POSTDOCTORAL FELLOW needed at the University of Wisconsin-Madison to study the mechanisms of control of replication of the AIDS virus using the SIV-infected rhesus macaque. Experience in molecular biology and cellular immunology required. Please send curriculum vitae and the names of three references to: **Dr. David Watkins, c/o Amanda Espinosa, 555 Science Drive, Madison, WI 53711. E-mail: abriggs@primate.wisc.edu.**

POSITIONS OPEN

DIVISION DIRECTOR
Physical Biosciences Division

The Lawrence Berkeley National Laboratory is seeking a Division Director for the Physical Biosciences Division. Berkeley Laboratory conducts pioneering research across a wide range of scientific disciplines with key efforts in fundamental studies of the universe; quantitative biology; nanoscience; new energy systems and environmental solutions; and the use of integrated computing as a tool for discovery. It is organized into 14 scientific divisions and hosts four U.S. Department of Energy (DOE) national user facilities. Berkeley Laboratory is located in the San Francisco Bay area on a 200-acre site in the hills above the University of California's Berkeley campus and is managed by the University of California for DOE.

Candidates must possess a distinguished record of scientific accomplishments in a discipline relevant to the research of PBD, and have proven experience with scientific management and development. Experience must include the ability to provide scientific and strategic leadership for a multidisciplinary group of scientists covering a variety of disciplines such as biology, microbiology, bioengineering, biophysics, physics, chemistry or related fields. This leadership position requires the ability to interact effectively with funding agencies, such as DOE, and demonstrated ability to initiate substantial new research efforts. Also required are superior interpersonal and communication skills needed to effectively build and maintain relationships with key internal and external stakeholders, and proven skills in building and leading collaborations among multidisciplinary teams. In addition, the candidate must have prior experience in effective organizational management and administrative oversight, demonstrated creativity in decision making and problem solving, experience in human resource management, and a commitment to mentoring and career development.

Learn more about this opportunity and apply at **website: http://cjo.lbl.gov/LBNLCareers/details.asp?jid=23175&p=1.**

Berkeley Laboratory is an Affirmative Action/Equal Opportunity Employer committed to the development of a diverse work force.

UNIVERSITY OF MARYLAND, BALTIMORE – SCHOOL OF MEDICINE

POSTDOCTORAL POSITIONS in thermoimmunobiology available to study the immunomodulatory effects of fever and its interaction with heat-shock pathways. Ongoing studies focus on transcriptional and posttranscriptional gene regulation that contributes to inflammation and the innate immune response. Candidates with strong background in biochemistry and proven experience in molecular biology including DNAse footprinting, in vitro transcription, RNA polysome analysis, and chromatin immunoprecipitation assays preferred. Please send cover letter, curriculum vitae, and three references to **e-mail: jhasday@umaryland.edu. Jeffrey D. Hasday, M.D., Department of Medicine, University of Maryland School of Medicine, HSF-2, Room S347, 20 Penn Street, Baltimore, MD 21201.**

POSTDOCTORAL RESEARCHER. Seeking a highly motivated individual to conduct NIH-funded research on mechanisms of the Type III secretion system and signal transduction in pathogenic bacteria by means of X-ray crystallography and electron cryomicroscopy in **Dr. Liang Tang's** laboratory at the Department of Molecular Biosciences, University of Kansas. Requires a Ph.D. in biochemistry or a related field, with a strong background in protein crystallography. For more information and to apply go to **website: https://jobs.ku.edu** and search for **job #00004831.** Review of applications begins August 1, 2009, and will continue until the position is filled. *Equal Opportunity/Affirmative Action Employer.*

OAK RIDGE National Laboratory

DIRECTOR
Center for Nanophase Materials Sciences (CNMS)

The Oak Ridge National Laboratory (ORNL), a premier science and energy laboratory, is seeking an outstanding research leader for the position of **Director, Center for Nanophase Materials Sciences (CNMS)**. The CNMS, one of five Department of Energy national nanoscience user facilities, is dedicated to the design, synthesis, characterization, and theory/modeling/simulation of nanoscale materials. The CNMS occupies a new, dedicated building with over 30 laboratories and a 10,000 sq. ft. nanofabrication clean room facility. Therefore, you will be provided with the ideal environment to create rich opportunities for collaborative research in a national laboratory environment.

Major responsibilities will include:

- Defining and leading an innovative research program
- Attracting and retaining outstanding research staff
- Managing a $20M annual operating budget and additional capital equipment budget

Qualifications include:

- Ph.D. in physical sciences, engineering or related field
- Greater than 10 years of professional research experience beyond the doctorate
- Greater than 8 years experience leading multi-disciplinary research groups

For a more detailed job description, and to apply, please visit our company's website at:
http://jobs.ornl.gov/ or **www.ornl.gov**

We are an Equal Opportunity Employer.

UNIVERSITY OF CALGARY — iseee

Canada Excellence Research Chair in Carbon Capture and Storage

With $10 million committed over a 7 year period, the Canada Excellence Research Chair (CERC) in Carbon Capture and Storage offers a world class funding opportunity for an outstanding researcher.

One of the pillars of the *University of Calgary*'s academic mission is innovative leadership in energy and the environment. You will play a significant role in the pursuit of that mission. You are already establishing your place amongst the world's leading researchers and developers of carbon capture and storage (CCS) technologies. Why not accelerate your work in Calgary, one of the world's energy capitals?

To fund the development and implementation of carbon capture and storage projects, the Government of Alberta is investing $2 billion in commercial-scale demonstration of carbon capture and storage over the next 10 years. The Canadian Government will invest an additional $1 billion over the next five years. This commitment creates the largest CCS demonstration and research investment in the world, right in the heart of Western Canada, home to the University of Calgary.

With carbon management in the fossil fuel sector positioned as a top research priority at the University there are already nearly 50 research faculty, along with hundreds of students and post-doctorate researchers doing work in this critical area. The University of Calgary has also recently been short-listed to lead a national research effort on fossil carbon management and the CERC would be expected to take a leadership role in this $50+ million research initiative.

Committed to integrated, multi-disciplinary research, the CERC will be contributing within the Institute for Sustainable Energy, Environment and Economy (ISEEE) at the University of Calgary. ISEEE provides leadership in engaging world-class research and education, for advancing sustainable energy, environment and the economy. The Institute consolidates and builds upon the knowledge and expertise in six faculties at the University of Calgary (the Schulich School of Engineering, Science, Social Sciences, Environmental Design, the Haskayne School of Business, and Law).

There is no more important area of research for Canada's resource rich economy and the global environment. The stakes are high. The time is now. The place is Calgary.

To explore this opportunity further, please forward your résumé to Hamilton Hall Soles/Ray & Berndtson at careers@hhsrb.ca or phone + (1) 403-410-6700 or submit your résumé and related information online at www.rayberndtson.ca/en/careers/8560 For further information on the CERC program visit www.cerc.gc.ca, and for information on ISEEE visit www.iseee.ca

GRANTS

FNP Foundation for Polish Science

WELCOME PROGRAMME
3rd call for proposals

Welcome programme is addressed to foreign scientists or Polish scientists returning to country, who wish to conduct scientific research in Poland with the participation of young researchers (master students, PhD students, and post-doctorate fellows).

The offered funding consists of stipends (tax exempt) for a group leader (up to 80 000* euro/year/), Master level students, PhD students, Postdocs (1100* euro/month) and grants amounting to 230 000* euro/year/group.

*the exact amount depending on the current exchange rate

The closing date for applications is 15 April 2010.
For further information visit: www.fnp.pl

The programme is financed from the Operational Programme Innovative Economy 2007-2013; measure 1.2 – Strengthening the human potential in the science sector

INNOVATIVE ECONOMY
NATIONAL COHESION STRATEGY

The Wellcome Trust–DBT India Alliance

Biomedical Research Careers Programme for India

The Wellcome Trust–DBT India Alliance provides opportunities for scientists at key stages of their research careers and funds science across the full spectrum of biomedical research – from fundamental molecular and cellular studies through to clinical and public health research.

Senior Fellowships

For outstanding scientists who wish to undertake independent, internationally competitive research in India.

The Fellowship provides five years' funding to support the Fellow and research expenses.

Candidates should have between five and ten years' research experience at a postdoctoral level, or clinical/veterinary equivalent, at the full application deadline.

Candidates need not be Indian nationals but must already be pursuing or intend to pursue an academic research career in India. Applications are particularly encouraged from scientists currently working outside India who wish to return there.

Early Career Fellowships

For the most promising newly qualified postdoctoral researchers to make an early start in launching their independent research careers, working in the best laboratories in India.

The Fellowship provides four years' funding to support the Fellow and research expenses. Fellows may normally spend up to 12 months outside their host institution working in other leading-edge laboratories within India or overseas.

Candidates should:

- be Indian nationals, but do not have to be resident in India during the application process
- have no more than 12 months' postdoctoral (or equivalent clinical) experience at the time of submission of a full application.

Applications will also be accepted from candidates in the final year of their PhD.

Deadlines for both schemes

Preliminary applications must be received no later than **14 September 2009**.
Full applications will be invited by 12 October 2009 for submission by 4 December 2009.

Further information and preliminary application forms are available at **www.wellcomedbt.org**

wellcome trust DBT
INDIA ALLIANCE

Careers with Mass Appeal

Alton J. Brann Endowed Professorship

The University of Massachusetts Boston (UMB) is inviting applications from senior scientists to conduct basic and translational research in an area related to the mission of the new joint Center for Personalized Cancer Therapy (CPCT), a partnership with the Dana Farber-Harvard Cancer Center (DF/HCC). The successful applicant will serve as UMB's academic leader for the CPCT. The position will be tenured at UMB with a joint appointment at the Dana-Farber Cancer Institute. The successful candidate will apply their vision to influence the direction and inspire the growth of the new Center, and work with a team of outstanding biomedical researchers.

Center for Personalized Cancer Therapy (CPCT)

The CPCT is a joint program between UMB, a leading urban public research university, and DF/HCC, a world leader in research and converting discoveries into improved cancer prevention, diagnosis, and treatment. The Center will be located on the UMB campus. The purpose of the CPCT is to bring together leading scientists from UMB and DF/HCC to focus on the multidisciplinary problem of diagnosing and treating the myriad of cancers that vary at the molecular level but remain indistinguishable in conventional clinical analyses. The initial mission of the CPCT is to develop reliable, affordable and specific tests using monoclonal antibodies to identify subtypes of common cancers. The CPCT will conduct basic and translational research to develop low-cost diagnostic tests that can be implemented in community hospital settings. Thus, a major goal of the Center is to provide affordable, cutting-edge cancer treatment tools as a means of mitigating racial, ethnic, and socioeconomic disparities in cancer outcomes.

Alton J. Brann Endowed Professorship

The successful candidate will assume the Alton J. Brann Endowed Professorship, an endowed Chair in the College of Science and Mathematics. UMass Boston is currently developing a $150 million Integrated Sciences Complex that will provide significant new campus research facilities including the permanent home for the CPCT and the Brann Chair laboratory. The Brann Professor is expected to have established a distinguished internationally recognized research program with a record of sustained funding. We expect that the successful candidate will work in an area of scientific relevance to the Center. A non-exclusive list of potential research emphases might include development and use of recombinant or synthetic antibody technologies; molecular pathology; or molecular diagnostics. The successful candidate will interact with biomedical faculty, develop training activities that take advantage of CPCT's unique opportunities, and interact with the CPCT Operations Director and the CPCT Scientific Advisory Committee. Leadership qualities, and the ability to translate a scientific vision into the building of a successful cancer research center are particularly sought. Appointment will be at the level of Full Professor with direct support from the Alton Brann Chair endowment. Considering the status of UMass Boston as New England's most diverse university, and the mission of CPCT, we are particularly interested in receiving applications from qualified minority candidates.

Review of applications will begin September 1, 2009, and continue until the position is filled. Please apply online with a cover letter, curriculum vitae, and names, addresses and telephone numbers of at least four references to: Andrew J. Grosovsky, Dean, College of Science and Mathematics: http://umb.interviewexchange.com/candapply.jsp?JOBID=14294

UMass Boston is an Affirmative Action, Equal Opportunity, Title IX employer, and encourages applications from minorities, women, and those with different abilities.

UMASS BOSTON

FACULTY POSITIONS AT YALE UNIVERSITY
Department of Molecular, Cellular and Developmental Biology

The Department of Molecular, Cellular and Developmental Biology at Yale University invites applications for faculty appointments as assistant, associate or full professor from individuals working in any area of molecular, cellular or developmental biology. The Department encourages applications from candidates using any experimental system (animals, microorganisms or plants) and biochemistry, computation, genetics, microscopy or molecular biology to investigate outstanding questions in contemporary biology at the cellular or molecular level. We expect successful candidates to develop active research groups, be interactive members of the faculty and participate in interdisciplinary research and training. Successful candidates should demonstrate communication skills commensurate with excellence in teaching at both the undergraduate and graduate levels.

During October 2009 the search committee will begin to screen applications and start to invite candidates to visit. Applications will close **December 1, 2009**. Submit an application, a *curriculum vitae* and a description of research interests to **mcdb.search@yale.edu**. Request at least three individuals submit letters of recommendation on your behalf to **mcdb.search@yale.edu**. Address correspondence to: **Faculty Search Committee, KBT 1204, Department of Molecular, Cellular and Developmental Biology, Yale University, P.O. Box 208103, New Haven, CT 06520-8103**.

Yale University is an Affirmative Action/Equal Opportunity Employer. Women and members of underrepresented minority groups are especially encouraged to apply.

WASHINGTON STATE UNIVERSITY

ASSISTANT/ASSOCIATE PROFESSOR
Pharmaceutical Sciences/Bioengineering/Nanomedicine

The Department of Pharmaceutical Sciences at Washington State University in Pullman, WA (**www.pharmacy.wsu.edu/PharmSci/**) invites applications for a full-time, 12-month tenure-track position at the rank of Assistant or Associate Professor to begin January 1, 2010. **Qualifications:** Applicants must have an earned doctorate in pharmaceutical sciences, bioengineering, biomolecular engineering or a related discipline; postdoctoral training; and ability/potential to contribute to the teaching and research missions of the department. **Responsibilities:** Candidates will be expected to: (a) teach at both the professional and graduate levels; (b) develop and maintain an extramurally funded research program; and (c) share in service to the Department, College and University. The successful candidate will receive a competitive start-up package and will be expected to establish an outstanding research program that will attract continued extramural funding. Preference will be shown to those whose research aligns with nanomedicine and delivery systems for drugs, genes, peptides, nucleic acids, or viral delivery. The successful candidate should have excellent communication and interpersonal skills, collegiality, and a strong global perspective. He/she should demonstrate the ability to contribute effectively in the department's teaching missions at both professional and graduate levels.

Screening of applicants will begin **September 1, 2009**. The application must include a letter of interest, *curriculum vitae*, statements of research goals and teaching interests, as well as the names, email addresses, and contact information for three references. Send applications to: **Ms. Paula Marley, Principal Assistant, Dept. of Pharmaceutical Sciences, College of Pharmacy, Washington State University, Pullman, WA 99164-6534; Email: bbr@wsu.edu; Phone: (509)335-5545; Fax: (509) 335-5902**. Applications should be mailed or emailed as PDF documents.

EO/AA/ADA

Director, MRC – University of Glasgow Centre for Virus Research

This is an excellent opportunity to lead and shape a new multi-disciplinary initiative in virology research targeting viruses of importance to human and animal health.

The Medical Research Council and University of Glasgow are jointly investing in a new Centre for Virus Research. The Centre will integrate molecular, clinical and veterinary virology, epidemiology and public health, and mathematical modelling to guide new approaches to the management of viral infections.

It is intended that the Centre will be located in a new building on the Garscube site adjacent to the Institute of Comparative Medicine providing excellent facilities and opportunities for cross-disciplinary working. Staff of the Centre will collaborate and network with scientists involved in virology research at other leading Universities nationally and internationally, in order to support cutting edge research programmes and to respond to national priorities regarding existing and newly-emerging viral infections that have a major impact on population health.

We seek a Director to lead this new initiative. The Director will have overall responsibility for the Centre's programme of research, including the MRC Virology Unit, and will participate in the planning of the new facility.

The Centre will combine the strengths of the current MRC Unit and University research programmes in herpes simplex, cytomegalovirus, hepatitis C, retroviruses and papilloma viruses as well as cross cutting themes including host-virus interactions, viral genomics, structural biology, epidemiology and mathematical modelling – with the overall goal of identifying new anti-viral approaches with clinical and veterinary application.

For this key role we seek a Director who:

- Is an internationally recognised virologist (PhD, MD or equivalent) with an excellent publication record and success in winning grants from major funders
- Has demonstrable breadth, leadership experience (or potential) and ability to work across disciplines
- Preferably has been involved in advising governments or other agencies in setting policies and priorities for virus research and/or control

Contractually, the Director will be an employee of the University of Glasgow, appointed at professorial level, with commensurate, excellent terms and conditions.

The MRC and University of Glasgow are both Equal Opportunity employers.

Further information please visit www.gla.ac.uk/jobs

To discuss your interest in strict confidence, please contact either Dr Marc Lambert or Dr Kevin Young at the RSA Group: 09421@theRSAgroup.com; +44 (0)1707 259333 closing date: Friday 28 August.

RSA, The Melon Ground, Hatfield Park, Hatfield, Herts AL9 5NB Tel +44 (0)1707 259333

RSA Executive Search

Nontraditional Careers:
Opportunities Away From the Bench

Webinar

Want to learn more about exciting and rewarding careers outside of academic/industrial research? View a roundtable discussion that looks at the various career options open to scientists across different sectors and strategies you can use to pursue a nonresearch career.

Now Available
On Demand
www.sciencecareers.org/webinar

Participating Experts:

Dr. Lori Conlan
Director of Postdoc Services,
Office of Intramural Training and Education
National Institutes of Health

Pearl Freier
President
Cambridge BioPartners

Dr. Marion Müller
Director, DFG Office North America
Deutsche Forschungsgemeinschaft
(German Research Foundation)

Richard Weibl
Director, Center for Careers in Science and Technology
American Association for the Advancement of Science

Produced by the
Science/AAAS Business Office.

Science Careers
From the journal *Science* AAAS

CGIAR Challenge Program "Climate Change, Agriculture and Food Security" (CCAFS) Six Theme Leaders

CCAFS is a major collaborative endeavour between the international agricultural (CGIAR) and global environmental change (Earth System Science Partnership, ESSP) research communities. The Program is launched in 2009 for a period of 10 years. For further details of the Program please consult:

www.cgiar.org/impact/challenge/index.html or www.essp.org/index.php?id=76

This new Program is now seeking candidates for the six positions of Theme Leader, which will provide continuity of vision and intellectual leadership for their given Research Theme, and share responsibility for integrating Theme research into the overall CCAFS.

The six Themes are:
1: Diagnosing vulnerability and analysing opportunities
2: Unlocking the potential of macro-level policies
3: Enhancing engagement and communication for decision-making
4: Adaptation pathways based on managing current climate risk
5: Adaptation pathways under progressive climate change
6: Poverty alleviation through climate change mitigation

The Theme Leaders will be appointed by the CCAFS Steering Committee and will report to the CCAFS Director.

Theme Leaders will be appointed on a part-time (≥50% of time) or full-time basis. For part-time appointees the remaining time would be funded by their home institution to enable them to continue their respective institution's activities.

The appointee will have the following key responsibilities:
- Demonstrate scientific leadership through producing high quality scientific papers, with colleagues and partners.
- Provide scientific leadership for planning, implementing and monitoring the Theme research agenda.
- Assist the Director in fund-raising, synthesis work, integration amongst Themes and ensuring an impact orientation.
- Keep in close contact with the Regional Facilitators to ensure that the Theme research activities in each region contribute to the overall achievements of the Program.

Essential qualifications and competencies:
- PhD or equivalent academic qualifications in agricultural and / or environmental sciences and demonstrated international standing in issues related to climate change, agriculture and food security.
- Demonstrated competency in communication and interpersonal skills, including extensive ability to motivate, inspire and promote team-work through negotiation and consensus-building.
- Interest and experience in ensuring that science outputs lead to outcomes and impact.
- Familiarity with the respective research agendas of the CGIAR and ESSP communities.
- Fluency in English, both written and spoken; and good working knowledge of other major international languages would be a considerable advantage.

For terms and conditions, please consult the full text of the vacancy announcement at the above websites.

A letter of application and CV in English with names and full contact details of three referees should be sent to:
The Challenge Program Chair,
Professor Thomas Rosswall,
thomas.rosswall@gmail.com by 10 September 2009.

The letter of application should clearly specify which of the six themes the candidate is applying for, and whether a candidate is seeking a full-time or part-time position. Where the applicant is part of a home institution that is offering support to CCAFS, the nature of such support should be outlined. For additional information about the position, please contact Thomas Rosswall.

Founded in 1911, The University of Hong Kong is committed to the highest international standards of excellence in teaching and research and has been at the international forefront of academic scholarship for many years. Of a number of recent indicators of the University's performance, one is its ranking at 26 among the top 200 universities in the world by the UK's *Times Higher Education Supplement*. The University has a comprehensive range of study programmes and research disciplines, with 20,000 undergraduate and postgraduate students from 50 countries, and a complement of 1,200 academic members of staff, many of whom are internationally renowned.

Tenure-Track Associate Professor/Assistant Professor in Environmental Science (Ref.: RF-2009/2010-9)

Applications are invited for appointment as Associate Professor/ Assistant Professor in Environmental Science in the Faculty of Science, from as soon as possible. The post will initially be made on a three-year term. Appointees who have demonstrated performance will be considered for tenure after satisfactory completion of a second three-year term.

The Faculty of Science is expanding on its research and teaching program in environmental science. We therefore encourage applications from well-qualified candidates with research expertise in the following areas: climate change, marine and oceanic sciences, atmospheric science, planetary science, geobiology, and natural hazards. Applicants with expertise in other areas under the general theme of environmental science will also be considered. Information about the Faculty can be obtained at http://www.hku.hk/science.

For Associate Professor level: applicants should be able to demonstrate excellence in teaching and research, and possess a proven record of high-quality scholarship and services. The appointee should be able to provide academic leadership in both research and teaching, and is also expected to supervise postgraduate students, conduct an ongoing active research agenda, obtain research grants, serve on committees within the University and external professional organizations.

For Assistant Professor level: applicants should possess good teaching and research skills and be able to demonstrate strong potential for research excellence. The appointee is expected to commit to high-quality scholarly research, submit grant proposals, publish in top-tier academic journals and supervise postgraduate students.

Annual salaries will be in the following ranges (subject to review from time to time at the entire discretion of the University):

Associate Professor : HK$661,980 – 1,023,720
Assistant Professor : HK$504,480 – 779,640
(approximately US$1 = HK$7.8)

The level of appointment and salary will be commensurate with qualifications and experience. The appointment will attract a contract-end gratuity and University contribution to a retirement benefits scheme, totalling up to 15% of basic salary, as well as leave, and medical/dental benefits. Housing benefits will be provided as applicable. At current rates, salaries tax does not exceed 15% of gross income.

For enquiries of the existing research activities and the specific job requirements, please write to Professor Sun Kwok, Dean of Science (e-mail: deansci@hku.hk). The application should include a curriculum vitae with a detailed publication list, a research plan, and a statement on teaching philosophy. **Further particulars and application forms** (152/708) can be obtained at http://www.hku.hk/apptunit/; or from the Appointments Unit (Senior), Human Resource Section, Registry, The University of Hong Kong, Hong Kong (**fax**: (852) 2540 6735 or 2559 2058; **e-mail**: senrappt@hku.hk). **Closes September 30, 2009**. Candidates who are not contacted within 3 months of the closing date may consider their applications unsuccessful.

The University is an equal opportunity employer and is committed to a No-Smoking Policy

POSITIONS OPEN

Two NIH-funded **POSTDOCTORAL POSITIONS** are available immediately to study signaling pathways that regulate the translational machinery. Current laboratory focus is on the abnormal regulation of protein synthesis in lymphoma cells and how this can be exploited for cancer therapy. Interested candidates must possess a recent Ph.D. with relevant experience in molecular biology. Priority will be given to U.S. citizens/permanent residents and candidates with experience in RNA technology. The laboratory is located in the Bressler Research Building with state-of-the-art facilities including core facilities for confocal microscopy, mass spectrometry, flow cytometry, bioinformatics, animal husbandry, and other techniques. The University of Maryland Marlene and Stewart Greenebaum Cancer Center is an NCI-designated cancer center and is located next to the Inner Harbor in downtown Baltimore. Interested candidates should e-mail curriculum vitae, statement of research interests, and contact information for three references to: **Ronald B. Gartenhaus, M.D., Associate Professor of Medicine, The University of Maryland School of Medicine, e-mail: rgartenhaus@som.umaryland.edu.**

POSTDOCTORAL POSITIONS
in Molecular Biology/Microscopy
University of Georgia
Complex Carbohydrate Research Center

Two positions are open at the postdoctoral level to work on a project to determine the functional significance of carbohydrate binding modules in the deconstruction of plant cell walls. (1) Molecular biology/protein biochemistry/enzymologist with experience. Applicants should have experience in green construction, protein expression and purification, and the enzymology of carbohydrate modifying enzymes. (2) Immunolocalization (fluorescence and immunogold) of proteins and polysaccharides. Demonstrated experience with light (visible and fluorescent) and electron microscopy (both transmission EM and scanning EM) is required. Experience with laser confocal microscopy is desirable. Preference will be given to candidates having prior experience with these techniques. All interested applicants should forward curriculum vitae and list of three references to: **Harry Gilbert, UGA/CCRC, 315 Riverbend Road, Athens, GA 30602-4712. E-mail: hgilbert@ccrc.uga.edu; fax: 706-542-4412**. Review of applications is ongoing and will continue until positions are filled. *Equal Employment Opportunity/Affirmative Action Employer.*

POSTDOCTORAL POSITIONS
in Cardiovascular Research

Positions are available in the Department of Molecular Cardiology at the Lerner Research Institute, Cleveland Clinic to study a newly discovered heart enzyme, corin, that processes cardiac hormones and regulates blood pressure (**website: http://www.lerner.ccf.org/moleccard/wu/**). We take molecular biology, cell biology, biochemical, and genetic approaches to define the biological function of corin and its role in cardiovascular disease such as hypertension and heart failure. Highly motivated recent graduates with an M.D. or Ph.D. with strong background of cardiovascular biology, proteases, and mouse models are encouraged to apply. Send your curriculum vitae and names of references to: **Qingyu Wu, M.D., Ph.D., Cleveland Clinic/ND50, 9500 Euclid Avenue, Cleveland, OH 44195. E-mail: wuq@ccf.org.**

POSTDOCTORAL POSITION available in the New York University Lung Cancer Biomarker Center to identify and characterize novel biomarkers in high-risk smokers for the early detection of lung cancer. Gene-environment interactions pursued. Experience with molecular biology techniques desirable. Ph.D. and/or M.D. degree and *green card or U.S. citizenship only.* **E-mail: william.rom@nyumc.org.**

POSITIONS OPEN

NEUROSCIENCE POSTDOCTORAL FELLOWS

NIH-funded Postdoctoral Fellow positions available to study nicotinic receptor functions in the etiology of autism, schizophrenia, and addiction. Significant experience in one or more techniques using molecular, cellular, transgenic, electrophysiology, and confocal imaging techniques and knowledge of neuroscience are desirable. The laboratory is part of the Interdisciplinary Neuroscience Signature Program and is located in the newly constructed Biomedical Research Tower with state-of-the-art facilities for proteomics, genomics, and imaging. Please send curriculum vitae and names of references to: **Rene Anand, Department of Pharmacology, 796 Biomedical Research Tower, 460 W. 12th Avenue, The Ohio State University College of Medicine, Columbus, OH 43210. E-mail: anand.20@osu.edu.** *OSUMC is an Equal Opportunity Employer.*

NIH-funded **POSTDOCTORAL** research position is available in the Department of Pediatrics at the Baylor College of Medicine in Houston, Texas, to study molecular regulation of cytochrome P4501A genes, in relation to oxygen-mediated lung injury in animal models and cell culture. We will use transgenic and knockout mouse models and utilize state-of-the-art techniques (chromatin immunoprecipitation, site-directed mutagenesis, in vivo bioluminescent imaging, liquid chromatography–mass spectrometry/mass spectrometry, microarray technology, confocal microscopy). The applicants are required to have a Ph.D. in a related field. Experience in molecular and cell biology is highly desirable. Please send your curriculum vitae to: **Dr. Bhagavatula Moorthy, e-mail: bmoorthy@bcm.edu.**

MARKETPLACE

Submission deadline August 1

"It's truly exhilarating to be recognized for your hard work. This prize will motivate young generations of scientists and encourage new discoveries."

Dr. Christine Jacobs-Wagner
Grand Prize winner 1997

The GE & Science Prize for Young Life Scientists. Rewarding brilliance since 1995.

Imagine standing on the podium at the Grand Hotel in Stockholm, making your acceptance speech. Imagine joining the ranks of those published in Science magazine and having your essay on your work in molecular biology read by your peers around the world. Imagine taking part in a seminar with the other Prize winners and Nobel Prize laureates and discussing your work with leaders in the field. Imagine what you could do with the US$25,000 prize money. Imagine this brilliant start to your career and where it could lead you. Now stop imagining, and make it a reality.

Dr. Christine Jacobs-Wagner did just that. In 1997, she entered in the GE & Science Prize for Young Life Scientists and won the grand prize. So why not you? If you are one of those who were awarded a Ph.D in 2008, then submit your 1000-word essay by August 1, 2009. Your brilliant idea could well be on its way to building a better reality, for you and for those around you.

All the information you need awaits you at: www.gelifesciences.com/science

GE & Science Prize for Young Life Scientists

imagination at work

Science AAAS

For the purpose of this prize, molecular biology is defined as "that part of biology which attempts to interpret biological events in terms of the physico-chemical properties of molecules in a cell".

(McGraw-Hill Dictionary of Scientific and Technical Terms, 4th Edition).